M1-9903-00-0005

초강력 펨토초 레이저마당 내의 원자조작을 통한 결맞는 X-선 광원 개발

Coherent X-Ray Source Development by Manipulating Atoms in a Super-Intense Femtosecond Laser Field

한국과학기술원

과 학 기 술 부

제 출 문

과학기술부 장관 귀하

본 보고서를 "초강력 펨토초레이저 마당내의 원자조작을 통한 결맞는 X-선 광원개발"과제의 보고서로 제출합니다.

2002 . 11. 30.

주관연구기관명 : 한국과학기술원

주관연구책임자 : 남 창 희

연 구 원 : 김 정 훈

〃 : 이 동 근

〃 : 유 태 준

〃 : CHEN Jing

편집순서 3

보고서 초록

과제관리번호		해당단계 연구기간	1999.10.16~2002.9.30	단계 구분	(1단계) / (3단계)
연구사업명	중 사 업 명	창의적 연구과제			
		-			
연구과제명		-			
	세부(단위)과제명	초강력 펨토초 레이저 마당내의 원자조작을 통한 결맞는 X-선 광원개발			
연구책임자	남 창 희	해당단계 참여연구원수	총 : 34.6 명 내부 : 34.6 명 외부 : - 명	해당단계 연구비	정부: 1,530,000,000 천원 기업: - 천원 계: 1,530,000,000 천원
연구기관명 및 소속부서명	한국과학기술원/ 물리학과		참여기업명	-	
국제공동연구	해당 없음				
위 탁 연 구	〃				

요약(연구결과를 중심으로 개조식 500자이내)	보고서 면수	415

1. 고출력 펨토초 레이저를 이용하여 결맞는 X-선 광원을 개발함. 펄스폭 20-30 fs, 출력 1-3 TW의 레이저 펄스를 Ar, Ne, He등의 기체 원자에 집속하여 극자외선/연 X-선 영역의 고차조화파를 발생하고 이의 분광구조를 연구함. 이를 통해 고차조화파의 비점진적 청색변이 특성을 규명하고 고차조화파 발생과정의 결맞는 조정(coherent control)을 성취함. 연속적으로 파장 가변할 수 있는 고차조화파 X-선 발생을 입증함.

2. 고차조화파 발생과정을 이론적으로 연구함. 강한 레이저장내의 원자상태를 양자역학적으로 계산하여 고차조화파의 분광구조를 설명할 수 있는 이론적 방법을 개발함. 단일원자 계산결과를 토대로 결맞는 합과 Wigner 분포 함수 방법을 도입하여 고차조화파 실험결과를 설명함.

3. 강력한 레이저와 원자와의 상호작용을 연구하기 위해 1kHz의 반복율을 갖는 10펨토초 0.1테라와트의 고출력 고반복 펨토초 티타늄 사파이어 레이저를 개발과 개발된 고출력 펨토초 레이저의 시공간적 특성을 조사함. 10펨토초 이하의 극초단 펄스(8,3 펨토초)를 갖는 기술을 확보함. 기사용중인 10 Hz, 20 펨토초 3 테라와트 티타늄 사파이어 레이저의 최적상태 운전과 개발된 고출력 펨토초 레이저의 시공간적인 특성을 SPIDER 장치와 CCD를 이용하여 조사하고 이를 바탕으로 레이저 성능의 최적화를 수행함.

색 인 어 (각 5개 이상)		
	한 글	고출력 펨토초 레이저, 고차조화파, 결맞는 엑스선, 파장가변 엑스선, 아토초 펄스
	영 어	Femtosecond high-power laser, High-order harmonics, Coherent x-rays, Wavelength tunable x-rays, attosecond pulse

편집순서 4

요 약 문

Ⅰ. 제 목

초강력 펨토초 레이저마당 내의 원자조작을 통한 결맞는 X-선 광원 개발

Ⅱ. 연구개발의 목적 및 필요성

본연구는 고출력 펨토초 레이저 기술 개발과 원자와 초강력 레이저장과의 상호작용 규명을 토대로 연속적으로 파장가변이 가능한 펨토초 고차조화파 엑스선 광원 (소형화된 싱크로트론)을 개발하고자 함. 강력한 펨토초 레이저마당 내의 원자조작을 통해 발생된 펨토초 결맞는 X-선 광원은 기존의 방사광가속기에서 방출하는 X-선이 갖지 못하는 펨토초의 짧은 펄스폭과 우수한 결맞음성을 가지고 있기 때문에 초고속 X-선 분광학, 비선형 X-선 광학 등에 활용되어 생물·화학 소재의 초고속 특성과 원자의 내부층 천이에 대한 초고속 특성을 규명하는데 활용할 수 있다. 뿐만 아니라 펨토초 레이저 펄스를 이용한 고차조화파 엑스선 광원개발은 크기의 소규모와 적은 유지보수비 등의 많은 장점으로 인하여 방사광 가속기를 사용하는 여러 분야에서도 그 필요성이 점차 증대되어 지고 있다.

Ⅲ. 연구개발의 내용 및 범위

1. 고출력 펨토초 레이저 기술 개발
- 강력한 레이저와 원자와의 상호작용을 연구하기 위해 1kHz의 반복율

을 갖는 10펨토초 0.1테라와트의 고출력 고반복 펨토초 티타늄 사파이어 레이저를 개발. 그리고 개발된 고출력 펨토초 레이저의 시공간적 특성을 조사.

2. 원자와 초강력 레이저장과의 상호작용을 규명

- 강력한 레이저장과 원자와의 상호작용에 의한 고차조화파 발생의 실험적 측정 및 분석과 전산시늉을 포함한 이론적 분석을 통하여 그 발생 메카니즘을 구체적으로 규명.

3. 파장가변 결맞는 엑스선 광원 개발

- 고차조화파의 결맞는 조절을 통하여 조화파의 선폭과 세기에 대한 최적화를 수행하고, 조화파의 청색변이를 이용하여 연속적으로 파장가변이 가능한 펨토초 고차조화파 엑스선 광원 (소형화된 싱크로트론)을 연구.

Ⅳ. 연구개발결과

1. 강력한 레이저와 원자와의 상호작용을 연구하기 위해 kHz의 반복률을 가지고 0.1 TW의 출력과 10 펨토초의 펄스폭을 갖는 티타늄 사파이어 레이저를 자체기술로 제작하였으며 이의 특성을 측정하였다. 기사용중인 10 Hz, 20 펨토초 3 테라와트 티타늄 사파이어 레이저의 최적상태 운전과 개발된 고출력 펨토초 레이저의 시공간적인 특성을 SPIDER 장치와 CCD를 이용하여 조사하였고 이를 바탕으로 레이저 성능의 최적화를 수행.

2. 이론적으로는 고차조화파의 시공간적인 위상정합 이론을 개발하고 이의 분석을 통해서 최적화된 고차조화파 발생조건을 규명. 아토초 펄스발생을 위한 고차조화파 이론을 연구.

3. 레이저 펄스의 처프를 이용한 고차조화파의 결맞는 조절로 조화파의 선폭과 세기를 최적화 시켰고, 펨토초 레이저 펄스에 의한 고차조화파의 강한 청색변이를 이용하여 연속적으로 파장가변이 가능한 고차조화파를 발생. 뿐만 아니라, 실험적으로 발생효율이 최적화된 고차조화파의 특성(발산각, 발생 에너지, 결맞음성) 등을 측정 분석하여 파장가변 펨토초 결맞는 엑스선 광원을 개발.

Ⅴ. 연구개발결과의 활용계획

1. 현재까지 초강력 레이저장에 의해 생성된 고차조화파의 특성조사를 성공적으로 수행하였으며, 파장가변 결맞는 엑스선을 발생시킬 수 있는 고차조화파의 청색변이에 대한 물리적 메카니즘을 이해할 수 있었고 펨토초 이하의 물리적인 특성 탐사를 가능케 하는 아토초 펄스를 발생을 구현할 수 있는 기본적인 실험결과를 얻었다. 이러한 파장가변 펨토초 결맞는 X-선 광원은 기존의 X- 선 광원으로 많이 활용되는 방사광 가속기를 보완할 수 있을 것으로 기대된다. 즉, 방사광가속기에서 방출하는 X-선이 갖지 못하는 펨토초의 짧은 펄스폭과 우수한 결맞음성은 X-선 간섭계, 초고속 X-선 분광학, 비선형 X-선 광학 등에 활용되어 생물·화학 소재의 초고속 특성과 원자의 내부층 천이에 대한 초고속 특성을 규명해 줄 것이다.

2. 펨토초 테라와트 레이저 개발과 극자외선 분광기술개발은 펨토초 레이저와 고출력 펨토초 레이저 기술의 국내 보급과 극자외선 분광기 기술의 국내 정착을 가져온다. 펨토초 레이저는 화학·물리 등의 기초과학 연구에서 그 활용도가 급격히 늘고 있으며, 초미세 가공이나 새로운 LASIK용 레이저로서 펨토초 레이저가 이용되기 시작하여 산업적·의료적 응용이 증대되고 있다. 이와 같은 고가의 고급레이저 기술인 펨토초 레이저 기술의 국산화는 국내 레이저 산업의 경쟁력 확보측면에서도 크게 이바지할 것으로 기대된다. 따라서, 이러한 고출력 펨토초 레이저기술은 물리·화학·생물분야등 기초과학분야 뿐만 아니라 공학·의료·군사 분야에서도 매우 필요한 기술로서 앞으로 활용도가 크게 증가될 것이다.

S U M M A R Y

I. Title

Coherent X-ray source development by manipulating atoms in a super-intense femtosecond laser field

II. Purpose and Signigicance of the Research

The current research aims to develop the high power femtosecond laser technology and to realize a tunable coherent femtosecond X-ray source through the understanding of the fundamental physical process in laser-atom interactions.

III. Contents and scope of the research

(1) Realization of a tunable coherent femtosecond X-ray source.

- Coherent control of high harmonics to realize a continuously tunable, coherent, femtosecond x-ray source, i.e. a tabletop synchrotron.

(2) Understanding the fundamental physical process in laser-atom interaction.

- The numberical simulation and the theoretical investigation of high-order harmonic generation for the deeper understanding of its generation mechanism and to explain some experimental results.

(3) Development of high power femtosecond laser technology.

- Generation of 10-fs, 0.1-TW pulses at 1 kHz repetition rate and characterization of the femtosecond pulse.

IV. Research Results

(1) We demonstrated the generation of tunable, coherent, ultrashort x-rays with low beam divergence and good coherence using high harmonics emitted from atoms driven by intense femtosecond laser pulses.

(2) We developed several simulation codes to investigate the high-order harmonic generation processes and the attosecond pulse formation. The development of a simulation code for the propagation calculation of high

harmonic generation has provided a deeper understanding of the propagation effects and enabled us to explain experimental results.

(3) We generated sub-10-fs high-power pulses with 1 kHz repetition rate and developed pulse characterization techniques. Tools to characterize femtosecond laser pulses, such as FROG and SPIDER together with an operating algorithm, were constructed. It successfully characterized the femtoseond pulses from Ti:sapphire laser oscillator and the 10-Hz CPA system.

V. Suggestions about applications of the research results

We have demonstrated the continuous wavelength tuning of high-order harmonics using the phenomenon of harmonic blueshift and the chirp control of harmonics using chirped femtosecond laser pulses, achieving spectral sharpness and brightness of the harmonics. The method developed can be easily implemented to most high-power femtosecond lasers; hence, the coherent control technique with chirped laser pulses can become a powerful tool in practical applications requiring sharp and strong XUV/soft x-ray radiation.

The coherent x-ray source, once developed, will open new application areas, just like lasers that have successfully found diverse applications. Lasers are nowadays need not only in basic science, engineering, medical science and military defense, but also in our daily life utilities such as audios, compact disc players, and bar code scanners. The development of a practical coherent x-ray source is believed to contribute to solving energy problem and human welfare, with possible applications including x-ray interferometry for diagnosing dense plasmas produced in laser fusion and x-ray hologram for a three-dimensional visualization of RNA, DNA, or living cells. Especially, coherent x-rays at 13 nm could be used as a metrological tool for EUV lithography optics.

Contents

1. Research Objectives and Evaluation Criteria

A. Proposed objectives

Final goal:

(1) Realization of a tunable coherent femtosecond X-ray source.

(2) Understanding the fundamental physical process in laser-atom interaction.

(3) Development of high power femtosecond laser technology.

First year goal:

(1) Construction of spectroscopic database needed for wavelength-tunable high harmonic X-rays in the wavelength range of 3 – 40 nm.

(2) Theory development of high harmonic generation, especially a calculation tool based on the time-dependent Schrodinger equation.

(3) Development of a femtosecond terawatt laser operating at 1 kHz - its design and initial setup.

Second year goal:

(1) Optimization of the conversion efficiency of high harmonic generation.

(2) Numerical simulation of propagation of the laser and high harmonic fields.

(3) Development of 10-fs, 0.1-TW laser operating at 1 kHz and new temporal characterization technique (spectral phase interferometry for direct electric-field reconstruction: SPIDER)

Third year goal:

(1) Harmonic generation with bright, low divergence, and coherent control of high harmonics to realize a continuously tunable, coherent, femtosecond x-ray source, i.e. a tabletop synchrotron.

(2) Theory development of spatio-temporal phase matching of high harmonics in the saturation intensity regime.

(3) Adaptive pulse shaping of amplified pulses and measurement and control of carrier-envelop phase of a femtosecond laser pulse.

B. Evaluation criteria

(1) High harmonic X-ray generation

- Whether there are any new findings in the HHG physics from the spectral structure analysis
- Whether the phase matching condition for efficient harmonic generation is obtained from the spectral structure analysis of high harmonic generation X-rays.
- Whether a tunable coherent femtosecond X-ray source is developed.
- Whether the coherent control of high-order harmonics is accomplished.
- Whether the characterization (energy yield, divergence, and coherence) of the high-order harmonic x-ray is accomplished.

(2) High harmonic theory development

- Whether there are new theoretical approaches achieved in the high harmonic generation, especially in the calculation of the time-dependent Schrodinger equation.
- Whether there are new theoretical analyses of experimental results.
- Whether the propagation code is developed and applied to the analysis of experimental results.
- Whether the harmonic spectral structure is analyzed to bring out the condition for an attosecond pulse formation.

(3) Up-to-date femtosecond laser technologies

- Whether operation of the existing laser system has been successful in supporting the high harmonic X-ray generation.
- Whether there are any novelties in the design of a new laser system, instead of copying other design.
- Whether the progress of the laser construction is properly done, along with cost reduction effort.
- Whether a Ti:sapphire laser with 10 fs and 0.1 TW at 1 kHz repetition rate is developed.
- Whether SPIDER technique is accomplished
- Whether the adaptive pulse shaping of amplified pulses using a micro-machined deformable mirror and genetic algorithm is successfully accomplished.

2. Current Trend and Future Directions

(1) High harmonic X-ray generation

Coherent control of high harmonic generation has become an important issue for the optimization of high-order harmonic generation processes. Access to deeper understanding of high harmonic generation physics, along with advancement of the characterization and control of femtosecond laser pulses, has opened the passage to a precise control of high harmonic processes. Absolute phase measurement and control techniques of femtosecond laser pulses have been intensively investigated in recent years, in part for the development of a new frequency standard using femtosecond lasers. This technological progress can help also the absolute phase control of pumping laser pulses used for high harmonic generation and enable the optimization of harmonic processes, such as spectral brightness and sharpness.

We have recently performed a systematic chirp analysis of high harmonics and shown that high harmonics could be positively chirped as well as negatively chirped. It has been known for some times that harmonics are negatively chirped due to dynamically induced chirp in a rapidly varying laser field. As applied laser intensity grew higher, it was found that a positive chirp was induced on the generated harmonics. We explained from a 1D simulation that a laser pulse, propagating through an ionizing medium, experiences a positive chirp in the leading edge due to the positive slope of refractive index change in time. When laser intensity exceeds the saturation intensity, harmonics are generated while the laser pulse is positively chirped, resulting in the generation of positively chirped harmonics. This positively chirped harmonics were compensated for using negatively chirped laser pulse and sharp and bright harmonics were generated. It shows that the application of appropriately chirped laser pulse is crucial in the optimization of harmonic processes, and demonstrated that the macroscopic response (the induced laser chirp due to the change of refractive index of the harmonic generation medium) should be taken into account as well as the microscopic response (the dynamically induced harmonic chirp due to the atomic response to the rapidly increasing laser field); the coherent control of harmonic generation should be based on the integral treatment of the interaction between a laser pulse and atoms, instead of an optical manipulation of atoms. Therefore, we are planning to continue the coherent control of harmonic generation processes with well-characterized femtosecond laser pulses in their chirp and phase parameters.

The realization of a continuously tunable x-ray source is one of the key issues in HHG

research. High-order harmonic produces only odd harmonics of the fundamental, so there is an inherent limitation on available wavelengths. This can limit applications of a high-order harmonic x-ray source. Several experimental methods have been recently proposed to realize the wavelength tuning of high harmonics. For example, it has been shown that driving atoms with laser pulses mixed from two different wavelengths can generate tunable harmonics [1]. In this method a laser pulse at the fundamental wavelength is mixed with a second pulse at a different wavelength, obtained by optical parametric generation. This mixing breaks the temporal symmetry of the laser pulse and produces harmonic spectra at sum and difference frequencies of the second laser pulse. In this case, however, the new harmonics added through mixing the two pulses are generally much weaker than those produced by the first laser pulse alone.

Another method that results in a shift of the harmonic wavelengths is the adjustment of the target position [2]. Because the applied laser intensity varies with target positions, the harmonics emitted at different target position exhibit different amounts of wavelength shift. The harmonic wavelength can be scanned, but the spectra widths of the harmonics at different target positions become quite broad as the target position is moved away from the laser beam focus. In addition, the spectral structure of the emitted harmonics becomes distorted because the phase matching conditions are sensitive to target position. Another method is the case of an optical parametric amplifier (OPA) [3]. The output harmonic spectrum can be made tunable by using OPA output. This technique also allowed to study HHG with pump wavelengths much longer than 0.8 μm (Ti:sapphire). Therefore, it could extend the cutoff wavelength using a longer wavelength pump, since the pondermotive energy is proportional to the square of a pumping laser wavelength. Recently, a high intensity optical parametric amplification was achieved [4]. The output signal of the OPA was tunable from 1.1 to 1.6 μm. The pulse energy at the output of the OPA was 400 μJ at a signal wavelength of 1.51 um. Using these pulses HHG experiments were performed by focusing the OPA output into a gas jet. The cut-off dependence on the wavelength of the driving field was demonstrated and the tunability of the HHG signal was also claimed, being the frequency of the 27^{th} harmonic of the 1.51 μm fundamental less than the frequency of the 35^{th} harmonic of the 1.22 μm fundamental. But the tuning of the harmonic wavelength through the OPA is not practical because the harmonic signal was weak due to the low pump energy until now, and, furthermore, harmonic spectra obtained using the OPA showed rather broad spectral widths and uneven intensity. Thus it would be desirable to tune harmonic wavelengths

without changing the laser spectrum.

We have proposed a method to continuously tune the harmonic wavelengths without modifying the laser spectrum. Our previous experimental results [5] on the harmonics from argon driven by 30-fs laser pulses showed a harmonic blueshift corresponding to twice the laser frequency, the interval between odd harmonics. When a laser intensity above the saturation intensity for optical-field ionization is applied to atoms, harmonic emission occurs in the leading edge of the laser pulse before all neutral atoms are ionized, and the nonadiabatic response of the atoms to a rapidly rising laser field results in a wavelength blueshift of the high harmonics. This nonadiabatic effect can induce a large blueshift of harmonic wavelengths [5, 6]. As shown in the results of the second year, we have demonstrated continuous tuning of high harmonics without sacrificing spectral sharpness, achieved through control of the laser intensity and chirp. However, the wavelength tuning range in harmonics from helium was from 73^{rd} to 101^{st} order, but to cover as wide wavelength region as possible, it is better to change the species of atom for the efficient harmonic generation and sufficient wavelength tuning in the required spectral range. For example, argon atom is proper for the wavelength tuning up to 41^{st} harmonic order, neon is for the harmonic order between 41^{st} and 71^{st}, and low-density helium is good for orders higher than 101. Consequently, by choosing proper species of atoms, we can extend the tunable wavelength range of high harmonic x-rays. The objective of forthcoming experiments is to demonstrate the continuous frequency tunablitiy of high harmonics in the whole spectral range between 23^{rd} to 121^{st} harmonics.

Another critical issue on HHG is the characterization of divergence and coherence properties of high harmonics for actual applications in many areas. Measurement of the spatial distribution can provide an insight into the processes governing high-order harmonic generation. From an application point of view, such studies bring some information on the degree of spatial coherence of the source, which ultimately determine our ability to refocus this radiation for use in applications. P. Salieres et al., [7] reported measurements of the spatial distribution of high-order harmonics generated in neon and argon with a 140 fs 825 nm laser. They showed that, using a short pulse laser, the harmonic fields are emitted in a narrow cone on the propagation axis. The profiles in the far field are structureless, unless the intensity is far above the saturation intensity. The distributions vary from almost Gaussian in the cutoff region to triangular or flat-top profiles for the harmonics in the plateau. The divergence seems to be essentially governed by whether the harmonics belong to the cutoff or

to the plateau, not much by the process order or the nature of the gas. In our work, we presented the measurement of the divergence of harmonics in a long gas jet pumped by intense 28-fs laser pulses. The measured divergence, 0.5 mrad for the 27^{th} harmonic from argon [8], is much smaller than those generated by other groups [9, 10]. This low beam divergence resulted from the large harmonic generation cross-section achieved by applying high intensity laser pulses over the saturation intensity to the long gas jet. In the coming year, we will measure the spatial and temporal coherence of bright, low divergence high-order harmonics from the long gas jet. This will verify the applicability of high harmonics as a coherent femtosecond x-ray source in many applications.

(2) Theory development of high harmonic generation

The introduction of the semiclassical two-step model [11,12] and the Lewenstein model [13] has contributed a lot to the understanding of the underlying mechanisms of high harmonic generation. Theses models have not only provided a simple picture that describes well the roles of the electron trajectories in forming rich structure in high harmonic spectra, but also produced theoretical results that allowed a direct comparison with some experimental results. The Lewenstein model has been successful in describing a single atom's response to laser fields, for most of its predictions have been in good agreement with exact numerical calculations of the time-dependent Schrödinger equation in a broad parameter region [13,14].

For a complete theoretical description of high harmonic generation, one needs to consider the propagation of high harmonics [15-17], as well as the single atom response. While many studies have been made on this problem in cases where the laser intensity is far below the ionization saturation intensity, less attention has been paid to the cases in which the laser intensity is too strong that plasmas produced during ionization processes induce changes in the phases and amplitudes of propagating waves. As the laser intensity available to experimental laboratories working in the area of high harmonic generation increases with the rapid development of laser technology, it is believed that future studies will be directed toward the high intensity regime, and the need for theoretical investigations of the effects of laser-produced plasmas on high harmonic generation will grow.

On ways to enhance the high harmonic conversion efficiency up to a level sufficient for applications, much effect has been devoted to the phase-matching problem of high harmonic generation [18,19]. Until now, most works addressing the phase-matching issue have been carried out in the low intensity regime where ionization is negligible. In these works, phase

matching of high harmonics are considered over the spatial volume in which the atomic gas is contained. However, when the laser intensity exceeds the saturation intensity, phase matching or mismatching among the high harmonics generated at different instants of the laser pulse duration becomes important, which naturally leads to temporal phase matching conditions. Thus, a complete description of phase matching should take into account both the spatial and temporal distributions of high harmonic phases (spatio-temporal phase matching). Recently, Christov et al. [20] suggested a new type of phase matching, which they referred to as an intra-atomic phase matching. Employing the evolutionary strategy process, they could optimize the phase of the laser field in such a way as to increase the intensity of a single harmonic by an order of magnitude. Basically, this intra-atomic phase matching considers only temporal phase matching of high harmonics, and thus can be viewed as a special case of the spatio-temporal phase matching.

(3) Up-to-date femtosecond laser technologies

Generation and characterization of sub-10-fs pulses is still a challenging area in the femtosecond laser technology. Recently, the generation of sub-10-fs pulses in the violet, visible, and near-infrared region has been demonstrated [21-23]. Especially for the generation of high-peak-power sub-10-fs pulses, continuum generation and pulse compression technique is widely used. A continuum is usually generated by a self-phase-modulation (SPM) process in various materials such as a fiber, sapphire block, or a hollow-core fiber filled with a noble gas, and then the induced SPM is compensated for by negative dispersion elements such as a grating pair, a prism pair, or chirped mirrors [24]. An adaptive pulse shaper using a deformable mirror or a spatial light modulator realized more perfect pulse compression [25], and adaptive pulse compression of visible pulses down to 4 fs was recently demonstrated [26].

The adaptive pulse shaper is a very good tool for coherent control of quantum dynamics as well as pulse compression with high-order dispersion compensation. Using a feedback control between laser pulses and interacting system, we can either grow up or suppress a particular signal from the system. This method has been applied in controlling various phenomena such as chemical reaction, molecular vibration, and nonlinear frequency conversion [27,28]. Recently, control of high harmonic generation using a deformable mirror coupled with a genetic algorithm was reported [29]. For the optimization of a highly complicated system, the genetic algorithm [30] has been proved to be very powerful because it can 'train' the given system to find an optimizing condition by itself. Thus self-learning

system based on the adaptive optics and genetic algorithm can be applied to many new areas.

With the advent of sub-10-fs pulses with few optical cycles, nonlinear optics based on the slowly-varying envelope approximation (SVEA) comes to face a new aspect. This approach disregards the electric carrier field relative to the envelope of the pulse. Electric field and its envelope travel at phase and group velocity, respectively, so that the difference between two velocities can cause a random walk of the offset between carrier and envelope in an unstabilized laser. For a few-cycle pulse, this random offset is very important because the pulse cannot be described any more by using only the envelope, i.e. the SVEA fails. Thus, the control of the carrier envelope phase (CEP) is crucial for the coherent control of high harmonic generation processes – extremely nonlinear processes. Measurement and control of the CEP have been intensively studied and demonstrated for the last 3 years [31-34]. Recently, the carrier-envelop phase in the amplified laser pulses was also measured [34]. This opens the possibility to generate high-order harmonics driven by CEP-controlled laser pulses. The technique of CEP control can be also utilized for the optical frequency metrology, and coherent synchronization and superposition of independent lasers.

References

[1] M. B. Gaarde, P. Antoine, A. Persson, B. Carre, A. L'Huillier, C.-G. Wahlstrom, *J. Phys. B* **29**, L163 (1996).

[2] C. Altucci, R. Bruzzese, C. de Lisio, M. Nisoli, S. Stagira, S. De Silvestri, O. Svelto, A. Boscolo, P. Ceccherini, L. Poletto, G. Tondello, P. Villoresi, *Phys. Rev. A* **61**, 021801(R) (1999).

[3] M. Bellini, Appl. Phys. B **70**, 773 (2000).

[4] B. Shan, A. L. Cavaliere, Z. Chang, Ultrafast Optics 2001, Poster No. 23 (2001).

[5] H. J. Shin, D. G. Lee, Y. H. Cha, K. H. Hong, C. H. Nam, *Phys. Rev. Lett.* **83**, 2544 (1999).

[6] J. B. Watson, A. Sanpera, K. Burnett, P. Knight, *Phys. Rev. A* **55**, 1224 (1997).

[7] P. Salières, T. Ditmire, K. S. Budil, M. D. Perry, and A. Lhuillier, *J. Phys.* B **27**, L217 (1994).

[8] D. G. Lee, "Bright, low-divergence high-order harmonic generation in a long gas jet," (in preparation)

[9] A. Rundquist, C. G. Durfee III, Z. Chang, C. Herne, S. Backus, M. M. Murnane, H. C.

Kapteyn, *Science*, **280**, 1412 (1998).

[10] Y. Tamaki, J. Itatani, M. Obara, and K. Midorikawa, *Phys. Rev.* A **62**, 063802 (2000).

[11] P. B. Corkum, Phys. Rev. Lett. **71**, 1994 (1993).

[12] K. J. Schafer, B. Yang, L. F. DiMauro, and K. C. Kulander, Phys. Rev. Lett. **70**, 1599 (1993).

[13] M. Lewenstein, Ph. Balcou, M. Y. Ivanov, A. L'Huillier, and P. B. Corkum, Phys. Rev. A **49**, 2117 (1994).

[14] T. Brabec and F. Frausz, Rev. Mod. Phys. **72**, 545 (2000).

[15] A. L'Huillier, Ph. Balcou, S. Candel, K. J. Schafer, and K. C. Kulander, Phys. Rev. A **46**, 2778 (1992).

[16] E. Priori, G. Cerullo, M. Nisoli, S. Stagira, S. De Silvestri, P. Villoresi, L. Poletto, P. Ceccherini, C. Altucci, R.Bruzzese, and C. de Lisio, Phys. Rev. A **61,** 063801 (2000).

[17] N. H. Shon, A. Suda, Y. Tamaki, and K. Midorikawa, Phys. Rev. A **63**, 063806 (2001).

[18] P. Salieres, A. L'Huillier, and M. Lewenstein, Phys. Rev. Lett. **74**, 3776 (1995).

[19] Ph. Balcou, P. Salieres, A. L'Huillier, and M. Lewenstein, Phys. Rev. A **55**, 3204 (1997).

[20] I. P. Christov, R. Bartels, H. C. Kapteyn, and M. M. Murnane, Phys. Rev. Lett. **86**, 5458 (2001).

[21] S. Sartania, Z. Cheng, M. Lenzner, G. Tempea, Ch. Spielmann, and F. Krausz, Opt. Lett. **22**, 1562 (1997).

[22] L. Gallmann, G. Steinmeyer, G. Imeshev, M. M. Fejer, J. –P. Meyn, and U. Keller, Ultrafast Optics 2001, Mon06 (2001).

[23] T. Kobayashi, A. Shirakawa, Appl. Phys. B **70**, S239 (2000).

[24] U. Morgner, F. X. Kartner, S. H. Cho, Y. Chen, H. A. Haus, J. G. Fujimoto, and E. P. Ippen, V. Scheuer, G. Angelow, and T. Tschudi, Opt. Lett. **24**, 411 (1999).

[25] E. Zeek, R. Bartels, M. M. Murnane, H. C. Kapteyn, and S. Backus, Opt. Lett. **25**, 587 (2000).

[26] A. Baltuska, T. Fuji, and T. Kobayashi, Ultrafast Optics 2001, Mon08 (2001).

[27] B. J. Pearson, J. L. White, T. C. Weinacht, and P. H. Bucksbaum, Phys. Rev. A **63**, 063412-1 (2001).

[28] A. Assion, T. Baumert, M. Bergt, T. Brixner, B. Kiefer, V. Seyfried, M. Strehle, and G. Gerber, Science **282**, 919 (1998).

[29] R. Bartels, S. Backus, E. Zeek, L. Misoguti, G. Vdovin, I. P. Christov, M. M. Murnane, and H. C. Kapteyn, Nature **406**, 164 (2000).

[30] J. F. Frenzel, IEEE Potentials **12**, 21 (1993).

[31] H. R. Teller, G. Steinmeyer, A. E. Dunlop, J. Stenger, D. H. Shutter, and U. Keller, Appl.

Phys. B 69, 327 (1999).

[32] D. J. Jones, S. A. Diddams, J. K. Ranka, A. Stentz, R. S. Windeler, J. L. Hall, and S. T. Cundiff, Science **288**, 635 (2000).

[33] A. Apolonski, A. Popper, G. Tempea, C. Spielmann, T. Udem, R. Holzwarth, T. W. Hansch, and F. Krausz, Phys. Rev. Lett **85**, 740 (2000).

[34] M. Kakehata, H. Takada, Y. Kobayashi, K. Torizuka, Y. Fujihira, T. Homma, and H. Takahashi, Ultrafast Optics 2001, Mon01 (2001).

3. Progress Analysis

A. Degree of objectives fulfillment

(1) High harmonic X-ray generation

(a) First year (1999)

The major objectives in this year have been set to demonstrate the continuous wavelength tuning as well as the construction of the spectroscopic database of high harmonic spectra. From high harmonics from Ne atoms driven by intense 27-fs laser pulses over the saturation intensity for the optical field ionization, the continuous wavelength tuning over two times the laser frequency was demonstrated. Besides, high harmonic spectra collected in a wide range of experimental parameters revealed that the laser chirp condition should be a crucial parameter in the generation of bright and sharp harmonic signals, which have not been appreciated by other research teams. From these results, we would like to claim the achievement of major objectives in this part.

Using Ne as an X-ray generation medium, the continuous tuning of harmonic wavelengths over two times the laser frequency was achieved in the 10 nm region. The wavelength tuning over the interval between odd harmonics, i.e. two times the laser frequency, is needed to provide a harmonic X-ray at any wavelength. Previously the strong blueshift of two times the laser frequency was observed in the 39th harmonic from Ar. The 39^{th} harmonic however disappeared at the low laser intensity; so, the continuous tuning could not be shown. Since Ne can withstand much stronger laser intensity due to its higher ionization potential than Ar, much higher order harmonics can be generated from Ne. It was demonstrated with the harmonics between the 65^{th} and 91^{st} orders that the harmonic wavelengths could be continuously tuned over two times the laser frequency by adjusting the laser intensity.

The spectral structure study based on the database collected over wide experimental parameters showed that the high harmonic generation process sensitively depended on the laser parameters, especially the laser chirp. This showed that, at relatively low laser intensity, positively chirped laser pulses could increase the harmonic intensity in the plateau region and observable harmonic orders were increased in the cutoff region, while at high laser intensity negatively chirped pulses increased the harmonic intensity in the plateau region. This is a new finding that does not agree with previous reports by others that observed the enhanced harmonic peaks in the plateau region only with positively chirped laser pulses, but no

enhancement with negatively chirped pulses. The experimental parameters, such as the position of interacting medium with respect to the laser focus and the laser confocal parameter and intensity, all affected the HHG processes. The collected spectral data of high harmonics would provide a guide for further investigation of spectral structure of high harmonics, especially for the best phase matching condition to achieve the highest harmonic conversion efficiency from a given driving laser.

The extension of high harmonic X-ray generation down to the water-window soft X-ray region (2.4–4.3 nm) was tried. The shortest wavelength of high harmonics observed was 4.3 nm, the carbon K-edge, corresponding to the 191st harmonic order (unshifted). Even though the experimental parameters were extensively varied, the high harmonics below 4.3 nm could not be observed. The increase of harmonic intensity toward the 4.3-nm region under a certain experimental condition indicated that there were high harmonic X-rays in the water-window region. Consequently, it is believed that the oil contamination on the grating surface and on the cooled X-ray CCD absorbed the harmonics in the water-window region. After replacing the grating with a new one and cleaning the CCD surface, the high harmonics below the carbon K-edge will certainly be measured by the end of this project year.

(b) Second year (2000)

The major objectives in this year have been set to find out the optimum condition for the maximum conversion of laser light to high harmonics as well as to find any new HHG physics from the spectral structure analysis. By applying intense 28-fs laser pulses over the saturation intensity for the optical field ionization, bright and low divergence harmonics were observed from Ar atoms. In addition, in the optimization processes, proper guidance of the refracting pumping pulse in the ionizing medium acting as a negative lens was achieved through the balancing of plasma defocusing and diffraction with nonlinear self-focusing, which made it possible to overcome the limitation of interaction volume for efficient harmonic generation in an ionizing medium. From these results, we would like to claim the achievement of the objectives in this part.

Efficient harmonic generation was achieved using a long argon gas jet pumped by intense 28 fs laser pulses. High harmonic generation in a long gas jet is a new approach, compared to that in a hollow core fiber or in a gas cell. The latter approaches have a limitation in acceptable beam size to the interaction medium; however, the adoption of the long gas jet removes this problem. The use of the long gas jet, on the hand, must overcome the refraction

problem in order to utilize the full medium length of the long gas jet. By balancing diffraction and plasma defocusing with nonlinear self-focusing, we could achieve a new optimum condition for efficient high-order harmonic generation. Under condition of a self-guided laser pulse, generated high-order harmonic signal (29^{th} harmonic from argon) was strong enough to saturate an x-ray CCD in one laser shot of 5 mJ and the measured divergence of the harmonics from 23^{rd} to 31^{st} order were 0.5 mrad (in FWHM). This divergence angle, being much smaller than those observed for high harmonics generated in hollow-core fiber (~1 mrad) and gas cell target (~2 mrad), was attributed to enlarged harmonic generation cross-section

The systematic study of experimental and theoretical high harmonic spectra reveals that the laser chirp condition for the generation of sharp and strong high-order harmonic changed from positive to negative as the applied laser intensity was increased. Based on this study, we demonstrated continuous wavelength tuning of high harmonics without sacrificing spectral sharpness, achieved through control of the laser intensity and chirp.

In the previous year, we demonstrated that the wavelengths of the harmonics between the 65^{th} and 91^{st} orders were continuously tuned over two times the laser frequency by adjusting only the laser intensity. Now by controlling not only incident laser energy but also laser chirp, continuous tuning of the high harmonics without losing spectral sharpness was achieved. The spectral widths were maintained within 0.7 ω_0 by adjustment of the laser chip condition. This represents direct proof that it is possible to generate a given harmonic at a specific frequency, a critical step in the realization of a continuously tunable high harmonic x-ray source.

(c) Third year (2001)

The major objectives in this year have been set to the realization of a continuously tunable, coherent, femtosecond x-ray source and the characterization of the coherence property of the generated harmonics. In addition, the output energy yield is to be measured using a well-calibrated x-ray photodiode, and the coherent control of high harmonics is to be investigated.

We have demonstrated the continuous wavelength tuning of high-order harmonics using the phenomenon of harmonic blueshift and the chirp control of harmonics with chirped femtosecond laser pulses for achieving spectral sharpness and high brightness for the harmonics. The wavelength tuning technique developed here requires only the rotation of a

half-wave plate to control the laser-energy and an adjustment of the grating separation in the pulse compressor for chirp control, both of which can be easily automated with a feedback control. Hence, the wavelength tuning method demonstrated here has a high potential as a practical tool for applications.

We here accomplished the coherent control of high-order harmonics using chirped femtosecond laser pulses for the production of sharp and strong harmonics. We here examined in detail the dependence of the output harmonic spectrum on the laser chirp condition in order to achieve the desired coherent control process. This work showed that the coherent control to achieve sharp harmonics should treat the interaction between atoms and a laser pulse as an integral system, not just as an optical manipulation of atoms. The method developed can be easily implemented in most high-power femtosecond lasers; hence, the coherent control technique with chirped laser pulses can become a powerful tool in practical applications requiring sharp and strong XUV/soft x-ray radiation.

We characterized the coherence properties and divergence of high-order harmonics generated from Ne and Ar atoms. The divergence of the 27^{th} harmonic (30 nm) generated from Ar was measured to be 0.5 mrad with energy of up to 4 nJ per pulse, easily saturating the CCD used in the KAIST soft x-ray spectrometer. The 61^{st} harmonic (13.5 nm) generated from Ne was measured to have a divergence of 0.7 mrad and energy of up to 0.3 nJ per pulse. The results show the lowest divergence ever reported. The degree of spatial coherence of high-order harmonics was measured using the double-pinhole interference experiments. The diameter of the pinholes and the distance between them were 10 μm and 100 μm, respectively. The measurements showed that the harmonic x-ray beam has complete spatial coherence over most of the beam cross section.

(2) Theory development of high harmonic generation

(a) First year (1999)

All the proposed objectives concerning the theoretical development of high harmonic generation have been more than fulfilled. Initially, we had planned to make a numerical tool for calculating the one-dimensional Schrodinger equation and to develop a theory that would explain the numerical and experimental findings. In the first fiscal year, by successfully achieving the proposed goals we were able to make significant progress in understanding the basic features of high harmonic generation.

Our theoretical accomplishments may be divided into two parts. In the first part, we proposed a numerical probing technique (the coherent sum method) that can resolve the complicated spectral structure in the single-atom high harmonic spectra obtained from the numerical simulation of the time-dependent Schrodinger equation. The coherent sum method can differentiate the contributions from different electron trajectories, and thus enables us to tell which trajectory contributes to which spectral line in the harmonic spectra. Since this technique can remove the intensity-sensitive harmonics from multiple recollisions and consequently provides a well-resolved spectrum, it has been successfully applied to the measurement of harmonic blueshift. In the second part, we investigated the time-frequency characteristics of high harmonics using the Wigner distribution function. Using this time-frequency analysis, we calculated for the first time the dynamically induced chirp of high harmonics, and demonstrated that the unexpectedly large harmonic blueshift observed experimentally is due mainly to the single-atom effect. We believe that the coherent sum method and the time-frequency analysis will become important tools not only in understanding the characteristic features of high harmonics, but also in analyzing the experimental results. In view of recent increasing interests in controlling and optimizing high harmonic generation processes using chirped laser pulses, the information revealed on the induced harmonic chirp will prove useful, and our analytic approach will surely draw attention from researchers working in this area.

(b) Second year (2000)

The research objectives proposed for this year included the numerical simulation of propagation of high harmonics and the theoretical investigation of the attosecond pulse formation from high harmonics. All these proposed objectives have been successfully fulfilled this year, and the development of a simulation code for propagation of high harmonics has provided a deeper understanding of the propagation effects and enabled us to explain some experimental results.

We developed a one-dimensional propagation code to investigate the self-phase modulation of laser pulses propagating through an ionizing gas and its effect on high harmonics generated in the medium. Numerical simulations taking into account the full three-dimensional effects are time-consuming tasks and seem to be practically beyond our computational facilities. Thus, in this year, we simplified the problem neglecting the 3D effects, and concentrated only on the 1D case that considers the propagation of the laser and harmonic fields along the propagation axis. By numerically solving the 1D propagation

equation, together with the Schrodinger equation (a numerical code for which was developed last year), both the single-atom and propagation effects were considered self-consistently. With the help of the simulation codes developed this year and last year, we were able to reproduce some experimental results obtained by using chirped pulses to control the high harmonic spectra.

As for the attosecond pulse generation, our numerical simulations have shown that after the propagation through the medium only the short trajectory component remains, with other components being suppressed due to their poor phase-matching conditions, leading to the generation of attosecond pulse trains. We have also found that the use of gases of very high densities has the effect of limiting the efficient generation of phase-matched high harmonics to a very narrow time interval on the leading edge of the laser pulse where the density of electrons produced during ionization process is substantially low. Based on this theoretical study, we predict that, without using ultrashort, few-cycle pulses as proposed by other research groups, it will be possible to reduce the harmonic pulse duration to a subfemtosecond time scale simply by increasing the gas density, while using laser pulses longer than a few tens of femtosecond.

Although some experimental results have been successfully explained with the help of the 1D simulation code developed this year, there still remain some other experimental results that need further theoretical investigation. We believe that the development of a 3D simulation code will be necessary to provide theoretical explanations for those experimental results.

(c) Third year (2001)

We here developed a code to calculate the time-frequency distribution functions and parallelized it to adapt to parallel computing. We analyzed the high harmonic signal in the time-frequency domain theoretically. We used Wigner and Husimi distribution functions to investigate the quantum mechanical nature of high harmonic generation, and compared the result obtained with the semiclassical calculation. The close agreement between the two results suggests that the two-step model can explain the process of high harmonic generation. Thus, the phenomenon of high harmonic generation is thus an example that shows a strong degree of quantum-classical correspondence.

We have compiled a code, for solving the three-dimensional Schrödinger equation numerically, to study the interaction between intense laser fields and atoms. A

one-dimensional code for solving Schrödinger equation code had already been developed earlier to investigate the harmonic generation process. However, it cannot be used to study real atoms because it is only a one-dimensional code wherein the actual three-dimensional features of the system are ignored. The 3D code has been used to investigate all the problems studied earlier using the 1D code. The results obtained using the 1D code have been confirmed. Moreover, the 3D code has been used to calibrate the ionization rate calculated by the ADK formula that is not consistent with experimental results.

In the case of interaction involving double ionization, we have calculated the momentum distribution of the recoil ions from laser induced single and double ionization process. It has been found that in both, single and double ionization cases, the distributions of the momentum parallel to the laser polarization show double-hump structures, which is due to the rescattering process, i.e. the interaction between the tunneled electron and the potential of the core. The result is compared with experiments and the limitations of the model are discussed. For the case of double ionization, theoretical calculations show that the minimum in the center of the distribution of the momentum parallel to the laser polarization decreases as the laser intensity decreases. However, the experimental observations indicate just the opposite behavior. Thus when the intensity of the driving laser decreases, the contribution from the rescattering ionization process of the second electron may diminish and other processes such as the process of rescattering excitation with subsequent tunneling, which are not included in the present model, may begin to dominate.

We have also calculated the frequency dependence of non-sequential double ionization of Ne. The non-sequential double ionization ratio increases as the wavelength decreases and reaches its maximum at about 250 nm, the lower limit of validity the semiclassical model ($I=1.0 \times 10^{15} W/cm^2$). Careful investigation of the trajectories shows that there are two categories of double ionization: "instant ionization" which is caused by the collision between the bound and tunneled electrons and "delayed ionization" that occurs through the excitation of the bound electron by the collision with the returned electron and subsequent ionization by the field. Based on the different time intervals for these two processes, a technique has been developed to identify the double ionization cases by limiting the time interval between the re-collision time and ionization time. It is found that "delayed ionization" gives rise to the a large probability for NSDI in the high frequency region.

(3) Operation and development of femtosecond terawatt lasers

(a) First year (1999)

The major role of the 10-Hz femtosecond terawatt Ti:sapphire laser in this project is to provide steadily high-power femtosecond laser pulses for high harmonic X-ray generation experiments. In this point of view, the operation of the 10-Hz laser system has been very successful so far. For more than 700 hours the laser system has been operated successfully during the first project year. Most of the operation time has been allocated mainly to high-harmonic generation experiments. Another important factor of the laser system is the precise characterization of the laser pulse. Due to the high sensitivity of generated high harmonics to the laser intensity profile and phase structure, it is desired to precisely characterize them in various conditions. We utilized a frequency-resolved optical gating (FROG) technique to fulfill this requirement. The laser pulse under consideration has been fully characterized in terms of intensity and phase. Further more, the spatial distribution of the pulse at the light-matter interaction region has been characterized by magnifying the focused beam on a CCD with an objective lens. Consequently, the beam size at the interaction region could be measured accurately and minimized by correcting any deformation of mirrors and spatial chirping. From this support the high harmonic generation experiments could be properly supported.

The development of a new 1-kHz high-power Ti:sapphire laser is another important mission of this project, and has been progressed well so far. The design of the laser system has been finished, and the initial setup is under progress. A long-cavity femtosecond Ti:sapphire oscillator, which is more preferable as a front-end oscillator due to its higher pulse energy and longer pulse separation, has been completed. For the temporal stretch of a femtosecond pulse to ~200-ps pulse duration, an Offner-triplet type pulse stretcher has been constructed with a low-aberration configuration. Currently, a preamplifier has amplified a nJ pulse to 1 mJ pulse, and a second amplifier and a pulse compressor will be added. The laser system will be completed on one optical table, and ~20-fs, ~0.1-TW pulses will be generated at 1 kHz. We expect the 1-kHz laser system to be a new versatile laser source for high-harmonic generation experiments due to its compactness and high average power.

(b) Second year (2000)

Main objective in the second year was the development of 10-fs, 0.1-TW, kHz laser. As a first step, the setup and operation of a 23-fs, 0.1-TW CPA Ti:sapphire laser was finished. We improved the performance of a long-cavity front-end oscillator and a pulse stretcher installed in the first project year, and added a 12-pass pre-amplifier, 5-pass second amplifier and a

high-efficiency pulse compressor. The obtained energy per pulse after the pulse compressor was 2.3 mJ with the pulse duration of 23 fs, giving a peak power of 0.1 TW at 1-kH repetition rate. As the next step, we designed and setup a hollow-core-fiber and chirped-mirror compression system to generate sub-10-fs pulses. We installed a 1-m hollow-core-fiber filled with noble gases and launched the 23 fs pulses using a focusing mirror to generation of continuum. We succeeded in generating continuum with a wavelength range from 500 nm to 1000 nm, supporting the pulse duration of 3 fs. By compensating for the positive dispersion with a chirped-mirror pair, we succeeded in compressing the pulse duration down to 8.8 fs. The output energy was about 0.05 mJ, giving a peak power of 6 GW, which will be further enhanced within the end of the project year.

Operation and maintenance of the 10-Hz CPA laser system to support the high-order harmonic generation (HHG) experiments was very successful. The laser was operated for over 1,400 hours without any degradation of output energy and pulse duration. The operation time was allocated mainly to HHG experiments and also to the experiment of laser and atomic cluster interaction. Chirped femtosecond pulses generated by adjusting the compressor, which induce many interesting phenomena in HHG, were analyzed using Wigner time-frequency distribution function. This laser system is now capable of routinely generating coherent X-rays emission through HHG and will be an important light source for the characterization and application of the coherent X-rays.

Another objective in this year was to develop a new diagnostic for measuring temporal shape and phase of femtosecond pulses, called a spectral phase interferometry for direct electric-field reconstruction (SPIDER) apparatus. We developed a SPIDER apparatus together with an operating algorithm. It successfully characterized the femtoseond pulses from Ti:sapphire laser oscillator and the 10-Hz CPA system. After improving the setup toward simpler configuration and adopted a fiber-optic on-board spectrometer, we are running this apparatus in a real-time, single-shot mode with a relatively simple setup. In addition to the new diagnostic technique, we are developing an adaptive pulse shaping system using a micro-machined deformable mirror. It is prepared for the Ti:sapphire laser oscillator and will be also applied to the CPA laser system soon. The combination of real-time pulse diagnostic and adaptive system will make it possible to coherently control the high-order harmonics and greatly extend the applicability of femtosecond laser pulses because it will open a way of actively controlling the temporal phase of the pulses.

(c) Third year (2001)

The main objective in the third year was the adaptive pulse shaping of high-power laser pulses and the measurement of the carrier-envelope phase (CEP) slip of mode-locked laser pulses. An acousto-optic pulse shaper was used successfully for the adaptive control of the 1-kHz Ti:sapphire laser system developed in the 2nd year, as it had more effective shaping ability than the pulse shaper based on a micro-machined deformable mirror. The power of an adaptive feedback control using this pulse shaper was demonstrated through the feedback control of chemical reactions induced by femtosecond laser pulses. Additionally, a new temporal characterization technique of sub-10-fs laser pulses was developed using an evolutionary algorithm, which is one of the optimization algorithms for adaptive feedback control, in combination with an interferometric autocorrelation measurement.

To measure the shot-to-shot CEP slip of mode-locked laser pulses, we set up a $2f$-to-f self-referencing interferometer. By probing the beat signal, generated in this interferometer, in time and frequency domain, we successfully measured the shot-to-shot CEP slip of the laser pulses. The control of the CEP slip was achieved by adjusting the related parameters, CEP stabilization through a feedback control is now under progress.

B. Self evaluation

(1) High harmonic X-ray generation

By successfully fulfilling the objectives set for the third year of the project as detailed above, we have achieved significant results on coherent x-ray generation that have global competitiveness in its quality: The wavelength tunability reported by us is the best technique among those reported to date, the beam divergence is the smallest ever reported and the harmonic conversion efficiency is as high as those reported by any world class research groups. We have demonstrated an effective and elegant method to coherently control the high harmonic spectral structure and have also showed that the harmonic x-ray beam has complete spatial coherence over most of the beam cross section.

The new findings on the high harmonic X-ray generation resulted in one paper published in Physical Review Letters and another paper published in Physical Review A. In addition three papers have been submitted to Physical Review Letters, Applied Physics Letters, and Optics Letters.

(2) Theory development of high harmonic generation

We have proposed a new model to explain the process of high harmonic generation. Time-frequency domain analysis of the dipole moment signal reveals that harmonic of different orders is generated at different times and that there are lambda structures in time-frequency distribution. This agrees with the semiclassical calculation.

A code for the numerical solution of three-dimensional time-dependent Schrodinger equation has been developed and successfully applied to the study of harmonic generation and ionization problems. It reproduces the main results obtained previous by the one-dimensional code and gives saturation intensities for optical field ionization of atoms consistent with experimental data, thus improving the results of the ADK formula. It is being currently used for further analysis of harmonic generation experiment, for example to investigate the interference of two temporally separated laser pulses.

The momentum distributions of recoil ions from laser induced single and double ionization have been studied. It was found that, not only in the case of double ionization but also in the case of single ionization, the distributions of the momentum, parallel to the polarization direction of the laser field, show a double-hump structure as a consequence of the rescattering. Furthermore, by comparing with experimental data we find that, as the intensity of the laser decreases, the rescattering ionization mechanism of the second electron calculated within our model does not dominate the process. In addition, the correlated emission of the electrons in the double ionization is also discussed and the effect of the repulsion between the emitted electrons is shown.

We also studied the frequency dependence of non-sequential double ionization (NSDI) of Ne. Investigation of the trajectories shows that there are two categories of double ionization: "instant ionization" and "delayed ionization." By limiting the time interval between the re-collision time and ionization time, the "delayed ionization" is identified to be the source of high probability of NSDI in short wavelength regime.

We have achieved the target set for the theoretical work and have reported new findings in the double ionization problem. Two papers have been published in Phys. Rev. A and one is under review in J. Phys. B.

(3) Operation and development of femtosecond terawatt lasers

We have improved the capabilities of the 1-kHz laser system developed in the 2nd year with regard to two aspects. First, an acousto-optic programmable dispersive filter (AOPDF) was installed to achieve adaptive pulse shaping of high-power femtosecond laser pulses and the other is the improvement of pulse quality of the high-power sub-10-fs pulses. We obtained 20-fs high-power laser pulses at 1 kHz from the laser system equipped with the AOPDF and routinely generated high-order harmonic x-rays using this laser. The adaptive control of the high-order harmonics was not achieved yet, but the laser system was applied to an adaptive feedback control of a chemical reaction induced by femtosecond laser pulses, demonstrating the equivalent capability of adaptive control of high-order harmonics. In addition, using the evolutionary algorithm utilized for the adaptive feedback control of the chemical reaction, we developed a new phase retrieval technique of sub-10-fs laser pulses from an interferometric autocorrelation (IAC) measurement. Next, the pulse duration of the high-power sub-10-fs pulses generated from a hollow-fiber/chirped-mirror compression system was reduced from 8.8 to 8.3 fs and the spatial and temporal pulse quality was significantly enhanced. We obtained a clean temporal pulse shape with a greatly suppressed wing structure and a nearly Gaussian spatial beam profile.

For the measurement of the shot-to-shot CEP slip of mode-locked laser pulses, a $2f$-to-f self-referencing interferometer was installed. After generating a one-octave continuum from a microstructure air-silica fiber by launching the mode-locked femtosecond pulses, we observed the beat signal between two 2-f frequency components produced in the interferometer. The beat signal was observed in time and frequency domain, yielding the successful measurement of the shot-to-shot CEP slip of the laser pulses. The control of the CEP slip was achieved by adjusting the related parameters, and the parameter dependence was measured, which gave us the basic information for the design and fabrication of the CEP stabilization loop. The active control through the feedback control is currently under development.

4. Planned Approaches for the Research (methods)

(a) First year (1999)

High harmonic generation (HHG) is a process that generates odd harmonics of laser frequency from atoms driven by an intense laser. Its wavelength range has reached up to the water-window soft X-ray region (λ = 2.4–4.3 nm). As the harmonic conversion efficiency is improving with the technological breakthrough of high power femtosecond lasers and with newly developed phase-matching techniques of high harmonics, the high harmonic X-rays possess a good potential as a coherent femtosecond X-ray source of a laboratory size. Even though the available wavelengths are numerous, the actual applicability of a high-harmonic X-ray source will be limited if only fixed, odd harmonic wavelengths are available. Therefore we proposed to develop a tunable, coherent, femtosecond X-ray source, i.e. a tabletop synchrotron based on HHG.

For the realization of a tunable coherent femtosecond X-ray source, the following idea was proposed: **By applying intense femtosecond laser pulses to atoms, high harmonic wavelengths can be tuned using the property of nonadiabatic blueshift of harmonic radiation.** When high harmonics are generated in a rapidly rising electric field, atoms see a nonadiabatic change of electric field in time, which results in the blueshift of harmonic wavelengths due to the deviation of atomic modulation from a periodic behavior. This property of harmonic blueshift may be utilized for the development of the tunable coherent femtosecond X-ray source.

The planned approaches to confirm the proposed idea are as fellows:

(1) Systematic investigation of high harmonic spectra with respect to experimental parameters, such as the kind of target atoms (Ar, Ne, He), laser parameters (pulse duration, intensity, confocal parameter), and the position of target with respect to laser focal spot. This will give physical pictures on the HHG mechanism and on the phase matching as well as on the blueshift.

(2) Theoretical approach for the understanding of spectral structure of high harmonics, especially the development of a calculation tool based on the time-dependent Schrodinger equation and the comparison with the results obtained from the strong field approximation.

(3) Development of femtosecond terawatt laser technologies to achieve 10 fs, 0.1 TW at 1 kHz rep rate and 20 fs, 10 TW at 10 Hz. The kHz Ti:sapphire laser system is going to be newly developed and the current 10 Hz Ti:sapphire laser system (20fs, 3TW) is going to be

upgraded.

The construction of spectroscopic data base on high harmonics will give the parameter range to achieve large tunability of high harmonic X-rays and will lead us to find out the optimum condition for efficient high harmonic generation. With the development of new theoretical tool, we aim at understanding the spectral structure of high harmonics that exhibits complicated structural composition. As the achievable parameter range of high harmonic generation is closely related with available laser parameters, such as pulse duration and intensity, the development of new femtosecond laser technologies is very crucial in meeting the proposed goal. In this sense, the current research team possesses a good potential to produce very challenging results since the high harmonic X-ray generation can be carried out using most advanced femtosecond laser technologies - the 10 Hz laser system is a homemade one and the kHz laser system is going to be developed also by the in-house team, with best laser technologies. The combination of above three ingredients, experimental outcome based on theory development and up-to-date femtosecond laser technology, will bring out challenging results to accomplish the proposed objectives.

(b) Second year (2000)

Recent advances in high-power femtosecond laser technology have made it possible to investigate the high harmonic generation processes in an unprecedented high-intensity, ultrashort pulse regime. Owing to the expectation that it may be utilized to develop ultrashort extreme ultraviolet sources, the subject of high harmonic generation has drawn considerable attention from the researchers working in the area of intense field-atom interaction. For diverse applications of the high harmonics as a coherent femtosecond x-ray source, however, the harmonic conversion efficiency still needs to be significantly increased. In the 2^{nd} year, we will systematically investigate the optimal conditions for efficient harmonic generation. We suppose that the use of a long gas medium to increase the number of atoms interacting with the laser may result in enhancement of harmonic conversion efficiency. We will develop a systematic technique to achieve coherence control of high harmonics by using chirped laser pulses, which is hoped to increase the efficiency of high harmonic generation by optimizing its spectral coherence property.

(1) Optimization of system parameters to achieve the maximum conversion efficiency of laser light to high harmonics. To significantly enhance the harmonic conversion efficiency, we will use a long gas jet, and carry out experiments in the saturation intensity regime while

varying the chirp condition of the incident laser. In this high intensity regime, ionization of atoms may change the refractive index of the medium affecting the propagation of laser and harmonic fields. By observing the visible images of plasma columns using a visible CCD, the optimum condition for the proper guidance of the refracting pulse will be searched.

(2) Development of a one-dimensional propagation code to calculate the self-phase modulation of laser pulses and its effect on high harmonics. The numerical tools developed in the first project year to calculate the single atom response will be extended to include the propagation effect for the direct comparison with experimental results. The time-frequency analysis will be applied to the analysis of macroscopic high harmonics, and optimal conditions for the attosecond pulse generation will be investigated.

(3) Development of a high-repetition-rate high-power femtosecond laser and systematic analysis of chirped femtosecond pulses. Generation of sub-tera-watt femtosecond laser pulses at a repetition rate of 1 kHz will make it possible to generate high-flux coherent X-ray through HHG. The information on the phase of the chirped laser pulses, which will be characterized by using the FROG technique and the time-frequency analysis, will help understand the features of HHG obtained by chirped femtosecond pulses.

The use of a slit nozzle as a nonlinear medium for the generation of high harmonics will provide a sufficient cross section of the harmonic generation volume, thereby increasing the harmonic conversion efficiency. Another approach that we will pursue to enhance the conversion efficiency is to control the high harmonic spectral structure by using chirped laser pulses. Adaptive optical system using a deformable mirror is a good solution for the active control of temporal characteristics of femtosecond laser pulses as well as spatial characteristics. Especially, a linear-type micro-machined deformable mirror (MMDM) is an ideal candidate for the temporal pulse shaping system because it is a low-cost and high-speed device with high deformation quality. The propagation model to be developed will provide physical explanation of experimental results, and guide us to find optimal experimental conditions for the efficient harmonic generation.

(c) Third year (2001)

In the previous year, we have investigated the spectral structure of the high-order harmonics and optimized the brightness of the harmonics by using the long gas jet target. Based on the previous studies, we proposed a method to continuously tune harmonic wavelengths without

changing the laser spectrum. We planned to develop the technique on the bases of harmonic blueshift of atoms for enough tuning and coherent control with chirped laser pulses for spectral sharpness. This will open a pathway to the realization of continuously tunable, coherent, femtosecond x-ray source by overcoming the weakness of harmonics – generation of only fixed harmonic wavelengths.

For the better understating of the experimental results, we targeted to develop the codes to calculate the time-frequency distribution functions and a three-dimensional time-dependent Schrödinger equation, which is hoped to enlarge our knowledge of physical processes in the harmonic generation.

In the laser part, an acousto-optic programmable dispersive filter (AOPDF) for an adaptive pulse shaping of high-power femtosecond laser pulses was planned to install for an adaptive feedback control of a chemical reaction induced by femtosecond laser pulses and also for the adaptive control of high-order harmonics. In addition, using the evolutionary algorithm utilized for the adaptive feedback control of the chemical reaction, we will develop a new phase retrieval technique of sub-10-fs laser pulses from an interferometric autocorrelation (IAC) measurement.

(1) Coherent control of high harmonics to realize a continuously tunable, coherent, femtosecond x-ray source and characterization of the beam properties (divergence and spatial coherence). To continuously tune the harmonic wavelengths, without modifying the laser spectrum, we apply the coherent control process of high-order harmonics with chirped femtosecond laser pulses. The coherent control process can be achieved by controlling both incident laser energy and laser chirp. The laser intensity is varied with the control of the incident laser energy using a half-wave plate and polarizers installed in front of the pulse compressor. The control of the incident laser energy is thus achieved without altering the focusing geometry. The laser spectrum is monitored while changing the laser energy to ensure that the spectrum was not modified. To cover as wide a wavelength region as possible, we select the species of atoms for efficient harmonic generation and sufficient wavelength tuning in the required spectral range.

Harmonic generation using a long gas jet will be performed to obtain bright high-order harmonics. When the driving laser pulses propagate in the ionizing long gas jet medium, the pulses are defocused by the electron density gradient in the transverse direction, which acts as

a negative lens. Therefore, proper guidance of the pumping laser pulse through the gas jet is required for efficient harmonic generation, together with low beam divergence. By observing the direct images of harmonic beams, the divergence is measured.

(2) Development of a code to calculate the time-frequency distribution functions and parallelizing it to adapt to parallel computing. Time-frequency analysis can be an ideal tool not only to understand the high harmonic generation but also to optimize the harmonic signal.

(3) Development of a code for solving three-dimensional time-dependent Schrodinger equation to study harmonic generation. For further theoretical investigations on harmonic generation, the numerical solution of three-dimensional time-dependent Schrödinger equation will be developed to study the interaction between intense laser fields and real atoms. It can be also used to examine the results obtained previous by the one-dimensional code. Understanding the ionization process is also very important in the study of harmonic generation. Compared to single ionization, the mechanism of double (multiple) ionization of atoms has not been adequately understood. The double ionization of atoms and ions will be studied using a semiclassical model.

(4) Adaptive pulse shaping of high-power laser pulses using an AOPDF and shot-to-shot CEP slip measurement using a $2f$-to-f self-referencing interferometer. The femtosecond high-power laser equipped with an adaptive pulse shaper allows an active control of femtosecond laser pulses and a self-learning experiment through a feedback algorithm. The shot-to-shot CEP slip can be measured and controlled in frequency domain using a one-octave spanned spectrum of mode-locked laser pulses. This experiment can be realized in the $2f$-to-f self-referencing interferometer.

5. Results

A. Research details

(a) First year (1999)

(1) High harmonic X-ray generation

The spectroscopic investigation of high harmonic X-rays revealed several interesting properties. First, the continuous tuning of harmonic wavelengths around 10 nm region was demonstrated. Using Ne as an X-ray generation medium, the continuous tuning of harmonic wavelengths over two times the laser frequency was achieved with the control of laser intensity. Second, the spectral structure study showed that, as the medium density was lowered, the highest observable harmonic order was increased though the harmonic intensity at the plateau region was reduced. Third, the spectral structure study also showed that the high harmonic generation process sensitively depended on the laser parameters, especially the laser chirp. This showed that, at relatively low laser intensity, positively chirped laser pulse could increase the harmonic intensity in the plateau region and observable harmonic orders were increased in the cutoff region, while at high laser intensity negatively chirped pulse increased the harmonic intensity in the plateau region. This is a new finding that does not agree with previous reports which observed the enhanced harmonic peaks only with positively chirped laser pulse, but no enhancement with negatively chirped pulse. In order to explain the observed high harmonic spectra a new theoretical approach should be explored that includes the spectral chirp in harmonics due to ionization as well as that due to the atomic chirp from the intensity-dependent harmonic phase. The experimental parameters, such as the position of interacting medium with respect to the laser focus and the laser confocal parameter and intensity, all affected the HHG processes. The collected spectral data of high harmonics would provide a guide for further investigation of spectral structure of high harmonics, especially for the best phase matching condition to achieve the highest harmonic conversion efficiency from a given driving laser. Fourth, the extension of high harmonic X-ray generation to the water-window soft X-ray region (2.4–4.3 nm) was tried. The shortest wavelength of high harmonics observed was 4.3 nm, the carbon K-edge, corresponding to the 191st harmonic order. Even though the experimental parameters were extensively varied, the high harmonics below 4.3 nm could not be observed, even though there was an increase of harmonic intensity toward the 4.3-nm region under a certain experimental condition. Consequently it is believed that the oil contamination on the grating surface and on the cooled X-ray CCD absorbed the harmonics in the water-window

region. After replacing the grating with a new one and cleaning the CCD surface, the high harmonics below the carbon K-edge will certainly be measured.

(2) Theory development of high harmonic generation

The development of HHG theory based on the numerical calculation of the time-dependent Schrodinger equation (TDSE) also progressed well. Previously the theory part was weak, even though there were very interesting experimental results. With the new development of analysis tools of high harmonic spectra, fruitful outcome from the interpretation of experimental results will be produced. The one-dimensional solution of TDSE was obtained using a soft core potential. The numerical solution of TDSE in the case of extremely short laser pulse (< 100 fs) does not show any harmonic peaks due to overlapping of several different components to a given harmonic order. In order to solve this problem, a coherent sum technique was developed that could remove harmonic components whose phases sensitively depended on laser intensity. In addition the Wigner distribution function is introduced, for the first time, to further analyze the temporal chirp of high harmonics, which can give the harmonic structure in the time-frequency domain. The coherent sum technique and the time-frequent domain analysis for the interpretation of TDSE results would become very powerful calculation tools not only in the advancement of HHG theory, but in the analysis of experimental results. Those methods made clear the chirp structure of high harmonics that has recently become a hot topic in HHG.

(3) Operation and development of femtosecond terawatt lasers

The operation of the existing laser for the HHG experiments and the new laser development progressed well as planned. First, as the experimental results of HHG sensitively depended on the laser parameters, it became very crucial to accurately characterize the temporal shape of laser pulse. Using the second-harmonic generation frequency-resolved optical gating technique, the temporal shape and phase was investigated with respect to the laser chirp adjusted by changing the distance between the compression gratings. The refinement of this measurement will be continued to figure out the correlation with harmonic experimental results that showed very sensitive change even without noticeable change in laser parameters. Second, the new kHz Ti:sapphire laser is another homemade laser system that incorporates up-to-date femtosecond laser technologies. The new femtosecond oscillator is based on a long-cavity design and constructed using only commercial optics (no custom-designed mirrors). It is still capable of producing very broad pulses with spectral width over 100 nm and with increased output energy (5 nJ) per pulse. The increased pulse interval in the long cavity oscillator will help to give a good prepulse contrast ratio, and the increased output

energy will alleviate the gain narrowing problem, resulting in broad amplified spectrum. The initial system construction was finished on one optical table. It will become a new compact driver for HHG with higher average power than the 10 Hz Ti:sapphire laser.

More detailed research results are given in the Appendix (I), as summarized in the below:

A . 1. High harmonic X-ray generation

A. 1. 1. Continuously tunable high harmonic X-ray generation from atoms in an intense femtosecond laser field

A. 1. 2. Nonadiabatic blueshift of high harmonics from Ar and Ne atoms in an intense femtosecond laser field

A. 1. 3. Control of the spectral structure of high harmonics using chirped laser pulses

A. 1. 4. Selection of high harmonics from a single quantum path for attosecond pulse generation

A. 2. Theory development of high harmonic generation

A. 2. 1. Coherent sum technique

A. 2. 2. Time-frequency analysis

A. 3. Operation and development of femtosecond terawatt lasers

A. 3. 1. Development of a 1 kHz femtosecond terawatt laser

A. 3. 2. Temporal structure of chirped laser pulses

A. 3. 3. Focused spot size and intensity measurement in a femtosecond terawatt Ti:sapphire laser

A. 3. 4. Incorporation of a cavity-dumped oscillator in a femtosecond terawatt Ti:sapphire laser

(b) Second year (2000)

(1) High harmonic X-ray generation

First, through the systematic investigation of laser propagation in an ionizing medium, proper guiding condition of laser pulse was found with a visible plasma column images and intense harmonics with very low beam divergence were observed when a gas jet was placed at the optimal position of laser propagation. The visible images of plasma column were captured on a visible CCD when 28 fs Ti:sapphire laser pulses with a peak intensity of 7×10^{15} W/cm^2 at the focused position were applied to a long gas jet from an 6 × 0.5 mm slit nozzle. When the gas jet was placed after the laser focusing point, laser pulse with enough strength for the

ionization of argon atoms could not propagate more than the first 1 mm, although the confocal parameter of the laser pulse in vacuum was 10 mm. The plasma column length became extended as the gas jet moved to before the focused position of the laser beam and, moreover, nearly uniform plasma column could be generated along the whole length of the gas jet at z = -7 mm. This experiment result shows that the guiding of laser beam, delivering the pumping laser pulse up to the end of medium, in a partially ionized medium was very sensitive on the target position. Collimated laser beam propagation could be achieved only at proper target position and density.

At the optimal position of laser propagation, intense, low divergence harmonics were observed. The 27^{th} harmonic from argon was strong enough to saturate our detection system with a singe shot of laser pulse. The measured divergence of the harmonic order from 23 to 31 was 0.5 mrad (in FWHM). This small divergence originated from a large harmonic generation cross section of the long gas jet. Since utilization of a long interaction medium also aids an efficient harmonic generation, the adoption of the long jet is expected to provide bright, low beam divergence harmonics.

Second, the coherent control of high-order harmonics by adjusting the chirp condition of femtosecond laser pulses were systematically investigated, for the first time, in experiment and theory. We showed that the laser chirp condition for the generation of sharp and strong high-order harmonics changed from positive to negative as applied laser intensity was increased. This cannot be explained by a single atom approach, and the laser chirp induced while propagating through an ionizing medium should be properly take into account. This demonstrates the importance of an integral treatment of the interaction between atoms and a pumping laser pulse for the proper coherent control of high-order harmonics. (This result is submitted to Phys. Rev. Lett.)

Third, continuously tunable spectral range was extended to 121^{st} order by applying a positively chirped pulse. The adoption of high-density medium enhance the blueshift as well as increase the harmonic signal level, facilitating the frequency tuning of harmonics in a strong signal level. But the highest observable harmonic order will rapidly decrease with medium density due to the plasma dispersion, which cause the phase mismatching of the harmonics and pumping laser pulses. So, to solve this problem, we utilize a new finding that the intensity of harmonic in the cutoff region and the highest harmonic order is drastically increases when the positively chirped laser pulse is applied at the relatively weak intensity of

1×10^{15} W/cm^2 for helium.

(2) Theory development of high harmonic generation

We developed a one-dimensional simulation code for propagation of the laser and high harmonic fields. Using the 1D simulation code, we have found that (i) the plasmas produced in the medium can induce a positive frequency chirp on the leading edge of the laser pulse and (ii) this plasma-induced chirp can lead to the generation of sharply peaked, chirp-free high harmonics. In some parameter regimes, the plasma-induced chirp can even cause high harmonics to become positively chirped.

The mechanism that shapes macroscopic high harmonic spectral lines was explained by making a comparison between the plasma-induced chirp and the dynamically induced chirp. The leading edge of the laser pulse, in which the laser frequency increases with time due to the phase modulation induced by plasmas, tends to generate positively chirped high harmonics. This effect is opposed by the dynamic single-atom effect that forces high harmonics to become negatively chirped. Depending on system parameters and harmonic order, one effect matches or dominates over the other. It is important to note that, even though the plasma-induced chirp broadens the laser spectrum, it can lead not only to broadening but also to narrowing of harmonic spectral lines. This indicates that using the plasma effect we can control the chirp and spectral line shape of high harmonics by increasing or decreasing the amount of the plasma-induced positive chirp relative to the dynamically induced negative chirp.

We also investigated optimal conditions for the attosecond pulse generation. We have found that by increasing the gas density we can make the free electrons produced in an ionizing medium induce severe phase mismatching among the harmonics generated at different positions, except on the front edge of the pulse where the electron density is very low. In this case, the efficient harmonic generation can be limited to a very narrow temporal region on the front edge of the pulse, and consequently the harmonic pulse width will be significantly reduced.

(3) Operation and development of femtosecond terawatt lasers

Operation of the existing laser for the HHG experiments and the new laser development progressed well, together with up-to-date femtosecond technologies such as SPIDER technique and adaptive pulse shaping technique. First, the development of the 23-fs, 0.1-TW

laser operating at the repetition rate of 1 kHz, and the hollow-core-fiber and chirped mirror compression system generating sub-10-fs pulses were finished. This laser consisted of a long-cavity Ti:sapphire laser delivering 12 nJ per pulse as a front-end oscillator, a Offner-type stretcher, a 12-pass pre-amplifier, a 4-pass second amplifier, and a high-efficiency compressor. We inserted a pellicle etalon in the pre-amplifier in order to obtain broadband spectrum over 80 nm. This laser itself will be a good source for the generation of large-flux high-order harmonics as well as 10-fs, 0.1-TW laser pulses. The hollow-core-fiber filled with noble gas converted the pre-compressed 23-fs pulses into continuum with the wavelength range covering 400 nm. By compensating for the residual dispersion using a chirped-mirror pair, we obtained 8.8-fs pulses. Second, we used Wigner distribution function (WDF) to analyze chirped femtoseond pulse generated by adjusting the grating separation in the compressor and suggested a graphical method to properly interpret instantaneous carrier frequency of the chirped pulses in WDF. This approach will help to understand a fundamental feature of carrier frequency in an ultrashort pulse. Third, we developed a real-time, single-shot SPIDER apparatus to characterize the temporal structure of femtosecond laser pulses. Because this diagnostic is compact and operates with high speed, it can substitute for the existing technique, frequency-resolved optical gating (FROG). Fourth, an adaptive pulse shaper using a micro-machined deformable mirror was developed for an active optimization of the Ti:sapphire laser oscillator. If this system is extended to the CPA system and supported by the real-time SPIDER, sensitive coherent control of the high-order harmonics will be possible.

More detailed research results are given in the Appendix (II), as summarized in the below:

A. 1. High harmonic X-ray generation

- A. 1. 1. Coherent control of high-order harmonics with chirped femtosecond laser pulses
- A. 1. 2. Continuously tunable high-harmonic x-rays from atoms in an intense femtosecond laser field
- A. 1. 3. Bright, low-divergence high-order harmonic generation in a long gas jet

A. 2. Theory development of high harmonic generation

- A. 2. 1. Self-phase modulation of laser pulse propagating in an ionizing medium.
- A. 2. 2. Propagation of high-order harmonics
- A. 2. 3. Attosecond pulse generation

A. 3. Operation and development of femtosecond terawatt lasers

- A. 3. 1. Development of a 1 kHz femtosecond terawatt laser

A. 3. 2. Temporal structure of chirped laser pulses

A. 3. 3. Graphical interpretation of instantaneous carrier frequency of chirped femtosecond pulses using the Wigner time-frequency distribution

A. 3. 4. Temporal characterization of femtosecond laser pulses using spectral phase interferometry for direct electric-field reconstruction (SPIDER)

A. 4. Emission of a hot electron jet from intense femtosecond laser-cluster interactions

(c) Third year (2001)

(1) High harmonic X-ray generation

First, we demonstrated the continuous wavelength tuning of high-order harmonics using the coherent control of high-order harmonic generation with chirped femtosecond laser pulses for spectral sharpness and brightness. Experiments on continuously tunable HHG were carried out using a femtosecond terawatt Ti:sapphire laser operating at 10 Hz. The laser spectrum was centered at 824 nm with a spectral bandwidth of 47 nm. Continuous tuning of high-order harmonics, without losing spectral sharpness, was achieved by controlling incident laser energy and laser chirp. The incident laser intensity was varied with the control of the incident laser energy using a half-wave plate and polarizers installed in front of the pulse compressor. The control of the incident laser energy was thus achieved without altering the focusing geometry.

To extend the tunable wavelength range, we changed the species of atom and achieved efficient harmonic generation and sufficient wavelength tuning in the required spectral range. Argon atom was chosen for the wavelength tuning up to 41^{st} harmonic order, neon was used for the harmonic order between 41^{st} and 71^{st}, and low-density helium was used for orders higher than 101. Consequently, by choosing proper species of atoms, we have extended the tunable wavelength range of high harmonic x-rays. (This result has been submitted to Phys. Rev. Lett.)

Secondly, the divergence and energy of the high-order harmonics were measured. Spectrally resolved divergence measurements of harmonics were carried out using a cylindrical mirror in the XUV spectrometer in place of the toroidal mirror. The spectral structure of the harmonics was examined in greater detail through these measurements. The measured divergence of the 27^{th} harmonic at 30 nm, generated from Ar was 0.5 mrad (FWHM) and the 61^{st} harmonic at 13.5 nm, generated from Ne, was also measured to have a divergence of 0.7 mrad. These small divergences of the harmonics generated in the long gas jet represents

definite evidence of a large harmonic generation cross section, diameter of 70 μm for harmonic generated from Ar, in comparison to those in a hollow-core fiber(1.5 mrad) and in a gas cell target(2 mrad). (This result will be published in App. Phys. Lett.)

To evaluate the photon number of the generated harmonics, we first measured the throughput of the XUV spectrometer by comparing the harmonic signals under identical harmonic generation conditions, but with and without the XUV spectrograph body in the system. The experimentally measured throughput was 6.7% at 29.4-nm (the wavelength of 27th harmonic). In addition, the absolute photon yields were measured using a calibrated XUV silicon photodiode (International Radiation Detectors Inc. AXUV-100). The sensitivity of the photodiode was estimated from the formula, $N_e = Q_{eff}\, h\nu/3.65$ eV, where N_e is the number of photoelectrons created by a single photon of energy $h\nu$ and Q_{eff} is a the effective quantum efficiency of the photodiode (77% at 29.4-nm wavelength). We measured energy yields for the 27th single harmonic from Ar of up to 4 nJ and for the 61st harmonic from Ne of up to 0.3 nJ per laser pulse.

Thirdly, we measured the degree of spatial coherence of high-order harmonics employing a double pinhole interference experiment. A thick Al-plate with two pinholes was placed 13 cm beyond the target to create the two wave fronts. The diameter of the pinholes was 10 μm. The diffracted wave fronts from the two pinholes interfere and the resulting interference fringe pattern was detected by an x-ray charge coupled device located 104 cm away from the pinhole plate. Here, the diffracted light of the pump laser was blocked by placing a 0.2 μm thick aluminum filter in front of the detector. Experimental results showed that the harmonic x-ray beams from Ne and Ar (wavelength of 13 nm for Ne and 30 nm for Ar) are highly coherent over almost the entire beam cross section.

(2) Theory development of high harmonic generation

We analyzed the high harmonic signal in the time-frequency domain theoretically. The Wigner and Husimi distribution functions were used to show the quantum mechanical nature of high harmonic signal, and the result was compared with the semiclassical calculations. The close agreement between the two results suggests that the two-step model is adequate to explain the process of high harmonic generation. The phenomenon of high harmonic generation is thus an example which is very good agreement with quantum-classical correspondence.

We developed a simulation code for three-dimensional time-dependent Schrodinger equation. Using this code, we confirmed the main results of harmonic generation obtained previously by using the one-dimensional code and obtained the saturation intensities for atoms that are consistent with the experimental observation.

We used a semiclassical rescattering model to study the momentum distributions of recoil ions from laser induced single and double ionization. It was found that not only in the case of double ionization but also in the case of single ionization, the distributions of the momentum parallel to the polarization direction of the laser field show a double-hump structure as a consequence of the rescattering. By comparison with experimental data we find that, as the intensity of the laser decreases, the rescattering ionization mechanism of the second electron calculated in our model does not dominate the process. In addition, the correlated emission of the electrons in the double ionization is discussed and the effect of the repulsion between the emitted electrons is shown.

The model was also used to study frequency dependence of non-sequential double ionization (NSDI) of Ne. We found that the ratio (Ne^{2+}/Ne^{+}), calculated for the laser intensity of $I=1.0x10^{15}$ W/cm^2, increases while the wavelength decreases down to about 250 nm, the limit of the applied model. Careful investigation of the trajectories shows that there are two categories $x10^{15}$W/cm^2, increases while the wavelength decreases down to about 250 nm, the limit of the applied model. Careful investigation of the trajectories shows that there are two categories of double ionization: "instant ionization" and "delayed ionization." By limiting the time interval between the re-collision time and ionization time, the "delayed ionization" is identified to be responsible for the high probability of NSDI in the short wavelength region.

(3) Operation and development of femtosecond terawatt lasers

We focused our attention on the performance improvement of the 1-kHz chirped-pulse amplification (CPA) laser system developed in the 2nd year and the measurements and control of the shot-to-shot CEP slip of mode-locked laser pulses.

First, we tried to improve the performance of the 1-kHz CPA laser system in two aspects. One is the installation of an acousto-optic programmable dispersive filter (AOPDF) for an adaptive pulse shaping of high-power femtosecond laser pulses and the other is the improvement of the pulse quality of high-power sub-10-fs pulses. We tried to obtain shorter

pulse duration than before, using the AOPDF, which enables reducing the gain narrowing effect in the laser spectrum and compensating for the residual high-order phase distortion of the laser pulses. As an application experiment of the AOPDF-equipped laser, we adaptively controlled a chemical reaction induced by femtosecond laser pulses, showing that the equivalent adaptive control can also be employed in the generation of the high-order harmonics. On the other hand, to generate the high-power sub-10-fs pulses with improved beam quality from a hollow-fiber/chirped-mirror compression system installed in the 2nd year, we accurately adjusted the laser energy, the pressure of gas and the alignment of launching optics. We investigated various conditions to suppress the wing structure in the temporal shape, and reducing the pulse duration and to obtain nearly Gaussian spatial beam profile.

Second, we tried to measure the shot-to-shot CEP slip of mode-locked laser pulses using a $2f$-to-f self-referencing interferometer. To generate a one-octave continuum, we launched the mode-locked femtosecond pulses into a microstructure air-silica fiber, and observed the beat signal between two 2-f frequency components produced in the interferometer which yielded the information of the shot-to-shot CEP slip of the laser pulses. We controlled the CEP slip by adjusting the related parameters, i.e., intracavity prism depth and intracavity laser energy, and measured the quantitative dependence of the shot-to-shot CEP slip on those parameters. The active control through the feedback control, based on the information given by these measurements, is currently being developed.

In addition, we developed a new phase retrieval technique of sub-10-fs laser pulses from an interferometric autocorrelation measurement. For this purpose, we used an evolutionary algorithm similar to that developed for the adaptive control of the chemical reaction. Because of the experimental simplicity of the IAC measurement, this technique allows an easy and simple characterization of sub-10-fs optical pulses.

More detailed research results are given in the Appendix (III), as summarized in the below:

A. 1. High harmonic X-ray generation

- A. 1. 1. Chirp analysis of high-order harmonics from atoms driven by intense femtosecond laser pulses
- A. 1. 2. Generation of high harmonics with low beam divergence and good wavelength tunability
- A. 1. 3. Wave-front phase measurements of high-order harmonic beams using the point-diffraction interferometry

A. 2. Theory development of high harmonic generation

A. 2. 1. Time-frequency analysis of high harmonic generation

A.2. 2. Ion momentum distribution for He single and double ionization in strong laser field

A. 2. 3. Frequency dependence of non-sequential double ionization

A. 3. Operation and development of femtosecond terawatt lasers

A. 3. 1. Performance improvement of a 1 kHz femtosecond high-power laser

A. 3. 2. Electric-field recovery of sub-10-fs laser pulses from interferometric autocorrelation using an evolutionary strategy

A. 3. 3. Measurement of shot-to-shot carrier-envelope phase slip of femtosecond laser pulses.

B. Research results

(a) First year (1999)

The most important achievement in this year for the realization of a tunable coherent femtosecond X-ray source is the demonstration of the wavelength tuning over two times the laser frequency using the harmonics in the orders from 65 (12.2 nm) to 91 (8.6 nm). In addition to the wavelength tuning using the nonadiabatic blueshift of high harmonics (introduced by this research group in Phys. Rev. Lett **83**, 2544(1999)), high harmonic signals were optimized, for given laser parameters, to obtain the brightest and sharpest harmonic signal by adjusting the laser chirp condition. The detailed description on this result is given in the Appendix A.1.1 that will be submitted to Nature with some refinements. This is a crucial achievement of an important milestone for the realization of a tunable coherent femtosecond X-ray source. The next milestone to tackle in the second year would be the generation of high harmonic X-rays with high conversion efficiency.

The spectral structure study of high harmonics revealed that the chirp structure of harmonics was much more complex than previously known. Depending on the experimental parameters taken for HHG, the sign of the harmonic chirp has changed. Previously, only negative harmonic chirp due to atomic chirp was thought to be crucial. However, the spectral structure study clearly showed that the harmonic chirp could be positive under intense laser field. This result suggest a new direction in the study of HHG physics. One paper on this finding is being prepared for submission to Physical Review Letters.

Another important achievement in this year is the development of theoretical calculation tools

based on the time-dependent Schrodinger equation. The introduction of the coherent sum technique and the time-frequency analysis in the interpretation of high harmonic spectra opened new theoretical methodology that would be very powerful in the correct analysis of experimental results. The coherent sum technique (Appendix A (I).2.1) will be published in Physical Review A, and the time-frequency analysis (Appendix A (I).2.2) is under the review process in Physical Review Letters. The latter explicitly revealed for the first time the dynamically induced harmonic chirp that would help to understand the chirped spectral structure of high harmonics, a hot topic in the recent high harmonic generation research.

(b) Second year (2000)

The most important achievement in this year is the generation of bright (> 1 nJ/pulse for 29^{th} harmonic from argon) and low beam divergence harmonics (< 0.5 mrad) using a long gas jet through proper guidance of the refracting laser pulse. The detailed description on this result is given in the Appendix A (II).1.3 that will be submitted to Physical Review Letters with some refinements. In addition to the efficient harmonic generation, we demonstrated continuous wavelength tuning of high harmonics without sacrificing spectral sharpness, achieved through control of the laser intensity and chirp. This opens a pathway to the realization of a continuously tunable, coherent, femtosecond x-ray source, i.e. a tabletop synchrotron. One paper on this finding was submitted to Science (Appendix A (II). 1.2).

Our one-dimensional numerical simulations revealed how the propagation of high harmonics modifies the single-atom harmonic spectra. First, those harmonic components depending sensitively on the laser intensity are suppressed, and thus the harmonic spectra are cleaned up. Second, when the laser intensity is very strong, the plasmas produced in the medium induce a positive frequency chirp on the leading edge of the laser pulses, which subsequently drive high harmonic to become positively chirped. Depending on system parameters and harmonic order, this leads to spectral line broadening or narrowing. Third, in addition to the single-atom blueshift, the self-phase modulation of laser pulses also induces a blueshift of high harmonics. These results are reported in a paper recently submitted to Physical Review A.

Main achievement in the femtosecond laser technology is the operation of a 23-fs, 0.1-TW CPA Ti:sapphire laser operating at the repetition rate of 1 kHz. The front-end oscillator was setup in a simple long-cavity type and delivered 12-fs laser pulses with the energy of 12 nJ at the repetition rate of 26 MHz. This oscillator efficiently offered high-peak-power (1 MW)

pulses to the CPA system without any reduction of laser spectrum. One paper regarding to the long-cavity Ti:sapphire oscillator is being prepared, and another one will be also written after full characterization of the 23-fs, 0.1-TW CPA Ti:sapphire laser. Further pulse shortening using a hollow-core-fiber and chirped-mirror compression system was succeeded, resulting in the generation of 8.8-fs pulses at 1 kHz. (Appendix A (II).3.1) The second achievement is the temporal characterization and time-frequency analysis of chirped femtosecond pulses. One paper on this topic is being prepared. Another achievement is the development of a real-time, single-shot SPIDER apparatus. One paper on this topic was published (Appendix A (II).3.3) in a domestic journal. One more paper on an adaptive pulse shaping (Appendix A (II).3.4) supported by SPIDER technique is being prepared.

(c) Third year (2001)

The most important achievement in this year has been the generation of continuously tunable high-order harmonics using the coherent control of high-order harmonic generation with chirped femtosecond laser pulses for spectral sharpness and brightness. The detailed description of this investigtion is given in the Appendix A.1.1 and A.1.2. In addition to the tunable harmonic generation, we demonstrated that the harmonic beam is highly coherent over almost the entire beam cross section (Appendix A (III).1.3). This result is reported in a paper recently submitted to Optics Letters.

In the harmonic theory part, we performed time-frequency analysis of high harmonic generation processes and found strong quantum-classical correspondence, which explains the success of the popular three-step model (Appendix A (III).2.1). Moreover, a fast code for time-frequency analysis based on parallel computing was developed.

The three-dimensional simulations of time-dependent Schrödinger equation repeated the main results of one-dimensional code and, in addition, gave the saturation intensities for atoms. Furthermore, the momentum distributions of recoil ions from laser induced single and double ionization and frequency dependence of double ionization were studied using a semiclassical model. The effect of rescattering is also found in the single ionization case as in the double ionization case. It is also found that when the intensity of the laser decreases, other mechanisms besides rescattering may dominate the process (Appendix A (III).2.2). Furthermore, we found that there are two categories- "delayeinstant ionization" and "delayed ionization", and the later is identified to be responsible for the high double ionization rate in the short wavelength region (Appendix A (III).2.3). These results were reported in a paper published in Phys. Rev. A and another paper has been submitted to J. Phys. B.

The main achievements in the laser part are: the performance improvement of the 1-kHz CPA laser system developed in the 2nd year, the shot-to-shot CEP slip measurement of mode-locked laser pulses, and the development of a new pulse characterization technique.

First, the performance improvement of the 1-kHz CPA laser system was tackled in two ways. On one hand, we provided an adaptive pulse shaping capability in the CPA laser by installing an AOPDF, and, on the other hand, we improved the temporal and spatial beam quality of high-power sub-10-fs pulses using a hollow-fiber/chirped-mirror compression system. With the help of the AOPDF, we obtained 20-fs high-power laser pulses at 1 kHz directly from the CPA laser and adaptively controlled a chemical reaction induced by femtosecond laser pulses. The latter result shows that an equivalent adaptive control can be applied in the generation of the high-order harmonics. We investigated various conditions for the continuum generation process in a hollow fiber filled with noble gas. We finally chose a 60-cm-long hollow fiber with a diameter of 0.32 mm filled with neon gas at the pressure of 2.6 bars and generated a continuum with a spectral width of 200 nm (in full width at half-maximum) and with a good spatial beam profile. The refined usage of the hollow-fiber/chirped-mirror compression made it possible to obtain high-power 8.3-fs pulses at 1 kHz with a good temporal and spatial beam quality. (described in appendix A (III). 3. 1)

Second, we measured the shot-to-shot CEP slip of mode-locked laser pulses using a $2f$-to-f self-referencing interferometer. The beat signal from the interferometer was observed in time and frequency domain, which revealed the shot-to-shot CEP slip of the laser pulses. The measured jitter of the shot-to-shot CEP slip was 2.7 mrad. The CEP slip was successfully controlled by the adjustment of the intracavity prism depth and the intracavity laser energy. The quantitative dependence of the shot-to-shot CEP slip on those parameters was also measured, which provided us with the quantitative information for the design of an active feedback control loop to stabilize the shot-to-shot CEP slip. (as described in appendix A (III). 3. 2)

Third, using an evolutionary algorithm, we developed a new phase retrieval technique of sub-10-fs laser pulses from an interferometric autocorrelation measurement. This algorithm worked well with numerically generated femtosecond pulses. In the experiments, we reliably characterized a 29-fs negatively chirped laser pulse and a sub-10-fs pulse with high-order phase distortion. (as described in appendix A (III). 3. 3)

6. Details of Research Achievements

A. Journal Papers

1. J. H. Kim, H. J. Shin, D. G. Lee, and C. H. Nam, "Enhanced spectral resolution of high-order harmonics by the coherent sum of dipole spectra," *Phys. Rev. A* **62**, 055402 (2000).
2. Y. H. Cha, K. H. Hong, and C. H. Nam, "Incorporation of a cavity-dumped oscillator in a long-wavelength injected femtosecond terawatt Ti:sapphire laser," *Opt. Commun.* **185**, 413 (2000).
3. T. Mocek, C. M. Kim, H. J. Shin, D. G. Lee, Y. H. Cha, K. H. Hong, and C. H. Nam, "Enhancement of soft X-ray emission from a cryogenically cooled Ar gas jet irradiated by 25 fs laser pulse," Appl. Phys. Lett. **76**, 1819 (2000).
4. T. Mocek, C. M. Kim, H. J. Shin, D. G. Lee, Y. H. Cha, K. H. Hong, and C. H. Nam, "Investigation of an optical-field-ionized oxygen plasma for a table-top soft X-ray laser," J. Korean Phys. Soc. **36**, 269 (2000).
5. T. Mocek, C. M. Kim, H. J. Shin, D. G. Lee, Y. H. Cha, K. H. Hong, and C. H. Nam, "Soft X-ray emission from small-sized Ne clusters heated by intense, femtosecond laser pulses," Phys. Rev. E **62**, 4461 (2000).
6. T. M. Jeong, C.-M. Chung, H. S. Kim, C. H. Nam, and C.-J. Kim, "Generation of Passively Q-switched and Mode-locked pulse from Nd:YVO4 Laser with Cr4+:YAG Saturable Absorber," Elec. Lett. **36**, 633 (2000).
7. H. Fiedorowicz, A. Bartnik, M. Szczurek, C. H. Nam, T. Mocek, H. J. Shin, Y. H. Cha, D. G. Lee, and K. H. Hong, "Femtosecond-pulse-driven soft X-ray laser studies using a gas puff target irradiated with a Ti:Sapphire laser," Opt. Appl. **30**, 93 (2000).
8. D. G. Lee, H. J. Shin, Y. H. Cha, K. H. Hong, and C. H. Nam, "Selection of high-order harmonics from a single quantum path for the generation of an attosecond pulse train," *Phys. Rev. A* **63**, 021801(R) (2001)
9. J. H. Kim, J. M. Yuan, W. K. Liu, and C. H. Nam, "Nonspreading wave packets of diatomic molecules: Generation and control," *Phys. Rev. A* 63, 043420 (2001).
10. H. J. Shin, D. G. Lee, Y. H. Cha, J. H. Kim, K. H. Hong, and C. H. Nam, "Nonadiabatic blueshift of high harmonic from Ar and Ne atoms in an intense femtosecond laser field," *Phys. Rev. A* **63** , 053407 (2001)
11. J. H. Kim, D. G. Lee, H. J. Shin, and C. H. Nam, "Wigner Time-Frequency Distribution of High-Order Harmonics," *Phys. Rev. A* **63** , 063403 (2001)

12. C. H. Nam, D. G. Lee, J. H. Kim, Y. H. Cha, and I. W. Choi, "High Harmonic Spectra from Neon Atoms in an Intense Femtosecond Laser Field," *J. Korean Phys. Soc.* **39**,873 (2001).
13. C. H. Nam, H. J. Shin, D. G. Lee, Y. H. Cha, K. H. Hong, and J. H Kim, "Tunable coherent femtosecond x-ray source driven by an intense femtosecond laser," *J. de Phys. IV* **11** (PR2), 345-350 (2001).
14. T. Mocek, C. M. Kim, H. J. Shin, D. G. Lee, Y. H. Cha, K. H. Hong, and C. H. Nam, "Interaction of intense, femtosecond laser pulse with small-sized Ne clusters," *J. de Phys. IV* **11** (PR2), 433-436 (2001).
15. H. Fiedorowicz, A. Bartnik, M. Szczurek, T. Mocek, H. J. Shin, Y. H. Cha, D. G. Lee, K. H. Hong, and C. H. Nam, "Investigations on femtosecond-pulse-driven soft x-ray lasers using a gas puff target irradiated with a Ti:Sapphire laser," *J. de Phys. IV* **11** (PR2), 197-200 (2001).
16. D. G. Lee, J. H. Kim, K. H. Hong, and C. H. Nam, "Coherent Control of High-Order Harmonics with Chirped Femtosecond Laser Pulses," *Phys. Rev. Lett.* **87**, 243902 (2001).
17. C. H. Nam, D. G. Lee, J. H. Kim, Y. H. Cha, and I. W. Choi, "High Harmonic Spectra from Neon Atoms in an Intense Femtosecond Laser Field," *J. Korean Phys. Soc.* **39**, 873 (2001).
18. J. H. Kim and C. H. Nam, "Plasma-induced frequency chirp of intense femtosecond lasers and its role in shaping high-order harmonic spectral lines," *Phys. Rev. A* **65**, 033801 (2002).
19. T. Mocek, C. M. Kim, H. J. Shin, D. G. Lee, Y. H. Cha, K. H. Hong, and C. H. Nam, "Investigation of soft x-ray emission from Ar clusters heated by ultrashort laser pulses," Laser Part. Beams **20**, 51-57 (2002).
20. L. M. Chen, J. J. Park, K.-H. Hong, J. L. Kim, J. Zhang, and C. H. NAM, "Emission of a hot electron jet from intense femtosecond laser-cluster interactions," Phys. Rev. E **66**, 025402(R) (2002).
21. L. M. Chen, J. J. Park, K. H. Hong, I. W. Choi, J. L. Kim, J. Zhang, and C. H. NAM, "Measurement of energetic electrons from atomic clusters irradiated by intense femtosecond laser pulses," Phys. Plasmas **9**, 3595-3599 (2002).
22. J. H. Sung, K.-H. Hong, Y. H. Cha, and C. H. Nam, "13-fs, 1-MW Ti:sapphire laser oscillator in a long-cavity configuration," Japan. J. Appl. Phys. **41**, L931-L934 (2002).
23. K.-H. Hong, J.-H. Kim, Y. H. Kang, and C. H. Nam, "Time-frequency analysis of chirped femtosecond pulses using Wigner distribution function," Appl. Phys. B **74**, S231-S236 (2002).

24. T. J. Yu, Y. H. Cha, and C. H. Nam, "Regenerative third-harmonic FM mode-locking in a bulk Nd:YLF laser," Japan. J. Appl. Phys. **41**, L471 (2002).
25. D. G. Lee, I. W. Choi, H. T. Kim, K. H. Hong, A. Bartnik, H. Fiedorowicz, and C. H. Nam, "Generation of bright low-divergence high-order harmonics in a long gas jet," Appl. Phys. Lett. (accepted).
26. Sung-Hae Lee, Kyung-Hoon Jung, Jae Hee Sung, Kyung-Han Hong, and Chang Hee Nam, "Adaptive quantum control of DCM fluorescence in the liquid phase," J. Chem. Phys. (accepted).
27. K.-H. Hong, J. H. Sung, Y. S. Lee, and C. H. Nam, "Temporal characterization of chirped femtosecond laser pulses," Opt. Commun. (accepted).
28. J. Chen and C. H. Nam, "Momentum distribution of single and double ionization," Phys. Rev. A (accepted).

B. International Conferences

(1) Invited presentation

1. C. H. Nam, H. J. Shin, D. G. Lee, Y. H. Cha, and K. H. Hong, "Tunable coherent femtosecond X-ray source drinven by an intense femtosecond laser," 7th Int. Conf. on X-ray Lasers, 19–23 June, 2000, Saint Malo, France.
2. C. H. Nam, H. J. Shin, D. G. Lee, Y. H. Cha, and J. H. Kim, "Tunable high harmonic generation from atoms driven by intense femtosecond laser," Atoms, Molecules and Quantum Dots in Laser Fields, 12–16 June, 2000, Pisa, Italy.
3. Y. H. Cha, K. H. Hong, J. H. Sung, and C. H. Nam, "Femtosecond terawatt Ti:sppphire laser at KAIST," Asia Pacific Laser Symposium, 21–26 August, 2000, Shanghai, China.
4. C. H. Nam, "VUV coherent source with high-order harmonics," OECD Global Science Forum on Compact High-Intensity Short Pulse Lasers, May 28-31, 2001, Kyoto, Japan.
5. C. H. Nam, D. G. Lee, H. T. Kim, K. H. Hong, I. W. Choi, J. H. Kim, "Efficient high-order harmonic generation using a long gas jet," SPIE's 46th Annual Meeting, July 29 – August 3, 2001, San Diego, USA
6. L. M. Chen, J. J. Park, K. H. Hong, J. Y. Kim, C. H. Nam, "Measurement of energetic hot electrons from atomic Xe and Ar clusters irradiated by intense femtosecond laser pulses," IFSA 2001, September 9-14, 2001, Kyoto, Japan (to be presented).
7. C. H. Nam, D. G. Lee, H. T. Kim, K. H. Hong, I. W. Choi, and J.-H Kim, "Coherent

Femtosecond X-Ray Source Based on High-Order Harmonics (Invited)," 14th Annual Meeting of the IEEE Laser & Electro-Optics Society, La Jolla, CA (Nov. 12-16, 2001).

8. C. H. Nam, H. T. Kim, K.-H. Hong, D. G. Lee, and J.-H. Kim, "High-order harmonics as a continuously tunable coherent femtosecond x-ray source (invited)," 8th Int. X-ray Laser Conference, Aspen, Colorado (May 24-31, 2002).
9. C. H. Nam, H. T. Kim, K-H. Hong, D. G. Lee, and J.-H. Kim, "Generation of high harmonics with low beam divergence and good wavelength tenability (invited)," 3rd Asia Pacific Laser Symposium, Osaka, Japan (Sep. 17-20, 2002).

(2) Contributed presentation

1. H. J. Shin, D. G. Lee, Y. H. Cha, K. H. Hong, and C. H. Nam, "Generation of high-order harmonics originated from a single quantum path," CLEO/QELS 2000, 7–12 May, 2000, San Francisco, USA.
2. T. Mocek, C. M. Kim, H. J. Shin, D. G. Lee, Y. H. Cha, K. H. Hong, and C. H. Nam, "Soft X-ray emission from small-sized Ar clusters heated by intense, femtosecond laser pulses," CLEO/QELS 2000, 8–12 May, 2000, San Francisco, USA.
3. D. G. Lee, H. J. Shin, Y. H. Cha, J.-H. Kim, C. H. Nam, "Control of the high-harmonic spectral structure for attosecond pulse generation," Atoms, molecules and quantum dots in Laser fields, 12–16 June, 2000, Pisa, Italy.
4. J. H. Kim, H. J. Shin, D. G. Lee, and C. H. Nam, "Enhanced spectral resolution of high-order harmonics by the coherent sum of dipole spectra," Atoms, molecules and quantum dots in Laser fields, 12–16 June, 2000, Pisa, Italy.
5. T. Mocek, C. M. Kim, H. J. Shin, D. G. Lee, Y. H. Cha, K. H. Hong, and C. H. Nam, "Soft X-ray emission from Ar clusters heated by ultrashort laser pulses," XXVI European Conference on Laser Interaction with Matter, 12–16 June 2000, Prague, Czech Republic.
6. T. Mocek, C. M. Kim, H. J. Shin, D. G. Lee, Y. H. Cha, K. H. Hong, and C. H. Nam, "Interaction of intense, femtosecond laser pulse with small-sized Ne clusters," 7th Int. Conf. on X-ray Lasers, 19–23 June, 2000, Saint Malo, France.
7. H. Fiedorowicz, A. Bartnik, M. Szczurek, T. Mocek, H. J. Shin, Y. H. Cha, D. G. Lee, K. H. Hong, and C. H. Nam, "Investigations on femtosecond-pulse-driven soft X-ray lasers," 7th Int. Conf. on X-ray Lasers, 19–23 June, 2000, Saint Malo, France.
8. C. H. Nam, T. Mocek, C. M. Kim, I. W. Choi, H. J. Shin, D. G. Lee, and Y. H. Cha, "Spectroscopic study of Ne clusters irradiated by an intense, femtosecond laser," Asia Pacific Laser Symposium, 21–26 August, 2000, Shanghai, China.
9. K. H. Hong, Y. H. Kang, Y, H. Cha, J. H. Kim, and C. H. Nam "Temporal characterization of compressor-controlled chirped pulses from a CPA Ti:sapphire laser,"

CLEO/Pacific Rim 2001, July 15-19, 2001, Chiba, Japan.

10. J. H. Kim, D. G. Lee, and C. H. Nam, "Time-Frequency Characterization of High-Harmonics Generation by Intense Femtosecond Laser Pulses," CLEO/Pacific Rim 2001, July 15-19, 2001, Chiba, Japan.
11. K. H. Hong, Y. H, Kang, Y. H. Cha, J. H. Kim, C. H. Nam, "Time-Frequency Analysis of Chirped Femtosecond Pulses Using the Wigner Distribution Function," Ultrafast Optics 2001, July 22-26, 2001, Montebello, Canada.
12. J. H. Kim, K. H. Hong, C. H. Nam, "Plasma-Induced Frequency Modulation of High-Order Harmonics," Ultrafast Optics 2001, July 22-26, 2001, Montebello, Canada.
13. Dong Gun Lee, Il Woo Choi, Hyung Taek Kim, Jung-Hoon Kim, and Chang Hee Nam, "Generation of low beam divergence harmonics using a long gas jet," Applications of High Field and Short Wavelength Sources IX, Palm Springs, California (Oct. 21-24, 2001).
14. Hyung Taek Kim, Dong Gun Lee, Jung-Hoon Kim, Il Woo Choi, and Chang Hee Nam, "Chirp analysis of high-order harmonics from atoms driven by intense femtosecond laser pulses," Applications of High Field and Short Wavelength Sources IX, Palm Springs, California (Oct. 21-24, 2001).
15. Hyung Taek Kim, I Jong Kim, Dong Gun Lee, Jong Ju Park, Kyung ?Han Hong, and Chang Hee Nam, "Highly Efficient High-order Harmonic Generation at 13 nm with a Long Gas Jet," 3rd Asia Pacific Laser Symposium, Osaka, Japan (Sep. 17-20, 2002).
16. Jae Hee Sung, Kyung-Han Hong, and Chang Hee Nam, "Generation of high-power sub-10 fs optical pulses at 1 kHz repetition rate," 3rd Asia Pacific Laser Symposium, Osaka, Japan (Sep. 17-20, 2002).

Appendix (I)

Research Results of FY 1999

A. 1. High Harmonic X-Ray Generation

A. 1. 1. Continuously Tunable High Harmonic X-Ray Generation from Atoms in an Intense Femtosecond Laser Field

When gaseous atoms are exposed to a strong laser field, i.e. an oscillating electromagnetic field, the periodic modulation of the electron motion in the atoms produces very high-order harmonics [1,2]. As with the recent advancement of femtosecond high power laser technologies, the shortest harmonic wavelengths reached the water-window x-ray region and the harmonic conversion efficiency was also greatly improved [3,4]. The high harmonic x-rays possess unique properties, such as good directionality and coherence as well as extremely short pulse duration, inherited from the driving laser [5-8]. As the gaseous medium carries an inversion symmetry, only odd harmonics of the laser frequency can be produced. Still obtainable harmonic wavelengths are numerous; however, the applicability of the harmonic x-ray source will be limited if only fixed, odd harmonic wavelengths are available. Though the synchrotron x-ray source can provide a continuously tunable x-ray radiation, its accessibility is limited and it cannot provide x-ray pulses shorter than a few tens of picosecond. Here we demonstrate, by applying an intense femtosecond laser pulses to atoms, the generation of continuously tunable high-harmonic x-rays, opening a way to realize a tabletop synchrotron.

The most reliable x-ray source so far has been synchrotrons that can provide bright x-rays in a wide wavelength range. For the last 30 years many fascinating experiments have been performed using the synchrotron beam lines throughout the world. One limitation imposed on synchrotron x-rays is that the pulse duration is longer than a few tens of picosecond, restricting the attainable temporal resolution to the picosecond range On the other hand, the high harmonic x-ray source can have much shorter duration, down to the femtosecond or even attosecond range, though its brilliance cannot compete with the synchrotron. Consequently, the high harmonic x-ray source can compliment the synchrotron x-ray source in the measurement of ultrafast phenomena.

The high harmonic x-rays have recently been applied to various areas. The high harmonics was used to diagnose near solid-density plasma produced by a subpicosecond laser [9]. The XUV interferometry using high harmonics was applied to probe laser-produced plasmas [10,11]. High harmonic x-rays were also useful in measuring the photoionizaton cross section and lifetime of excited He states, due to their short pulse duration [12,13]. The high harmonic x-rays were valuable as a light source for photoemission spectroscopy that could measure the energy relaxation kinetics in quartz [14] and ultrafast electron transport in semiconductors [15]. As the range of available

high harmonic wavelengths with sufficient strength for metrology increases with the improvement of HHG techniques, it is anticipated that the applications of high harmonic x-rays will be quickly expanded to many areas.

High harmonic generation (HHG) is a process that emits harmonic radiation from the periodic modulation of the electron motion in an atom by a strong laser pulse. With the application of intense femtosecond laser to achieve efficient harmonic generation in very high orders, atoms are exposed to rapidly varying laser field, and the electron motion in the atom deviates from the periodic one. This causes the emitted harmonic radiation to shift its frequencies from the odd harmonics of the driving laser frequency [16]. Here only the HHG from neutral atoms is considered since the phase matching condition for the coherent growing of emitted harmonics is much more severe to satisfy in the case of harmonics from ions. In the case of the laser intensity exceeding the saturation intensity for the optical field ionization, the high harmonics are emitted mainly in the leading edge of the laser pulse because of the depletion of neutral atoms before the peak of the laser pulse. The neutral atoms then can see only the rapidly increasing electric field, and as a result the high harmonics emitted experience frequency shift due to the nonadiabatic change of the electric field seen by the atoms. The harmonic frequency shift in the rising edge occurs towards a shorter wavelength, i.e blueshift. This property of harmonic blueshift can be applied to the realization of the continuously tunable x-ray source.

The HHG experiment on non-adiabatic blueshift was performed with a femtosecond terawatt Ti:sapphire laser operating at 10 Hz. The Ti:sapphire laser implemented the long-wavelength injection method to generate a broad amplified spectrum in the chirped-pulse amplification (CPA) Ti:sapphire laser [17]. The laser beam was focused into a gas jet for HHG. The full width at half maximum of the gas-density profile was about 700 μm. The high harmonic spectra were detected by a flat-field extreme-ultraviolet (XUV) spectrometer equipped with a back-illuminated X-ray charge-coupled device (CCD) with 330 × 1,100 pixels (Princeton Instruments). In order to block a stray laser light two Zr filters of 0.2-um thickness were installed in front of the CCD. Intensity control.

For the generation of large nonadiabatic blueshift intense femtosecond laser pulses are applied to Ne atoms. The condition to generate strong high harmonics also requires the application of an intense laser pulse to the atoms before all neutrals are ionized. High harmonic spectrum from 47^{th} to 97^{th} orders from Ne atoms is shown in Fig. 1. The applied laser pulse had the duration of 27 fs, intensity of $1x10^{16}$ W/cm^2, and wavelength of 817 nm. The peak gas density at the interaction region was $3x10^{18}$ cm^{-3}. The wavelength calibration of the spectrometer was done using the argon spectral lines from Ar^{7+} ions produced by interacting the high-density argon gas jet with the laser pulse. Here the harmonic of 53^{rd} order was observed at the position of 55^{th} order, having a blueshift of two times the laser frequency, and the harmonic of 93^{rd} order was observed at the position of 97^{th} order, a blueshift of four times the laser frequency. This is very large frequency shifts, enough to cover the frequency interval between odd harmonics.

High harmonics can be blueshifted due to the self-phase modulation (SPM) of the driving laser in an ionizing medium [18,19]. The nonadiabatic blueshift of harmonics from atoms in a rapidly increasing laser field is basically a single atom effect, while the SPM effect is a result of the propagation of the driving laser pulse through interacting medium. These two effects have different origins and characteristic behaviors, which are readily distinguishable. In the inset of Fig. 1, the fractional frequency shift, plotted with respect to the harmonic order, increases with order. This is one of the evidences predicted by HHG theory that the observed blueshift comes from the nonadiabatic effect In the case of the blueshift due to the SPM effect, the fractional frequency shift should be constant. Furthermore, the measurement of harmonic blueshift over the gas density does not show much density dependence of the blueshift, which confirms that the blueshift is mainly due to the nonadiabatic effect.

The strong blueshift of high harmonics from atoms driven by intense femtosecond pulses is also confirmed in the numerical calculation of the time-dependent Schrodinger equation. Under the experimental condition of 27 fs and $1x10^{16}$ W/cm^2, the single atom calculation gives a complicated spectral structure even for the short trajectory component of high harmonics, and the harmonic peaks of different orders cannot be distinguished. This problem however can be resolved using the time-frequency domain

analysis method. By calculating the Wigner distribution the high harmonic frequency distribution in time can be obtained, which enables the precise estimation of the harmonic blueshift. It also reveals that the high harmonics contain large induced negative chirp and the spectrum of one harmonic order overlaps with adjacent orders. The experimentally observed discrete harmonic peaks however are believed to come from the restructuring of harmonic spectrum during the propagation through the medium. Since the HHG medium is partially ionized during the strong harmonic generation, the free electrons induce a phase-mismatch among harmonics generated at different positions; it limits the coherent growing of harmonics in the trailing part of the harmonic pulse. It consequently shortens the harmonic pulse train and also reduces the spectral broadening so that the well-resolved harmonic peaks are observed. When the spectral modification due to the propagation effect is taken into account, a good agreement is reached between the experiment and calculation.

The large induced chirp in high harmonic spectral structure shown in the single atom calculation is not a promising feature in the application of HHG. It means that the high harmonics have broad spectral structure and, consequently, low intensity. It is known that the harmonic chirp can be compensated for by using a chirped laser pulse. For this purpose the generation of chirped pulses is achieved by changing the distance between the compression gratings that is the last stage in the CPA laser system. This method of generating chirped pulse does not modify the amplified laser spectrum. It is an important feature since in a CPA laser the modification of the laser chirp before amplification means the modification of the amplified spectral structure that is directly linked with the temporal profile of the laser output. The comparison of experimental data is therefore much more direct when the laser chirp is controlled at the last stage. The final laser output is characterized using the frequency-resolved optical gating technique.

When chirped laser pulses are applied to atoms, it is observed that the spectral structure of high harmonics is very sensitively modified. Figure 2 shows the change of harmonic intensity and line width of the 65^{th} harmonic from Ne with respect to the laser chirp. The duration of a chirp-free laser pulse is 27 fs and its intensity is $5x10^{15}$ W/cm^2 at the energy of 3.0 mJ. The gas jet is placed 2 mm after the laser focus to maximize the

harmonic intensity by optimizing the phase matching condition. In the case of the low laser intensity, the use of positively chirped laser pulses enhances the harmonic intensity and sharpens the harmonic line width. This agrees with the previous report by Z. Chang et al. that showed the negative harmonic chirp could be compensated with a positively chirped laser pulse. As the laser intensity is increased, an opposite feature is observed; the negatively chirped laser pulse produces stronger harmonic intensity and sharper spectral width. This kind of behavior has not been observed before. Since it cannot be explained just by considering the atomic chirp, the harmonic chirp composition should be investigated as well with other effects, such as the contribution from SPM. The result in Fig. 2 provides an important basis for the optimization of the HHG process.

The tunability of high harmonic x-rays is sought on the basis of the result in Fig. 2. Figure 3 shows the spectral images of high harmonics obtained by controlling the laser energy and chirp condition. Other experimental parameters not specified are same as in Fig. 2. For the harmonics of orders between 65 and 91, the spectral image clearly shows the continuous frequency shift over two times the laser frequency. Here we arrange the spectral data with nearly equal frequency intervals for the cases of Figs. 3 (a) – (e). The frequency difference between Figs. 3 (e) and (f) is much larger than other cases due to the sensitive intensity dependence of harmonic blueshift at low laser intensity. In this case the precise control of harmonic frequency can be achieved with much more elaborate control of laser energy. This result shows that the continuous frequency tuning over $2\omega_0$, the frequency interval between odd harmonics, can be achieved just by controlling the laser energy and chirp, a critical step towards the realization of a continuously tunable high harmonic x-ray generation.

The continuously tunable high harmonic x-ray source can be applied to many unexplored areas. It will enable the measurement of energy-resolved ultrafast phenomena in surface physics study, the fast excitation of specific state of atoms/ions or biological process, ... It will be useful also as a seeding pulse to an x-ray laser. Instead of starting an x-ray laser from an amplified spontaneous emission (ASE), the x-ray laser injection-seeded from a high harmonic x-ray can have much better coherence property

and shorter pulse duration than those achievable with an x-ray laser based on ASE. For instance, the Ne-like Ag x-ray laser at 10.0 nm seeded by the 79th harmonic, similar to the condition given by Fig. 3, may have a duration in a subpicosecond range, contrary to the usual duration of several hundred picoseconds. Therefore, the addition of tunability to the high harmonic x-ray source will make the applications of high harmonic x-rays much more diverse.

References

[1] A. Mcpherson, G. Gibson, H. Jara, U. Johann, T. S. Luk, I. McInyre, K. Boyer, and C. K. Rhodes, J. Opt. Soc. Am. B **4**, 595 (1987).

[2] M. Lewenstein, Ph. Balcou, M. Yu. Ivanov, A. L'Huillier, and P. B. Corkum, Phys. Rev. A **49**, 2117 (1994).

[3] M. Schnürer, Ch. Spielmann, P. Wobrauschek, C. Streli, N. H. Burnett, C. Kan, Phys Rev. Lett. **80**, 3236 (1998).

[4] E. Constant, D. Garzella, P. Breger, E. Mével, Ch. Dorrer, C. Le Blanc, F. Salin, and P. Agostini, Phys. Rev. Lett. **82**, 1668 (1999).

[5] P. Salières, T. Ditmire, K. S. Budil, M. D. Perry, and A. L'Huillier, J. Phys. B **27**, L217 (1994).

[6] J. Peatross and D. D. Meyerhofer, Phys. Rev. A **51**, R906 (1995).

[7] M. Bellini, C. Lyngå, A. Tozzi, M. B. Gaarde, T. W. Hansch, A. L'Huillier, and C. –G. Wahlström, Phys. Rev. Lett. **81**, 297 (1998).

[8] P. Salières, A. L'Huillier, and M. Lewenstein, Phys. Rev. Lett. **74**, 3776 (1995).

[9] W. Theobald, R. Häßner, C. Wülker, and R. Sauerbrey, Phys. Rev. Lett. 77, 298 (1996).

[10] D. Descamps, et at., Opt. Lett. **25**, 135 (2000).

[11] P. Salières, L. Le Déroff, T. Auguste, P. Monot, P. d'Oliveira, D. Campo, J. –F. Hergott, H. Merdji, and B. Carré, Phys. Rev. Lett. **83**, 5483 (1999).

[12] M. Gisselbrecht, D. Descamps, C. Lyngå, A. L'Huillier, C. –G. Wahlström, and M. Meyer, Phys. Rev. Lett. **82**, 4607 (1999).

[13] J. Larsson, E. Mevel, R. Zerne, A. L'Huillier, C. –G. Wahlström, and S. Svanberg, J. Phys. B **28**, L53 (1995).

[14] F. Quéré, Phys. Rev. B **61**, 9883 (2000).

[15] A. Ruttenberger, P. Leiderer, M. Probst, and R. Haight, Phys. Rev. B **56**, 12092 (1997).

[16] H. J. Shin, D. G. Lee, Y. H. Cha, K. H. Hong, and C. H. Nam, Phys. Rev. Lett. **83**, 2544 (1999).

[17] Y. H. Cha, Y. I. Kang, and C. H. Nam, J. Opt. Soc. Am. B **16**, 1220 (1999).

[18] C.-G. Wahlström, J. Larsson, A. Persson, T. Starczewski, S. Svanberg, P. Salières, Ph. Balcou, and Anne L'Huillier, Phys. Rev. A **48**, 4709 (1993).

[19] K. Miyazaki and H. Takada, Phys. Rev. A **52**, 3007 (1995).

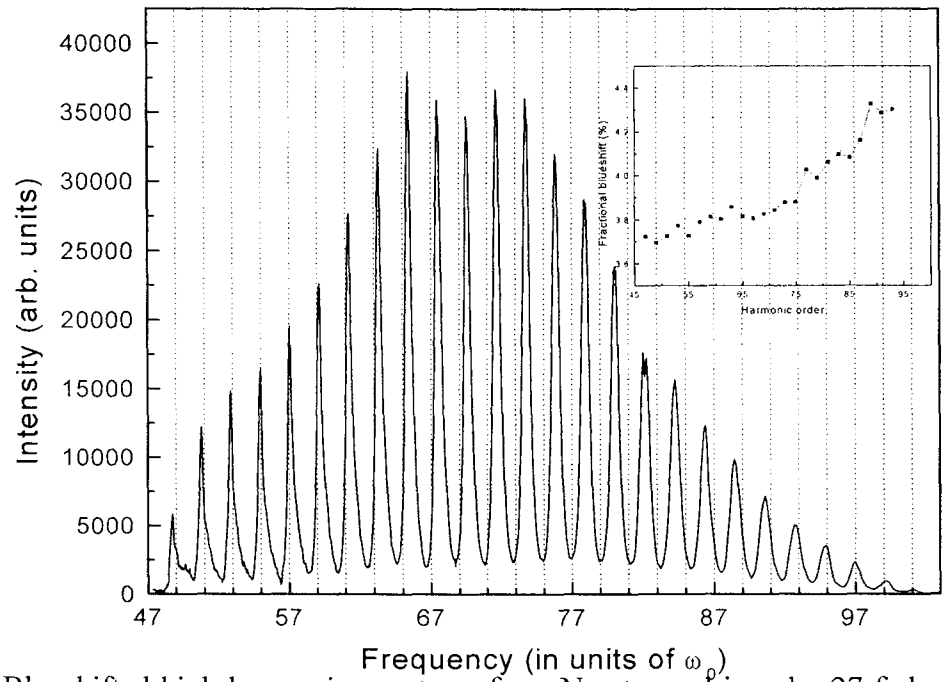

Fig. 1. Blueshifted high harmonic spectrum from Ne atoms driven by 27 fs laser pulse with the intensity of 1×10^{16} W/cm^2. The inset shows the fractional blueshift with respect to harmonic order.

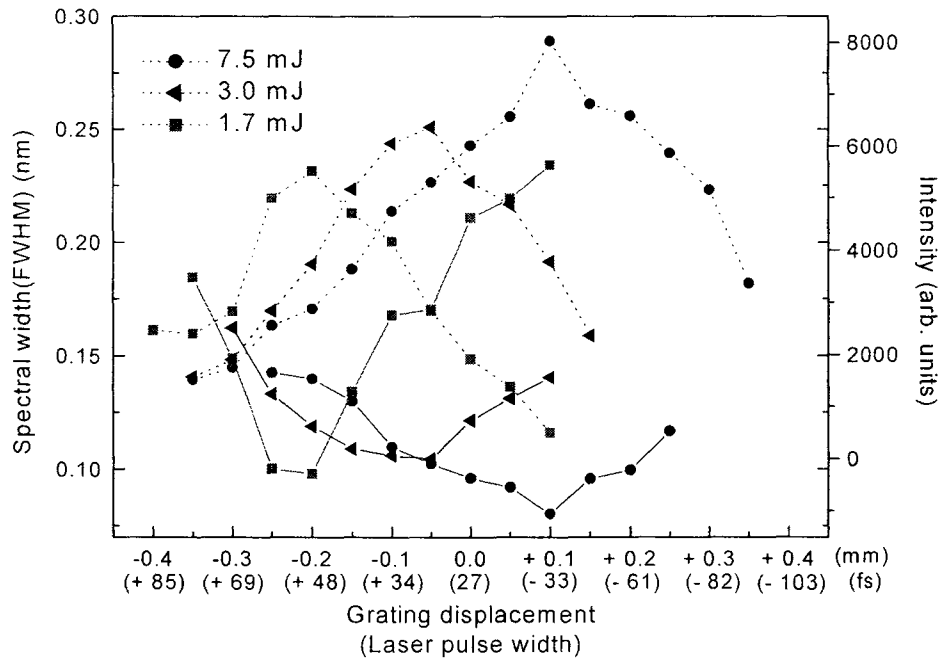

Fig. 2. Intensity and spectral width optimization of the 65th harmonic from Ne achived with the adjustment of the grating separation in the pulse compressor. The duration of chirped pulses measured with the FROG technique is given in the parenthesis.

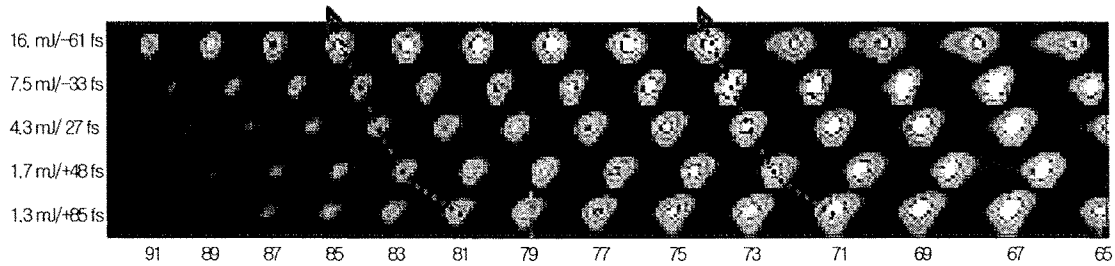

Fig. 3. Wavelength-tunable high harmonic generation from Ne atoms. For the given laser energy, the laser chirp condition was selected to obtain sharpest and brightest signals.

A. 1. 2. Nonadiabatic Blueshift of High Harmonics from Ar and Ne Atoms in an Intense Femtosecond Laser Field

Strong blueshift of high harmonics was observed when intense femtosecond Ti:sapphire laser pulses were applied to Ar and Ne. The blueshift was systematically investigated for various experimental parameters, such as laser intensity, laser pulse duration, and gas density. We observed the harmonic blueshifts of two times the laser frequency in the 39th harmonic from Ar and five times the laser frequency from Ne in the 99th harmonic from Ne. A semiclassical calculation predicted the inverse proportionality of the blueshift to the laser pulse duration, which was confirmed in the experiment done with 30-fs and 80-fs pulses. The density dependence of blueshift showed that the self-phase modulation in an ionizing medium was not a major factor of the observed blueshift. The experimental results along with theoretical calculations showed that the observed blueshift resulted from the nonadiabatic effect due to the rapid increase of a femtosecond laser electric field.

I. Introduction

High-harmonic generation (HHG) in noble gases is a rapidly developing subject in the field of laser-atom interactions [1-4]. HHG has attracted much attention since it is promising as a coherent femtosecond X-ray light source in a tabletop scale. HHG also provides very fundamental information on the interaction between atom and strong laser field. Rapid development of intense femtosecond lasers has prompted great progresses in HHG research. The improved performance of ultrashort lasers have extended the wavelength range of HHG and increased the harmonic conversion efficiency as atoms can be exposed to intense laser field before significant ionization of neutral atoms is being made [5,6]. In addition, theoretical studies showed that XUV pulses with attosecond duration could be generated using the high harmonics obtained under a proper phase-matching condition [7,8].

Harmonics produced by an ultrashort intense laser pulse showed new phenomena that had not been observed in harmonics generated by a relatively long and weak laser pulse. One of these phenomena is the frequency shift of high harmonics. The frequency shift of harmonics was seen with the laser pulses longer than 100 fs [9,10]. It could be understood by considering the change of refractive index during ionization that modulated the wavelength of a propagating laser pulse — the self-phase modulation (SPM) effect in an ionizing gas. In our previous work [11], we reported that a large blueshift could be generated due to the nonadiabatic effect from the rapid increase of the ultrashort laser field when the duration of the driving laser pulse was shorter than 30 fs.

The observed blueshift of the 39th harmonic from Ar was large enough to shift the interval between neighboring odd harmonics.

In this paper we present the systematic investigation of the nonadiabatic blueshift generated by intense femtosecond laser pulses. The dependences of the harmonic blueshift on various experimental parameters, such as laser intensity, pulse duration, gas density, and gas species, are measured. The blueshift due to the nonadiabatic effect is distinguished from that due to SPM in experimental results. The observed results are analyzed using the semiclassical theory. The origin of the observed blueshift is studied, and the characteristic behavior of the harmonic blueshift is obtained. The harmonic blueshift is quantitatively calculated and compared with the observed results.

This paper is organized as follows: In Sec. II, we present the theoretical analysis of the nonadiabatic blueshift using the semiclassical theory. The systematic investigation of harmonic blueshift in Ar and Ne atoms is given in Sec. III. Finally, we conclude in Sec. IV.

II. Calculation of nonadiabatic blueshift

When gaseous atoms are driven by an intense femtosecond laser pulse, the atoms experience the nonadiabatic change of the laser electric field. The high-harmonic emission from these atoms reflects the nonadiabatic effect and the harmonic frequencies deviate from usual odd harmonics of the driving laser frequency. If the applied laser intensity is stronger than the saturation intensity for the optical-field ionization (OFI), the HHG occurs only in the rising edge of the laser pulse and the high harmonics experience blueshift. The nonadiabatic blueshift is different from the blueshift due to SPM in an ionizing medium that the nonadiabatic effect is basically a single atomic effect. In this section, the semiclassical theory based on the SFA model will be used to calculate the nonadiabatic harmonic blueshift since it is relatively simple to calculate and easy to understand the underlying physics of the blueshift, as compared to a quantum-mechanical method such as the numerical calculation of TDSE. The dependences of harmonic blueshift on the laser intensity and the harmonic order are

obtained.

According to the semiclassical two step model, an electron first tunnels the atomic potential modified by the laser field and appears in the continuum. Harmonics are then emitted when the electron driven by the oscillating laser electric field returns to the atom. High-harmonic emission from a single atom can be obtained by calculating the dipole acceleration of a returning electron which is ionized and accelerated by an oscillating electric field. The harmonic spectrum is then obtained from the power spectrum of the dipole acceleration. In the SFA model, the atomic dipole moment is calculated using a saddle-point method [12]. Since the major contribution to the dipole moment calculation in the SFA model comes from the stationary points of the electron wavefunction, the semiclassical theory in which the electron trajectory corresponds to the stationary points basically gives very similar result to the SFA result.

From the SFA model, the phase, θ_q, of the q^{th} harmonic emitted by the electron may be written as [12,13]

$$\theta_q = S(t_q) - q\omega_0 t_q, \tag{1}$$

where ω_0 is the laser frequency and t_q corresponds to the returning time of the electron with the kinetic energy of $q\hbar\omega_0 - E_I$, where E_I is the ionization potential of an atom. The classical action, $S(t_q)$, which is the accumulated phase of the wavefunction of an electron that released from an atom at time t' and returns to the ion at time t_q, is given by

$$S(t_q) = \frac{1}{\hbar}\int_{t'}^{t_q} dt[\frac{1}{2}m_e v(t)^2 + E_I], \tag{2}$$

where the first term in the integrand is the kinetic energy of the electron. The effect of the atomic potential is assumed to be small between t' and t_q, so that the action actually describes the motion of an electron freely moving in the laser field. The action, however, includes the effect of the binding potential through its dependence on E_I.

The fractional frequency shift of the q^{th} harmonic is then calculated by considering the rate of harmonic-phase change:

$$\frac{\Delta\omega_q}{\omega_q} = \frac{1}{q\omega_0}\frac{\Delta\theta_q}{\Delta t} = \frac{2I_p}{\pi}\frac{1}{q}\left(\frac{d\theta_q}{dI}\right)_{I_p}\frac{\delta E}{E}, \quad (3)$$

where I_p is the laser intensity at the time of harmonic generation and δE is the electric-field variation of a laser pulse during a half-optical cycle. Here, the fractional frequency shift is expressed with two terms: the intensity-dependent harmonic phase and the relative electric-field variation. The former, $\frac{2I_p}{\pi}\frac{1}{q}\left(\frac{d\theta_q}{dI}\right)_{I_p}$ in Eq. (3), describes the dependence of harmonic frequency shift on the laser intensity and the harmonic order. The latter, $\frac{\delta E}{E}$, is the relative electric-field variation of a driving laser that does not depend on the harmonic order.

As the power spectrum of the dipole acceleration gives the high-harmonic spectrum, the temporal distribution of the dipole acceleration was examined. The dipole acceleration of an Ar atom driven by a 30-fs Gaussian laser pulse was calculated using the SFA model. The neutral depletion was taken into account by the Ammosov-Delone-Krainov formula [14,15]. Figure 1(a) shows the envelope of the electric field of a 30-fs Gaussian laser pulse and Fig. 1(b) shows the relative electric-field variation of the laser pulse. Figures 1(c) and (d) show the temporal distributions of the dipole acceleration for harmonics between the 21st and 39th orders from an Ar atom driven by a laser pulse with peak intensities of 3.0×10^{14} and 9.0×10^{15} W/cm^2, respectively. In the case of Fig. 1(c), with the laser intensity of 3.0×10^{14} W/cm^2, the actual laser intensity, I_p at the time of maximum dipole acceleration is about 2.5×10^{14} W/cm^2. When the laser intensity is increased to 9.0×10^{15} W/cm^2, much stronger than the saturation intensity of Ar ($\approx3\times10^{14}$ W/cm^2), I_p is about 3.2×10^{14} W/cm^2. Consequently, the actual laser intensity, I_p at the time of maximum dipole acceleration is almost constant, varying only 30 % even though the peak laser intensity increased by 30 times. There is, however, a big difference in the HHG condition. As the laser intensity becomes stronger, the harmonic generation occurs earlier in time. This means that HHG occurs while atoms see larger electric-field variation, as seen in Fig. 1(b).

According to the semiclassical theory, two different electron trajectories within one optical cycle can occur with same recolliding kinetic energy; two electron trajectories, called short and long trajectories, contribute to one harmonic order in the plateau region of high harmonics. In Fig. 2 the harmonic phase of the 31st order from an Ar atom is given with respect to the laser intensity at the time of harmonic emission. Above the threshold intensity of the 31st harmonic, the two trajectories behave differently, but both have positive slopes. Consequently, the sign of the frequency shift of high harmonics follows that of the electric-field variation in Fig. 1(b), i.e. positive in the leading edge and negative in the trailing edge. When the laser intensity is similar to or less than the saturation intensity, high harmonics are generated mostly near the peak of the laser pulse where the electric-field variation is small. The frequency shift then results in the spectral broadening of the high harmonics due to the combination of small harmonic blueshift in the rising edge and small redshift in the falling edge of the laser pulse. On the other hand, when the laser intensity exceeds the saturation intensity, the high harmonics are generated mainly at the rising edge and the frequency shift occurs only toward the blue side. If the laser intensity increases further, the high harmonics are generated much earlier in time and reflect the nonadiabatic change of the laser field seen by the atom.

The intensity-dependent harmonic phase can be examined from the term, $\frac{1}{q}(\frac{d\theta_q}{dI})_{I_p}$, in Eq. (3). This term was calculated for an Ar atom in the laser intensity of 3.0×10^{14} W/cm^2 since most of the harmonics are emitted around this intensity when the peak laser intensity exceeds this intensity. The result is shown in Fig. 3. The first part of Eq. (3) increases with harmonic order for the short trajectory component and decreases for the long trajectory component. The two branches meet at the 53rd order, the cutoff order for the laser intensity, I_p. As a result, the fractional blueshift increases for the short trajectory with harmonic order, while it decreases for the long trajectories. Consequently this behavior of harmonic blueshift can provide a valuable information on which electron trajectory contributes to observed harmonic spectrum.

The functional behavior of the fractional frequency shift is primarily determined by the

relative electric-field variation, the second term in Eq. (3). The first part of Eq. (3) does not vary much with the laser intensity for a given harmonic order. The dependence of harmonic blueshift on the laser intensity then follows the functional shape of the electric-field variation. Therefore, the intensity dependence of the nonadiabatic blueshift of high harmonics can be understood if the electric-field variation at the time of strong harmonic emission is estimated.

In the case of a Gaussian laser pulse, the laser intensity has the following form:

$$I = I_0 \exp(-\alpha \frac{t^2}{\tau^2}), \tag{4}$$

where α is a constant and τ is the laser pulse duration. In this case the time of the maximum dipole acceleration can be expressed by the incident laser intensity I_0 and the laser intensity at the time of maximum harmonic emission I_p:

$$t = -\tau \sqrt{\frac{1}{\alpha} \ln(I_0 / I_p)}. \tag{5}$$

From this, the second part of Eq. (3) can be calculated as

$$\frac{\delta E}{E} = \frac{T}{2\gamma} \sqrt{\alpha \ln(I_0 / I_p)}, \tag{6}$$

where T is a optical period of the laser pulse. Equation (6) gives a very important relation between the harmonic blueshift and the laser pulse duration: the relative frequency shift of harmonics is inversely proportional to the laser pulse duration. Therefore, a short laser pulse is more efficient in making blueshift than a long laser pulse.

Figure 4 shows the electric-field variations of 30-fs and 80-fs laser pulses. In this calculation, I_p was assumed as a constant, 3×10^{14} W/cm^2. The electric-field variation is zero at the laser intensity of I_p , 3×10^{14} W/cm^2. The electric-field variation then starts to increase rapidly to a significant value as the laser intensity is increased up to 2×10^{14} W/cm^2. It then slightly increases more as the intensity is raised further. For a sech^2 pulse the relative electric-field variation is given in Fig. 4 as dotted lines for 30-fs and 80-fs pulse durations. In this case, the electric-field variation increases rapidly until the laser intensity is increased from 3×10^{14} to 1×10^{15} W/cm^2, but it does not increase any more to

a saturated value above 1×10^{15} W/cm^2. Since the electric-field variation changes with the temporal shape of the laser pulse, the accurate determination of the pulse shape is important for the proper estimation of harmonic blueshift.

III. Observation of nonadiabatic blueshift of high harmonics

A. Experimental setup

The HHG experiment was performed with a femtosecond terawatt Ti:sapphire laser operating at 10 Hz. The optical layout of the laser system is shown in Fig. 5. It utilized a long wavelength injection method to generate a broad amplified spectrum necessary for producing ultrashort laser pulse [16]. The Ti:sapphire laser consisted of a femtosecond oscillator, a reflective-type grating pulse stretcher, two multi-pass amplifiers, and a grating pulse compressor in vacuum. The pulses from a femtosecond Ti:sapphire oscillator were stretched to about 200-ps pulses. A single pulse was then selected by a Pockels cell at 10 Hz repetition rate, and amplified by two multi-pass amplifiers pumped by a frequency-doubled Q-switched Nd:YAG laser. The amplified pulse was compressed using a grating compressor installed in a vacuum chamber. The temporal characteristics of the laser pulse was measured using a second-harmonic generation frequency-resolved optical gating (FROG) technique [17]. The measured temporal shape of the laser pulse was close to Gaussian and had no significant frequency chirping

For HHG, the laser beam was focused into a gas jet target by a 60-cm focal length spherical mirror. The full width at half maximum of the gas density profile in the interaction region was about 700 μm. The generated harmonics were detected by a flat-field extreme ultraviolet (XUV) spectrometer equipped with a back-illuminated X-ray charge-coupled device (CCD). The XUV spectrometer consisted of a toroidal mirror, slit and varied line-spacing concave grating (1200 line/mm). The toroidal mirror was installed in front of the entrance slit to compensate for the astigmatism occurring at a grazing-incidence concave grating, and to enhance X-ray collection efficiency [18]. X-ray filters made of Al or Ti were inserted in front of the X-ray CCD to block stray laser light. Two 0.2-μm Al filters were used in the wavelength region of 18-35 nm and two Ti

filters of 0.1 and 0.2 μm were used in the wavelength region below 18 nm.

For the systematic inquiry of the blueshift of high harmonics, it needed to vary the laser intensity without changing any other laser parameters. For this purpose, the laser energy was controlled before the grating pulse compressor using a combination of a half-wave plate and dielectric polarizers. Just rotating the half-wave plate, the laser intensity could be controlled by a factor of 30. Great care was taken to prevent any spectral modulation during the energy control since it can affect the temporal shape of the laser pulse, even if the modulation is small.

B. Experimental result

The theoretical study in Sec. II shows that the nonadiabatic blueshift of high harmonics occurs when atoms are driven by an intense femtosecond laser pulse. In this section, we present experimentally observed harmonic spectra and compare them with the theoretical prediction. The harmonic spectra from Ar and Ne were obtained with laser intensities above the saturation intensity. Both harmonic spectra from Ar and Ne explicitly showed large blueshifts in their observed wavelengths. The detailed analysis of the harmonic blueshift is performed to find out its dependences on the gas density, laser intensity, pulse duration, and harmonic order.

High-harmonic spectra from Ar were obtained with 30-fs laser pulses of intensities in the range from 3×10^{14} W/cm^2 to 9×10^{14} W/cm^2. The spectral images of high harmonics between 23rd and 39th orders on the X-ray CCD are shown in Figs. 6(a)-(f). The unshifted harmonic positions are marked by dotted lines with harmonic orders. The 27th harmonic, marked with short solid lines, clearly showed the increase of blueshift with the laser intensity. At the laser intensity of 3×10^{14} W/cm^2, close to the saturation intensity for Ar, the 27th harmonic appeared very near the unshifted wavelength. As the laser intensity was increased, an appreciable blueshift was observed. At the laser intensity of 9×10^{15} W/cm^2, the 27th harmonic was observed at the middle of the 27th and the 29th harmonic positions, i.e. the blueshift as large as the laser frequency.

Using Ne, much higher order harmonics in the 10 nm wavelength region could be observed. The harmonic blueshift in Ne is smaller than that in Ar under same condition due to tighter binding of electrons in Ne, on the other hand, allows the generation of much higher order harmonics. Figure 7 shows the harmonic spectra obtained from Ne gas driven by 23-fs laser pulses with intensities of 2×10^{16} and 7×10^{16} W/cm^2. The blueshift of the 67th harmonic was about three times the laser frequency at the laser intensity of 2×10^{16} W/cm^2 and increased to about four times the laser frequency at the laser intensity of 7×10^{16} W/cm^2.

As is clearly seen in Figs. 6 and 7, the blueshift of harmonics increases with harmonic order. The 39th harmonic from an Ar gas generated at the laser intensity of 9×10^{15} W/cm^2 was observed at the position of the unshifted 41st harmonic: the blueshift of the 39th order harmonic corresponded to two times the laser frequency. The blueshifts of the 67th and the 99th harmonics from Ne gas at the laser intensity of 7×10^{16} W/cm^2 were increased to four times and five times the laser frequency, respectively. These are very large frequency shifts, enough to cover the interval between odd harmonics. In the following subsections, the blueshift of high harmonics is analyzed in terms of their dependences on the gas density, laser intensity, harmonic order, and laser pulse duration.

1. Density dependence of blueshift

The density dependence of harmonic blueshift was examined to determine the origin of large observed blueshift. The blueshift of high harmonics has two origins: nonadiabatic and SPM effects. The former is due to the rapid increase of the laser electric field, as explained in Sec. II. The latter is due to the SPM of a laser pulse propagating in an ionizing medium. The frequency shift of the laser spectrum due to SPM can be written as

$$\begin{aligned}\Delta\omega &= -\frac{\omega_0}{c}\int\frac{\partial n_r}{\partial t}dz \\ &= \frac{\omega_0}{2n_c c}\frac{\partial \bar{n}_e}{\partial t}\ell,\end{aligned} \tag{7}$$

where n_r is the refractive index of an ionizing medium, $\bar{n}_e$ is the averaged electron density along the propagation length of the laser pulse, n_c is the critical density, and ℓ is the medium length. In an ionizing phase, the sign of the frequency shift, $\bar{n}_e \Delta\omega$, is always positive. Since the OFI rate is independent of medium density, the frequency shift due to the SPM in an ionizing gas is proportional to the gas density. Therefore by examining the density dependence of the blueshift of harmonics, the contribution to the blueshift from the SPM effect can be determined.

The density dependence of the harmonic blueshift from Ar was examined by changing the gas density. Figure 8 shows the observed high-harmonic spectra from Ar with 30-fs, 9×10^{15} W/cm^2 laser pulses. Unshifted harmonic positions are marked by dotted lines. Harmonic spectra reflect the density effect; the peak intensities of harmonics were approximately proportional to the square of the gas density. This shows that the coherent growing of harmonic intensity occurs as the number of harmonic generation increases. The result of Fig. 8, however, shows that the effect of SPM on the harmonic blueshift was not significant. The amount of the harmonic blueshift at the Ar density of 1×10^{18} cm^{-3}, however, was just 25 % larger than that at the density of 1×10^{18} cm^{-3}, even though the gas density was increased five times.

The density dependence of the blueshift from Ar gas was more closely inspected in Fig. 9. The peak density of Ar was varied from 1×10^{17} to 8×10^{17} cm^{-3}. The dotted lines show the blueshift extrapolated to zero gas density. The blueshift due to the SPM effect can be estimated by subtracting the zero density value obtained by the extrapolation from the observed blueshift. For the 27th harmonic generated at the Ar density of 1×10^{17} cm^{-3}, it is only 6 % of the total blueshift. The fractional blueshift increased linearly with the gas density and the slopes of the density-dependent fractional blueshift for different harmonic orders were nearly same as expected. This is the consequence of the blueshift due to the SPM effect since the SPM in an ionizing gas is proportional to the medium density and the fractional blueshift does not depend on the harmonic order. The amount of blueshift extrapolated to zero gas density, however, was still significant. Therefore the observed blueshift should have another mechanism than SPM, the nonadiabatic blueshift, since the SPM effect should disappear at the zero density.

2. Intensity dependence of blueshift

The theoretical analysis on the nonadiabatic blueshift in Sec. II predicted the characteristic behavior of the nonadiabatic blueshift with respect to the laser intensity. Though the blueshift due to SPM also increases with laser intensity, it is not considered seriously here since its contribution is small, as shown in the density dependence of blueshift. The experimental result is compared with the theoretical prediction by the semiclassical theory.

Figure 10 shows the laser intensity dependence of harmonic blueshift in Ar obtained with 30-fs and 80-fs laser pulses. In the case of the blueshift of harmonics obtained with 30-fs laser pulses, the blueshift increased rapidly to a significant value when the laser intensity was increased from 3×10^{14} to 2×10^{15} W/cm^2. It then slightly increased further as the laser intensity was raised to 9×10^{15} W/cm^2. It is exactly the same behavior as predicted theoretically in Fig. 4.

The quantitative comparison on the harmonic blueshift over peak laser intensity between the experimental result and the theoretical estimation is made in Fig. 11. The experimentally observed fractional frequency shifts of the 27th harmonic from Ar are plotted with theoretical results for 30-fs and 80-fs Gaussian laser pulses in Fig. 11. The Ar density was 2×10^{17} cm^{-3}. The blueshift of harmonics only from the short electron trajectory was considered in the calculation since the poor phase matching of the harmonics from the long trajectory makes them less visible [13]. For the quantitative comparison, however, the propagation effect of HHG should be considered. If only a single-atom response is considered, the harmonic intensity would be strongest at the time of maximum dipole acceleration. At this moment about 30 % of neutral atoms are ionized by the driving laser pulse. As a result, the harmonics generated at this moment need not yield the maximum observed harmonic intensity since the phase matching of harmonics during propagation is less favorable than the harmonics emitted earlier in time; it would provide a lower bound of the fractional frequency shift. The upper bound of the fractional frequency shift can be estimated by considering the lowest possible laser intensity to generate a given harmonic, i.e. the threshold intensity for a given

harmonic order [13]. The shaded area shows the lower and the upper bounds of the calculated fractional frequency shift. If we consider the fact that the experimentally observed blueshift of the 27th harmonic obtained with an Ar density of 2×10^{17} cm^{-3} contains the blueshift of about 10 % due to the SPM effect, as shown in Fig. 9, the observed blueshift matches well the calculated range. For the laser intensity above 1×10^{15} W/cm^2 in which the ionization of Ar is significant, the blueshift of harmonics have values close to the upper bound — harmonics emitted as early as possible, indicating the importance of the propagation effect. Therefore, the experimentally observed frequency shift can be reasonably well explained by the nonadiabatic blueshift estimated from the semiclassical theory.

3. Order dependence of blueshift

In the semiclassical theory, the nonadiabatic blueshift depends on the harmonic order. In Fig. 3, the blueshift of harmonics from the short trajectory increases linearly with harmonic order, while the blueshift of harmonics from the long trajectory decreases with harmonic order. In the experimental results the harmonic blueshift increased with harmonic order. Therefore, the assumption that the observed harmonics are generated from the short trajectory can be justified by the behavior of the blueshift with harmonic order.

Figure 12 shows the order dependence of the harmonic blueshift obtained with the laser intensity of 9×10^{15} W/cm^2 and Ar density of 2×10^{17} cm^{-3}, along with the calculated result from the semiclassical theory. The blueshift increased linearly with values close to the upper bound of the calculated fractional blueshift as harmonic order increased. The blueshift of the 39th harmonic from Ar with the 30-fs laser pulse was about 60 % larger than the blueshift of the 25th harmonic. Since the fractional blueshift due to the SPM effect has no order dependence, this result can be used as one of evidences showing that the major factor of the blueshift observed in this experiment is not due to the SPM effect but due to the nonadiabatic effect from the rapid increase of the 30-fs laser field.

4. Effect of Laser pulse duration on blueshift

As shown in Eq. (6), the relative electric-field variation of a laser pulse at the time of maximum harmonic emission is inversely proportional to the laser pulse duration. Accordingly, the nonadiabatic blueshift should be inversely proportional to the laser pulse duration also. The laser pulse duration effect on the blueshift was shown in the experimental results. In Fig. 10 the characteristic behavior of the blueshift on the laser intensity was very similar for the harmonics obtained with the 30-fs laser pulses and with the 80-fs laser pulses. The blueshifts of harmonics generated by 30-fs laser pulses were larger than those by 80-fs laser pulses for all laser intensities and harmonic orders. The ratio between the blueshifts of the 27th harmonic generated by 30-fs and 80-fs laser pulses at the laser intensity of 9×10^{15} W/cm^2 was about 2.5. It agrees well with the expected value of 2.7 and confirms the dependence of the nonadiabatic blueshift on the laser pulse duration. This provides an important measure in estimating the amount of harmonic blueshift when laser pulses of different durations are used.

In addition, the laser pulse shape effect can be considered. In Fig. 4, the shape of the electric-field variation is different for different temporal shape laser pulse. The electric-field variation of a sech^2 shape laser pulse increases very rapidly to a certain value below 1×10^{15} W/cm^2 and does not increase much after the laser intensity. For a Gaussian shape laser pulse, the electric-field variation increases rapidly to a certain value below 3×10^{15} W/cm^2. Furthermore, it increases continuously above the laser intensity even though the slope is reduced. In the experimental result, Fig 10, the blueshifts increased rapidly below the laser intensity of 3×10^{15} W/cm^2 and increased further above the laser intensity for 30-fs and 80-fs laser pulses. It ascertains the FROG measurement in which the temporal shape of the laser pulse was more close to a Gaussian.

IV. Conclusion

We have presented the detailed study of the blueshift of high harmonics generated by intense femtosecond laser pulses. Using the semiclassical theory based on the strong-field approximation, the observed large harmonic blueshift was analyzed. The observed blueshift originated mainly from the nonadiabatic effect due to the rapid increase of the laser electric field. The density dependence of blueshift showed that the SPM was not a major factor of the observed large blueshift. The characteristic behavior of the harmonic blueshift in the laser intensity and the order dependences further confirmed that the observed blueshift mainly was caused by the nonadiabatic effect. The experimental result also showed that the harmonic blueshift was inversely proportional to the laser pulse duration, agreeing with the prediction by the semiclassical calculation.

As the harmonic blueshift increased with applied laser intensity, the harmonic wavelengths could be changed simply by adjusting the applied laser intensity. The adjustment of laser intensities could be done by controlling the laser energy before the pulse compressor without changing any other parameters. In this way, the blueshifts of two times the laser frequency in the 39th harmonic from Ar and five times the laser frequency in the 99th harmonic from Ne were achieved. These blueshifts were large enough to cover the whole frequency interval between adjacent odd harmonics. This is an important demonstration of large harmonic blueshift that can provide a tool to realize a tunable coherent femtosecond XUV light source, or a tabletop synchrotron.

References

[1] A. Mcpherson, G. Gibson, H. Jara, U. Johann, T. S. Luk, I. McInyre, K. Boyer, and C K. Rhodes, J. Opt. Soc. Am. B **4**, 595 (1987).

[2] P. B. Corkum, Phys. Rev. Lett. **71**, 1994 (1993).

[3] J. J. Macklin, J. D. Kmetec, and C. L. Gordon III, Phys. Rev. Lett. **70**, 766 (1993).

[4] A. L'Huillier and P. Balcou, Phys. Rev. Lett. **70**, 774 (1993).

[5] Schnürer, Ch. Spielmann, P. Wobrauschek, C. Streli, N. H. Burnett, C. Kan, K. Ferencz, R. Koppitsch, Z. Cheng, T. Brabec, and F. Krausz, Phys. Rev. Lett. **80**, 3236 (1998).

[6] E. Constant, D. Garzella, P. Breger, E. Mével, Ch. Dorrer, C. Le Blanc, F. Salin, and P. Agostini, Phys. Rev. Lett. **82**, 1668 (1999).

[7] P. Antoine, A. L'Huillier, and M. Lewenstein, Phys. Rev. Lett. **77**, 1234 (1996).

[8] I. P. Christov, Phys. Rev. A **60**, 3244 (1999).

[9] C.-G. Wahlström, J. Larsson, A. Persson, T. Starczewski, S. Svanberg, P. Salières, Ph Balcou, and A. L'Huillier, Phys. Rev. A **48**, 4709 (1993).

[10] K. Miyazaki and H. Takada, Phys. Rev. A **52**, 3007 (1995).

[11] H. J. Shin, D. G. Lee, Y. H. Cha, K. H. Hong, and C. H. Nam, Phys. Rev. Lett. **83**, 2544 (1999).

[12] M. Lewenstein, P. Salieres, and A. L'Huillier, Phys. Rev. A **52**, 4747 (1995).

[13] C. Kan, C. E. Capjack, R. Rankin, and N. H. Burnett, Phys. Rev. A **52**, R4336 (1995).

[14] M. Lewenstein, Ph. Balcou, M. Yu. Ivanov, A. L'Huillier, and P. B. Corkum, Phys. Rev. A **49**, 2117 (1994).

[15] M. V. Ammosov, N. B. Delone, and V. P. Krainov, Sov. Phys. JETP **64**, 1191 (1986)

[16] Y. H. Cha, Y. I. Kang, and C. H. Nam, J. Opt. Soc. Am. B **16**, 1220 (1999).

[17] K. H. Hong, Y. H. Cha, C. H. Nam, and J. D. Park, J. Korean Phys. Soc. **33**, 315 (1998).

[18] I. W. Choi, J. U. Lee, and C. H. Nam, Appl. Opt. **36**, 1457 (1997).

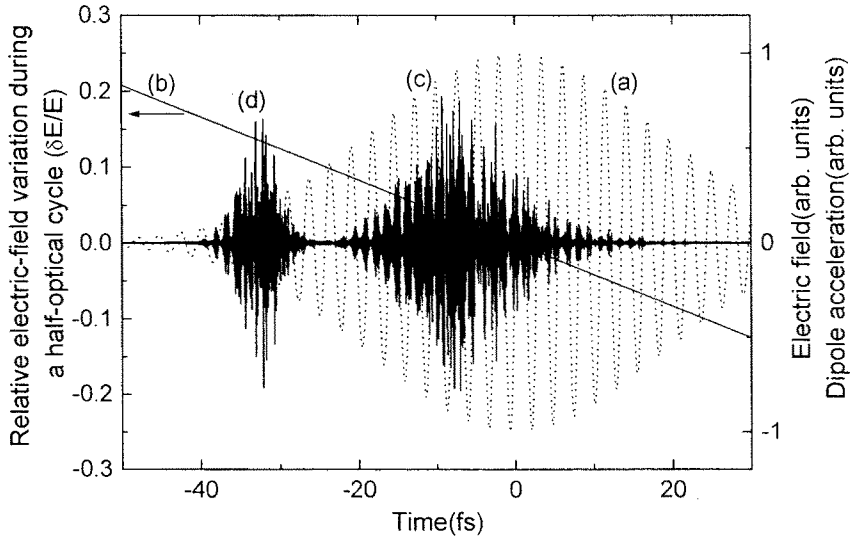

1. Electric-field profile (a), relative electric-field variation (b) of a 30-fs, Gaussian laser pulse, and calculated dipole acceleration of a recolliding electron at the laser intensities of 3×10^{14} (c) and 9×10^{15} W/cm^2 (d).

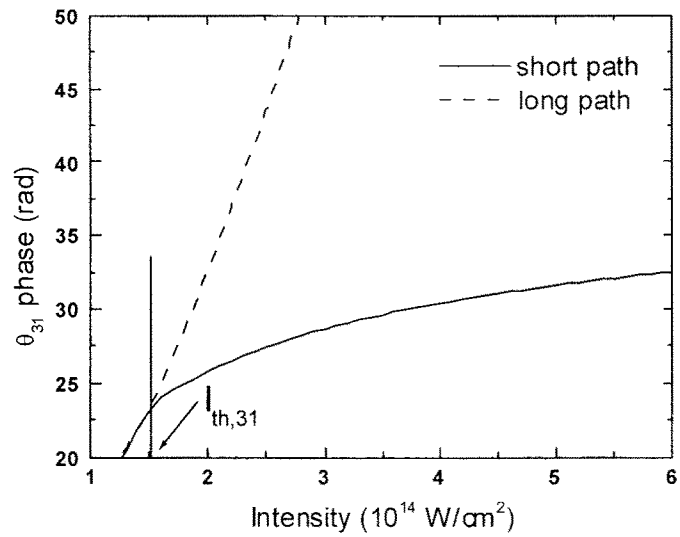

Fig. 2. Intensity-dependent phase of the 31st harmonic from Ar driven by a 30-fs laser pulse. Solid line indicates the harmonic phase of the short trajectory and dashed line indicates the harmonic phase of the long trajectory. $I_{th,31}$ is the threshold laser intensity of the 31st harmonic.

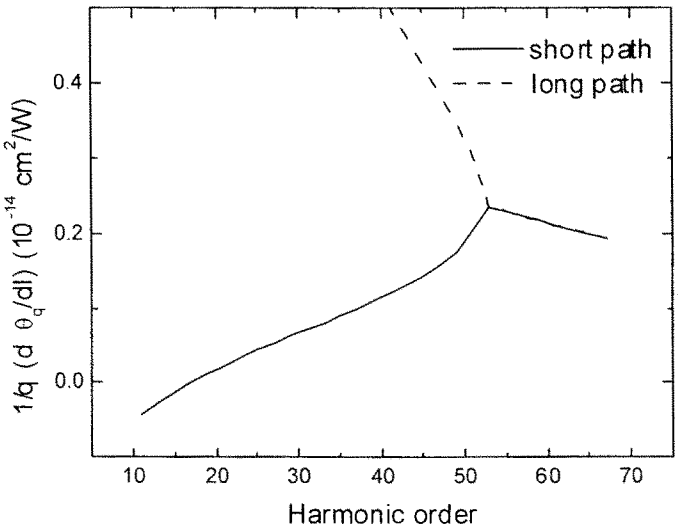

Fig. 3. Order dependence of the intensity-dependent phase term, $(1/q)(d\theta_q/dI)$, obtained from Ar at the laser intensity $I_h=3\times10^{14}$ W/cm^2. Solid line indicates the intensity-dependent phase term for the short trajectory and dashed line indicates that for the long trajectory.

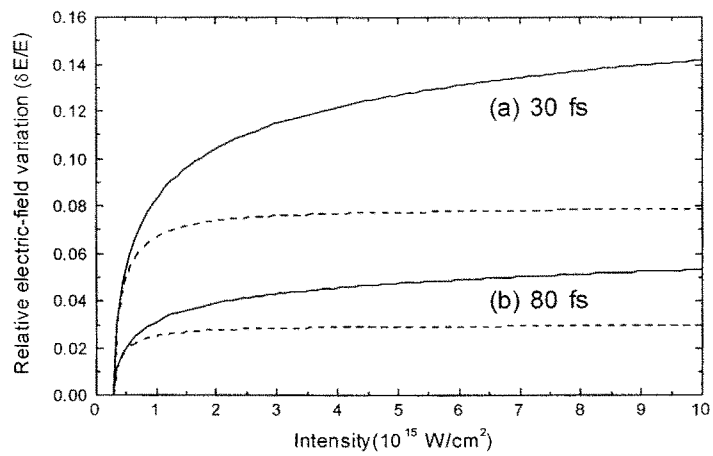

Fig. 4. Relative electric-field variation at the time of maximum harmonic emission. The solid lines are the relative electric-field variations of 30-fs and 80-fs Gaussian laser pulses and the dotted lines are the relative electric-field variations of sech^2 shape laser pulses.

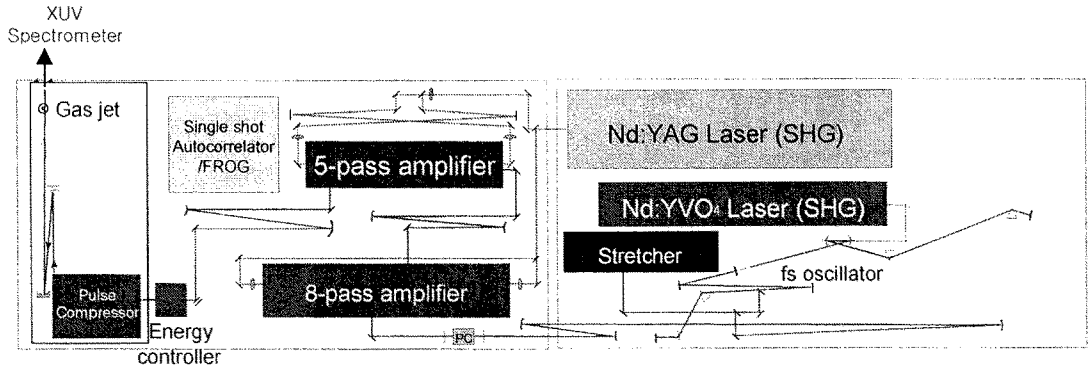

Fig. 5. Optical layout of the femtosecond terawatt Ti:sapphire laser and experimental setup for the blueshift of high harmonics.

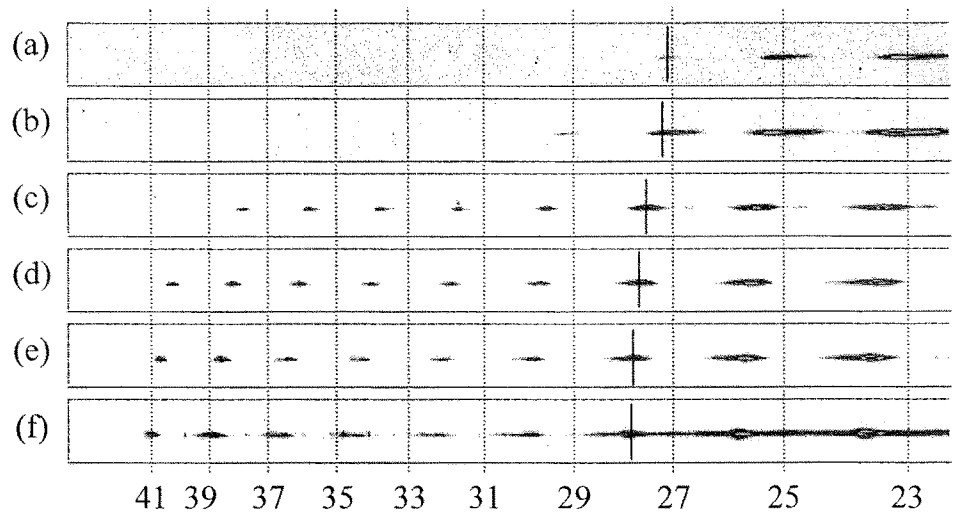

Fig. 6. Images of high-harmonic spectra on the X-ray CCD obtained from Ar driven by 30-fs Ti:sapphire laser pulses with the wavelength centered at 813 nm. The peak gas density at the interaction region was 8×10^{17} cm^{-3}; laser intensities were 3×10^{14} (a), 5×10^{14} (b), 9×10^{14} (c), 2×10^{15} (d), 3×10^{15} (e), and 9×10^{15} W/cm^2 (f).

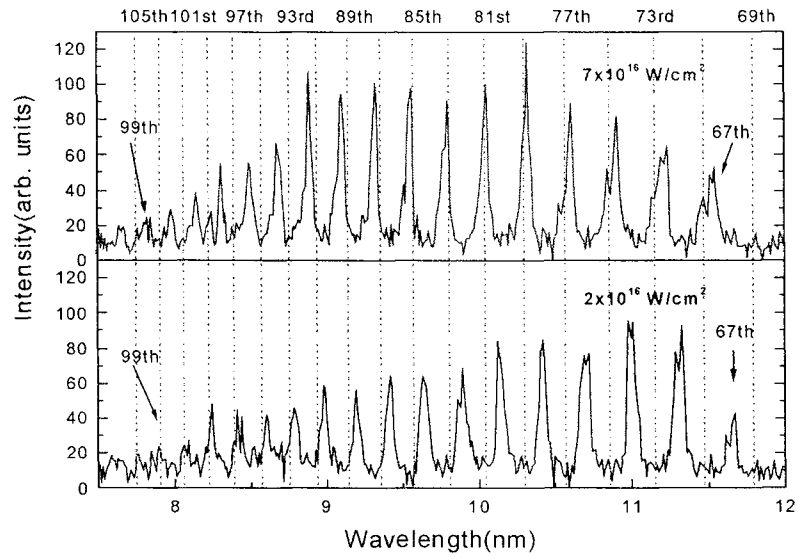

Fig. 7. High-harmonic spectra obtained from Ne driven by a 23-fs Ti:sapphire laser centered at 814 nm. The peak gas density at the interaction region was 3×10^{18} cm^{-3}; laser intensities were 7×10^{16} (a) and 2×10^{16} W/cm^2 (b).

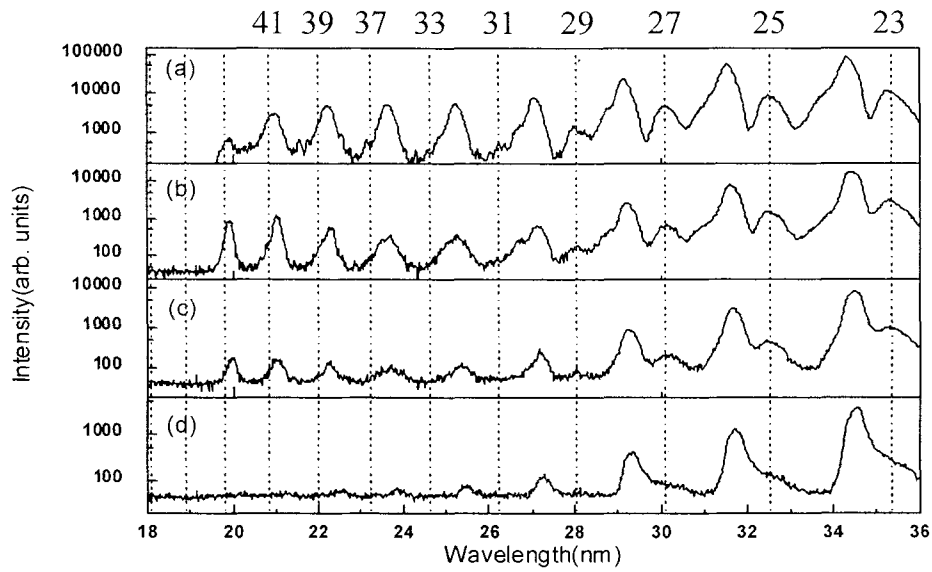

Fig. 8. High-harmonic spectra obtained from Ar driven by a 30-fs Ti:sapphire laser centered at 813 nm. The laser intensity was 9×10^{15} W/cm^2, and the peak gas densities at the interaction region were 1×10^{18} (a), 8×10^{17} (b), 4×10^{17} (c), and 2×10^{17} cm^{-3} (d). Unshifted wavelengths of the harmonics were plotted by dotted lines.

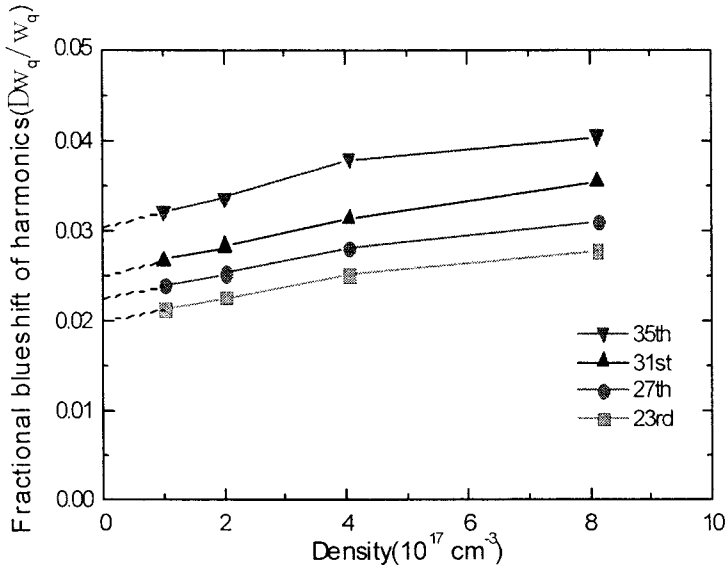

Fig. 9. Fractional blueshift of harmonics from Ar driven by a 30-fs laser pulse with respect to the gas density. The laser intensity was 9×10^{15} W/cm^2.

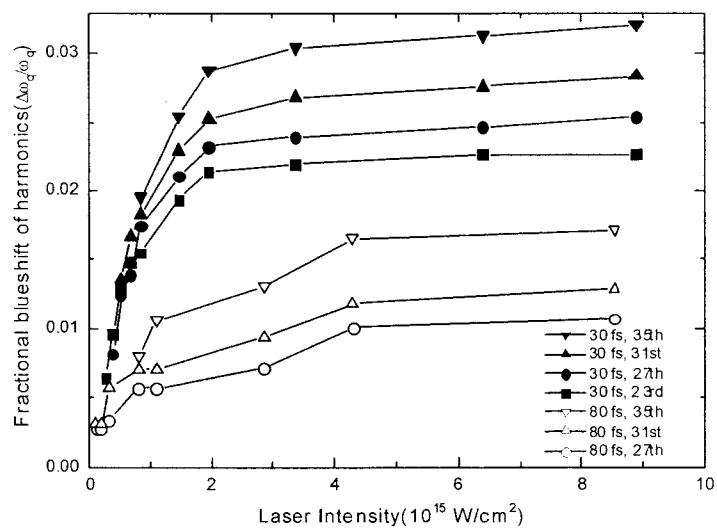

Fig. 10. Fractional blueshift of harmonics from Ar driven by a 30-fs laser pulse with respect to the applied laser intensity. The gas density was 2×10^{17} cm^{-3}.

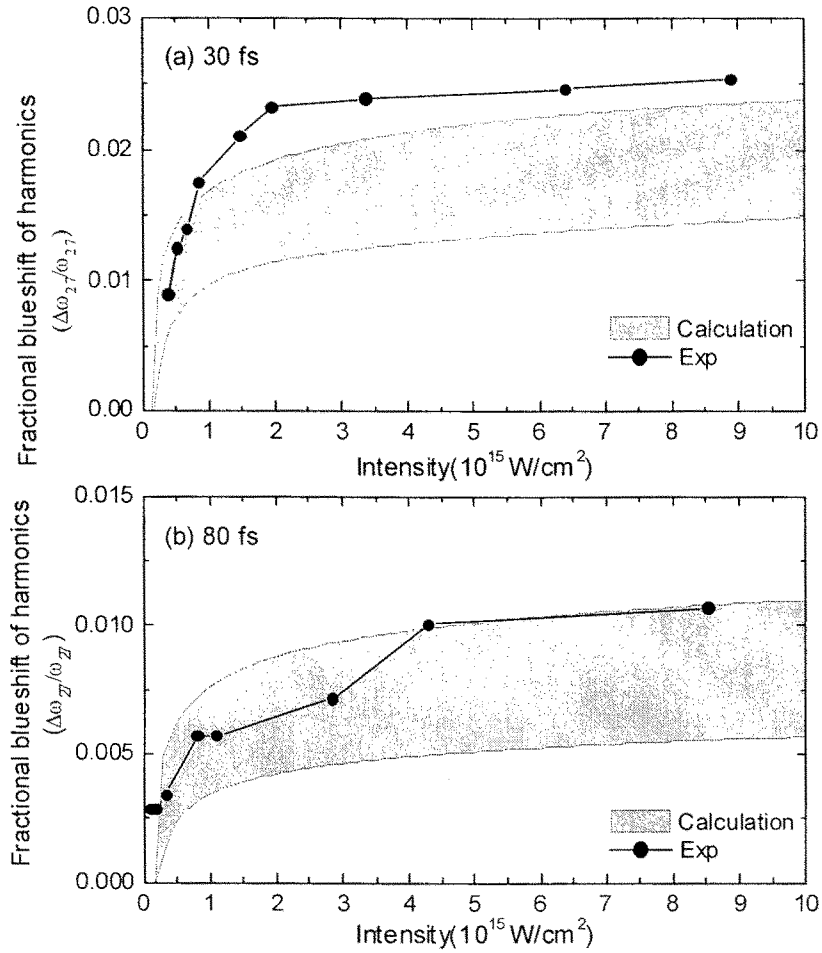

Fig. 11. (a) Intensity dependence of the fractional blueshift of the 27th harmonic obtained from Ar. Solid line with circles indicates the experimental result obtained with an Ar density of 2×10^{17} cm^{-3} and the laser pulse duration of 30 fs. The lower bound of the shaded area was calculated by assuming the harmonic generation at the maximum dipole acceleration; the upper bound was determined by assuming it at the threshold intensity of the 27th harmonic. (a) Fractional blueshift of the 27th harmonic obtained with 30-fs laser pulses and (b) with 80-fs laser pulses.

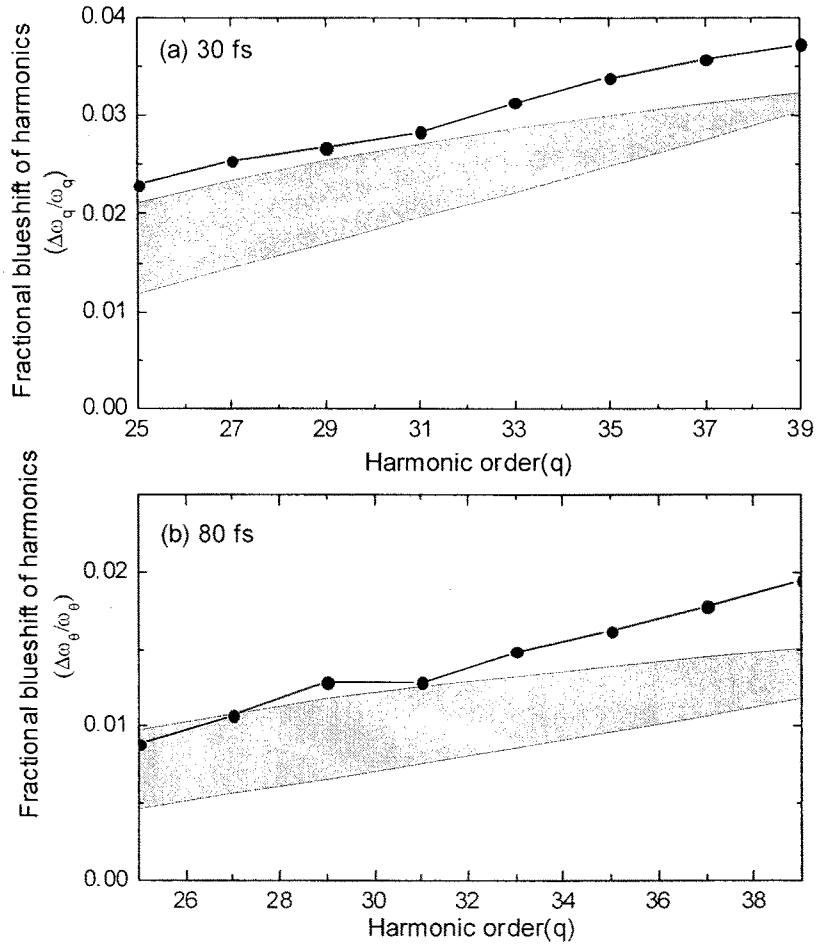

Fig. 12. (a) Order dependence of the fractional blueshift of harmonics obtained from Ar with the laser intensity of 9×10^{15} W/cm^2. The solid line with circles indicates the experimental result obtained at Ar density of 2×10^{17} cm^{-3} and the shaded area was calculated result by the semiclassical theory. (a) Fractional blueshift of harmonics obtained with 30-fs laser pulses and (b) with 80-fs laser pulses.

A. 1. 3. Control of the Spectral Structure of High Harmonics using Chirped Laser Pulses

We investigate the spectral structure of high harmonics generated from He and Ne gases driven by intense femtosecond laser pulses, with emphasis on the effect of the laser chirp on the detailed spectral structure. By adjusting the chirp condition of the driving laser pulse, we can sharpen the spectral width of high harmonics in the plateau region, and extend the cutoff to a much shorter wavelength region. Experimental results demonstrate that the ionization effect on the harmonic chirp becomes important as the laser intensity increases greater the saturation intensity.

Since the first experimental observation of high harmonic generation in a neon gas in 1987 [1], considerable attention has been directed towards understanding the physics behind this highly nonlinear process and exploring its characteristics under various experimental conditions. Recent experimental achievements, such as the demonstration of high harmonic generation with cutoff reaching the water-window x-ray region [2] and the enhancement of conversion efficiency to 10^{-5} [3], shed lights on the idea that a reliable extreme ultraviolet or soft x-ray source can be developed utilizing the high harmonics. The coherent light source so realized may find its applications in diverse scientific and technological research areas [4-7]

The spectral structure of high harmonics, that is important for the study of the harmonic generation process [8] and for the attosecond pulse formation from high harmonics in the plateau [9] or cutoff region [10], have been investigated for various experimental conditions. For example Z. Chang et al. [11] showed that the spectral width of the harmonics was asymmetric to the laser chirp direction and a positively chirped laser pulse could compensate the negatively chirped harmonic pulses which originated from the temporal variation of the intensity-dependent harmonic phase [12]. Moreover, T. Sekikawa et al. [13] compressed the pulse width of the fifth harmonic to 13 fs by compensating the negative harmonic chirp with a positively chirped laser pulse. These experiments were carried out at relatively low intensities below the saturation intensity of the atom where the effect of ionization on high harmonic generation was not significant. In the above-saturation regime, however, the effect of the laser chirp on the harmonic spectral structure has not been well understood until now. In this high intensity regime, ionization of the atoms could induce the phase mismatch between the fundamental and harmonic due to the production of free electrons [14], and self-phase

modulation (SPM) of the fundamental pulse [15,16] could severely change the harmonic phase through the propagation of the ionizing medium.

In the present work we experimentally demonstrated that harmonic wavelength could be extended to the short wavelength with positively chirped laser pulses and also presented the laser chirp effect on the harmonics in the plateau for different pump laser intensities and gas densities. The harmonic chirp, which would be determined by the temporal variation of the intensity-dependent harmonic phase and also by the self phase modulation (SPM) of the laser pulse in the ionizing medium, could be reduced and then the peak intensity of each harmonic would be enhanced with the proper choice of the pump laser chirp. Although the conversion efficiency of the harmonics in the plateau would not depend much on the laser chirp, the intensity and spectral width of each harmonic could be very sensitive to the chirp of the laser pulse. The reparation of the harmonic chirp for the intense and near transform limited pulse is important for applications that require good temporal coherence for the interferometers in the XUV region [6] and as a seed of the x-ray laser experiment for the improvement of the coherence of the x-ray laser beam.

We examined the effect of introducing various amounts of chirp on harmonic production in helium and neon. The experiments were performed with a femtosecond terawatt Ti: sapphire laser operating at 10 Hz. The detailed description of the laser system is given elsewhere [17]. The laser spectrum was centered at 817 nm with a spectral bandwidth of 47 nm. The laser beam was focused into a gas jet with a nozzle of 0.2-mm diameters. The full width at half maximum of the gas density profile was about 0.7 mm. The peak gas density was varied from 1×10^{17} to 3×10^{18} cm^{-3}. The generated high harmonics were detected by a flat-field extreme-ultraviolet (XUV) spectrometer equipped with an X-ray charge-coupled device (CCD) with 330×1100 pixels (Princeton Instruments). Ti and Zr filters with a total thickness of 400 nm and 300 nm, respectively, were used in front of CCD to block the scattered laser light in the XUV spectrometer.

The observed high harmonic spectra from helium as a function of the laser chirp clearly

showed the enhancement of the harmonics to the short wavelength region with positive laser chirp and improvement of the spectral resolution of the harmonics in the plateau with negative chirp. High harmonic spectra between 44 Å and 180 Å are shown in Fig. 1. The x-ray with wavelength shorter than the carbon absorption edge, 43.7 Å, was absorbed by the carbon impurity on the surface of grating or CCD detector. Adjusting the separation of the grating in the pulse compressor could easily vary the chirp of the pump laser pulse. In Fig. 1 the peak laser intensity is 1×10^{17} W/cm^2, the transform limited pulse duration is 27 fs, and center wavelength is 817 nm.

As the laser chirp goes to the positive direction, harmonic cutoff was extended to the carbon absorption edge (43.7 Å), but the spectrum lost the sharp peaks and only quasi-continuum like structure was remained. As shown in Fig. 2, even though we reduced the peak laser intensity to 3×10^{16} W/cm^2, observable shortest wavelength was extended with positively chirped laser pulse. This effect is like the result of neon with the laser intensity of 4×10^{15} W/cm^2 at the transform limited pulse duration, as shown in Fig. 3. To get the efficient harmonic signal around the wavelength from 60 Å to 180 Å, two Zr filters with 0.2 and 0.2-μm thickness were installed in front of the detector. The maximum harmonic order around 81st was extended to more than 101st harmonic order when laser was positively chirped to +57 fs, as shown in Fig. 3. These experimental results conclusively show that the extension of the cutoff with positively chirped laser pulse is general characteristic of the high harmonic, irrelevant to atomic species and the peak intensity of the laser pulse, when the laser intensity is above the saturation intensity.

In the semiclassical model, maximum order of the harmonics is determined by the maximum kinetic energy of the returning electron to the mother atoms [18]:

$$q_c\omega_0 = I_p + 3.17U_p, \quad (1)$$

where U_p is the ponderomotive energy, ω_0 is the photon energy of the pump laser pulse and I_p is the ionization potential of the atom. In the high intensity, ionization of the atom would limit the harmonic generation intensity to the maximum laser intensity before the atoms were totally ionized. In our experimental conditions, dominant harmonics are generated at the earlier time than the peak of the laser pulse. So red-shifted fundamental

pulse will drive the high harmonic generation when the positively chirped laser pulse is applied. The ponderomotive energy at the saturation intensity, which is expressed as

$$U_p = 9.33 \times 10^{-14} \times I_{sat} \lambda^2, \quad (3)$$

should be increased and result in the generation of higher-order harmonics with longer wavelength, λ (in μm), driving pulse, although the saturation intensity, I_{sat} (in W/cm^2), of the chirped laser pulse is similar within the experimental range according to the Ammosov-Delone-Krainov (ADK) ionization rate calculations [19].

For the experimental result in Fig. 2, wavelength of the laser field at the harmonic generation time can be changed from 790 nm to 850 nm as the chirped laser pulse duration is changed from -61 fs (- negative chirp) to +69 fs (+ positive chirp). So, the maximum harmonic photon energy can be increased about 16 % according to Eq. (2). But the observed maximum photon energy is increased more than 44 %, and also the experiment result with neon (see Fig. 3) shows a larger increase in the maximum photon energy than the estimation based on the wavelength shift of the laser field. So with single atom response, it is not enough to understand the extension of observable highest harmonic order with positively chirp laser pulse. For further understanding of the experiment results, it is required to consider the propagation effect, especially in the cutoff region.

In the plateau, clearly distinguished harmonic peaks are observed with negatively chirped laser pulse (see Fig. 1). The direction of the laser chirp for the sharp harmonic peaks is opposite to the result of Z. Chang et al. [11] where they used the laser intensity lower than the saturation intensity and the density of the interaction medium, 8 torr, is about ten times lower than our case of 76 torr. The observed harmonic spectra showing the more detailed structure depending on the amount of the laser chirp are shown in Fig. 4. Each harmonic spectrum is normalized with its peak intensities. The laser parameter and atomic density are the same as in Fig. 1. For the enhancement of the harmonic photon signal in the plateau, 60 Å~ 180 Å, Zr filter was installed instead of Ti filter in front of the CCD. Each harmonic peak in Fig. 4 was blueshifted (redshifted) with negatively (positively) chirped laser pulse and spectral widths of the harmonics were decreased with negatively chirp lasered pulses. The presented experimental results say

that the negatively chirped laser pulse reduces the harmonic chirp, namely observed harmonics are positively chirped at this experimental condition.

To understand the harmonic chirp in the rapidly ionizing medium, we systematically carried out the harmonic generation experiments with neon at different pump laser intensities. The summarized results are presented in Fig. 5. The spectrum width of the harmonics from 63^{rd} to 67^{th} depending on the grating displacement at three different laser energies, 7.5, 3.0, and 1.7 mJ/pulse, are shown in Fig. 5. The chirped pulse width at every grating displacement is also written on the x-axis of the graph. To get rid of the effects of the harmonics from long quantum path on the harmonic spectrum, the gas jet position was moved to + 2 mm after the laser focusing position [20]. At each laser energy the amount of the laser chirp for the optimization of the harmonic spectral width is different (see Fig. 5). According as the laser energy increases, the chirp of the laser pulse needed for the smallest spectral width goes to the negative direction. This experimental result clearly showed that harmonic could have negative or positive chirp depending on the laser intensity.

Harmonics are known to be negatively chirped when they are generated around the peak intensity of the laser pulse. As the laser intensity is increased, ionization of the atom will play in altering the harmonic chirp via self phase modulation of the fundamental pulse. The WKB phase shift due to the free electron induced refractive index modification is [14]

$$\theta_{WKB} = \frac{\pi z}{\lambda_0}\frac{n_e}{n_c}. \qquad (2)$$

where z is propagation distance, n_e is electron density, and n_c is critical density of the pump laser wavelength, λ_0. The WKB phase shift in time, self phase modulation, will make positive chirp of the laser pulse until about 50 % of the atoms are ionized and then will induce a negative chirp. From the ADK calculation of tunneling ionization rate, rapid increasing electric field made larger chirp of the laser field when the peak intensity of the laser pulse was increased. If we consider the phase mismatch between fundamental pulse and harmonic pulse, WKB phase shift in the propagating medium will diminish the harmonic generated at ionized medium. When the product of the

medium length and density is approximately larger than $n_c\lambda_0 / q(\approx 2\times10^{15}\,\mathrm{cm}^{-2}$ for 63rd harmonic), only harmonic generated before the 50 % of the ionization of the atom will survive after propagation of the medium. In our experiment condition, $n_0 \times z$ is about 2×10^{17} cm^{-2}. So, harmonic would experience only the positively chirped laser field.

The intensity-dependent phase will also cause the harmonic chirp but the amount of the atomic chirp will decreases as laser intensity increase when the intensity above the saturation intensity is applied. Because the atomic chirp caused by the intensity dependent phase is approximately proportional to the second derivative of temporal shape of the laser intensity envelope and atomic chirp will decrease when the harmonic generation time comes to be earlier with higher laser intensity. So higher peak intensity would possibly make the positively chirped harmonic.

The harmonic chirp caused by the self phase modulation of the fundamental pulse would be decreased at low density of the medium. As shown in Fig. 6 optimization position of laser chirp is changed from negative chirp quantity at high pressure to transform limited case at low atomic pressure. This pressure dependence of the laser chirp for the optimization of the harmonic spectrum quite well demonstrates the roles of self phase modulation of the fundamental pulse in the rapidly ionizing medium.

In summary, we have investigated the laser chirp effect on harmonic generation. In helium and neon gases, we observed the expansion of the cutoff order with positively chirped laser pulse. These results suggest that laser chirp might be used to improve the harmonic generation efficiency at short wavelength region. And we also experimentally demonstrated that the chirp of the harmonics are not simply negatively chirped but could have different chirp depending on the laser intensity and density of the interaction medium.

Reference

[1] A. Mcpherson et al., J. Opt. Soc. Am. B **4**, 595 (1987).

[2] Z. Chang, A. Rundquist, H. Wang, M. Murnane, and H. C. Kapteyn, Phys. Rev. Lett. **79**, 2967 (1997).

[3] Y. Tamaki, J. Itatani, Y. Nagata, M. Obara, and K. Midorikawa, Phys. Rev. Lett. **82**, 1422 (1999).

[4] A. Rettenberger, and P Leiderer, Phys. Rev. B **61**, 9883 (2000).

[5] M. Gisselbrecht, D. Descamps, C. Lynga, A. L'Huillier, C. –G. Wahlstrom, and M. Meyer, Phys. Rev. Lett. **82**, 4607 (1999).

[6] P. Salieres, L. Le Deroff, T. Auguste, P. Monot, P. d'Oliveira, D. Campo, J. –F. Hergott, H. Merdji, and B. Carre, Phys. Rev. Lett. **83**, 5483 (1999).

[7] W. Theobald, et al., Phys. Rev. Lett. **77**, 298 (1996).

[8] C. Kan, C. E. Capjack, and R. Rankin, Phys. Rev. A **52**, R4336 (1995).

[9] P. Antoine, A. L'Huillier, and M. Lewenstein, Phys. Rev. Lett. **77**, 1234 (1996).

[10] K. J. Schafer, and K. C. Kulander, Phys. Rev. Lett. **78**, 638 (1997).

[11] Z. Chang, A. Rundquist, H. Wang, I. Christov, H. C. Kaypteyn, and M. M. Murnane, Phys. Rev. Lett. **58**, R30 (1998).

[12] M. Lewenstein, P. Salieres, and A. L'Huillier, Phys. Rev. A **52**, 4747 (1995).

[13] T. Sekikawa, T. Ohno, T. Yamazaki, Y. Nabekawa, S. Watanabe, Phys. Rev. Lett. **83**, 2564 (1999).

[14] C. Kan, N. H. Burnett, C. E. Capjack, and R. Rankin, Phys. Rev. Lett. **79**, 2971 (1997).

[15] W. M. Wood, C. W. Siders, and M. C. Downer, Phys. Rev. Lett. **67**, 3523 (1991).

[16] S. C. Rae and K. Burnett, Phys. Rev. A **50**, 3438 (1994).

[17] Y. H. Cha, Y. I. Kang, and C. H. Nam, J. Opt. Soc. Am. B **16**, 2872 (1999).

[18] M. Lewenstein, Ph. Balcou, M. Yu. Ivanov, A. L'Huillier, and P. B. Corkum, Phys. Rev. A **49**, 2117 (1994).

[19] M. V. Ammosov, N. B. Delone, and V. P. Krainov, Zh. Eksp. Teor. Fiz. **91**, 2008 (1986) [Sov. Phys. JETP **64**, 1191 (1986)].

[20] P. Salieres, P. Antoine, A. De Bohan, and M. Lewenstein, Phys. Rev. Lett. 81, 5544 (1998).

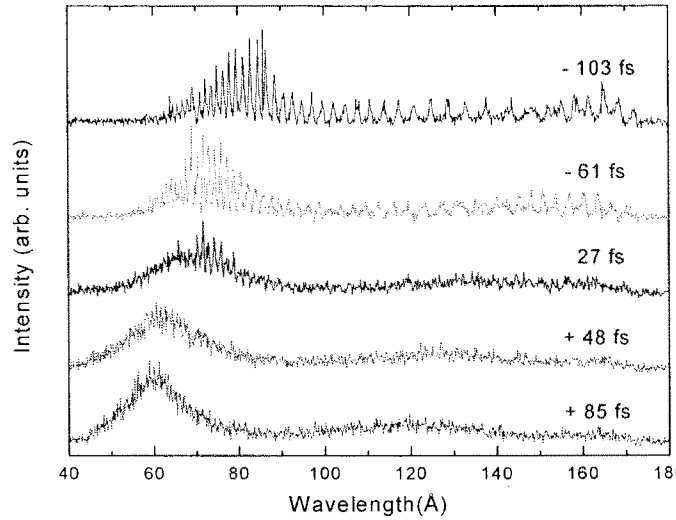

Fig. 1. Experimentally measured harmonic spectra from helium with positively (+ sign) and negatively (- sign) chirped laser pulses. The peak laser intensity is 1×10^{17} W/cm^2 in the chirp-free case and the laser energy per pulse is fixed to 18 mJ.

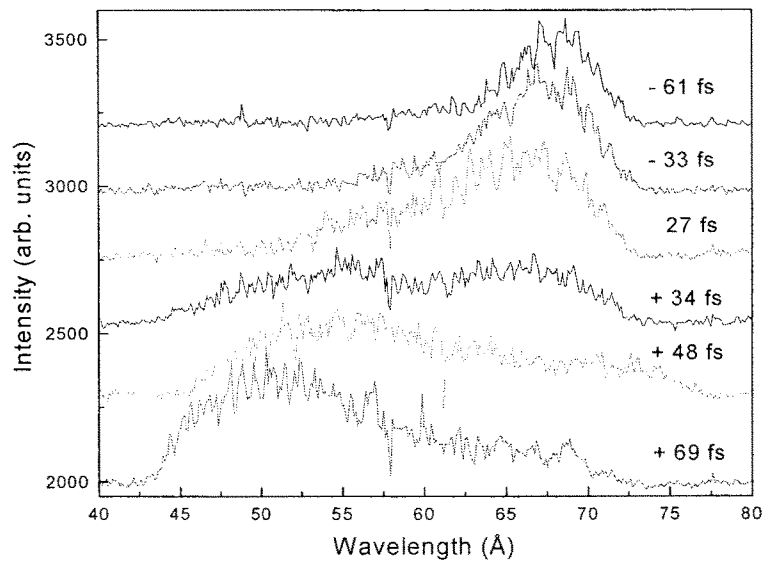

Fig. 2. Harmonic spectra generated in helium with the fixed laser energy of 9 mJ for various laser pulse chirps. The peak intensity of the chirp-free pulse is 3×10^{16} W/cm^2

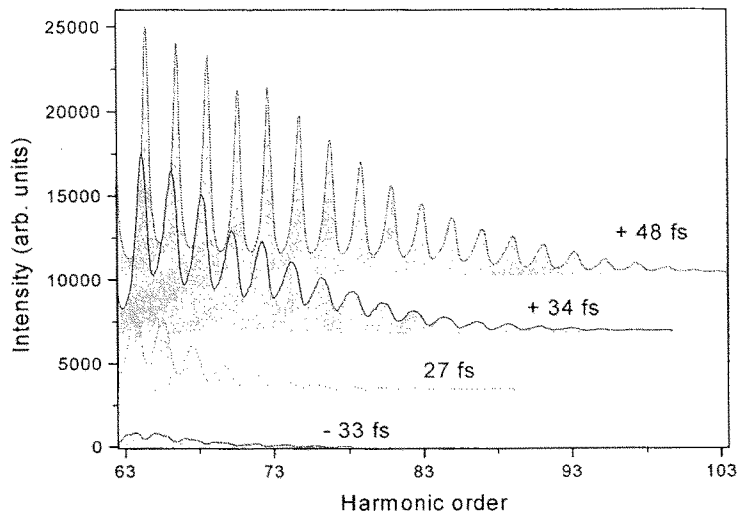

Fig. 3. Harmonic spectra from neon atoms obtained with chirped laser pulses. The peak intensity of the transform limited pulse is 4×10^{15} W/cm^2 and the laser energy was fixed.

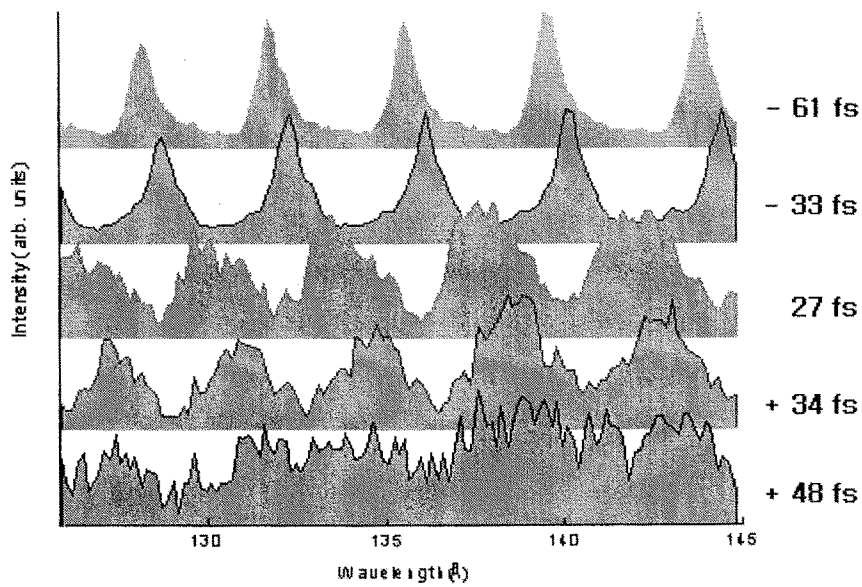

Fig. 4. Harmonic emission from helium obtained with chirped laser pulses. The experimental parameters are same as in Fig. 1.

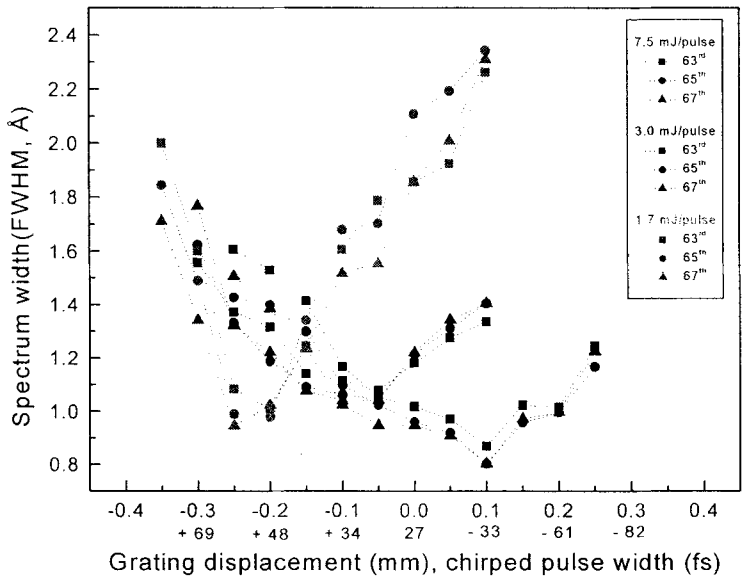

Fig. 5. Compensation Spectral widths of the harmonics from neon with respect to the laser chirp condition and energy. Chirp-free pulse width is 27 fs.

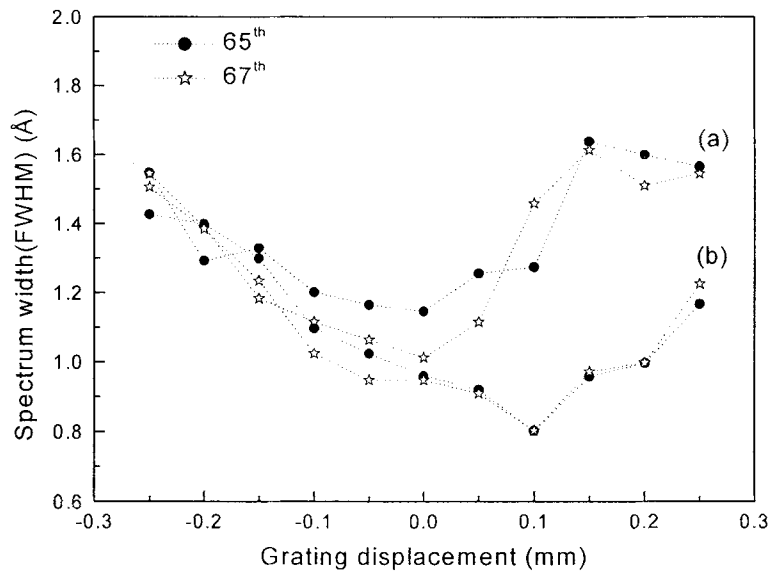

Fig. 6. Change of spectral widths of harmonics generated by chirped laser pulses with the neon density. Comparison of spectral widths of the harmonics from neon at different gas density. The peak gas density is (a) 8×10^{17} cm^{-3} and (b) 3×10^{18} cm^{-3}.

A. 1. 4. Selection of High Harmonics from a Single Quantum Path for Attosecond Pulse Generation

By applying an intense 28-fs laser pulse to a helium gas jet, spectrally resolved high harmonics from different quantum paths were obtained. The selection of high harmonics from a single quantum path could be achieved by controlling the phase matching condition. The comparison of the observed harmonic spectrum with a calculation indicated that an attosecond pulse train with a single pulse of 150 as duration per half-optical cycle was produced.

There has been extensive effort to extend the limit of ultrashort pulse generation to the attosecond range [1-3]. Ultrashort pulse technology has recently made considerable progress due to the advancement of Ti:sapphire laser technology. The shortest pulse directly produced from a Ti:sapphire laser reached within a factor of two to the theoretical limit of 3 fs [4]. The achievement of even shorter pulse duration in the attosecond range necessitates the application of much shorter wavelength radiation. The high harmonic generation (HHG) in the extreme ultraviolet region is well suited in this respect. The existence of wide plateau region in high harmonic spectra is attractive not only for efficient harmonic generation but also for the formation of attosecond pulses. The regularly spaced spectral structure of high harmonics may resemble that of a mode-locked laser when a proper phase-locking condition is met between different orders. The HHG theory however showed that the high harmonics in the plateau region were contributed from several different kinds of quantum paths, which would destroy the phase relation of harmonics from a single quantum path [2,5-7].

The understanding of the HHG processes has proceeded well with theoretical developments, especially the strong-field approximation (SFA) model [8,9]. The SFA model showed that the phase of dipole moment induced on an atom by a driving laser depended on the laser intensity and that the harmonic phase directly followed this intrinsic atomic phase. This property of intensity-dependent harmonic phase played a crucial role in the proper interpretation of experimental results [10,11]. It also showed that several different kinds of quantum paths existed in an ionized electron motion driven by the laser field [5,12], being consistent with the semiclassical model [13] that provided the basic picture of HHG, i.e. tunneling ionization under strong laser field, acceleration of an ionized electron along the electric field, and generation of high

harmonics during recombination. If the contribution from several quantum paths were added together to generate high harmonic emission, different harmonic orders would have randomly-distributed harmonic phase values, as confirmed by a theoretical calculation based on a single-atom response [2,7]. Consequently, the selection of high harmonics from a single quantum path will be required to obtain high harmonics with well-defined phase relation and to generate attosecond pulses [2,14].

In this Rapid Communication, we present spectrally resolved high harmonics from different quantum paths and show that high harmonics from a single quantum path can be selected by controlling the phase matching condition. P. Antoine et al. [2] proposed the generation of an attosecond pulse train using high-order harmonics from a single quantum path; however, it has not been experimentally demonstrated yet. Two quantum paths, called short and long quantum paths, are known to contribute mainly to the harmonics in the plateau region, which correspond to the pre-3.17 and post-3.17 electron trajectories used in the semiclassical model, respectively [12]. As the two quantum paths have different ionizing and returning times, they experience different electric fields and their harmonic phases behave differently. Their contribution to high harmonics can be spectrally separated if an intense femtosecond laser field is applied because the harmonic blueshift of the two paths would not be equal [12]. As the phase matching condition for the two paths is quite distinctive, the selection of high harmonics from one of these two paths is achieved by choosing a proper geometrical condition for phase matching [2,15]. Finally we show that single quantum-path high harmonics can form an attosecond pulse train.

With the application of intense femtosecond laser field to atoms, blueshifted harmonic spectrum can be generated due to the intensity-dependent harmonic phase and also due to the self-phase modulation (SPM) of the fundamental laser pulse during the propagation in a rapidly ionizing medium [10]. If the laser intensity is much stronger than the saturation intensity for optical-field ionization, high harmonics are emitted in the leading edge of the laser pulse before all neutral atoms are ionized. In this case HHG occurs while the atoms are nonadiabatically exposed to a rapidly growing laser field. The intensity-dependent harmonic phase would then result in the nonadiabatic blueshift

of harmonic spectrum. Since the significantly different behavior of the harmonic phases for the two quantum paths results in an unequal amount of harmonic blueshift, the high harmonics from the two quantum paths can be spectrally resolved.

In a rapidly rising field, the contribution of the SPM effect to harmonic blueshift may become large as well because of a rapid ionization process. In an ionizing medium the refractive index change is proportional to the ionization rate of the medium and the spectrum of the propagating laser shifts to shorter wavelength [16,17]. This blueshift of the fundamental wavelength generates the blueshift of high harmonics. The SPM effect on blueshift can be distinguished from the nonadiabatic effect in its density and order dependence [10]. As the fractional frequency shift is the same for all orders, the contribution from the SPM effect to harmonic blueshift, however, can be deducted by appropriately correcting the wavelength of the driving laser.

Experimental verification on the generation of spectrally resolved high harmonics from different quantum paths was pursued by driving He atoms with intense 28-fs Ti:sapphire laser pulses. Helium was chosen because the analysis of an experimental result was relatively simple. Helium is also advantageous in identifying the long quantum-path component since He experiences smaller blueshift than other atoms because of its highest ionization potential among neutral atoms. The saturation intensity for the optical field ionization of He is about 1×10^{15} W/cm^2 for 28 fs pulses. So the experiment was performed with a focused laser intensity of 6×10^{15} W/cm^2. At this intensity the highest harmonic order could reach at about 300 when the cutoff harmonic is assumed to occur at 99 % ionization of He atoms. By choosing harmonic orders around 30, high harmonics in the plateau region, far from the cutoff, could be observed, which would help to readily distinguish the high harmonics from different quantum paths.

The experiment on the spectrally resolved high harmonics from different quantum paths was performed with a femtosecond terawatt Ti:sapphire laser operating at 10 Hz. The Ti: sapphire laser utilized a long-wavelength injection method to generate a broad amplified spectrum [18]. The laser spectrum was centered at 820 nm with a spectral bandwidth of 40 nm. The laser beam was focused into a gas jet with a nozzle of 200-μm

diameter. The small nozzle was used to confine the interaction region well within the confocal parameter of 4 mm used in the experiment. The full width at half maximum of the gas density profile at the interaction region was about 700 μm, and the peak gas density was 3×10^{18} cm^{-3}. The generated high harmonics were detected by a flat-field extreme-ultraviolet (XUV) spectrometer [19] equipped with an X-ray charge-coupled device (CCD) with 330×1100 pixels (Princeton Instruments). The resolving power of the spectrometer was better than 1000 at the observation region. Al X-ray filters with a total thickness of 0.4 μm were used in front of CCD to block scattered laser light in the XUV spectrometer.

The high harmonics obtained by placing the gas jet at the tight focusing position of the laser clearly showed that the spectral structure consisted of two components. High harmonic spectrum between orders 21 and 39 is shown in Fig. 1(a). Here the harmonic spectrum was blueshifted due to SPM and nonadiabatic effects. As the nonadiabatic effect of the short quantum-path harmonics from He was estimated to be negligible in the observed orders, the SPM contribution could be easily estimated. At the wavelengths given by the SPM-corrected laser wavelength of 798 nm divided by harmonic orders, sharp-peaked signals appeared, as shown in the upper scale of Fig. 1(a). At the positions between the sharp signals, broadly-peaked signals were observed. These sharp-peaked and broadly-peaked harmonic signals clearly showed the existence of two components in high harmonics.

For the identification of these two components a single atom harmonic spectrum was calculated using the SFA model. The dipole moment at time t of an electron ionized at time t-τ and moving along an electric field of a linearly polarized laser, E(t), may be written in atomic units as [8,9]

$$\begin{aligned} x(t) = i\int_0^{\infty} d\tau \left(\frac{\pi}{\varepsilon + i\tau/2}\right)^{3/2} & a^*(t)\, d^*(P_s(t,\tau) - A(t)) \\ & \times E(t-\tau)\, a(t-\tau)\, d(P_s(t,\tau) - A(t-\tau)) \\ & \exp[-iS_s(t,\tau)] + c.c., \end{aligned} \tag{1}$$

where $d(P_s\text{-}A)$ is the dipole moment of the field-free ground-continuum transition,

$P_s(t,\tau)$ is the stationary canonical momentum, a(t) is the ground state amplitude, and ε is an infinitesimal positive constant. The stationary canonical momentum is defined as

$$P_s(t,\tau) = \frac{1}{\tau}\int_{t-\tau}^{t} dt' A(t'), \tag{2}$$

where A(t) is the vector potential of the electric field. The phase term, S_s, is the quasiclassical action, describing the motion of an electron moving along the electric field,

$$S_s(t,\tau) = \int_{t-\tau}^{t} dt[\frac{1}{2}\{P_s(t',\tau) - A(t')\}^2 + I_p], \tag{3}$$

where I_p is the ionization potential of the atom.

Here only the harmonic spectrum for an electron returning within one optical cycle ($\tau < 2\pi/\omega_0$) was calculated since the contribution from longer electron paths from multiple encounters would not be efficient. The harmonic spectrum calculated using 798 nm as the fundamental wavelength is shown in Fig. 1(b). By choosing appropriately the returning time of the ionized electron, the SFA calculation clearly showed that the sharp-peaked signal at the odd harmonic wavelengths came from the short quantum path (τ_1) and the weak broadly peaked signal between odd harmonics came from the long quantum path (τ_2). This is the first high harmonic spectrum that clearly identified the high harmonics from the two quantum paths.

The harmonic spectrum in Fig. 1(a) contained several interesting features. First, the amount of harmonic blueshift was larger for the long quantum path than that for the short quantum path. The nonadiabatic blueshift of the short quantum path is negligible in He at these orders for the given condition, while that of the long path is clearly observable. This confirms the fact that the harmonic phase variation is much larger for the long quantum path than for the short quantum path. Second, the measured spectral bandwidths of harmonics from the short quantum path (τ_1) closely matched the calculated value within 15 % difference. This means that the propagation effect did not significantly change the spectral structure of high harmonics from each atom.

The selection of high harmonics from a single quantum path can be ac hieved by considering the phase behavior of the two components. The harmonic phase is determined by two dominant contributions [15]: (1) the intrinsic atomic phase, i.e. the intensity-dependent harmonic phase, and (2) the geometrical Gouy phase induced by focusing the fundamental beam. The gradient of the total harmonic phase, $\frac{\partial \Phi_{tot}}{\partial z}$ along the propagation axis of the laser pulse is shown in Fig. 2 for the two components. This shows that the phase matching conditions of the two high harmonic components are quite different. The phase gradient of the long path harmonics is small only near the focused position, z = 0; however, that of the short path is still favorable at the interaction region away from z = 0. Therefore, by choosing the target position away from the focused position, the short path component can be selected and high harmonics from a single quantum path only can be generated.

By placing the gas jet at z = 2 mm after the laser focusing, the high harmonic spectrum from the short quantum path was obtained. As shown in Fig. 3(a), the observed harmonic spectrum showed single-component harmonics. The laser intensity at the target was 3×10^{15} W/cm^2, and the wavelength shift for the SPM correction was -8 nm. By comparing this spectrum with a single atom calculation in Fig. 3(b), obtained by restricting the electron returning time to the short quantum path ($\tau < 4.08/\omega_0$), it could be easily identified that the short quantum path caused the observed harmonic spectrum. This kind of behavior was predicted by HHG theory [6,14,15]; however, it is the first experimental realization to confirm the prediction. This became plausible by applying the intense femtosecond laser field, since high harmonics were generated only at the leading edge, while the laser field was growing rapidly, so that high harmonics experienced only blueshift. In this way the high harmonics only from the short quantum path could be produced, which should be suitable for the generation of attosecond pulses.

The temporal structure of selected high harmonics was obtained by the inverse Fourier transformation of the harmonic spectrum of the single atom calculation. When both the short and long path harmonics were included, the temporal reconstruction of the

harmonics of orders between 23rd and 39th showed that two pulses per half-optical cycle were generated (Fig. 4(a)). When only the short path harmonics were used, an attosecond pulse train with one pulse per half-optical cycle was generated and the pulse width was about 150 as, as shown in Fig. 4(b). Here the obtained spectral and temporal structures reproduced features observed in the results obtained by the propagation calculation [2,6,14]. The duration of the attosecond pulse train in Fig. 4(b) was about 7 fs; however, it should be shorter than the calculated duration since the spectral widths of observed harmonics were about two times broader than the calculated values. As the effective phase-matched medium length was longer at z = 2 mm than at the focused region, harmonics generated at earlier times before significant ionization occurred would experience better phase-matching than those generated later, although the later harmonics would have stronger signals according to the single atom calculation [12]. Consequently, the broader spectral width means that the duration of HHG was shorter than that predicted by the single atom calculation due to the effect of propagation, which would have its significance in the generation of a single attosecond pulse, instead of an attosecond pulse train.

Even though the single-atom calculation could not take into account the propagation effect, the comparison with the experimental result showed that the restriction on the returning time of the ionized electron to the ionic core was effective in considering the propagation effect. One important role of the propagation effect is to filter out the harmonic component with poor phase matching, which was proved by restricting the returning time of the ionized electron. The other important effect of propagation would be the shift of fundamental laser frequency due to SPM in a rapidly ionizing medium. The calculation by Christov et al. [3] showed that the phase relation between different orders was not destroyed during propagation even in a rapidly ionizing medium and the attosecond pulse generation could be achieved using intense femtosecond pulses. Therefore, high harmonic in the plateau region, generated by an intense femtosecond laser, can be effectively utilized for the generation of attosecond pulses.

In conclusion, we could spectrally distinguish high harmonics from short and long quantum paths and select high harmonics originated from the short quantum path by

controlling the phase matching condition. It was shown that 9 plateau harmonics could be added to generate an attosecond pulse train with a single 150-as pulse per half-optical cycle. The utilization of a larger number of harmonics in the plateau region will result in the formation of even shorter pulses.

References

[1] P. B. Corkum, N. H. Burnett, and M. Y. Ivanov, Opt. Lett. **19**, 1870 (1994).

[2] P. Antoine, A. L'Huillier, and M. Lewenstein, Phys. Rev. Lett. **77**, 1234 (1996).

[3] I. P. Christov, M. M. Murnane, and H. C. Kapteyn, Phys. Rev. A **57**, R2285 (1998).

[4] U. Morgner, F. X. Kärtner, S. H. Cho, Y. Chen, H. A. Haus, J. G. Fujimoto, and E. P. Ippen, Opt. Lett. **24**, 411 (1999).

[5] M. Lewenstein, P. Salières, and A. L'Huillier, Phys. Rev. A **52**, 4747 (1995).

[6] P. Salières, P. Antoine, A. de Bohan, and M. Lewenstein, Phys. Rev. Lett. **81**, 5544 (1998)

[7] F. L. Kien, K. Midorikawa, and A. Suda, Phys. Rev. A **58**, 3311 (1995).

[8] M. Lewenstein, Ph. Balcou, M. Yu. Ivanov, A. L'Huillier, and P. B. Corkum, Phys. Rev. A **49**, 2117 (1994).

[9] A. L'Huillier, M. Lewenstein, P. Salières, and Ph. Balcou, Phys. Rev. A **48**, R3433 (1994).

[10] H. J. Shin, D. G. Lee, Y. H. Cha, K. H. Hong, and C. H. Nam, Phys. Rev. Lett. **83**, 2544 (1999).

[11] C. Lynga, M. B. Gaarde, C. Delfin, M. Bellini, T. W. Hänsch, A. L'Huillier, and C. G. Wahlström, Phys. Rev. A **60**, 4823 (1999).

[12] C. Kan, C. E. Capjack, and R. Rankin, Phys. Rev. A **52**, R4336 (1995).

[13] P. B. Corkum, Phys. Rev. Lett. **71**, 1994 (1993).

[14] P. Antoine, D. B. Milosević, A. L'Huillier, M. B. Gaarde, P. Salières, and M. Lewenstein, Phys. Rev. A **56**, 4960 (1997).

[15] P. Balcou, P. Salières, A. L'Huillier, and M. Lewenstein, Phys. Rev. A **55**, 3204 (1997).

[16] W. M. Wood, C. W. Siders, and M. C. Downer, Phys. Rev. Lett. **67**, 3523 (1991).

[17] S. C. Rae and K. Burnett, Phys. Rev. A **50**, 3438 (1994).

[18] Y. H. Cha, Y. I. Kang, and C. H. Nam, J. Opt. Soc. Am. B **16**, 2872 (1999).

[19] I. W. Choi, J. U. Lee, and C. H. Nam, Appl. Opt. **36**, 1457 (1997).

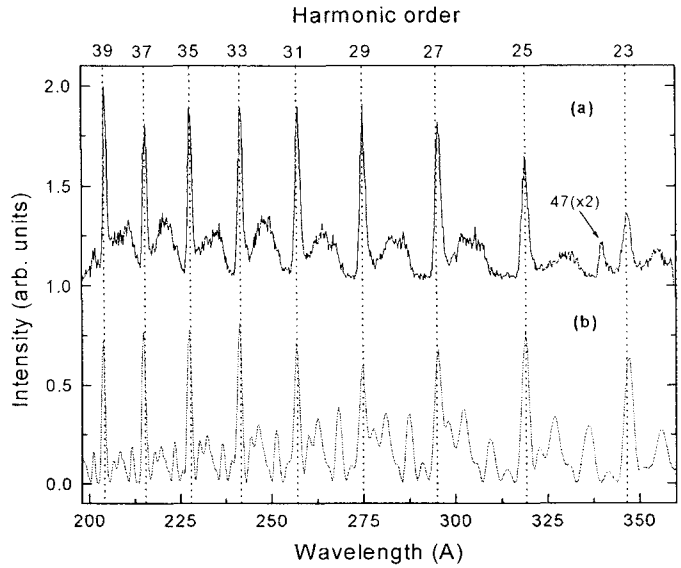

Fig. 1. (a) Experimentally obtained high harmonic spectrum from Heat z = 2 mm. The laser intensity was 3×10^{15} W/cm^2. (b) Calculated high harmonic spectrum obtained by restricting the returning time to less than $4.08/\omega_0$, corresponding to the short quantum-path harmonics.

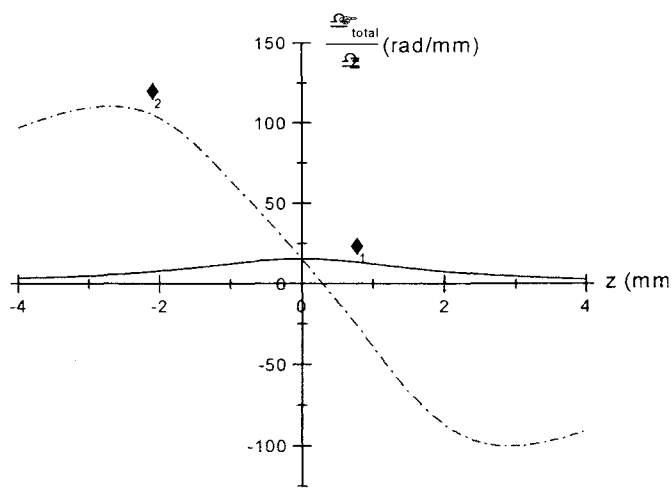

Fig. 2. Gradient of the total harmonic phase along the laser propagation direction. (τ_1: the short quantum-path component and τ_2: the long quantum-path component.)

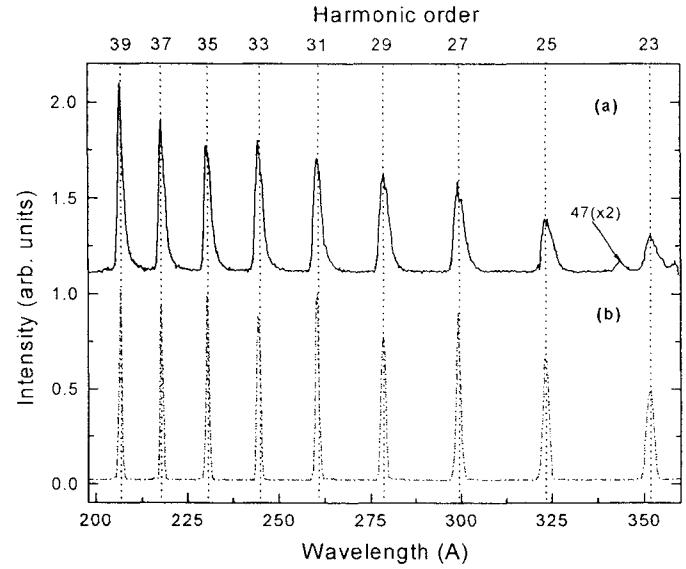

Fig. 3. (a) Experimentally obtained high harmonic spectrum from He at z = 2 mm. The laser intensity was 3×10^{15} \$W/cm^2. (b) Calculated high harmonic spectrum obtained by restricting the returning time to less than $4.08/\omega_0$, corresponding to the short quantum-path harmonics.

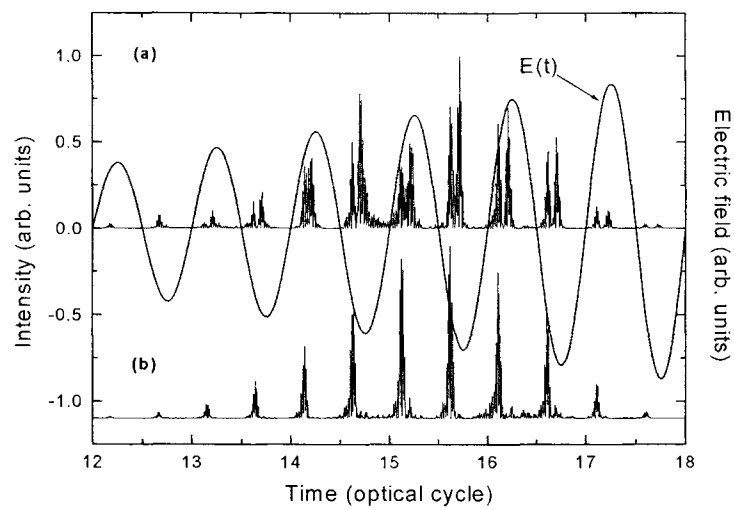

Fig. 4. Temporal reconstruction of high harmonic spectra of orders from 23 to 39, shown with the temporal profile of 28-fs electric field. The electron returning time was restricted to $\tau < 2\pi/\omega_0$ (a) and $\tau < 4.08/\omega_0$ (b). The time is indicated with respect to the peak of the laser pulse.

A. 2. Theory Development of High Harmonic Generation

The nonlinear multiphoton process of high harmonic generation in atomic gases under the influence of intense laser fields has received considerable attention [1-3] owing to the expectation that the coherent radiation generated during the process may be utilized to develop ultrashort extreme ultraviolet (XUV) sources. The ultrashort duration of high-order harmonics generated in the form of a single pulse or a train of pulses [4,5] is believed to be able to pave the way for time-resolved studies of ultrafast physical processes occurring on attosecond time scales. Moreover, the highest frequency part of high harmonic spectra can now reach the water-window region [6] where biological applications are rich. The temporal and spatial coherences of high harmonics necessary for these applications have been demonstrated to be of good quality [7]. Much effort [8,9] is currently being devoted to controlling and optimizing the temporal, spectral and coherence properties of high harmonics, and enhancing the high harmonic generation efficiency. In order to accomplish these goals successfully, it is essential to comprehend in full detail the time-frequency characteristics of high harmonics and their dependence on system parameters.

It has been known that the emission spectra from the harmonic generation process extend over a broad spectral range and contain many discrete odd harmonics of the incident fundamental field. According to recent theoretical and experimental studies [10-12], the high-order harmonics can be blueshifted by applying intense short laser pulses. The observed blueshift is so large that it can sweep the interval between neighboring odd harmonics [12]. Thus, in principle, continuously tunable XUV sources with extremely large tunable ranges could be realized.

In this theoretical part of the report, we develop two novel approaches:

First, a numerical probing technique is developed that can resolve the spectral structures of high-order harmonics obtained from the solutions of the Schrodinger equation. This

method can accurately locate the high harmonics in frequency domain, which otherwise might be impossible due to the intricate structures of mid-plateau harmonics in the short drive pulse regime. Resolved fine spectra reveal that the high harmonics contain several components whose phases have different intensity dependences, in accordance with the prediction of semiclassical approaches. The present technique is applied to the measurement of the harmonic blueshift induced by intense femtosecond pulses.

Second, we investigate the time-frequency characteristics of high-order harmonics generated in atomic gases by intense femtosecond laser pulses using the Wigner distribution function. We calculate the dynamically induced chirp of high harmonics both quantum mechanically and semiclassically, and observe a good agreement between them as long as the tunneling effect is properly taken into account. Using the present time-frequency analysis, we demonstrate that the large harmonic blueshift measured recently is due mainly to the single-atom effect.

A. 2. 1. Coherent Sum Technique

Calculations of the time-dependent Schrodinger equation (TDSE) for a single atom have displayed the characteristic features of high harmonic generation, such as the plateau and cut-off in the high harmonic spectra. However, they usually exhibit harmonic spectra with complicated noisy profiles in the plateau region when the pulse duration is reduced to several tens of femtoseconds, which renders the identification of each individual harmonic unattainable unless special resolution techniques are brought in. We suppose that the complicated spectral structure has been a main obstacle to the detailed analyses of the harmonic profiles in the plateau region and their blueshifts based on the TDSE approach or Lewenstein model [13] for short drive pulses, while a few studies [10,11] have been made on this subject only in the regime where somewhat resolved harmonic spectra are attainable. The appearance of the intricate structure is due to the fact that many electron trajectories contributing to a given harmonic order cause the harmonic spectrum to split into several parts [11], and as the width of the incident laser pulse decreases the split spectral lines begin to overlap and interfere with adjacent harmonic lines of different orders. To systematically investigate the high harmonics, in

particular the location of harmonic components in frequency domain and the amount of their blueshifts as a function of laser parameters, essentially required is thus the ability to differentiate the contributions from different trajectories.

In this subsection, we propose a simple method that can resolve the complicated structures of high harmonic spectra in the mid-plateau region. The dipole phase associated with each trajectory of an ionized electron has its own distinctive intensity dependence [11,13,14], and if dipole spectra at some different laser intensities are added only the components corresponding to the trajectories whose dipole phases (or actions) have less sensitive dependences on intensity will survive, while other components will disappear due to destructive interference. This property is exploited in suppressing insignificant harmonic components and consequently obtaining well-resolved harmonic spectra. Using this technique, we successfully extract some interesting features predicted by semiclassical approaches from the exact solutions of the TDSE.

The semiclassical approaches employing the classical concept of "ectron trajectories" [13-15] have provided an intuitive picture that describes well the underlying mechanism of high harmonic generation. An important prediction of these approaches and the quantum-path analysis [16,17] is that for a given harmonic order q there exist several electron trajectories contributing to the harmonic generation. Dominant contributions are made by those electrons that, once acquiring the kinetic energy $K=q\hbar\omega_0 - I_p$ (where I_p is the ionization potential) from the interaction with the oscillating laser field after tunneling ionization, return to and recombine with the parent ion within one optical cycle after the ionization emitting photons of energy $q\hbar\omega_0$. There are two such electron trajectories per half optical cycle, and one of them (long trajectory) is released earlier from and returns later to the core, spending more time in the continuum, than the other (short trajectory). In the cut-off region, the two trajectories are barely distinguished from each other and have the common release time $t_0=0.31\ \mathrm{rad}/\omega_0$, recombination time $t_r=4.40\ \mathrm{rad}/\omega_0$, and excursion time $\tau=4.08\ \mathrm{rad}/\omega_0$(the time spent by the electron during its stay in the continuum), when the driving field varies in time as $\cos(\omega_0 t)$. The recollisions between the rest ion and the returning electron that occur after one optical cycle can also contribute to the harmonic generation in the

plateau region, and in some cases they manifest themselves in secondary peaks of high harmonics. Recently, based on the Lewenstein model, Kan et al. [11] reported results that clearly demonstrated these. For short laser pulses that have time-varying intensities, they showed that the intensity-dependent dipole phase gives rise to different blueshifts for different trajectories, leading to the emergence of split spectral lines. An experimental demonstration of the spectral line splitting due to the two primary trajectories has been carried out just lately [18].

To assist in gaining a concrete understanding, we produced a dipole acceleration spectrum, similar to that obtained by Kan et al. [11], in Fig.1 by numerically solving the one-dimensional (1D) TDSE for a neon atom exposed to a 160-fs, 800-nm laser pulse with a peak intensity of $I=10^{15}$ W/cm^2. In Fig.1, the high harmonic peaks corresponding to the two primary trajectories mentioned above are denoted by τ^s_q (short trajectory) and τ^l_q (long trajectory). The secondary peaks related to the trajectories with longer excursion times can be seen near the primary harmonic peaks. It is clear that the split spectral lines observed from the calculations [11] based on the Lewenstein model can also be seen in our calculation obtained from the solution of the TDSE that takes into account the effects of the Coulomb potential. We note that, because the atom is completely ionized on the rising side of the pulse at the applied laser intensity that exceeds the saturation intensity for the optical field ionization, only the blueshifts of harmonic lines are observed.

The resolution of the split spectral lines, however, begins to deteriorate when the pulse width decreases below 100 fs, as can be seen from Fig. 2(a) where the pulse width is chosen to be 80 fs. The harmonic lines in the mid-plateau region shown in Fig 2(a) are smeared with complicated structure, and it should be emphasized that this is not a numerical artifact but the effect of interference between the split harmonic lines. In the case of Fig. 2(a), the blueshift of harmonic lines corresponding to secondary recollisions is so large that the secondary harmonic lines overlap and interfere with the next primary harmonic lines, which makes a precise location of the harmonic lines a difficult task. In the cut-off region, however, the spectral lines are still well resolved due to the lack of secondary recollisions in this region. Our discussion here will be focused on the issue of

how to resolve the complicated spectral lines in the plateau region and measure the blueshift of high harmonics even in the cases of drive pulses shorter than 100 fs.

The distinct intensity dependence of the dipole phase of each trajectory, which is the main reason for the complicated harmonic structure, can be taken advantage of in constructing an efficient way to eliminate the contributions from certain trajectories, and thereby enhancing the spectral resolution of the harmonic lines which we are interested in. If we add a large number of dipole spectra (not squared) obtained at different laser intensities, the components whose phases depend sensitively on the intensity are more likely to experience destructive interference and will not survive the sum. Here, by solving the 1D TDSE we obtain dipole acceleration spectra for N pulses with slightly different peak intensities I_i's uniformly chosen from the region between $I-\Delta I/2$ and $I+\Delta I/2$, and add the resulting spectra as follows [19]:

$$d(\omega) = \frac{1}{N}\sum_{i=1}^{N} d_i(\omega) \qquad (1)$$

where $d_i(\omega)=|d_i(\omega)|\exp\{-i\Phi_i(\omega)\}$ is the dipole spectrum for a pulse with peak intensity I_i. If ΔI is small, the variation in the dipole amplitude $|d_i(\omega)|$ may be negligible. However, the dipole phase $\Phi_i(\omega)$ of a certain harmonic component could experience a significant variation $\Delta\Phi$ even with a small intensity fluctuation. We assume that those harmonic components with phase variations greater than 2π do not survive the sum of Eq. (1). The survival condition for a specific harmonic component can then be written as

$$\Delta\Phi = \left|\frac{\partial\Phi}{\partial I}\right|\Delta I < 2\pi \qquad (2)$$

In order to determine the optimal intensity variation ΔI, we follow the semiclassical approaches and use the following approximate expression for the phase of the q-th harmonic [11,14]:

$$\Phi = \frac{S(t_0, t_r)}{\hbar} - q\omega_0 t_r \qquad (3)$$

Here, S is the classical action of the electron that is released from the ion at t_0 with zero initial velocity and returns to the ion at t_r, and is given by

$$S(t_0, t_r) = \int_{t_0}^{t_r} dt \left[\frac{p(t)^2}{2m_e} + I_p \right] \qquad (4)$$

where p is the mechanical momentum of the free electron placed in the laser field with frequency ω_0. Displayed in Fig. 3 is the derivative of the dipole phase with respect to the laser intensity for the two primary trajectories, where the dipole phase is calculated at a constant laser intensity. The dipole phases associated with the trajectories corresponding to secondary recollisions have far more sensitive dependences on laser intensity than those associated with the two primary trajectories, and the dipole phase gradients for those trajectories are too large to be seen in the scale adopted in Fig. 3. The survival condition (2) along with Fig. 3 allows the estimation of an appropriate value of ΔI to select some harmonic components.

Figures. 2(b) and (c) show the dipole spectra obtained in the way described above. The variation in the intensity is $\Delta I/I=2.6\%$ for Fig. 2(b) and $\Delta I/I=8\%$ for Fig. 2(c), and N=20 pulses are considered for both cases. The results clearly indicate that, by properly choosing the intensity variation ΔI, we can remove some unwanted components and obtain clean dipole spectra that now can readily be used to track the primary harmonic lines. For example, in Fig. 2(b), the secondary peaks that complicated the spectral structure do not satisfy the survival condition (2) and are thus removed, and only the peaks associated with the two primary trajectories τ^s_q and τ^l_q are observed. A further increase in ΔI can remove the τ^l_q component by making its phase variation $\Delta\Phi$ greater than 2π. At the intensity variation ΔI chosen in Fig. 2(c), only the τ^s_q component satisfies Eq. (2) and remains undestroyed.

The selection of some harmonic components by the present technique can also be viewed clearly when we inspect the harmonic generation in time domain. By taking the harmonics between $44\omega_0$ and $60\omega_0$ from the three dipole spectra in Fig. 2, we get the temporal profiles shown in Fig. 4. Whereas there appear several sub-femtosecond pulses in Fig. 4(a), only two pulses are visible per half optical cycle in Fig. 4(b) when $\Delta I/I=2.6\%$. The release time t_0, recombination time t_r and excursion time τ shown in Fig. 4(b) are calculated classically at the instantaneous laser intensity at which the sub-femtosecond pulses are emitted, and these characteristic times have little harmonic-order dependences for q in the range considered. The classical analysis reveals that the pulses in Fig. 4(b) are emitted at the recombination times t^s_r and t^l_r of the two primary trajectories. As we move to times earlier than that depicted in Fig. 4(b), the τ^s and τ^l pulses approach each other and then merge together when the instantaneous intensity corresponds to the cut-off intensity of the harmonics considered. In the case of Fig. 4(c) with $\Delta I/I=8\%$, only one pulse (τ^s) per half optical cycle is seen.

Since the present technique provides well-resolved spectra, one important application of it would be the measurement of the blueshift of high harmonics in the single-atom dipole spectra. As an illustration, we present in Fig. 5 the blueshift measured for two different pulse widths. Generally, as shown in Fig. 5, the harmonic blueshift $\delta\omega$ increases as the pulse width decreases. Also shown in the figure are the semiclassical calculations obtained from the relation

$$\delta\omega = \frac{\partial\Phi}{\partial I}\frac{\partial I}{\partial t} \qquad (5)$$

Both the terms $\partial\Phi/\partial I$ and $\partial I/\partial t$ are calculated at the moment when the q-th harmonic generation reaches its maximum. It is obvious that the semiclassical calculations are in good agreement with the TDSE calculations.

In experiments, there are two sources for the blueshift, namely, the single-atom effect [10-12] considered in this work and the self-phase modulation of propagating waves

which is induced mainly by the free electrons produced in an ionizing medium [20,21]. To explore favorable conditions for the development of tunable coherent XUV sources, one may need to investigate the single-atom and propagation effects on the blueshift separately. Our resolution technique can serve as a convenient tool for investigating the single-atom blueshift.

A direct implication of the present study is that, with a typical intensity variation along the propagation axis that may be caused by a focusing geometry in real experiments, well-resolved harmonic peaks could be observed. For instance [18], for a gas of 700-μm thickness, a confocal parameter of b=4 mm results in $\Delta I/I = 3\%$ along the propagation direction if the gas is centered at the focus z=0 mm (or $\Delta I/I = 34\%$ if the gas is centered at z=2 mm behind the focus), which is comparable to the intensity variation considered in the present study. The mechanism behind this phenomenon shares the same root as the previous findings [8,22] that by taking into account the geometric effects in propagation calculations well-resolved harmonics are observed. In both cases, those harmonic components with phases robust to changes in system parameters are added constructively while others disappear due to their poor phase matching conditions.

In summary, we have presented here a method that can resolve the complicated structures in the single-atom high harmonic spectra. This method can efficiently differentiate the contributions from different electron trajectories and thus provides a conclusive knowledge that which trajectory contributes to which spectral line in the harmonic spectra. It has always been of fundamental importance to derive features of classical theories from the exact solutions of quantum theories and inspect the correspondence between them. The present work demonstrates that the predictions of the semiclassical trajectory analyses on the high harmonic generation can be for the most part reproduced by the exact quantum mechanical calculations, which strongly supports the semiclassical descriptions. The new resolution technique introduced here has played a crucial role in arriving at this conclusion. Finally, we mention that an alternative but consistent explanation of blueshift in terms of the analysis of the

periodicity and recollision has been given by Watson et al. [23].

A. 2. 2. Time-Frequency Analysis

Thanks mainly to the semiclassical interpretation[17,24] and the Lewenstein model [13] incorporating the strong field approximation, the underlying mechanism and characteristic features of high harmonic generation have been uncovered to a great degree. One of subtle but important predictions made by these approaches and the quantum-path analysis [16,17] is that each high harmonic consists of two dominant components associated with the short and long electron trajectories that return to and recombine with the parent ion within one optical cycle after tunneling ionization. For a short laser pulse that has a time-varying instantaneous intensity, the two trajectory components experience different amounts of frequency shift depending on time, and hence different spectral broadenings, because their phases have different intensity dependencies. Several experimental and theoretical studies [8,25] have directly or indirectly shown that high harmonics do have time-varying frequencies, all arriving at the same conclusion that they are negatively chirped. In these studies, the dipole phase has been assumed to depend linearly on the laser intensity, i.e., $\Phi(t)=\alpha I(t)$ where α is a constant specific to each trajectory [16]. Thus, the time-dependence of the dipole phase has been supposed to directly follow the pulse shape I(t).This assumption, however, appears to lead to incorrect predictions in certain parameter regions, as will be demonstrated in this work. To the best of our knowledge, a complete description of the induced chirp of high harmonics given in a detailed manner based on a quantitative analysis is still missing.

In this subsection, we present calculations of the induced harmonic chirp obtained from the numerical solutions of the time-dependent Schrodinger equation (TDSE). The Wigner distribution [26,27] that has been proven powerful for investigating quantum states in phase space is employed in our time-frequency domain analysis. It is found that when the laser intensity exceeds the saturation intensity for the optical field ionization, the chirp induced in the two trajectory components can have opposite signs, i.e., the

long trajectory component can be positively chirped while the short trajectory component is negatively chirped. We immediately note that this finding cannot be explained by the simple expression $\Phi=\alpha I$, since this is bound to predict that the two trajectory components will experience chirps of different amounts but with the same sign [16]. We present a precise semiclassical analysis that resolves this discrepancy and reproduces the quantum mechanical calculations remarkably well. Finally, using the present time-frequency analysis we show that the unexpectedly large blueshift observed recently [12] is indeed due largely to the single-atom response to the rapidly increasing laser intensity, which confirms the semiclassical interpretation presented there [12].

The variation in time of the frequency of high harmonics, which is not revealed by a standard Fourier analysis, can be exposed effectively by means of distribution functions defined in (two-dimensional) time-frequency domain. Among a broad class of time-frequency distributions [28], we here choose to use the Wigner distribution that is defined by

$$W(t,\omega)=\frac{1}{\pi}\int_{-\infty}^{\infty}E^{*}(t-t')E(t+t')e^{-2i\omega t'}dt' \qquad (6)$$

where E(t) is a time signal under inspection. We will substitute for E(t) a suitably frequency-windowed dipole acceleration that is calculated from the one-dimensional TDSE.

A clear insight into how the Wigner distribution grasps the fine detail of the time-frequency characteristics of high harmonics can be gained from Fig.6 (a), which was obtained for a neon atom exposed to an 80-fs, 800 nm pulse with a peak intensity of $I=3.6\times10^{14}$ W/cm^2. In obtaining Fig.6(a), we eliminated the contributions from multiple recollisions that deteriorate the resolution of the Wigner distribution using the method of coherent sum [29]. It can be seen that, near the center of the incident pulse (t=0) where a major portion of the 47th harmonic is emitted, there exist two peaks having different slopes. The peak with a smaller slope corresponds to the short trajectory component (τ^{s}) and that with a larger slope to the long trajectory component (τ^{l}). In

this region, both components are negatively chirped and almost symmetric about the center, and the expression $\delta\omega=\partial\Phi/\partial t=\alpha\partial I/\partial t$ can provide a good description of the chirp. It is estimated from the figure that $\alpha=4$ and 20×10^{-14} rad/Wcm^{-2} for the short and long trajectory components respectively. As we move from the center to the edges of the pulse, we observe that the two components become curved and eventually meet each other when the instantaneous laser intensity coincides with the cutoff intensity for the 45th harmonic ($t=\pm11$).

For a comparison of the above result with the semiclassical calculation, we use the following approximate expression for the phase of the q-th harmonic [11,14]:

$$\Phi = \frac{1}{\hbar}\int_{t_0}^{t_r}\left[\frac{1}{2}m_e v(t)^2 + I_p\right]dt - q\omega_0 t_r \qquad (7)$$

where I_p is the ionization potential, and the integration is the classical action of the electron that is released from the core at t_0, and returns to the core at t_r with the kinetic energy $K=q\hbar\omega_0-I_p$. The instantaneous frequency variation of the q-th harmonic can then be calculated by

$$\delta\omega = \frac{\partial\Phi}{\partial I}\frac{\partial I}{\partial t} \qquad (8)$$

We are here also interested in inspecting the limitation of the statement of the semiclassical two-step model [15,24] that when ionization occurs the electron is released from the ionic core with zero initial velocity ($v_0=0$). Under this assumption, t_0 and t_r take real values. On the other hand, if we use the accurate initial velocity that is calculated from the relation $m_e v_0^2/2+I_p=0$, we come by complex-valued t_0 and t_r [14]. We consider both cases and compare them below.

The semiclassically calculated time-dependence of the 45th harmonic frequency is displayed in Fig.6(b) where the dotted and solid curves represent the results for the

electron released with $v_0=0$ and $\pm i(2I_p/m_e)^{1/2}$ respectively. Comparison between Figs.6(a) and (b) shows that both curves simulate well the exact quantum mechanical result near the center of the laser pulse. Although $\partial\Phi/\partial I$ depends on the laser intensity as can be seen from the inset in Fig.6(b), in the limited region near the center of the pulse it can be assumed to be constant and set to $\partial\Phi/\partial t=\alpha$. Then α determined from the inset in Fig.6(b) agrees well with the result estimated earlier from Fig.6(a). However, as the instantaneous laser intensity decreases to the cutoff intensity for the 47th harmonic (near $t=\pm 11$), the two curves begin to separate from each other, with the solid curve following closely the quantum calculation shown in Fig.6(a). This indicates that the imaginary-valued initial velocity that leads the electron to move along a ghost trajectory [30] in complex plane causing the action to take a complex value plays an important role in the cutoff region. In other words, the tunneling effect that is properly taken into account by allowing physical variables to take complex values has a noticeable influence in this region.

As the laser intensity grows greater than the saturation intensity, the harmonic chirp begins to behave in a more complicated manner than the equation $\Phi=\alpha I$ can describe. This can be clearly illustrated by Fig.7(a) that was obtained at $I= 10^{15}$ W/cm^2. In this saturation regime, only the blueshifted part ($t<0$) is observed. It is apparent that the signs of the induced chirps are opposite for the two trajectory components. Considering that one of these components can be selected by suitably changing the position of the gas jet relative to the laser focus [5], the positively chirped long trajectory component should not be neglected, but need be treated as importantly as the negatively chirped short trajectory component. The complicated spurious structure between the two harmonic peaks is attributed to the inherent nature of the Wigner distribution [28] that may be suppressed by using other distribution, such as the Husimi [27] or the Choi and Williams [28] distribution.

The fact that the two trajectory components can have chirps with opposite signs strongly suggests that α should be a variable. When the laser intensity is lower than the saturation intensity, high harmonics are generated mostly over a limited intensity range

near the center of the pulse, where α may be assumed to be constant. In contrast, in the saturation regime, high harmonics are generated over a relatively broad intensity range on the rising side of the pulse until the atom is completely ionized, and furthermore the harmonic generation process lasts for a very short period of time. In this case, the rate of change in the harmonic frequency can be significantly affected by a small variation in α. In fact, as the inset in Fig.6(b) shows, the intensity-dependence of $\partial\Phi/\partial I$ cannot be ignored and α itself should thus be considered as a intensity-dependent variable [17]. The precise semiclassical calculation performed based on Eqs.(7) and (8) is presented in Fig.7(b). It is found to be in good agreement with the quantum mechanical result shown in Fig.7(a).

Another advantage of the present time-frequency analysis using the Wigner distribution over the conventional Fourier analysis is prominently visible when the induced chirp becomes so big that neighboring harmonics of different orders overlap one another making it nearly impossible to distinguish individual harmonics exhibited by the Fourier spectrum. This situation is encountered in particular when the laser intensity is so strong that high harmonics undergo a huge blueshift. To make this point clear we present in Fig.8 the experimentally obtained high harmonic spectrum together with the one calculated from the TDSE for a neon atom exposed to a 27 fs, 817 nm laser pulse of intensity $I=10^{16}W/cm^2$. Our experimental setup was described elsewhere [12]. In Fig.8(b), harmonic components other than the short trajectory component were removed by the method of coherent sum [29]. Whereas the experiment yields well-resolved harmonic peaks, the numerical spectrum is smeared with complicated structure, in this case, owing to the large chirp induced in the short trajectory component. Note in Fig.8(a) that the 85th harmonic is blueshifted to $88.5\omega_0$. The large blueshift experimentally observed, however, cannot be directly compared with the numerical result because of the complicated numerical spectrum. The use of the Wigner distribution overcomes this difficulty impressively.

Shown in Fig.9 is the Wigner distribution corresponding to Fig.8(b). There appear two different kinds of stripes parallel to horizontal dotted lines, one with only peaks (red) and the other with alternate peaks and valleys (blue). The former corresponds to odd

order harmonics, while the latter lying between the odd order harmonic stripes are artifacts pertaining to the Wigner distribution [28] that do not represent any meaningful harmonic signals. A similar striped pattern appears parallel to vertical dotted lines. Any valuable information is contained only in those stripes guided by the vertical dotted lines. Note that there is one such stripe per half optical cycle. This means that the time marginal of the Wigner distribution consists of a train of ultrashort pulses with two pulses bursting per optical cycle, in accordance with the semiclassical prediction. In spite of the large frequency variation greater than $2\omega_0$ (the interval between adjacent harmonics), individual harmonics are readily distinguishable in this time-frequency domain. Counting the harmonic order from the fundamental directly up to a given harmonic, we can determine the frequency of the harmonic. For example, we find that as time evolves the 85th harmonic sweeps from $90\omega_0$ to $87\omega_0$ with a peak near 87.5-$88.2\omega_0$. Even though this single-atom numerical peak for the 85th harmonic is slightly below the experimentally observed one, it is obvious at least that the experimental 85th harmonic falls within the range of the maximum variation of the numerical 85th harmonic frequency.

The small discrepancy between the experimental blueshift and the single-atom result, and the mechanism behind the appearance of discrete experimental harmonic peaks in this far above saturation regime could be connected with the propagation effect. The free electrons produced in an ionizing medium induce phase-mismatching in propagating waves and limit the coherent growing of the trailing edge of harmonic pulses, and consequently shorten the width of the harmonic pulse train retaining only the front part [11]. Because the short trajectory component is negatively chirped, the center of the 85th harmonic will then be pushed toward a higher frequency region. This may account for the small discrepancy in the harmonic blueshift mentioned above. In addition, the net spectral broadening caused by the chirp will be somewhat reduced (see Fig.9), which may result in well-resolved harmonic peaks. This implies that, in the saturation regime, the ionization effect should be taken into account in discussing the phase-matching condition as well as the geometric effect associated with the laser focusing (the Gouy phase) and the intensity-dependent dipole phase. In particular, the ionization effect may modify the time-frequency characteristics of high harmonics in

the way just described. Finally, the propagation effect on the blueshift relating to the self-phase modulation arising from the time-varying refractive index due to ionization would be fairly smaller than the single-atom effect.

In conclusion, we have demonstrated the usefulness of distribution functions in investigating the time-frequency characteristics of high harmonics. This approach has enabled us to enjoy the novel opportunity of exploring several interesting aspects of high harmonics: the dynamically induced chirp, the tunneling effect near the cutoff laser intensity, and the single-atom effect on the blueshift. We believe that the information revealed on the induced harmonic chirp will be crucial in achieving an efficient control of spectral structure of high harmonics for the optimization of high harmonic generation processes.

References

[1] Atoms in Intense Laser Fields, edited by M. Gavrila (Academic Press, New York,1992), and references therein.

[2] M. Protopapas, C. H. Keitel, and P. L. Knight, Rep. Prog. Phys. **60**, 389 (1997).

[3] P. Salieres, A. L'Huillier, Ph. Antoine, and M. Lewenstein, Adv. At. Mol. Opt. Phys. **41**, 83 (1999).

[4] G. Farkas and C. Toth, Phys. Lett A **168**, 447 (1992); S.E. Harris et al., Opt. Commun. **100**, 487 (1993); N.A. Papadogiannis et al., Phys. Rev. Lett. **83**, 4289 (1999).

[5] Ph. Antoine et al., Phys. Rev. Lett. **77**, 1234 (1996).

[6] C. Spielmann et al., Science **278**, 661 (1997); Z. Chang et al., Phys. Rev. Lett. **79**, 2967 (1997).

[7] M. Bellini et al., Phys. Rev. Lett. **81**, 297 (1999); L. Le Deroff et al., Phys. Rev. A **61** 043802 (2000).

[8] P. Salieres et al., Phys. Rev. Lett. **81**, 5544 (1998).

[9] P.B. Corkum et al., Opt. Lett. **19**, 1870 (1994); A. Rundquist et al., Science **280**, 1412 (1998); Y. Tamaki et al., Phys. Rev. A **59**, 4041 (1999); R. Bartels et al., Nature **406**, 164 (2000).

[10] J. B. Watson, A. Sanpera, and K. Burnett, Phys. Rev. A **51**, 1458 (1995).

[11] C. Kan, C. E. Capjack, R. Rankin, and N. H. Burnett, Phys. Rev. A **52**, R4336 (1995).

[12] H. J. Shin, D. G. Lee, Y. H. Cha, K. H. Hong, and C. H. Nam, Phys. Rev. Lett. **83**, 2544 (1999).

[13] M. Lewenstein, Ph. Balcou, M. Yu. Ivanov, A. L'Huillier, and P. B. Corkum, Phys. Rev. A **49**, 2117 (1994).

[14] M. Lewenstein, P. Salieres, A. L'Huillier, Phys. Rev. A **52**, 4747 (1995).

[15] P. B. Corkum, Phys. Rev. Lett. **71**, 1994 (1993).

[16] M. B. Gaarde, F. Salin, E. Constant, Ph. Balcou, K. J. Schafer, K. C. Kulander, and A. L'Huillier, Phys. Rev. A **59**, 1367 (1999).

[17] Ph. Balcou, A. S. Dederichs, M. B. Gaarde, and A. L'Huillier, J. Phys. B 32, 2973

(1999).

[18] D. G. Lee, H. J. Shin, Y. H. Cha, K. H. Hong, and C. H. Nam, Phys. Rev. A, submitted.

[19] Equivalently, using the linearity of the Fourier transform, one may first add the dipole accelerations, i.e., $d(t)=\Sigma d_i(t)/N$, and then make a Fourier transform to get the same dipole spectrum of Eq. (1)

[20] A. L'Huillier, Ph. Balcou, S. Candel, K. J. Schafer, and K. C. Kulander, Phys. Rev. A **46**, 2778 (1992).

[21] S. C. Rae, K. Burnett, and J. Cooper, Phys. Rev. A **50**, 3438 (1994).

[22] M. B. Gaarde, Ph. Antoine, A. L'Huillier, K. J. Schafer, and K. C. Kulander, Phys. Rev. A **57**, 4553 (1998).

[23] J. B. Watson, A. Sanpera, K. Burnett, and P. L. Knight, Phys. Rev. A **55**, 1224 (1997).

[24] K.J. Schafer et al., Phys. Rev. Lett. **70**, 1599 (1993).

[25] Z. Chang et al., Phys. Rev. A **58**, R30 (1998); C. Altucci et al., Phys. Rev. A **58**, 3934 (1998); T. Sekikawa et al., Phys. Rev. Lett. **83**, 2564 (1999).

[26] M. Hillery et al., Phys. Rep. **106**, 121 (1984).

[27] H.W. Lee, Phys. Rep. **259**, 147 (1995).

[28] L. Cohen, Proc. IEEE **77**, 941 (1989).

[29] J.H. Kim, H.J. Shin, D.G. Lee, and C.H. Nam, Phys. Rev. A (to be published).

[30] M. Kus et al., Phys. Rev. Lett. **71**, 2167 (1993).

[31] P. Salieres et al., Phys. Rev. Lett. **74**, 3776 (1995); Ph. Balcou et al., Phys. Rev. A **55**, 3204 (1997).

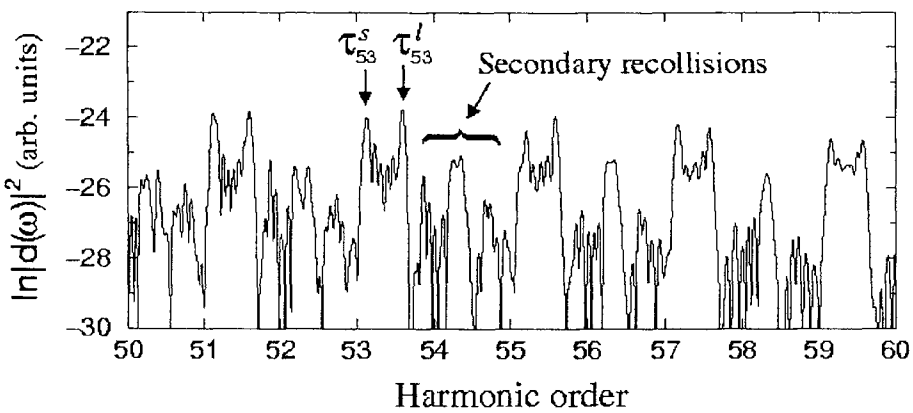

Fig.1. High harmonic spectrum in the mid-plateau region from a neon atom irradiated by an 160 fs (FWHM) Gaussian laser pulse with λ=800 nm and intensity I=10^{15} W/cm^2.

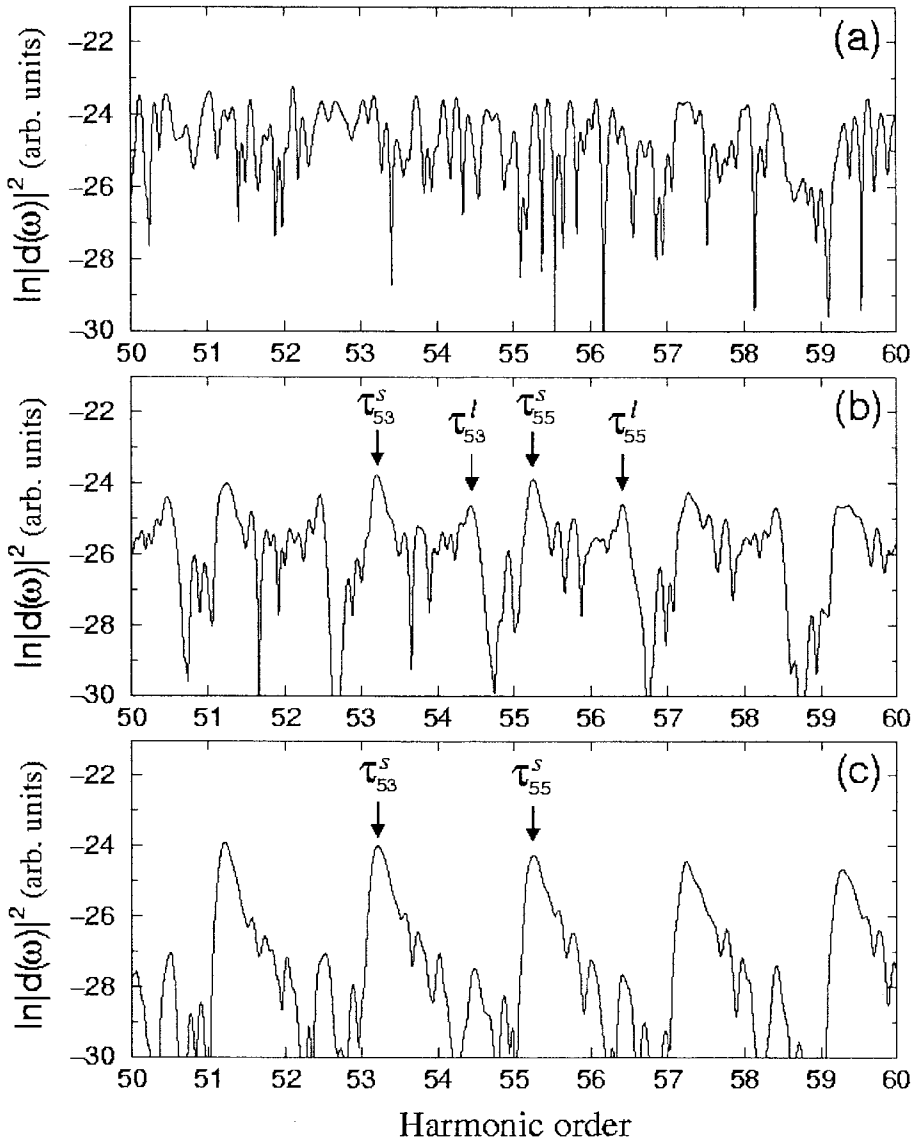

Fig.2. Same as Fig. 1 except that the pulse width is 80 fs. (a) Spectrum for a single pulse. (b) Spectrum after the sum of Eq. (1), where N=20 dipole spectra are used with $\Delta I/I=2.6\%$. (c) Same as (b) except $\Delta I/I=8\%$.

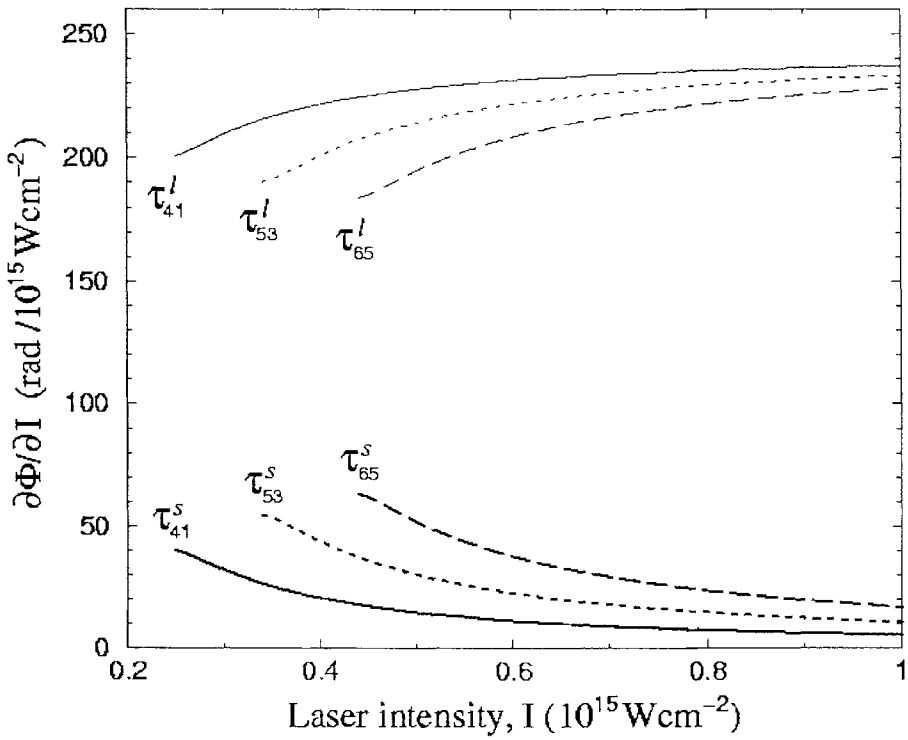

Fig.3. Dipole phase gradients of τ^s_q and τ^l_q trajectories for a neon atom placed in a constant-intensity field with λ=800 nm.

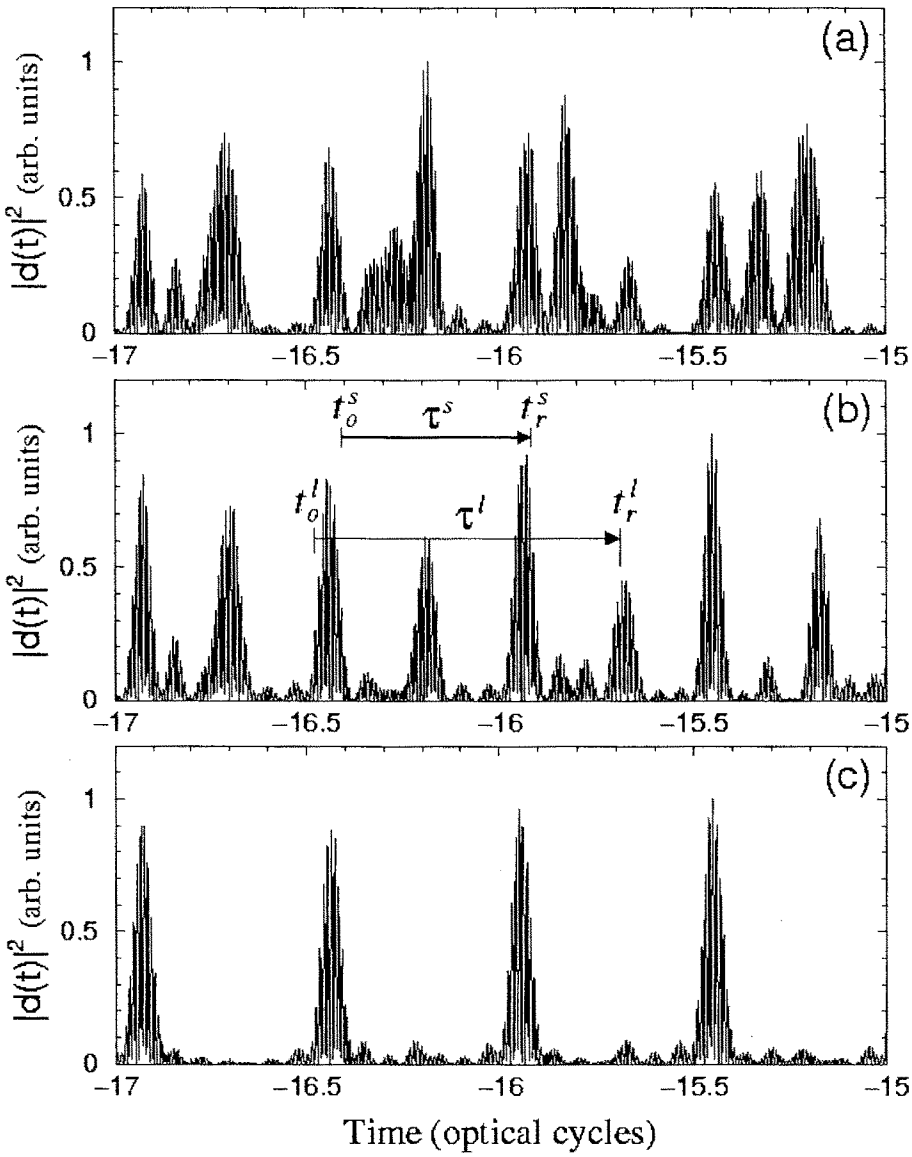

Fig.4. Temporal profiles of high harmonics between $44\omega_0$ and $60\omega_0$. The incident laser pulse is centered at t=0. In (a), (b), and (c), same parameters are used as in Figs. 2(a), (b), and (c), respectively. The release time t_0, recombination time t_r and excursion time τ for the two primary trajectories in (b) are calculated classically.

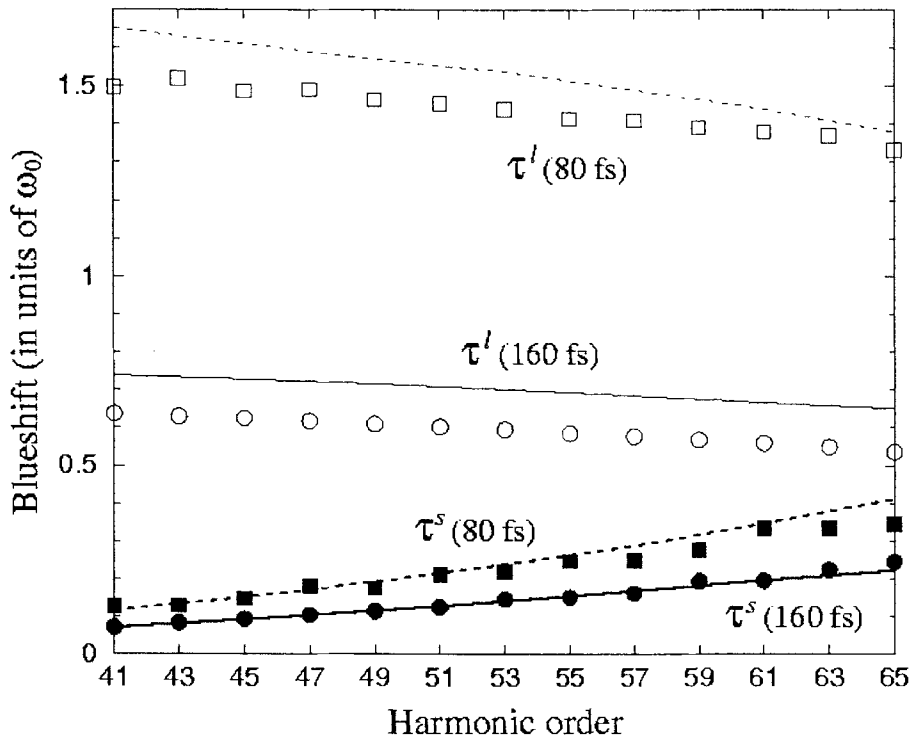

Fig.5. Blueshift of τ^s_q and τ^l_q components for 160 and 80 fs pulses with wavelength 800 nm and intensity I=10^{15} W/cm^2. Filled circles stand for the τ^s_q components at 160 fs, open circles the τ^l_q components at 160 fs, filled squares the τ^s_q components at 80 fs, and open squares the τ^l_q components at 80 fs. Solid and dotted curves represent the semiclassical calculations of Eq. (5) at 160 and 80 fs respectively.

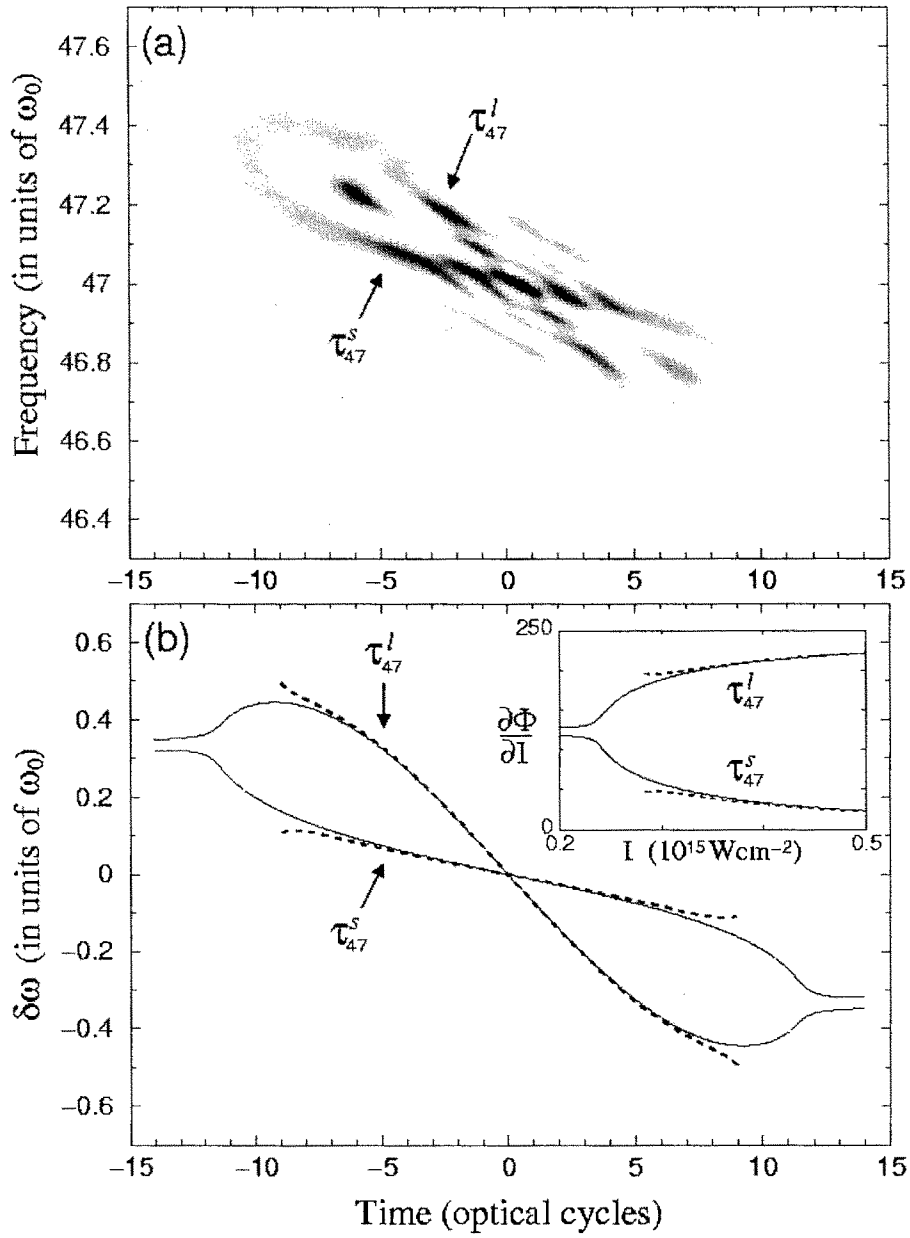

Fig.6. (a) Wigner distribution of the 47th harmonic (windowed between $46.5\omega_0$ and $47.5\omega_0$ from a neon atom irradiated by an 80 fs (FWHM) Gaussian laser pulse (centered at t=0) with a wavelength λ=800 nm and a peak intensity $I=3.6\times10^{14}$ W/cm^2. Only positive values are plotted. (b) Frequency variation of the 45th harmonic calculated semiclassically. The inset shows the dipole phase gradient (in units of 10^{-15} rad/Wcm^{-2}) as a function of the laser intensity.

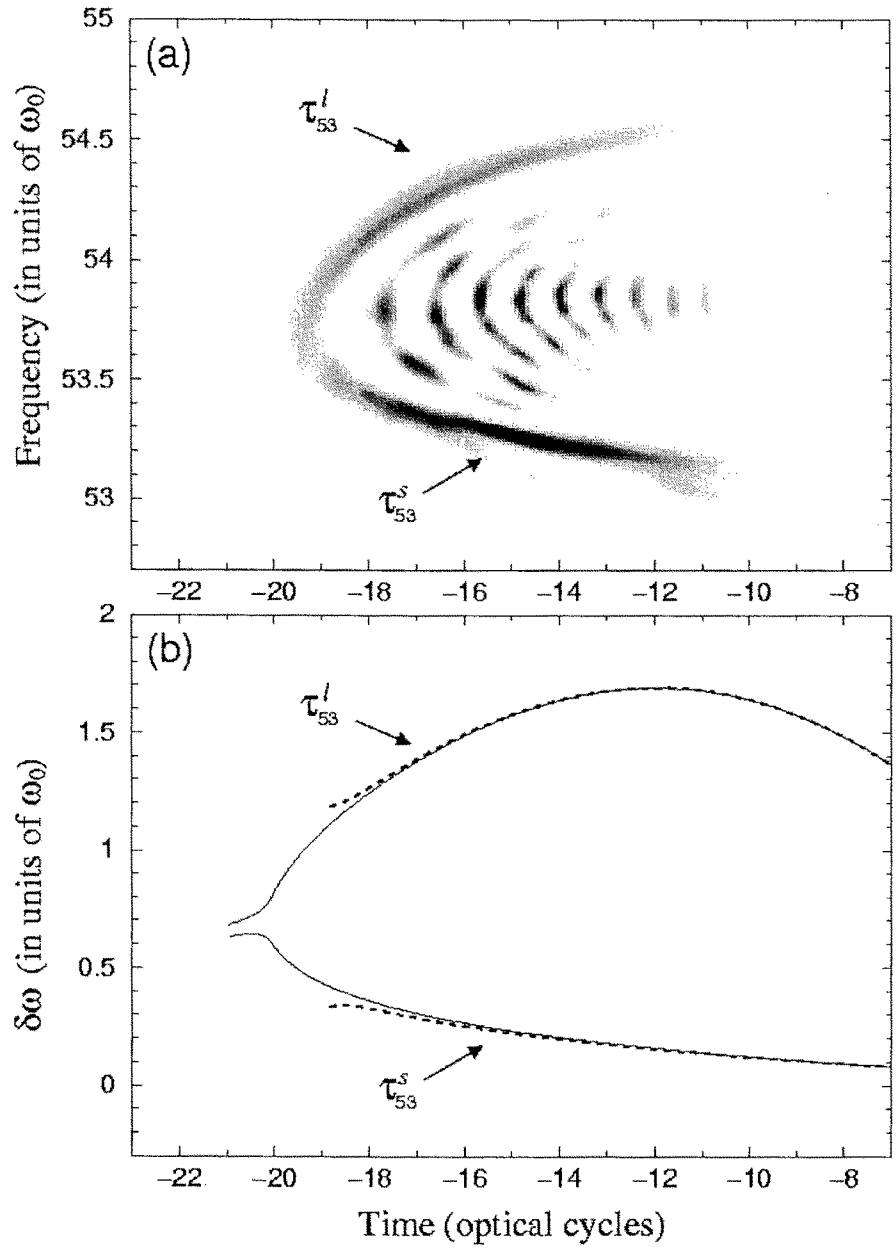

Fig.7. (a) Wigner distribution of the 53rd harmonic (windowed between $52.8\omega_0$ and $54.7\omega_0$) for the same parameters as in Fig.6 except that $I=10^{15}$ W/cm^2. Only positive values are plotted. (b) Frequency variation of the 53rd harmonic calculated semiclassically.

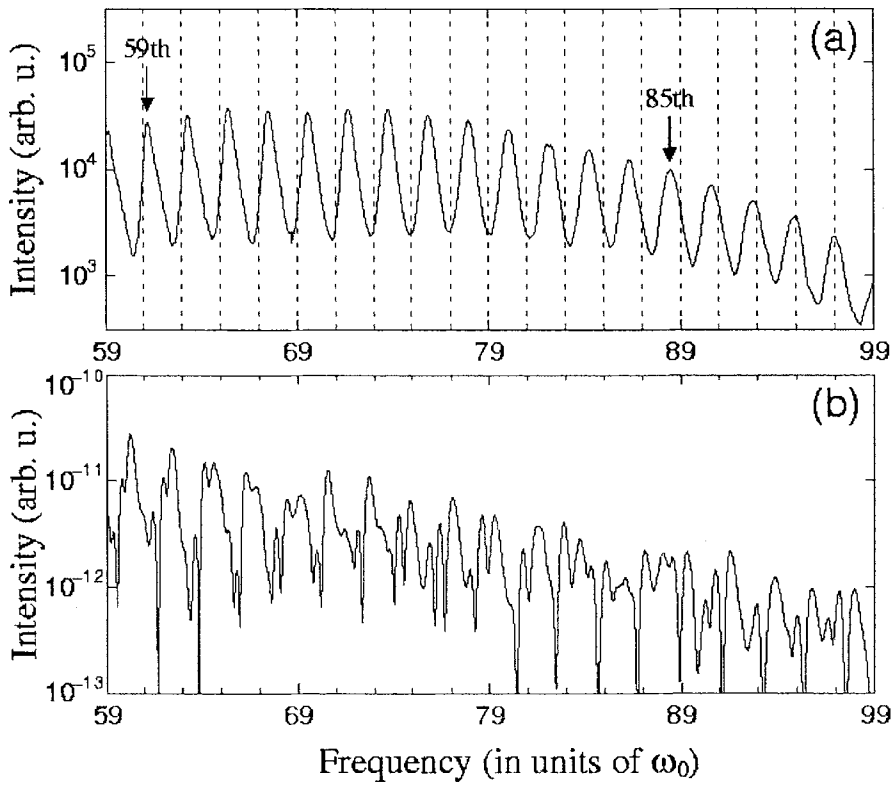

Fig.8. (a) Experimental high harmonic spectrum from a neon gas of density 3×10^{18} cm^{-3} irradiated by an 27 fs, 817 nm laser pulse of intensity $I=10^{16}$ W/cm^2. (b) Single-atom calculation for (a) (only the short trajectory component is shown).

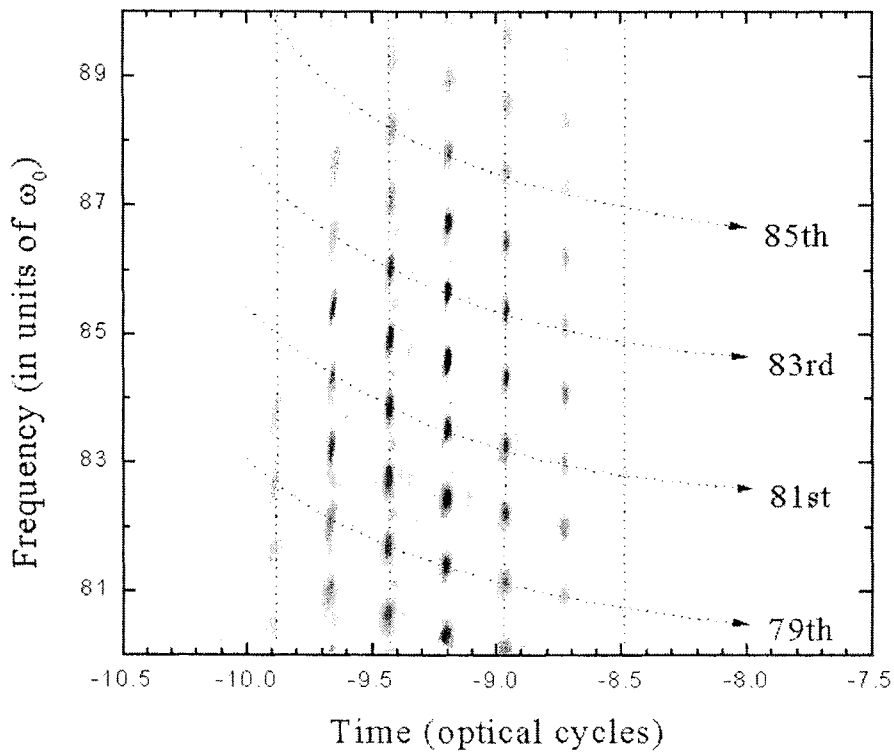

Fig.9. Wigner distribution of single-atom high harmonics windowed between $75\omega_0$ and $95\omega_0$ for the same parameters as in Fig.8.(b). Positive values are colored red and negative values are colored blue (in arbitrary units)

A. 3. Operation and Development of Femtosecond Terawatt Lasers

A. 3. 1. Development of a 1 kHz Femtosecond Terawatt Laser

I. Introduction

Femtosecond terawatt lasers can produce very intense pulses in the femtosecond range and provide the unique environment in which very high electric field lasts only for a few tens of femtoseconds. The extremely short duration of the femtosecond laser pulses also results in the spatially localized electromagnetic field, another unique environment. Due to their intensity or temporal and spatial localization, they have been applied to many research fields, such as their high-harmonic generation, X-ray laser, and attosecond pulse generation, and are still expanding their new application areas.

In the development of a femtosecond terawatt laser it should be noted that very short pulse can cause the damage of optical components because of nonlinear self-focusing even before a pulse is amplified to a desired level. This problem can be solved by using the technique of chirped-pulse amplification (CPA). CPA is a unique technique for the amplification of the femtosecond pulse in which a pulse is stretched by a factor of 1000-10000, amplified to a desired level, and finally compressed close to its initial pulse duration. Due to the advent of the CPA technology there has been great advancement in power level, pulse duration, compactness and repetition rate of high-power laser systems, and, currently, most high-power lasers are developed based on the CPA technique.

A femtosecod terawatt Ti:sapphire laser based on the CPA technique has been greatly advanced and widely spread in past several years because Ti:sapphire is a very attractive gain medium for the generation and the amplification of femtosecond pulses in terms of its very broad gain profile, high saturation fluence, and good physical property[1-5].

Recently, in spite of its lower power level, a 1-kHz high-power Ti:sapphire laser is showing more versatile aspects in many application fields than a ~10-Hz laser system due to its compactness, high average power, and high-repetition rate[6,7].

In this research, we designed and built an initial setup of a 1-kHz femtosecond terawatt Ti:sapphire laser based on the CPA. The expected power and pulse duration are about 0.1 TW and 20 fs, respectively.

II. Design points and set up of a 1-kHz femtosecond terawatt Ti:sapphire laser

The 1-kHz femtosecond terawatt Ti:sapphire laser is composed of a femtosecond oscillator, a pulse stretcher, amplifying stages, and a pulse compressor, as shown in Fig. 1. The total system is installed on one optical table of 1.2 m X 3.0 m.

1. Femtosecond Ti:sapphire oscillator

For the generation of femtosecond pulses as seeds to amplifying stages, a Kerr-lens mode-locked Ti:sapphire oscillator is typically used. Kerr-lens mode-locking (KLM) utilizes a nonlinear self-focusing effect (Kerr effect) behaving like a fast saturable absorber in a specific resonator condition. Due to its simplicity and non-resonant property, KLM has been widely used for the short pulse generation in many kinds of lasers. In addition to KLM, proper dispersion compensation is necessary to reach a femtosecond regime of pulse duration. Because most of optical materials such as Ti:sapphire, BK7, and fused silica have positive group-delay dispersion (GDD), negative GDD should be added to compensate for the positive GDD inside a cavity including Ti:sapphire. Such negative GDD can be easily realized by installing a prism pair anti-parallel to each other inside a cavity, and the amount of negative GDD can be controlled by adjusting the separation between two prisms.

A typical setup of a KLM Ti:sapphire laser is given in Fig. 2. It is composed of a Ti:sapphire crystal, two concave mirrors, a flat rear mirror, an output coupler, and a prism pair. The Ti:sapphire crystal positioned between two concave mirrors is not only a

gain medium but also a nonlinear medium for KLM. To insure the high laser intensity at the crystal, the crystal is located at the tightly focused beam mode between two concave mirrors, and the focused beam mode size is determined by the radius of the concave mirrors. The smaller radius of concave mirrors forms more tightly focused beam mode at the Ti:sapphire crystal, and this also helps to lower the lasing threshold. Typically, a ~10-cm radius is used.

For the optimal dispersion compensation inside a cavity, the thickness of a Ti:sapphire crystal should be small. On the other hand, the Ti:sapphire crystal should be thick enough to absorb 80-90% of a pumping power. These two contradictory restrictions can be solved by using a thin Ti:sapphire crystal with a high absorption coefficient. The selection of a prism material is also important because the amount of high order dispersion is mainly determined by the prism material. Fused silica is widely used due to its small high-order dispersion. To determine the prism separation for the optimal dispersion compensation, it should be noted that the prism material itself has positive GDD while the geometric configuration of the prism pair anti-parallel to each other has negative GDD.

A femtoseoncd oscillator as a front-end laser of a high-power laser system has another desirable requirements such as a broad output spectrum and a high output pulse energy. Because the gain-narrowing effect reduces an amplified spectral width during amplification, a broader input spectrum is favorable to obtain a broad amplified spectrum. The high pulse energy has advantage in suppressing amplified spontaneous emission (ASE) and the gain-narrowing effect. The broad output spectrum can be achieved by the used of broadband, low-dispersion mirrors and the careful dispersion compensation. The high pulse energy, however, is not easy to obtain due to the limited pump power of less than 5 W, and 1-2 nJ of a pulse energy is a typical value with a ~10-fs pulse duration. To overcome the limited pump power in increasing the pulse energy, a cavity-dumping technique or a long-cavity oscillator is used. The cavity-dumping technique can generate femtosecond pulses of more than 30 nJ but requires a complicated set up to install a cavity dumper inside a cavity. The long-cavity oscillator can generate 5-10 nJ pulses with a relatively simple configuration[8].

In this research, we developed a long-cavity femtosecond Ti:sapphire oscillator, as shown in Fig. 3. The Ti:sapphire crystal (Crystal systems) is 3-mm-long and highly doped with an absorption coefficient of 6.8/cm at 532 nm. It is mounted in a copper block and water-cooled to ~20 ^{o}C. A frequency-doubled Nd:YVO_4 laser (Millennia V, Spectra-Physics) is used to pump the Ti:sapphire crystal with a pump power of up to 5 W. The two concave mirrors have a 10-cm radius, and the Ti:sapphire crystal is installed between them. The pump beam is focused by a lens of a 10-cm focal length and goes through one of the concave mirror to longitudinally pump the crystal. For the dispersion compensation inside the cavity, a fused silica prism pair is used with a separation of ~50 cm. The lengths of two arms were initially set to 60 cm and 95 cm, respectively. With a 10% output coupler, the cw power was 450 mW at a 3.6-W pumping. The KLM condition can be found by adjusting the position of the concave mirrors, the Ti:sapphire sapphire crystal, and the pump beam focusing lens. The KLM could be started by moving a prism or tabbing a mirror, and the mode-locked power was ~350 mW at a 3.6-W pumping. The repetition rate was ~100 MHz and the pulse energy was 3.5 nJ.

For a long-cavity set up of the Ti:sapphire laser, the arm of 60 cm was lengthened to 260 cm using a 1:1 telescope with two concave mirrors of a 50-cm focal length. The image at the output coupler was image relayed to a new output coupler position not to affect the lasing condition. With a long-cavity set up, the cw power was ~400 mW and the mode-locked power ~300 mW at a 3.6-W pumping. The repetition rate of the oscillator was lowered to 40 MHz with a long-cavity set up, and the pulse energy was increase to 6.7 nJ. Fig.4 shows a typical output spectrum of mode-locked pulses from the long-cavity Ti:sapphire laser. The transform-limited pulse duration of the spectrum was ~9 fs.

2. Pulse stretcher

The femtosecond pulse from the front-end oscillator should be temporally stretched before amplification to prevent damage of amplifying stages. The basic idea of pulse stretching is decomposing and unfolding spectral components of a femtosecond pulse in time domain by using a diffraction grating. Figure 5 shows a pulse stretcher composed of a grating, a convex mirror, a concave mirror, and flat mirrors. The grating diffracts

each spectral components of an incident pulse to a different diffraction angle. The concave and the convex mirrors form a telescope of −1 magnification, and each diffracted spectral components passing the telescope returns to the grating with the same incident angle as its diffraction angle. Therefore, each spectral components propagates parallel but along different paths after second diffraction at the grating, which yields a frequency dependent propagation delay through the stretcher.

The stretched pulse duration is determined by a following formula.

$$\Delta t = -2 \cdot \frac{\lambda^3 \cdot Z}{2\pi c^2 d^2 \cos^2 \theta} \cdot \Delta \varpi$$

where λ is a center wavelength of a input pulse, c the speed of light, d a grating constant, θ a diffraction angle of the center wavelength, $\Delta\varpi$ a bandwidth of a input pulse, and Z effective separation of a grating and its image. We used a gold-coated 1400 l/mm grating (Spectrogon), a concave mirror of a 30-cm focal length, and a convex mirror of a 15-cm focal length. The expected pulse duration after the pulse stretcher is ~200 ps with an incident angle of 45°, a 800-nm center wavelength, an effective separation of 20 cm and the bandwidth of ~80 nm.

The aberration in a stretcher should be kept low because it results in spatial chirping and unexpected modulation of pulse structure. To minimize the aberration, the Offner-triplet type stretcher was used[9], and the pulse was image-flipped vertically and horizontally in the stretcher to compensate for the residual aberration.

It was found that the spectrum after the stretcher was severely cut on the short wavelength side, as shown in Fig 6. This is due to the limited bandwidth of the concave and the convex mirrors which are dielectric-coated. The transmission bandwidth of the stretcher can be improved by replacing the dielectric-coated mirrors with metal-coated ones.

3. preamplifier

A preamplifier amplifies the input pulse of nJ level to a mJ level. Therefore, a very high gain of ~10^6 is necessary in a preamplifier. There are two kinds of preamplifier widely

used for the femtosecond pusles. One is a regenerative amplifier which capture an input pulse into a resonator and releases it after amplification inside the resonator with 10-20 round-trips. The regenerative amplifier has a relatively high efficiency but a complicated configuration because a Pockels cell and polarizing beam splitters should be used inside the resonator to capture and release a pulse. Further more, due to a large amount of dispersion inside a resonator, it is difficult to achieve precise dispersion compensation at a pulse compressor. The second type of preamplifier is a multipass amplifier which is composed of only a gain medium and several mirrors. Although its efficiency is not so high as the regenerative amplifier, it has advantages in terms of simple configuration and minimal amount of dispersion.

Figure 7 shows the preamplifier we designed. It is a ring-type ten-pass amplifier composed of a Ti:sapphire crystal, two concave mirrors of 50-cm and 45-cm focal lengths, and flat mirrors[10]. The Ti:sapphire crystal is 6-mm long and has an absorption coefficient of 4.5/cm at 532 nm. It is pumped by a 5-W average power from a frequency-doubled Nd:YLF laser (Merlin, Positive light), and the pump beam is focused to the crystal by a len of a 50-cm focal length. To suppress thermal problems by the high average pump power, the crystal is cooled by the combination of TE and water cooling.

At the preamplifier, especially, operating at a high-repetition rate of 1 kHz, the ASE problem is one of the most serious problem. The 1-kHz pump laser typically has pulse duration of more than 200 ns which is long compared to the round-trip time of the preamplifier, and ASE can be built up even before the injection of a seed pulse. The confocal configuration of the two concave mirrors of different focal lengths helps to suppress the ASE due to its unstable-type resonator characteristics. For further suppression of the ASE, a Pockels cell is used in the passes at the preamplifier. After 5 passes, the pulse is picked and selected out by the Pockels cell, and only the selected pulse makes another 5 passes at the preamplifier. This could significantly reduce the ASE because most of ASE is blocked after 5-passes. An amplified energy of ~0.5 mJ is expected at the preamplifier.

4. Power amplifier

In contrast to a preamplifier, a gain at a power amplifier is low, but the extracted energy should be high. Therefore, the efficiency should be maximized in a power amplifier. Figure 8 shows the power amplifier we designed. It is also a ring-type four-pass amplifier composed of a Ti:sapphire crystal, two concave mirrors of a 50-cm focal length, and flat mirrors. The Ti:sapphire crystal is 6-mm long, of a 4.5/cm absorption coefficient, and pumped by a 15-W average power from the frequency-doubled Nd:YLF laser. For the efficient amplification, the mode matching between the pump and the laser beams should be optimized. The ring-type amplifier is advantageous in mode matching because the beam size at the gain medium can be easily adjusted to a optimal value. Due to the high pump power, the Ti:sapphire crystal should be cooled by TE and water cooling. The amplified energy is expected to be ~4 mJ at the power amplifier.

5. Pulse compressor

The amplified pulse is compressed closed to its original pulse duration at a pulse compressor to generate a high peak power. A pulse compressor performs a reverse action against a pulse stretcher; the unfolded spectral components of the stretched pulse are effectively recombined to form a femtosecond pulse. The pulse compressor we designed is shown in Fig. 9. It is composed of two 1480 l/mm gratings and flat mirrors.

To obtain minimal pulse duration, the dispersion accumulated through the laser system should be carefully compensated for, and the slightly different grating constant from the stretcher is more advantageous in minimizing residual high-order dispersion. With an incidence angle of 52.684° and an 40-cm separation between two gratings, up-to third-order dispersion of the laser system including a total 84-cm length of Ti:sapphire can be compensated for.

References

[1] C. P. J. Barty, C. L. Gordon III, and B. E. Lemoff, Opt. Lett. **19**, 1442 (1994).

[2] J. Zhou, C.-P. Huang, M. M. Murnane, and H. C. Kap-teyn, Opt. Lett. **20**, 64 (1995).

[3] J. P. Chambaret, C. Le Blanc, G. Cheriaux, P. Curley, G. Darpentigny, P Rousseau, G. Hamoniaux, A. Antonetti, and F. Salin, Opt. Lett. **21**, 1921 (1996).

[4] C. P. J. Barty, T. Guo, C. Le Blanc, F. Raksi, C. Rose-Petruck, J. Squier, K. R. Wilson, V. V. Yakovlev, and K. Yamakawa, Opt. Lett. **21**, 668 (1996).

[5] Y. H. Cha, Y. I. Kang, and C. H. Nam, J. Opt. Soc. Am. B **16**, 1220 (1999).

[6] S. Backus, C. G. Durfee III, G. Mourou, H. C. Kapteyn, and M. M. Murnane, Opt. Lett. **22**, 1256 (1997).

[7] S. Sartania, Z. Cheng, M. Lenzner, G. Tempea, Ch. Spielmann, and F. Krausz, Opt. Lett. **22**, 1562 (1997).

[8] S. H. Cho, B. E. Bouma, E. P. Ippen, and J. G. Fujimoto, Opt. Lett. **24**, 417 (1999).

[9] G. Cheriaux, P. Rousseau, F. Salin, and J. P. Chambaret, Opt. Lett. **21**, 414 (1996).

[10] S. Backus, J. Peatross, C. P. Huang, M. M. Murnane, and H. C. Kapteyn, Opt. Lett. **20**, 2000 (1995).

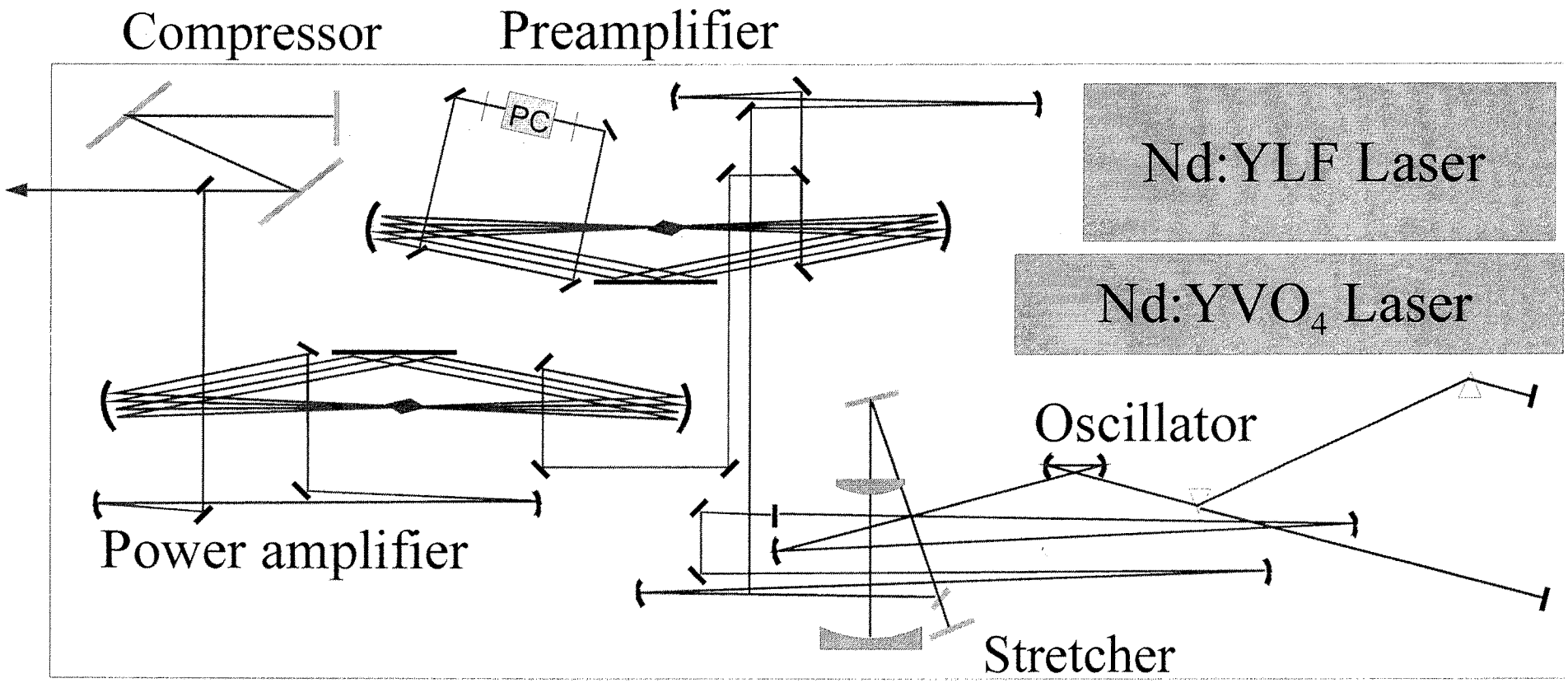

Fig. 1. Layout of a 1-kHz femtosecond terawatt Ti:sapphire laser.

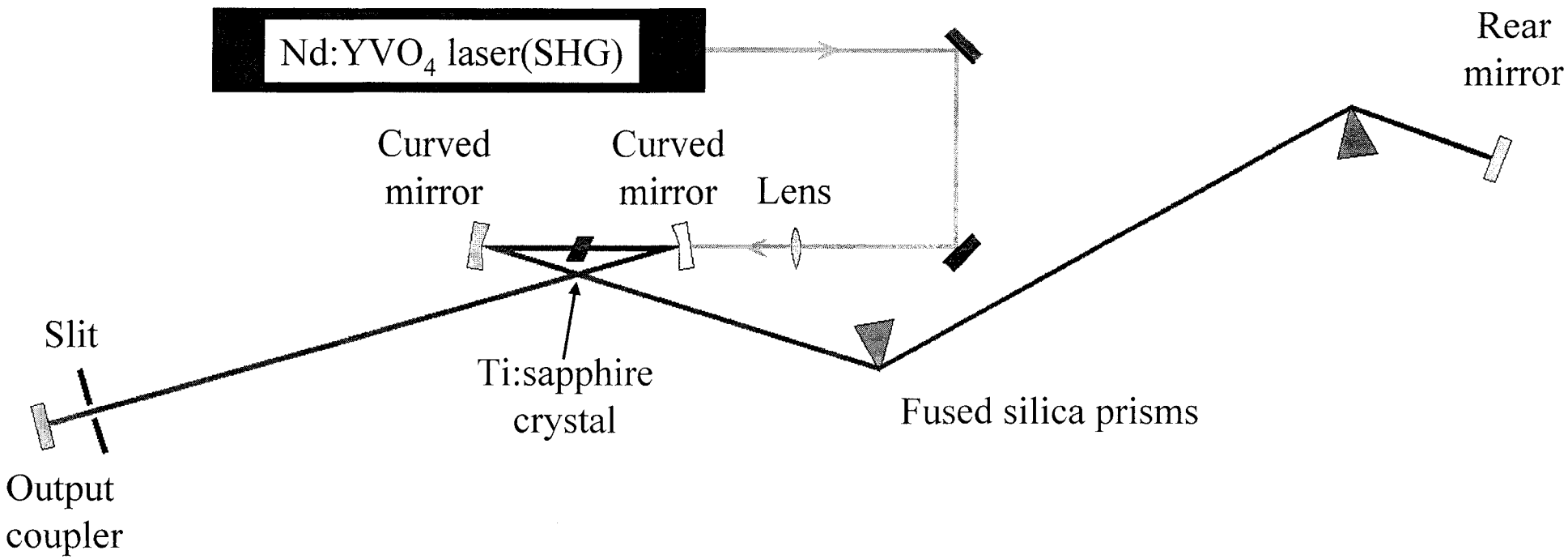

Fig. 2. Schematics of a Kerr-lens mode-locked Ti:sapphire laser.

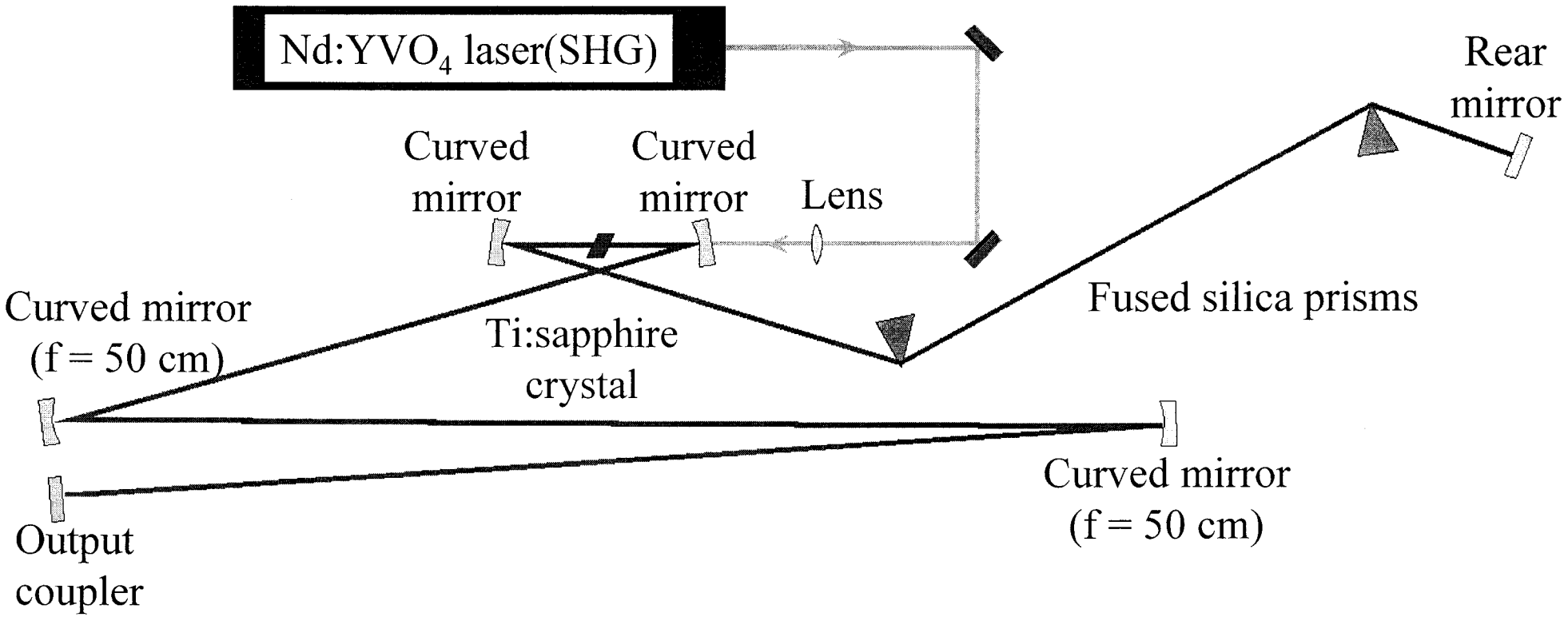

Fig. 3. Schematics of a long-cavity Kerr-lens mode-locked Ti:sapphire laser.

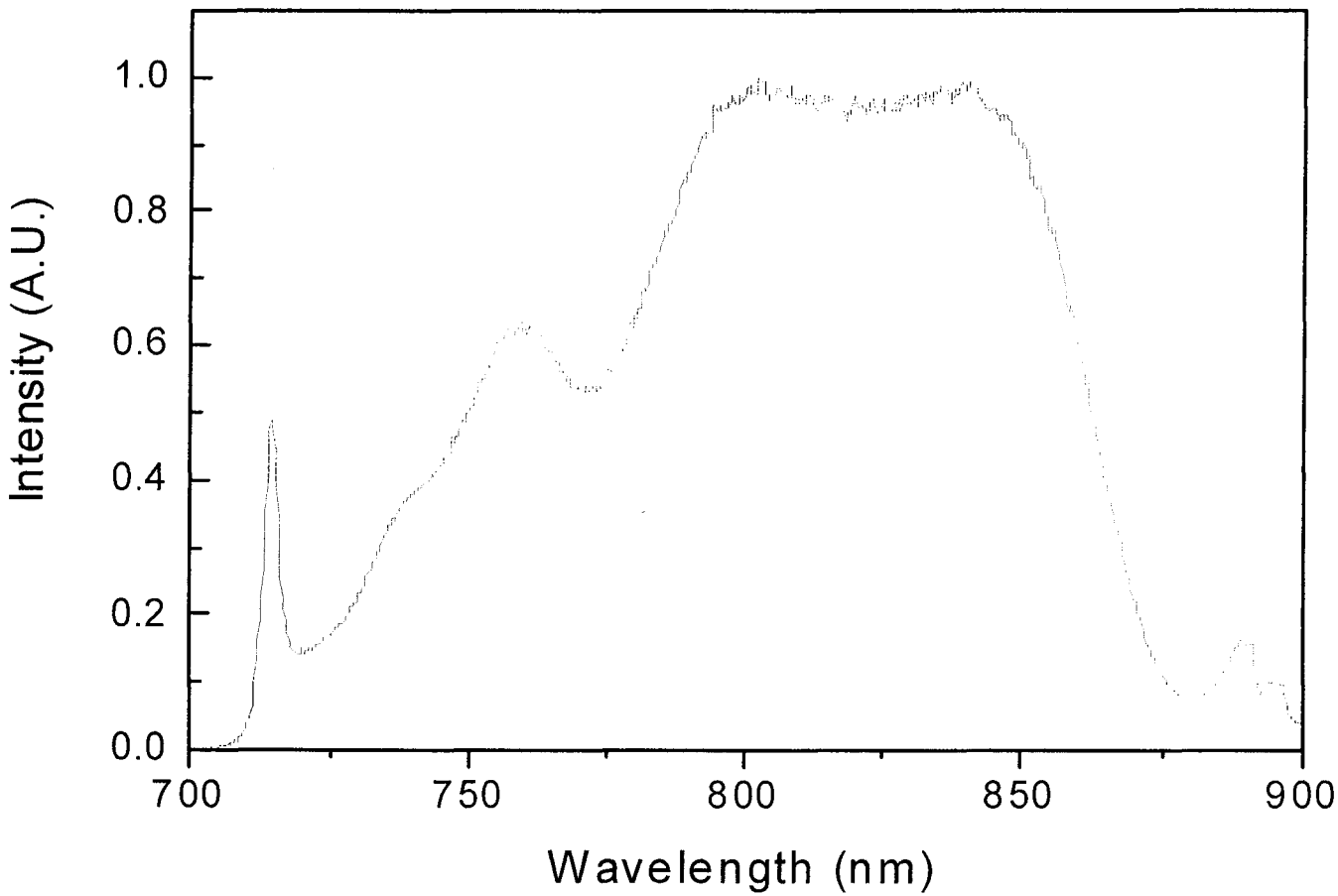

Fig. 4. Spectrum of a long-cavity femtosecond Ti:sapphire oscillator

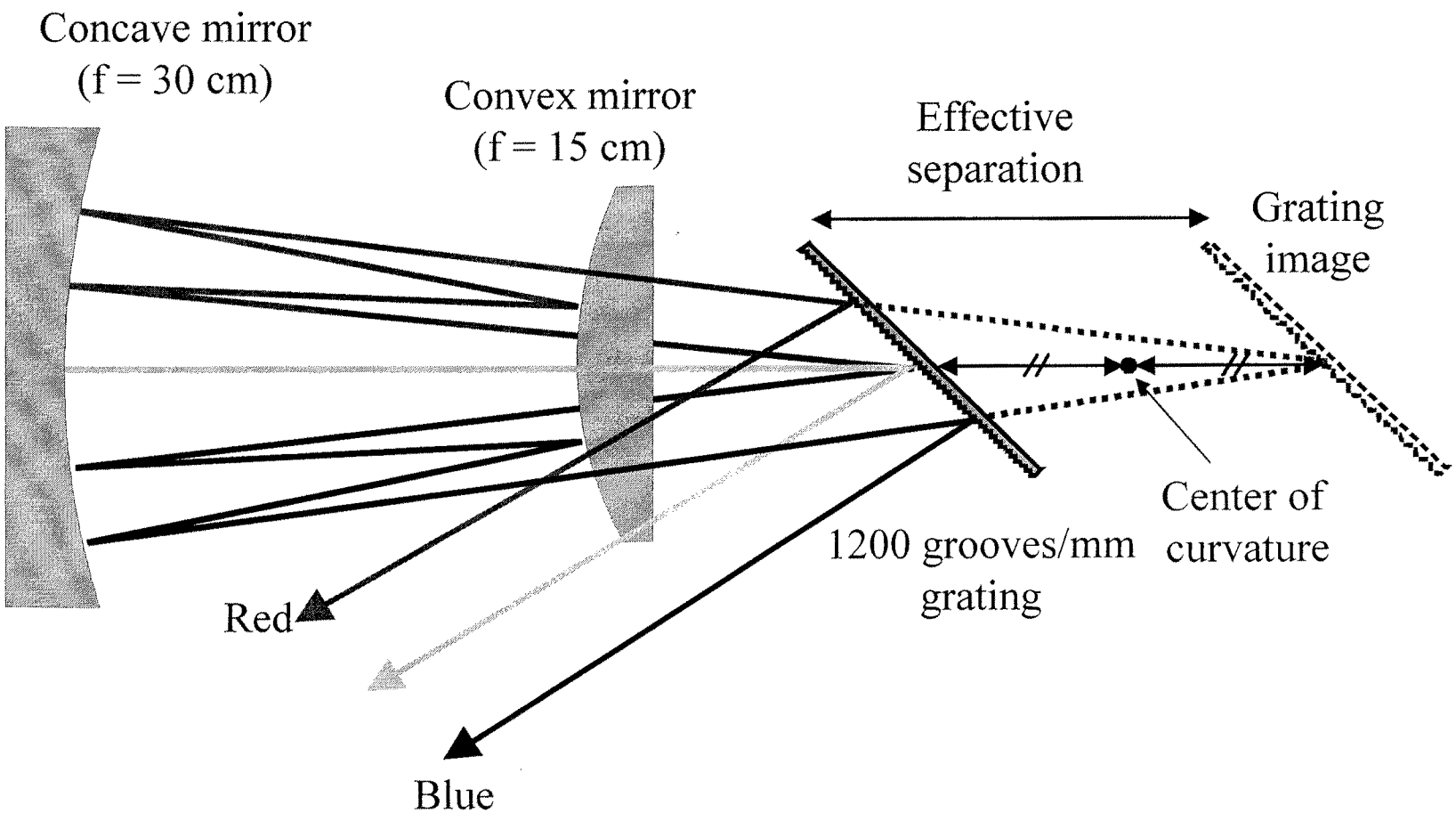

Fig. 5. Schematics of a Offner-triplet type pulse stretcher

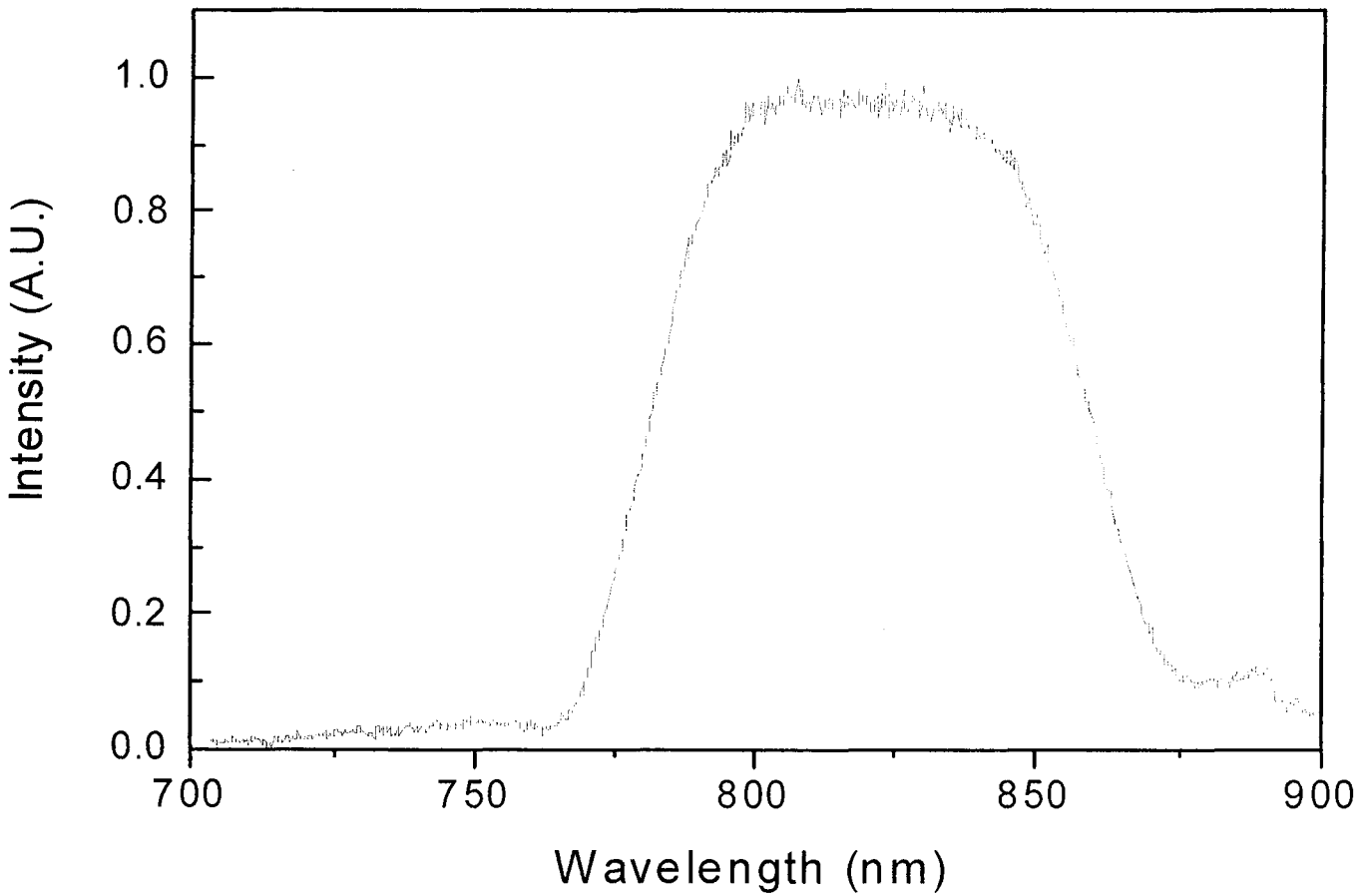

Fig. 6. Spectrum of a stretched pulse.

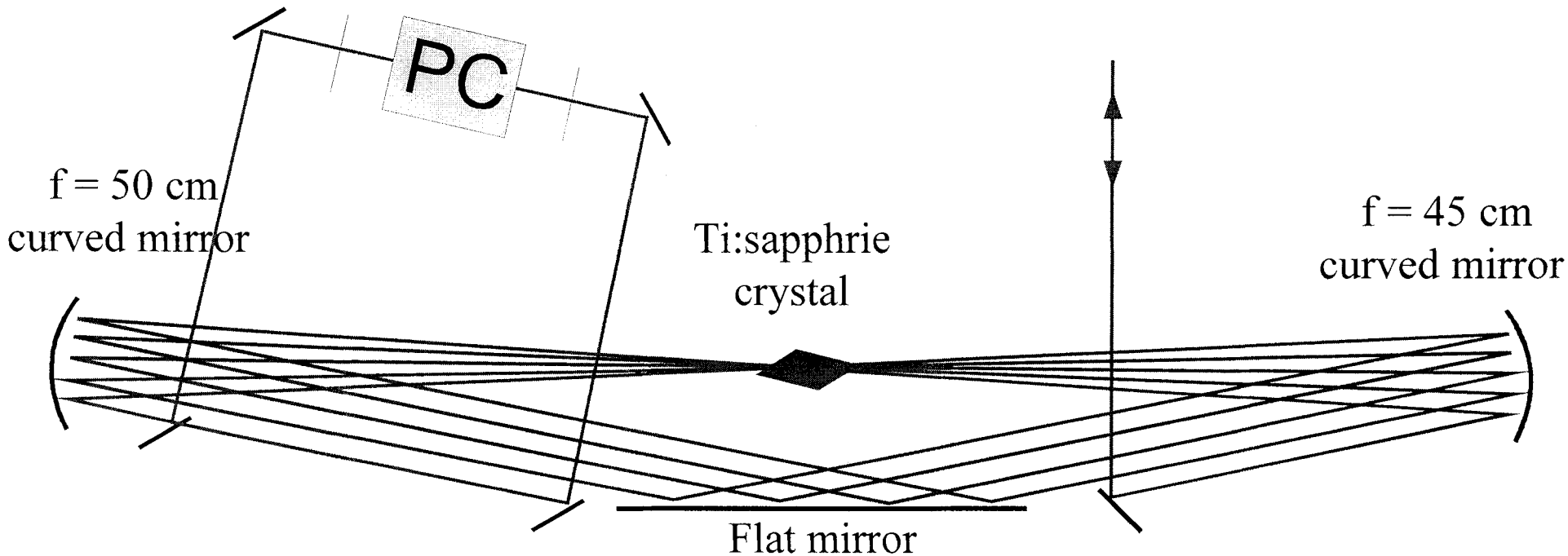

Fig. 7. A ring-type ten-pass preamplifier.

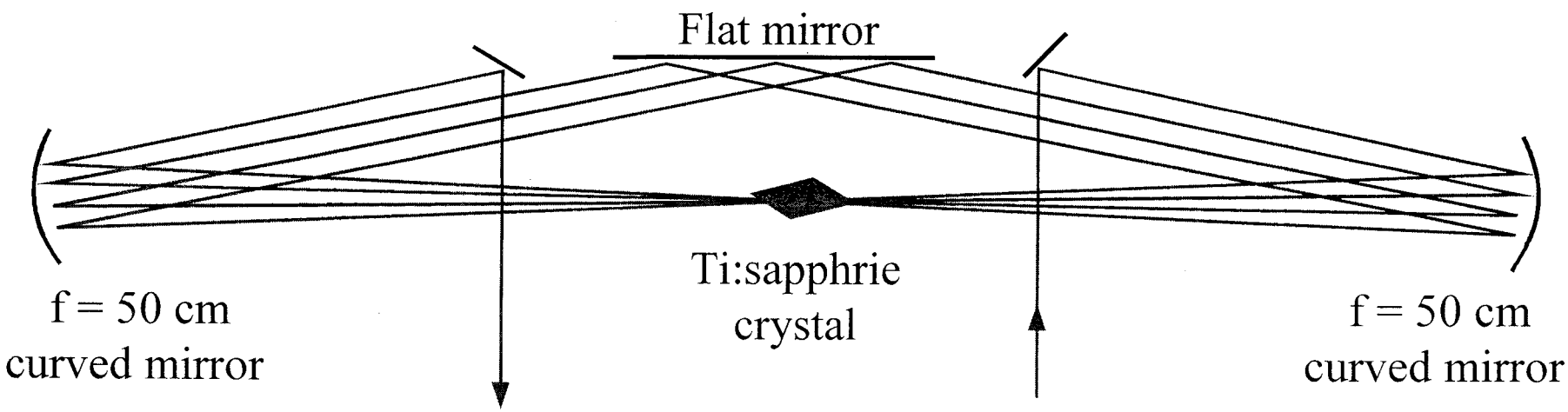

Fig. 8. A ring-type four-pass power amplifier.

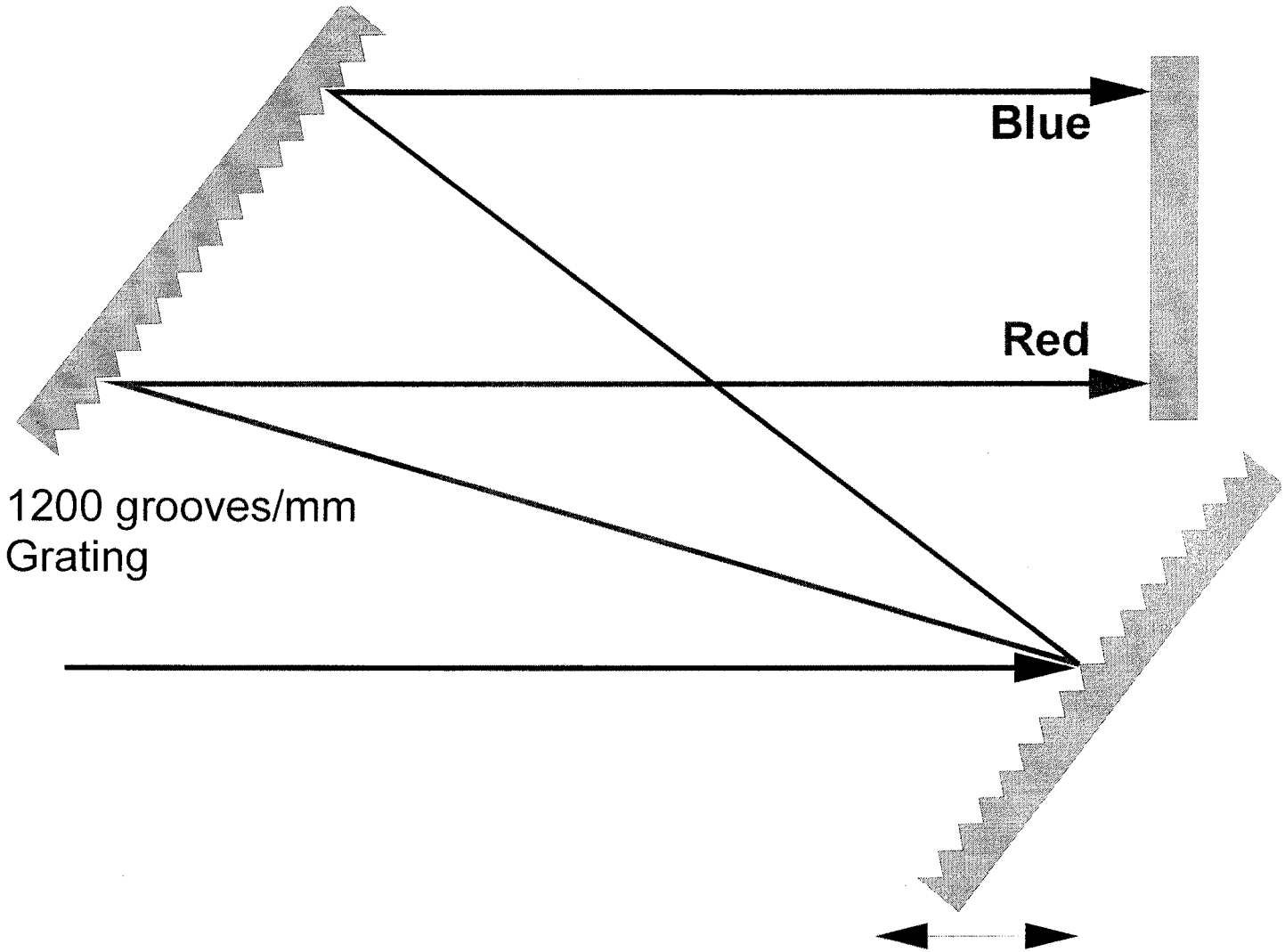

Fig. 9. Schematics of a pulse compressor.

A. 3. 2. Temporal Structure of Chirped Laser Pulses

I. Introduction

A chirped pulse amplification (CPA) laser system uses a pulse stretcher to avoid an optical damage induced by laser pulses of high peak power during amplification. After sufficient amplification, the stretched pulses are sent to a pulse compressor that has an inverse geometry of the stretcher. This is the main concept of the CPA technique that enables the generation of terawatt laser pulses in the femtosecond region [1].

An ultrashort pulse with broadband spectrum can be stretched by a strongly dispersive optical element such as diffraction grating, prism, and glass block because each of frequency components in the pulse will experience different path length when the pulse passes through it. The stretched pulse has a unique temporal structure with its spectral component arranged in time domain, so this is called 'frequency chirping' and can be described mathematically in terms of group delay dispersion (GDD). Positive GDD induces 'positive chirping' in the sense that the frequency increases with time, and negative GDD 'negative chirping' in the contrary meaning. The function of a stretcher in a CPA laser system is to load a strong positive chirping, so that low frequency component is located at the leading part of the pulse, resulting in pulse broadening. Stretching factor is determined by the amount of GDD induced by the stretcher. We can guess the function of a compressor is to shorten the pulse duration by compensating the given positive GDD through loading negative one using an inverse geometry. To achieve these conjugate schemes, most CPA laser systems use diffraction gratings as dispersive elements both in the stretcher and in the compressor [2-5].

According to the principle of a CPA system explained above, the shortest possible pulse duration is obtainable by perfect compensation of dispersion remaining in a pulse. On the other hand, we can intentionally impose positive or negative chirping on the pulse by the imperfect dispersion compensation. Controlling the chirping state of pulses is important feature of a high power laser, especially for HHG experiments because the

amount of frequency shift in a HHG spectrum is found to be very sensitive to the intensity profile and chirping state of the driving pulse [6,7]. Therefore, the careful control and characterization of driving laser pulse is absolutely necessary to find out more exact relationship between a HHG spectrum and the phase structure of the laser.

The precise information of a laser pulse should include intensity (or amplitude) and phase profile. Among a lot of attempts to characterize the intensity and the phase of femtosecond laser pulses, frequency-resolved optical gating (FROG) technique has been proven to be a very reliable method [8-10]. We used the FROG technique to characterize femtosecond pulses generated from a CPA laser system in a variety of compressor conditions and compared the measured results with a calculated ones.

II. FROG setup

Figure 1 shows the second-harmonic generation (SHG) FROG setup used to characterize the chirped pulses from a 10-Hz, CPA femtosecond Ti:sapphire laser in KAIST [11]. SHG FROG experiment is easy to understand in that it is an extended version of a simple autocorrelation which also uses SHG.

A 30-μm-thick type-I BBO crystal was utilized as a SHG medium to generate an autocorrelation signal. Two replicas of the laser pulse are line-focused on the crystal with a crossing angle of ~3° by a cylindrical mirror in order to realize a single-shot geometry. The line image of the second-harmonic signal was relayed into a spectrometer slit using a lens, and then, a two-dimensional image of the frequency-resolved signal was obtained in a 16-bit charge-coupled device (CCD) located at the end of the spectrometer. Second harmonic and fundamental backgrounds were blocked on the way of the image relay. Because the obtained image (FROG trace) is spanned in a time-frequency domain, the calibration in both directions should be made. The frequency calibration was naturally achieved by the spectrometer, and the time delay calibration was possible with a translator shown in Fig.1 because a spatial shift of the signal induced by the translator is proportional to a temporal one in a single-shot scheme as shown in Fig. 2. This single-shot FROG is a very useful tool for the pulse

characterization of a low-repetition-rate laser because the temporal pulse structure can be fully resolved even with a single pulse.

In the actual acquisitions, we accumulated 5 shots to see an average effect of the pulse shape as in HHG experiments which are usually preformed with hundreds of laser shots. The compressor grating was scanned from –0.5 mm to +0.5 mm along the incidence direction of the laser pulse, and the zero position of the grating was set to be the location of minimum pulse duration.

III. FROG algorithms and retrieval of electric field

Mathematical formula expressing a SHG FROG trace is following.

$$I_{FROG}(\omega,\tau)=\left|\int_{-\infty}^{\infty}E(t)E(t-\tau)\exp(i\omega t)dt\right|^2 \qquad (1)$$

Several algorithms such as basic FROG algorithm and generalized projections [12] have been known in order to retrieve the E(t) from this trace. All the FROG algorithms are basically using iterative Fourier and inverse Fourier transforms and achieve convergence by use of two constraints during the iterations. FROG error after k iterations, $G^{(k)}$, is defined as a root-mean-square average across the entire trace of the difference between the experimental FROG trace and the retrieved FROG trace and can be written as

$$G^{(k)}=\sqrt{\frac{1}{N^2}\sum_{i,j=1}^{N}\left|I_{FROG}(\omega_i,\tau_i)-I_{FROG}^{(k)}(\omega_i,\tau_j)\right|^2}\,, \qquad (2)$$

where I_{FROG} and $I_{FROG}^{(k)}$ are the experimental and retrieved trace, respectively, which are always normalized to a peak of unity.

The obtained FROG trace was processed using commercially available FROG algorithms to find out the intensity and phase profile of E(t). Independent FROG algorithms are automatically tried to achieve lower FROG error. We used 256 Fourier transform grids in the process, resulting in a typical FROG error of 0.4 % for various pulses after about 50 to 200 iterations depending on the FROG traces. In the case of SHG FROG, both E(t) and E(-t) generate the same FROG trace. Therefore, we must

specify whether we retrieved E(t) or E(-t) after getting a convergent result from a FROG trace. This problem of inherent phase ambiguity, which will be explained again in next section, could be avoided from the knowledge about the relationship between a grating distance from the grating zero position and the direction of chirping: a plus value of the relative grating distance yields a positive chirping, and vice versa. There was, however, difficulty in determining the direction of phase around the grating zero position since the phase structure is nearly flat and a little complicated around here. This is for the reason that GDD is mostly compensated around this position, and that the phase is dominated by higher order dispersions. So we decided the phase direction by comparing the intensity shape at this position with neighboring ones rather than analyzing the phase direction.

IV. Experimental result

We characterized the pulse structure with respect to the compressor grating position. Figure 3 shows typical SHG FROG traces in the case of relative grating position of –0.5 mm (a), 0.0 mm (b), and +0.5 mm (c), respectively. Due to the inherent characteristics of a second-order nonlinear effect, a SHG FROG trace is always symmetric along the time-delay axis, and the retrieved pulse from the SHG FROG trace has a time-reversal ambiguity; the propagation direction of the retrieved pulse cannot be determined. In spite of this shortcoming, however, the SHG FROG can be successfully utilized for the characterization and optimization of a CPA laser system because, in the most of cases, the temporal direction of the retrieved pulse can be easily determined as was discussed in the previous section in our case. Even though Fig. 3 (a) and (c) look very similar to each other, we can determine the direction of the chirping from the information of grating position.

Retrieved E(t)'s by FROG algorithms are shown in Fig. 4. The x-axis is time evolution in femtosecond, the left y-axis the pulse intensity, and while the right y-axis the pulse phase that is expressed as the relative angular frequency from center. As the center wavelength of the spectrum was 820 nm, the center angular frequency was 2.2987 rad/fs actually. Therefore the range of the relative angular frequency from –0.5 rad/fs to 0.5

rad/fs is corresponding to the wavelength range from 1048 nm to 674 nm. Scanning step of the grating distance was 0.05 mm at the grating position from –0.1 mm to 0.1 mm, and was 0.1 mm at the other positions. The retrieved electric fields whose pulse duration is the closest to mean value at each grating position were selected in Fig.4.

Increasing angular frequency with time evolution simply means the pulse was positively chirped, but the phase structure is more complicated than we can guess. The phase in the low intensity region seems to be more easily modulated than that around the peak by residual high-order dispersions. But abrupt leaps of the phase in the region of extremely low intensity can be explained as a numerical truncation error occurring on the way of usual Fast Fourier Transform (FFT). We can find this phenomenon even when we execute a FFT with a spectrum of flat phase to get a transform-limited pulse as shown in Fig. 5(h). But this does not change a global picture of the pulse because the phase under zero or very low intensity comparable to a noise level is actually meaningless. Moreover a HHG signal is not affected by this low intensity part unless the pulse intensity is very high, and even under a high intensity laser field, the ionization probability of electron grows enough to prevent a proper observation of HHG signal.

V. Comparison between the calculated and measured pulse structure

To check if we got reasonable pulse structures for each grating distance, we calculated phase shift induced by our compressor. For this, we used a ray tracing formulae for two parallel gratings [13], and executed a FFT, in together with the spectrum of the pulse to obtain temporal intensity and phase. We must consider several parameters for the calculation. Two parameters of our grating compressor system that determine the phase shift were the number of grooves, which was 1200 lines/mm for both the gratings, and the incidence angle to the normal direction to the first grating, which was 46^{o}. Another parameter was the normal distance between two gratings, which was varied by the grating scan. It should also considered that the direction of grating scan has a fixed angle with the normal direction of the grating and that moving distance of the grating is to be doubled for the double pass scheme of the compressor. For simplicity, we assumed that the dispersion accumulated through the laser system was completely compensated

for at the compressor with the grating zero position.

Figure 5 shows the result of calculation. Electric fields at each grating position were found to be the time-reversed versions of the opposite-sided ones across the grating zero position. The result measured by FROG, however, indicates that the pulses on the conjugate grating position are not exactly in a time-reversed feature with each other, as shown in Fig. 4. This is mainly due to residual high order dispersions that were not compensated by the compressor, and secondly due to fluctuations of amplification system. The residual high order dispersions can be reduced by changing the incidence angle to the compressor or to the stretcher, and adjusting a prism pair for fourth-order dispersion compensation which was inserted in front of the stretcher. These adjustments will make it possible to get a shorter pulse duration at the grating zero position, too. But unsymmetrical feature is not important for the purpose of HHG experiments. As for the fluctuations, several factors can be present such as the energy fluctuation of pumping source, the spectrum fluctuation of Ti:sapphire oscillator pulses, and fine vibrations due to imperfect mechanical isolation.

We can compare the measured pulses with the calculated ones quantitatively in terms of pulse duration and the linear chirp parameter. Figure 6 shows the pulse durations at each grating position for the measured and calculated case. The measured pulse durations below the grating position of -0.3 mm are consistently smaller than calculated ones while in the other region the measured ones follow the calculated ones relatively well.

For a quantitative comparison of the phase structure, we can use linear chirp parameter which can be defined in following Talyor's series of temporal phase:

$$\varphi(t) = \varphi(t_0) + \varphi'(t)(t-t_0) + \frac{1}{2}\varphi''(t)(t-t_0)^2 + \frac{1}{3!}\varphi'''(t-t_0)^3 + \cdots \quad , \tag{3}$$

$$\begin{aligned} \omega(t) &= -\frac{d\varphi(t)}{dt} \\ &= -\varphi'(t_0) - \varphi''(t)(t-t_0) - \frac{1}{2}\varphi'''(t-t_0)^2 - \frac{1}{3!}\varphi^{(4)}(t-t_0)^3 \cdots \quad , \\ &= \omega_0 + a(t-t_0) + b(t-t_0)^2 + c(t-t_0)^3 + \cdots \end{aligned} \tag{4}$$

where the parameter a represents the first-order chirping and is dominant except the

condition of GDD is nearly zero. Using this parameter, we can say of a pulse whether it was positively chirped or negatively chirped. Figure 7 is the comparison of this quantity at each grating position. For a consistent comparison, the phase values within full width at half maximum (FWHM) of the pulse intensity were selected, which also makes it possible to avoid the fluctuating frequency in the vicinity of the pulse. The linear chirp parameter a was obtained by performing a polynomial fitting to the selected angular frequency curve with $t_0 = 0$ in Eq. (4) and then finding out the linear coefficient. The linear chirp parameter is maximum at –0.2 mm and minimum at +0.2 mm in both the measured and calculated cases. Two curves show better agreement with each other as the absolute value of the grating distance becomes larger. This is because the influence of uncompensated high-order dispersions get reduced whereas the GDD induced by the compressor grating becomes dominant, as the grating is moved to a farther position from zero.

V. Conclusion

We characterized laser pulses from the femtosecond CPA Ti:sapphire laser at KAIST using a FROG. The grating distance of the compressor was scanned from –0.5 mm to 0.5 mm so as to change the pulse durations and the amount of chirping. The measured pulse duration and the linear chirping parameter were in good agreement to the calculated ones.

We could change the pulse duration and the amount of chirping through the grating scan although this did not mean we were able to control the pulse completely as we want. Resultantly, through this partial control of the pulse supported by FROG measurement, we could improve the tunability of HHG spectrum and find out some useful information on the physical process of HHG driven by chirped pulses.

References

[1] Yong Ho Cha, "System configuration and operational characteristeics of a femtosecond terawatt Ti:sapphire laser based on a long-wavelength injection method," Ph.D thesis, 2000, KAIST.

[2] C. P. J. Barty, C. L. Gordon III, and B. E. Lemoff, Opt. Lett. **19**, 1442 (1994).

[3] Y. H. Cha, Y. I. Kang, and C. H. Nam, J. Opt. Soc. Am. **B 16**, 1220 (1999).

[4] S. Bachus, C. G. Durfee III, G. Mourou, H. C. Kapteyn, and M. M. Murnane, Opt. Lett. **22**, 1256 (1997).

[5] K. Yamakawa, M. Aoyama, S. Matsuoka, T. Kase, Y. Akahane, and H. Takuma, Opt. Lett. **23**, 1468 (1998).

[6] J. Zhou, J. Peatross, M. M. Murnane, and H. C. Kapteyn, Phys. Rev. Lett. **76**, 752 (1996).

[7] Z. Chang, A. Rundquist, H. Wang, I. Christov, H. C. Kapteyn, and M. M. Murnane Phys. Rev. A **58**, R30 (1998).

[8] D. J. Kane and R. Trebino, J. Opt. Soc. Am. **A 10**, 1101 (1993).

[9] B. Kohler, V. V. Yakovlev, and K. R. Wilson, J. Squier, K. W. DeLong, and R. Trebino, Opt. Lett. **20**, 483 (1995).

[10] K. H. Hong, Y. H. Cha, and C. H. Nam, J. Kor. Phys. Soc. **33**, 315 (1998).

[11] Y. H. Cha, Y. I. Kang, K. H. Hong, C. H. Nam, Newphysics **37**, 469 (1997).

[12] K. W. DeLong, D. N. Fittinhoff, R. Trebino, B. Kohler, and K. Wilson, Opt. Lett. **19**, 2152 (1994).

[13] E. B. Treacy, IEEE J. Quan. Electron. **QE-5**, 454 (1969).

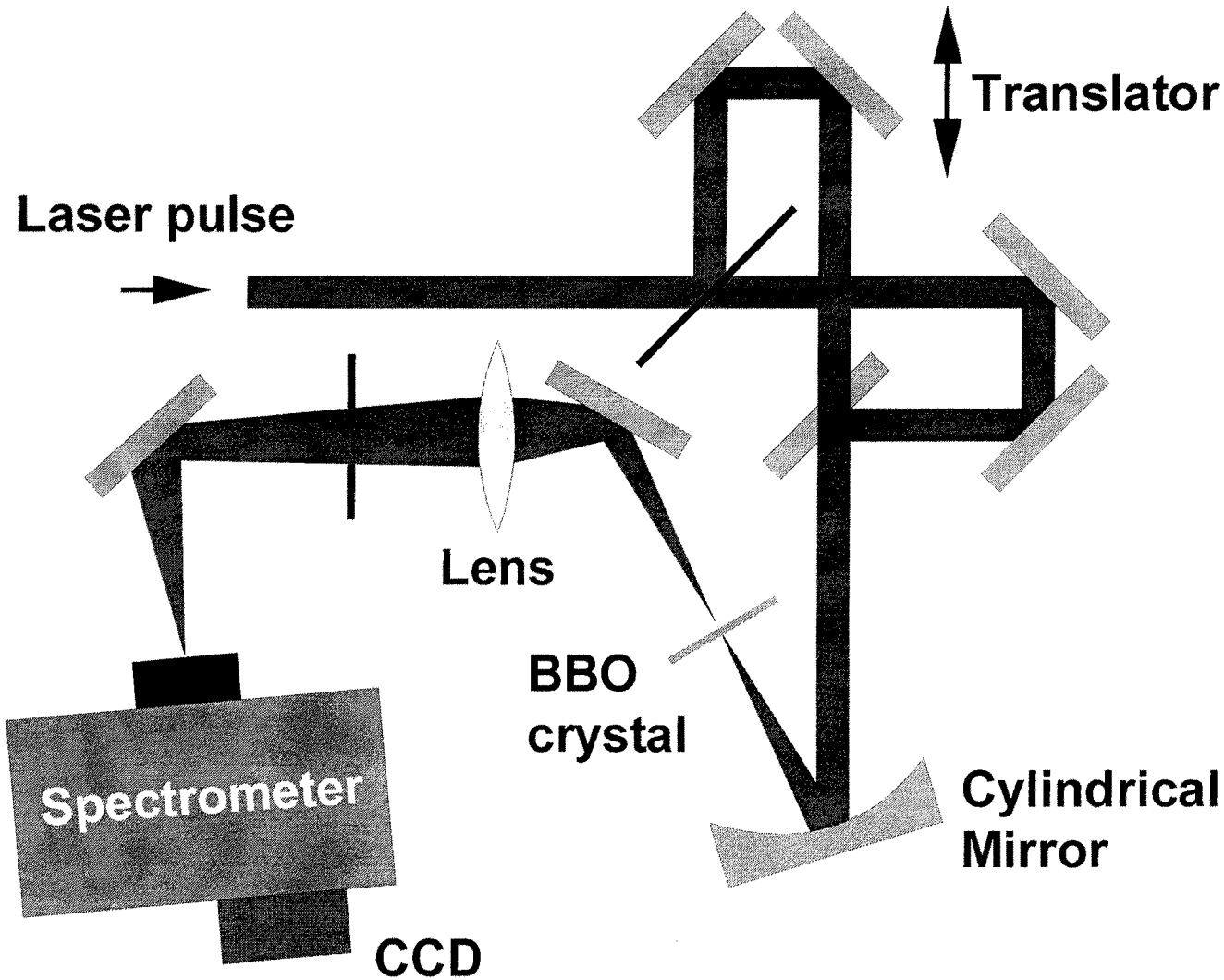

Fig. 1. Experimental layout of a SHG FROG.

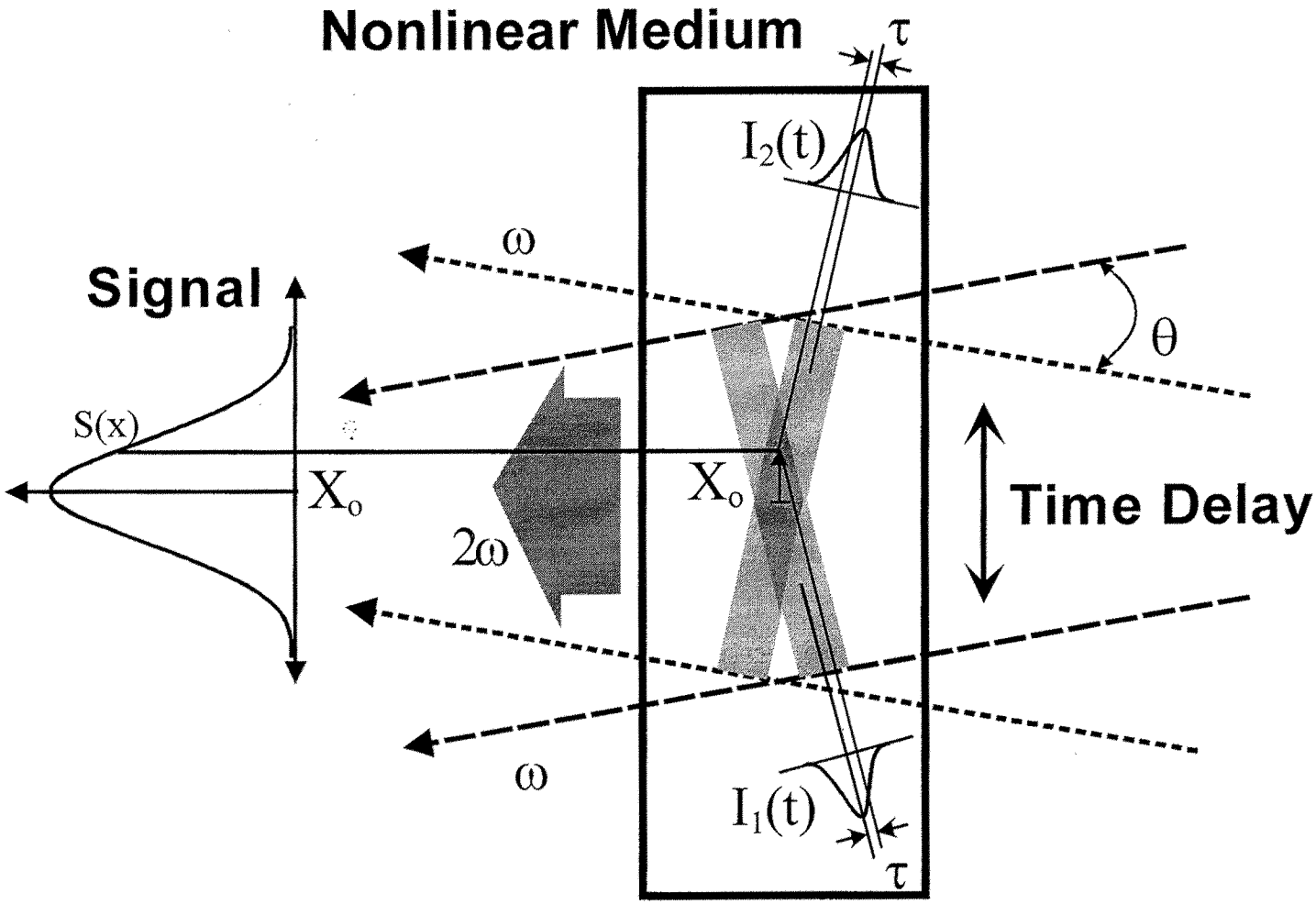

Fig.2 Schmatics of a single-shot measurement. The time delay between two pulses is represented spatially.

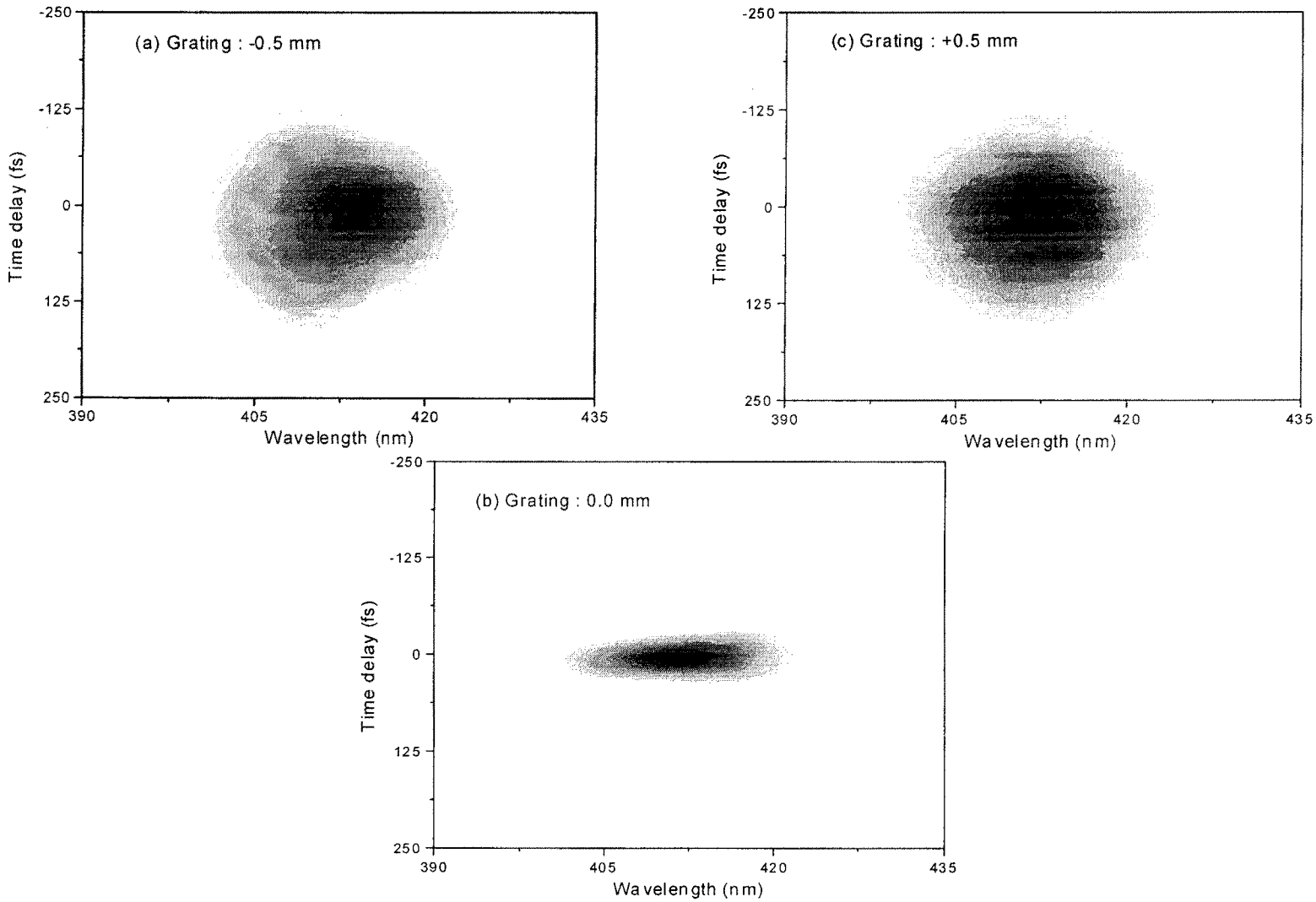

Fig. 3. FROG traces at the grating position of (a) +0.5 mm, (b) -0.5 mm, and (c) 0 mm

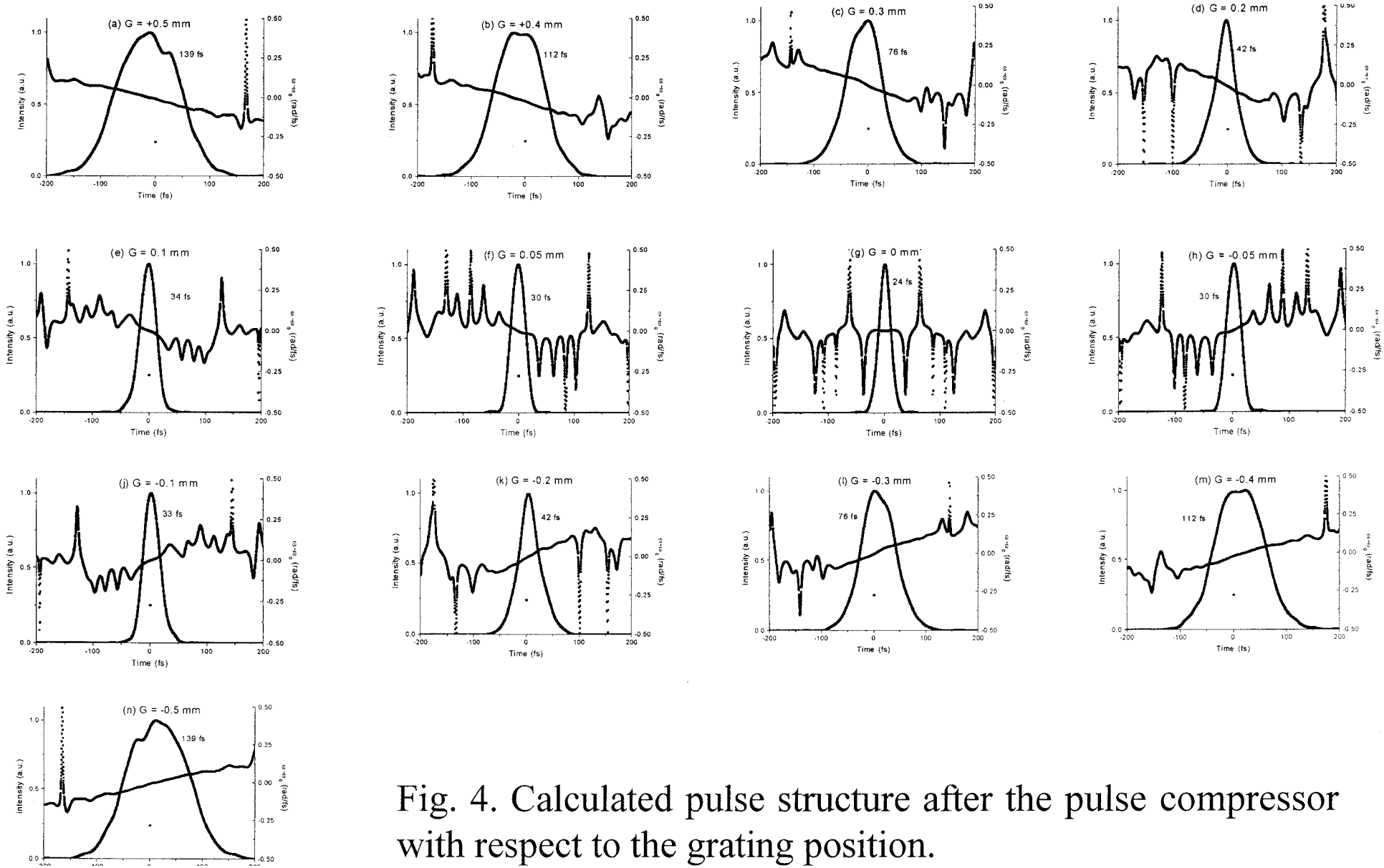

Fig. 4. Calculated pulse structure after the pulse compressor with respect to the grating position.

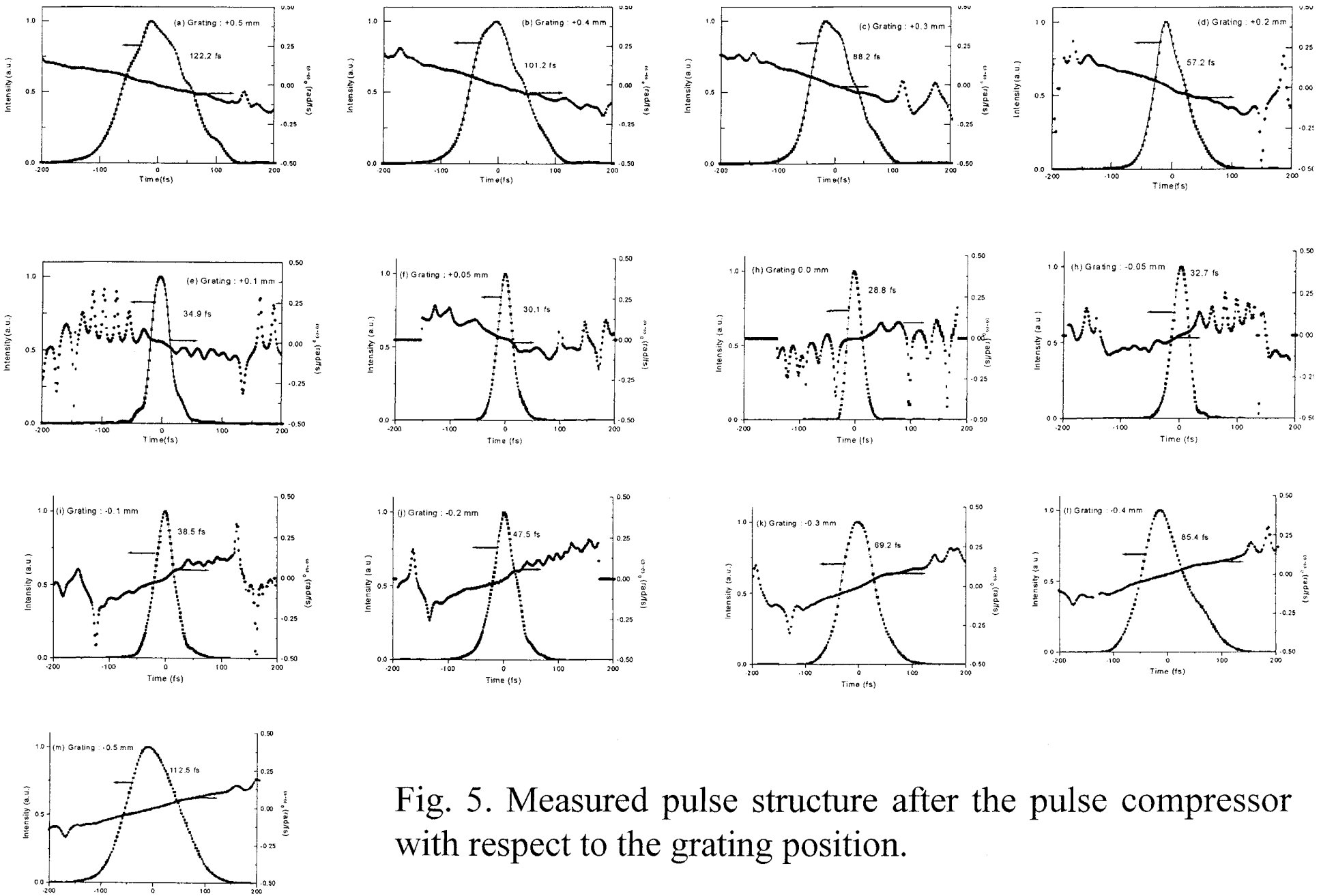

Fig. 5. Measured pulse structure after the pulse compressor with respect to the grating position.

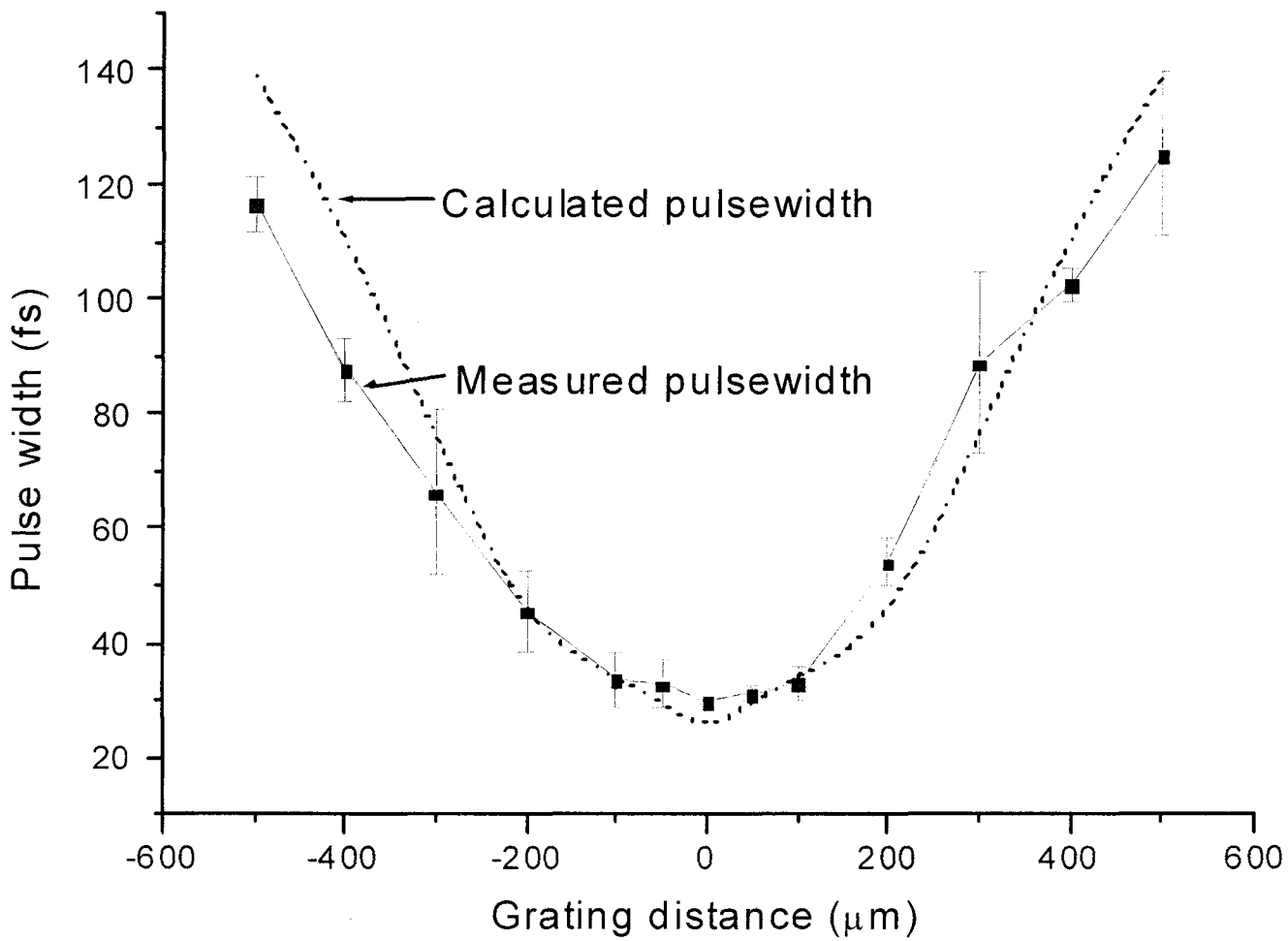

Fig. 6. Measured and calculated pulse duration with respect to the grating position.

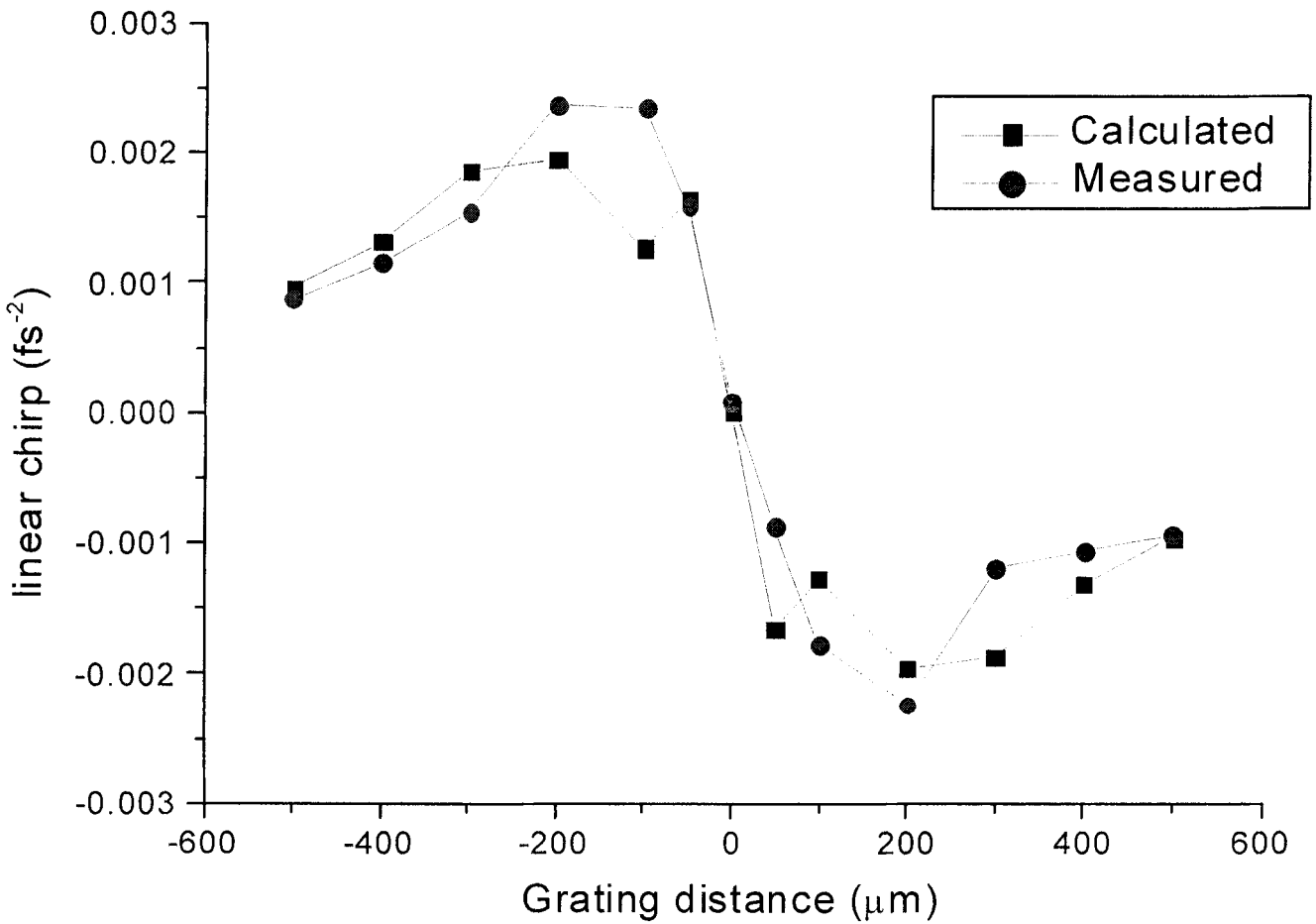

Fig. 7. Measured and calculated linear chirp at the center of pulses with respect to the grating position.

A. 3. 3. Focused Spot Size and Intensity Measurement in a Femtosecond Terawatt Ti:sapphire Laser

I. Introduction

In the light-matter interaction experiments such as high harmonic generation (HHG) [1] and laser-induced x-ray generation [2], the peak intensity of a driving pulse is one of the most important parameters capable of changing overall feature of the physical process. There are three factors that determine the intensity of a laser pulse: pulse energy, pulse duration, and the size of beam area. While the pulse energy can be measured simply by a commercial energy meter, the measurement and optimization of pulse duration and beam size is not easy. The pulse duration was well characterized by the FROG technique in our experiments as explained in the previous section. In this section, we measured the focused beam size in the interaction region where HHG signal is generated.

In our laser system, we have two ways of controlling the laser energy. The first is to adjust the transmission through a polarizer by rotating the polarization direction of a pulse using a $\lambda/2$ wave plate, and the second is to use various sizes of apertures in front of the compressor. In the latter case, the focused beam size is inversely proportional to the aperture size, whereas there is no change of the focused beam size in the former case. We measured the focused beam size with several apertures and compared it to the diffraction-limited size. From the measured beam size, the peak intensity of the pulse at the focused region was calculated.

II. Measurement and result

The beam diameter at the pulse compressor in our CPA Ti:sapphire laser is about 35 mm but the beam cross section is cut by an aperture to adjust the pulse energy delivered to a target. As the aperture size was changed from 8 to 30 mm, not only the pulse energy but also the focused beam size was changed. For the direct measurement of the beam size focused by a concave mirror of a 60-cm focal length, we used a CCD that can the image

in real time. Because the pixel size of the CCD element was relatively large (>10 μm), we couldn't obtain sufficient resolution to determine the beam size which is estimated to be as small as 40 μm in diameter. A microscope objective lens of 10x magnification was used to overcome this resoluton problem. For the exact calibration of the magnified beamsize, a drawing of two parellel lines with a distance of 0.5 mm was located at the focused position, and the number of pixels between the two lines seen in the CCD was counted. From the calibration, 1 pixel in the CCD was found to represent 1.0 μm.

When we firstly observed the foucused beam image by the CCD, it was found that the beam shape was not round and strongly elliptical, especially for the large aperture size of 30 mm, as shown in Fig. 1. Such a distorted beam shape should be fixed becuase it severly degrades the performace of the high-power laser in terms of intensity and spatial uniformity at a target. To find the reason of the distorted beam shape, we checked all the mirrors from the compressor to the target, and it was found that the two flat mirrors used in the compressor caused the problem. The flat mirrors have a large area of 120X60 mm, but a thin thickness of 12 mm. Therefore, the mirror surface was easily deformed when mounted, and the deformed surface caused the distorted beam shape. It was found that the only ~1-λ deformation on the mirror surface over the beam cross section can yield a significant distortion of the focused beam shape. We replaced the flat mirrors by new ones with thick substrates to minimize the deformation on the surface.

Another reason of the elliptically focused beam shape was spatial chirping. The spatial chirping means that the spectral components of laser pulses are spatilly decomposed and arranged across the beam cross section, and it usually causes an ellipitical beam shape. Because the spatial chirping is usually induced by the imperfect parallelism of two diffraction gratings in the compressor, it is very important to keep the two gratings parallel to each other. To obtain a round focused beam shape without spatial chirping, we carefully adjusted the grating angle while monitoring the beam image on the CCD.

Figure 2 shows the focused beam shape after the correction described above. The corrected beam was simply round in shape even with the largest aperture, and the beam size was inversely proportional to the aperture size. This confirms that the intensity at

the focused region can be effectively adjusted by changing the aperture size. Further more, the measured beam size was very close to the diffraction-limited value of a Gaussian beam shape, as shown in Fig. 3, where the beam size was defined at the pulse intensity decreased to 14 % ($1/e^2$) of the peak. Therefore, the intensity at the focus could be effectively maximized.

The intensity at the focus calculated from the beam size, pulse duration, and the transmitted energy through apertures is shown in Fig. 4. By changing the aperture, the intensity could be successfully adjusted from ~3×10^{17} to ~2×10^{15} W/cm^2 at the maximum pulse energy. Such a wide range of intensity tunability is very useful, especially for the control of HHG which is very sensitive to the driving intensity.

III. Conclusion

We chracterized the focused beam shape using a CCD and a microscope objective lens. The distorted beam shape caused by deformed mirrors and spatial chirping was found and successfully corrected by the replacement of the mirrors and the careful adjustment of the pulse compression gratings. The corrected beam shape was clearly round and the beam size was nearly diffraction-limited. With the measured beam size, the intensity delivered to the focus could be successfully estimated.

References

[1] H. J. Shin, D. G. Lee, Y. H. Cha, K. H. Hong, and C. H. Nam, Phys. Rev. Lett. **83** 2544 (1999).

[2] T. T. Mocek, C. M. Kim, H. J. Shin, D. G. Lee, Y. H. Cha, K. H. Hong, and C. H Nam, Appl. Phys. Lett.. **76**, 1819 (2000).

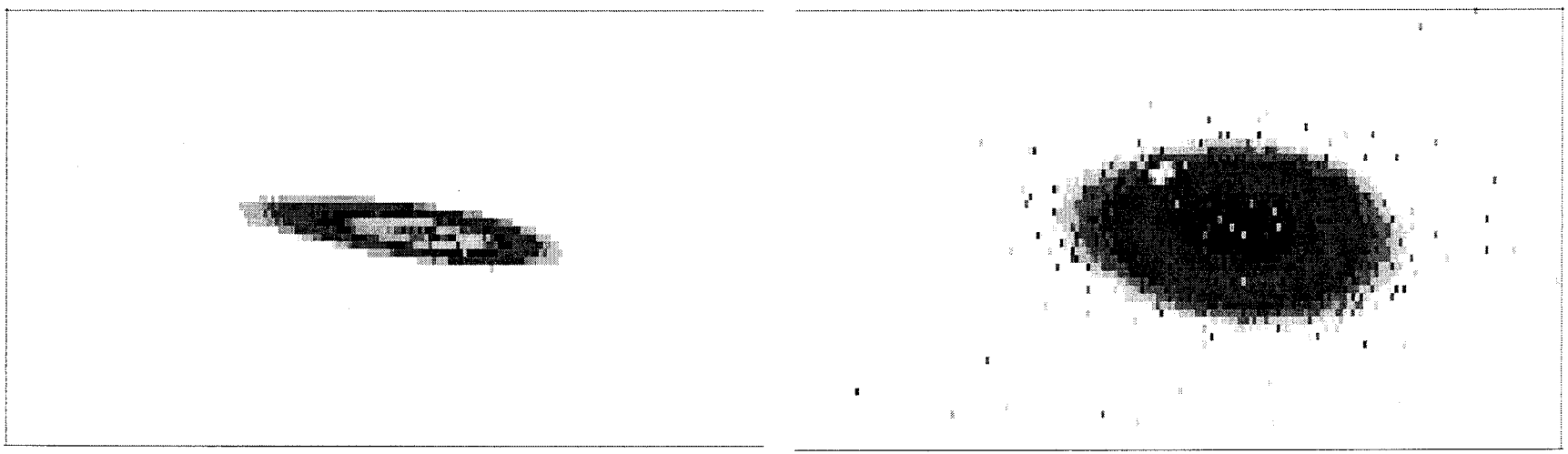

30 10

Fig. 1. Focused beam image observed by the CCD and the objective lens. The number below the image is the inlet aperture diameter.

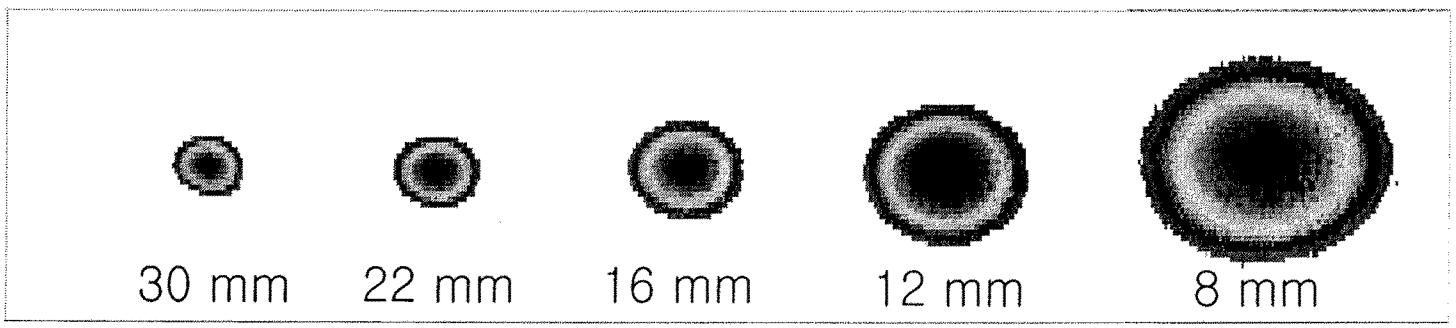

Fig. 2. Focused beam image after the removal of the deformed mirrors and spatial chirping. The number below the image is the aperture size.

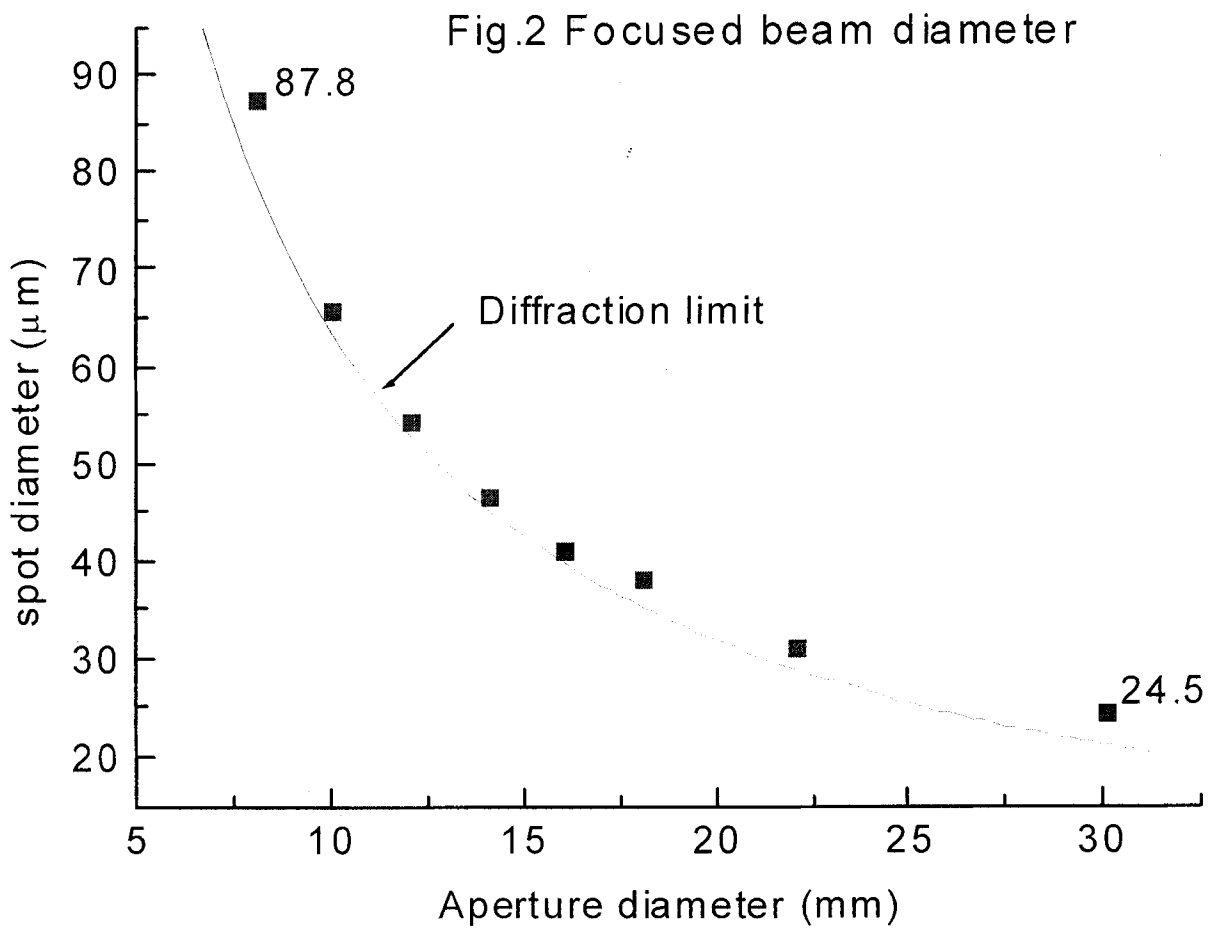

Fig. 3. Focused beam size with respect to the aperture size. The solid line is the diffration-limited beam size of a Gaussian beam.

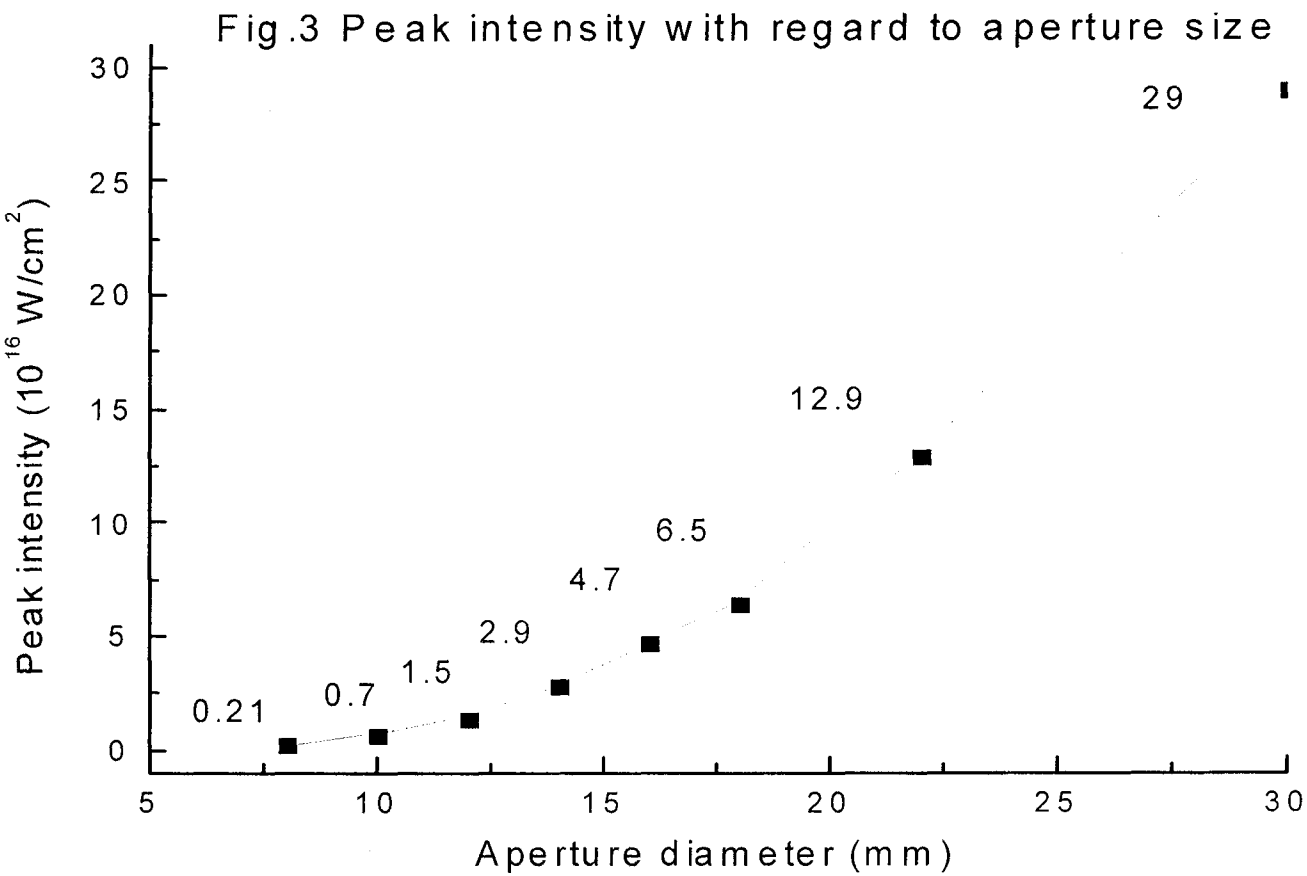

Fig. 4. Intensity at the focus calculated from the measured beam size with respect to the aperture size.

A. 3. 4. Incorporation of a Cavity-Dumped Oscillator in a Femtosecond Terawatt Ti:sapphire Laser

I. Introduction

In the past several years high-power Ti:sapphire lasers based on the chirped-pulse amplification technique have been greatly improved in terms of peak power and pulse duration. The excellent property of Ti:sapphire such as high saturation fluence, broad gain profile and good thermal characteristics has enabled the development of a number of sub-50-fs multiterawatt lasers with efficient and compact amplifiers[1-3]. With the development of unique techniques such as a regenerative pulse shaping[4] or a long-wavelength injection method[5] the pulse duration has been reduced to a sub-20-fs regime at a terawatt power level. Using the former technique an 18-fs, 100-TW Ti:sapphire laser was recently constructed[6]. Such high-power Ti:sapphire lasers are becoming common and useful tools in many research fields.

A typical configuration of high-power Ti:sapphire lasers starts with a femtosecond Ti:sapphire oscillator based on the Kerr-lens mode locking (KLM). Because a KLM-assisted Ti:sapphire oscillator can routinely generate ~10-fs pulses with a very broad spectral width of ~100 nm, it has been utilized as an ideal front-end oscillator in a high power Ti:sapphire laser. However, its small pulse energy of nJ level needs a very high gain of more than 10^8 to achieve a terawatt power level and the high gain causes two problems - amplified spontaneous emission (ASE) and gain narrowing. ASE, which is generated from a high-gain amplifier and can precede main pulses, should be kept as low as possible because it may change target properties prior to the arrival of main pulses. For the suppression of ASE, a spatial filtering technique or a saturable absorber has been generally used. The spatial filtering, however, yields a complicated system configuration, and the saturable absorber an undesirable modulation of laser pulses[2]. The gain narrowing effect, which is caused by the finite gain bandwidth of a gain medium, reduces an amplified spectral width and, consequently, broadens the amplified pulse duration. Although the gain-narrowing problem can be relaxed by the regenerative pulse shaping[4] or the long-wavelength injection method[5], it is still an unavoidable

problem in constructing high-power Ti:sapphire laser systems.

Because both ASE and gain narrowing are caused by a very high gain at amplifiers, they can be suppressed simply by decreasing the gain. On the other hand, an enough gain for a desired output power is necessary in a high power laser system. These two contradictory problems can be simultaneously challenged by adopting a cavity-dumped oscillator which can generate femtosecond pulses with a 10-100 times higher energy without significant degradation of pulse duration. In the past several years, a number of cavity-dumped Ti:sapphire lasers using acousto-optic modulators or electro-optic devices have been developed, and sub-20-fs pulses of several tens of nJ have been successfully demonstrated at a repetition rate of more than 100 kHz[7-9]. Such cavity-dumped pulse should be more appropriate as a seed in a high power laser because a smaller gain is needed to achieve a same power level, yielding less ASE and gain narrowing. The cavity-dumped laser is also effective in suppressing the femtosecond prepulses because the prepulses are initially selected out during the dumping process. This is an important feature because the prepulses as well as ASE affect a target and should be kept low enough. Typically, the reduction of prepulses by a factor of 10-1000 is expected depending on the dumping performance of cavity-dumped lasers.

In this paper we adopted a cavity-dumped laser in a femtosecond terawatt Ti:sapphire laser and showed that ASE and prepulses could be significantly suppressed. The gain narrowing effect was also reduced and, in combination with the long-wavelength injection method, a broad amplified spectrum could be generated.

II. Development of a cavity-dumped Ti:sapphire oscillator

The cavity-dumped Ti:sapphire laser that we developed is shown in Fig. 1. Its configuration was slightly modified from that of a typical X-folded type Kerr-lens mode-locked laser. The cavity was composed of four concave mirrors, a flat output coupler, a Ti:sapphire crystal, a fused silica Bragg cell as a dumper, and fused silica prisms for the dispersion compensation. The Ti:sapphire crystal positioned between two concave mirrors of a 5-cm focal length was 0.15-wt.%-doped, 4.75-mm long, and

pumped by a frequency-doubled Nd:YVO_4 laser. The fused silica Bragg cell (Camac Inc.) was 3.56-mm-long and installed between two concave mirrors of 10-cm and 5-cm focal lengths. We installed the Bragg cell at the end of the prism side rather than the output coupler side to generate a broad spectrum by minimizing the spectral filtering effect, which is caused by nonlinear self-focusing of a chirped pulse inside the cavity\cite{10}. To compensate for the additional dispersion from the Bragg cell one more prism pair was added and the total prism separation was lengthened to 85 cm. The repetition rate was reduced from 90 MHz to 74 MHz due to the extension of the cavity-length.

The installation of a cavity dumper requires very careful control of operation parameters The Bragg cell was driven by 9-ns, 6-W RF pulses synchronized with laser pulses, and double-pass interferometric scheme was used for the efficient dumping process. Because the dumping efficiency is very sensitive to the dumper position and the phase of driving RF pulses, especially in the double-pass scheme, we had to adjust these parameters carefully to maximize the dumping efficiency. Figure 2 shows the pulse evolution inside the cavity during the dumping process. The dumping efficiency was about 50% at the dumping repetition rate of 167 kHz. The dumped pulse energy was more than 30 nJ, which is about 30 times higher than that without the dumper. In spite of the dumper installation, there was no significant degradation of the mode-locked pulse quality. The spectral width and pulse duration of the dumped pulse was 76 nm and 17 fs, respectively, as shown in Fig. 3.

III. Prepulse suppression

The first visible advantage of the incorporation of the cavity-dumped laser is the improvement of the contrast ratio between the preceding and main femtosecond pulses. Because the dumping process itself is a kind of pulse selection, the preceding pulse is naturally suppressed. For the acousto-optic dumping, however, the contrast ratio is usually limited to about 100:1 due to a practical limit of a cavity-dumping system. The RF driver (CD2000, Camac Inc.) used for the cavity-dumping generated about 10-ns RF pulses and required a reference signal in the range of 70-100 MHz from the cavity-

dumped laser. Therefore, the round-trip time of the cavity-dumped laser cannot be longer than 14 ns, which is not long enough to prevent the preceding laser pulse from being dumped by the leading edge of the acoustic wave packet of about 10-ns duration. With the 74-MHz repetition rate of the cavity-dumped laser, the measured contrast ratio between the preceding and dumped pulses was better than 100:1. The total contrast ratio in combination with a Pockels cell was improved from 500:1 to better than 50000:1. The contrast ratio can be further improved by using an advanced RF driver generating more sharply rising and shorter RF pulses[8] or an electro-optic dumping[9].

IV. Amplification of a dumped pulse

The pulse from the oscillator was stretched to about 240 ps by an all-reflective Offner-triplet type stretcher[11] with a 1200 lines/mm grating (Richardson Grating Laboratory) and amplified by a preamplifier. The preamplifier was a bow-tie type, multipass amplifier composed of four concave mirrors and a 7-mm long, 0.25 wt.%-doped Ti:sapphire crystal. The four concave mirrors in a confocal configuration had slightly different radii of curvature of 1000 and 900 mm because this kind of multipass amplifier produces less ASE[3,12]. The preamplifier was pumped by a 50-mJ green pulse from a frequency-doubled Nd:YAG laser, and the number of passes at the preamplifier was adjusted appropriately to boost the input pulse energy to mJ level. Before the incorporation of the cavity-dumped laser the input pulse energy at the preamplifier was 0.3 nJ, and the eight-pass configuration was needed to obtain a 3.5-mJ amplified energy, yielding a total gain of more than 10^7. With the adoption of the cavity-dumped laser, on the other hand, the input pulse energy at the preamplifier was increased to 10 nJ, and the seven-pass configuration was enough to generate the same amplified energy of 3.5 mJ, yielding a total gain of 3.5×10^5.

A high gain amplifier inevitably generates ASE during the amplification. The upper limit of ASE preceding the main pulses can be estimated by measuring the ASE without the injection of a seed pulse. The eight-pass preamplifier generated 0.5 mJ of ASE without the injection of seed pulse, which is about 14\% of the amplified energy. Although the injection of seed pulse significantly reduces the total amount of ASE[13],

it is difficult to assure that the ASE preceding the main pulse is sufficiently reduced. With the adoption of the cavity-dumped laser, the seven-pass preamplifier generated 0.06 mJ of ASE without the injection of seed pulse; the ASE was significantly suppressed compared to that with the eight-pass preamplifier. The reduced number of passes at the preamplifier should guarantee the suppression of ASE preceding the main pulses when a seed pulse is injected.

The high gain preamplifier can cause a severe gain-narrowing problem and reduce the amplified spectral width. To relax the gain-narrowing problem and generate a broad amplified spectrum at the preamplifier, we used the long-wavelength injection (LWI) method[5]. The LWI method utilizes the gain saturation effect to compensate for the gain narrowing effect by preparing the input spectrum on the long wavelength side of the gain peak and amplifying the pulse to a saturated fluence level. The mirror set in the Ti:sapphire oscillator was selected to generate the input spectrum centered at 820 nm, and the pulse was amplified to a fluence level of 1.8 J/cm^2 corresponding to the 3.5-mJ amplified energy. As a result, a broad amplified spectrum of a 52-nm width could be obtained at the eight-pass preamplifier, as shown in Fig. 4(a).

The decrease of the total gain with the adoption of the cavity-dumped laser was effective in generating an even broader amplified spectrum at the preamplifier when combined with the LWI method. The spectrum of the dumped pulse was prepared on the long-wavelength side of the gain peak as shown in Fig. 3, and the dumped pulse was amplified at the seven-pass preamplifier. Because the total gain at the seven-pass preamplifier was reduced by more than an order of magnitude, a broader amplified spectrum of a 65-nm width was generated as shown in Fig. 4(a).

To increase the amplified energy to a 100-mJ level, the amplified pulse from the preamplifier was up-collimated to 6 mm in diameter and further amplified at a five-pass power amplifier. The power amplifier was composed of flat mirrors and a 7-mm long, 0.25 wt.%-doped Ti:sapphire crystal with anti-reflection coating on both sides. The crystal was pumped on both sides by the frequency-doubled Nd:YAG laser, and the amplified pulse energy was 130 mJ at a pumping energy of 450 mJ. The amplified

spectrum after the power amplifier became 57 nm, improved from 49 nm without the incorporation of the cavity-dumper, as shown in Fig. 4(b).

For the optimization of the output power by compressing the amplified pulse close to its transform-limited pulse duration, the careful control of high-order dispersion throughout the laser system is required. To compensate for the dispersion of the laser system up to fourth-order, we installed a SF10 prism pair after the stretcher, and the amplified pulse was compressed by a pulse compressor with two 1200 lines/mm gratings at the final stage. The compressed pulse duration measured by a single-shot autocorrelator with a 25- m-thick BBO crystal was 20 fs assuming the pulse shape obtained by inverse Fourier transform of the laser spectrum, as shown in Fig. 5. Although the transform-limited pulse duration calculated by inverse Fourier transform of the spectrum was reduced from 19 fs to 18 fs after the incorporation of the cavity-dumped laser, we could not obtain shorter pulse duration, which could be because of higher-order dispersion. The output pulse energy after the compressor was 60 mJ, yielding 3-TW pulses.

V. Conclusion

In conclusion, we developed and incorporated a cavity-dumped Ti:sapphire laser as a front-end oscillator in a femtosecond terawatt Ti:sapphire laser system. Due to the 30 times higher energy of the dumped pulse we could reduce the number of passes from eight to seven at the preamplifier with the same amplified energy, and the seven-pass preamplifer generated much less ASE than the eight-pass one. The decreased gain at the preamplifier resulted in the relaxation of the gain-narrowing effect, and a broad amplified spectrum supporting 18-fs pulse duration could be obtained in combination with the long-wavelength injection method. Another advantage of the cavity-dumped laser was the improvement of the contrast ratio between the preceding and main femtosecond pulses, which was naturally achieved by the initial dumping process. After the compression of the amplified pulses, we could obtain 20-fs, 3-TW pulses.

References

[1] C. P. J. Barty, C. L. Gordon III, and B. E. Lemoff, Opt. Lett. **19**, 1442 (1994).

[2] J. Zhou, C.-P. Huang, M. M. Murnane, and H. C. Kap-teyn, Opt. Lett. **20**, 64 (1995).

[3] J. P. Chambaret, C. Le Blanc, G. Cheriaux, P. Curley, G. Darpentigny, P Rousseau, G. Hamoniaux, A. Antonetti, and F. Salin, Opt. Lett. **21**, 1921 (1996).

[4] C. P. J. Barty, T. Guo, C. Le Blanc, F. Raksi, C. Rose-Petruck, J. Squier, K. R. Wilson, V. V. Yakovlev, and K. Yamakawa, Opt. Lett. **21**, 668 (1996).

[5] Y. H. Cha, Y. I. Kang, and C. H. Nam, J. Opt. Soc. Am. B **16**, 1220 (1999).

[6] K. Yamakawa, M. Aoyama, S. Matsuoka, T. Kase, Y. Akahane, and T. Takuma, Opt Lett. **23**, 1468 (1998).

[7] M. S. Pshenichnikov, W. P. de Boeij, and D. A. Wiersma, Opt. Lett. **19**, 572 (1994)

[8] A. Baltuska, Z. Wei, M. S. Pshenichnikov, D. A. Wiersma, and Robert Szipocs, Appl. Phys. B **65**, 175 (1997).

[9] G. N. Gibson, R. Klank, F. Gibson, and B. E. Bouma, Opt. Lett. **21**, 1055 (1996).

[10] I. P. Christov, V. D. Stoev, M. M. Murnane, and H. C. Kapteyn, Opt. Lett. **21**, 1493 (1996).

[11] G. Cheriaux, P. Rousseau, F. Salin, and J. P. Chambaret, Opt. Lett. **21**, 414 (1996).

[12] P. Georges, F. Estable, F. Salin, J. P. Poizat, P. Grangier, and A. Brun, Opt. Lett. **16**, 144 (1991).

[13] S. Backus, J. Peatross, C. P. Juang, M. M. Murnane, and H. C. Kapteyn, Opt. Lett. **19**, 2000 (1995).

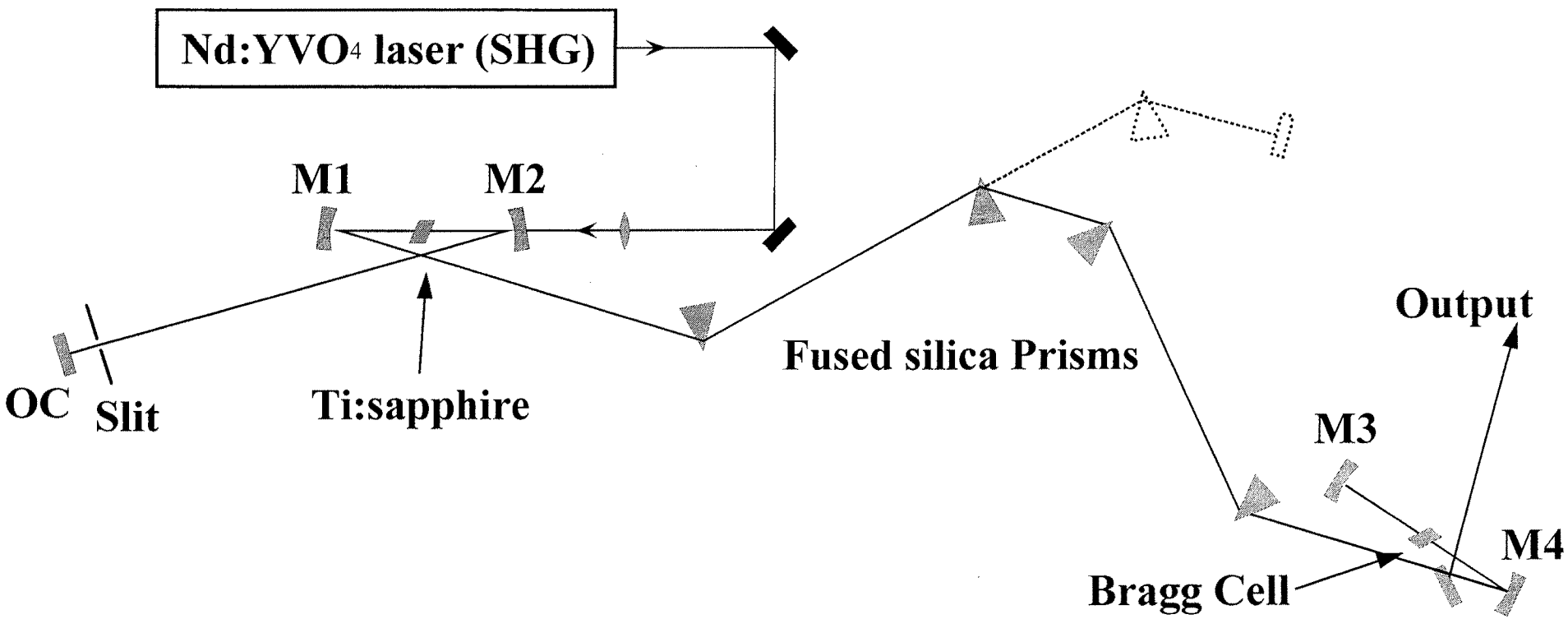

Fig. 1. Experimental setup of a cavity-dumped Ti:sapphire laser: M1-M3, R = 10 cm mirrors; M4, R = 20 cm mirror; OC, output coupler; L, f=10 cm lens; Bragg cell, 3.56-mm fused silica acousto-optic modulator.

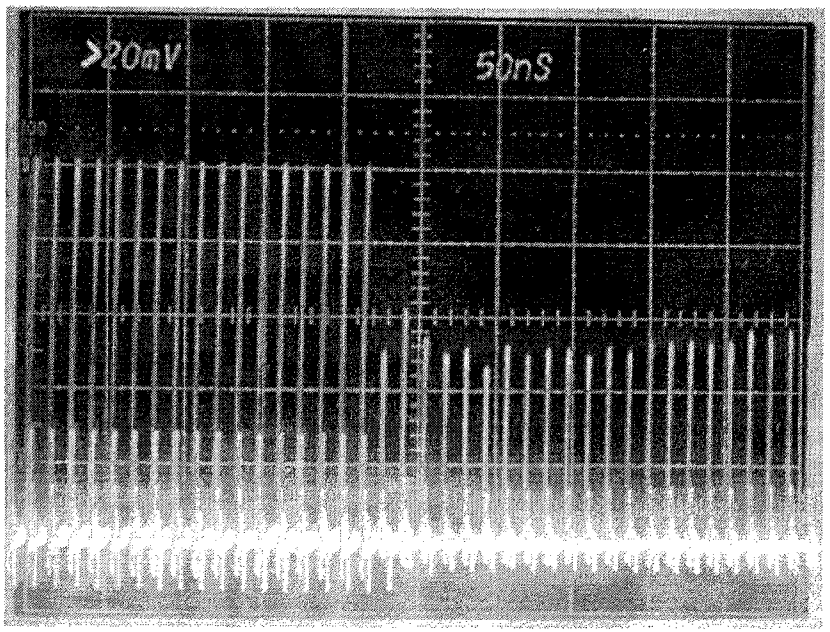

(a)

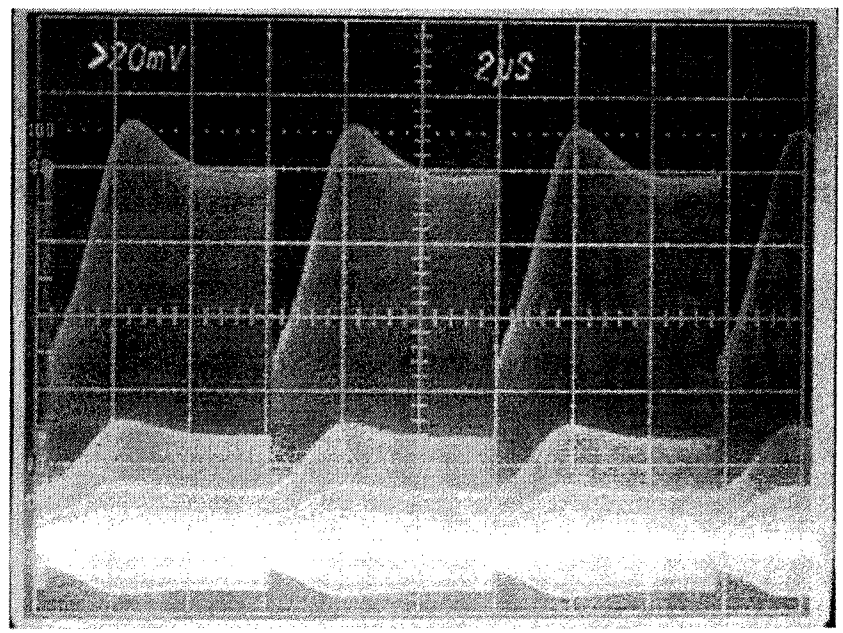

(b)

Fig. 2. Intracavity laser pulse train during dumping ((a) 50 ns/div., (b) 2 μs/div.). The dumping efficiency was 50%, and the repetition rate was 167 kHz.

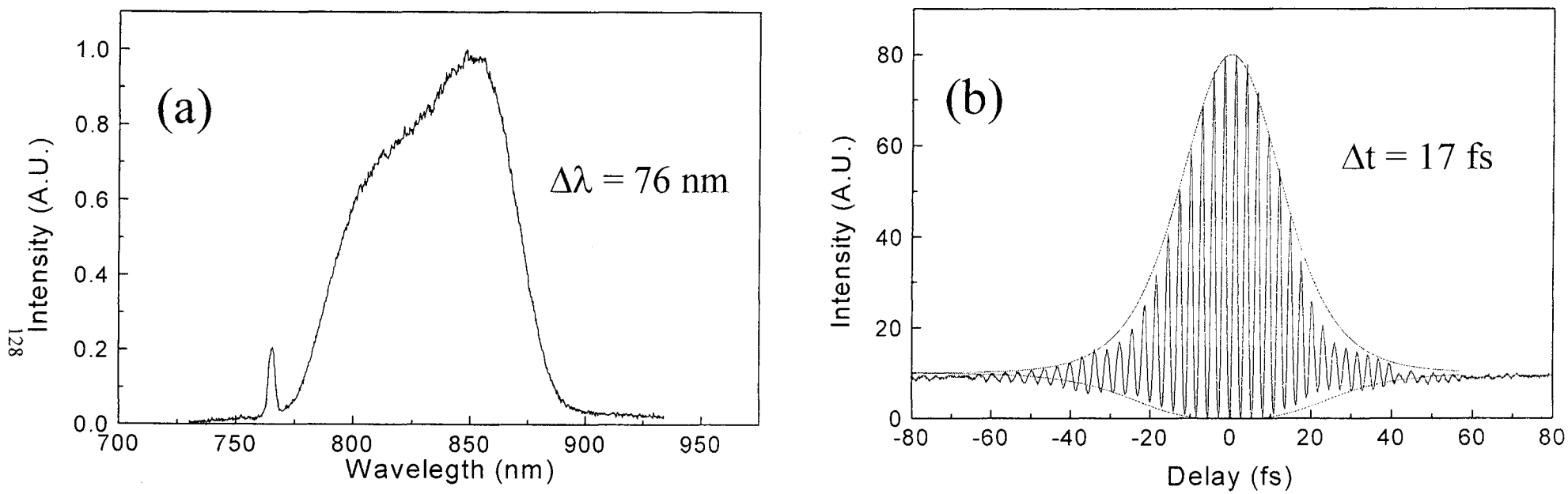

Fig. 3. (a) Spectrum and (b) interferometric autocorrelation of cavity-dumped pulses. Thespectral width was 76 nm and the pulse duration was 17 fs.

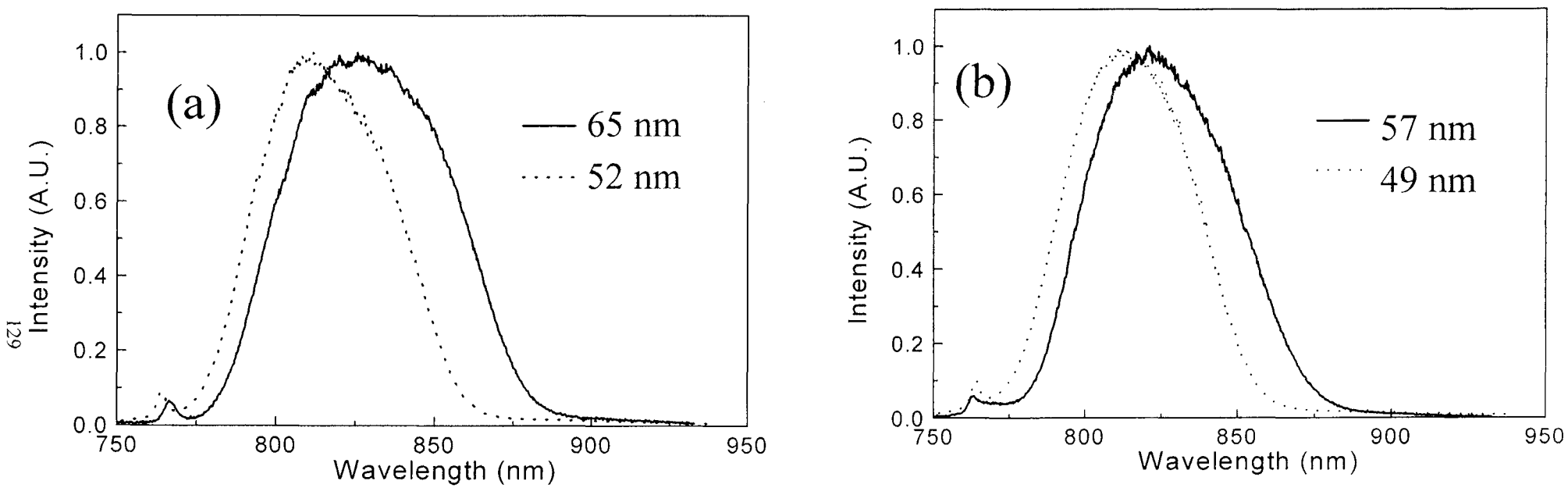

Fig. 4. Amplified spectra before (dotted line) and after (solid line) the incorporation of the cavity-dumped laser at (a) the preamplifier and (b) the power amplifier.

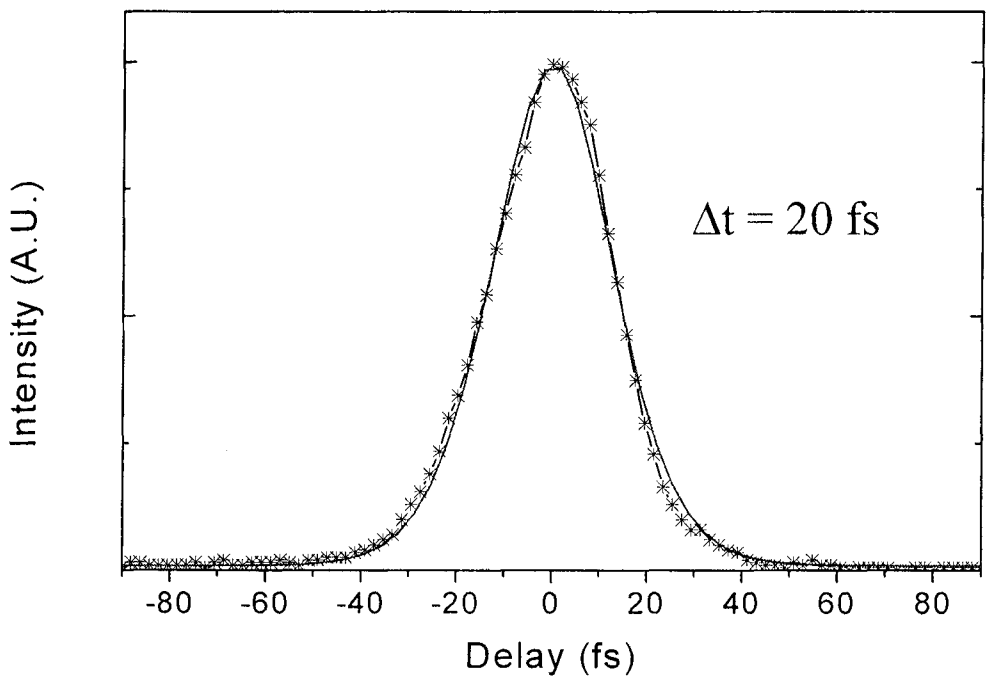

Fig. 5. Single-shot autocorrelation trace of a compressed laser pulse and its fit curve to a pulse shape obtained by inverse Fourier transform of the laser spectrum. The pulse duration was 20 fs.

Appendix (II)

Research Results of FY 2000

A. 1. High Harmonic X-Ray Generation

A. 1. 1. Coherent Control of High-Order Harmonics with Chirped Femtosecond Laser Pulses

High-order harmonics were coherently controlled using chirped femtosecond laser pulses for the production of sharp and strong harmonics. As the laser intensity was increased above the saturation intensity for optical-field ionization, the laser chirp needed to suppress harmonic chirp in the plateau region changed from positive to negative. We showed that the modification of a laser chirp condition in a rapidly ionizing medium should be included for the proper coherent control of high-order harmonics, necessitating the integral treatment of the interaction between atoms and a driving laser pulse.

Coherent control of quantum dynamics in atoms, molecules, and condensed matter has generated a wide range of interesting results [1-4]. The coherent control of the interaction process between a laser light and matter can be achieved by manipulating the temporal shape or spectral configuration of the interacting light. Recent advances in the generation and characterization techniques of ultrashort laser pulses made practical to prepare precisely defined laser pulses, and frequency-synthesized or chirped laser pulses have been applied to optically control interaction processes [1,2]. As a result, the coherent control technique has made plausible the selective excitation or ionization of atoms, selective chemical reactions, and atomic wave packet control [2-4]

The coherent control process can be applied to high-order harmonic generation (HHG) for the production of sharp and strong harmonics. HHG can be described as an interaction between a laser pulse and atoms. According to the semiclassical model of HHG that gives a good insight into the interaction process, high-order harmonic emission occurs through the repetition of following three steps - tunnel ionization of an atom in an intense laser field, acceleration of the ionized electron along the laser electric field, and recombination of the returned electron with the parent ion [5]. As the response of atoms to the applied laser field determines the high harmonic process, the temporal structure, i.e. amplitude and phase, of the laser field directly administers high harmonics emitted. For instance, rapidly varying laser intensity of ultrashort laser pulses can affect the phase of the electronic wave packet of a driven atom in such a way that a negative frequency chirp is induced in high-order harmonics [6,7]. Because atoms respond to every optical cycle of the laser pulse, this dynamically induced harmonic chirp, or equivalently the spectral structure of high-order harmonics, can be coherently controlled

by appropriately shaping the temporal structure of the laser pulse. There have been some attempts to apply the coherent control concept to HHG [6,8,9]; however, a systematic approach to this has not been made yet.

For proper coherent control of HHG, the interaction between atoms and a driving laser pulse has to be treated comprehensively. The intensity and spectral width of each harmonic can be sensitive to the temporal profile of a driving laser pulse, especially the chirp condition. Chang *et al.* [6] showed that the spectral shape of the harmonics was asymmetric to the laser chirp direction and that a positively chirped laser pulse could compensate for a dynamically induced, negative harmonic chirp. Sekikawa *et al.* [10] compressed the pulse width of the fifth harmonic to 13 fs by compensating for the negative harmonic chirp with a positively chirped laser pulse. Both of these experiments were carried out at relatively low intensities (below the saturation intensity), where dynamically induced harmonic chirps could be compensated for by positively chirped laser pulses and the effect of ionization on HHG was not significant. At laser intensity above the saturation intensity for optical field ionization (OFI), as required to induce a large frequency shift [11,12] or to significantly extend the cutoff order of harmonics [13], the ionization of atoms in the leading edge of the laser pulse is not negligible. This ionization effect was not previously appreciated in the estimation of the harmonic phase, but the self-phase modulation (SPM) of the laser pulse propagating in an ionizing medium alters its spectral structure and temporal shape. In other words, atoms modify the chirp condition of a driving laser pulse, which will be directly transferred to the frequency chirp of harmonics. Consequently, the coherent control to achieve sharp harmonics should treat the interaction between atoms and a laser pulse as an integral system, not just as an optical manipulation of atoms. In this Letter we systematically examine the relation between the laser chirp condition and the harmonic spectral structure for the development of a proper coherent control process, and demonstrate that the laser chirp needed for the production of sharp harmonics changes from positive to negative as applied laser intensity increases, due to the laser chirp modification in an ionizing medium.

We examined the effect of a laser chirp condition on the spectral structure of high-order harmonics emitted from neon atoms. The experiments were performed with a femtosecond terawatt Ti:sapphire laser operating at 10 Hz [15]. The laser spectrum was centered at 817 nm with a spectral bandwidth of 47 nm. The pulse duration measured with a second-harmonic generation (SHG) frequency-resolved optical gating (FROG) method was 28 fs. The laser intensity was varied by adjusting the laser energy with a

half-wave plate and polarizers installed before the pulse compressor, without changing the focusing geometry. While changing the laser energy, it was assured that the laser spectrum was not modified. The laser beam was focused into a gas jet with a nozzle of 0.2-mm diameter. This small nozzle was selected to minimize the geometrical effect in HHG, which will help simplifying the analysis of high-order harmonics. The peak gas density was 3×10^{18} cm^{-3}, and the full width at half maximum of the gas density profile was about 0.7 mm. The spatial profile of the focused beam was measured with a charge-coupled device (CCD) coupled with a microscope objective lens, which showed the central Airy disc contained 70 % of the energy. The generated high-order harmonics were detected by a flat-field extreme ultraviolet (XUV) spectrometer equipped with a back-illumination X-ray CCD with 330 × 1100 pixels (Princeton Instruments). Two Zr filters with a total thickness of 400 nm were used in front of CCD to block scattered laser light in the XUV spectrometer.

The laser chirp condition was controlled by changing the grating separation in the pulse compressor. The laser chirp may be adjusted also by changing the setting in the pulse stretcher. This however is not directly connected to the chirp condition of a final output. The amplified laser spectrum and also the final laser pulse shape will depend on an initial laser chirp condition, since the gain narrowing and gain saturation in amplifiers will occur differently. Consequently, the laser chirp control at the pulse compressor is definitely preferable since it does not change the laser spectrum and provides a predictable temporal structure of the final laser output.

The control of the distance between two pulse compression gratings provides linearly chirped laser pulses. The reduction of the grating separation from the chirp-free condition generates positively chirped pulses and the increase of it provides negatively chirped pulses. The pulse duration and phase information of chirped laser pulses were characterized with the SHG FROG technique. It showed a close match to the theoretical estimation obtained from the ray tracing formula for a grating pulse compressor [16] in combination with a measured laser spectrum; the pulse duration to the grating separation was almost quadratic, except a small asymmetry of the pulse duration to the chirp direction [17]. At the chirp-free condition the laser pulse duration was 28 fs. The increase of the grating separation by 0.5 mm from the chirp-free setting produced negatively chirped pulses of 120 fs, while the reduction by 0.5 mm produced positively chirped pulses of 115 fs.

For the generation of sharp harmonics the spectral broadening by the dynamically

induced harmonic chirp should be appropriately compensated for by controlling the chirp condition of driving laser pulses. Figure 1 shows the harmonic spectra obtained with a chirp-free 28 fs laser pulse and with negatively and positively chirped pulses. The peak laser intensity of the chirp-free pulse was 2×10^{15} W/cm^2, comparable to the OFI saturation intensity of neon. The chirped pulses were obtained while keeping the same laser energy. To get rid of harmonics from the long quantum path, the gas jet was placed at 2 mm after the laser focusing position so that only harmonics from the short quantum path could have a favorable phase matching condition [12]. With chirp-free pulses, harmonics up to the 77th order were observed. With negatively chirped pulses, the harmonics became broadened and weak, and the highest observed harmonic order was reduced. With positively chirped pulses, the harmonics in the plateau region became sharp and strong, which is consistent with the observation by Chang *et al.* [6]. The positively chirped pulse of 48 fs enhanced the peak intensity of the 67th harmonic by a factor of 5. This result shows that positively chirped pulses compensated for the negative harmonic chirp, and sharp and strong harmonics were generated. In this case the harmonics in the cutoff became drastically enhanced. It should be noted that the cutoff order was greatly extended to 101 with the positively chirped pulse of 69 fs, though the peak laser intensity was decreased with positive chirping. A further increase of chirped pulse duration made the harmonic signal broadened and weaker, eventually making the spectral structure quasi-continuous. This is a new observation and will help extending the wavelength limit of high-order harmonics toward a short wavelength region.

As the laser intensity was increased over the saturation intensity, the chirp structure contained in the harmonics changed dramatically. High-order harmonic spectra for the case of the chirp-free laser intensity of 1×10^{16} W/cm^2 are shown in Fig. 2. The chirp-free pulse of 28 fs produced high-order harmonics up to the 101st order. The control of laser chirp in this case produced very different behavior from that of the lower laser intensity in Fig. 1. With positively chirped pulses the harmonic spectra in the plateau became weaker and broader than that of the chirp-free case. This kind of behavior is quite contrary to the lower intensity case in Fig. 1. The understanding of this observation should be based on the more general case that takes into account the temporal modification of laser pulses occurring during the propagation through an ionizing medium. As positively chirped pulses were applied, all observed harmonics became broadened and the spectral structure was lost. On the other hand, with negatively chirped pulses the plateau harmonics behaved very differently, compared to the lower intensity case; they became sharp and strong, but the cutoff harmonics turned

out to be weak and disappearing. This also shows the importance of applying properly conditioned laser pulses for the generation of sharp and strong high-order harmonic at a certain order.

The observed spectral behavior of high harmonics, especially its dependence on laser intensity and chirp condition, can be explained by considering the effect of SPM-induced chirp on high harmonics. When applied laser intensity is sufficiently strong, the laser pulse propagating in a rapidly ionizing medium experiences a strong SPM due to the rapid change of refractive index in time [18], which induces a blueshift in the laser spectrum. Because the change in the refractive index is not a linear function of time during the pulse duration, different parts of the laser pulse experience different amounts of blueshift. Figure 3 shows the temporal variation of spectra of laser pulses propagating through a neon gas, obtained by numerical calculations of the one-dimensional (1D) wave equation [19]. The Wigner distribution, defined by $W(t,\omega)=\frac{1}{\pi}\int E^*(t-t')E(t+t')e^{-2i\omega t'}dt'$, clearly shows that the laser frequency increases with time in the leading edge, and then decreases back to its original frequency in the remaining part of the pulse. We note that only the positively chirped leading edge of the pulse is important in the high harmonic generation process, since the depletion of atoms and plasma-induced phase mismatch forbide efficient harmonic generation in the remaining part of the pulse. It can be seen from Fig. 3 that the amount of the positive chirp (the slope of the Wigner distribution) in the leading edge increases as the laser intensity increases. When this SPM-induced positive chirp becomes large enough, it can overcompensate the dynamically-induced negative chirp, changing the overall sign of the harmonic chirp from negative to positive. This explains why the effective laser chirp to comensate the harmonic chirp should be negative in the strong intensity regime (see Fig. 2).

To further explain the change in the optimal laser chirp conditions in the saturation intensity regime, we present in Fig. 4(a) the Wigner distribution of high harmonics, obtained after propagating 0.7-mm long neon medium with density of 1×10^{18} cm^{-3}. The peak laser intensity was 1.2×10^{16} W/cm^2. The propagation was calculated by using a recently developed 1D model [19], in which the single-atom response was calculated at 200 different positions in the medium by numerically solving the 1D Schrödinger equation, and the propagation of laser and harmonic fields are considered in 1D space along the propagation axis. Although our 1D model does not allow direct quantitative comparison with experimental results because of the neglect of spatial effects, it does

provide a basic description of the effect of the SPM-induced chirp on high harmonics. It can be seen in Fig. 4(a) that, due to strong SPM, high harmonics undergo very large positive chirp and consequently overlap with neighboring harmonics of different orders, resulting in a quasi-continuum structure in the plateau region of the harmonic spectrum. Since the SPM-induced chirp is larger than the dynamically induced chirp, the incident laser pulse should be negatively chirped to suppress the dominant SPM-induced positive chirp. In Fig. 4(b), we show that, using a negatively chirped laser pulse of 100 fs, the SPM-induced positive chirp was largely compensated for and sharp harmonics could be produced. Therefore, the experimental and theoretical results in Figs. 2-4 show that for the generation of sharp and strong high harmonics we should take into account the effect of atoms on a propagating laser pulse; the proper coherent control of high harmonics must be based on the integral treatment of the interaction between atoms and a driving laser pulse.

In conclusion, we have shown that high harmonic generation processes could be coherently controlled using chirped femtosecond laser pulses to produce sharp and strong harmonic spectra. For an efficient coherent control of high harmonic generation, a proper laser chirp condition should be chosen to suppress the harmonic chirp that broadens high harmonics and reduces their peak intensities. Specifically, at relatively low laser intensity high harmonics experience mostly the dynamically induced negative chirp, which could be controlled by positively chirped laser pulses. In contrast, when the laser intensity well exceeds the saturation intensity for optical field ionization, the SPM-induced positive laser chirp becomes appreciable and the harmonic chirp can change its sign from negative to positive. In this case, the laser pulse should be negatively chirped to suppress the harmonic chirp and thereby to produce sharp harmonics. Since the current method can be easily implemented to most high-power femtosecond lasers, the coherent control technique with chirped laser pulses will become a powerful tool for actual applications requiring sharp and strong harmonic signal.

References

[1] N. Dudovich, B. Dayan, S. M. G. Faeder, and Y. Siberberg, Phys. Rev. Lett. **86**, 47 (2001).

[2] J. Cao, C. J. Bardeen, and K. R. Wilson, Phys. Rev. Lett. **80**, 1406 (1998).

[3] W. S. Warren, H. Rabitz, and M. Dahleh, Science **259**, 1581 (1993).

[4] J. Arlt, C. Weiss, G. Torosyan, and R. Beigang, Phys. Rev. Lett. **79**, 4774 (1997).

[5] M. Lewenstein, Ph. Balcou, M. Yu. Ivanov, A. L'Huillier, and P. B. Corkum, Phys. Rev. A **49**, 2117 (1994).

[6] Z. Chang, A. Rundquist, H. Wang, I. Christov, H. C. Kaypteyn, and M. M. Murnane, Phys. Rev. Lett. **58**, R30 (1998).

[7] J. -H. Kim, D. G. Lee, H. J. Shin, and C. H. Nam, Phys. Rev. A **63**, 063403 (2001).

[8] P. Saliéres, P. Antoine, A. de Bohan, and M. Lewenstein, Phys. Rev. Lett. **81**, 5544 (1998).

[9] R. Bartels, S. Backus, E. Zeek, L. Milsoguti, G. Vdovin, I. P. Christov, M. M. Murnane, and H. C. Kapteyn, Nature **406**, 164(2000).

[10] T. Sekikawa, T. Ohno, T. Yamazaki, Y. Nabekawa, S. Watanabe, Phys. Rev. Lett. **83** 2564 (1999).

[11] H. J. Shin, D. G. Lee, Y. H. Cha, K. H. Hong, and C. H. Nam, Phys. Rev. Lett. **83**, 2544 (1999); H. J. Shin, D. G. Lee, Y. H. Cha, J. -H. Kim, K. H. Hong, and C. H. Nam, Phys. Rev. **63**, 053407 (2001).

[12] D. G. Lee, H. J. Shin, Y. H. Cha, K. H. Hong, J. -H. Kim, and C. H. Nam, Phys. Rev. A **63**, 021801(R) (2001).

[13] Z. Chang, A. Rundquist, H. Wang, M. M. Murnane, and H. C. Kapteyn, Phys. Rev. Lett. **79**, 2967 (1997).

[14] J. -H. Kim, H. J. Shin, D. G. Lee, and C. H. Nam, Phys. Rev. A **62**, 055402 (2000).

[15] Y. H. Cha, Y. I. Kang, and C. H. Nam, J. Opt. Soc. Am. B **16**, 2872 (1999).

[16] E. B. Treacy, IEEE J. Quant. Elec. **QE**-5, 454 (1969).

[17] K. H. Hong, J. H. Sung, Y. H. Kang, Y. H. Cha, and C. H. Nam (in preparation).

[18] C. Kan, N. H. Burnett, C. E. Capjack, and R. Rankin, Phys. Rev. Lett. **79**, 2971 (1997).

[19] J. -H. Kim and C. H. Nam, Phys. Rev. Lett. (submitted).

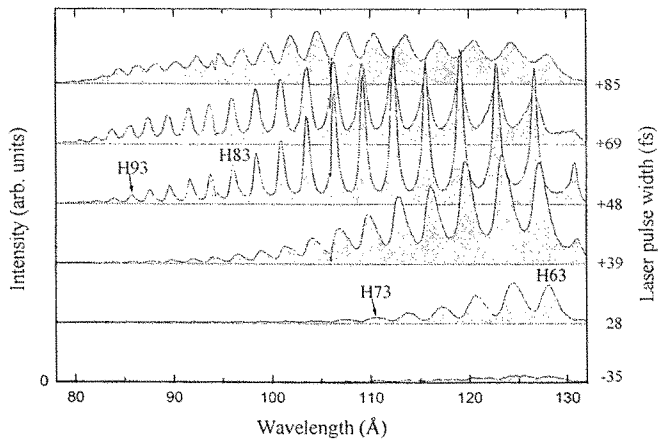

Fig. 1. Experimentally observed harmonic spectra from neon driven by femtosecond laser pulses with different laser chirps. Positively (+ sign) and negatively (- sign) chirped laser pulses were generated with the same laser energy as that of the chirp-free pulse. The pulse duration and peak laser intensity of the chirp-free pulse were 28 fs and 2×10^{15} W/cm^2, respectively. 'H*n*' denotes the nth harmonic.

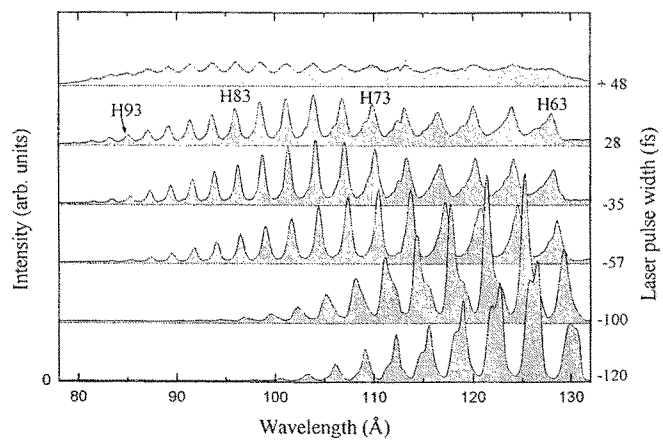

Fig. 2. Experimentally observed harmonic spectra from neon driven by femtosecond laser pulses with different laser chirps. The peak laser intensity of the chirp-free 28 fs pulse was 1×10^{16} W/cm^2.

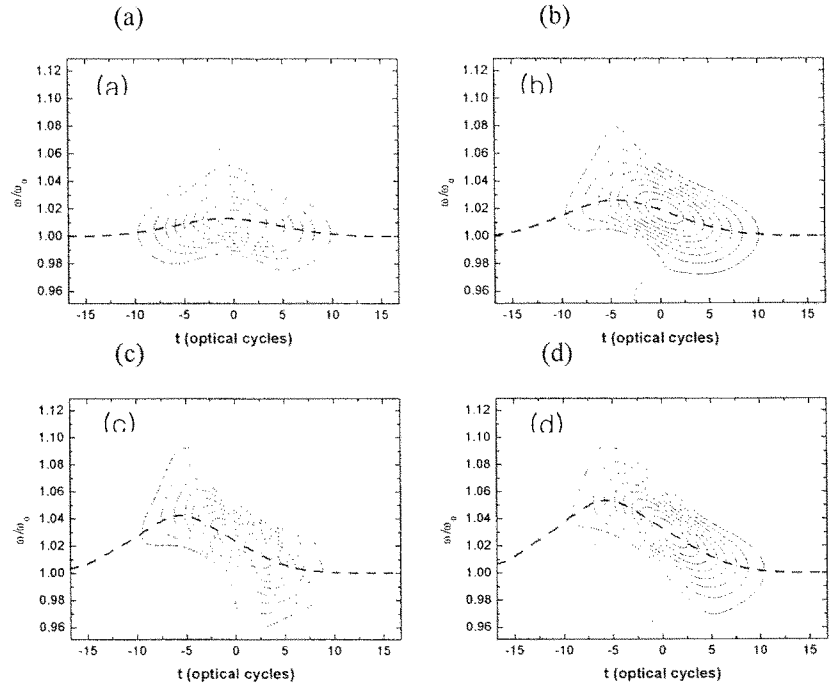

Fig. 3. Wigner distribution of the 30-fs, 800-nm laser pulse propagating through a 0.7-mm long neon gas of density 1×10^{18} cm^{-3}. The laser intensity is given by (a) $I = 1 \times 10^{15}$ W/cm^2, (b) $I = 3 \times 10^{15}$ W/cm^2, (c) $I = 6 \times 10^{15}$ W/cm^2, (d) $I = 1 \times 10^{16}$ W/cm^2.

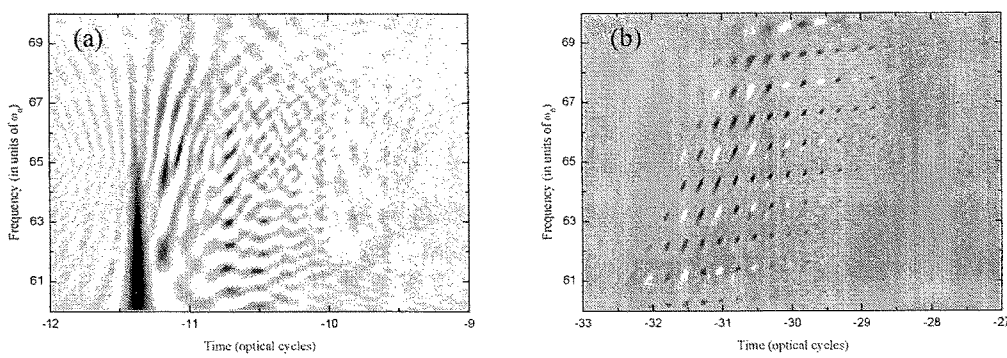

Fig. 4. Wigner distribution of high-order harmonics obtained after propagation. (a) Chirp-free 28 fs pulse. (b) Negatively chirped pulse, -100 fs.

A. 1. 2. Continuously Tunable High-Harmonic X-rays from Atoms in an Intense Femtosecond Laser Field

The high harmonics emitted from gaseous atoms driven by intense femtosecond laser pulses can cover a wide wavelength region, up to water-window x-rays. When intense laser pulses shorter than 30 fs are applied, the resulting harmonic emission reflects the atomic response to the rapidly varying laser field, and the emission wavelengths are blueshifted from the regular harmonic wavelengths. We demonstrate continuous wavelength tuning of high harmonics without sacrificing spectral sharpness, achieved through control of the laser intensity and chirp. This opens a pathway to the realization of a continuously tunable, coherent, femtosecond x-ray source, i.e. a tabletop synchrotron.

When gaseous atoms are exposed to a strong laser field, the periodic modulation of the electrons' motion produces high harmonics of laser frequency. High harmonics possess unique properties such as good coherence [1,2] and low beam divergence [3], as well as extremely short pulse duration [4, 5], inherited from the driving laser. Although numerous harmonic wavelengths can be obtained, the applicability of a harmonic x-ray source is restricted if only fixed harmonic wavelengths, set by the laser wavelength divided by odd integers, are available. A synchrotron x-ray source can provide continuously tunable x-ray radiation; however, access to synchrotron sources is limited and they usually generate x-ray pulses longer than a few tens of picoseconds [6]. The addition of tunability to harmonic x-ray sources, on the other hand, would offer tunable, coherent, femtosecond x-ray pulses with a peak brightness far greater than that of synchrotron x-ray pulses. Harmonic x-ray sources would be suitable for applications such as ultrafast atomic and molecular spectroscopy, and in photoelectron spectroscopy for characterization of chemical and biological materials. In this report we demonstrate that by simply adjusting the applied laser intensity and laser chirp we can achieve continuous wavelength tuning of high harmonics without sacrificing spectral sharpness and brightness.

Wavelength tuning of high harmonics has been attempted using several different approaches. For example, it has been shown that driving atoms with laser pulses mixed from two different wavelengths could generate tunable harmonics [7]. In this method a laser pulse at the fundamental wavelength was mixed with a second pulse at a different wavelength, obtained by optical parametric generation. This mixing broke the temporal

symmetry of the laser pulse and produced harmonic spectra at sum and difference frequencies of the second laser pulse. In this case, however, the new harmonics added through mixing the two pulses were generally much weaker than those produced by the first laser pulse alone. Another method that resulted in a shift of the harmonic wavelengths was the adjustment of the target position with respect to the laser beam focus [8]. Because the applied laser intensity varied with target position, the harmonics emitted at different target positions exhibited different amounts of wavelength shift. The harmonic wavelengths could be scanned, but the spectral widths of the harmonics at different target positions became quite broad as the target position was moved away from the laser beam focus. This procedure also led to a double-peaked harmonic signal. In addition, the spectral structure of the emitted harmonics became distorted because the phase matching conditions are sensitive to target position. Another possibility is the tuning of harmonic wavelengths through control of the laser wavelength. Tuning of the harmonic wavelength through control of the oscillator spectrum, however, is not practical because adjustment of the oscillator spectrum cannot be directly transferred to the final laser spectrum due to gain narrowing and gain saturation processes in a chirped-pulse amplification (CPA) laser [9]. Moreover, the shortest possible pulse duration in the CPA femtosecond laser, which is needed for the production of very high harmonics [10] and good conversion efficiency [11], requires the use of the entire obtainable laser spectrum. This requirement severely limits the spectral tuning range of the laser. Thus it would be desirable to tune harmonic wavelengths without changing the laser spectrum.

We propose a method to continuously tune the harmonic wavelengths without modifying the laser spectrum. Our previous experimental results [12] on the harmonics from argon driven by 30-fs laser pulses showed a harmonic blueshift corresponding to twice the laser frequency, the interval between odd harmonics. When a laser intensity above the saturation intensity for optical-field ionization is applied to atoms, harmonic emission occurs in the leading edge of the laser pulse before all neutral atoms are ionized, and the nonadiabatic response of the atoms to a rapidly rising laser field results in a wavelength blueshift of the high harmonics. This nonadiabatic effect can induce a large blueshift of harmonic wavelengths [12, 13]. However, the range of continuous tuning in the harmonics from argon was limited, and control of the laser intensity for the harmonic blueshift was accompanied by a modification of the spectral shape and brightness of harmonics, not a promising feature for realistic applications of harmonic x-rays. To achieve continuous tuning, the harmonic blueshift should be much larger than twice the laser frequency. In addition, the dynamically induced negative harmonic chirp

[14, 15] due to the rapid variation of laser intensity during harmonic generation results in a broadening of the harmonic spectrum, which should be appropriately compensated for to achieve sharp harmonics. Consequently, we explored the wavelength tunability of high harmonic x-rays on the basis of the harmonic blueshift in helium atoms using chirped femtosecond laser pulses. The objective of these experiments was to demonstrate that this method could provide sufficient tuning of high harmonics without losing spectral sharpness.

Experiments on continuously tunable HHG were carried out using a femtosecond terawatt Ti:sapphire laser operating at 10 Hz. The laser was a typical CPA laser, except that a long-wavelength injection method was implemented to obtain a broad, amplified spectrum [9]. The laser spectrum was centered at 824 nm with a spectral bandwidth of 47 nm. The pulse-shape closely matched a 26-fs Gaussian, up to 3% of peak laser intensity. A helium gas jet was placed 2 mm after the laser beam focus to generate single-peaked harmonics [16]. The helium gas profile in the interaction region was peaked at 3×10^{19} cm^{-3}, with a full width at half maximum of about 0.5 mm. High harmonic spectra were detected by a flat-field extreme-ultraviolet (XUV) spectrometer equipped with a back-illuminated x-ray charge-coupled device (CCD) with $330 \times 1{,}100$ pixels (Princeton Instruments). Two zirconium filters of thickness 0.2 μm were installed in front of the x-ray CCD to block stray laser light.

The wavelength tunability of high harmonics was investigated by controlling the incident laser energy and laser chirp. The blueshift of high harmonics was first scanned with adjustment of the applied laser intensity. The laser intensity was varied with the control of the incident laser energy using a half-wave plate and polarizers installed in front of the pulse compressor. Control of the incident laser energy was achieved without altering the focusing geometry. The laser spectrum was monitored while changing the laser energy to ensure that the spectrum was not modified, preventing any change in the temporal profile of the laser pulse. Any modification of the harmonic spectral profile incurred during the laser intensity scan could be fixed by adjusting the laser chirp. Laser chirp control was achieved by adjusting the grating distance in the pulse compressor. Although adjustment of the grating distance also affected the harmonic wavelengths [17], a sharp harmonic at a specific wavelength could be generated through iteration of these two steps, achieving simultaneous control of the spectral position and spectral width of the harmonics.

Helium was selected as the target medium because it is capable of providing a

sufficiently large blueshift in the wavelength region near 10 nm. The harmonic intensity and range of observed harmonic orders depend on the target medium and laser parameters. Decreasing the atomic number of the rare gas comprising the target medium decreases the intensity of the harmonics, but enhances the highest obtainable harmonic order. The harmonic blueshift of a low atomic number medium is small, but it can be improved by operating at short wavelengths, because the amount of harmonic blueshift increases with harmonic order [12]. The relatively weak harmonic intensity in helium was enhanced by use of a high-density medium as the target. Thus, the high-density helium gas jet provided strong harmonics with a sufficiently large blueshift in the wavelength region near 10 nm.

A strong blueshift of the high harmonics was generated in the intense femtosecond laser field used in these experiments. The high harmonic spectrum from helium atoms driven by a chirp-free 26-fs laser pulse is shown in Fig. 1. The peak laser intensity was 2×10^{16} W/cm^2, well in excess of the saturation intensity for optical-field ionization of helium under a 26-fs laser pulse (3×10^{15} W/cm^2). Under this intense laser field, helium atoms were rapidly ionized in the leading edge of the laser pulse, allowing strong harmonic generation only in the leading edge [18]. The harmonics emitted in this case were strongly blueshifted. The harmonic of 55th order was blueshifted more than two times the laser frequency and the harmonic of 97th order more than four times the laser frequency (see Fig. 1). As the harmonic order was increased, the harmonic blueshift became large enough for continuous tuning of harmonic wavelengths over the frequency interval between adjacent harmonics.

Both the nonadiabatic effect [12, 13] and self-phase modulation (SPM) [19, 20] of the driving laser pulse contribute to the blueshift of harmonic wavelengths observed in Fig. 1. The nonadiabatic effect is basically a single atom effect, because it comes from the atomic response to the rapidly rising intense laser field. On the other hand, the blueshift due to SPM is a result of the propagation of the driving laser pulse through the harmonic generation medium. In an ionizing medium the refractive index decreases with time, which causes SPM of the propagating laser pulse [21]. The SPM then causes a blueshift of the laser spectrum and, as a result, the high harmonics are also blueshifted. Estimation of the relative contributions of the nonadiabatic and SPM effects based on the order dependence of the harmonic blueshift [12], showed that about 25% of the blueshift of the 79th harmonic in Fig. 1 was due to the nonadiabatic effect, with the SPM effect accounting for the remainder. Because the SPM effect increases with medium density, the adoption of a high-density medium enhances the blueshift as well

as increasing the harmonic signal level, facilitating the wavelength tuning of harmonics in a strong signal level.

The high harmonics from atoms driven by intense femtosecond pulses can possess very different chirp structures depending on the experimental parameters. For example, Fig. 2 shows the harmonics from a 26-fs chirp-free laser pulse with the relatively weak intensity of $1x10^{15}$ W/cm^2, and those from a positively chirped laser pulse of 130 fs. In the chirp-free case the observed harmonics are limited to the 55^{th} order. The harmonic emission changes dramatically when the positively chirped laser pulse is applied. This pulse enhances the intensity of the 55^{th} harmonic by more than an order of magnitude. In addition, the highest harmonic order is drastically increased from 55 for the chirp-free 26-fs laser pulse to 121 for the positively chirped 130-fs laser pulse, in spite of the decrease of the peak laser intensity by a factor of 5. This result clearly shows the importance of applying properly chirped laser pulses in HHG.

High harmonic spectra are affected by induced harmonic chirp, i.e. the wavelength of a certain harmonic may decrease (positive chirp) or increase (negative chirp) during its generation. The chirp structure of high harmonics can be clearly shown using the Wigner distribution function [22], which provides a representation of the temporal variation of harmonic frequencies in the time-frequency domain. This chirp analysis method has been used to show that, because atoms respond to every optical cycle of a driving laser pulse, the harmonic chirp can be compensated for using appropriately chirped laser pulses. At the relatively low laser intensity used to obtain the results in Fig. 2, dynamically induced negative chirp was mostly responsible for the harmonic chirp. In this case a positively chirped laser pulse was shown to compensate for the negative harmonic chirp and produce significantly enhanced harmonics. Consequently, the use of a positively chirped laser pulse to compensate for a negative harmonic chirp improved the spectral characteristics of the harmonics, leading both to sharply enhanced brightness and to significantly increased number of observed harmonic orders.

Continuous tuning of the high harmonics without losing spectral sharpness was achieved by controlling the incident laser energy and laser chirp. Spectral images of the continuously tuned high harmonics obtained from helium atoms are presented in Fig. 3. The wavelength of the harmonic spectrum was calibrated using the argon spectral lines from Ar^{7+} and Ar^{8+} ions. Figure 3A shows that the harmonic wavelengths decrease as the laser parameters are adjusted from Spectrum (I) to Spectrum (V), and that the harmonic frequencies of order greater than or equal to 73 in Spectrum (I) overlap with or exceed those of the next higher-order harmonics in Spectrum (V). Continuous

wavelength tuning of sharp harmonics was achieved by changing the laser parameters from a negatively chirped 35-fs, 11-mJ pulse in Spectrum (I) (Fig. 3A) to a positively chirped 130-fs, 1.0-mJ pulse in Spectrum (V). Here we tuned the harmonic frequencies such that the 79^{th} harmonics of the 5 spectra in Fig. 3A had equal frequency intervals between neighboring spectra, demonstrating the continuous wavelength tuning capability. The wavelength shifts of the 79^{th} harmonic of the 5 harmonic spectra can be fitted by a straight line, as shown in Fig. 3B. The spectral widths were maintained within 0.7 $_0$ by adjustment of the laser chirp condition. This represents a direct proof that it is possible to generate a given harmonic at a specific wavelength by controlling the incident laser energy and laser chirp, a critical step in the realization of a continuously tunable high harmonic x-ray source. The continuous tuning range of harmonics below the 71^{st} order was slightly less than the full tuning range. The extension of the full tuning range to longer wavelength should be achievable using a higher medium density. Alternatively, adoption of a medium of higher atomic number such as neon, argon, or xenon, would also facilitate tuning to longer wavelengths because of larger blueshift of these atoms. The proposed method can be easily implemented in most harmonic experiments that use CPA lasers, because the continuous wavelength tuning is accomplished simply by adjusting the angle of the half-wave plate (for laser energy control) and the grating distance in the pulse compressor (for chirp control).

The results in Fig. 3A show that the amount of the laser chirp needed to produce sharp harmonics decreases with increasing the incident laser energy. This interesting result can be understood as follows. As the laser intensity is increased above the saturation intensity, the SPM of the propagating laser pulse induces a positive laser chirp in the leading edge of the laser pulse [17]. The induced positive laser chirp in turn generates a positive harmonic chirp, which offsets the effect of the dynamically induced negative harmonic chirp and causes the net harmonic chirp to decrease. As a result, the laser chirp needed to compensate for the harmonic chirp becomes smaller, and eventually the sign of the laser chirp for the production of sharp harmonics changes from positive to negative [17]. This phenomenon is directly represented in Fig. 3A, which shows a decrease in the laser chirp needed for the generation of sharp harmonics with increasing incident laser energy. At the largest laser energy (Spectrum (I) of Fig. 3A), the net harmonic chirp became positive, and a negatively chirped laser pulse was required to produce sharp harmonics. In this case the SPM-induced chirp exceeded the dynamically induced chirp. The control of HHG with appropriately chirped laser pulses is therefore crucial to generate sharp and bright harmonics.

We have demonstrated the continuous wavelength tunability of high harmonics based on harmonic blueshift due to the nonadiabatic and SPM effects and on control of harmonic chirp using chirped femtosecond laser pulses. The wavelength tuning method proposed here requires only rotation of the half-wave plate for laser-energy control and adjustment of the grating distance in the pulse compressor for chirp control, which can be automated with a feedback control using a genetic algorithm [23]. Hence, the wavelength tuning method demonstrated here has strong potential as a practical tool that will allow the application of high harmonic x-ray sources to many unexplored areas. Tunable harmonic x-ray sources open the pathway to XUV/x-ray nonlinear optics, x-ray absorption spectroscopy, and photoelectron spectroscopy in atomic, molecular, and biological materials, with superb coherence and ultrashort time resolution not accessible with synchrotron x-ray sources. Tunable high harmonics should also prove useful as seeding pulses for x-ray lasers. Instead of starting an x-ray laser from an amplified spontaneous emission (ASE), an injection-seeded x-ray laser from a high harmonic x-ray has much better coherence properties and shorter pulse duration than those achievable with an x-ray laser based on ASE. Therefore, the tunability of high harmonic x-ray sources will significantly increase the diversity and versatility of the applications of high harmonic x-rays.

References

[1] L. Le Deroff, P. Salieres, B. Carre, D. Joyeux, D. Phalippou, *Phys. Rev. A* 61, 0433802 (1999).

[2] M. Bellini, C Lyngå, A. Tozzi, M. B. Gaarde, T. W. Hänsch, A. L'Huillier, C. –G. Wahlström, , *Phys. Rev. Lett.* 81, 297 (1998).

[3] A. Rundquist, C. G. Durfee III, Z. Chang, C. Herne, S. Backus, M. M. Murnane, H. C. Kapteyn, *Science* 280, 1412 (1998).

[4] M. Drescher, M. Hentschel, R. Kienberger, G. Tempea, C. Spielmann, G. A. Reider, P. B. Corkum, F. Krausz, *Science* 291, 1923 (2001).

[5] P. M. Paul, E. S. Toma, P. Breger, G. Mullot, F. Auge, Ph. Balcou, H. G. Muller, P. Agostini, *Science* 292, 1689 (2001).

[6] There have been efforts to generate subpicosecond x-ray pulses from a synchrotron by modulating an electron bunch with a femtosecond laser pulse or scattering femtosecond laser pulse with a high-energy electron beam; see, for example, (24).

[7] M. B. Gaarde, P. Antoine, A. Persson, B. Carre, A. L'Huillier, C.-G. Wahlstrom, *J. Phys. B* 29, L163 (1996).

[8] C. Altucci, R. Bruzzese, C. de Lisio, M. Nisoli, S. Stagira, S. De Silvestri, O. Svelto, A. Boscolo, P. Ceccherini, L. Poletto, G. Tondello, P. Villoresi, *Phys. Rev. A* 61, 021801(R) (1999).

[9] Y. H. Cha, Y. I. Kang, and C. H. Nam, *J. Opt. Soc. Am. B* 16, 1220 (1999).

[10] Z. Chang, A. Rundquist, H. Wang, M. M. Murnane, H. C. Kapteyn, *Phys. Rev. Lett.* 79, 2967 (1997).

[11] M. Schnurer, Z. Cheng, M. Hentschel, G. Tempea, P. Kálmán, T. Brabec, F. Krausz, *Phys. Rev. Lett*. 83, 722 (1999).

[12] H. J. Shin, D. G. Lee, Y. H. Cha, K. H. Hong, C. H. Nam, *Phys. Rev. Lett*. 83, 2544 (1999).

[13] J. B. Watson, A. Sanpera, K. Burnett, P. Knight, *Phys. Rev. A* 55, 1224 (1997).

[14] Z. Chang, A. Rundquist, H. Wang, I. Chrstov, H. C. Kapteyn, M. M. Murnane, *Phys. Rev. A* 58, 30(R) (1998).

[15] P. Salières, P. Antoine, A. Bohan, M. Lewenstein, *Phys. Rev. Lett*. 81, 5544 (1998).

[16] D. G. Lee, H. J. Shin, Y. H. Cha, K. H. Hong, J.-H. Kim, C. H. Nam, *Phys. Rev. A* 61, 21801(R) (2001).

[17] D. G. Lee, J.-H. Kim, K. H. Hong, C. H. Nam, *Phys. Rev. Lett*. (submitted).

[18] C. Kan, C. E. Capjack, R. Rankin, *Phys. Rev. A* 52, 4336(R) (1995).

[19] P. Villoresi, P. Ceccherini, L. Poletto, G. Tondello, C. Altucci, R. Bruzzese, C. de Lisio, M. Nisoli, S. Stagira, G. Cerullo, S. De Silvestri, O. Svelto, *Phys. Rev. Lett*. 85,

2494 (2000).
[20] C.-G. Wahlström, J. Larsson, A. Persson, T. Starczewski, S. Svanberg, P. Salieres, P. Balcou, A. L'Huillier, *Phys. Rev. A* 48, 4709 (1993).
[21] Wm. M. Wood, C. W. Siders, M. C. Downer, *Phys. Rev. Lett*. 67, 3523 (1991).
[22] J.-H. Kim, D. G. Lee, H. J. Shin, C. H. Nam, *Phys. Rev. A* 63, 63403 (2001).
[23] B. J. Pearson, J. L. White, T. C. Weinacht, P. H. Bucksbaum, *Phys. Rev. A* 63, 63412 (2001).
[24] R. W. Schoenlein, S. Chattopadhyay, H. H. W. Chong, T. E. Glover, P. A. Heimann, C. V. Shank, A. A. Zholents, M. S. Zolotorev, *Science* 287, 2237 (2000).

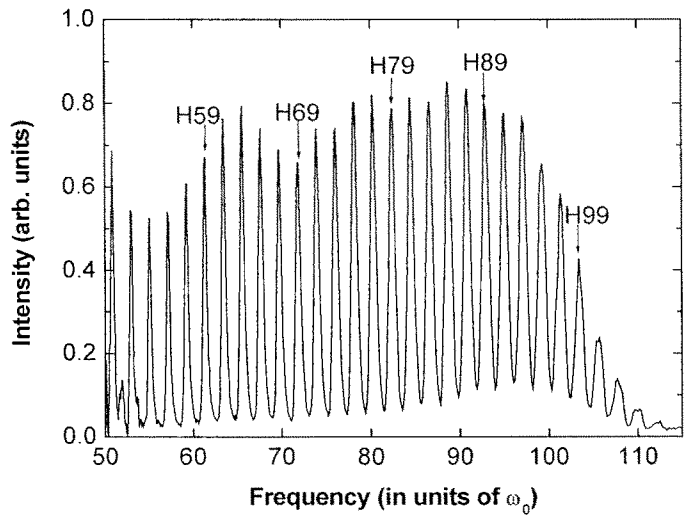

Fig. 1 Strongly blueshifted harmonic spectrum from helium atoms driven by a chirp-free 26-fs laser pulse with an intensity of 2×10^{16} W/cm^2. The incident laser energy was 11 mJ, the same as in Spectrum (I) of Fig. 3A. The peak helium density was 3×10^{19} cm^{-3} and the full-width at half maximum of the helium profile was 0.5 mm. 'Hn' denotes the harmonic of order n.

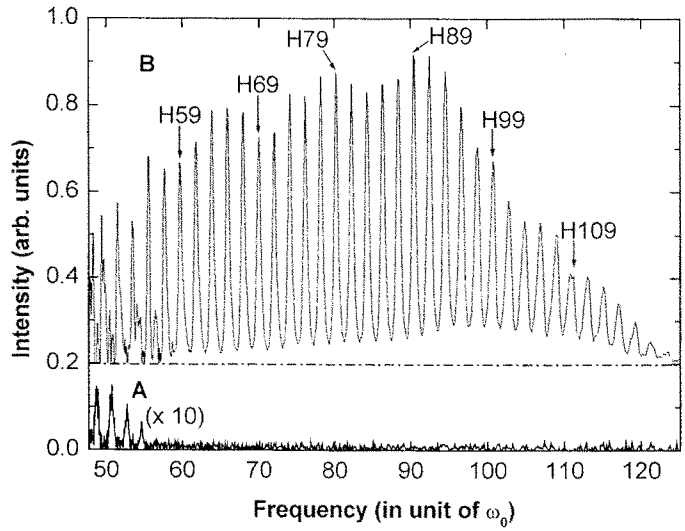

Fig. 2 Enhancement of high harmonics with chirped femtosecond laser pulses. (A) Harmonics produced by a chirp-free 26-fs laser pulse with an intensity of $1x10^{15}$ W/cm^2. The incident laser energy was 1.0 mJ, the same as in Spectrum (IV) of Fig. 3A. The harmonic intensity is magnified by a factor of 10 to make it comparable to that of Fig. 2B. The harmonics are broad and the highest observed order is 55. (B) Harmonics produced by a positively chirped 130-fs laser pulse with the same laser energy as in Fig. 2A. An offset of +0.2 is added for clarity. The harmonics become stronger using the chirped pulse, and the highest harmonic order is extended to 121.

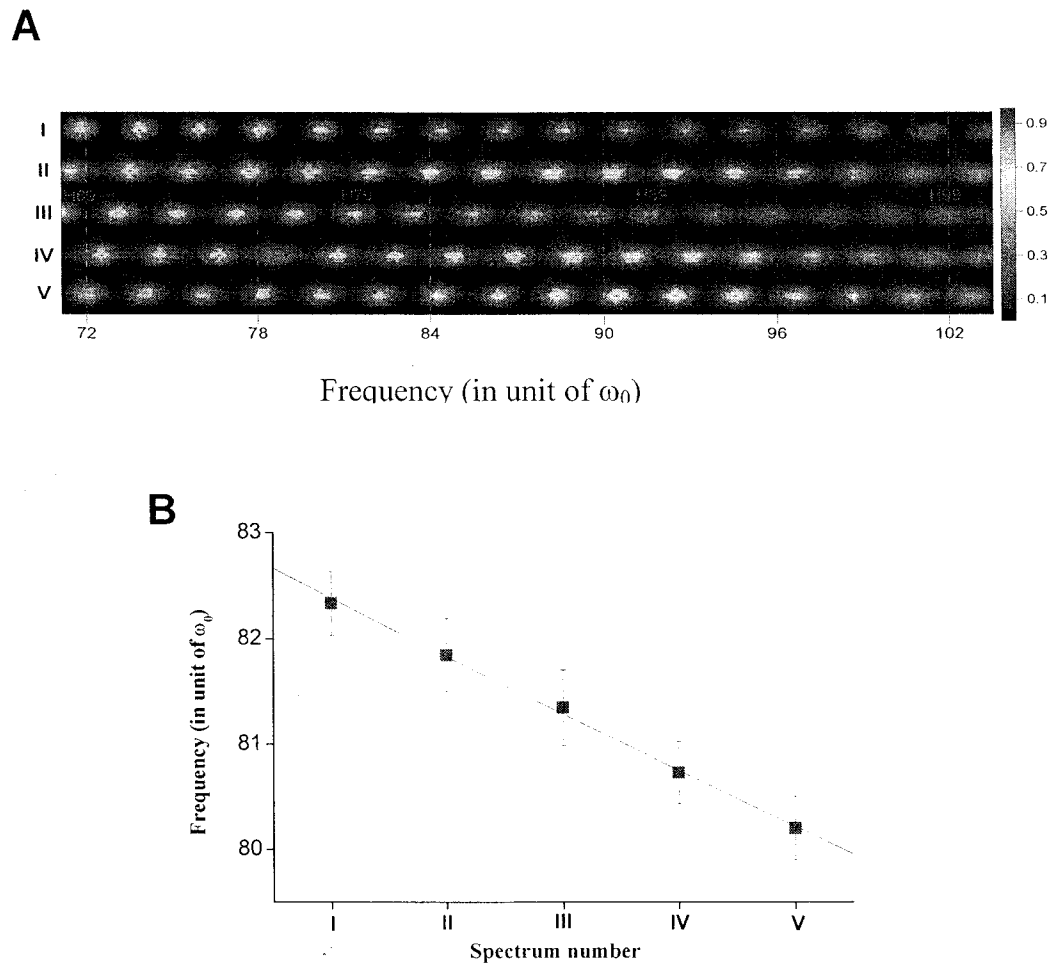

Fig. 3 Continuously wavelength-tuned high harmonics generated from helium atoms driven by intense femtosecond laser pulses. The wavelength tuning was achieved by adjusting the incident laser energy and laser chirp. The laser energy was varied using a half-wave plate and polarizers, and the laser chirp was adjusted by changing the grating distance in the pulse compressor. (A) Spectral images of harmonics taken using an x-ray CCD. Five spectral images of high harmonics were prepared such that the wavelength of the 79th harmonic could be tuned with even frequency intervals between neighboring spectra. The laser energy and chirped pulse duration were (I) 11 mJ and –35 fs, (II) 5.9 mJ and +34 fs, (III) 4.1 mJ and +43 fs, (IV) 1.8 mJ and +58 fs, (V) 1.0 mJ and +130 fs, respectively. (B) Frequency and spectral width of the 79th harmonics of the 5 spectra shown in Fig. 3A.

A. 1. 3. Bright, low-divergence high-order harmonic generation in a long gas jet

We have investigated efficient harmonic generation in a long gas jet using intense 28 fs pulses. We experimentally demonstrated that, by balancing diffraction and plasma defocusing with nonlinear self-focusing, a new optimum condition for efficient high-order harmonic generation could be reached. Under condition for a self-guided beam, the 27th harmonic from argon with energy larger than 1 nJ and divergence less than 0.5 mrad was produced with 5 mJ pumping laser pulse.

After the development of high power laser technique, it is possible to generate much higher order harmonics through very higher nonlinear process, where the laser field is sufficiently so high that the Coulomb potential of the atoms are significantly modified and atoms can be ionized through the tunneling process. The high-order harmonics generated in such a nonperturbative regime has several distinctive characteristics. Especially, the existence of the wide plateau region, the spectral region of almost constant intensity independent of harmonic order, made it possible to obtain the harmonics the wavelength of which is shorter than 10 nm with reasonably high conversion efficiency [1,2]. This can be applied to the formation of the attosecond pulses [3,4], and a number of applications that use the coherent X-ray sources in the XUV region. However, many more applications would be possible if the process were made more efficiently. So the extensive studies have been devoted to increase both its efficiency and the photon flux. To improve the number of photons in macroscopic gas medium the phase-matching condition has to be fulfilled and also the propagation of the pumping laser pulse has to be well controlled to deliver sufficient laser energy to as many atoms as possible.

For efficient harmonic generation, uniform pumping of a long interaction volume is needed. Harmonic generation in a hollow-core fiber showed good performance for this purpose [5]. The cross section of the harmonic generation volume, however, is severely limited, restricting maximum-coupling laser energy. On the other hand, harmonic generation using a gas jet does not have such limitation, but it has to overcome the refraction of laser pulses in an ionizing medium [6,7], since the ionization of atoms is unavoidable for efficient harmonic generation process. Because of an electron density gradient in the transverse direction, the laser pulse is defocused as it propagates through the medium; the ionizing medium acts as a negative lens. Therefore, proper guidance of the refracting pumping laser pulse is important for optimizing harmonic generation volume as well as the density of atom.

In this Letter, we present experimental results of high-order harmonics in a long gas jet pumped by intense 28-fs laser pulses. A 6-mm slit nozzle and high intensity laser pulses over the saturation intensity were applied to generate an elongated interaction medium and to cover a large volume of atoms with high laser intensity. The refraction of the laser pulses in ionizing medium was observed with a visible charge-coupled device (CCD). Good phase matching between the driving laser pulses and generated harmonic signal was obtained by optimizing laser parameters, medium density, and target position.

Figure 1 shows the visible images of the plasma column captured on a visible charge coupled device (CCD) along the laser propagation when 28 fs Ti:sapphire laser pulses with a peak intensity of 7×10^{15} W/cm^2 at the focusing position were applied into a long argon gas jet from an 6×0.5 mm slit nozzle. The peak gas density and spatial width in the transverse direction are about 65 Torr and 700 μm (FWHM), respectively. A focusing method was applied for the measurement of the spatial and temporal density of the gas jet. An IR blocking filter was installed in front of the CCD to eliminate strong background at the laser wavelength. As shown in Fig. 1, when gas jet was placed at z = +3 mm after the laser focus (the entrance of the interaction medium was positioned at the focused position of the laser beam), laser pulse could not propagate more than the first 1 mm due to the plasma defocusing effect, although the confocal parameter of the laser pulse, b = 10 mm, in vacuum was long enough to provide high intensity over the saturation intensity for optical field ionization in the whole gas jet medium. The plasma column length became extended as the gas jet moved to before the laser focus and, moreover, nearly uniform plasma column could be generated along the whole length of the gas jet at z= -7 mm. It showed that the guiding of the laser beam, delivering the pumping laser pulse up the end of medium, in a partially ionized medium was very sensitive to the target position.

With the same experimental condition as in Fig. 1, we detected the high-order harmonics with an X-ray CCD detector (Princeton Instruments). The harmonic signal was resolved with a flat-field XUV spectrometer. It consists of a toroidal mirror (for compensation of astigmatism in a grazing-incidence concave grating to achieve spatially resolved spectral image), or cylindrical mirror (for the measurement of divergence), and grazing-incidence concave grating. Two Al-filters with a total thickness of 0.4 μm was installed in front of the CCD to block scattered laser light in the XUV spectrometer. Figure 2 shows the experimental results of 27th harmonic energy from argon depends on target position and peak gas density. The medium length

is sufficiently long for efficient harmonic generation because it corresponds to about 3 times the absorption length (L_{abs} = 2.1 mm for 27 harmonic) of 65 torr argon [8]. In contrary to the previous results [9,10] performed with comparatively low peak intensity (< 10^{15} W/cm^2) and short medium length (< 1 mm), the harmonic energy increases as the gas jet is moved away before the focusing position, reaches maximum at -7 mm and then decreases (see Fig. 2(a)). At the optimized condition, harmonics were so strong that it could saturate our detection system in a single shot of 5 mJ laser pulse. The harmonic energy generated by the converging laser beam was more than two orders of magnitude larger than that obtained with the gas jet after the focused position. Although the intensity at the time for the observed harmonic generation (1-2 × 10^{14} W/cm^2) is somewhat less than the intensity required for the full ionization of the argon (> 7 × 10^{14} W/cm^2), the optimized position coincides with the position with the long plasma column in Fig. 1. And at the optimization position, the harmonic signal is quite sensitive to the gas jet density, 6 % deviation of the density drops the signal to an order of magnitude as shown in Fig. 2(b).

The observed results are consistent with what can be expected from the refraction effect due to free electrons on the propagation of the incident laser. This can induce a significant defocusing of the laser pulse and can therefore decrease the coherence length and limit the actual intensity present in the interaction volume. By placing the gas jet before the laser focus, we could reduce the defocusing in plasma. The balance between plasma defocusing, diffraction, and nonlinear self-focusing lead to a new optimum condition that harmonics could be generated over a long medium length and large transverse cross section of the interaction region (the size of the pumping laser will be larger than that of focal position).

At optimized experimental conditions, beam divergence of harmonics was measured after replacing the toroidal mirror in the XUV spectrometer with a cylindrical mirror. Figure 3 shows the observed harmonic spectra for harmonics 23 to 31. The measured divergence of harmonics was 0.5 mrad (in FWHM). This small divergence compared with harmonics generated in hollow-core fiber [5], ~ 1 mrad, and in gas cell target [11], ~ 2 mrad, result from enlarged harmonic generation cross-section. All observed harmonics are strongly blueshifted due to SPM in an ionizing gas [12] and nonadiabatic blueshift of an single atom [13], and we also find that in our experimental conditions 27th harmonic are particularly stronger than other adjacent orders and this single order possesses more than 45 % of the total energy of detected harmonics (see Fig. 3(b)). Recently, Bartels *et al.* [14] reported where they actively controlled the temporal

envelope of 25 fs laser pulses to stand only 27th harmonic out than other orders. In our case, the optimization process by manipulation of the propagation of the laser pulse at proper atomic density might be similar effects on enlargement of specific harmonic order because the sensitive of self-phase and amplitude modulation (SPAM) of the fundamental laser pulse through the propagation in the rapidly ionizing medium [15] was also involved in efficient harmonic generation.

To evaluate the photon number of the observed harmonics, the throughput of the XUV spectrometer was measured by comparing harmonic signals under identical condition with and without the spectrometer in the system. The sensitivity of the CCD was also measured with the calibrated photodiode (AXUV-100) using 27th harmonic source. We have measured energy yields of up to 1 nJ per pulse for 27th single harmonic corresponding to a conversion efficiency of 2×10^{-7} by 5 mJ, 28 fs laser pulses.

In conclusion we could convert a large amount of laser energy to high-order harmonics with high conversion efficiency. Optimization of the harmonic generation volume, not a simple extension of medium length and density, could overcome the limit set by the neutral absorption of the X-rays for the high flux harmonic generation which is necessity in many applications. In addition to low beam divergence and easiness of laser alignment, the harmonic generation in a long gas jet will provide a pathway to efficient harmonic generation with a large pumping energy, because there is no restriction in the transverse dimension of harmonic generation medium. Further studies of the laser propagation in nonlinear medium relating the high-order harmonic generation would help to increase the X-ray yields much more.

References

[1] Y. Tamki, J. Itatani, Y. Nagata, M. Obara, and K. Midorikawa, Phys. Rev. Lett. **82**, 1422 (1999).

[2] M. Schnürer, Z. Cheng, M. Hentschel, G. Tempea, T. Brabec, and F. Krausz, Phys. Rev. Lett. **83**, 722 (1999).

[3] P. Antoine, A. L'Huillier, and M. Lewenstein, Phys. Rev. Lett. **77**, 1234 (1996).

[4] D. G. Lee, H. J. Shin, Y. H. Cha, K. H. Hong, J. -H. Kim, and C. H. Nam, Phys. Rev. A **63**, 021801(R) (2001).

[5] A. Rundquist, C. G. Durfee III, Z. Chang, C. Herne, S. Backus, M. M. Murnane, H. C. Kapteyn, Science, **280**, 1412 (1998).

[6] W. P. Leemans, C. E. Clayton, W. B. Mori, K. A. Marsh, P. K. Kaw, A. Dyson, and C Joshi, Phys. Rev. A **46**, 1091 (1992).

[7] C. Altucci, T. Starczewski, E. Mevel, and C. -G. Wahlstrüm, J. Opt. Soc. Am. B **13**, 148 (1996).

[8] E. Constant, D. Garzella, P. Breger, E. Mével, Ch. Dorrer, C. Le Blanc, F. Salin, and P. Agostini, Phys. Rev. Lett. **82**, 1668 (1999).

[9] Ph. Balcou, C. Cornaggia, A. S. L. Gomes, L. A. Lompré, and A. L'Huillier, J. Phys. B **25**, 4467 (1992).

[10] P. Salieres, A. L'Huillier, and M. Lewenstein, Phys. Rev. Lett. **74**, 3776 (1995).

[11] Y. Tamaki, J. Itatani, M. Obara, and K. Midorikawa, Phys. Rev. A **62**, 063802 (2000).

[12] C. -G. Wahlström, J. Larsson, A. Persson, T. Starczewski, and S. Svanberg, Phys. Rev. A **48**, 4709 (1993).

[13] H. J. Shin, D. G. Lee, Y. H. Cha, K. H. Hong, and C. H. Nam, Phys. Rev. Lett. **83**, 2544 (1999); H. J. Shin, D. G. Lee, Y. H. Cha, J. -H. Kim, K. H. Hong, and C. H. Nam, Phys. Rev. A **63**, 053407 (2001).

[14] R. Bartels, S. Backus, E. Zeek, L. Milsoguti, G. Vdovin, I. P. Christov, M. M. Murnane, and H. C. Kapteyn, Nature, **406**, 164 (2000).

[15] Kan, N. H. Burnett, C. E. Capjack, and R. Rankin, Phys. Rev. Lett. **79**, 2971 (1997)

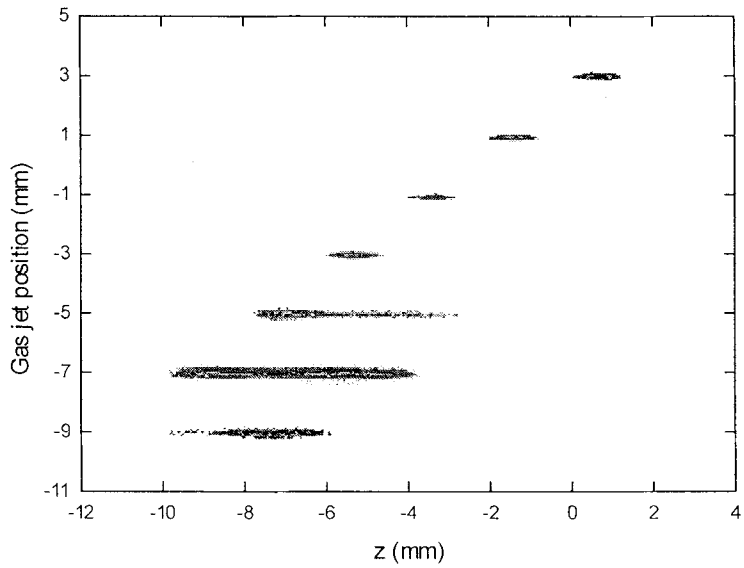

Fig. 1. Visible images of Ar plasma column obtained at different positions of the 6-mm gas jet relative to the focal position, with a focused intensity of 7×10^{15} W/cm^2, of 28-fs pulses. Laser pulses propagate from the left to right and, in vacuum, laser pulses are focused at z = 0.

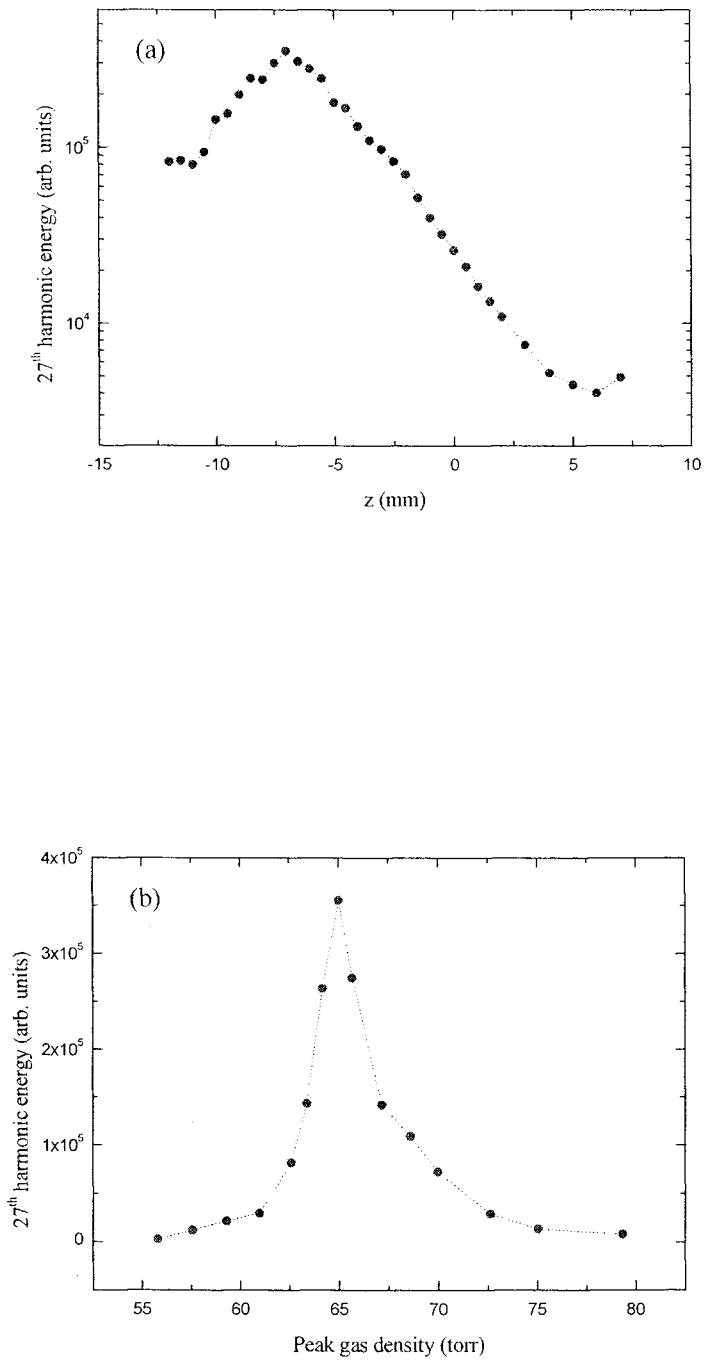

Fig. 2. Harmonic yield as a function of (a) the focus-jet relative position and (b) peak gas density at a fixed laser-pulse energy.

(a)

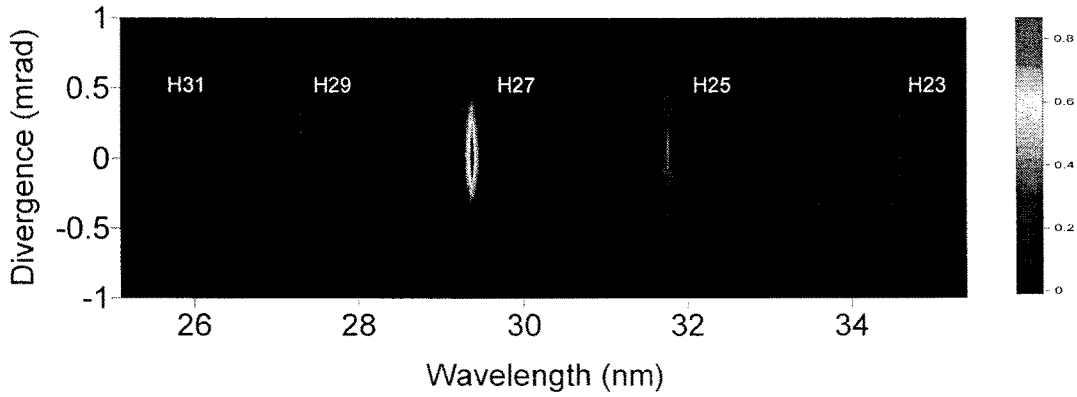

(b)

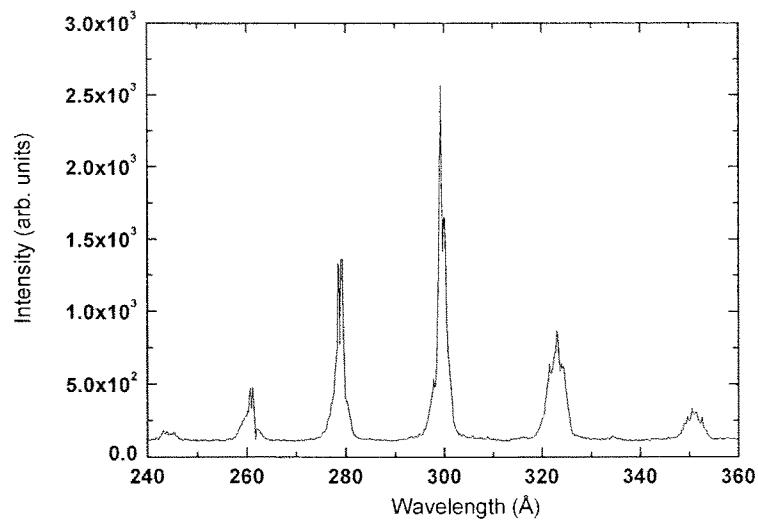

Fig. 3. (a) divergence measurement of high-order harmonics from a long argon gas jet with a 6-mm slit, (b) single-shot harmonic spectrum.

A.2. Theory development of high harmonic generation

We investigate the self-phase modulation of intense femtosecond laser pulses propagating in an ionizing gas and its effects on collective properties of high-order harmonics generated in the medium. Plasmas produced in the medium are shown to induce a positive frequency chirp on the leading edge of the propagating laser pulse, which subsequently drives high harmonics to become positively chirped. In certain parameter regimes, the plasma-induced positive chirp can help to generate sharply peaked high harmonics, by compensating for the dynamically-induced negative chirp that is caused by the steep intensity profile of intense short laser pulses.

A.2.1. Self-phase modulation of laser pulse propagating in an ionizing medium

Recent remarkable progress in high-power femtosecond laser technology has provided a novel opportunity to investigate high-order harmonic generation processes in an unprecedented high-intensity, ultrashort pulse regime. While necessary for generating high-order harmonics with wavelength extremely short compared to the laser wavelength, the use of lasers in this regime has some other important merits: the harmonic conversion efficiency is dramatically enhanced, and the harmonic pulse duration can be reduced to a subfemtosecond time scale.

As the laser pulse evolves into the high-intensity, ultrashort regime, high harmonic emission begins to exhibit complicated spectral features, such as harmonic line broadening, blueshifting, splitting, and smearing. All of these features are absent in the high harmonic spectra observed for lasers with weak intensity well below the ionization saturation intensity and long pulse duration (longer than a few hundred femtoseconds) that show well-defined narrow harmonic peaks almost exactly at odd multiples of the fundamental laser frequency. The involved spectral features showing up for intense short laser pulses can be satisfactorily accounted for, at least at the single-atom level, in terms of decomposition of high harmonics into quantum-path components, and different behaviors of the quantum-path components, in laser fields with rapidly-varying instantaneous intensity. Since high-intensity laser pulses can ionize atoms producing plasmas that can affect propagating waves, a proper understanding of macroscopic high harmonic structure necessitates a detailed knowledge of the plasma-related propagation

effect as well as the single-atom effect. It is known that an increase in electron density during the laser pulse duration causes the refractive index of a medium to decrease with time, which leads to frequency upshifting and spectral broadening of the laser pulse. Because the change in the driving laser spectrum should be reflected in the harmonic conversion, one might expect that harmonic spectral lines would likewise be blueshifted and broadened. In reality, however, the harmonic spectrum exhibits behavior more complicated than this expectation, as demonstrated in this paper. As a matter of fact, there is another source that can affect the harmonic spectral line shape: the dynamically-induced harmonic chirp (dynamic chirp) that is brought about by a steep pulse envelope. The observed spectral behavior of high harmonics can only be understood through inspecting the temporal variation of harmonic frequency caused by the plasma-induced change in the laser frequency, in close connection with the dynamic chirp.

In this paper, we elucidate how the plasma effect modulates the spectrum of an intense femtosecond laser pulse, and discuss its subsequent influence and the effect of laser focusing on macroscopic high harmonic spectra. It is shown that the plasmas induce a positive frequency chirp on the leading edge of the laser pulse up to the point at which a maximum blueshift is attained, and a negative chirp on the remaining part of the laser pulse. Depending on the relative amount of the plasma-induced chirp compared to the dynamic chirp, not only broadening but also narrowing can occur in high harmonic spectral lines. We demonstrate these using a one-dimensional (1D) model, in which the atomic response to the laser is calculated from the 1D Schroedinger equation, and propagations of the laser and harmonic fields are considered in 1D space along the propagation axis.

In order to see how the laser field E_1 is affected by the plasmas (whose effects are dominated by electrons) produced in the medium, we begin by finding a solution of the 1D wave equation:

$$\frac{\partial^2 E_1(x,t)}{\partial x^2} - \frac{1}{c^2}\frac{\partial^2 E_1}{\partial t^2} = \frac{\omega_p^2(w,t)}{c^2} E_1, \qquad (1)$$

where $\omega_p(x,t) = \omega_0 [N_e(x,t)/N_{cr}]^{1/2}$ is the local plasma frequency, and ω_0 is the laser frequency. The critical plasma density N_{cr} is given in Gaussian units by $N_{cr} = m_e \omega_0^2 / 4\pi e^2$, where m_e is the electron mass. To calculate the electron density $N_e(x,t)$, we use the ADK model, and consider sequential tunneling ionization up to as high stages of ionization as needed, neglecting collisional ionization that is of little

significance in the parameter regions in which high harmonic generation experiments are commonly carried out. At the present gas pressures (<100 Torr) much lower than 1 atm, the energy loss and temporal broadening of the laser are negligible; thus, we may ignore the amplitude modulation of the laser field. Assuming the Gaussian incident pulse $E_1(x,t) = E_0 \exp\left[-(2\ln 2/\Delta t^2)(t-x/c)^2 - i\omega_0(t-x/c)\right]$ that is a solution to Eq.(1) in free space with Δt being the full width at half maximum (FWHM) of the pulse, we may then write the solution of Eq.(1) in the medium as

$$E_1(x,t) = E_0 \exp\left[-(2\ln 2/\Delta t^2)(t-x/c)^2 - i\omega_0 t + i\int^{x} n(x',t-|x-x'|/c)\frac{\omega_0}{c}dx'\right], \quad (2)$$

where $n(x,t) = \left[1 - N_e(x,t)/N_{cr}\right]^{1/2}$ is the refractive index of the medium. This expression turns out to be a good approximate solution of Eq.(1) under the conditions $N_e/N_{cr} << 1$ and $c^{-1}\int^{x}(\partial n/\partial t)dx' << 1$, which are satisfied in the parameter regions considered in this paper.

To confirm that Eq.(2) indeed closely approximates the exact solution, we present in Fig.1 some typical spectra of 30-fs laser pulses at the exit of the medium (Ne gas) calculated from Eq.(2), along with those obtained from direct numerical calculations of Eq.(1). Use of the explicit expression in Eq.(2) of course significantly reduces the computational time. Upon comparison, it is obvious that the approximate solutions presented in Fig.1(a) agree well with the exact numerical results in Fig.1(b) in the parameter regions considered. It can be seen that, as the gas density increases and/or as the laser intensity increases, the spectrum shifts toward a higher-frequency region and becomes broader.

More detailed features of the laser pulse passing through the medium can be revealed with the help of the Wigner distribution function, that allows a view of temporal variation of the laser spectrum. The Wigner distributions, calculated under the same conditions as in Fig.1, are displayed in Fig.2. It can be observed that, owing to the phase modulation induced by plasmas produced in the medium, the laser frequency increases with time (becomes positively chirped) in the leading edge, and then decreases (becomes negatively chirped) back to the original frequency in the remaining part of the pulse. We note that at the moment when the plasma-induced chirp changes sign from positive to negative, the production rate of electrons reaches its maximum. This moment

at which the laser experiences a maximum blueshift, comes earlier in time as the laser intensity increases, as can be seen from Fig.2.

When focused laser beams are used, as in usual high harmonic generation experiments, due regard should also be paid to the focusing effect that can change the amplitude and phase of the laser field. In fact, in three-dimensional (3D) simulations this focusing effect could have been automatically considered. Apparently, however, the 1D wave equation in Eq.(1) cannot deal with this effect. Nevertheless, via Eq.(2) the focusing effect can be taken into account along the propagation axis as follows:

$$E_{1f}(x,t) = E_1(x,t) f(x) \exp[i\Phi_f(x)], \qquad (3)$$

where $f(x) = \left[1 + 4(x/b)^2\right]^{-1/2}$ and $\Phi_f(x) = -\tan^{-1}(2x/b)$ represent, respectively, the amplitude and phase changes due to the focusing, and b is the confocal parameter. The laser field given in the form of Eq.(3) now suitably describes the phase modulation induced by plasmas and the focusing effect along the axis, and can be used for discussing the phase matching issue of harmonics generated on the propagation axis.

A.2.2 Propagation of high-order harmonics

We next discuss the propagation of high harmonic fields. Since the change in the refractive index in the presence of plasmas is much smaller for higher-frequency waves, we may ignore here the plasma effect. Then the Green function method enables us to write a solution of the 3D wave equation $\nabla^2 E_h - c^{-2}(\partial^2 E_h / \partial t^2) = 4\pi c^{-2}(\partial^2 P / \partial t^2)$ in the following integral form:

$$E_h(\vec{r},t) = -\int \frac{1}{c^2 |\vec{r}-\vec{r}'|} \frac{\partial^2 P(\vec{r},t')}{\partial t'^2} d^3 r', \qquad (4)$$

where t' is the retarded time defined by $t' = t - |\vec{r}-\vec{r}'|/c$, and the laser-induced polarization P is given in terms of the gas density N_0 and the atomic dipole moment d by $P(\vec{r}',t') = N_0 d(\vec{r}',t')$. Equation (4) clearly indicates that the harmonic field E_h at t is determined by the coherent sum of the dipole accelerations of atoms in the medium calculated at the retarded time t'.

In our 1D calculations, a medium lies on the propagation axis, and the integration in Eq.(4) is performed in practice over the 1D space along the axis. The medium, a Ne gas of length l = 700 μm at 28 Torr, is uniformly discretized by 200 points, and at each point the dipole acceleration is calculated by numerically solving the 1D Schroedinger equation for an atom in the laser field E_{1f} given in Eq.(3), with $\Delta t = 30$ fs, $\lambda = 800$ nm, $b = 4$ mm, and $I = 1\times10^{15}$ W/cm^2 at the entrance of the medium. After suitably weighted by a constant factor to yield the correct gas density, the results are then added according to Eq.(4) to give E_h.

The high harmonic spectrum calculated in the above way is presented in Fig.3, which shows the respective roles played by the laser focusing and plasmas in the formation of macroscopic harmonic fields. In Fig.3(b), we neglect the plasma effect by setting $n(x,t) = 1$ to concentrate only on the focusing effect. Both the focusing and plasma effects are fully considered in Fig.3(c), and for comparison we present in Fig.3(a) a single-atom spectrum calculated for an atom located at the entrance of the medium. Whereas the single-atom spectrum in Fig.3(a) is smeared with a complicated structure in the plateau region, the macroscopic harmonic spectrum in Fig.3(b) exhibits discrete harmonic peaks. This is because the intensity-sensitive harmonic components (the long quantum-path component and multiple-recollision components), which give rise to the

complicated structure, are suppressed due to their poor phase-matching conditions, leaving only the short quantum-path component. Here we emphasize that the variation in the laser intensity caused by the focusing as represented by $f^2(x)$ is mainly responsible for this cleaning up of the harmonic spectrum. At very low gas densities, we may observe a harmonic spectrum similar to that shown in Fig.3(b). However, at the gas density used in Fig.3(c), a further change in the harmonic spectrum is caused by the plasma effect: harmonics of low order (43rd and below) undergo spectral broadening, while higher-order harmonics get sharpened.

The plasma-induced harmonic line broadening and narrowing are detailed in Figs.4 and 5, respectively. The mechanism that shapes high harmonic lines can be explained by making a comparison between the plasma-induced chirp and the dynamically-induced chirp. Considering that only the leading edge of the laser pulse, where the depletion of neutral atoms is not severe and the electron density is low, is important for the phase-matched harmonic generation, we focus only on this part of the laser pulse. The leading edge of the laser pulse, in which the laser frequency increases with time due to the plasma effect (Fig.2), tends to generate positively chirped high harmonics. This effect is opposed by the dynamic single-atom effect that, in the present case, forces high harmonics to become negatively chirped. Depending on system parameters and harmonic order, one effect matches or dominates over the other. For instance, for the low-order harmonics in Fig.4, the dynamic negative chirp is very small [Fig.4(b)], and the plasma effect dominantly affects the time-frequency characteristics of high harmonics in such a way as to make high harmonics become positively chirped [Fig.4(d)], leading to spectral line broadening [Fig.4(c)]. In contrast, the dynamic negative chirp of higher-order harmonics in Fig.5(b) is substantially large, and the plasma-induced positive chirp more or less cancels out the dynamic chirp [Fig.5(d)], resulting in harmonic line narrowing [Fig.5(c)]. In both cases of Figs.4 and 5, the plasma effect blueshifts the central frequencies of high harmonics.

In conclusion, we have investigated the plasma-induced phase modulation of intense femtosecond laser pulses and its effects on macroscopic high harmonic spectra, using a simple but accurate 1D model. It has been shown that the plasmas produced in the medium induce a positive frequency chirp on the leading edge of the laser pulses. Strikingly, the plasma-induced chirp, which broadens the laser spectrum, can lead not only to broadening but also to narrowing of harmonic spectral lines. The underlying mechanism has been explained by comparing the plasma-induced positive chirp with the dynamically-induced negative chirp. In stark contrast to the widely reported finding

(in regimes well below saturation) that high harmonics are negatively chirped, this study clearly demonstrates that, under laser fields of high intensity and gas pressures not too low, high harmonics can become free of chirp, or even become positively chirped, thanks to the plasma effect. This suggests a way to control the chirp and spectral line shape of high harmonics using the plasma effect.

A.2.3. Attosecond pulse generation

In this section, we discuss the generation of an attosecond pulse train or a single attosecond pulse. It has been known that, when a large number of high harmonics are selected by using a suitable frequency filter, the harmonic pulse can take the form of a train of attosecond pulses in the time domain [25-27]. This means that the phases of high harmonics are properly locked, just as the equally spaced spectral modes of phase-locked lasers. The attosecond pulse can be applied to the time-resolved studies of ultrafast physical processes taking place on attosecond time scales. From a practical point of view, it may be required that the harmonic pulse train contain only a single attosecond pulse.

To achieve this goal, some methods have been proposed in the past. For instance, Corkum et al. [28] have proposed to use two perpendicularly polarized laser pulses possessing slightly different frequencies. The polarization of the mixed fields will then change as time evolves, allowing only a short time interval of the pulse to have linear polarization. Since harmonics are effectively generated only when the polarization of the laser becomes linear, the harmonic pulse width generated by the two mixed laser pulses can be very short, possibly shorter than one femtosecond. Another method to generate a single attosecond pulse is to use a few-cycle laser [3,5,29]. Because the time duration for which the laser intensity is greater than that required for the generation of certain high harmonics is very short in this case, the harmonic emission occurs only for a limited time shorter than the laser pulse width, making it possible for the harmonic pulse train to contain only a single attosecond pulse.

Since the presence of many quantum path components can complicate the phases of high harmonics as a result of interference, which prevents the generation of a regular temporal series of harmonic pulses, one needs to select only one quantum path component among many possible quantum paths. Selection of a single quantum path component can be accomplished by controlling system parameters affecting the phase-matching conditions, such as the position of the gas jet relative to the laser focus. In Fig.6, we present the temporal profile of high harmonics obtained by locating the gas medium at 2 mm behind the focus. Harmonic components other than the short quantum-path component are suppressed due to phase-mismatching, and as a result the harmonic pulse train consists of a series of attosecond pulses separated by one half optical cycle.

The underlying mechanism of suppression of certain harmonic components can be

explained in terms of the intensity dependent intrinsic dipole phase. The dipole phases associated with different quantum paths have different intensity dependences. As the geometric focusing effect makes the atoms distributed along the propagation axis experience different amplitudes of laser field, the harmonics generated from the medium will have different intrinsic phases depending on the position of the atoms. When high harmonics are added coherently during the propagation, those harmonic components having phases sensitively depending on the laser intensity will experience severe phase mismatching and consequently disappear. The phase associated with the short quantum path has the weakest intensity dependence, and thus the corresponding harmonic component is most robust against the phase mismatching caused by the geometric focusing effect.

Comparison between Fig.6(a) and (b) [or (c) and (d)] reveals that the plasma effect causes the width of the harmonic pulse train to be reduced toward the front edge, where the density of electrons produced during the ionization process is low. This indicates that the plasma-induced phase mismatch can be taken advantage of to shorten the pulse train. Considering that the plasma effect increases as the gas density grows, we predict that, if the gas density is sufficiently high, the phase matched harmonic generation will be limited within a narrow time interval on the leading edge of the pulse such that only a single attosecond pulse is contained in the harmonic pulse train. Fig.7 shows the temporal profile of high harmonics of orders between 100 and 120. Displayed in Fig.7(a) is the single-atom calculation, and Fig.7(b) shows the macroscopic high harmonics obtained from a neon gas of density 1×10^{19} cm^{-3}. While there exist several attosecond pulses in Fig.7(a), only two attosecond pulses can be seen in Fig.7(b) that correspond to the short quantum path component. If we increase further the gas density, only one attosecond pulse can survive after propagation.

References

[1] C. Spielmann, N. H. Burnett, S. Sartania, R. Koppitsch, M. Schnurer, C. Kan, M. Lenzner, P. Wobrauschek, and K. C. Kulander, Science **278**, 661 (1997).

[2] Z. Chang, A. Rundquist, H. Wang, M. M. Murnane, and H. C. Kapteyn, Phys. Rev. Lett. **79**, 2967 (1997).

[3] C. Kan, N. H. Burnett, C. E. Capjack, and R. Rankin, Phys. Rev. Lett. **79**, 2971 (1997).

[4] M. Shnurer, Z. Cheng, M. Hentschel, G. Tempea, P. Kalman, T. Brabec, and F. Krausz, Phys. Rev. Lett. **83**, 722 (1999).

[5] K. J. Schafer and K. C. Kulander, Phys. Rev. Lett. **78**, 638 (1997).

[6] D. G. Lee, H. J. Shin, Y. H. Cha, K. H. Hong, J. H. Kim, and C. H. Nam, Phys. Rev. A **63**, 021801(R) (2001).

[7] J. B. Watson, A. Sanpera, and K. Burnett, Phys. Rev. A **51**, 1458 (1995).

[8] C. Kan, C. E. Capjack, R. Rankin, and N. H. Burnett, Phys. Rev. A **52**, R4336 (1995).

[9] H. J. Shin, D. G. Lee, Y. H. Cha, K. H. Hong, and C. H. Nam, Phys. Rev. Lett. **83**, 2544 (1999); H. J. Shin, D. G. Lee, Y. H. Cha, J. H. Kim, K. H. Hong, and C. H. Nam, Phys. Rev. A **63**, 053407 (2001).

[10] J. H. Kim, H. J. Shin, D. G. Lee, and C. H. Nam, Phys. Rev. A **62**, 055402 (2000).

[11] M. B. Gaarde, F. Salin, E. Constant, Ph. Balcou, K. J. Schafer, K. C. Kulander, and A. L'Huillier, Phys. Rev. A **59**, 1367 (1999).

[12] Ph. Balcou, A. S. Dederichs, and A. L'Huillier, J. Phys. B **32**, 2973 (1999).

[13] E. Yablonovitch, Phys. Rev. A **10**, 1888 (1974).

[14] S. C. Wilks, J. M. Dawson, and W. B. Mori, Phys. Rev. Lett. **61**, 337 (1988).

[15] Wm. M. Wood, C. W. Siders, and M. C. Downer, Phys. Rev. Lett. **67**, 3523 (1991).

[16] S. C. Rae and K. Burnett, Phys. Rev. A **46**, 1084 (1992).

[17] P. Chessa, E. De Wispelaere, F. Dorchies, V. Malka, J. R. Marques, G. Hamoniaux, P. Mora, and F. Amiranoff, Phys. Rev. Lett. **82**, 552 (1999).

[18] J. H. Kim, D. G. Lee, H. J. Shin, and C. H. Nam, Phys. Rev. A **63**, 063403 (2001).

[19] M. V. Ammosov, N. B. Delone, and V. P. Krainov, Sov. Phys. JETP **64**, 1191 (1986)

[20] A. E. Siegman, *Lasers* (Oxford University Press, Oxford, 1986).

[21] P. Salieres, Ph. Antoine, A. de Bohan, and M. Lewenstein, Phys. Rev. Lett. **81**, 5544 (1998).

[22] The laser pulse experienced by atoms in the case of Fig.3(b) resembles in form that used in our previous discussions on the coherent sum method [10] and the time-frequency analysis [18]. Thus, the slope of the Wigner distributions shown in Figs.4(b)

and 5(b) gives the dynamic chirp.

[23] C. Altucci, C. Delfin, L. Roos, M. B. Gaarde, A. L'Huillier, I. Mercer, T. Starczewski, and C. G. Wahlstrom, Phys. Rev. A **58**, 3934 (1998).

[24] T. Sekikawa, T. Ohno, T. Yamazaki, Y. Nabekawa, and S. Watanabe, Phys. Rev. Lett. **83**, 2564 (1999).

[25] G. Farkas and C. Toth, Phys. Lett. A **168**, 447 (1992).

[26] S. E. Harris, J. J. Macklin, and T. W. Hansch, Opt. Commun. **100**, 487 (1993).

[27] Ph. Antoine, A. L'Huillier, and M. Lewenstein, Phys. Rev. Lett. **77**, 1234 (1996).

[28] P. B. Corkum, N. H. Burnett, and M. Y. Ivanov, Opt. Lett. **19**, 1870 (1994).

[29] I. P. Christov, M. M. Murnane, and H. C. Kapteyn, Phys. Rev. Lett. **78**, 1251 (1997).

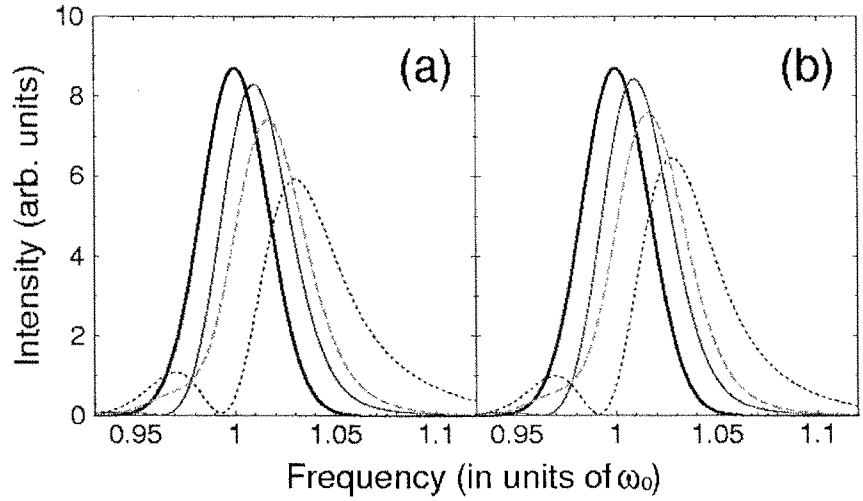

Fig.1. (a) Laser spectra obtained from Eq. (2) for a 30-fs (FWHM) laser pulse of wavelength λ=800 nm after propagating through a Ne gas medium of length l=700 μm. The laser intensity and gas density are given by $I = 1\times10^{15}$ W/cm^2 and $N_0 = 1\times10^{18}$ cm^{-3} (28 Torr) (thin solid line); $I = 1\times10^{15}$ W/cm^2 and $N_0 = 3\times10^{18}$ cm^{-3} (85 Torr) (dotted line); $I=3\times10^{15}$ W/cm^2 and $N_0 = 1\times10^{18}$ cm^{-3} (dashed line). The spectrum of the incident laser pulse is drawn by a thick solid line. (b) Laser spectra obtained by direct numerical calculations of Eq.(1) for the same parameters as in (a).

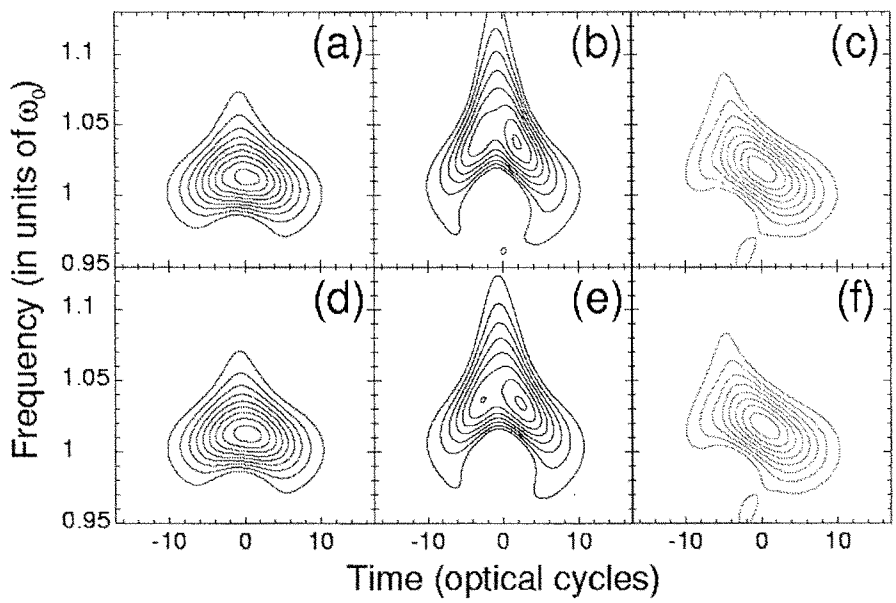

Fig.2. Wigner distributions of the laser pulses specified in Fig.1. In (a)-(c) [(d)-(f)], the same parameters are used as for the thin solid, dotted and dashed lines in Fig.1(a) [Fig.1(b)], respectively. Only positive contour lines are shown

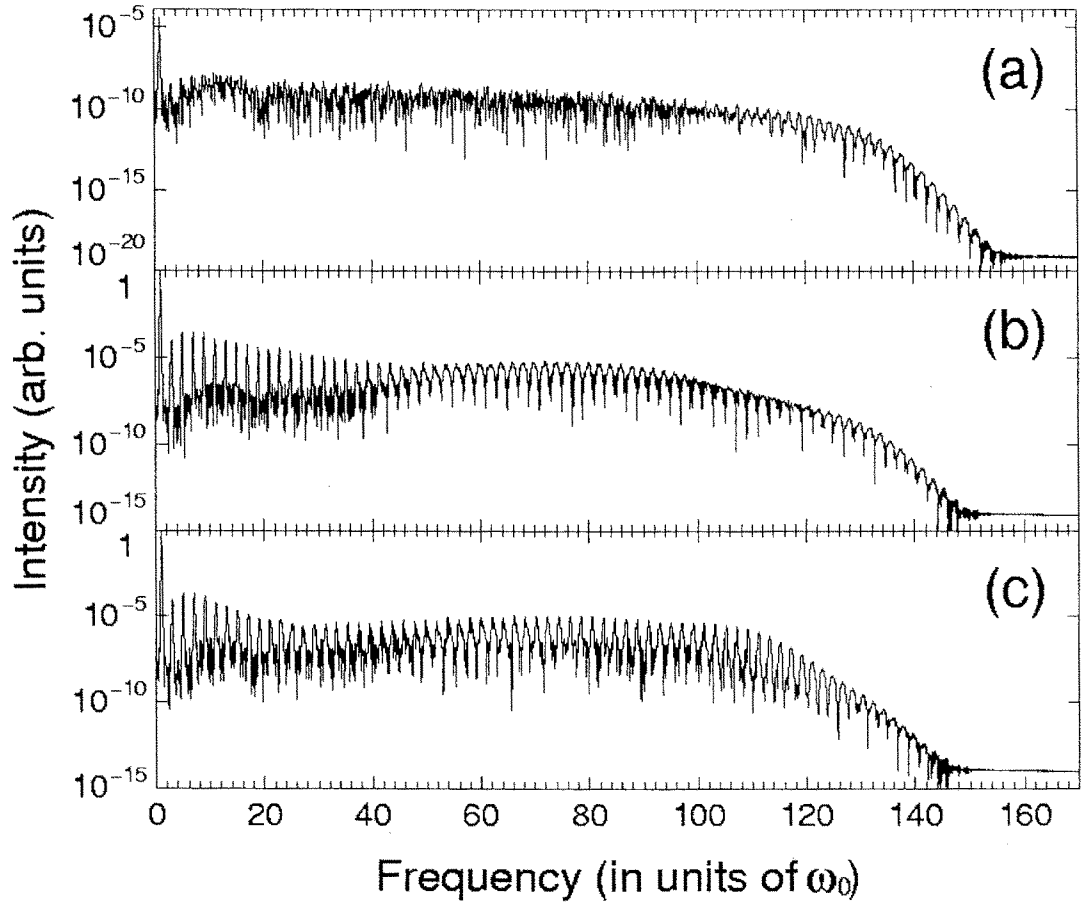

Fig.3. (a) Single-atom harmonic spectrum for a Ne atom placed at the entrance of the medium. (b) Macroscopic harmonic spectrum (in the far field, on the axis) considering only the effect of laser focusing. (c) Macroscopic harmonic spectrum taking into account both the focusing and plasma effects. A Ne gas medium of density $N_0 = 1\times10^{18}$ cm^{-3} and length l = 700 μm is irradiated by a 30-fs (FWHM) Gaussian laser pulse of wavelength λ = 800 nm. The medium is centered at x = 2 mm behind the focus, and because of focusing (b = 4 mm) the laser intensity decreases from $I = 1\times10^{15}$ W/cm^2 at the entrance to $I = 0.7\times10^{15}$ W/cm^2 at the exit of the medium.

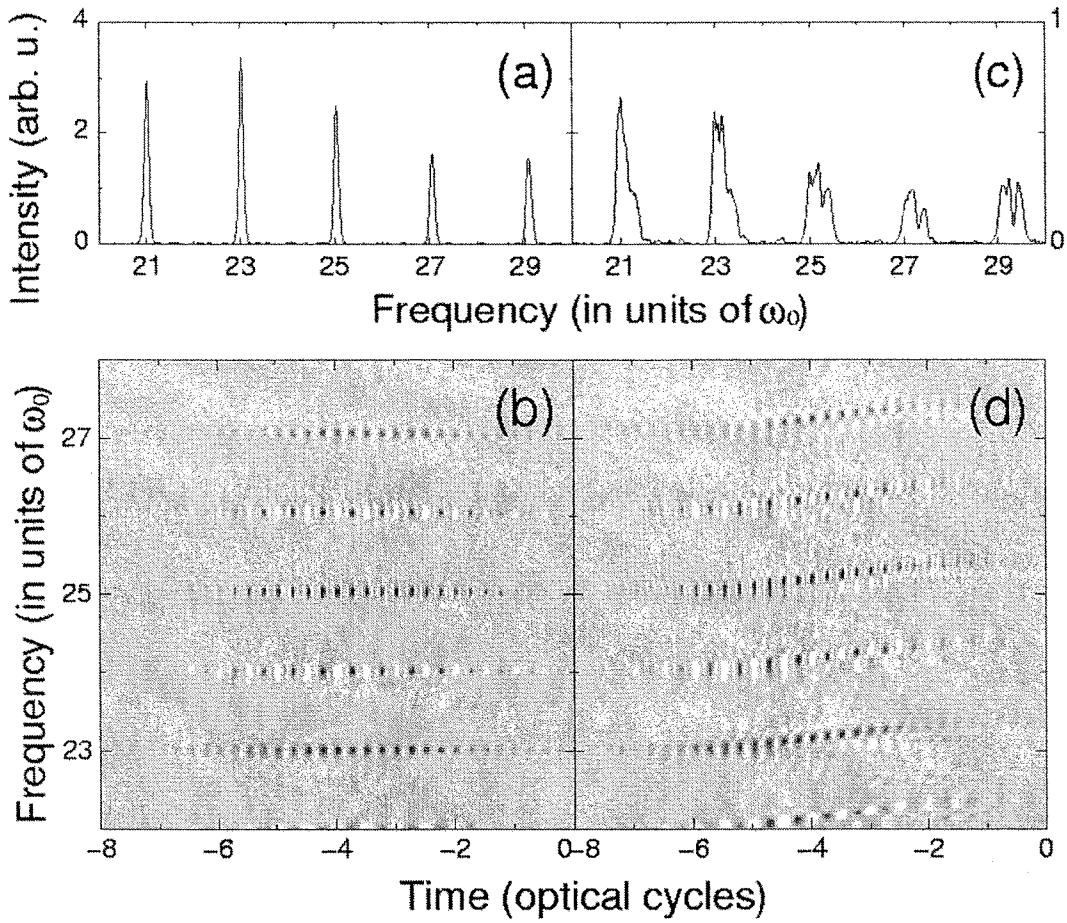

Fig.4. (a) Enlarged view (on a linear scale) of Fig.3(b) between 20 ω_0 and 30 ω_0 (only the focusing effect is considered). (b) Wigner distribution of the harmonics chosen in (a) (c) [(d)] Same as (a) [(b)] except that harmonics are chosen from Fig.3(c) (both the focusing and plasma effects are considered). Positive and negative values of the Wigner distribution are colored black and white, respectively.

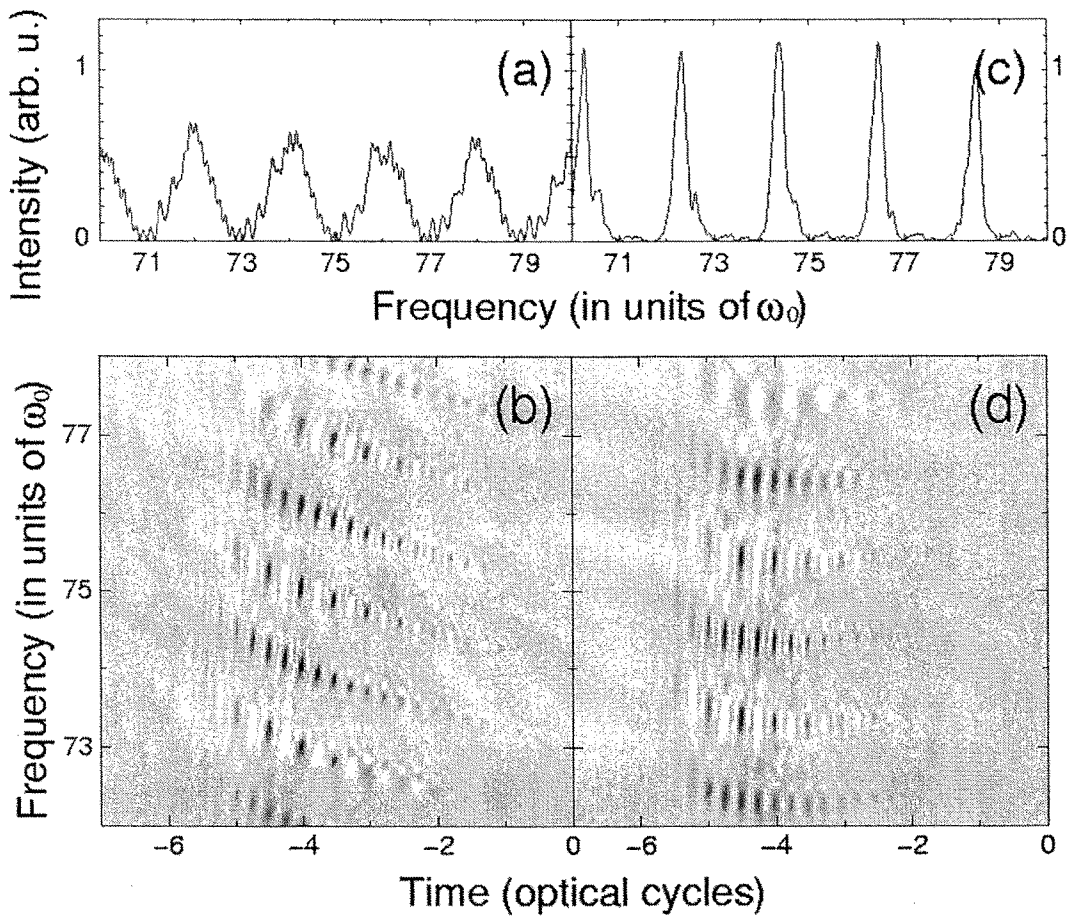

Fig.5. Same as Fig.4 except that harmonics between 70 ω_0 and 80ω_0 are chosen here.

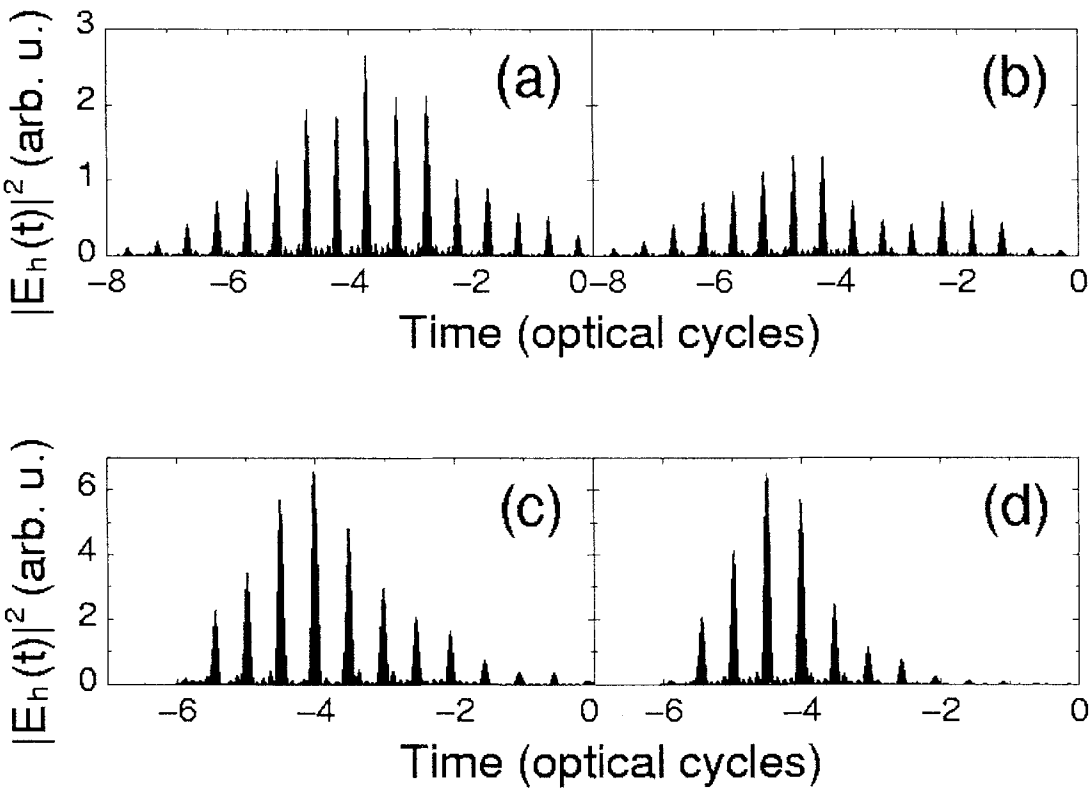

Fig.6. Temporal profiles of the harmonics selected in Figs.4 (a), 4(c), 5(a), and 5(c) are presented in (a), (b), (c), and (d), respectively.

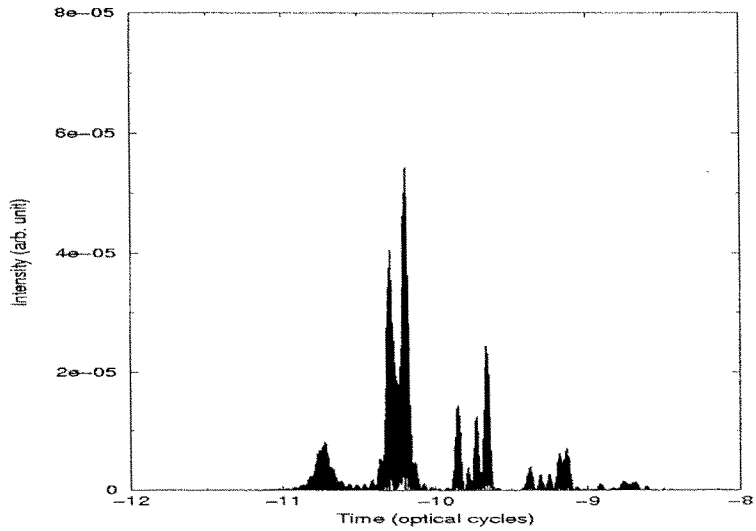

(a)

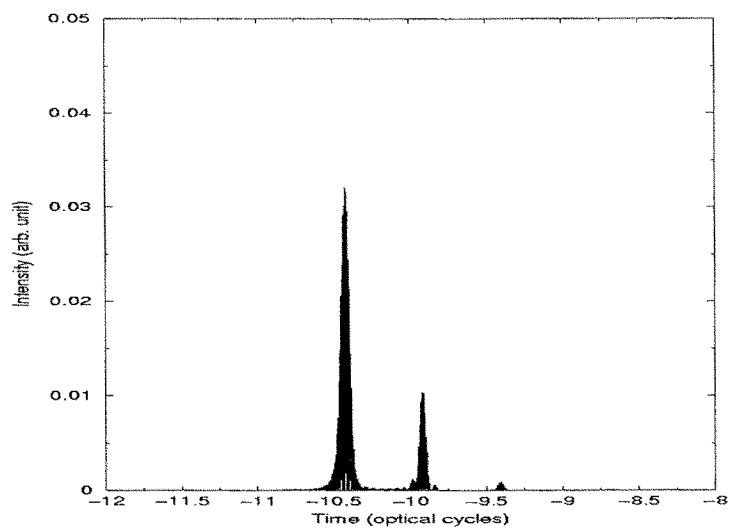

(b)

Fig.7. Temporal profiles of high harmonics windowed between 100 ω_0 and 120 ω_0 for Ne irradiated by a 30-fs, 800-nm laser pulse of intensity 1×10^{16} W/cm^2. (a) single-atom calculation. (b) after propagation through a 0.7-mm long neon gas of density 1×10^{19} cm.

A. 3 Operation and Development of Femtosecond Terawatt Lasers

A. 3. 1. Development of a 1-kHz Femtosecond Terawatt Laser

I. Introduction

Femtosecond terawatt lasers can produce very intense pulses in the femtosecond range and provide the unique environment in which very high electric field lasts only for a few tens of femtoseconds. The extremely short duration of the femtosecond laser pulses also results in the spatially localized electromagnetic field, another unique environment. Due to their intensity or temporal and spatial localization, they have been applied to many research fields, such as their high-harmonic generation, X-ray laser, and attosecond pulse generation, and are still expanding their new application areas.

The increase in average power capability of pump lasers and the development of ultrashort-pulse laser sources has resulted in the development of high repetition rate, ultrashort-pulse laser systems capable of several watts average power. In spite of its lower power level, a 1-kHz high-power Ti:sapphire laser is showing more versatile aspects in many application fields than a ~10-Hz laser system due to its compactness, high average power, and high-repetition rate[1-4].

Amplification of ultrashort pulses at high energy with high-repetition rate requires careful consideration of several different key factors. In particular, the thermal lensing effect is one of the most serious problems. Also, gain narrowing of the spectrum and high-order spectral phase distortion must be controlled carefully in order to attain very high peak powers.

In this Report, we designed and built an setup of a 1-kHz femtosecond terawatt Ti:sapphire laser based on the CPA. The measured peak power and pulse duration were about 90 GW and 23 fs, respectively.

II. Set up of a 1-kHz femtosecond terawatt Ti:sapphire laser

The 1-kHz femtosecond terawatt Ti:sapphire laser is composed of a femtosecond

oscillator, a pulse stretcher, amplifying stages, and a pulse compressor, as shown in Fig. 1. The total system was installed on one optical table of 1.2 m X 3.0 m.

1. Femtosecond Ti:sapphire oscillator

Ti:sapphire lasers generating ultrashort pulses by Kerr-lens mode-locking have been widely utilized for seeding high-power solid-state amplifier systems. Standard Kerr-lens mode-locked (KLM) Ti:sapphire oscillators typically generate pulses with an energy of a few nJ at a repetition rate of about 100 MHz. A femtosecond oscillator as a front-end laser of a high-power laser system needs high output pulse energy because it has advantage in suppressing amplified spontaneous emission (ASE) and the gain-narrowing. Cavity dumping can be used to increase the pulse energy at the reduced repetition rates. Sub 20-fs pulses with a pulse energy of >30 nJ were obtained from the oscillator at a repetition rate of 1 kHz using the cavity dumping technique. However, cavity dumping is a relatively complex and expensive method because it requires an electro-optic or acousto-optic modulator, rf drive electronics and complex alignment. Recently, several methods that are much simpler and less expensive were demonstrated[5]. We demonstrate a process to obtain pulses with high energy directly from a KLM Ti:sapphire laser by using a long cavity configuration.

The energy per pulse from the laser can be increased by reducing the repetition rate which depends on the cavity length. If the end-mirrors of the standard oscillator are moved farther apart to increase the cavity length, the alignment sensitivity will increase, so the stable region of the cavity will be reduced. However, if the cavity length is extended by use of image relay method[6], the laser cavity mode and nonlinear focusing behavior will be preserved while lowering the repetition rate. The image relay method can be achieved by simply adding a few curved mirrors to the standard oscillator.

We setup a dispersion-compensated Kerr-lens mode-locked Ti:sapphire laser as shown in Fig. 2. The laser is pumped with a frequency-doubled diode-pumped Nd:YVO_4 laser (Millennia; Spectra-Physics, Inc). The gain medium was a 3-mm-long Brewster-cut Ti:sapphire crystal that has an absorption coefficient of 7.8 cm^{-1}, and the focusing mirrors with 10-cm radius of curvature were used in a folded-X cavity. Group delay dispersion (GDD) was compensated for by installing a pair of fused-silica prisms at intracavity with a separation of 520 mm. In our setup, the image relay was achieved using two pairs of equal concave mirrors (f = 0.5 m). The mirrors were setup apart from each other as much as 2f. Using this design, we could reproduce exactly the beam at the plane 4f apart from the previously position of the output coupler. In consequence, we

added 4 m to the standard-cavity path length of 1.15 m, and the mode-locking was operated at a 26.5-MHz repetition rate. To compensate for the additional dispersion due to the long air path, the prism separation was increased as much as 5 cm. This makes it possible to operate the laser at the same dispersion condition as that of the normal cavity configuration, so that the laser spectrum does not become narrow. This phenomenon indicates that the dispersion due to the additional air path cannot be neglected and has to be compensated for to keep the laser mode-locking in the negative dispersion regime.

In Fig 3, the mode-locked laser pulse train of 26.5-MHz repetition rate or 38-ns pulse separation is shown. Pulse duration was measured by spectral phase interferometry for direct electric-field reconstruction (SPIDER). The reconstructed pulse intensity and phase in the time domain are shown in Fig. 4(a). We obtained a pulse duration of 12.8 fs with an average power of 200 mW at a pumping power of 3.2 W. The corresponding output pulse energy was 8 nJ. The spectral bandwidth of the laser pulse was 120 nm centered at 800 nm as can be seen in Fig. 4(b).

2. Pulse stretcher

Before passing through the stretcher, the femtosecond pulse from the front-end oscillator propagates through an SF-10 prism pair, introduced for high-order phase compensation. The distance between the prisms is 11 cm.

The pulse is temporally stretched before amplification to prevent damage of amplifying stages. The basic idea of pulse stretching is decomposing and unfolding spectral components of a femtosecond pulse in time domain by using a diffraction grating. Figure 5 shows a pulse stretcher composed of a grating, a convex mirror, a concave mirror, and flat mirrors. The grating diffracts each spectral components of an incident pulse to a different diffraction angle. The concave and the convex mirrors form a telescope of –1 magnification, and each diffracted spectral components passing the telescope returns to the grating with the same incident angle as its diffraction angle. Therefore, each spectral component propagates parallel but along different paths after second diffraction at the grating, which yields a frequency dependent propagation delay through the stretcher.

We used a gold-coated 1400 l/mm grating (Spectrogon), a concave mirror of a 30-cm focal length, and a convex mirror of a 15-cm focal length. The pulse duration after the pulse stretcher was ~260 ps with an incident angle of 45°, a 800-nm center wavelength and an effective separation of 19 cm. To prevent cutting on the short wavelength side of

the spectrum due to the limited bandwidth of the concave and the convex mirrors which are dielectric-coated, we used the gold-coated mirrors instead of the dielectric-coated ones. As a result, we could get the spectrum with the bandwidth of ~100 nm.

The aberration in a stretcher should be kept low because it results in spatial chirping and unexpected modulation of pulse structure. To minimize the aberration, the Offner-triplet type stretcher was used[7].

3. Preamplifier

After passing through the stretcher, the 26.5-MHz repetition-rate pulse train is reduced to 1 kHz using a DKDP Pockels cell between crossed BK7 polarizers. This permits transmission of a single pulse during a 10-ns window that is timed to the laser oscillator through a digital delay generator. The extinction of the polarizers and the Pockels cell is >2000. After the Pockels cell, the pulse is injected into a preamplifier.

Figure 6 shows a schematic of the preamplifier. The amplifier is a ring-type 12-pass amplifier composed of an coated Brewster-cut Ti:sapphire crystal, a flat gold mirror and two dielectric-coated focusing mirrors of 45-cm and 50-cm radius.[8] The Ti:sapphire crystal is 6-mm long and has an absorption coefficient $4.5cm^{-1}$ at 532 nm. The preamplifier produces 0.8 mJ of amplified output energy when pumped with 8-W average power from a frequency-doubled Nd:YLF laser (Merlin, Positive light). To suppress thermal problems by the high average pump power, the crystal is cooled by the combination of TE cooler and water cooling.

One of the major problems with high-average-power ultrafast systems is thermal lensing induced by the heat load of the large pump laser fluence on the amplifier crystal. This thermal lensing can lead to a mismatch between the pump and the laser modes in subsequent passes through the laser amplifier and to possible damage. In the case of the preamplifier, the beam is approximately at a waist when passing through the crystal. This minimizes the effect of lensing on the beam divergence. A mask, consisting of a series of small holes through which the beam passes on each transit through the ring, was inserted into the amplifier to control the beam size. This mask reduces ASE as well as compensating for thermal lensing. If the beam in the amplifier ring is not restricted by the mask, the spot size on the curved mirrors grows on each successive pass. Simultaneously, the beam is focused to a smaller spot size in the amplifier crystal resulting in damage to the crystal.

The minimum output pulse width from the amplifier is bandwidth-limited. As the method to overcome the limitation imposed by gain-narrowing, the modulation of the spectral losses can be use. We introduced into the preamplifier a 2-μm-thick pellicle whose transmission is directly proportional to the inverse of the gain profile. The pellicle was oriented at an angle with respect to the beam to position the minimum in transmission at 800 nm. Fig. 7(a) shows the output spectrum out of a preamplifier without a pellicle. The spectral bandwidth at FWHM is 43 nm. With a pellicle, the resulting spectrum shows a bandwidth of 80 nm at FWHM. In the fig. 7(b), the red line is the increased spectrum, the blue line the 100-nm input spectrum and the dotted line the spectrum modulated by the transmission of the pellicle.

4. Power amplifier

Figure 8 shows the power amplifier. It is also a ring-type four-pass amplifier composed of a Ti:sapphire crystal, two concave mirrors of a 50-cm focal length, and flat mirrors. The Ti:sapphire crystal is 6-mm long, of a 4.5/cm absorption coefficient, and pumped by a 12-W average power from the frequency-doubled Nd:YLF laser. For the compensation for thermal lensing, the mask was used. Due to the high pump power, the Ti:sapphire crystal was cooled by TE and water cooling. Unlike to the preamplifier, the crossing point of the various passes is moved out of the focal region to prevent the damage to the crystal. The ring design allows the flexibility to move this crossing point anywhere in the cavity. The output energy was ~2.6 mJ. Thus, the pump-to-output conversion efficiency is approximately 22%.

5. Pulse compressor

The amplified pulse is compressed closed to its original pulse duration at a pulse compressor to generate a high peak power. A pulse compressor performs a reverse action against a pulse stretcher; the unfolded spectral components of the stretched pulse are effectively recombined to form a femtosecond pulse. The pulse compressor is shown in Fig. 9. It is composed of two 1480 l/mm gratings and flat mirrors.

To obtain minimal pulse duration, the dispersion accumulated through the laser system should be carefully compensated for, and the slightly different grating constant from the stretcher is more advantageous in minimizing residual high-order dispersion. With an incidence angle of 52.648° and an 16.3-cm separation between two gratings, up-to fourth-order dispersion of the laser system including a total 84-cm length of Ti:sapphire can be compensated for. After compression, the ouput energy was 2.0 mJ, given the compressor efficiency of ~77%.

5. Pulse width measurement

The output pulses from the amplifier were characterized by use of the frequency-resolved optical gating (FROG). The pulse duration was ~23 fs, as shown in the fig. 10. Thus, the peak power was ~90 GW.

III. Set up of a gas-filled hollow fiber compressor

Ultrashort pulses can be generated by extracavity compression techniques. A method for optical pulse compression based on the interplay between self-phase modulation (SPM) and group velocity dispersion (GVD) that arise during the propagation of short light pulses in single-mode optical fibers was introduced[9]. The propagation of the pulse along the optical fiber spectrally broadens and chirps the laser pulse as a result of the combined action of SPM and GVD. The increased spectral bandwidth of the output pulse enables to generate a compressed pulse shorter in duration than the input pulse. However, the use of single-mode optical fibers limits the pulse energy to a few nanojoules due to both material damage and appearance of high order nonlinearities. A novel compression technique which in particularly suitable for ultrashort pulses of high energy was introduced[10]. Pulse spectral broadening is achieved by SPM in a hollow fiber made of fused silica and filled with noble gases at high pressure. This technique presents the advantages of a guiding element with a large diameter mode and of a fast nonlinear medium with high threshold for multiphoton ionization.

The amplified and recompressed pulses are coupled into a 95 cm long fused-silica capillary with an inner diameter of 260 μm as shown in fig. 11. The capillary is kept straight in a V groove on an aluminum bar placed in a plastic tube that is filled with argon. The fused-silica windows are 0.7-mm thick to minimize nonlinearities. The Kerr nonlinearity of the argon imposes SPM on the pulse propagating down the waveguide. High-order transverse modes can be suppressed by the higher propagation loss that they experience in the leaky waveguide and by a proper matching of the Gaussian input beam to the fundamental EH_{11} mode.

The broadened spectrum that experienced SPM and four-wave mixing processes in the capillary is shown in Fig. 12(a) for input pulse energy of 0.9 mJ and a pressure of 0.9

bar, which supports the transform-limited pulse duration of 3 fs as shown in Fig. 12(b). Input pulses yielded the 0.13 mJ output pulses. After recollimation by an R = 2.4 m gold mirror the beam is reflected five times off ultrabroadband chirped mirrors for pulse compression. The mirrors exhibit a high reflectivity over the wavelength range of 600-1000 nm, and are designed to have approximately constant negative group-delay dispersion. The pulse duration was measured using FROG technique. Figure 13 shows the intensity profile of the compressed pulses with the duration of 8.8 fs. The pulse profile was very complicated due to the complicated spectrum and uncompensated spectral phase distortion. Thus, we have potential compressibility of the pulse duration if we efficiently compensate for the residual phase distortion.

References

[1] S. Backus, C. G. Durfee III, G. Mourou, H. C. Kapteyn, and M. M. Murnane, Opt. Lett. **22**, 1256 (1997).

[2] S. Sartania, Z. Cheng, M. Lenzner, G. Tempea, Ch. Spielmann, and F. Krausz, Opt. Lett. **22**, 1562 (1997).

[3] Charles G. Durfee, III, Sterling Backus, Margaret M. Murnane, and Henry C. Kapteyn, IEEE J. Selected Topics in Q. E. **4**, 395 (1998)

[4] Catherine Le Blanc, Emmanuel Baubeau, Francois Salin, Jeff A. Squier, Christopher P. J. Barty, and Christian Spielamann, IEEE J. Selected Topics in Q. E. **4**, 407 (1998)

[5] S. H. Cho, B. E. Bouma, E. P. Ippen, and J. G. Fujimoto, Opt. Lett. **24**, 417 (1999).

[6] J. T. Hunt, J. A. Glaze, W. W. Simmons, and P. A. Renard, Appl. Opt. **17**, 2053 (1978)

[7] G. Cheriaux, P. Rousseau, F. Salin, and J. P. Chambaret, Opt. Lett. **21**, 414 (1996).

[8] S. Backus, J. Peatross, C. P. Huang, M. M. Murnane, and H. C. Kapteyn, Opt. Lett. **20**, 2000 (1995).

[9] H. Nakatsuka, D. Grischkowsky, and A. C. Balant, Phys. Rev. Lett. **47**, 910(1981)

[10] M. Nisoli, S. De Silvestri, and O. Svelto, Opt. Lett. **68**, 2793(1996)

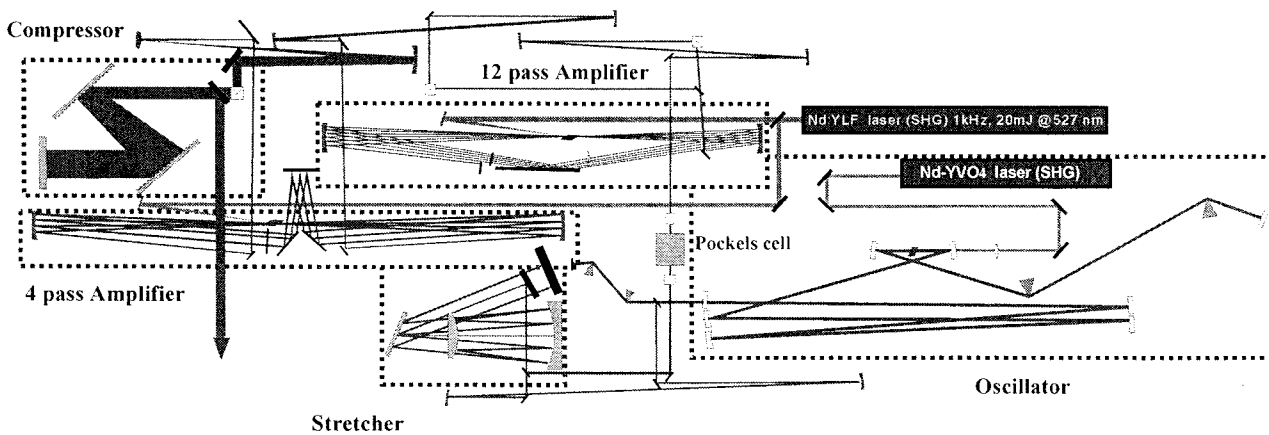

Fig. 1. Layout of a 1-kHz femtosecond terawatt Ti:sapphire laser.

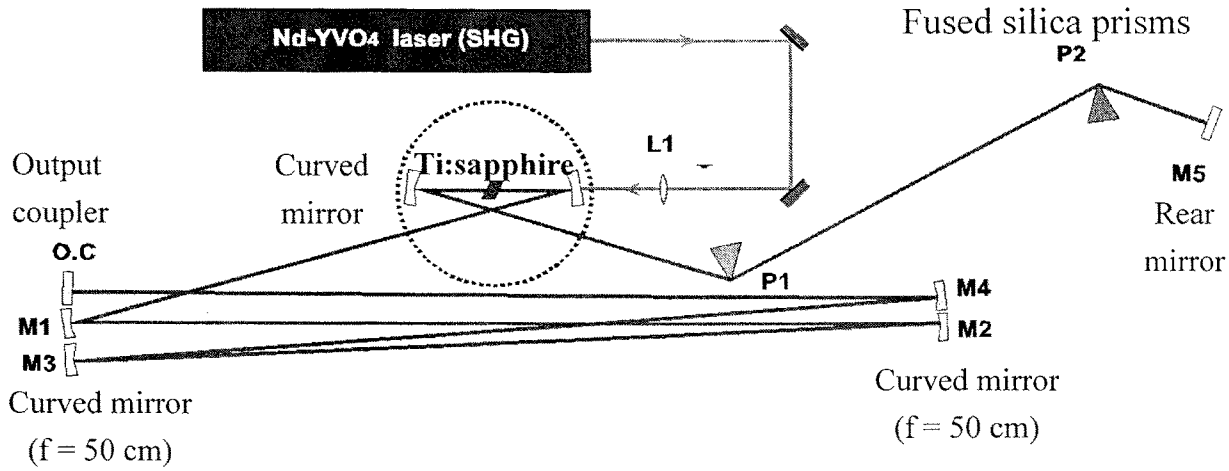

Fig. 2. Schematics of a long-cavity Kerr-lens mode-locked Ti:sapphire laser.

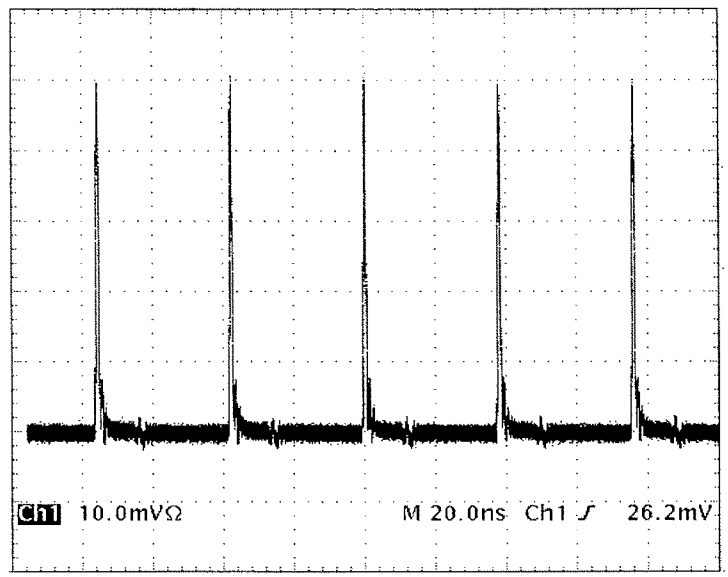

Fig. 3. Mode-locked laser pulse train of 26.5 MHz repetition rates or 38 ns pulse separation

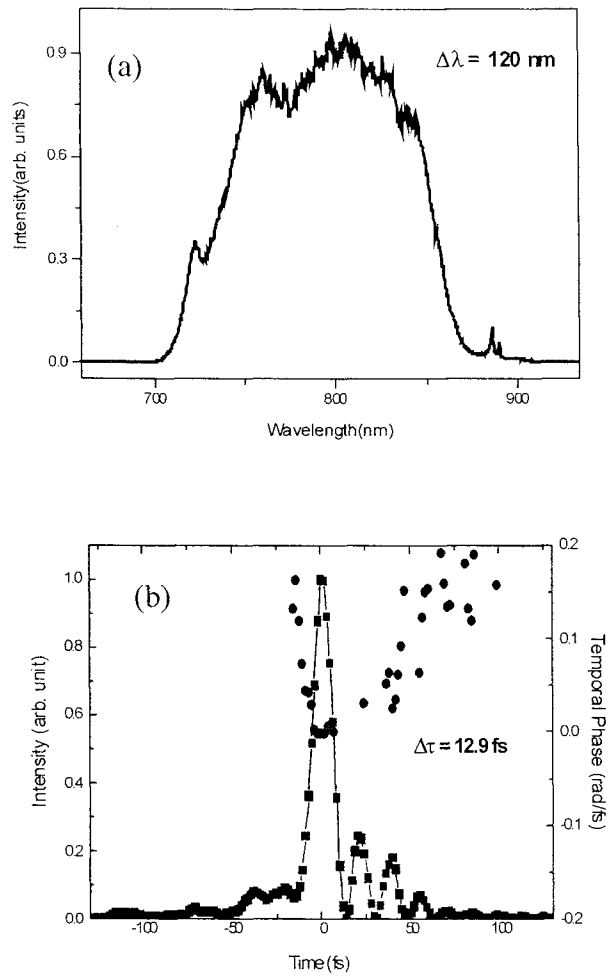

Fig. 4. Reconstructed temporal intensity profile and phase (a) and associated spectrum bandwidth of 120 nm (b) from a Ti:sapphire oscillator

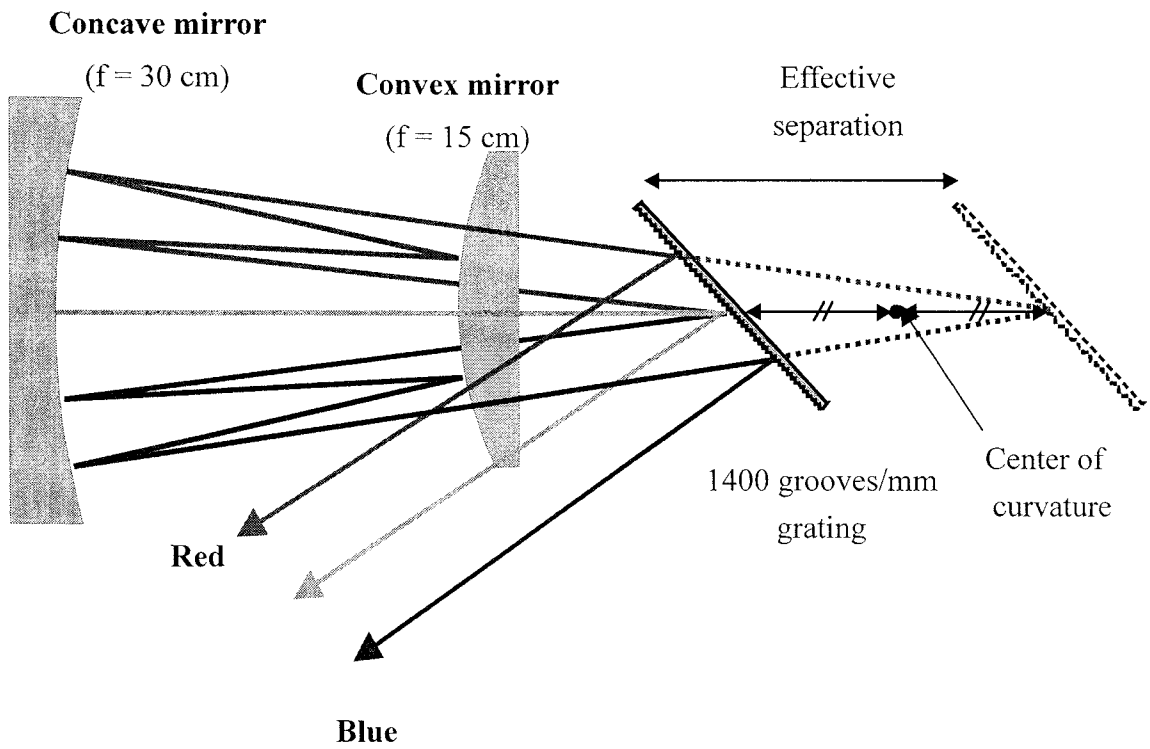

Fig. 5. Schematics of a Offner-triplet type pulse stretcher

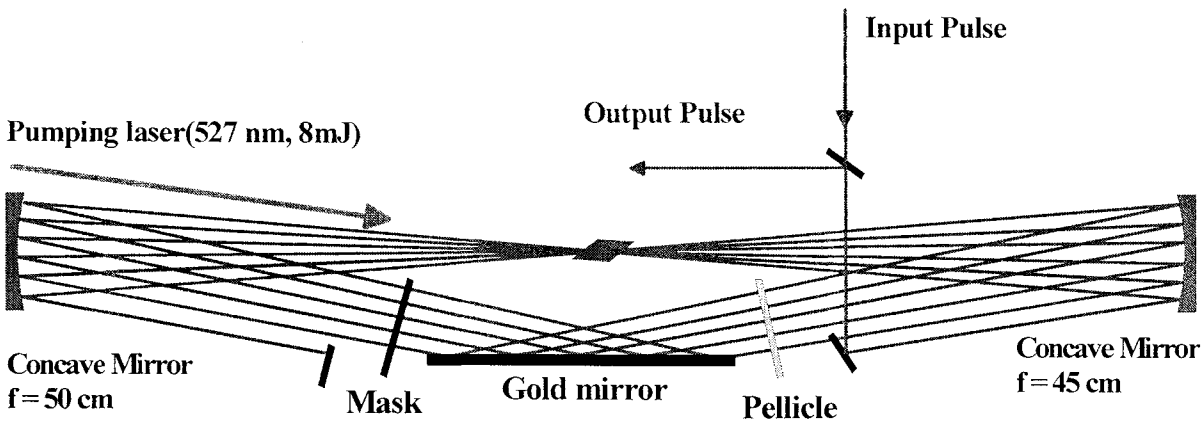

Fig. 6. A ring-type 12-pass preamplifier.

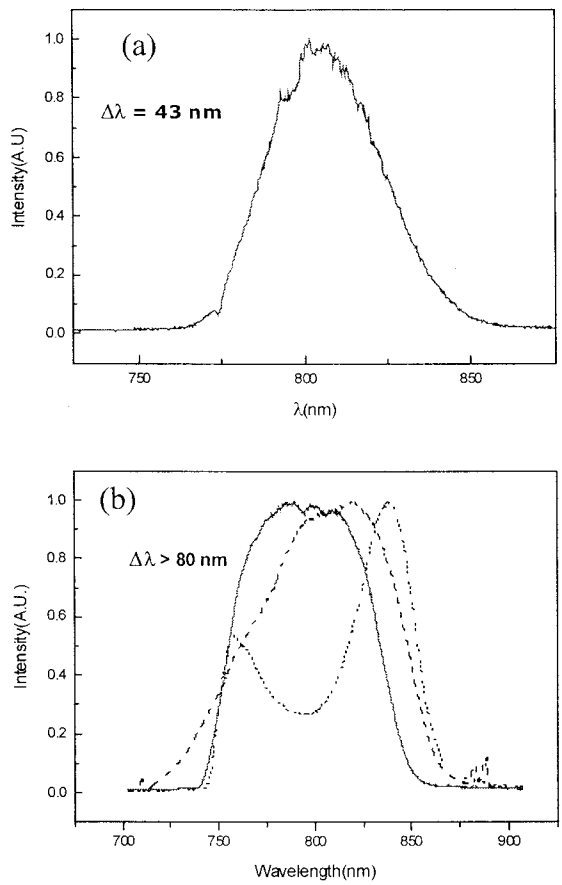

Fig. 7. Spectra of the amplified laser pulses. The output spectrum out of a preamplifier without a pellicle is shown in (a). The dashed line in (b) is the input spectrum, the dotted line, the spectrum modulated by the transmission of the pellicle, and the solid line, the resulting spectrum.

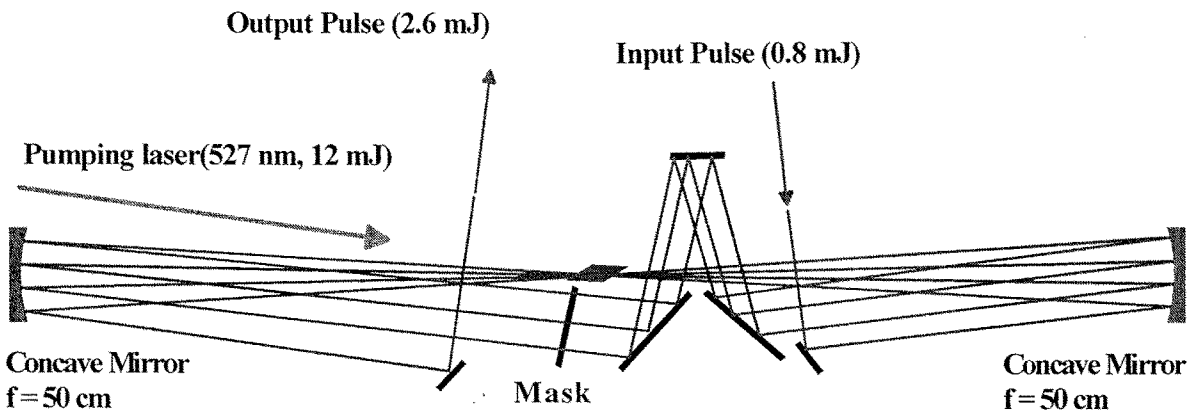

Fig. 8. A ring-type four-pass power amplifier.

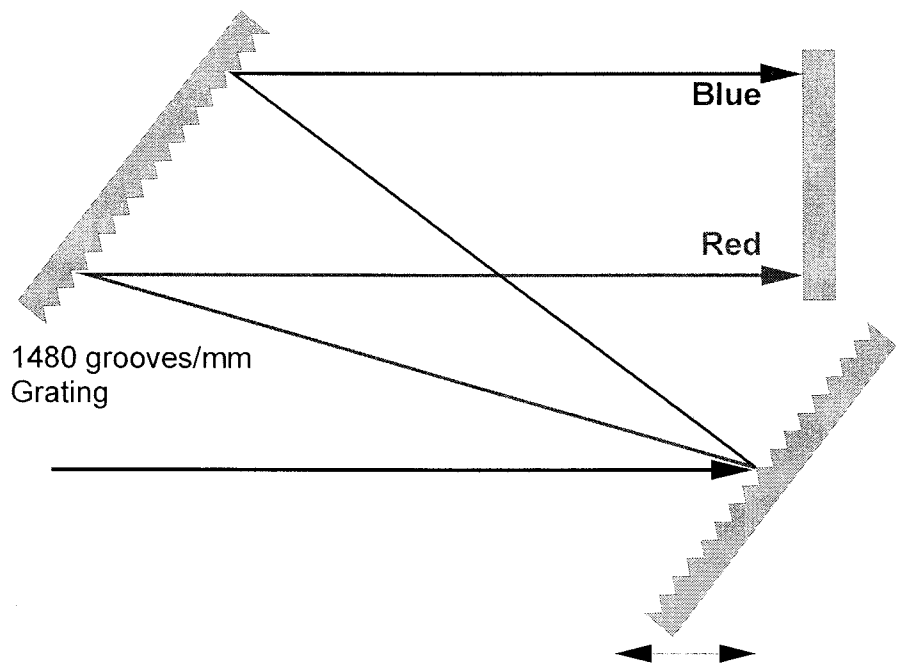

Fig. 9. Schematics of the pulse compressor.

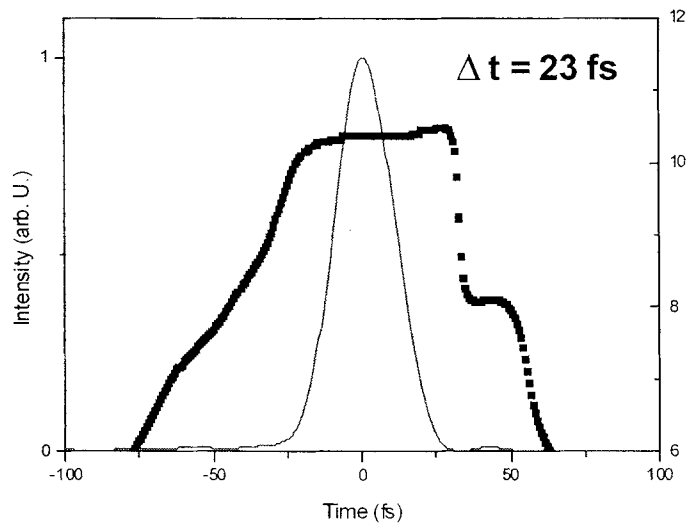

Fig. 10. The output pulse shape: the solid line is the temporal pulse shape, and the dotted line is the phase profile.

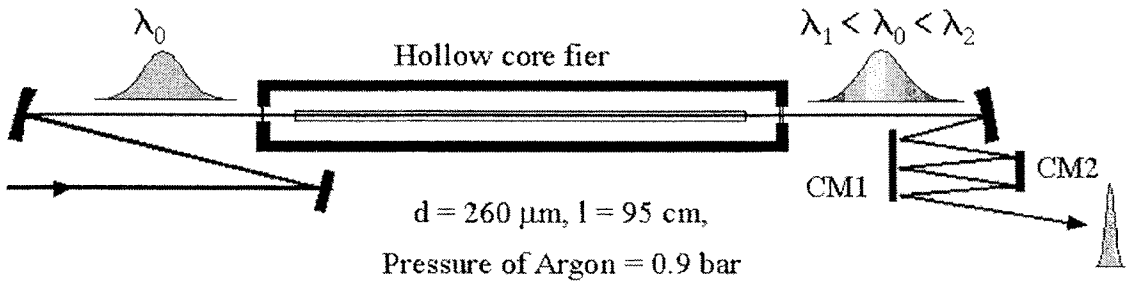

CM1,2 : Ultrabroad-band chirped mirror

Fig. 11 Experimental setup of hollow-core fiber compression system

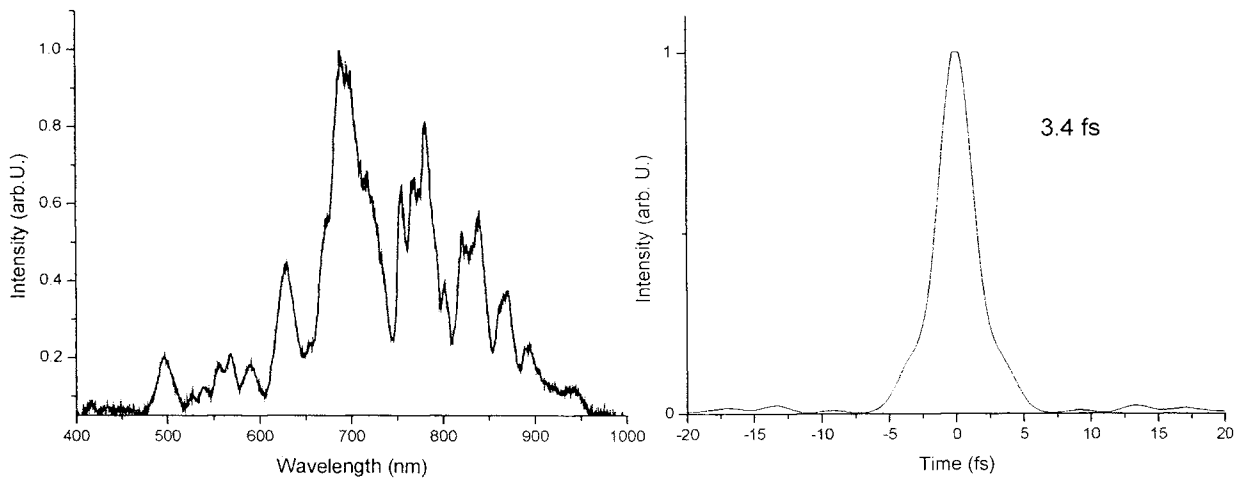

(a) (b)

Fig. 12 Broadened spectrum (a) by SPM and four-wave-mixing processes and the transform-limited pulse (b) supported by the spectrum.

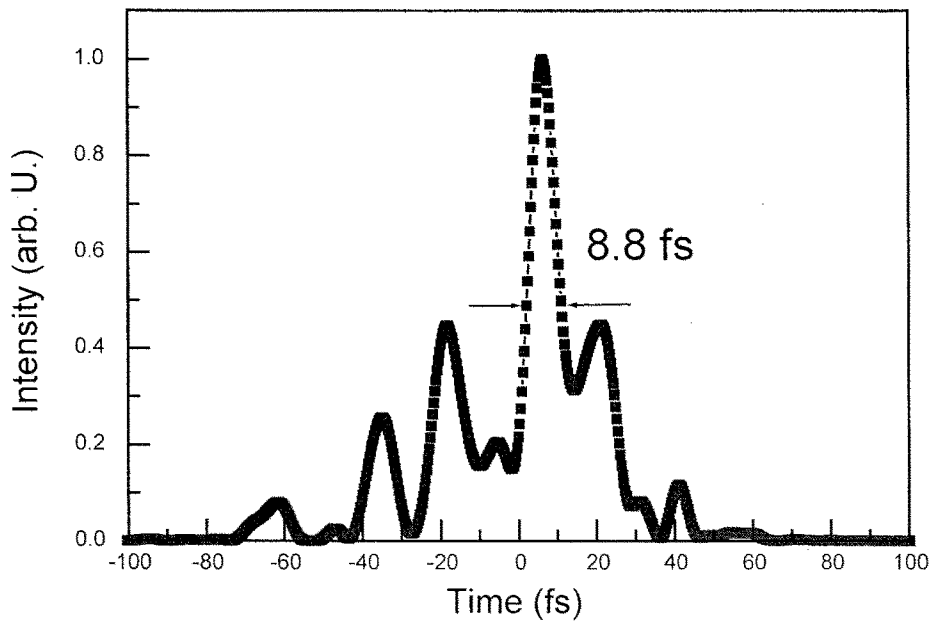

Fig. 13 Measured pulse profile after compression with the chirped mirrors. Several sub-peaks comparable to the main peak still exist due to the complicated spectral structure and uncompensated spectral phase distortion.

A. 3. 2. Graphical Interpretation of Instantaneous Carrier Frequency of Chirped Femtosecond Pulses using the Wigner Time-Frequency Distribution

I. Introduction

Time-dependent phase is a very important characteristic with an ultrashort laser pulse, especially in femtosecond regime. This characteristic mainly comes from the broadband spectrum of femtosecond laser pulses whose spectral intensity or spectral phase is easily modulated by optical elements such as glass block, prism, and grating. The frequency chirp induced by material or angular dispersion and the spectral filtering by etalon effect are good examples of such modulations. Any modification in either the spectral intensity or spectral phase of the laser pulses directly changes the temporal intensity and phase. Measurement of the time-dependent phase of femtosecond laser pulses has been intensively investigated since early 1990's, and frequency-resolved optical gating (FROG) and spectral phase interferometry for direct electric-field reconstruction (SPIDER) proved to be successful techniques among a lot of attempted ones[1,2]. Temporal phase measurement using those techniques also showed that femtosecond pulses usually do not have constant phase in time.

A time-dependent phase also implies a time-dependent carrier frequency. The relation between these two quantities is given by $\omega(t) = \omega_0 - \frac{d\varphi}{dt}$, where $\omega(t)$ is the time-dependent carrier frequency and φ is the temporal phase. This time-dependent carrier frequency is usually called 'instantaneous (carrier) frequency' of the pulse, meaning that the carrier frequency at time t is ω. We can quantitatively analyze the amount of laser chirp using this relationship after measuring the temporal phase. But, this interpretation sometimes fails because this quantity is generally not consistent with the Fourier spectral component at time t[3]. Recently, many efforts to interpret this 'instantaneous frequency' with proper meaning have been made in the analysis of frequency-modulation (FM) and amplitude-modulation (AM) signal with multiple frequency components[4-6]. However, the problem with the interpretation of instantaneous (carrier) frequency of an ultrashort laser pulse has not been noticed yet.

Time-frequency distribution functions are appropriate to interpret the instantaneous carrier frequency, which is a time-frequency-coupled quantity, because they simultaneously express the temporal and spectral behavior of ultrashort laser pulses by

revealing time-resolved spectral structure, whereas standard Fourier analysis shows only the averaged information in time and frequency domain. Wigner distribution function (WDF) is the simplest among a lot of time-frequency distribution functions and has a good marginal property. For this reason, it has been widely used in the representation of quantum particles in phase space[7], and, since adopted as a tool for the description of ultrashort pulses[8], it has been applied for the measurement of amplitude and phase of ultrashort laser pulses[9,10] and analysis of the error criteria of pulse characterization techniques[11]. It also played a significant role in analyzing a complicated structure of high-order harmonics generated by intense ultrashort pulses[12].

The WDF has mathematical relation with instantaneous carrier frequency and group delay of an ultrashort pulse, which makes it possible to analyze laser chirp quantitatively using the WDF. In this report, we propose a graphical method to find out instantaneous carrier frequency and group delay in the WDF of a Gaussian chirped pulse. After showing that the instantaneous carrier frequency defined by $\omega(t) = \omega_0 - \frac{d\varphi}{dt}$ is not the same with the instantaneous Fourier spectral component in the case of a femtosecond laser pulse with a broad and continuous spectrum, we will determine instantaneous Fourier spectral components of complicated femtosecon pulses using the graphical method proposed.

II. Description of Gaussian Chirped Pulses using WDF

The WDF for the electric field in time domain, *E(t)*, is defined as :

$$W(t,\omega) = \frac{1}{\pi}\int_{-\infty}^{+\infty} E(t+\frac{1}{2}t')E^*(t-\frac{1}{2}t')\exp(-i\omega t')dt' \qquad (1)$$

The equivalent definition is possible using the electric field in frequency domain, $\tilde{E}(\omega)$, and is written as:

$$W(t,\omega) = \frac{1}{\pi}\int_{-\infty}^{+\infty} \tilde{E}^*(\omega+\frac{1}{2}\omega')\tilde{E}(\omega-\frac{1}{2}\omega')\exp(-i\omega' t)d\omega \qquad (2)$$

The usefulness of this representation comes mainly from its good marginal property: the time marginal defined by the integration along ω-axis represents the intensity profile, and the frequency marginal, the integration along *t*-axis, the spectrum profile. Thus, this representation directly expresses how the carrier frequency changes with time evolution of the pulse and how the group delay with regard to the laser frequency. For a

quantitative time-frequency analysis on the laser chirp, two important parameters are linear chirp parameter given by the second derivative of the temporal phase at time zero with minus sign or $\alpha = -d^2\varphi/dt^2\big|_{t=0}$, and group-delay dispersion (GDD) defined by the second derivative of the spectral phase at the center frequency or, $\beta = d^2\tilde{\varphi}/d\omega^2\big|_{\omega=\omega_0}$ because they represent the variation of the instantaneous carrier frequency and the group delay, respectively.

A chirped Gaussian pulse gives a direct formulation to find out the carrier frequency and the group delay in the WDF. The linear chirp parameter of a Gaussian pulse can be expressed in terms of GDD, β [13]:

$$\alpha = \frac{4\beta}{T_{G0}^2 + 4\beta^2}, \tag{3}$$

where *chirp-free* pulse duration of full-width at half maximum (FWHM) $T_p = \sqrt{2\ln 2}T_{Go}$. Figure 1 is the linear chirp parameter for the chirped pulses with a continuous change of GDD when T_p = 24 fs. We can find that a maximum and a minimum point exist when $\beta = +\frac{T_{Go}^2}{2}$ and $-\frac{T_{Go}^2}{2}$, respectively. The intensity-normailized WDF for the Gaussian chirped pulse with a GDD of β can be explicitly written as

$$W(t,\omega) = \exp\left[-\frac{2}{T_{G0}^2}\left(t^2 - 2\beta\omega t + \frac{T_{G0}^2 + 4\beta^2}{4}\omega^2\right)\right] \tag{4}$$

Figure 2 shows the Wigner distribution for the chirped pulse when β= 225 fs^2, and T_p = 24 fs. The Wigner contours are in the shape of ellipse whose major axis is rotated by θ with regard to the ω-axis.

By looking into Eq. (4), we can find the way of proper analysis of the group delay and instantaneous carrier frequency. For a frequency ω, the WDF is at maximum when $t_{\max} = \beta\omega$. If the ω is scanned across the laser spectrum, these points make a line with a slope of β as to the ω-axis. Because β is the GDD of the chirped pulse, this line represents the group delay. With the same principle, for a fixed time *t*, the WDF is at maximum when $\omega_{\max} = 4\beta/(T_{G0}^2 + 4\beta^2)t \equiv \alpha t$. When *t* is scanned across the pulse, this line represents the instantaneous carrier frequency with a slope of linear chirp

parameter, α. The group delay and the instantaneous carrier frequency is shown in Fig.2 (b) and (c). We will call this graphical method to be 'local-maximum tracing (LMT)' method for convenience.

The angle θ in Fig. 2 monotonously increases from $-\frac{\pi}{2}$ to $\frac{\pi}{2}$ as GDD changes from $-\infty$ to $+\infty$. However, the linear chirp parameter which has a maximum and a minimum as shown in Fig. 1 cannot be explained in terms of this angle but should be obtained using the slope of line (c) in Fig. 2. Why the absolute value of the linear chirp parameter has a decreasing point is that it does not catch up the pulse broadening induced by the increase of GDD. In case that the absolute value of GDD is large or the Wigner contours has a large ellipticity, we can see from Eq. (3) that the GDD is inverse to the linear chirp parameter, and that three lines (a), (b), and (c) in Fig. 2 are overlapped. Thus, the simple approach using the angle θ is valid in this case.

In the chirped Gaussian pulse, the instantaneous carrier frequency $\omega(t) = \omega_0 - \frac{d\varphi}{dt}$ is well defined and consistent with the instantaneous Fourier spectral components because the WDF always has positive value and symmetric temporal and spectral profile. However, two quantities do not exactly match each other in an arbitrary chirped pulse. Sometimes the instantaneous carrier frequency is out of range determined by laser spectrum.

III. Instantaneous carrier frequency of an arbitrary laser pulse

Figure 3 is the temporal and spectral structure of a chirped femtosecond pulse with a double-peak spectrum, where the group delay (d) linear increases with frequency. The instantaneous carrier frequency (b) is beyond the laser spectrum (c) around the valley of laser intensity profile or envelope. A lot of examples having this kind of structure can be given. This means that the instantaneous carrier frequency, $\omega(t)$, cannot be interpreted as 'carrier frequency at time t' in general.

Why $\omega(t)$ is not consistent with the instantaneous Fourier spectral component can be explained with mathematical description of $\omega(t)$ using WDF. By a direct calculation of the frequency average over the Wigner distribution, we can find out the instantaneous carrier frequency. For $E(t) = A(t)e^{i\{\omega_0 t - \varphi(t)\}}$, the frequency averaged at time t is calculated as follows:

$$
\begin{aligned}
<\omega>_t &\equiv \frac{\int_{-\infty}^{\infty} d\omega W(t,\omega)\omega}{\int_{-\infty}^{\infty} d\omega W(t,\omega)} \\
&= \left[\iint_{-\infty}^{\infty} d\omega dt' \omega A(t+\frac{1}{2}t') e^{-i\left\{\omega_0 t+\frac{1}{2}\omega_0 t'-\varphi(t+\frac{1}{2}t')\right\}} A(t-\frac{1}{2}t') e^{i\left\{\omega_0 t-\frac{1}{2}\omega_0 t'-\varphi(t-\frac{1}{2}t')\right\}} e^{-i\omega t'} \right] / |A(t)|^2 \\
&= i\frac{d}{dt'}\left[A(t+\frac{1}{2}t')A(t-\frac{1}{2}t') e^{-i\left\{\omega_0 t'+\varphi(t+\frac{1}{2}t')-\varphi(t-\frac{1}{2}t')\right\}} e^{-i\omega t'} \right]_{t'=0} / |A(t)|^2 \qquad (5) \\
&= \omega_0 - \frac{d\varphi(t)}{dt}.
\end{aligned}
$$

With the same principle, the time averaged at frequency ω, $<t>_\omega$, is found to be the group delay when it is calculated with the WDF in frequency domain. More discussion on the time and frequency average over the general distribution functions can be found in [14]. The frequency or time average in a linearly chirped Gaussian pulse is the same as the frequency or time at which the Wigner distribution is maximum along the time or frequency axis because of its single-peaked and symmetric structure in time and frequency domain. Thus, a Gaussian-like chirped pulse can be directly analyzed using the LMT method. However, complicated pulses of which WDF have large negative region have large deviation between $\omega(t)$ and instantaneous Fourier spectral component.

In order to find out the Fourier spectral component at time t, we can get an idea from the WDF of chirped Gaussian pulse. When an arbitrary pulse is represented in time-frequency domain using WDF, its Wigner distribution around local maxima can be approximated to that of the chirped Gaussian. Thus, the LMT method is also useful even to the analysis of complicated pulses. In the next section, we will find out the instantaneous Fourier spectral component of two kinds of pulse other than Gaussian using LMT method.

IV. Time-frequency analysis of various chirped pulses

The first example is a chirped pulse with a spectrum double-peaked at $\omega_0 \pm 0.4$ rad/fs, which was already shown in Fig.3. To find out the instantaneous Fourier spectral component using the LMT method, Wigner distribution of this pulse was plotted in Fig.4. Whereas the group delay (c) is linear to frequency and exactly the same with the line obtained by LMT method, the instantaneous carrier frequency (a) is nonlinear to time and is not limited within the laser spectrum. The Fourier spectral components are localized at (b), which consists of three dotted lines. The temporal shape of this pulse

also consists of three parts. The carrier frequency from center of –0.4 rad/fs is dominant at the leading sub-pulse, and +0.4 rad/fs, at the following sub-pulse. At the main part of the pulse, the carrier frequency was chirped around the center frequency, and the ± 0.4 rad/fs components also exist.

The second example is a chirped pulse whose phase is distorted by third-order dispersion (TOD) or quadratic group delay. The WDF of this pulse is shown in Fig. 5. The instantaneous carrier frequency (a) is constant through the pulse whereas the instantaneous Fourier spectral components (b) are decomposed to two dominant frequencies in the leading part. The group delay difference between the given value (c) and obtained value by LMT method (d) comes from the existence of the negative region in the leading part. The peak position of the pulse is before t=0, in other word, is determined by (d) rather than (c) as shown in the intensity profile.

The pulse whose phase is distorted by TOD is easily observed in a chirped-pulse amplification (CPA) system. Figure 6 is an experimental data measured using frequency-resolved optical gating (FROG) technique from a CPA Ti:sapphire laser. (a) is the instantaneous carrier frequency, (b) is the instantaneous Fourier components, and (c) is the group delay. The line (c) shows that this pulse has TOD with zero GDD, thus it can be analyzed as described in the same way with the theoretically generated pulse.

V. Conclusion

We showed that the instantaneous carrier frequency defined by $\omega(t) = \omega_0 - \frac{d\varphi}{dt}$ is usually not supported by Fourier spectral components at time t. To solve the problem occurring from this discrepancy, we proposed a graphical method (LMT method) in time-frequency representation using WDF of a chirped Gaussian pulse. Using the LMT method, the instantaneous carrier frequencies of chirped pulses having double-peak spectrum and distorted by TOD were analyzed. We could quantitatively discompose the instantaneous Fourier spectral components of these pulses, which will be very helpful to understand the carrier frequency of a femtosecond pulse.

References

[1] B. Kohler, V. V. Yakovlev, K. R. Wilson, J. Squiffer, K. W. DeLong, and R. Trebino, Opt. Lett. 20 483 (1995).

[2] C. Dorrer, B. de Beauvoir, C. Le Blanc, J.-P. Rousseau, S. Ranc, P. Rousseau, J.-P Chambaret, F. Salin, Opt. Lett. 24 1644 (1999).

[3] L. Mandel, Amer. J. Phys. 42, 840 (1974).

[4] B. Ristic and B. Boashash, IEEE Trans. Signal Processing 44, 1549 (1996).

[5] P. J. Loughlin, IEEE Signal Processing Lett. 4, 123 (1997).

[6] W. Nho and P. J. Loughlin, IEEE Signal Processig Lett. 6, 78 (1999).

[7] E. Wigner, Phys. Rev. 40, 749 (1932).

[8] J. Paye: IEEE J. Quantum Electron. QE-28, 2262 (1992).

[9] R. Gase, J. Opt. Soc. Am B 14, 2915 (1997).

[10] I. A. Walmsley and V. Wong, J. Opt. Soc. Am B 13, 2453 (1996).

[11] S. Yeremenko, A. Baltuska, M. S. Pshenichnikov, and D. A. Wiersma, Appl. Phys B 70, S109 (2000).

[12] J. H. Kim, D. G. Lee, H. J. Shin, C. H. Nam, Phys. Rev. A 63, 063403 (2001).

[13] J-.C. Diels, W. Rudolph, Ultrashort Laser Pulse Phenomena, Ch.1, Academic Press USA, 1996.

[14] L. Cohen, Proc. IEEE 77, 941 (1989).

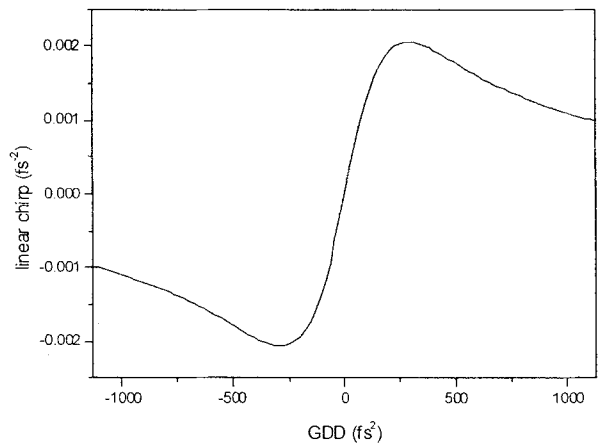

Fig.1 Linear chirp parameter versus GDD of chirped Gaussian pulses. Chirp-free pulse duration is 24 fs.

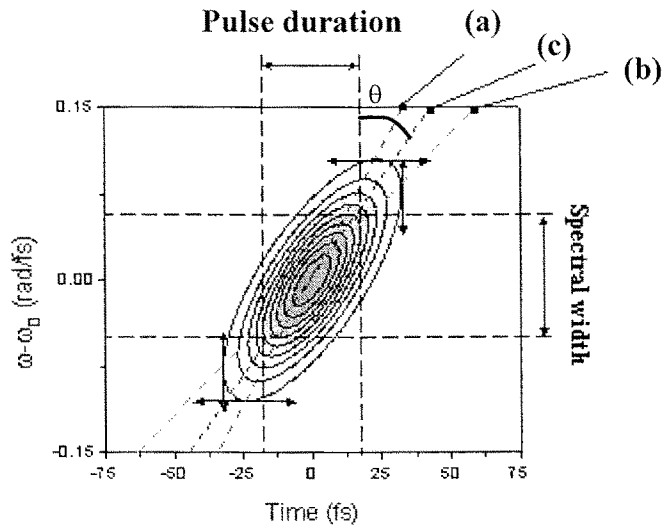

Fig. 2 Graphical interpretation of the WDF of a chirped Gaussian pulse. (a) is group delay line (function of w), (b) is instantaneous carrier frequency (function of t), and (c) is the major axis of the ellipse formed by Wigner contour (rotation angle of q with regard to w-axis).

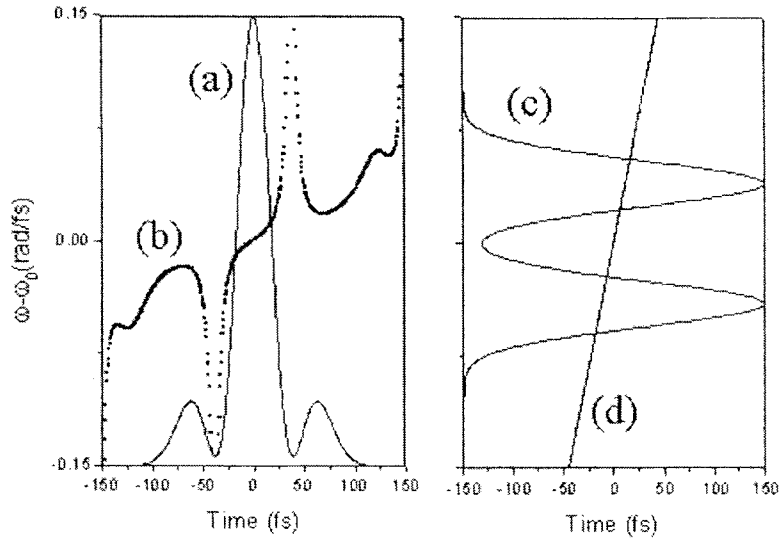

Fig. 3 Chirped pulse with a double-peak spectrum. Instantaneous carrier frequency (b) can be out of laser spectrum(c). (a) is the temporal intensity profile, and (d) is group delay (function of w).

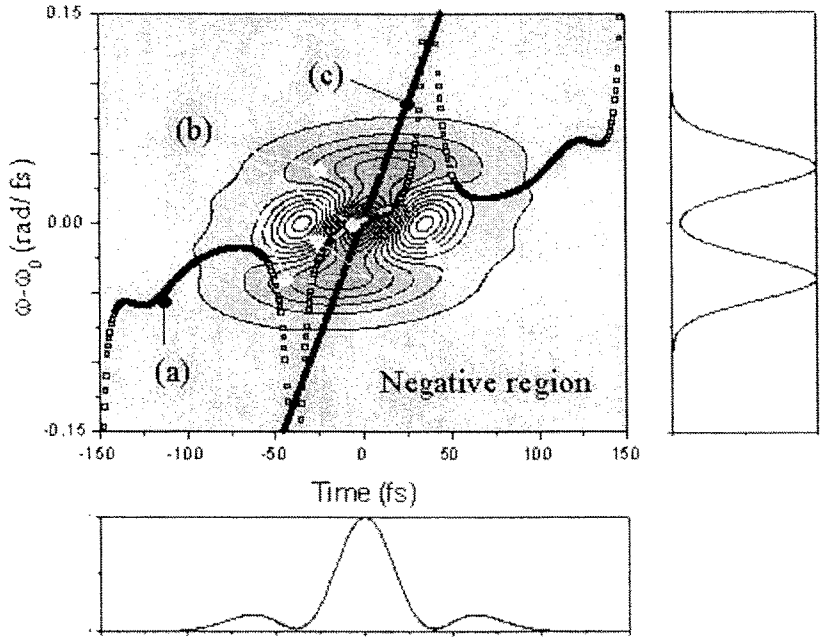

Fig. 4 Wigner distribution of chirped pulse with a double-peak spectrum. Instantaneous carrier frequency, dotted line (a), is out of laser spectrum while the instantaneous Fourier spectral components, dashed lines (b) obtained using LMT method are localized in the spectrum. Solid line (c) is the group delay, and time and frequency marginals are shown in bottom and right sides.

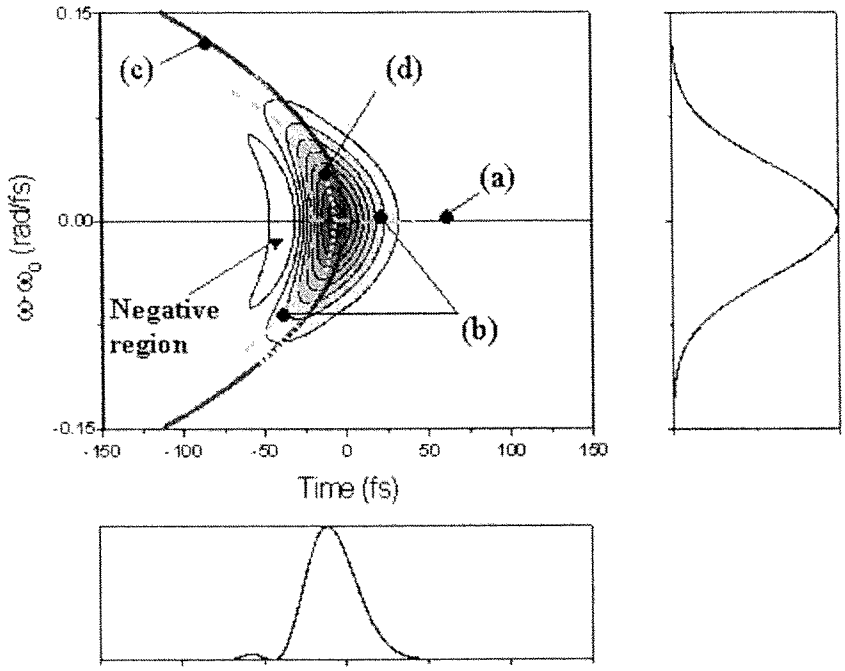

Fig. 5 Wigner distribution of a chirped pulse distorted by TOD. Instantaneous carrier frequency (a) is constant through the pulse, whereas Fourier spectral components are decomposed into two parts in the leading edge of the pulse (b). The peak of the pulse, where the group delay is 0, is corresponding to the group delay (d) obtained using LMT method rather than the given group delay (c).

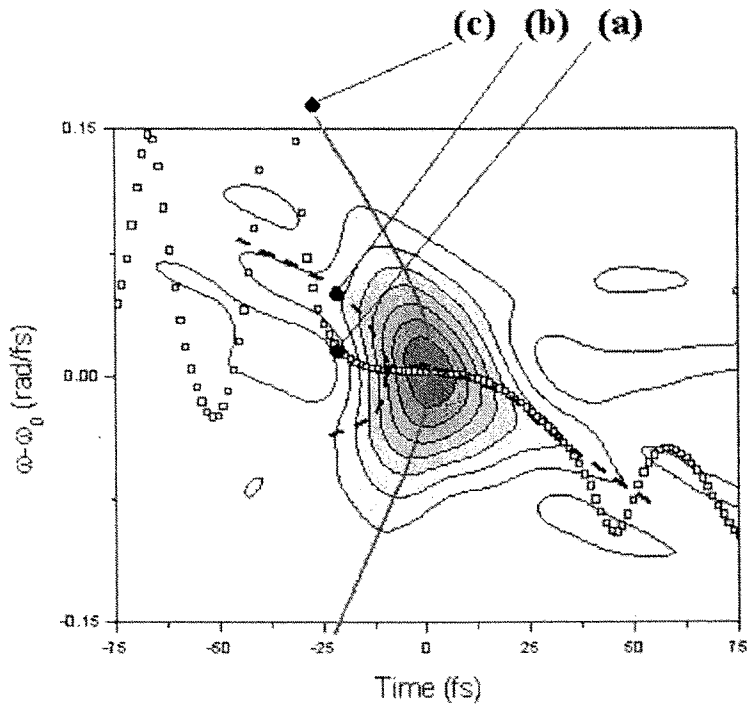

Fig. 6 Wigner distribution of experimental measured pulse distorted by TOD. Instantaneous carrier frequency is (a), the Fourier spectral component is (b), and group delay is (c).

A.3.3 Temporal characterization of femtosecond laser pulses using spectral phase interferometry for direct electric-field reconstruction (SPIDER)

I. Introduction

Since Spence *et al.* generated a 60 fs ultrashort laser pulse from Ti:sapphire laser using Kerr-lens mode-locked technique in 1991, research for generating a shorter pulse has been accelerated, so that sub-10-fs pulses became available from Ti:sapphire laser.[1-3] Ultrashort pulses have wide applications in chemistry, biology and semiconductor engineering because they opened femtosecond time resolving spectroscopy.[4] After amplification of femtosecond pulses using chirped pulse amplification(CPA) technique. we can obtain a high power pulse above tera watt(10^{12} W; TW). The CPA lasers are small-scale coherent and incoherent X-ray source.[5,6]

Temporal characterization of femtosecond laser pulses is a critical issue because there is no electronic detector that can directly measure a femtosecond signal. So we should use an optical method to measure it. Traditional methods for the characterization are intensity autocorrelations and interferometric autocorrelation. But we must assume a pulse shape in these measurements, which make it impossible to get a accurate information about pulse phase. In 1993, D. J. Kane *et al.* introduced a frequency resolved optical gating (FROG) technique with several following algorithms, to fully characterize femtosecond pulses.[7] In 1998, another technique for a perfect characterization of ultrashort pulse was introduced by C. Iaconis *et al.* named a spectral phase interferometry for direct electric-field reconstruction(SPIDER).[8] This technique is being adopted by many research groups because it is much faster than FROG.

In this report, we designed a SPIDER apparatus and characterized femtosecond pulses. As an independent cross-check of the accuracy of the method, we compared the interferometric autocorrelation (IAC) signal calculated from the SPIDER data with a separately measured IAC.

II. SPIDER setup and electric-field reconstruction algorithm

After obtaining a SPIDER signal, we should find the pulse information with SPIDER algorithm. It composed of the following processes. (1) The incident pulse is divided to

two parts by a beamsplitter. One of the pulses is divided again by another beamsplitter to produce a pair of pulses, which are aligned with a fixed time delay by a Michelson - type interferometer. The other pulse is stretched to several hundred times of input pulse duration by heavily dispersive material(or grating pair). (2) Both the pulse pair and strongly chirped pulse are overlapped at nonlinear crystal for sum-frequency generation (SFG). At this moment, two SFG spectra generated by those three pulses are sheared to each other. (3) We obtain spectral phase information from the following equation:

$$I(\omega) = |E(\omega) + E(\omega + \Omega)|^2 = I(\omega) + I(\omega + \Omega) + |E(\omega)||E(\omega + \Omega)| \cdot \cos\{\varphi(\omega) - \varphi(\omega + \Omega) + \omega\tau\},$$

where $I(\omega)$ represents the spectrum generated by two sheared pulses. (4) We get phase information of above equation using a Fourier filtering process and by subtracting $\omega\tau$ term by calibration. (5) We reconstruct a spectral phase from a concatenation method. So we can obtain a perfect temporal characteristic of pulse along with spectral amplitude information.

The SPIDER setup is illustrated in Fig. 1. The p-polarized incident pulse is divided into two parts by a 50% femtosecond beamsplitter. One pulse generates a pair of pulses with a time delay τ between two determined by a Michelson-type interferometer. Another pulse is strongly stretched to about 4 ps by a 8-cm long SF10 material. The Michelson-type interferometer is composed of a 50% femtosecond beamsplitter and two aluminum mirrors. The polarization of the pulse pair from the interferometer is changed by 90° by a periscope. And pulse pair after the periscope is overlapped with strongly chirped pulse using a horizontal translator T2. The overlapped pulses are focused on a 30-μm thick type-II BBO(β-BaB_2O_4) crystal for spectrally sheared SFG, and the resultant SPIDER signal is recorded on a spectrometer. Here we locate a flipper in front of the SPIDER setup to compare the result with that of an IAC technique.

In the measurement of the femtosecond pulse shape using a SPIDER, it is necessary to control the amount of spectral shearing. Since the spectral shearing Ω has some relation with time delay τ given by Eq. (1), we can control Ω by time delay τ.

$$\Omega = \frac{\Delta\omega\tau}{\Delta t} = \frac{\tau}{\phi''} \qquad (1)$$

There are three factors to be considered for a proper management of SPIDER signal. One is Whittaker-Shannon sampling theory[9], and another is the range for the Fourier filtering. The third we must consider is the resolution of spectrometer. We confirmed that the spacing of our spectrum data was sufficient for Whittaker-Shannon sampling theory, so we could obtain a satisfactory temporal range after fast Fourier

transformation (FFT). From the resolution of spectrometer, we can determine the upper bound of τ to get a right result. Since our spectrometer has a resolution about 0.115 THz/pixel(0.0679 nm/pixel), it should be satisfied $\tau \leq 2.90$ ps to get the 3 point per a fringe. We can determine the lower bound of τ from the Fourier transformation of SPIDER signal.

To get a right Fourier filtering of AC part, it is necessary to make distinction between the component at $\omega=0$ and $\omega=2\pi/\tau$ after the FFT processing. For this, we adjust the time delay τ within a boundary shown in Fig. 3. Since the spectral phase can be reconstructed only at an interval of Ω given by Eq. (1), the resolution of the spectral phase will be determined by Ω, which means that a large spectral shearing makes a large error. On the other hand, too small spectral shearing also results in a large error because the SPIDER signal will become sensitive to noise due to the high-frequency modulation of spectrum. It was indicated by M. E. Anderson *et al.*[10] that error is small when $\Omega/\Delta\omega$ is between 4% and 35% and the smallest at $\Omega/\Delta\omega \approx 23$ %. In our SPIDER setup, the group delay dispersion ϕ'' of stretched pulse was 12720 fs^2 , and the time delay τ was 272 fs. Thus, we obtain $\Omega/2\pi$ of 3.4 THz and $\Omega/\Delta\omega$ of about 7.7 %.

The SPIDER algorithm is based on the algorithm of Takeda *et al.*[11] with addition of a concatenation method. In this algorithm, we get the phase information of the SPIDER signal with following equation.

$$\phi_\omega(\omega)-\phi_\omega(\omega+\Omega)-\omega\tau = \arg\left[D^{filtering}(\omega)\right], \quad (2)$$

where $D^{filtering}(\omega)$ means Fourier high-pass filtering. If we subtract $\omega\tau$ from left side of equation, we can obtain a spectral phase difference at Ω spacing. So it is important to determine $\omega\tau$ precisely. We obtained $\omega\tau$ in the same setup only by shifting the axis of BBO by 45° with the strongly chirped pulse blocked. After subtracting $\omega\tau$ from Eq. 2, we performed a concatenation process to get a spectral phase. Spectral phase $\theta(\omega)$ is defined by

$$\theta(\omega) \equiv \phi_\omega(\omega)-\phi_\omega(\omega-\Omega). \quad (3)$$

Thus, We can reconstruct the spectral phase using a concatenation method as follows:

$$\begin{aligned}
&\vdots \\
&\phi_\omega(\omega_0-2\Omega) = -\theta(\omega_0-\Omega)-\theta(\omega_0) \\
&\phi_\omega(\omega_0-\Omega) = -\theta(\omega_0) \\
&\phi_\omega(\omega_0) = 0 \\
&\phi_\omega(\omega_0+\Omega) = \theta(\omega_0+\Omega) \\
&\phi_\omega(\omega_0+2\Omega) = \theta(\omega_0+2\Omega)+\theta(\omega_0+\Omega) \\
&\vdots
\end{aligned} \quad (4)$$

where a phase offset at center frequency, $\phi_\omega(\omega_0)$, was set to be zero because it doesn't make any influence on the pulse duration and frequency chirp.

To obtain an electric field in time, we should obtain spectral amplitude together with spectral phase. Typically spectral amplitude is independently measured. But it was also suggested that the spectral amplitude is measurable together with SPIDER signal from rebuilt spectrometer.[12] Anyway, the electric field can be obtained from the inverse Fourier transform of the measured spectral amplitude and phase :

$$E(t) = \frac{1}{2\pi}\int_{-\infty}^{\infty} d\omega \left\{\sqrt{I(\omega)}e^{i\phi(\omega)}\right\}e^{i\omega t} \qquad (5)$$

III. Measurement of ultrashort pulse using SPIDER

Using the SPIDER apparatus, we reconstruct femtosecond pulses generated from the Ti:sapphire oscillator described in A.3.1. Figure 2 shows a measured SPIDER signal recorded on the spectromer, and Figure 3 is the Fourier transform of the signal to perform a Fourier filtering. After filtering and concatenation described in the previous section, spectral phase was reconstructed as shown in Fig. 4. As the final process, we performed the inverse Fourier transform to get the temporal intensity and phase shown in Fig. 5. The dotted line in Fig. 5 is the transform-limited pulse and the solid line, the measured pulse. The result of SPIDER shows that pulse duration is 19.4 fs, while the transform-limited pulse duration, 13.6 fs. Figure 6 shows the comparison between an IAC signal measured (open circle) and reconstructed by the SPIDER result (solid curve). Figure 6 indicates the two data fit very well.

Figure 7 shows the reconstructed IAC signal in full range and its envelope. Even though the envelope comes from a 15-fs pulse whose shape is assumed to be sech^2, it shows a good fit to the IAC signal. This means that an IAC result may have some problem of underestimation of the pulse duration due to the assumption of the pulse shape. In the same way, if we assume the pulse shape to be Gaussian, the pulse duration is different from that of original pulse only by 5%. We can find that the pulse duration can be much different depending on the assumption of the pulse shape. Therefore, a direct pulse characterization technique such as SPIDER is necessary in the sub-20-fs regime.

IV. Single-shot real-time operation

After initial setup of the SPIDER apparatus, some improvements was made for high-

performance operation. First, we adopted a collinear-type SFG setup instead of a non-collinear-typed one because it has smaller error when we subtract $\omega\tau$ value from the phase term of SPIDER signal. The setup of collinear-type SPIDER is illustrated in Fig. 8. We made the SPIDER setup simpler through the reduction of number of mirrors only by adding one more femtosecond beamsplitter to the previous SPIDER apparatus.

Second, we upgraded the SPIDER apparatus to characterize the pulse in a single-shot scheme. It was achieved by using a broadband fiber spectrometer and a band-pass optical filter. In a typical SPIDER setup, the laser spectrum is measured independently, but we simultaneously measured it with a broadband fiber spectrometer that covers a spectrum range from fumdamental to second harmonic spectra. As a result, we could obtain two spectra in a single-shot. One of the problems is that the intensities of two signals are so different that we must control the relative intensity level, but the band-pass filter made it possible to greatly reduce the fundamental spectrum without suppressing the second harmonic spectrum. The other problem is that the fundamental spectrum has some modulation due to the Michelson-type interferometer, which can be solved by performing the Fourier filtering to remove the modulatioin. The single-shot scheme is very useful to characterize the amplified pulse from a CPA system because the amplified pulse has the spectrum fluctuation by shot-to-shot.

Along with the single-shot operation, it is necessary to characterize a pulse in a real-time experiment. The fast algorithm of SPIDER that includes several times of FFT and additive calculations enables a real-time measurement of the pulse intensity and phase. After the acquisition of the SPIDER data from the spectrometer, we process it with a fast SPIDER algorithm coded in C++ language. Now the repetition rate of 0.3 Hz is available for the data acquisition and electric-field reconstruction using a Pentium PC with a clock speed of 100 MHz. We expect the repetition rate to be enhanced by using a faster PC and improving the structure of the code.

V. Conclusion

We designed and fabricated a SPIDER apparatus to characterize femtosecond pulses. For the accuracy check of SPIDER measurement, we get an IAC signal at the same time and compared it with the reconstructed IAC signal from the SPIDER result. They showed a good agreement with each other. The conventional, but unjustified, method of fitting a sech^2 pulse to the IAC deceivingly yielded a pulse duration of 15 fs or 18 fs in the case of fitting a Gaussian pulse whereas the SPIDER result indicated that the pulse

duration was 19 fs. For the characterization of femtosecond pulses with a broadband spectrum of which shape is far from $sech^2$ or Gaussian, the SPIDER technique was proved to be very powerful. We also upgraded the SPIDER apparatus for the single-shot, real-time operation. For this purpose, we changed the SFG setup from non-collinear to collinear type, which made easier calibration possible, and adopted a broadband fiber spectrometer with high-speed performance in combination with a band-pass filter.

For its high reconstruction speed, the SPIDER technique is expected to be more widely used than FROG technique that requires relatively long time for the pulse reconstruction.

Reference

[1] I. D. Jung, F. X. Kartner, N. Matuschek, D.H. Sutter, F. Morier-Genound, G. Zhang, and O. Keller, Opt. Lett. **22**, 1009 (1997).

[2] J. Herrmann, V. P. Kalosha, and M. Muller, Opt. Lett. **22**, 236 (1997).

[3] Ch. Spielman, T. Brabec, and F. Krausz, Opt. Lett. **22**, 1884 (1997).

[4] A. Assion, T. Baumert, M. Bergt, T. Brixner, B. Kiefer, V. Seyfried, M. Strehle, G. Gerber, *Science* **282**, 919 (1998).

[5] H. J. Shin, D. G. Lee, Y. H. Cha, K. H. Hong, and C. H. Nam, Phys. Rev. Lett. **83**, 2544 (1999).

[6] T. Mocek, C. M. Kim, H. J. Shin, D. G. Lee, Y. H. Cha, K. H. Hong, and C. H. Nam, Phy. Rev. E **62**, 4461 (2000).

[7] R. Trebino and D. J. Kane, J. Opt. Soc. Am. A **10**, 1101 (1993).

[8] C. Iaconis and I. A. Walmsley, Opt. Lett. **23**, 792 (1998).

[9] J. W. Goodman, Introduction to Fourier Optics (McGraw-Hill, New York, 1988) chapter 2.

[10] M. E. Anderson, L. E. E. de Araujo, E. M. Kosik, I. A. Walmsley, Appl. Phys. B **70** S85 (2000).

[11] M. Takeda, H. Ina, and S. Kobayashi, J. Opt. Soc. Am. **72**, 156 (1982).

[12] C. Dorrer, Opt. Lett. **24**, 1532 (1999).

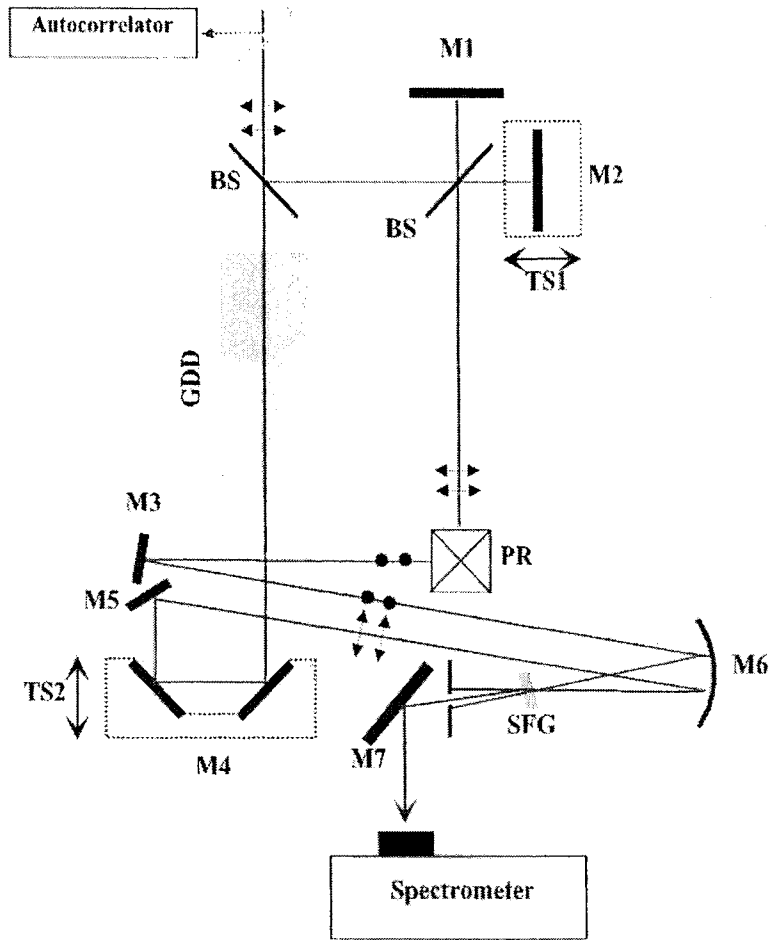

Fig. 1 Experimental setup of SPIDER apparatus. M1, M2, M3, M4, M5, M7: aluminum mirror, BS: beamsplitter, PR: polarization rotator (Periscope), M6: gold-coated spherical mirror, TS1, TS2: horizontal translator, GDD: highly dispersive material (SF10 glass), SFG: type-II BBO crystal

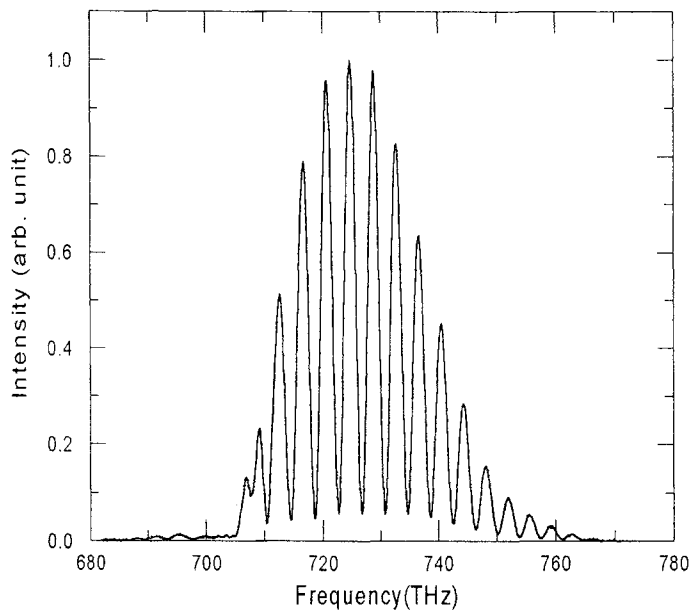

Fig. 2 SPIDER signal captured in the spectrometer

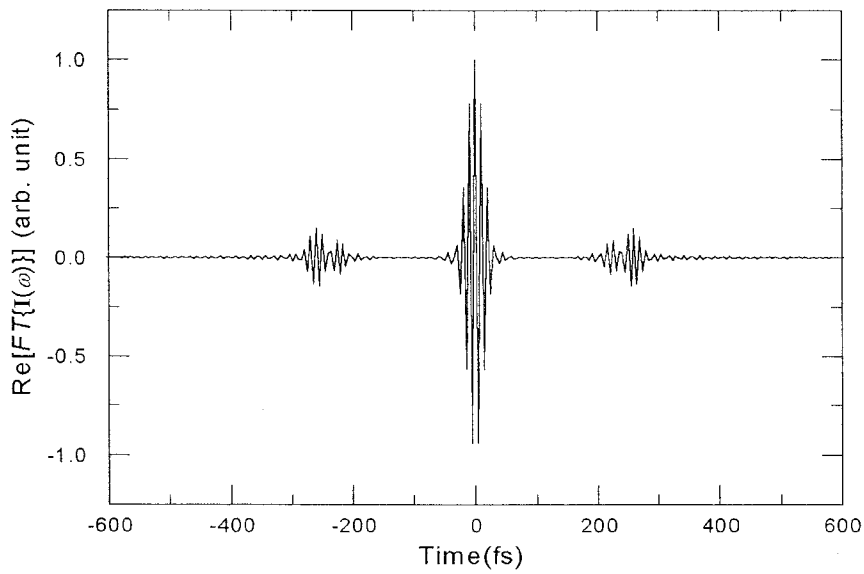

Fig.3 Fourier transform of the SPIDER signal.

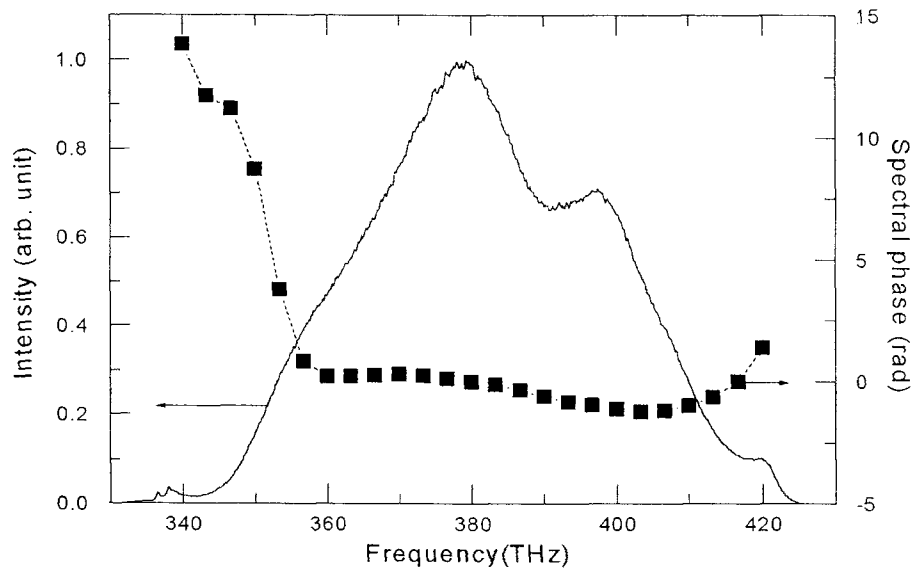

Fig. 4 Spectral phase from SPIDER algorithm and fundamental spectrum

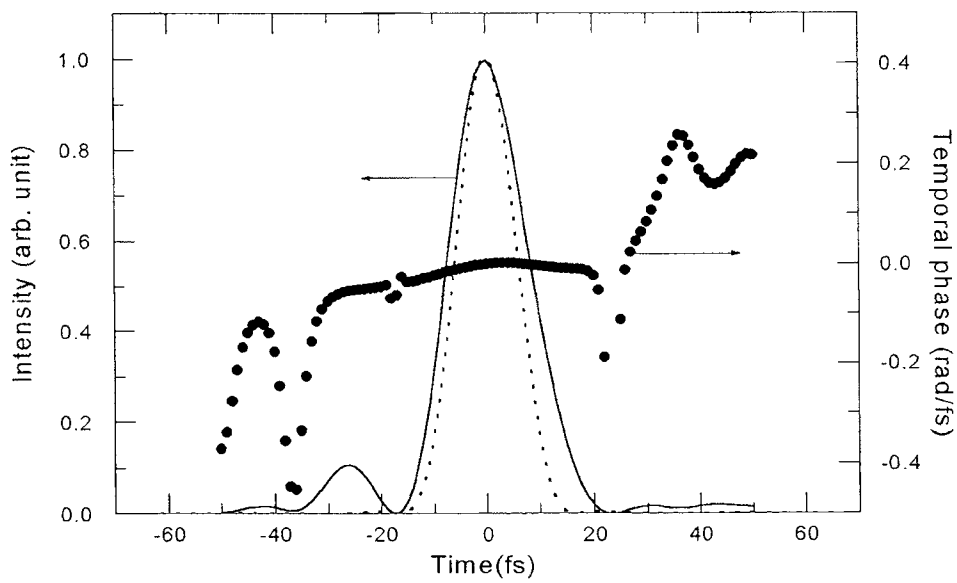

Fig. 5 Temporal phase (closed circles) and intensity profile (solid line) from the SPIDER measurement and corresponding transform-limited pulse (dotted line).

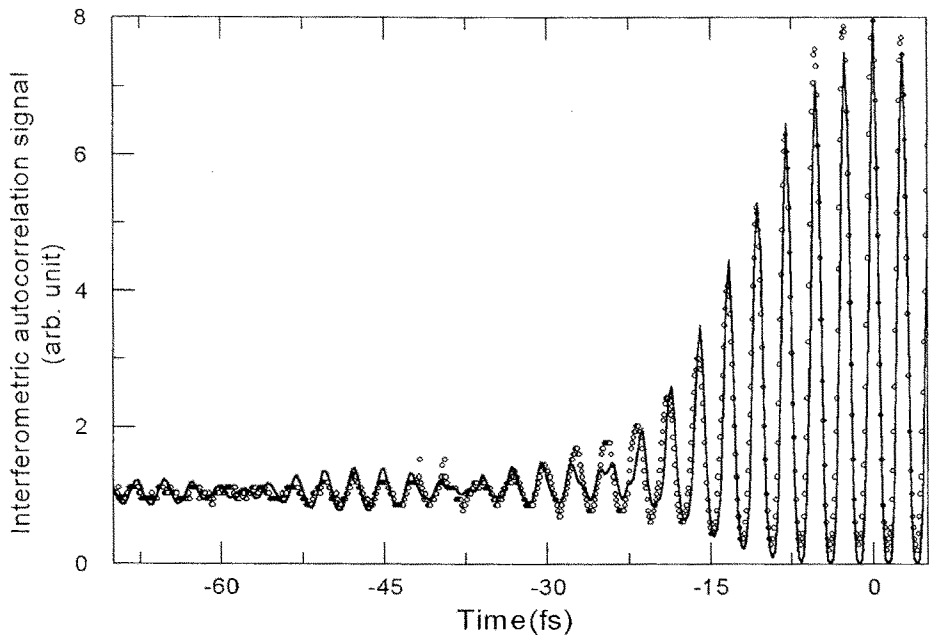

Fig. 6. Interferometric autocorrelation signals from really measured (open circle) and reconstructed from the SPIDER result (solid line).

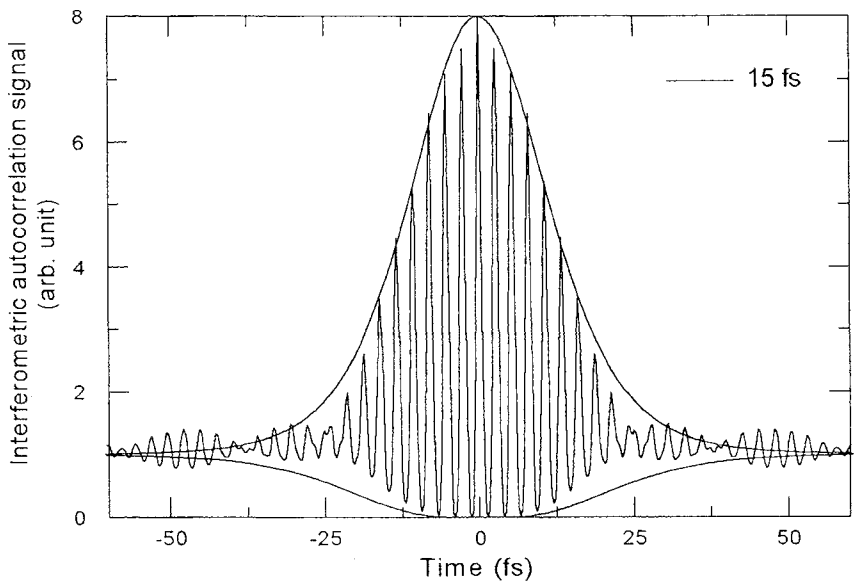

Fig. 7. Interferometric autocorrelation signal in full range reconstructed from the SPIDER result and its envelope fitted by a 15-fs $sech^2$ pulse.

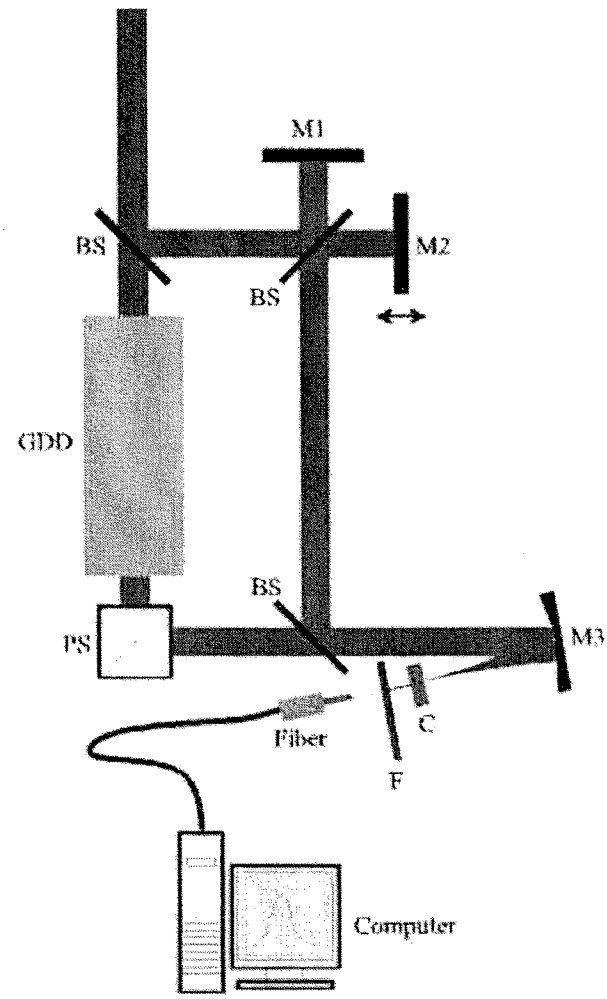

Fig. 8 Real-time, single-shot SPIDER apparatus. A broadband fiber spectrometer and a band-pass filter were used.

A. 3. 4. Adaptive pulse compression using a micro-machined deformable mirror

I. Introduction

Femtosecond pulses are easily modulated by the dispersion of optical elements because of their broadband spectra. The group delay dispersion (GDD) induced the optical elements yields pulse broadening effect, thus the GDD should be efficiently removed in the pulse so as to compress the pulse duration. Positively chirped pulse broadened by usual optical elements such as BK7, fused silica, and SF10 can be compression using negative-GDD elements such as prism, grating, and chirped-mirror pair. However, these 'passive' dispersion-compensation elements have the limitation in compressing the pulse because of residual dispersion. To overcome the limitation of passive elements, active devices such as liquid crystal and acousto-optic modulator was used recently.[1]

Deformable mirror that has been used for the wave-front correction is one of good candidates to overcome the limitation. Micro-machined deformable mirror (MMDM), which was given birth to by semiconductor production technology, is a low-cost and fast deformable mirror. In 1999, it was firstly used for an active and adaptive pulse compression of femtosecond pulses, and for the generation of optimized high-order harmonics.[2,3]

In this Report, we setup an adaptive pulse shaper using an MMDM and compressed the positively chirped pulse by feedback control using genetic algorithm (GA).[4]

II. Setup of adaptive pulse compressor

Experimental setup of the adaptive pulse compressor is shown in Fig. 1. Positively chirped pulses from a Ti:sapphire oscillator are dispersed by a prism, and then imaged on the MMDM using a focusing mirror with a geometry of magnification 1. Here we used a SF10 prism instead of a diffraction grating to obtain higher throughput efficiency and a focusing mirror with a large focal length (1.25 m) to utilize the full surface of MMDM. The MMDM (OKO technologies) is in linear type with the dimension of 1 inch and has 19 actuators. Each actuator is controlled by digitized DC voltage from 0 to 255 V interfaced by a Pentium PC.

To compress the pulse duration, we maximized the second-harmonic (SH) signal generated by the pulse because shorter pulse duration will yield higher SH peak intensity. The SH signal was detected on a spectrometer (PC2000, Ocean Optics) to feedback the peak value to the MMDM. As a feedback algorithm to maximize the SH signal, we used GA which realizes the natural principle of 'survival of the fittest' in a simulation or an experiment.

The procedure of a simple GA is shown in Fig. 2. First, a random population is generated. Population consists of a number of individuals and is refreshed with the evolution of generation. We set the voltage array loaded to the MMDM as an individual, and a population consists of 10 to 20 individuals. Thus, we must capture the SH signal for 10 to 20 times for one population. Second, the individuals are selected by fitness, the peak intensity of the SH signal, where a better individual is selected more frequently. And then, the individuals are crossovered and mutated at a certain rate to improve the population fitness. A new generation begins with the evaluation of the fitness (capturing SH signal) and repeats the following processes until a criterion is fulfilled.

The temporal characterization of the pulse before and after compression was performed using spectral interferometry for direct electric-field reconstruction (SPIDER).[5] The experimental setup was described in A.3.3.

III. Experimental result

The intensity and phase profile of uncompressed pulse is shown in Fig. 3. The pulse duration was 84 fs, and the instantaneous carrier frequency showed the positive chirp. The transform-limited pulse duration determined by the laser spectrum was calculated to be 19.5 fs.

We set the number of individuals to be 20, crossover rate to be 0.5, and mutation rate to be 0.1. One individual was generated within one second, so that 50 generations were completed in 15 minutes. The evolution of the population fitness with number of generation is plotted in Fig. 4, which indicates that the fitness was enhanced up to 4.5 times of that generated by flat voltage array. During the evolution of generation, the best individual was always recorded. Figure 5 is the SPIDER result for the compressed pulse using the adaptive pulse compressor with the best individual. The pulse duration was reduced from 84 fs to 23 fs. We have room to compress the beam further because the

transform-limited pulse duration is 19.5 fs, but it was not achieved with several trials. This is because the spectral phase shown in Fig. 5(b) was not flattened at the marginal region of the spectrum. This situation can be improved if we use the spectral phase curve itself as the fitness.

We tried controlling the SH spectrum by adaptive pulse shaping, too. By maximizing a particular wavelength of SH spectrum, we could control the SH spectrum within limited degree. Figures 6 shows the result of controlled spectra maximized at 413 nm and 425 nm, respectively, where the SH center wavelength is originally 419 nm. In the results, the SH spectra was maximized at 415 nm and 423 nm, respectively. The temporal pulse shapes in Figs. 6(b) and (d) are very different. Especially, the pulse profile in Fig. 6(b) was very complicated, which is hard to be estimated without the adaptive pulse shaping system. This pulse shaping system can be used for the general coherent control experiment using femtosecond laser pulse.

IV. Conclusion

We setup an adaptive pulse compressor using an MMDM in combination with GA. 84-fs pulses were compressed down to 23 fs using this system after 15-minute optimization process. Further compression can be achieved by adopting the spectral phase curve measured by SPIDER as the fitness in GA. The SH spectra were also controlled using this system, where the maximization of the peaks at the wavelength of 415 nm or 423 nm was demonstrated. The adaptive pulse shaper will be used for the spectral phase optimization of the amplified pulses in a CPA laser.

References

[1] A. M. Weiner, D. E. Leaird, J. S. Patel, and J. R. Wullert, IEEE J. Quantum Electron. **28**, 908 (1992).

[2] E. Zeek, K. Maginnis, S. Backus, U. Russek, M. Murnane, G. Mourou, H. Kapteyn, and G. Vdovin, Opt. Lett. **24**, 493 (1999).

[3] R. Bartels, S. Backus, E. Zeek, L. Misoguti, G. Vdovin, I. P. Christov, M. M. Murnane, and H. C. Kapteyn, Nature **406**, 164 (2000).

[4] J. F. Frenzel, IEEE Potentials **12**, 21 (1993).

[5] Y. H. Kang, K. H. Hong, C. H. Nam, 한국광학회지(Hankook Kwanghak Hoeji) **12** 219 (2001).

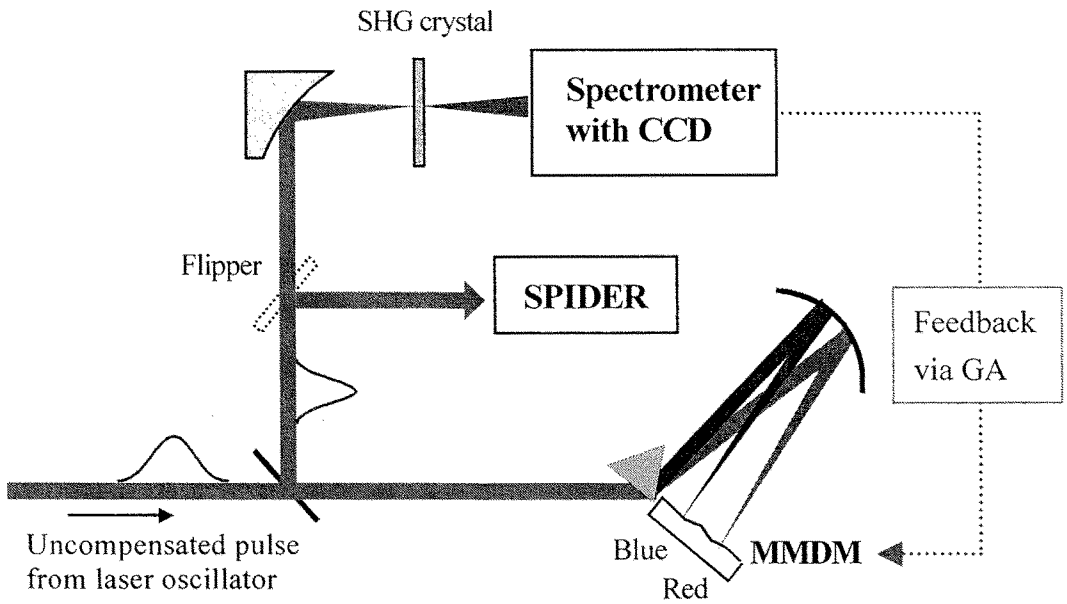

Fig. 1 Experimental setup of adaptive pulse compressor.

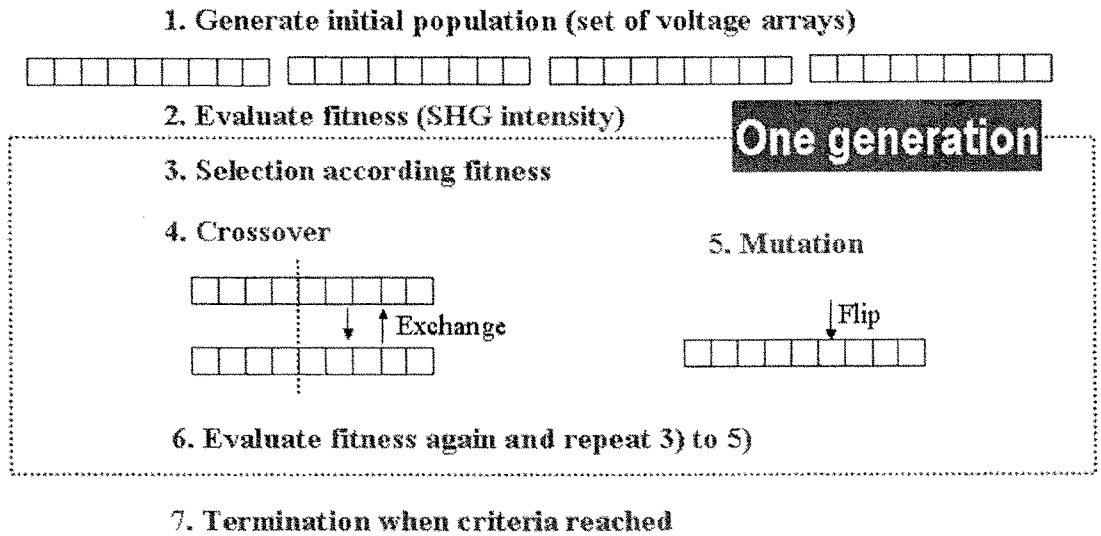

Fig. 2 Procedure of simple GA. The process follows the principle of survival of the fittest.

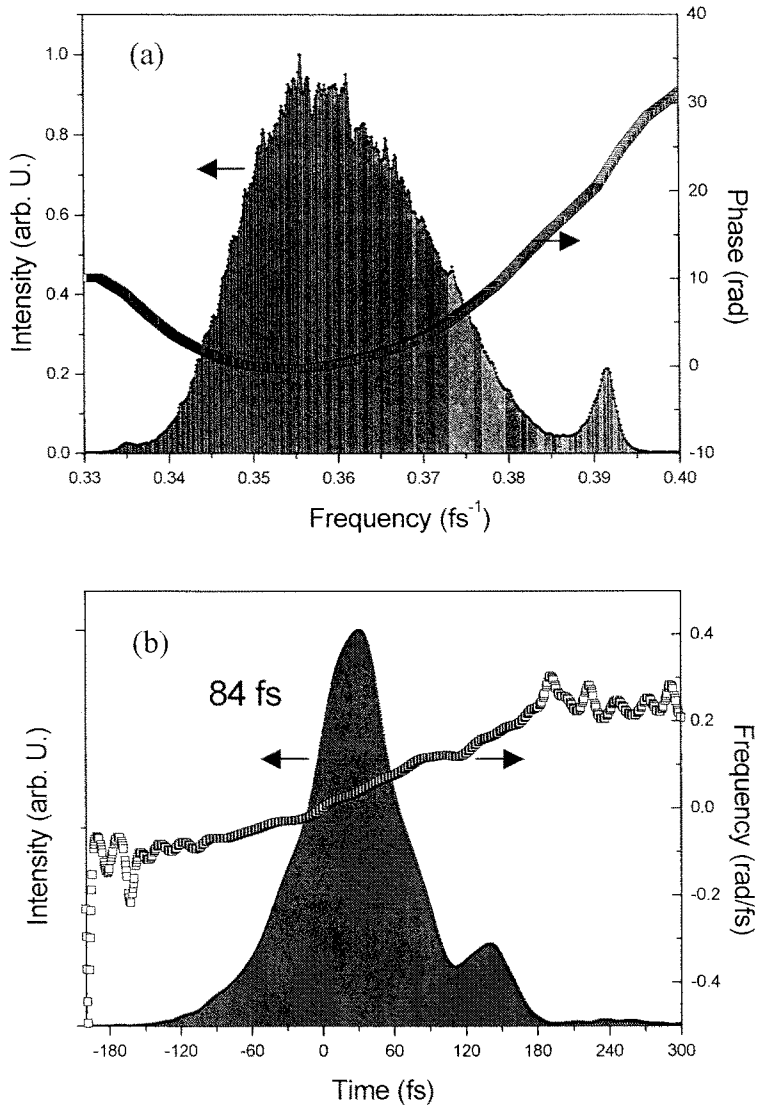

Fig. 3 Spectral (a) and temporal (b) characteristics of chirped pulse uncompressed

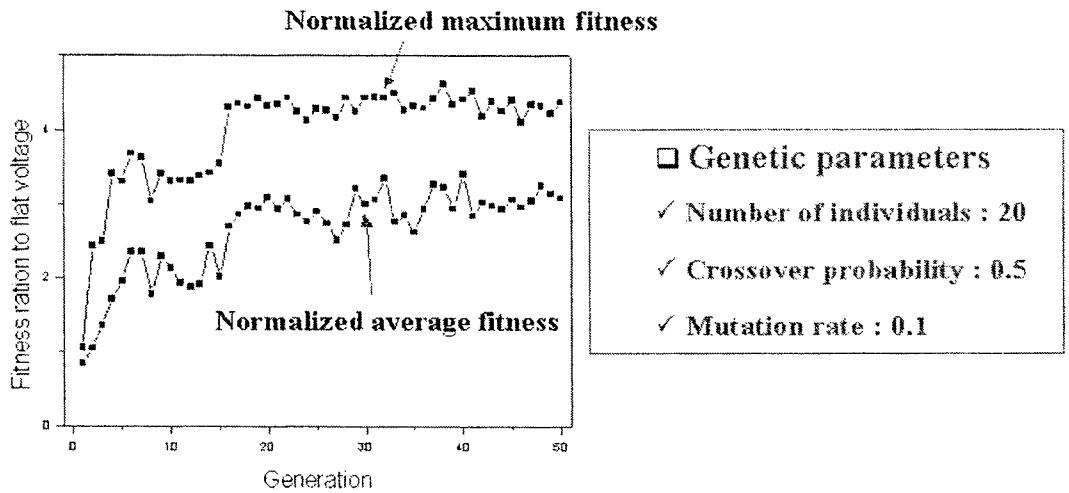

Fig. 4 Evolution of population versus evolution of generation. The fitness is being enhanced with evolution of generation and then stagnates after 16^{th} generation.

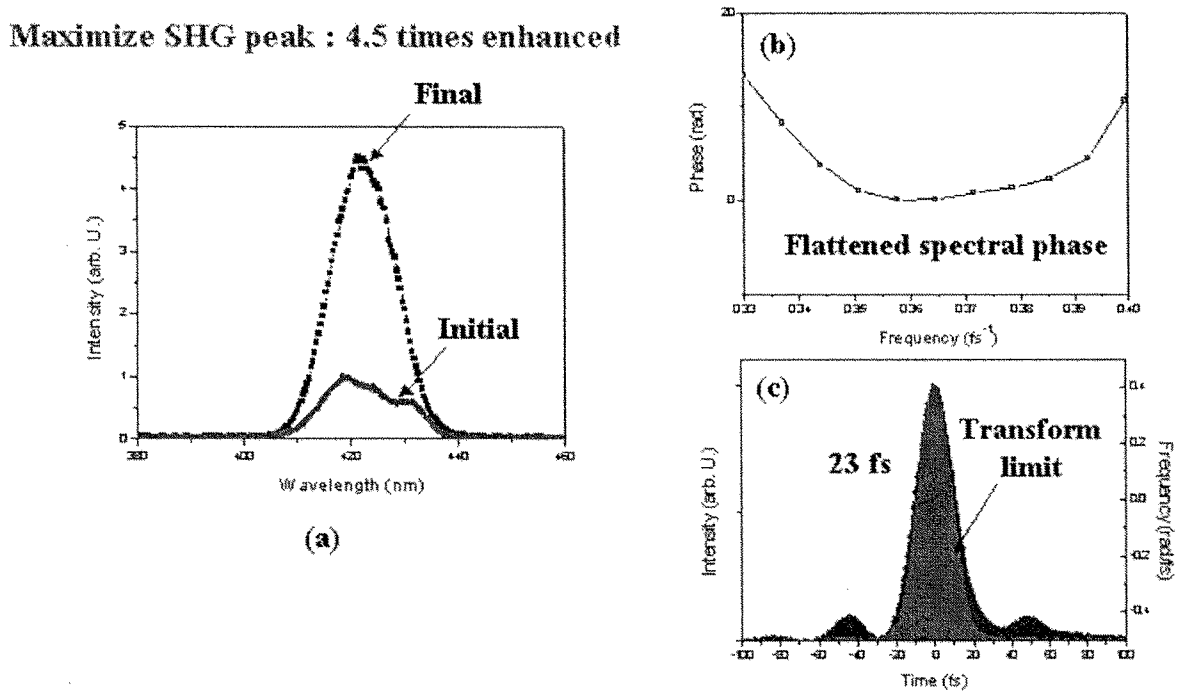

Fig. 5 Pulse compression result. The SHG peak intensity was enhanced up to 4.5 times , (a) the spectral phase became flattened, (b) and the pulse duration was reduced, (c) The spectral phase at marginal region of the spectrum should become more flattened for further compression.

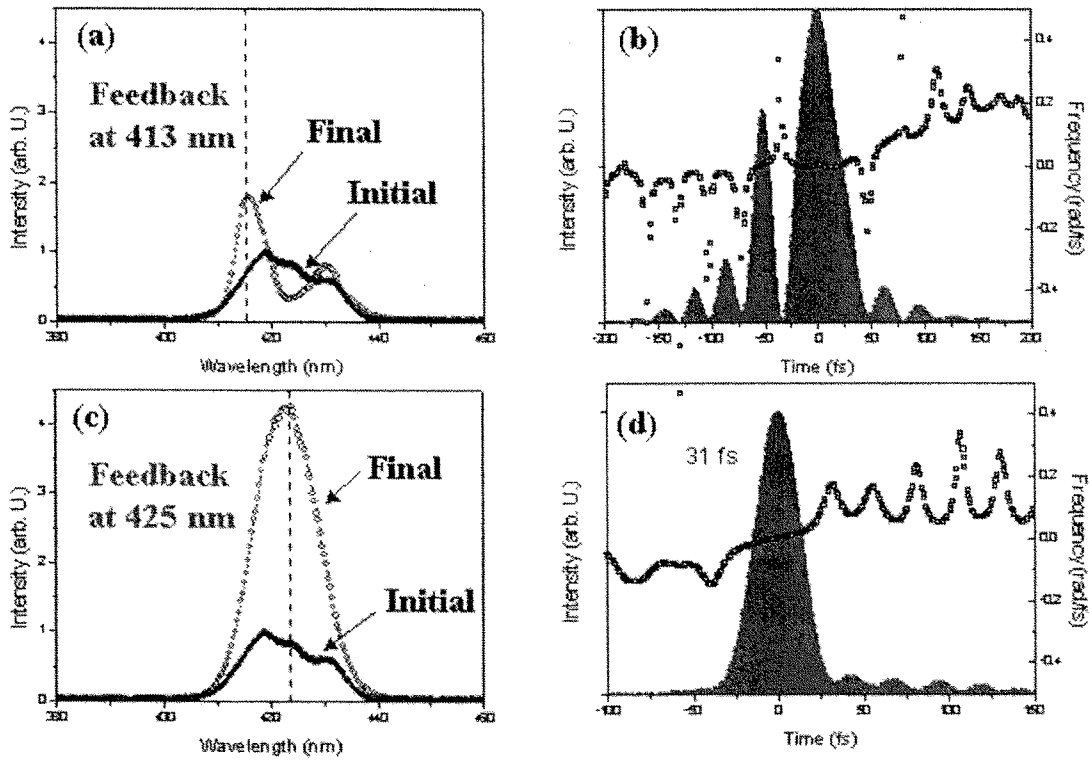

Fig. 6 The control of peak wavelength of SH spectrum using the adaptive pulse shaper. The peak at 415 nm was maximized when the feedback was done at 413 nm(a), and corresponding temporal profile was very complicated(b). The peak at 423 nm was also maximized when the feedback was done at 425 nm(c). The signal was enhanced over 4 times. The corresponding pulse shape was relatively simple.

A. 4. Emission of a hot electron jet from intense femtosecond laser-cluster interactions

Hot electrons with energy higher than 50 keV were detected from the interaction of a laser pulse of duration 28 fs and intensity $1x10^{17}$ W/cm^2 with Ar clusters. Emission of a directional hot electron jet was observed along the laser propagation direction when the femtosecond laser pulse interacted with high local density atomic clusters. Channel betatron resonance is believed to be the main accelerating mechanism for this directional hot electron jet.

The interaction of intense ultrashort laser pulses with van der Waals-bonded atomic clusters has been intensively studied. The high local density within a cluster, coupled with low average-density gas, creates a unique condition for effective coupling of an intense laser pulse with interacting medium. It has been observed that cluster targets could absorb incident laser energy very efficiently [1], producing strong extreme ultraviolet (XUV) emission [2] along with high-energy electrons [3] and ions [4]. These observations are much different from the irradiation of gas targets, in which low energy electrons and small yield of XUV radiation are produced. In addition, T. Ditmire [5] has demonstrated nuclear fusion reactions in laser–cluster interactions.

Compared to soft x rays and high energy ions produced by intense irradiation of clusters electron measurement from laser-cluster interaction has not received much attention. Until now, to our knowledge, only Y. L. Shao [3] presented a study on hot electrons. It showed that, at modest laser intensity, rapid collisional heating of electrons in the cluster yielded an electron distribution that exhibited two distinct peaks - warm and hot electrons - with energies ranging up to 3 keV. The warm electrons came from the collisional heating early in the pulse. The hot electrons, on the other hand, resulted from extensive collisional heating of electrons in the bulk of the cluster. The hot electrons appeared to be an evidence for a resonance in the electron heating when the cluster electron density drops to three times the critical density, called "giant" resonance. These results indicated that the interaction of an intense laser pulse with atomic clusters efficiently coupled laser energy to electrons. The laser intensity used, however, was rather low ($1x10^{16}$ W/cm^2) and pulse width was 150 fs. Consequently, additional

experimental results are needed for extensive understanding of the laser-cluster interactions at higher laser intensity with various kinds of cluster parameters, especially at shorter pulse duration.

Hot electrons generated by intense laser pulses incident on rare gas targets have attracted much attention because of their relevance to advanced concept accelerators and radiation sources [6]. High electron beam can be generated mainly through two mechanisms. One is the forward Raman scattering or self-modulated laser wake-field acceleration (LWFA) [8]. With laser intensities well above 10^{18} W/cm^2, relativistic self-channeling is stimulated as the laser intensity exceeds the critical power given by $P_{RSF} \approx 17(n_c / n_e)$ GW [7], where n_c is the critical density ($= 1.7 \times 10^{21}$ cm^{-3} at 820 nm). When combined with ion inertia that provides an electrostatic restoring force, laser field can drive a high amplitude electron plasma wave. Through this process, some of laser energy is converted into a longitudinal electrostatic laser wake field, propagating at nearly the speed of light, which continuously accelerates electrons in the direction of laser propagation so that electron energy can reach GeV level in a distance as short as a centimeter. This kind of mechanism is considered dominant at low gas density and high laser power. The second acceleration mechanism that exists at high gas density but comparably low laser power is the direct laser acceleration (DLA) at the channel betatron resonance (CBR). It was first described by Pukhov [9] when the laser power overcomes significantly the critical power for self-focusing. Strong self-generated static electric and magnetic fields can confine energetic electrons in relativistic laser channel. The relativistic electrons make transverse oscillations at the betatron frequency $\omega_\beta \approx \omega_p / (2\gamma)^{1/2}$ in these fields while drifting along the channel, in which γ is the relativistic factor and ω_p is the plasma frequency. When ω_β coincides with the laser frequency, the channel betatron resonance results in an effective energy transfer between laser wave and electrons. The increments of energy gain from the transverse electrostatic channel field are then converted into increments of longitudinal energy gain via $v \times B$ interaction. The DLA can be stimulated at comparably lower intensity than LWFA but at higher gas densities. Gahn [10] reported on the observation of electron beams generated by DLA in an experiment with a gas target.

In this Letter, we report, for the first time, the observation of a hot electron jet emission from the interaction of laser pulses with modest intensity ($1x10^{17}$ W/cm^2) with atomic clusters. And we show that this phenomenon exists only when linearly polarized laser pulses are incident on clusters, and that these hot electrons are generated by the DLA with CBR heating mechanism.

The experiments were carried out with a chirped pulse amplification (CPA) Ti:Sapphire laser operating at 820nm at a repetition rate of 10 Hz. The laser delivered 28 fs, 30 mJ pulses. The Ti:Sapphire oscillator was operated in a long cavity mode (45 MHz), which lowered the ratio of prepulse to main pulse below 10^{-5}. The linearly polarized laser beam was focused with a f /45-cm spherical mirror, yielding a peak intensity of about $1x10^{17}$ W/cm^2. A $\lambda/4$ waveplate was used when a circularly polarized light was needed. The atomic Ar clusters were produced with a pulsed gas jet with a nozzle diameter of 0.2 mm. With sufficiently high backing pressure, clusters are formed in the gas jet flow due to the cooling associated with an adiabatic expansion of the gas into vacuum [11]. The jet was operated at a backing pressure up to 22 bars.

For large rare gas clusters, the final mean cluster size (atoms per cluster) has been shown to be reasonably well predicted by the expression $\langle N\rangle=33(\Gamma^*/1000)^{2.35}$ (for $\Gamma^*>1000$), where Γ^* is the dimensionless Hagena parameter given by $\Gamma^*=k[d/\tan(\alpha)]^{0.85}P_0T_0^{-2.29}$ [11], where k=1650 for Ar and the other parameters are defined in Ref. 14. Experiments have shown that for $\Gamma^*>2000$ the condensed fraction in the cluster beam is above 90% [12]. The cluster size estimation based on the Hagena parameter gives a reasonable agreement with other methods such as the Rayleigh scattering [13].

The main diagnostic for the measurement of hot electrons was a 45^0 focusing magnetic spectrometer, placed in a permanent magnetic field of B = 650 Gauss. An array of LiF thermoluminescent dosimeter (TLD) pieces (model GR-200F) was used as detectors. Recent development of ultra-sensitive LiF TLD provided thin TLD for hot electron detection [14]. The energy range of this instrument covered from 7 keV to 1 MeV. The collection angle of the spectrometer was in the order of $5x10^{-3}$ sr. Its energy resolution was better than 5%. The background of these TLDs that were heat-treated at 240^0C was less than 10 μGy. In some cases, we also piled up several Al foil wrapped TLD pieces to

detect hot electrons. After deconvolution, an electron spectrum was obtained. With TLDs attached inside of a hemisphere, the angular distribution of hot electron emission was measured. Soft x-ray emission was measured using a space-resolving, flat field XUV spectrometer described in Ref 15. We also used a calorimeter to measure a laser absorption rate in laser-cluster interactions and a visible CCD to measure a plasma length.

Hot electron angular distribution was measured in the horizontal plane with hemispherically installed detectors. Array of TLD detectors wrapped with 18 μm thick Al foil was placed on the inner side of the hemisphere. This Al foil is capable of blocking energetic ions, scattered laser light, majority of soft x-rays and electrons with energy below 50 keV. Consequently, this system is suitable for the detection of energetic electrons. The hot electrons angular distribution is shown in Fig. 1(a) obtained with a laser intensity of $1x10^{17}$ W/cm^2 and Ar backing pressure of 20 bars. The gas nozzle was cooled down to the temperature of -70^0C using a cooling chamber [16]. At this temperature and Ar backing pressure, an average cluster radius of about 40±8 Å was inferred from a Rayleigh scattering measurement [16].

A sharply directional hot electron jet emission was observed along the laser propagation direction. The angular divergence of the hot electron jet is less than 30^0 at FWHM. The highest TLD dose is nearly several tens of mGy, which is about 1000 times higher than that in the transverse emission. Figure 2 shows that the hot electron spectra measured in the forward and transverse directions. It also shows that the electron flux in the forward direction is much higher than that in the transverse direction even if we integrate the whole spectrum. Another important feature is the difference in electron temperature: in the forward direction, hot electron temperature for maxwellian distribution can be as high as 250 keV. But in the transverse direction, it is only 60 keV. It indicates that electrons are strongly accelerated along the laser propagation direction.

This result would not be observed if clusters are disassembled while other conditions are kept the same. For the sake of verifying the hot electron jet emission detected is really generated through the interaction of intense laser pulse with atomic clusters, 7% of the laser pulse was split as a prepulse and injected 80 ps before the main pulse. This

prepulse was still strong (>10^{15} W/cm^2) enough to make clusters heated and expanded. Most clusters are completely disassembled when the main pulse comes 80 ps after the prepulse, according to the expansion time scale for clusters [17], especially at the central part of the focal spot. With the prepulse, observed electron angular distribution was much different from the prepulse-free case. As in Fig. 1(b), electron flux decreased dramatically and jet emission in the forward direction was nearly absent. Thus, we can draw a conclusion that the hot electron jet observed in the prepulse-free case was really generated from irradiated clusters. In another experiment, a circularly polarized laser pulse was incident on cluster. No hot electrons were detected by TLD in hemisphere and also in the electron spectrometer, which means that measured hot electrons are unique for linearly polarized laser interacting with atomic clusters.

It is of great importance to determine the emission mechanism of the hot electron jet at our experimental conditions. Inverse Bremsstrahlung (IB) cannot generate high-energy electrons at this modest laser intensity [18]. The result obtained with circularly polarized laser pulses also verifies this assertion. It is not possible for these electrons to come from photoelectrons through high-order above-threshold ionization (ATI) process because the ponderomotive energy (average energy of sinusoidally oscillating free electrons) $U_p = e^2 E_0^2 / 4 m_e \omega^2$ is less than 6 keV at this intensity [19]. These photoelectrons cannot pass through the 18-μm Al foil and also the direction of the electron emission from ATI is along the laser polarization [20]. Only two kinds of mechanism can produce hot electrons along the laser propagation direction - LWFA and CBR. The laser intensity to stimulate the LWFA is in the relativistic regime, much higher than the laser intensity used in our experiments. The observation that the emission of a hot electron jet was absent in the cases of the prepulse and of the circularly polarized pulse rules out the possibility of LWFA because the hot electron emission cannot be greatly affected by a prepulse or by laser polarization in the case of LWFA [8]. Therefore, LWFA cannot be the mechanism to generate the hot electron jet at our experimental conditions, i.e. linearly polarized laser-cluster interactions.

CBR, on the other hand, can occur in the interaction of high-local-density cluster with a laser at modest intensity. CBR is a resonance process, which means a laser pulse can efficiently couple with a medium under appropriate conditions. This assumption is supported by our laser energy absorption measurement. Figure 3 shows the laser absorption rate for Ar with respect to different backing pressure. The absorption rate becomes as high as 50% at the backing pressure of 20 bars. It indicates a strong laser-cluster coupling at this condition. But if clusters were destroyed by a prepulse, the

interaction becomes much weaker and the absorption rate is less than 10%. Even the majority of this 10% absorption may come from the cluster-prepulse interaction.

The observed electron spectrum also supported this conclusion. Figure 4 shows the hot electron spectrum measured in the transverse direction. These hot electrons that reach energy above 100 keV should come from the giant resonance [21], resulting from resonantly driven electrons in expanding clusters by the incident laser pulse. This may be further confirmed by the peak electron energy and electron temperature and the measurements of cluster expansion dynamics. The electron spectrum in the case of the interaction with prepulse in Fig. 4 shows that the hot electron flux is dramatically reduced and the electron energy drops monotonically. The results that the hot electrons in the case without prepulse are much larger in quantity and have much higher energy than those from the interaction with prepulse are an evidence that the hot electrons in the case without prepulse are generated in the laser-cluster interaction through the giant resonance process. The hot electron spectra in the transverse direction, which is distinguished from LWFA of which the electron emission occurs only along the laser propagation direction, indicates that the giant resonance is the first process of CBR. Electrons are first heated by the giant resonance process and then accelerated along the laser propagation direction through a VxB drift by a self-generated azimuthal magnetic field

The second important feature to show the stimulation of CBR is that the laser power must exceed the critical power for laser self-channeling. The gas density at our experiment was $6x10^{18}$ cm^{-3}. At this laser intensity and gas temperature, Ar^{8+} can be generated when intense laser pulses interact with clusters [16]. This means the average electron density can be close to $5x10^{19}$ cm^{-3}. Under this electron density, the laser power used, 1.1 TW, can satisfy the CBR threshold set by the critical power P_{th} (=0.6TW). On the other hand, in the case with a prepulse most clusters are destroyed before the arrival of the main pulse; so, the electron density cannot be as high as that without prepulse. Since the CBR threshold power is inversely proportional to n_e, it should increase with decreasing n_e; however, the laser power used in the experiment cannot significantly exceed the threshold power for the CBR stimulation. Thus no jet emission was observed in the case with prepulse.

A direct method to verify the CBR stimulation may be to detect the formation of a plasma channeling [10]. We measured the plasma length to prove that a plasma channel could be formed in our laser-cluster experiments. The visible images of plasmas generated by laser pulses with and without prepulse are shown Fig. 5(a) and (b), respectively. The gas temperature was cooled up to -70^0 C. The plasma length obtained with a prepulse was about 500 μm (Fig. 5(a)), and this length did not change significantly at different gas temperature. In the case without prepulse, the plasma length increased by more than a factor of 2, reaching 1400 μm (Fig. 5(b)), and the plasma volume and brightness were increased with cooling. Thus, in this case the plasma channel was formed, stimulating the CBR heating.

For the laser self-channeling or -focusing which is very important to stimulate CBR and its also a feature of it, can be explained in other way besides the increment of electron density. the gas clustering will cause the plasma anisotropic distribution, it will also cause the enhancement for the laser self-focusing according to numerical simulations from L. M. Chen and H. Lin [23] because clustering will lead to enhancement for the fluctuation mode.

In conclusion, we observed a directional hot electron jet emission when intense femtosecond laser pulses with a duration of 28 fs and intensity of $1x10^{17}$ W/cm^2 interacted with Ar clusters. Experimental results, showing the polarization dependence, prepulse effect and channel formation, indicate that the hot electron jet emission comes from the CBR when the intense femtosecond laser pulse efficiently couples with clusters. There can be two applications for this new result: (1) The threshold laser intensity for generating an electron accelerator can be decreased through clustering of a high-pressure gas. It will be a new method to generate the electron beam source in a weak relativistic laser system. (2) If this method is applied to a relativistic laser system with an intensity over $1x10^{18}$ W/cm^2, the electron accelerator may be more efficient than the previous results, giving a direction for future works.

References

[1] T. Ditmire, R. A. Smith, J. W. G. Tisch, and M. H. R. Hutchinson, Phy. Rev. Lett. **78**, 3121 (1997).

[2] T. Mocek, C. M. Kim, H. J. Shin, D. G. Lee, Y. H. Cha, K. H. Hong, and C.H. Nam, Phys. Rev. E 62, 4461 (2000).

[3] Y. L. Shao, T. Ditmire, J. W. G. Tisch, E. Springate, J. P. Marangos, and M. H. R. Hutchinson, Phys. Rev. Lett. **77**, 3343 (1997).

[4] T. Ditmire, J. W. G. Tisch, E. Springate, M. B. Mason, N. Hay, R. A. Smith, J. Marangos, and M. H. R. Hutchinson, Nature, **386**, 54 (1997).

[5] J. Zweiback, R. A. Smith, T. E. Cowan, G. Hays, K. B. Wharton, V. P. Yanovsky, and T. Ditmire, Phys. Rev. Lett. **84**, 2634 (2000).

[6] T. Tajima and J. M. Daeson, Phys. Rev. Lett. **43**, 267 (1979).

[7] C. Max, J. Arons, and A. B. Langdon, Phys. Rev. Lett. **33**, 209 (1974).

[8] A. Modena et al., Nature **377**, 606 (1995); R. Wagner, S.-Y. Chen, A. Maksimchuk, and D. Umstadter, ____**78**, 3125 (1997); D. Gordon, K. C. Tzeng, C. E. Clayton, A. E. Dangor, V. Malka, K. A. Marsh, A. Modena, W. B. Mori, P. Muggli, Z. Najmudin, D. Neely, C. Danson, and C. Joshi, ___**80**, 2133 (1998).

[9] A. Pukhov, Z. –M. Sheng, and J. Meyer-ter-Vehn, Phys. Plasmas **6**, 2847 (1999).

[10] C. Gahn, G. D. Tsakiris, A. Pukhov, J. Meyer-ter-Vehn, G. Pretzler, P. Thirolf, D. Habs, and K. J. Witte, Phys. Rev. Lett. **83**, 4772 (1999).

[11] O. F. Hagena and W. Obert, J. Chem. Phys. **56**, 1793 (1972).

[12] J. Wörmer, V. Guzielski, J. Stapelfeldt, and T. Möller, Chem. Phys. Lett. **159**, 321 (1989).

[13] J. S. Zweiback, Ph.D thesis, University of California, 1999 (UCRL Report No. LR-134008).

[14] L. M. Chen, J. Zhang, H. Teng, Q. L. Dong, Z. L. Chen, T. J. Liang, L. Z. Zhao, and Z. Y. Wei, Phys. Rev. E **63**, 036403 (2001); L. M. Chen, J. Zhang, Q. L. Dong, H. Teng, T. J. Liang, L. Z. Zhao, and Z. Y. Wei, Phys. Plasmas **8**(6), 2925 (2001).

[15] I. W. Choi, J. U. Lee, and C. H. Nam, Appl. Opt. **36**, 1457 (1997).

[16] T. Mocek, C. M. Kim, H. J. Shin, D. G. Lee, Y. H. Cha, K. H. Hong, and C. H. Nam Appl. Phys. Lett. **76**, 1819 (2000).

[17] J. Weiback, T. Ditmire, and M. D. Perry, Phy. Rev. A **59**, R3166 (1999).

[18] D. F. Price, R. M. More, R. S. Walling, G. Guethlein, R. L. Shepherd, R. E. Stewart, and W. E. White, Phys. Rev. Lett. **75**, 252 (1995).

[19] B. Walker, B. Sheehy, L. F. DiMauro, P. Agostini, K. J. Schafer, and K. C. Kulander Phys. Rev. Lett. **73**, 1227 (1994).

[20] C. I. Moore, A. Ting, T. Jones, E. Briscoe, B. Hafizi, R. F. Hubbard, and P. Sprangle, Phys. Plasmas **8**, 2481 (2001); C. I. Moore, A. Ting, K. Krushelnick, E. Esarey, R. F. Hubbard, B. Hafizi, H. R. Burris, C. Manka, and P. Sprangle, Phys. Rev. Lett. **79**, 3909 (1997).
[21] L. M. Chen, J. J. Park, K. H. Hong, I. W. Choi, J. Y. Kim, C. H. Nam, (to be submitted).
[22] T. Ditmire, R. A. Smith, and M. H. R. Hutchinson, Opt. Lett. **23**, 322 (1998); T. Ditmire and R. A. Smith, Opt. Lett. **23**, 618 (1998).
[23] L. M. Chen and H. Lin, Phys. Plasmas **8**, 2974 (2001).

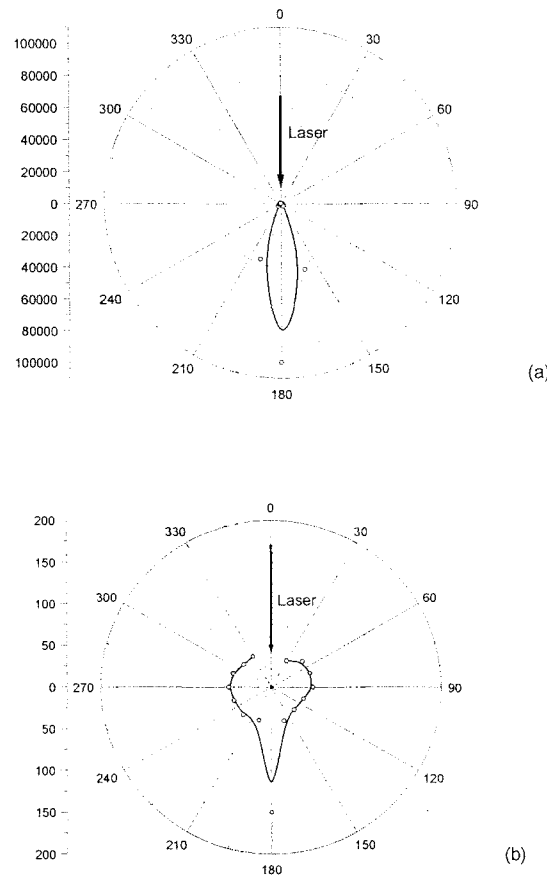

Fig 1. Angular distribution of hot electrons at horizontal plane with energy over 50 keV. (a) Laser pulse of an intensity $1x10^{17}$ W/cm^2 was interacting with Ar clusters, and (b) the same laser pulse, but containing a prepulse at 80 ps in advance, was incident on clusters.

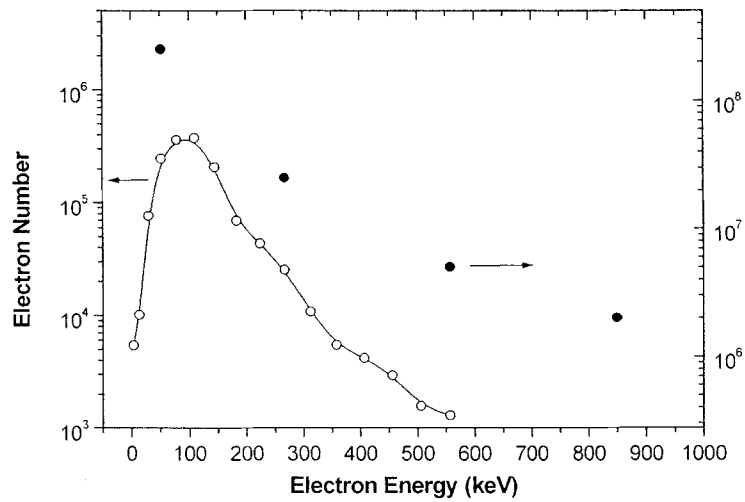

Fig. 2. Hot electron spectra measured along the longitudinal direction (solid circle) and transverse direction (open circle).

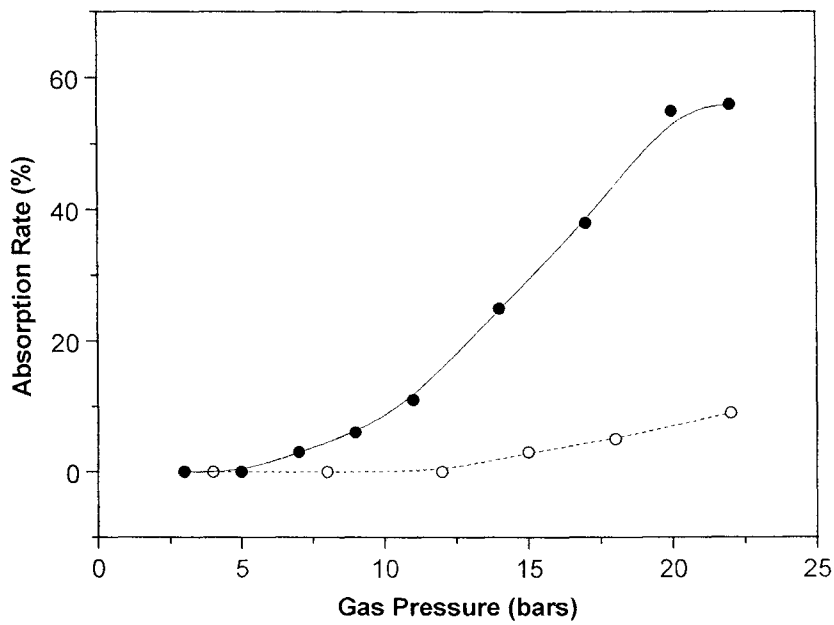

Fig. 3. Laser absorption rate with respect to the backing pressure of Ar in the case of a laser pulse without a prepulse (solid circle) and with a prepulse 80 ps in advance (open circle). The laser intensity was $1x10^{17}$ W/cm^2.

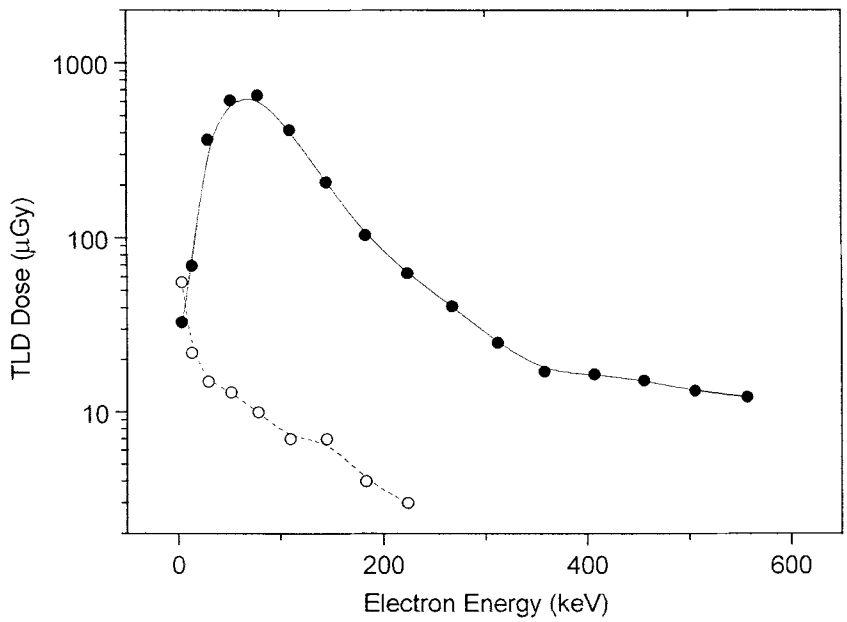

Fig. 4. Typical electron spectrum in the transverse direction without any prepulse (solid circle) and with a prepluse at 80 ps before the main pulse (open circle).

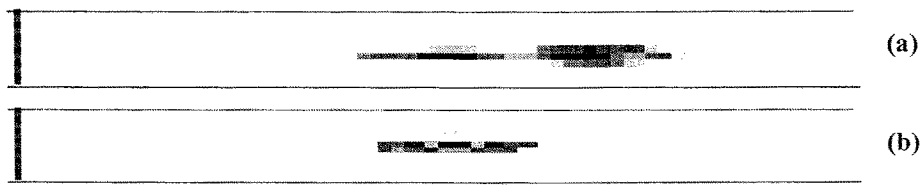

Fig. 5. Plasma length observed with a laser pulse with prepulse 80 ps in advance (a) and without prepulse (b).

Appendix (III)

Research results of FY 2001

A. 1. High harmonic x-ray generation

A. 2. Theory of high harmonic generation

A. 3. Development of high power femtosecond laser technology

A. 1. High Harmonic X-Ray Generation

A. 1. 1. Chirp analysis of high-order harmonics from atoms driven by intense femtosecond laser pulses

Chirp structure of high-order harmonics was analyzed using chirped femtosecond laser pulses. Harmonic spectra obtained from Ne and He gases showed that harmonic chirp was generated due to the induced positive laser chirp in a rapidly ionizing medium as well as the dynamically induced negative chirp.

Atoms driven by laser pulses of ionizing intensity can radiate high-order harmonics in the soft-x-ray region. High-order harmonics have attracted much attention due to their unique features such as good coherence [1], ultrashort time duration [2], and tabletop scale. Recently, the rapid progress of intense femtosecond laser technique has led to the generation of high harmonics with wavelength with in the 'water-window' x-ray region [3.4], attosecond pulse duration [5,6] and high brightness [7,8].

The semi-classical explanation [9] of high-order harmonic generation provides a physical understanding of the process. According to this model, high harmonics are generated due to the repetition of three successive processes – tunneling ionization, acceleration of the ionized electron in the intense laser field and recombination of the accelerated electron with the ionic core. Through the acceleration and recombination of the ionized electron, the harmonics acquire a dynamically induced phase that depends on the laser intensity. Especially, the rapidly changing laser intensity can induce a negative harmonic chirp. This dynamically induced negative chirp of the harmonics has been studied both experimentally and theoretically [10-12].

High-order harmonic generation is intrinsically related to the ionization of the medium. While propagating through an ionizing medium, the laser field can be temporally modulated, which leads to self-phase modulation (SPM). This in turn affects the harmonic generation and the harmonics can become chirped. Previously, we have reported that the ionizing medium induces a positive chirp on the leading edge of propagating laser pulses and the harmonics also became positively chirped [13]. Therefore, two different types of chirp, i.e., the dynamically induced chirp and the SPM-induced chirp, can affect the spectral structure of high harmonics. Near the saturation laser intensity for the optical field ionization (OFI), the harmonic spectrum

can still be broad and weak, even though the target medium is positioned for good phase matching. This is because of the chirp of harmonics that is competitively induced by both, the SPM of fundamental field and the dynamic process of harmonic generation.

In this paper, the chirp structure of high-order harmonics was investigated using chirped femtosecond laser pulses. Applied laser intensity is around the OFI saturation intensity and the observed spectral region was between 11 nm and 17 nm. Two different gases, Ne and He, were used in the experiments to examine the dependence of harmonic chirp on the atomic species.

The experiments were performed with a chirped pulse amplification Ti:sapphire laser operating at 10Hz. For the reduction of gain narrowing the long wavelength injection method was used [14]. The laser spectrum had a center wavelength of 824 nm and a 50-nm bandwidth. The output pulse duration was 25 fs as measured using a second-harmonic generation (SHG) frequency-resolved optical gating (FROG) technique. A half-wave plate and polarizers were placed in front of the pulse compressor for the control of laser intensity. The laser beam was focused into a gas jet, puffed from a 0.5-mm diameter circular nozzle, using a spherical mirror with 60-cm focal length. Gas density profile in the interaction region had a width of 0.5 mm (FWHM). The gas density was controlled over a range from 10^{17} to 10^{19} cm^{-3} by adjusting the time delay between the seeding time of a laser pulse and the gas jet opening time. The peak gas density used in the experiment was 3×10^{19} cm^{-3} for both Ne and He. Gas jet was positioned 1 mm before the laser focus to achieve a strong harmonic signal. The spatial profile of focused beam was measured with a 12-bit charge-coupled device (CCD), after magnification using a microscope objective lens. It showed a clear Airy pattern that closely matched a truncated Gaussian profile calculated from diffraction theory, and the central Airy disk contained 70 % of the full laser energy. The generated harmonics were detected by a flat-field extreme ultraviolet (XUV) spectrometer equipped with a back-illumination X-ray CCD with 400x1340 pixels (Princeton Instruments). Two Zr filters with a total thickness of 400 nm were placed in front of the CCD to block scattered laser light.

The chirp of laser pulses was controlled by changing the separation of the grating pair in the pulse compressor, which varied the linear chirp of femtosecond laser pulses [15, 16]. Decreasing the spacing between the two gratings, with respect to the chirp-free separation, provided positively chirped pulses, while increasing it produced negatively

chirped pulses. The spectral phase and the duration of chirped laser pulses were measured at various grating separation using the SHG FROG method, which showed a close match to the calculated temporal characteristics using a ray tracing formula for a grating pulse compressor. Chirp-free pulses of 25-fs duration were generated at the optimum grating separation (l=0), positively chirped pulses of 102 fs at l=-0.5 mm and negatively chirped pulses of 107 fs at l=+0.5 mm. The dependence of temporal pulse width on the grating separation was almost quadratic to the laser chirp except for a small asymmetry [16].

Harmonic chirp is generated by both the dynamically induced negative chirp and the SPM-induced positive chirp. The dynamically induced harmonic chirp is basically a single atom effect. However, the SPM-induced harmonic chirp is a macroscopic effect since it arises due to the change of refractive index with time. Thus, the latter becomes important at high density of the gas medium. For the given medium density, the SPM-induced harmonic chirp will become important as applied laser intensity increases. Recent calculations [13] showed that the harmonic could possess positive chirp due to the SPM-induced laser chirp. Consequently, a proper analysis of harmonic chirp is crucial for the production of strong and sharp harmonics.

Harmonic spectra obtained from neon for various chirp conditions of laser pulses are shown in Fig. 1 wherein the laser chirp was adjusted in the pulse compressor; the laser energy was kept constant. In the case of Fig. 1 (a), the laser intensity, $1x10^{15}$ W/cm^2, for the chirp-free pulse was below the saturation intensity ($1.6x10^{15}$ W/cm^2 for 98% ionization with 25-fs pulses), and sharp and strong harmonics were obtained with positively chirped laser pulses (negative change in the grating separation corresponds to positive laser chirp). This means that the negative harmonic chirp, dominated by the dynamically induced harmonic chirp, was compensated by the positively chirped laser pulses. In contrast, negatively chirped laser pulses generated broad and weak harmonic spectra. At this laser intensity, positively chirped 47-fs laser pulses (grating separation of -100 μm) were most effective in removing harmonic chirp and thereby achieving sharp harmonics.

As the laser intensity increased over the saturation intensity, the chirp structure of harmonics changed dramatically. With the chirp-free laser intensity of 5×10^{15} W/cm^2 (Fig. 1 (b)), the harmonics generated by chirp-free or positively chirped laser pulses were almost smeared out. On the other hand, negatively chirped pulses generated

narrow and intense harmonics. This means that the SPM-induced positive chirp was greater than the dynamically induced negative chirp of harmonics and the resulting positive harmonic chirp was compensated by the negatively chirped laser pulses. The optimized chirp condition was achieved by negatively chirped 107-fs pulses (grating separation of +500-μm) that generated the 61st harmonic stronger by more than a factor of 5 than that of the chirp-free case. These results are in agreement with our previous work on the coherent control of high-order harmonics from neon [17].

Next, harmonics from helium were obtained for comparison with the Ne results. Figure 2 shows the dependence of the harmonic spectra of He on laser chirp. At the laser intensity of $1x10^{15}$ W/cm^2, which is below the saturation intensity ($2.4x10^{15}$ W/cm^2 for 98 % ionization) [Fig 2 (a)], the optimal laser chirp condition was achieved with the grating separation of -200 μm (positively chirped 54-fs pulse). At this laser intensity, the dynamically induced negative chirp of harmonics dominated and positively chirped laser pulses produced sharp harmonics. When the laser intensity was increased to $5x10^{15}$ W/cm^2 [Fig. 2 (b)], the sign of optimized laser chirp was changed from positive to negative. In this case, the grating separation of +300 μm (negatively chirped 47-fs pulse) generated narrow and strong harmonics, due to the increase of SPM-induced positive chirp. At this optimum chirp condition, the 63rd harmonic had a bandwidth of 0.6 Å and the intensity was stronger by a factor of 2 over that of the chirp-free case. Thus, harmonics from helium showed a behavior similar to that of neon regarding the chirp structure.

The change of the optimum laser chirp needed for the production of strong harmonics for the cases of Ne and He are shown in Fig. 3. Laser pulses with chirp-free intensity of $(1\text{-}5)x10^{15}$ W/cm^2 were applied to Ne and He of density $3x10^{19}$ cm^{-3}. In the case of Ne, positively chirped laser pulses (negative grating separation) generated strong harmonics at the laser intensity of $1x10^{15}$ W/cm^2, but negatively chirped pulses (positive grating separation) were needed for the laser intensity above $2x10^{15}$ W/cm^2. In the case of He, the transition occurred for the laser intensity at $3x10^{15}$ W/cm^2. In general, the harmonics from Ne contained larger positive chirp than those from He. This indicates that the SPM effect in Ne is stronger than in He, due to lower ionization potential. A detailed theoretical investigation is given in following section.

The different chirp structure between helium and neon can be explained by considering the different SPM-induced chirp of harmonics. When sufficiently intense laser pulses

propagate in a rapidly ionizing medium, the rapid change of refractive index in time can cause a strong SPM, which induces a blueshift of the incident laser spectrum. Different parts of the pulse experience different amounts of blueshift due to the nonlinear time dependence of the refractive index of the medium. The time evolution of the laser field in the ionizing medium was obtained by numerically solving the one-dimensional (1D) wave eqation,

$$\frac{\partial^2 E_1(x,t)}{\partial x^2} - \frac{1}{c^2}\frac{\partial^2 E_1}{\partial t^2} = \frac{\omega_p^2(x,t)}{c^2} E_1, \tag{1}$$

where $\omega_p(x,t) = \omega_0[N_e(x,t)/N_{cr}]^{1/2}$ is the local plasma frequency. The critical plasma density N_{cr} is given in Gaussian units by $N_{cr} = m_e\omega_0^2/4\pi e^2$, where m_e is the electron mass. The electron density $N_e(x,t)$ is given by

$$N_e(x,t) = N_0 - N_0 \exp[-\int_{-\infty}^{t} w(x,t')dt'], \tag{2}$$

where N_0 is the initial gas density, and $w(x,t')$ is the ionization rate calculated from the Ammosov-Delone-Krainov model [18].

The SPM-induced frequency shift of the laser pulse and its time dependence can be clearly shown with the help of the Wigner distribution [12] function defined by

$$W(t,\omega) = (1/\pi)\int E^*(t-t')E(t+t')e^{-2i\omega t'}dt', \tag{3}$$

where the $E(t)$ is the laser field obtained by a direct numerical calculation froSm Eq. (1). Figure 4 shows the Wigner distribution of laser fields with intensity between $1x10^{15}$ W/cm^2 and $5x10^{15}$ W/cm^2 propagating through neon and helium. The dotted line connects the peak points of the distribution at specific times. For the chirp free laser intensity of $1x10^{15}$ W/cm^2, the Wigner distribution of the laser field that propagated through the helium gas was almost the same as the initial pulse distribution. At this intensity, the dynamically induced harmonic chirp can easily dominate the whole chirp of harmonics. However, the chirp induced by SPM for the neon gas is not negligible and can reduce the dominant, dynamically induced negative chirp of harmonics. As the laser

intensity increases above the saturation intensity, the harmonic generation occurs only in the leading edge of the pulse due to the depletion of atoms. After the generation of free electrons, the plasma-induced phase mismatch can be too severe for the harmonics to build up and consequently only the positively chirped leading edge of the laser pulse is important for generating high harmonics. At the laser intensity higher than the saturation intensity, plasma-induced positive chirp of the laser pulse can exceed the dynamically induced negative chirp, changing the overall sign of the chirp from negative to positive. This can account for the resilt in the case of Fig. 1 (b) and Fig. 2 (b) wherein the laser intensity of $5x10^{15}$ W/cm^2 is well above the saturation intensity for both neon and helium. However, the amount of the SPM-induced chirp for these two gases was quite different as shown in Fig. 4 (c) and (d). The positive chirp in the leading edge of the laser pulse was about two times higher for neon than for helium and the harmonics from neon were more positively chirped than those generated from helium. This explains why laser pulses with higher negative chirp were necessary for neon than helium to produce sharp harmonics.

We have presented experimental and theoretical study on the chirp structure of high-order harmonics generated by intense femtosecond laser pulses. The harmonic chirp is induced by two different processes, one having a microscopic origin (dynamically induced negative chirp) and the other a macroscopic origin (SPM-induced positive chirp). The net chirp of high-order harmonics was determined by the competition between these two processes. Change in the sign of the harmonic chirp was observed near the saturation intensity. The effects of the SPM-induced chirp on the harmonic structure were important when the laser intensity was well above the OFI saturation intensity. The harmonics from neon were more positively chirped than from helium. The time-frequency analysis using the Wigner distribution function showed that this occurred because of the different amount of SPM-induced chirp for neon and helium. Since the high-power femtosecond laser based on the chirped pulse amplification technique can easily generate linearly chirped pulses, the approach discussed in this paper provides a useful method for the generation of sharp and strong high-order harmonics.

References

[1] L. Le Déroff, P. Saliéres, B. Carré, D. Joyeux, and D. Phalippou, "Measurement of the degree of spatial coherence of high-order harmonics using a Fresnel-mirror interferometer," Phys. Rev. A **61**, 043802 (2000).

[2] P. B. Corkum, N. H. Burnett, and M. Y. Ivanov, "Subfemtosecond pulses," Opt. Lett. **19**, 1870 (1994).

[3] C. Spielmann, N. H. Burnett, S. Sartania, R. Koppitsch, M. Schürer, C. Kan, M. Lenzer, P. Wobrauschek, and F. Krauz, "Generation of coherent x-rays in the water window using 5-femtosecond laser pulses," Science **278**, 661 (1997).

[4] Z. Chang, A. Rundquist, H. Wang, M. M. Murnane, and H. C. Kapteyn, "Generation of Coherent soft x rays at 2.7 nm using high harmonics," Phys. Rev. Lett. **79**, 2967 (1997).

[5] M. Drescher, M. Hentschel, R. Kienberger, G. Tempea, C. Spielmann, G. A. Reider, P. B. Corkum, F. Krausz, "X-ray pulses approaching the attosecond frontier," Science **291**, 1923 (2001).

[6] P. M. Paul, E. S. Toma, P. Breger, G. Mullot, F. Augé, P. Balcou, H. G. Muller, and P. Agostini, "Observation of a train of attosecond pulses from high harmonic generation," Science **292**, 1689 (2001).

[7] M. Nisoli, E. Priori, G. Sansone, S. Stagira, G. Cerullo, S. D. Silvestri, C. Altucci, R. Bruzzese, C. D'Lisio, P. Villoresi, L. Poletto, M Pascolini, G. Tondello, "High-brightness high-order harmonic generation by truncated Bessel beams in the sub-10-fs regime," Phys. Rev. Lett. **88**, 003902 (2002).

[8] D. G. Lee, I. W. Choi, H. T. Kim, K.-H. Hong, A. Bartnik, H. Fiedorowicz, and C. H. Nam, "Generation of bright low-divergence high-order harmonics in a long gas jet," Appl. Phys. Lett. **81**, 3726 (2002).

[9] M. Lewenstein, P. Balcou, M. Y. Ivanov, and A. L'Huillier, "Theory of high-harmonic generation by low-frequency laser field," Phys. Rev. A **49**, 2117 (1994).

[10] Z. Chang, A. Rundquist, H. Wang, I. Christov, H. C. Kapteyn, and M. M. Murnane, "Temporal phase control of soft-x-ray harmonic emission," Phys. Rev. A **58**, R30 (1998)).

[11] T. Sekikawa,T Ohno,T. Yamazaki,Y. Nabekawa, and S. Watanabe, "Pulse

compression of a high-order harmonic by compensating the atomic dipole phase," Phys. Rev. Lett. **83**, 2564 (1999).

[12] J. -H. Kim, D. G. Lee, H. J. Shin, and C. H. Nam, "Wigner time-frequency distribution of high-order harmonics," Phys. Rev. A **63**, 063403 (2001).

[13] J, -H. Kim and C. H. Nam, "Plasma-induced frequency chirp of intense femtosecond lasers and its role in shaping high-order harmonic spectral lines," Phys. Rev. A **65**, 033801 (2002).

[14] Y. H. Cha, Y. I. Kang, and C. H. Nam, "Generation of a broad amplified spectrum in a femtosecond terawatt Ti : sapphire laser by a long-wavelength injection method," J. Opt. Soc. Am. B **16**, 1220 (1999).

[15] K.-H. Hong, J.-H. Kim, Y. H. Kang, and C. H. Nam, "Time-Frequency Analysis of Chirped Femtosecond Pulses using Wigner Distribution Function," Appl. Phys. B **74**, S231 (2002).

[16] K. –H. Hong, Y. H. Kang, Y. H. Cha, J. –H. Kim, and C. H. Nam, in Technical Digest of Ultrafast Optics Conference, Montebello, Canada, 2001 (Optical Society of America, Washington, DC, 2001), p. 247.

[17] D. G. Lee, J. –H. Kim, K. -H. Hong, and C. H. Nam, "Coherent control of high-order harmonics with chirped femtosecond laser pulses," Phys. Rev. Lett. **87**, 243902 (2001).

[18] M. V. Ammosov, N. B. Delone, and V. P. Kraĭnov, "Tunnel ionization of comlex atoms and of atomic ions in an alternating electromagnetic field," Sov. Phys. JEPT **64**, 1191 (1986).

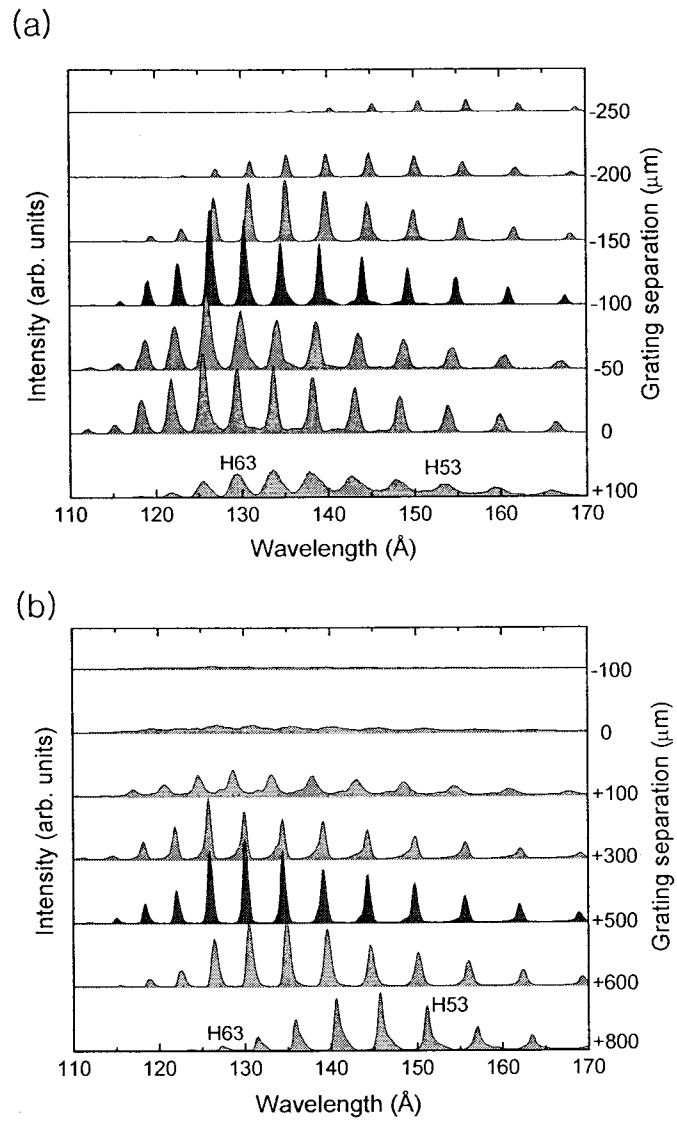

Figure 1. Harmonic spectra from neon of density $3x10^{19}$ cm^{-3} driven by femtosecond laser pulses with different laser chirp (different grating separation). Chirped laser pulses were generated with the same laser energy. The negative grating separation means laser pulses are positively chirped. The pulse duration of the chirp-free pulse was 25 fs, and the laser intensities were (a) $1x10^{15}$ W/cm^2 and (b) $5x10^{15}$ W/cm^2. 'H*n*' denotes the *n*th order harmonic.

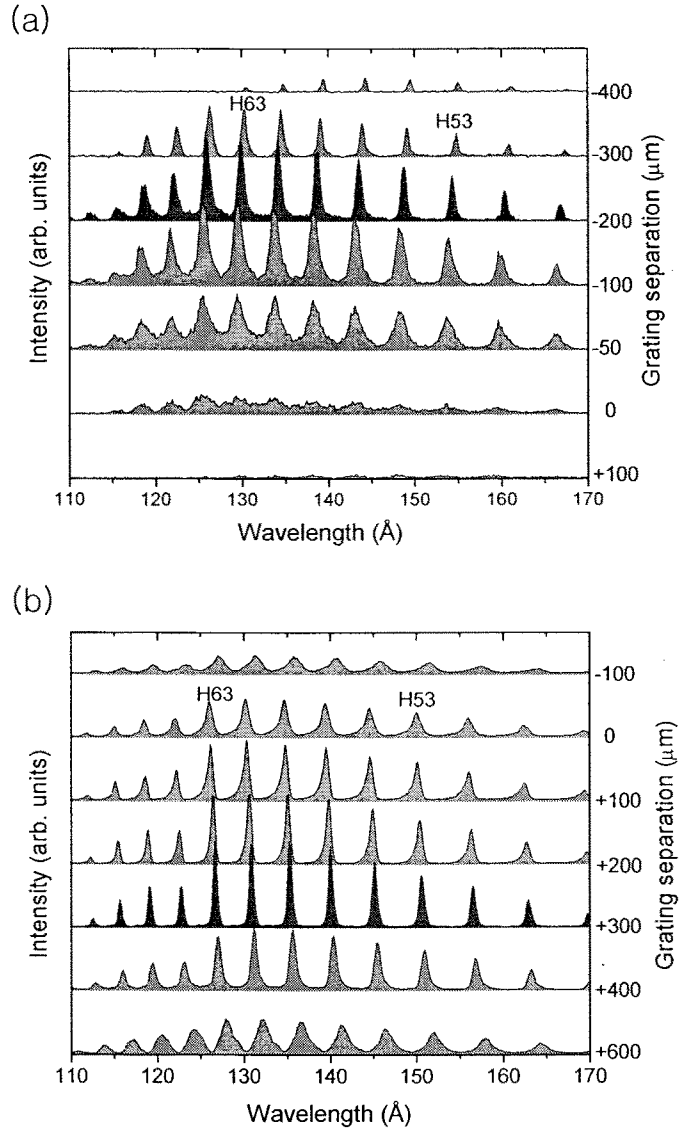

Figure 2. Harmonic spectra from helium of density 3×10^{19} cm^{-3} driven by femtosecond laser pulses with different laser chirp (different grating separation). The pulse duration of the chirp-free pulse was 25 fs and the laser intensities were (a) 1×10^{15} W/cm^2 and (b) 5×10^{15} W/cm^2.

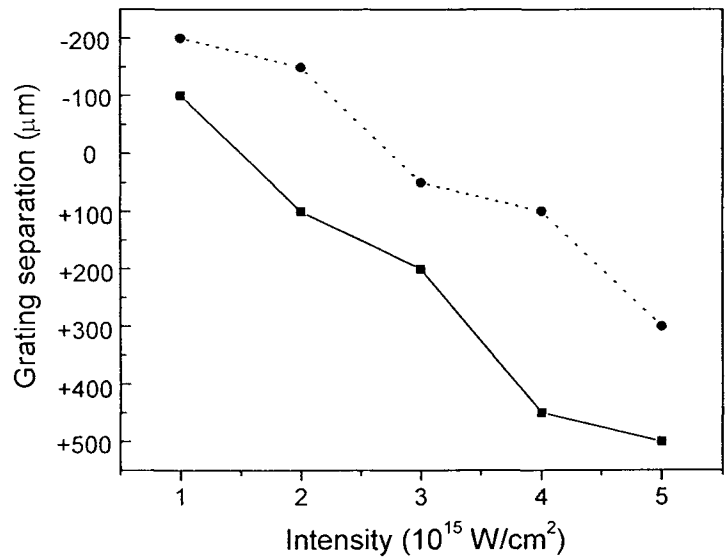

Figure 3. Optimal laser chirp conditions for the 63rd harmonic from Ne and He. Laser pulses with chirp-free intensity of (1-5)x10^{15} W/cm^2 were applied. Filled squares with solid lines refer to Ne and circles with dotted lines refer to He.

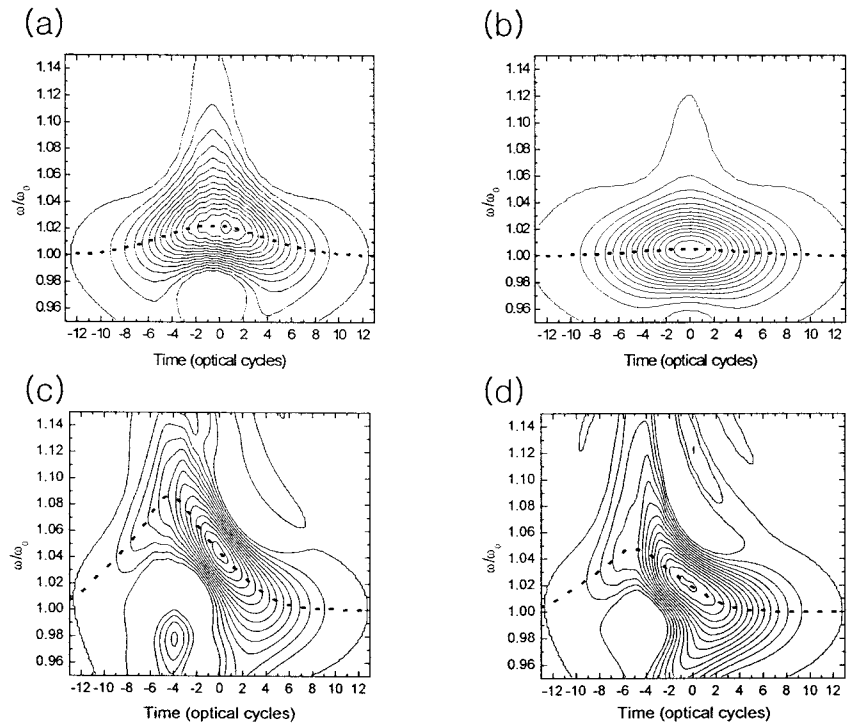

Figure 4. Wigner distribution of the 26-fs, 825-nm laser pulse after propagating through a 0.5-mm long gaseous medium of density $2x10^{18}$ cm^{-3}. The dotted line connects the peak points of the distribution at specific times. The gas species and laser intensity used in four different cases are (a) neon, $I_0=1x10^{15}$ W/cm^2, (b) helium, $I_0=1x10^{15}$ W/cm^2, (c) neon, $I_0=5x10^{15}$ W/cm^2, and (d) helium, $I_0=5x10^{15}$ W/cm^2.

A. 1. 2. Generation of high harmonics with low beam divergence and good wavelength tunability

With the application of appropriately chirped laser pulses, harmonic chirp can be coherently controlled so that sharp harmonics be produced. Using the strong blueshift property and coherently controlling harmonic generation process, we demonstrated a continuously tunable high-order harmonic generation, without losing spectral sharpness.

With the technological advancement of compact ultrashort high-power lasers, investigations on intense field physics are widely pursued. When intense ultrashort laser pulses are exposed to atoms or molecules, highly nonlinear effects that had never been observed before have appeared. Among these effects, high-order harmonic generation (HHG) due to a repetitive modulation of an electron motion in an atom by the strong laser field has received much attention. These harmonics have good prospects as coherent ultrashort light sources in the soft x-ray wavelength region.

The harmonics generated by the coherent interaction between the laser field and atoms have several novel properties such as low beam divergence [1], ultrashort pulse duration [2] and spatial coherence [3] which is better than any other currently available x-ray source such as x-ray laser [4] and radiation from synchrotron [5]. Due to the inversion symmetry in gaseous medium, harmonics are allowed only in odd orders. This makes the harmonic x-rays an x-ray source at fixed frequencies with an interval of two times the laser frequency. The harmonic x-ray source can be operated at numerous frequencies; however, it will be a limitation in actual applications. Therefore, the realization of a continuously tunable x-ray source is one of the key issues in HHG research. In addition, the generation of low beam divergence harmonics is important for applications.

Several experimental methods [6, 7] have been recently proposed to realize the wavelength tuning of high harmonics. Until now, the tuning of the harmonic wavelength without changing the laser spectrum has not been demonstrated yet.

In this report, we show the experimental results on continuous tuning of harmonic wavelength and on high harmonic generation with low beam divergence. A large blushift of harmonic wavelengths is accomplished by introducing the laser intensity above the saturation intensity for optical-field ionization, and spectral width and intensity of harmonics are optimized through the coherent control process with chirped laser pulses. For the generation of low beam divergence harmonics, a long gas jet is adopted as a target medium and the condition for self-guided propagation of the driving laser pulse is obtained.

To achieve a continuous tuning, we have proposed to utilize strong harmonic blueshift [10]. For sufficient wavelength tuning that can cover the frequency interval between

adjacent harmonics, the harmonic blueshift should be much larger than two times the laser frequency. In addition, the harmonic chirp [8, 9], due to the rapid variation of laser intensity and the self-phase modulation of the driving laser pulses in the ionizing medium, results in the broadening of harmonic spectrum, which should be appropriately compensated for to achieve sharp harmonics. Therefore, we explore the wavelength tunability of high-order harmonic x-rays on the bases of large blueshift of harmonic wavelengths for enough tuning and coherent control with chirped laser pulses for spectral sharpness.

When an intense femtosecond laser pulse is applied to atoms, high-order harmonics experience strong blueshift due to the nonadiabatic and self-phase modulation (SPM) effects [10]. The nonadiabatic response of atoms to the rapidly increasing laser field results in the nonadiabatic blueshift of harmonics. The femtosecond laser pulse propagating through the rapidly ionizing medium experiences a wavelength blueshift, resulting in the blueshift of harmonics. This harmonic blueshift increases with the increase of applied laser intensity. The harmonic spectrum in Fig. 1 shows strongly blueshifted harmonics that were generated from a helium gas jet driven by 25 fs Ti:sapphire laser pulses. The gas density profile at the interaction region was peaked at $3x10^{19}$ cm^{-3} with the full width at half maximum of about 500 μm, and the laser spectrum was centered at 824 nm with a spectral bandwidth of 45 nm. The high-order harmonic spectra were detected by a flat-field extreme-ultraviolet (XUV) spectrometer equipped with a back-illuminated x-ray charge-coupled device (CCD) with 330 × 1,100 pixels (Princeton Instruments). In Fig. 1 the harmonic of 51^{st} order was blueshifted more than two times the laser frequency and the harmonic of 81^{st} order more than four times the laser frequency. As the harmonic order increases, the harmonic blueshift becomes large enough to cover the frequency interval between adjacent harmonics so that continuous tuning of harmonic wavelengths becomes feasible.

To achieve the wavelength tuning of harmonics without sacrificing the spectral sharpness, the spectral structure of harmonics needs to be controlled. Though the spectrum in Fig. 1 shows the potential wavelength tuning capability of the harmonics accessible by controlling the laser intensity, the modification of the spectral shape and brightness of harmonics is accompanied during the tuning process. The experimental results shown in Fig. 2 clearly illustrate how we can solve this problem. While maintaining applied laser energy constant, but scanning laser chirp from positive to negative by adjusting the grating distance in the pulse compressor, harmonic spectra are acquired. Figure 2 shows that the harmonic intensity and spectral sharpness are very sensitive to the chirp condition of the applied laser pulse and the negatively chirped 47-fs laser pulse produce much brighter harmonics than those generated by the chirp-free pulses. This shows how we can achieve the generation of spectrally sharp harmonics by controlling laser chirp.

High-order harmonics generated with intense femtosecond laser pulses possess chirped spectral structure. In relatively low laser intensity, the harmonic chirp is governed mostly by the dynamically induced, negative chirp. On the other hand, when the laser intensity is higher than the saturation intensity, the SPM-induced harmonic chirp

becomes dominant, making the net harmonic chirp positive. The chirp structure of high-order harmonics can clearly be shown with the time-frequency domain analysis using the Wigner distribution function [9]. Since atoms respond to every optical cycle of a driving laser pulse, the harmonic chirp can be compensated for by using appropriately chirped laser pulses. In the low intensity case a positively chirped laser pulse can compensate for the negative harmonic chirp and produce sharp harmonics. At high laser intensity the laser chirp needed to compensate for the harmonic chirp changes from positive to negative due to strong SPM effect, as in the case of Fig. 2. Consequently, the experimental results in Fig. 2 demonstrate the necessity and importance of the coherent control of high-order harmonics with appropriately chirped laser pulses.

Applying the two important physical mechanisms of strong harmonic blueshift and coherent control of high-order harmonic generation, we have successfully demonstrated continuously tunable high-order harmonic generation in the 10 nm region without sacrificing spectral sharpness, as shown in Fig. 3. The tuning of the harmonic spectrum was carried out by simultaneously controlling laser intensity (to control the amount of blueshift) and laser chirp (to optimize the spectral brightness). The laser parameters at each harmonic spectrum in Fig. 3 were changed from negatively chirped 110-fs, 11-mJ pulse in Spectrum (I) (Fig. 3) to positively chirped 44-fs, 1.0-mJ pulse in Spectrum (V). For the extension of the spectrum of tunable harmonic generation to a much longer wavelength region, we change the target atom with neon, having lower ionization potential than helium. In Fig. 4, the tuning spectrum with neon in the 13 nm region without losing the spectral sharpness was shown.

Along with the tunability of high-order harmonics, the generation of low-divergence harmonics is also important in applications requiring bright harmonic x-ray beam. Gas-filled hollow fiber has been used for efficient harmonic generation [11]. The cross section of harmonic generation volume in this case is severely limited, restricting the maximum cross section of a harmonic source. If generated harmonic beam is close to the transform-limited one, the beam divergence of the harmonics is inversely proportional to the source size. For the generation of low divergence harmonics, the increase of harmonic generation cross section is required.

For the generation of efficient and low-divergence high-order harmonics, we adopted a 6-mm and 9-mm long argon gas jet. This target can provide a long uniform medium along the laser propagation direction and the cross section of gas jet is much larger than the diameter of the laser beam, so there is no restriction in harmonic source size due to the medium. When harmonics are generated in a long gas jet, the refraction effect of driving laser pulse in the ionizing medium becomes non-negligible. Therefore, proper guidance of the pumping laser pulse through the gas jet is required for low beam divergence harmonic generation.

In our experiments we found a proper guiding condition of the laser beam by controlling the target position relative to the laser focus. A uniform visible image of plasma column was generated along the entire length, 6-mm, of the argon jet at the target position (z) of 7 mm before the laser focus and strong 27^{th} harmonic was generated. Fig. 5 and Fig. 6 show the experimental result of spectrally resolved

divergence measurement of high-order harmonics from argon and neon, respectively. That were obtained by applying a single laser pulse with an intensity of 1.6 x 10^{15} W/cm^2. The measured divergence of harmonics was 0.5 mrad (FWHM) for argon and 0.7 mrad for neon. This small divergence of the harmonics from argon generated in the long gas jet represents a definite evidence of a large harmonic generation cross section, reaching a diameter of 70 μm.

In conclusion, we have presented the experimental results on continuous tuning of high harmonics from helium by applying the coherent control process and demonstrated the generation of low-divergence harmonics through the use of self-guided laser pulses in a 6-mm long argon gas jet.

References

[1] P. Salieres, T. Ditmire, M. D. Perry, A. L'Huillier, and M. Lewenstein, *J. Phys. B* **29**, 4771 (1996).

[2] T. E. Glover, R. W. Schoenlein, A. H. Chin, and C. V. Shank, *Phys. Rev. Lett.* **76**, 2468 (1996).

[3] T. Ditmire, E. T. Gumbrell, R. A. Smith, J. W. G. Tisch, D. D. Meyerhofer, and M. H. Hutchinson, *Phys. Rev. Lett.* **77**, 4756 (1996).

[4] R. E. Burge, G. E. Slark, M. T. Browne, X.-G. Yuan, P. Charalambous, X.-H. Cheng, C. L. S. Lewis, A. MacPhee, and D. Neely, *J. Opt. Soc. Am. B* **14**, 2742 (1997).

[5] K. Fezzaa, F. Comin, S. Marchesini, R. Coisson, and M. Belakhovsky, *J. X-ray Sci. and Technol.* **7**, 12 (1997).

[6] M. B. Gaarde, P. Antoine, A. Persson, B. Carre, A. L'Huillier, C.-G. Wahlstrom, *J. Phys. B* **29**, L163 (1996).

[7] C. Altucci, R. Bruzzese, C. de Lisio, M. Nisoli, S. Stagira, S. De silvestri, O. Svelto, A. Boscolo, P. Ceccherini, L. Poletto, G. Tondello, P. Villoresi, *Phys. Rev. A* **61**, 021801(R) (1999).

[8] Lee, D. G., Kim, J. –H., Hong, K. H. & Nam, C. H. Coherent control of high-order harmonics with chirped femtosecond laser pulses. *Phys. Rev. Lett.* **87**, 243902 (2001).

[9] Kim, J. –H. & Nam, C. H. Plasma-induced frequency chirp of intense femtosecond lasers and its role in shaping high-order harmonic spectral lines. *Phys. Rev. A* **63**, 63403 (2001).

[10] Shin, H. J., Lee, D. G., Cha, Y. H., Hong, K. H. & Nam, C. H. Generation of nonadiabatic blueshift of high harmonics in an intense femtosecond laser field. *Phys. Rev. Lett.* **83**, 2544-2547 (1999).

[11] A. Rundquist, C. G. Durfee III, Z. Chang, C. Herne, S. Backus, M. M. Murnane, and H. C. Kapteyn, *Science* **280**, 1412-1415 (1998).

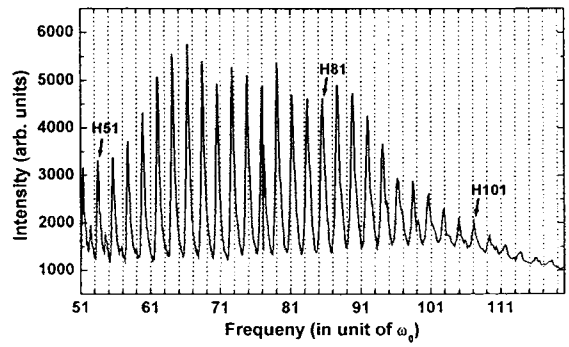

Fig. 1 Blueshifted harmonic spectrum from helium atoms driven by a chirp-free 25-fs laser pulse with an intensity of 2×10^{16} W/cm^2. 'H*n*' denotes the harmonic of the order *n*.

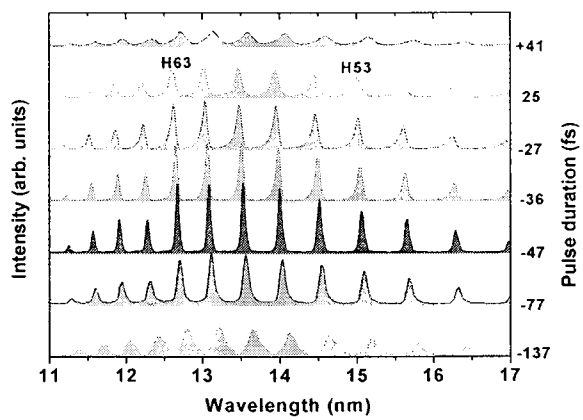

Fig. 2 Harmonic spectra from helium of density 3×10^{19} cm^{-3} driven by femtosecond laser pulses with different laser chirp. The pulse duration of the chirp-free pulse was 25 fs and the laser intensity was 3×10^{15} W/cm^2.

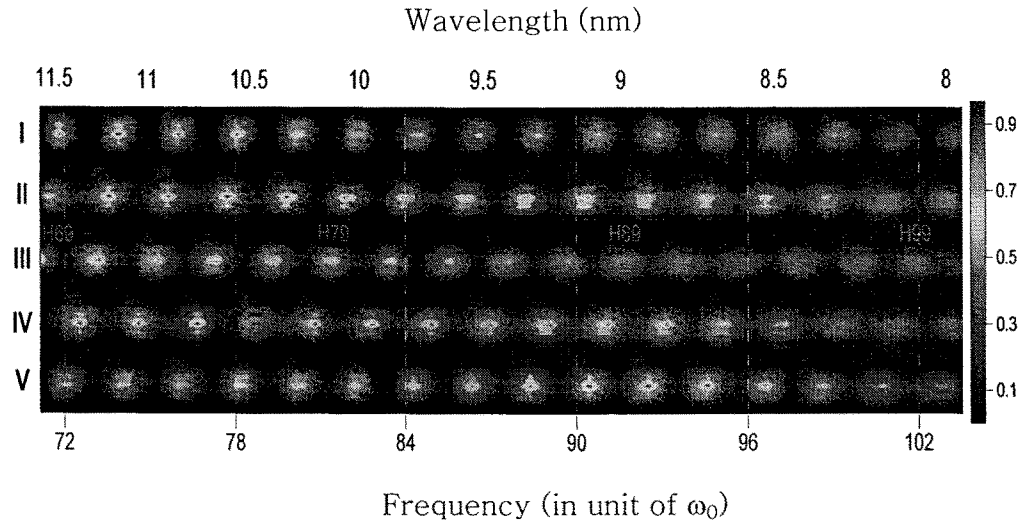

Fig. 3 Continuously wavelength-tuned high-order harmonics generated from helium atoms driven by femtosecond laser pulses. The laser energy and chirped pulse duration were (I) 11 mJ and –110 fs, (II) 5.9 mJ and -87 fs, (III) 4.1 mJ and -47 fs, (IV) 1.8 mJ and 26 fs, (V) 1.0 mJ and +44 fs, respectively. The wavelength tuning with optimized harmonics was achieved by simultaneously adjusting incident laser energy and laser chirp.

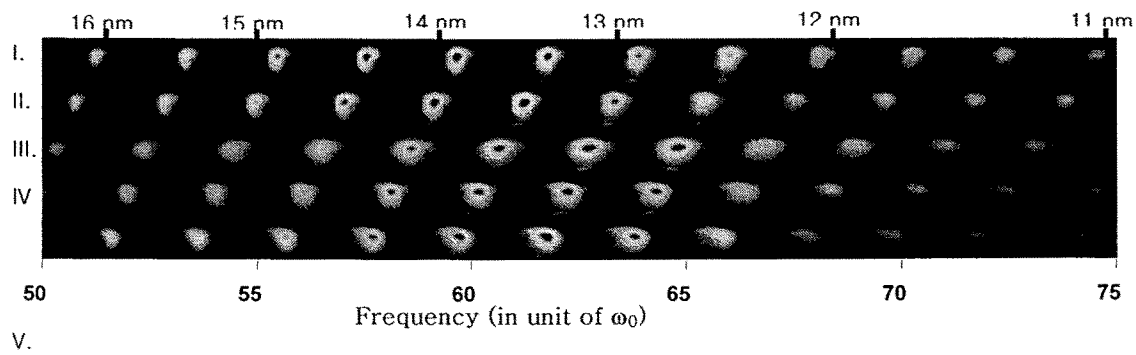

Fig. 4 Continuously wavelength-tuned high-order harmonics generated from neon atoms driven by femtosecond laser pulses. The laser energy and chirped pulse duration were (I) 3.5 mJ and –227 fs, (II) 0.9 mJ and -62 fs, (III) 0.4 mJ and -26 fs, (IV) 0.3 mJ and +27 fs, (V) 0.2 mJ and +30 fs, respectively.

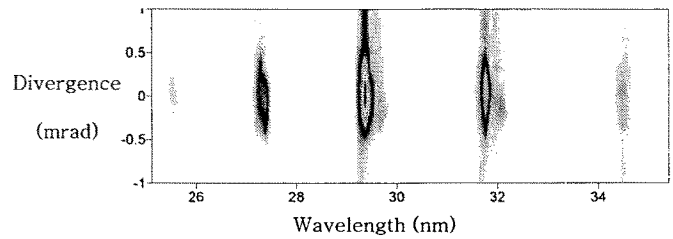

Fig. 5 Spectrally resolved divergence measurement of high-order harmonics obtained with a 6-mm long argon jet placed at z = -7 mm.

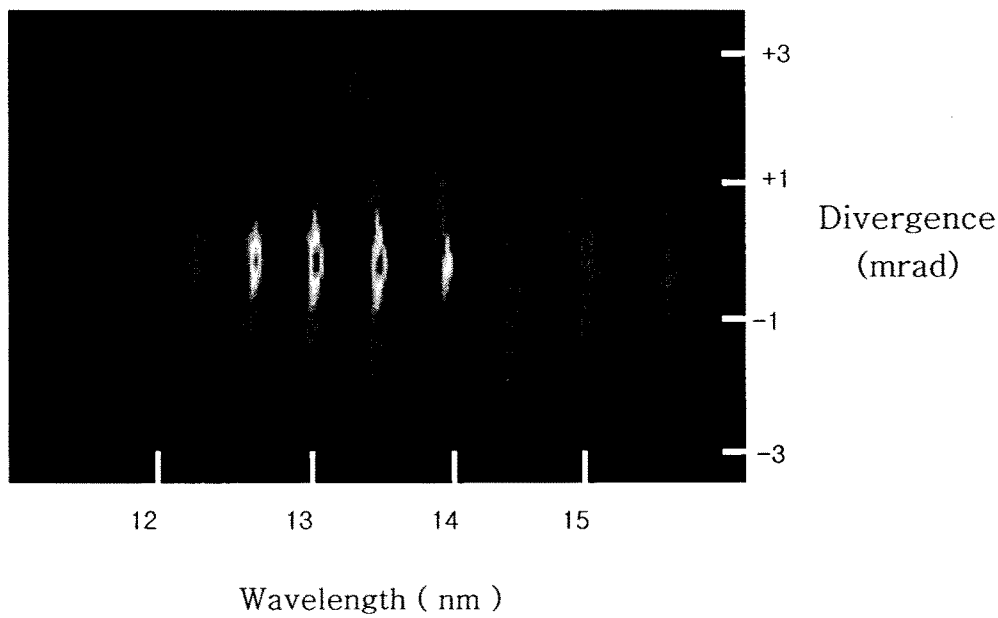

Fig. 6 Spectrally resolved divergence measurement of high-order harmonics obtained with a 9-mm long neon jet placed at z = -15 mm.

A. 1. 3. Wave-front phase measurements of high-order harmonic beams using the point-diffraction interferometry

We report the wave-front phase measurement of high-order harmonics employing the point-diffraction interferometry. The high-order harmonics generated in a gas-filled hollow tube showed excellent spatial coherence over nearly the whole cross-section of the harmonic beams. Using this coherent harmonic source in the extreme ultraviolet/soft x-ray region we have demonstrated the operation of a point diffraction interferometer and measured the wave-front phase of high-order harmonics.

The high-order harmonics, generated by the highly non-linear interaction between atoms and intense laser pulses, have good prospects as coherent light sources in the extreme ultraviolet (EUV)/soft x-ray wavelength region. The high-order harmonic generation (HHG) have several novel properties such as low divergence [1-3], ultrashort duration [4] and spatial coherence [5-7] which is better than any other currently available EUV/soft x-ray source such as x-ray laser [8] and synchrotron [9,10]. This coherent ultrashort EUV/soft x-ray source has already been used in several areas of science and the applications are expanding rapidly. The possibility of performing interferometry in the EUV/soft x-ray range has been demonstrated by an interference experiment using two spatially separated sources of harmonic radiations [11]. The recent work by Bartels et al.[7] applied HHG to record a Gabor hologram, which proves superb coherence property of high-order harmonics. These works demonstrate strong potential of HHG as coherent EUV/soft x-ray sources.

A conventional method for testing the quality of EUV optical components used in EUV lithography, x-ray microscopy and holography is the point-diffraction interferometry (PDI) in which the aberrations of optics can be obtained from a wave-front phase measurement [12]. In this technique, a plate with a very small pinhole is used to generate a spatially coherent beam from synchrotron radiation. The pinhole in the membrane generate a spherical reference wave-front by diffraction and this interferes with the wave-front from a test optical component with reduced intensity due to the semi-transparent nature of the membrane. From the analysis of the resulting interference pattern, the information on the aberrations of optical components can be obtained. The investigations by Goldberg et al.[12] showed that the degree of spatial coherence of the

probing beam critically affected the results of measurements in the PDI. Hence, the use of the first pinhole, to improve the coherence, is indispensable, but this is accompanied by a significant reduction of source intensity. Therefore, HHG, with its superb spatial coherence and high intensity, can be a far better alternative source for the metrology of EUV optics.

In this Letter, we demonstrate the measurement of the wave-front phase of a harmonic beam using the PDI method. To ensure successful operation of the PDI method, we first measure the degree of spatial coherence of HHG employing a double pinhole interference experiment and show that the harmonic beam is highly coherent over almost the entire beam cross section.

The degree of spatial coherence was measured using the experimental setup shown in Fig. 1. We focused 20-fs Ti:sapphire laser pulses, with 0.35 mJ energy per pulse and 1 kHz repetition rate, into a 30-torr argon filled hollow-tube target using a f/83 focusing mirror to generate high-order harmonics. The core diameter and length of the hollow-tube target were 350 μm and 4-cm, respectively. The harmonic spectrum obtained using a flat-field soft x-ray spectrometer showed that the 27th harmonic at 30.7 nm was dominant and was accompanied by much weaker neighboring harmonics. Here, we controlled the Ar gas density such that the 27th harmonic contained more than 68 % of the total detected harmonic energy. The spectral width of harmonics determined by the three harmonics from 25th to 29th was about 4 nm. A thick Al-plate with two pinholes was placed 13 cm beyond the target to create the two wave fronts. The diameter of the pinholes and the distance between them were 10 μm and 100 μm, respectively. The diffracted wave fronts from the two pinholes interfere and the resulting interference fringe pattern was detected by an x-ray charge-coupled device located 104 cm away from the pinhole plate. The diffracted light of the pump laser was blocked by placing a 0.2 μm thick aluminium filter in front of the detector.

The interferogram of the harmonic beam acquired with 100 laser shots and the intensity plot along a horizontal line passing through the center of the fringe image are shown in Fig. 2. The fringe visibility at points away from the center of the fringe pattern decreases due to the broad spectrum and divergence of the harmonic beams. Considering the low beam divergence of about 1 mrad (in $1/e^2$) in our experiment, the reduction of visibility in this experiment comes from the broad spectrum of the harmonic beam. The spatial coherence can thus be determined from the fringe visibility

at the central part of the interferogram in which the visibility is less affected by the broad spectrum. The intensity plot in Fig. 2(b) shows that the visibility at the center is 1, which indicates that the two points in the beam, separated by 100 μm, are completely coherent. The harmonic beam size at the pinhole plate, estimated by scanning the beam with a single pinhole plate, was found to be 130 μm (full-width at half maximum). Hence, the above measurements show that the harmonic beam has complete spatial coherence over most of the beam cross section.

We, next, performed the measurement of the wave-front phase of the generated harmonic beams using the PDI method. As the PDI plate, 1 μm thick aluminium foil with a 10 μm pinhole was used. The thickness of the foil and the diameter of the pinhole were determined by carrying out a ray-tracing simulation for the propagation of both interfering beams – the beam transmitted through the Al foil and the beam diffracted by the pinhole in the foil - taking into account complex electric field amplitudes for the two beams. The Al-foil thickness and the hole diameter corresponded to the case wherein the simulation yielded a comparable intensity and beam diameter for both interfering beams at the detection plane. The PDI plate was mounted on a motorized x-y stage to adjust the relative position between the harmonic beam and pinhole. The radius of the harmonic beam recorded at the detector is about 1.3 mm (in $1/e^2$). When we moved the pinhole position to the center of the transmitted harmonic beam, a point-diffracted reference beam was generated and it interfered with the incident harmonic beam. The interferogram obtained with 10,000 laser shots is shown in Fig. 3(a) and the intensity plot, along a horizontal line passing through the center of the interferogram, in Fig. 3(b). Figure 3(a) shows good concentric fringes, implying that the wave front of harmonic beam in the far-field is spherical. Though the fringe visibility decreases at the outer region due to broad spectrum contained in several harmonic orders used, the visibility of fringes in Fig. 3(b) is greater than 50 % for almost the entire region of the interferogram.

The far-field amplitude, u(r), of the point-diffracted reference beam for a uniformly illuminated circular aperture of radius a is expressed in the form,

$$u(r) \approx i4\pi N e^{-i\pi N(r/a)^2} \times \frac{2J_1(2\pi ar / L\lambda)}{2\pi ar / L\lambda}, \qquad (1)$$

where J_1 is the 1st order Bessel function, L is the distance from the pinhole to the

detector, λ is the source wavelength and the Fresnel number N is defined by

$$N \equiv \frac{a^2}{z\lambda}. \tag{2}$$

The Fresnel number for our experimental conditions is $<10^{-3}$ and, also, the detection position, z, is sufficiently larger than the Rayleigh range, $z_r \equiv \pi a^2 / \lambda \cong 2.6(mm)$ for a circular aperture. Therefore, in the far-field approximation, the wave-front phase of the point-diffracted beam in the experiment can be considered as a spherical wave-front with a phase equal to $\pi N(r/a)^2$.

Using the phase information of 11 constructive and destructive interference fringes shown in Fig. 3, the wave-front of the harmonic beam was constructed. The wave-front phase of the harmonic beam was found to be nearly spherical with a radius of 1.197 m. The root-mean-square(rms) error of the optical-path difference(OPD), which is defined as the standard deviation of the measured OPD between the wave-front of the harmonic beam and a spherical wave-front of radius R(z) = 1.197 (m), and the measurement error are plotted in Fig. 4. The measurement error, mainly determined by the CCD pixel size of 24 μm was less than 24 Degree (= λ /15) at the edge of the fringe pattern. The OPD rms error is comparable with the measurement error for radial distances less than 1.1 mm and, at the edge of the fringe, the error is increased to ≅ 60 Degree (=λ /6). Considering our measurement accuracy, it is clear that the wave-front of the harmonic beam deviates slightly from a perfectly spherical shape and that the deviation, which increases with distance from the center, is measurable in this PDI setup. The measurement of the wave-front phase information together with an intensity profile of the harmonic beams is important from the viewpoint of improving the beam quality and it gives all the properties of the propagating beam, which is essential for designing the EUV optics for various applications.

In summary, we have demonstrated a point-diffraction interferometer using the excellent spatial coherence of high-order harmonics and measured the wave-front phase of a harmonic beam. The experimental results from PDI showed that the generated harmonic beam can be considered as a spherical wave within a phase error of λ /15 at the central two-thirds part of the harmonic beam. With a slight improvement of wave-front quality so as to obtain a phase error less than λ /20, harmonic EUV sources will become a powerful compact tool for the metrology of EUV optics.

References

[1] P. Salières, T. Ditmire, M. D. Perry, A. L'Huillier, and M. Lewenstein, J. Phys. B **29**, 4771 (1996).

[2] Y. Tamaki, J. Itatani, M. Obara, and K. Midorikawa, Phys. Rev. A **62**, 63802 (2000)

[3] D. G. Lee, H. T. Kim, K. H. Hong, C. H. Nam, I. W. Choi, A. Bartnik, and H. Fiedorowicz, App. Phys. Lett. **81**, 3726 (2002).

[4] M. Paul, E. S. Toma, P. Breger, G. Mullot, F. Auge, Ph. Balcou, H. G. Muller, P. Agostini, Science **292**, 1689 (2001).

[5] T. Ditmire, E. T. Gumbrell, R. A. Smith, J. W. G. Tisch, D. D. Meyerhofer, and M. H. Hutchinson, Phys. Rev. Lett. **77**, 4756 (1996).

[6] L. Le Déroff, P. Salières, B. Carré, D. Joyeux, and D. Phalippou, Phys. Rev. A **61**, 43802 (2000).

[7] R. A. Bartels, A. Paul, H. Green, H. C. Kapteyn, M. M. Murnane, S. Backus, I. P. Christov, Y. Liu, D. Attwood, C. Jacobsen, Science **297**, 376 (2002).

[8] Y. Liu, M. Seminario, F. G. Tomasel, C. Chang, J. J. Rocca, and D. T. Attwood, Phys Rev. A **63**, 033802 (2001).

[9] K. Fezzaa, F. Comin, S. Marchesini, R. Coisson, and M. Belakhovsky, J. X-ray Sci. and Technol. **7**, 12 (1997).

[10] C. Chang, P. Naulleau, E. Anderson, and D. Attwood, Opt. Common. **182**, 25 (2000).

[11] D. Descamps, C. Lyngå , J. Norin, A. L'Huillier, C.-G. Wahlström, J. -F. Hergott, H. Merdji, P. Salières, M. Bellini, and T. W. Hänsch, Opt. Lett. **25**, 135 (2000).

[12] K. A. Goldberg, R. Beguiristain, J. Bokor, H. Medecki, D. T. Attwood, K. Jackson, E. Tejnil, and G. E. Sommargren, J. Vac. Sci. Technol. B **13**, 2923 (1995).

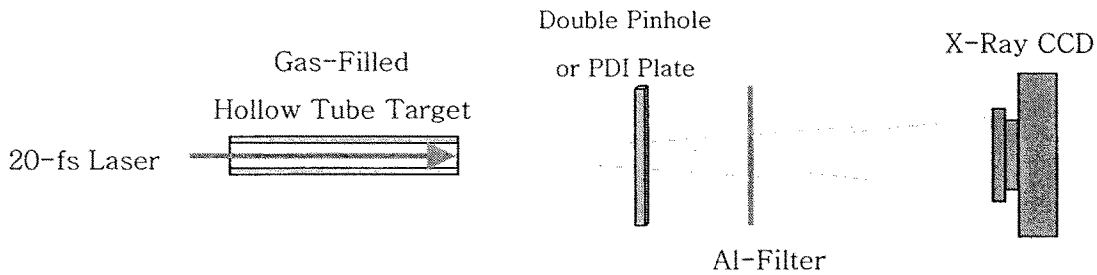

Fig. 1. Schematic diagram of the experimental setup for the measurement of spatial coherence with double pinholes and of high-order harmonic wave-front phase with a PDI.

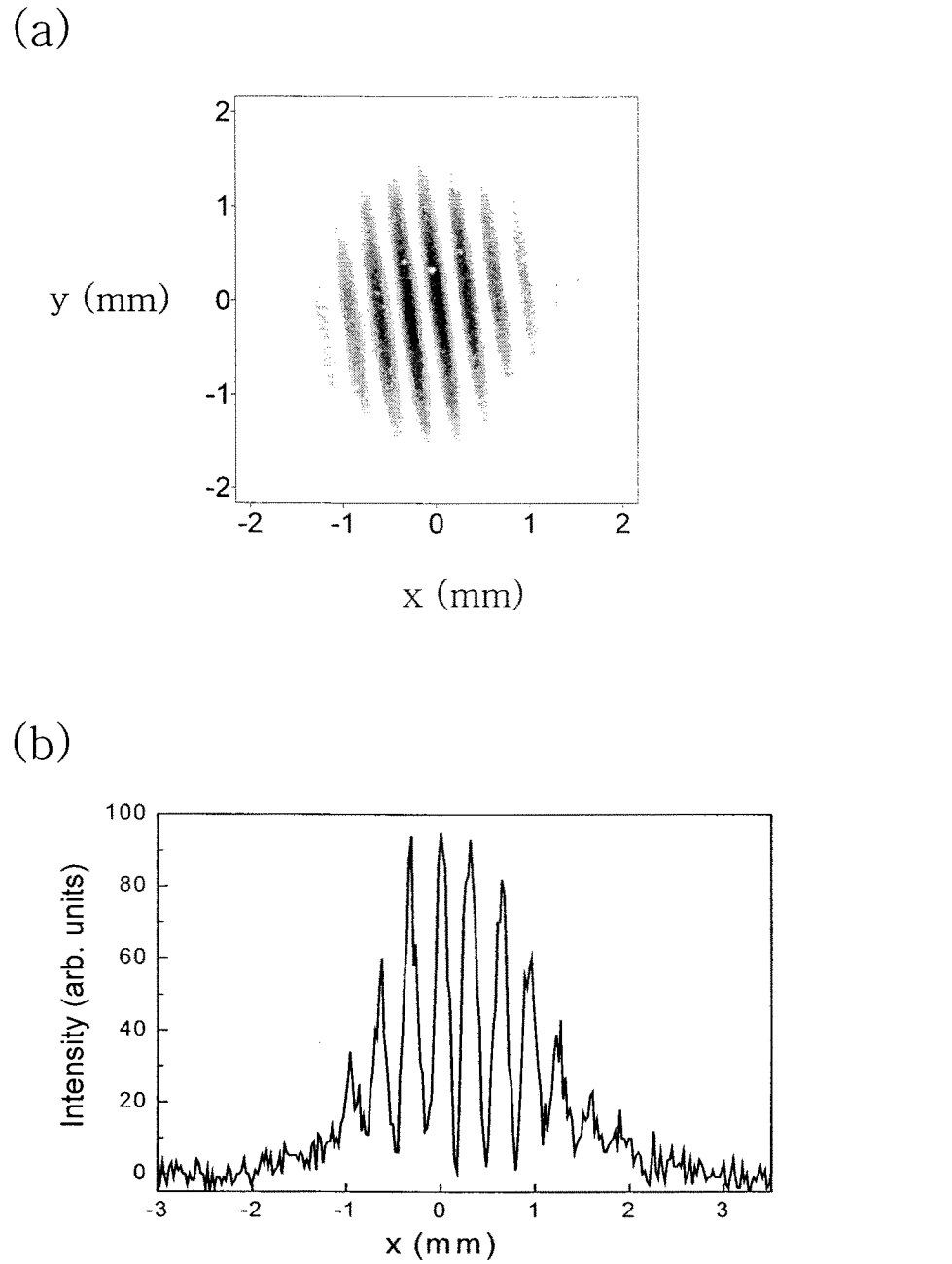

Fig. 2. Interferogram of harmonic beam diffracted by double pinholes separated by 100 μm. (a) fringe image and (b) the intensity profile of interferogram along a horizontal line passing through the center.

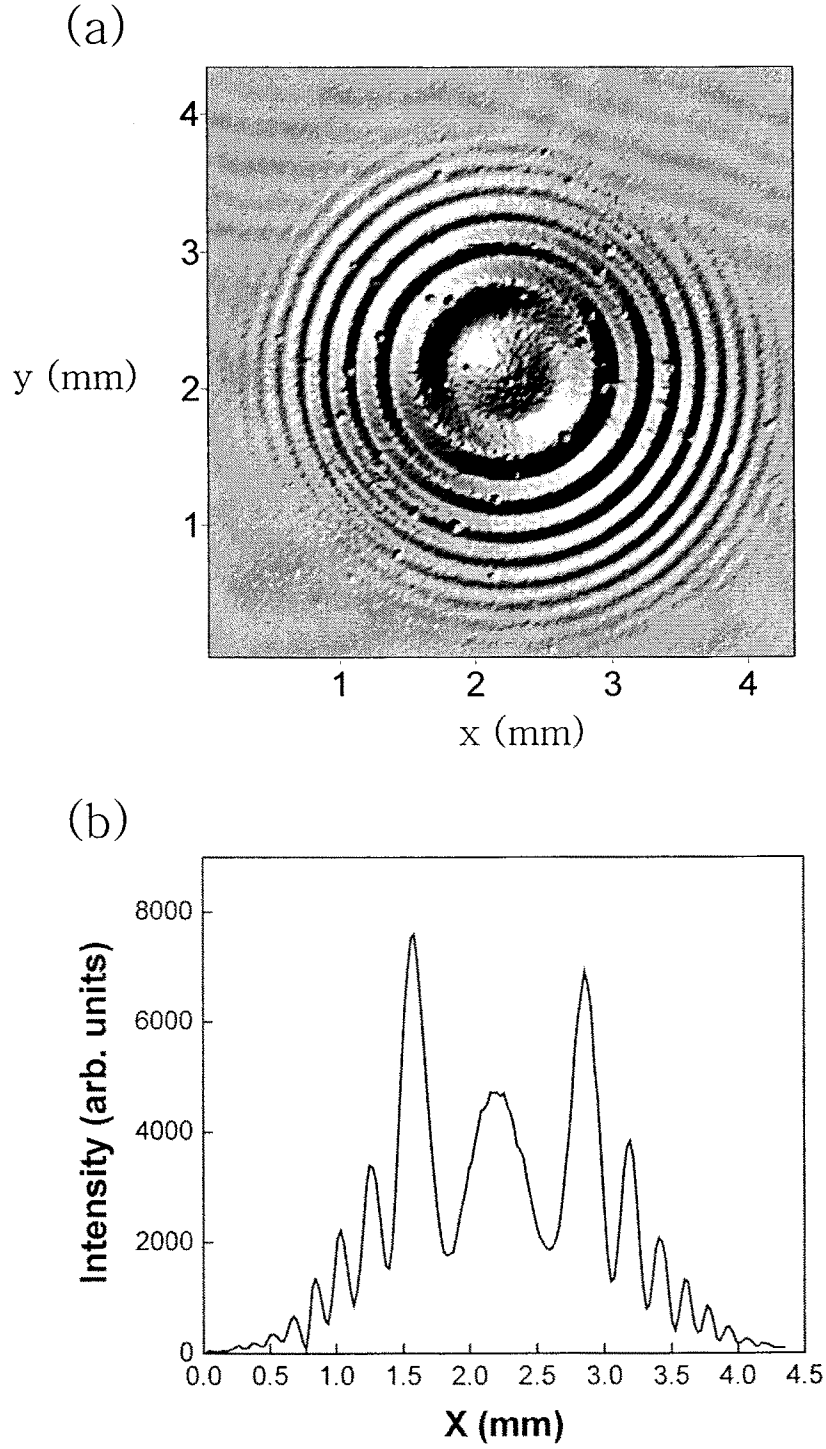

Fig. 3. (a) Interferogram recorded with a PDI plate having a 10-μm pinhole when the pinhole was positioned at the center of harmonic beam and (b) the intensity profile of interferogram along a horizontal line passing through the center.

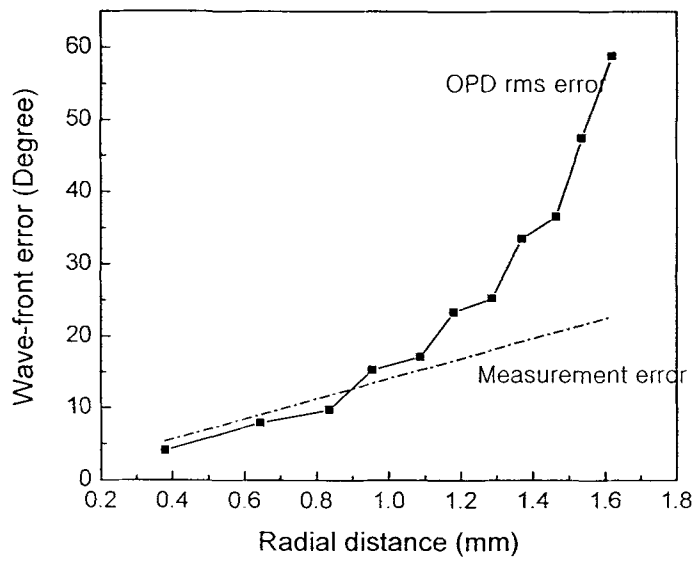

Fig. 4. The OPD rms error and measurement error along the radial position of the interferogram shown in Fig. (3).

A. 2. Theory of high harmonic generation

A. 2. 1. Time-frequency analysis of high harmonic generation

The conceptual understanding of high-order harmonic generation in atomic gases irradiated by high-power laser pulses is provided by the semiclassical two-step model [1, 2]. The maximum photon energy is determined by the simple formula, $I_p+3.17U_p$, where I_p is the ionization potential and U_p is the ponderomotive energy. Quantum-mechanical approaches [3, 4] not only confirm this semiclassical interpretation but also provide further useful information such as the phase of the dipole moment. There are many electron paths that yield the same photon energy [5, 6, 7], among which the two paths ("long" and "short") are shorter than one optical cycle contribute dominantly to the generation of high-order harmonics[8, 9]. The dipole moments produced by the two paths interfere with each other, giving rise to a complicated structure in the midplateau region of the spectrum [10, 11]. Under certain conditions, however, the contribution of only one of these two paths satisfies the phase-matching condition [12], leading to a simpler spectral and temporal profile amenable to theoretical analysis. There also exist numerical techniques such as the coherent sum method [11] which select the contribution of only one path is not sensitive to the laser intensity and thus help to resolve the complicated structure of high-order harmonics. Theoretical time-frequency analysis using the Wigner distribution function, combined with the coherent sum method, reveals a good agreement between the quantum-mechanical calculations based on the time-dependent Schrödinger equation and the semiclassical calculations [13].

We wish to study the question of when each harmonic is emitted. We assume that

the electron is initially in the ground state of the atom. Under the influence of the laser field, a part of the electron wave packet tunnels out and, when the direction of the laser field is reversed, recombines to the ground state. For our analysis we compute one-dimensional time-dependent Schrödinger equation for Ne atom using the soft-core potential. The laser pulse incident on the atom is assumed to be a Gaussian pulse of width (FWHM) 160 fs (=59.96 optical cycles), center frequency ω_L =800 nm, and peak intensity 3×10^{14} W/cm^2.

We turn to a time-frequency analysis of the dipole acceleration using the Wigner and Husimi distribution functions [14]. While the dipole acceleration yields only the temporal information and the power spectrum only the spectral information, the time-frequency distribution functions provide both temporal and spectral information simultaneously [15]. The Wigner distribution function of the dipole acceleration $\ddot{d}(t)$ can be defined as

$$W(t,\omega)=\frac{1}{\pi}\int_{-\infty}^{\infty}\ddot{d}^{*}(t-t')\ddot{d}(t+t')e^{-2i\omega t'}dt'$$

While positive and negative regions that appear alternately in the Wigner distribution may cancel each other when physically meaningful marginal distributions are computed, regions having predominantly either positive or negative values may carry physical significance. There are regions having predominantly positive values and these regions occur at times the laser field amplitude takes on the maximum or minimum value. Near the cutoff, the Wigner distribution takes on predominantly positive values at times which high-order harmonics near the cuttoff are emitted. On the other hand, in the plateau region the Wigner distribution shows a complex structure, reflecting the complex dynamics involving the generation of harmonics in the plateau region. Perhaps a clearer picture of the time-frequency structure emerges when the Husimi

distribution [14] (or the Garbor transform [16, 17])

$$H(t,\omega)=\frac{1}{2\pi}\left(\frac{\kappa}{\pi}\right)^{1/2}\left|\int_{-\infty}^{\infty}e^{-\kappa(t'-t)^2/2}\ddot{d}(t')e^{-i\omega t'}dt'\right|^2$$

is used. Here one has the freedom of choosing the value of the smoothing parameter κ depending on the desired accuracy in the temporal *vs.* spectral information. It is seen that, as κ is increased, one gains the temporal information but loses the spectral information. The Husimi distribution exhibits the Λ structure not clearly seen in the Wigner distribution, indicating that photons of a given harmonic frequency in the plateau region are emitted mainly at two different times within one half optical cycle. The separation between these two times decreases as the harmonic order is increased toward the cutoff. The complex structure exhibited by the Wigner distribution in the plateau region is caused by the effects of interference between the two paths (short and long) that yield the same photon energy and by the effects of multiple recollisions. Such effects can be largely eliminated by the coherent sum method in which a large number of dipole acceleration spectra obtained at slightly different laser peak intensities ranging between $I-\Delta I/2$ and $I+\Delta I/2$ are added. When ΔI is suitably chosen, contributions from the long path and multiple recollisions which produce dipole phases depending sensitively on the laser intensity can be effectively erased. Only the left half of the Λ structure remains when the coherent sum is performed. This suggests that the left half of the Λ structure represents the contribution from the short path. We show below that this result is consistent with the semiclassical analysis.

According to the semiclassical analysis, the electron after tunneling out through the barrier at time t is accelerated by the laser field, subject to the initial

condition $x(t)=0$ and $v(t)=0$. The electron then returns to the nucleus after time τ and radiates energy equal to its kinetic energy at that time plus the ionization energy I_p. One thus has, as the final condition, $x(t+\tau)=0$, and the energy of the photon emitted at time $t+\tau$ is given by

$$\hbar\omega = I_p + \frac{1}{2}mv^2 .$$

If we plot this ω/ω_L with respect to the return time, we obtain the semiclassical results. Comparing the short path contribution, one can confirm that the Wigner and Husimi distributions obtained by the coherent sum method represent the contribution from the short path and that quantum-mechanical and semiclassical calculations yield good agreement.

In conclusion, information on the times at which high-order harmonics in the plateau region (as well as the low-order harmonics) are emitted can be obtained using the time-frequency analysis based on the Wigner and Husimi distibutions. The Wigner and Husimi distributions exhibit a characteristic Λ structure in the midplateau region, indicating that photons of a given harmonic frequency are emitted at two different times corresponding to the return times of the short and long paths. We have found that the Wigner and Husimi distributions computed quantum mechanically can be explained with the simiclassical three-step model. The phenomenon of high-harmonic generation is thus an example that shows a strong degree of quantum-classical correspondence.

Reference

[1] J. L. Krause, K. J. Schafer, and K. C. Kulander, Phys. Rev. Lett. **68**, 3535 (1992)

[2] K. J. Schafer, B. Yang, L. F. DiMauro, and K. C. Kulander, Phys. Rev. Lett. **70**, 1599 (1993).

[3] A. L'Huillier, M. Lewenstein, P. Saliéres, Ph. Balcou, M. Yu. Ivanov, J. Larsson, and C. G. Wahlstrom, Phys. Rev. A **48**, R3433 (1993).

[4] M. Lewenstein, Ph. Balcou, M. Yu. Ivanov, A. L'Huillier, and P. B. Corkum, Phys. Rev. A **49**, 2117 (1994).

[5] P. Saliéres, A. L'Huillier, and M. Lewenstein, Phys. Rev. Lett. **74**, 3776 (1995).

[6] M. Lewenstein, P. Salieres, and A. L'Huillier, Phys. Rev. A **52**, 4747 (1995).

[7] Ph. Balcou, A. S. Dederichs, M. B. Gaarde, and A. L'Huillier, J. Phys. B **32**, 2973 (1999).

[8] M. Bellini, C. Lynga, A. Tozzi, M. B. Gaarde, T. W. Hansch, A. L'Huillier, and C. G. Wahlstrom, Phys. Rev. Lett. **81**, 297 (1998).

[9] D. G. Lee, H. J. Shin, Y. H. Cha, K. H. Hong, J. H. Kim, and C. H. Nam, Phys. Rev. A **63**, 021801(R) (2001).

[10] C. Kan, C. E. Capjack, R. Rankin, and N. H. Burnett, Phys. Rev. A **52**, R4336 (1995).

[11] J. H. Kim, H. J. Shin, D. G. Lee, and C. H. Nam, Phys. Rev. A **62**, 055402 (2000).

[12] Ph. Antoine, A. L'Huillier, and M. Lewenstein, Phys. Rev. Lett. **77**, 1234 (1996).

[13] J. H. Kim, D. G. Lee, H. J. Shin, and C. H. Nam, Phys. Rev. A **63**, 063403 (2001).

[14] H. W. Lee, Phys. Rep **259**, 147 (1995).

[15] L. Cohen, Time-Frequency Analysis (Prentice Hall, NJ, 1995).

[16] C. F. de Morrisson Faria, M. Dorr, and W. Sander, Phys. Rev. A **58**, 2990 (1998).

[17] Ph. Antoine, B. Piraux, and A. Maquet, Phys. Rev. A **51**, R1750 (1995).

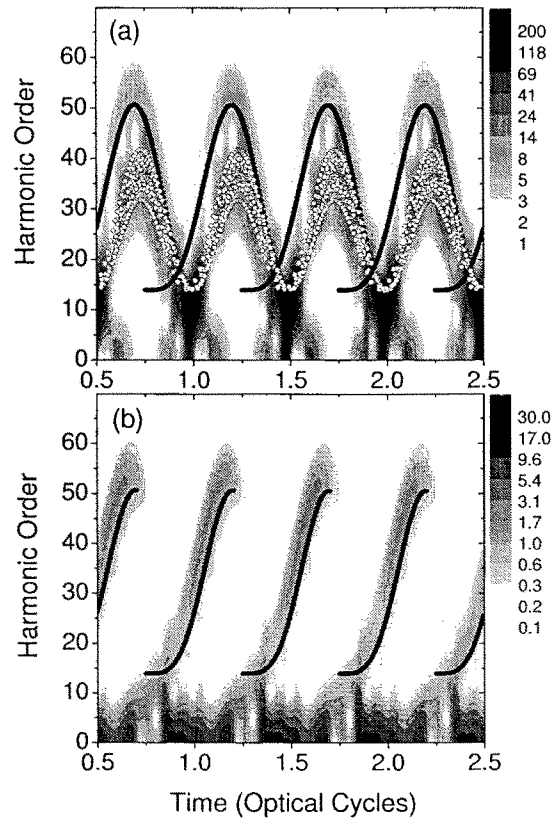

Fig. 1. (a) The contribution from the short and long paths within one optical cycle (solid curve) and from multiple recollisions (open circles) calculated using the semiclassical method. Shown in the background is the Husimi distribution with $\kappa = 0.1$. (b) The contribution from the short path (solid circles) calculated using the semiclassical method. Shown in the background is the Husimi distribution computed using the coherent sum method with $\kappa = 0.1$.

A. 2. 2. Ion momentum distributions for He single and double ionization in strong laser fields

Using a semiclassical rescattering model, the momentum distributions of recoil ions from laser induced single and double ionization are obtained. Not only in the case of double ionization but also in the case of single ionization, the distributions of the momentum parallel to the polarization direction of the laser field show a double-hump structure as a consequence of the rescattering. By comparing with experimental data we find that, as the intensity of the laser decreases, the rescattering ionization mechanism of the second electron calculated within our model does not dominate the process. In addition, the correlated emission of the electrons in the double ionization is discussed and the effect of the repulsion between the emitted electrons is shown.

Among the achievements in the field of interaction between atoms and intense laser pulses, the recognition of the rescattering process [1-3] was one of the most important steps to advance the understanding of the behaviour of atoms in laser field. The rescattering process can be understood from a simple quasiclassical notion: Once an electron subject to a strong field, has undergone a transition into continuum from its initial bound state, its motion is dominated by its interaction with the laser field. In the case of linearly polarized laser field, a majority of these electrons will be driven back into the vicinity of the ion core and undergo elastic or inelastic scattering, or recombine with the core and emit a high-energy photon. This mechanism is the so-called rescattering process. It is commonly believed that rescattering is responsible for many distinct experimental observations, such as the cut-off in high-order harmonic generation, a plateau formed by high-order ATI peaks [1,2] and the singular angular distributions of the photoelectrons in the plateau regime [3-8].

Since a surprisingly high ion yield in double and multiple ionization of atoms in intense, linearly polarized laser pulses was first observed [9], many-electron dynamics in intense laser fields has been studied intensively both in theoretical and experimental investigations. Especially in recent years, double and multiple ionization of rare gas atoms in intense laser fields has attracted more and more attention. It is well known that double ionization can occur either by a stepwise process or by so-called nonsequential double ionization (NSDI) mechanisms. It is commonly accepted that in the stepwise process occurring mainly above the saturation intensity for the single ionization (the

intensity at which the neutral target atoms are fully depleted in the interaction volume), the electrons are ionized sequentially, i.e. the probability of the stepwise double ionization is determined by the independent product of the probability of single ionization of the neutral atoms and that of the singly charged ions. In contrast, the mechanism of NSDI, which occurs primarily in the intensity domain near and below the saturation intensity, is still under dispute [2,10-21].

Among the various mechanisms developed, three are rather important. Fittinghoff *et al.* [10] suggested that the second electron could be shaken-off by a nonadiabatic change of the potential caused by the emission of the first electron. This mechanism is known to dominate the double ionization of helium after the absorption of single photons with energies beyond 1 keV [22]. The rescattering process has also been proposed to explain NSDI by Corkum [2] and Kuchiev [19]. In this model, the second electron is ionized due to a collision of the first tunneled electron with the parent ion after free propagation during about half an optical cycle in the external laser field. Becker and Faisal [15,23] proposed a "correlated energy sharing" model based on the intense-field many-body S-matrix theory, derived by rearranging the usual S-matrix series. This model includes short-time electron correlation and the rescattering mechanism.

Recently, measurements of the distributions of the recoil momentum of doubly charged He [24], Ne [25] and Ar [26-29] in the NSDI region have been reported and have led to intensive theoretical and experimental investigations on the topic during the last two years [30-46]. In the NSDI region, all the distributions show a remarkably broad double-hump distribution for the recoil momentum parallel to the laser field polarization direction and a narrow single-hump distribution in the perpendicular direction. These characteristic features are believed to serve as a test of various models and rule out the mechanisms based on an instantaneous release of two (or more) electrons at a phase where the field maximizes, such as "shaken-off" and "collective tunneling" [31]. It is already known that the positions of these maxima are consistent with kinematical constraints set by the "rescattering model" [25,30,33,34,36].

In this paper, we calculate the recoil momentum of singly and doubly ionized ions of He using a semiclassical rescattering model developed recently [37]. This model has been applied to quantitatively reproduce the excessive double ionization of He observed in experiments and has gained success in the explanation of the momentum distribution of recoiled He^{2+} ions [36,37]. This model has also been used to study the photoelectron

spectra, angular distribution and correlated electron emission in NSDI [45,46].

We begin by briefly presenting the semiclassical rescattering model adopted in the previous calculations [36,37]. The ionization of the first electron from a bound to continuum state is treated by tunneling ionization theory. The subsequent evolution of the ionized electron and the bound electron in the combined Coulomb potential and laser field is described by the classical Newtonian equations. To emulate the evolution of the electron wave packet, a set of trajectories is launched with initial conditions obtained from the wave function of the tunneled electron.

Evolution of the two-electron system after the tunnel ionization of the first electron is determined by the classical equations of motion (in atomic units),

$$\frac{d^2\mathbf{r}}{dt^2} = \mathbf{E}(t) - \nabla(V_{ne} + V_{ee}) \quad (1)$$

Here $\mathbf{E}(t)=(0,0,F(t))$ is the electric field and $F(t)=F\cos(\omega t)$. The indices i=1 and 2 refer to the tunnel ionized and the bound electron with ionization potentials I_{p1} and I_{p2}, respectively. The potentials are $V_{ne}=-2/|\mathbf{r}_i|$ and $V_{ee}=1/|\mathbf{r}_1-\mathbf{r}_2|$, respectively.

The initial condition of the first, i.e. the tunneled electron, is determined by an equation including an effective potential [36,37]. The initial velocities are set to be $v_z=0, v_x=v_{per}\cos(\Theta)$ and $v_y=v_{per}\sin(\Theta)$. The weight of each trajectory is proportional to $w(t_0,v_{per})=w(0)\hat{w}(1)$ [47]. Here $w(0)$ is the tunneling rate in the quasistatic approximation and $\hat{w}(1)=(2|I_{p1}|)^{1/2}/(\varepsilon\pi)\ \exp(-v_{per}^2(2|I_{p1}|)^{1/2}/\varepsilon)$ is the quantum-mechanical transverse velocity distribution.

The initial condition of the second, i.e. the bound electron is determined by assuming that the electron is in the ground state of He^{1+} and that its initial distribution is a microcanonical distribution [37,48].

Under the condition of the experiment [24], the recoil momentum of the ion, $\mathbf{P}$, satisfies $\mathbf{P}\approx-\mathbf{p}_e$ or $-(\mathbf{p}_{e1}+\mathbf{p}_{e2})$ corresponding to singly or doubly ionized ions, respectively. Here p_e is the momentum of the ionized electron for single ionization, and $\mathbf{p}_{e1}$ and $\mathbf{p}_{e2}$ are the momenta of the two ionized electrons for double ionization, respectively. We need to calculate the momentum distribution of the ionized electrons. The parameters for our calculation are chosen as $I_{p1}=0.9$ a.u. (24.12 eV), $I_{p2}=2$ a.u. (54.4 eV), $\omega=0.05642$ a.u. ($\lambda_l=800$nm) and F=0.0935 a.u., 0.141 a.u. and 0.174 a.u., corresponding to I=2.9 x

10^{14}W/cm^2, 6.6 x 10^{14}W/cm^2 and 1.0 x 10^{15}W/cm^2, respectively. The calculation of the single ionization is quite trivial. But the calculation of the double ionization is a little complicated. In the first step of our computation, 1- 2 x 10^5 points are randomly distributed in the parameter volume $-\pi/2<\phi_0<\pi/2$, $v_{per}>0$ and $0<\theta<2\pi$ where $\phi_0=\omega t_0$. The trajectories are traced until at least one electron has moved to such a position that $r_i>200$. About 300 trajectories are found to lead to double ionization in our calculations. In the second step, the parameter volume is carefully chosen according to the parameters obtained in the double ionization cases [37]. It is pointed out in Ref.[37] that most double ionization yields come from the region $-0.2<\phi_0<0.4$ with a tail up to$\phi_0=1.2$. Moreover, the parameter volume of the initial perpendicular velocity component also gets reduced depending on the calculations of the first step. Finally, about 1- 2 x 10^4 double ionization cases are obtained in about 1- 2 x 10^6 random traces. Then these cases are traced until $t_f=13T$ to obtain the distribution of the momenta of the electrons; here T is the period of the laser field. In the calculations, the field strength is a constant during $t_0<t<10T$ and is turned off in a cosine-squared shape during the last three periods.

Figure 1 shows the momentum distributions of singly ionized He parallel and perpendicular to the laser polarization. It is interesting to note that the distributions of the momenta parallel to the polarization display a double-hump structure, similar to that for double ionization. For comparison, the momentum distribution obtained without considering the interaction between the tunneled electron and the core is also shown in Fig. 1, which presents a single-peak structure, in contrast. This comparison clearly shows that the double-hump structure in the distribution of single ionization also appears because of the interaction between the electron and the core, i.e. the recollision. This can be seen more clearly in Fig. 2, which shows the distribution of phase ϕ_0 corresponding to different final momenta. Since the momentum values obtained in our simulation is continuous, the momentum labeled in Fig. 2, for example p_e =0.35 a.u., means the momentum in the interval $[p_e-\delta p\ p_e+\delta p]$, where δp is chosen as 0.1 a.u. As stated above, we choose $-\pi/2<\phi_0<\pi/2$ in the simulation and obtain the distribution. However, the momentum distributions shown in Fig. 1 and Fig. 3 are obtained by reflecting the distribution relative to 0 and adding them together. It is well known that, in the semiclassical picture, the tunneled electron, with momentum equal to zero, is ionized around the peak of the laser field, i.e. $\phi_0=0$, and has the largest probability, which gives the single-peak located at zero in the distribution. But with the rescattering effect included, most of the electrons ionized near the peak of the field will return to the core with nonzero momentum, interact with the core (rescattering) and the field and

finally acquire non-zero momenta. It can thus be seen in Fig. 2 that, when the momentum changes from zero to 0.25 a.u., the peak of the distribution shifts from about -0.1 to about zero and the probability (the area under the curve) also increases. When the momentum increases to 0.35 a.u., the location of the peak moves to about 0.05 and the probability reaches the maximum, corresponding to the location of the peak at p_e =0.35 a.u. in Fig. 1c. If the momentum increases further, the peak of the distribution shifts further but the probability begins to decrease.

Our results are qualitatively consistent with the experimental data [24,25]. The experimental results, however, did not indicate the double-hump structure in the momentum distribution along the laser polarization, possibly due to limited resolution. There are several reasons for the discrepancy between our simulation and the experiments. First, a constant amplitude field is used in our simulation. In fact, the contributions at different times during the laser pulse and at different positions in the focusing volume with different laser intensities may smear out the theoretical predicted structures in actual experiments. Second, the resolution of the measurement in the experiment was probably not high enough. Since the space between the two peaks in the distribution is small, as seen in Fig. 1, it may be difficult to resolve the detailed structure in experiments. Third, the semiclassical model is believed to overestimate the rescattering effect since the interaction between the electron and the field is treated classically without considering the quantum effects such as diffusion [8]. Fourth, compared to a high energy electron with large momentum, a low energy electron with small momentum has a higher probability to undergo inelastic collisions with the ion. It may then recombine with the ion or excite the bound electron and be simultaneously captured to form a doubly excited bound state of He that is only classically allowed. This can be confirmed by examining the phase distribution that leads to atomic He after evolution as shown in Fig. 2 (thick solid line). It is clearly seen that the phases leading to recombination focus in the region where the momentum is small. This classical recombination effect indeed deepens the valley between the maxima in the momentum distribution. However, it will not completely smear out the characteristics of the distribution if the classical recombination effect is avoided because of the fact that the main contribution to the peak of the momentum distribution is from the cases with phases around zero. This has the highest probability and is slightly influenced by the classical recombination effect (in the quantum picture, the electron also has some probability to recombine with the ion). Furthermore, to avoid the formation of the doubly excited bound state of He, further calculations have been done by using the

Coulomb approximation to simulate the potential of He^+ instead of the bound electron. These results are also presented in Fig. 1 and show slightly shallower valleys and closer distances between the peaks in the momentum distributions. It is noted that a similar calculation of the momentum distribution for single ionization of Ne is reported in Ref. [49], where no double-hump structure in the momentum distribution was observed. However, because they use a classical Monte Carlo method to calculate the ionization process, the tunneling ionization that plays a very important role cannot be included and the distribution, especially in the small momentum part, is not correct for comparison with experimental result [49]. In addition, it is clearly seen in Fig. 1 that, the width of the distribution obtained by including rescattering is narrower than that of the distribution without considering rescattering and is more consistent with the experimental data [24,25]. In our opinion, this is also the consequence of the interaction between the electron and the ionic potential. Since the ionic potential is an attractive one, it will reduce the momentum of the ejected electron and then leads to a narrower momentum distribution. On the other hand, the excitation of the bound electron by the inelastic collision with the tunneled electron and the recombination of the tunneled electron will also reduce the width of the momentum distribution. In summary, the double-hump effect of single ionization may be overestimated in the semiclassical model due to its classical aspect. However, it can still be seen in the Fig. 1 of Ref [24] that there is at least a plateau structure around the center. This kind of effect needs to be examined in future experiments.

We next turn our discussion to the double ionization process. Figure 3 shows the distributions of momenta for double ionization. The results are qualitatively consistent with the experimental data presented by Weber *et al.* [24], whereas in the experiment the double peak structure is much less pronounced. All the distributions of momenta parallel to the polarization display the structure of well separated double peaks, which is believed to be a consequence of the rescattering mechanism of the nonsequential double ionization. It can be understood as follows. For simplification, it is assumed that only the electron that tunnels out at t_a has enough kinetic energy to ionize the bound electron when it returns back to the ion at time t_b (only consider $-T/4< t_a <T/4$ according to the symmetry of the laser field as stated above). It is known that, in the absence of an external field, the sum of the momentum of the two electrons after impact-ionization is a single-hump distribution with a central maximum [50]. In the presence of the external field the ionized electrons will be accelerated by the field. Then the maximum of the sum-momentum distribution moves up or downwards (according to $-T/4< t_a <T/4$ or

T/4< t_a <3T/4) by a magnitude dependent on the time at which the electrons are ionized and thus finally forms a double-hump structure with a central minimum. Moreover, it can be seen from Fig. 3 that when the intensity increases, the absolute value of the momentum with maximum probability increases. This is reasonable since more intense field will accelerate the electron with larger momentum.

Another interesting feature that can be observed from Fig. 3 is that, when the intensity decreases, the minimum between the two peaks also decreases relatively. This can be understood by examining Fig. 4 that shows the angular distributions of two emitted photoelectrons in double ionization. Here the asymmetry with respect to 90° (perpendicular to the polarization direction of the field) in the figures is due to our choice of the phase in the interval$\phi_0 \in [-\pi/2, \pi/2]$. The angular distribution of the electron with initial phase in $[\pi/2, 3\pi/2]$ will be the mirror image of that with respect to 90°. So the total angular distribution, i.e. the distribution observed in the experiment, is the sum of the two contributions and will be symmetrical with respect to 90°. The distribution with I=2.9 x 10^{14}W/cm^2 is more concentrated on the negative direction than those with I=6.6 x 10^{14}W/cm^2 and 1.0 x 10^{15}W/cm^2. This effect can be understood as follows: neglecting the core potential, the final momentum of the ionized electron can be expressed as

$$p = -\frac{q}{\omega} F \sin(\omega t_c) + p_c,$$

(2)

where t_c is the collision time and p_c is the momentum of the electron just after collision. For simplification, we assume

$$p_c = \sqrt{2(3.17U_p - I_{p2})},$$

(3)

which means that all the excess energy is gained by only one electron. In the case of I=2.9 x 10^{14}W/cm^2, we have F/ω=1.66 a.u. and p_c=0.59 a.u.. Since the phase ωt_c is mainly in the interval from 3π /2 to 2π, i.e. $\sin\omega t_c < 0$, the final momenta of electrons are mainly in the negative direction. This gives rise to the shift of the maximum to the opposite direction in the angular distribution of He^{2+} compared with that of single ionization [45]. In fact, the excess energy is shared by two electrons, and consequently almost all the electrons will be driven to the negative direction in this condition. In the cases of I=6.6 x 10^{14}W/cm^2 and 1.0 x 10^{15}W/cm^2, we have F/ω=2.5 a.u.,3.07 a.u. and p_c =2.43 a.u.,3.31 a.u.. Thus more and more of the ionized electrons cannot be driven to

the negative direction as the intensity increases. This leads to the fact that the minimums between the peaks become less pronounced with increasing intensity.

However, it is obvious that this trend is not consistent with the experimental observations [24]. In the experiments, on the contrary, the minimum between the peaks increases relatively as the intensity decreases. This discrepancy indicates that when the intensity decreases to a value well below the saturation intensity, the simple rescattering ionization mechanism does not dominate the process. Other mechanisms giving rise to central peak distribution of the momentum parallel to the polarization should be introduced. For example, the process of rescattering excitation with subsequent tunneling has been shown to become important for an Ar target as the intensity decreases [28].

Similar to the situation in single ionization, it may happen that the cross section of the recapture of one electron by the ion is overestimated in the classical calculations and this effect will deepen the valley as the intensity decreases which puts our conclusions on a weak ground. We examine the probability of recapture by counting the number of the events for which the total energies of both electrons have been once above zero during the evolution but finally end up as single ionization. This number is quite small and increases as the intensity decreases, but is in any case less than 10\% of all double ionization events when the intensity is $2.9 \times 10^{14} W/cm^2$. Thus, this limitation of the model should not influence the conclusion obtained above.

The momentum correlation between the two emitted electrons is also shown in Fig. 5 that presents the density plot of the distribution of the momentum components parallel to the polarization of the laser field. It is clearly seen that the emitted electrons have a strong tendency to fly to the same side of the ion in the polarization direction, which is consistent with the experiments [27] and previous simulations [41,46]. In addition, when the intensity decreases, the emitted electrons show an even stronger trend to acquire similar momenta parallel to the laser field. This is also consistent with the above analysis.

Figure 6 presents the momentum correlation between the electrons with different relative transverse momenta. Here the relative transverse momentum is defined as $\Delta p=((p_{1x}-p_{2x})^2+(p_{1y}-p_{2y})^2)^{1/2}$. A dependence of the correlation pattern on the transverse momentum can be observed. Comparing Fig. 6 with Fig. 5b, if the relative transverse

momentum is large, the density along the diagonal line increases, which means that both the electrons are more likely to have similar parallel momenta. In contrast, if the relative transverse momentum is small, the density along the diagonal line decreases, indicating that the electrons tend to have different parallel momenta. This dependence can be explained as the repulsion effect in the correlation between the emitted electrons [29,51]

In summary, by using a semiclassical rescattering model, we have calculated the momentum distribution of recoil ions from laser induced single and double ionization. It has been found that in both cases of single and double ionization, the distributions of the momentum parallel to the polarization show a double-hump structure. Analysis shows that the double-hump structure in single ionization is also the consequence of the rescattering, i.e. the interaction between the tunneled electron and the potential of the core, similar to that in the case of double ionization. The result is compared with experiments and the limitations of the model are discussed. For double ionization, the calculations show that the minimum in the center of the distribution of the momentum parallel to the laser polarization decreases as the laser intensity decreases. This is not consistent with the experimental observations indicating a contrary tendency. Thus, it can be concluded that, when the intensity of the laser decreases, the contribution from the rescattering ionization process of the second electron will diminish and other processes, which are not included in the present model, may begin to dominate.

In addition, the correlated emission of electrons in double ionization is observed in the density plot of the distribution of the momentum components, of both the emitted electrons, parallel to the polarization. Comparison with experiments yields qualitative consistency. Finally, the evidence of the repulsion between the emitted electrons is observed in the momentum correlation between the electrons with different relative transverse momenta.

References

[1] J. L. Krause, K. J. Schafer, and K. C. Kulander, Phys. Rev. Lett. **68**, 3535 (1992).

[2] P. B. Corkum, Phys. Rev. Lett. **71**, 1994 (1993).

[3] G. G. Paulus, W. Nicklich, F. Zacher, P. Lambropoulos and H. Walther, J. Phys. B **52** L249 (1996).

[4] W. Becker, A. Lohr and M. Kleber, J. Phys. B **27** L325 (1994).

[5] M. Lewenstein, K. C. Kulander, K. J. Schafer and P. H. Bucksbaum, Phys. Rev. A **51**, 1495 (1995).

[6] D. Bao, S. G. Chen and J. Liu, Appl. Phys. B **62** 313 (1996).

[7] B. Hu, J. Liu, S. G. Chen, Phys. Lett. A **236**, 533 (1997).

[8] J. Chen, J. Liu, S. G. Chen, Phys. Rev. A **61**, 033402 (2000).

[9] A. L'Huiller *et al.*, Phys. Rev. A **27**, 2503 (1983).

[10] D. N. Fittinghoff *et al.*, Phys. Rev. Lett. **69**, 2642 (1992).

[11] B. Walker *et al.*, Phys. Rev. Lett. **73**, 1227 (1994).

[12] T. Brabec, M. Y. Ivanov and P. B. Corkum, Phys. Rev. A **54**, R2551 (1996).

[13] J. B. Watson *et al.*, Phys. Rev. Lett. **78**, 1884 (1997).

[14] A. Becker and F. H. M. Faisal, J. Phys. B **29**, L197 (1996).

[15] A. Becker and F. H. M. Faisal, J. Phys. B **32**, L335 (1996).

[16] K. J. LaGattuta and J. S. Cohen, J. Phys. B **31**, 5281 (1998).

[17] K. C. Kulander, J. Cooper and K. J. Schafer, Phys. Rev. A **51**, 561 (1995).

[18] D. N. Fittinghoff *et al.*, Phys. Rev. A **49**, 2174 (1994).

[19] M. Yu. Kuchiev, J. Phys. B **28**, 5093 (1995).

[20] B. Sheehy *et al.*, Phys. Rev. A **58**, 3942 (1998).

[21] W. C. Liu *et al.*, Phys. Rev. Lett. **77**, 520 (1999).

[22] V. Schmidt, *Electron Spectrometry of Atoms using Synchrotron Radiation* (Cambridge University Press, Cambridge, England, 1997).

[23] A. Becker and F. H. M. Faisal, Phys. Rev. A **59**, R1742 (1999).

[24] Th. Weber *et al.*, Phys. Rev. Lett. **84**, 443 (2000).

[25] R. Moshammer *et al.*, Phys. Rev. Lett. **84**, 447 (2000).

[26] Th. Weber *et al.*, J. Phys. B **33**, L127 (2000).

[27] Th. Weber *et al.*, Nature (London) **405**, 658 (2000).

[28] B. Feuerstein *et al.*, Phys. Rev. Lett. **87**, 043003 (2001).

[29] R. Moshammer *et al.*, Phys. Rev. A **65**, 035401 (2001).

[30] A. Becker and F. H. M. Faisal, Phys. Rev. Lett. **84**, 3546 (2000).

[31] U. Eichmann *et al.*, Phys. Rev. Lett. **84**, 3550 (2000).

[32] B. Witzel, N. A. Papadogiannis and D. Charalambidis, Phys. Rev. Lett. **85**, 2268 (2000).
[33] B. Feuerstein *et al.*, J. Phys. B **33**, L823 (2000).
[34] M. Lein *et al.*, Phys. Rev. Lett. **85**, 4707 (2000).
[35] H. W. van der Hart and K. Burnett, Phys. Rev. A **62**, 013407 (2000).
[36] J. Chen *et al.*, Phys. Rev. A **63**, 011404(R) (2001).
[37] L. B. Fu *et al.*, Phys. Rev. A **63**, 043416 (2001).
[38] V. R. Bhardwaj *et al.*, Phys. Rev. Lett. **86**, 3522(2001).
[39] G. L. Yudin and M. Yu. Ivanov, Phys. Rev. A **63**, 033404 (2001).
[40] K. Sacha and B. Eckhardt, Phys. Rev. A **64**, 053401 (2001).
[41] S. P. Goreslavskii *et al.*, Phys. Rev. A **64**, 053402 (2001).
[42] E. R. Peterson and P. H. Bucksbaum, Phys. Rev. A **64**, 053405 (2001).
[43] M. Dammasch *et al.*, Phys. Rev. A **64**, 061402(R) (2001).
[44] R. Lafon *et al.*, Phys. Rev. Lett. **86**, 2762(2001).
[45] J. Chen *et al.*, Phys. Rev. A **66**, 043410 (2002).
[46] L. B. Fu *et al.*, Phys. Rev. A **65**, 021406(R) (2002).
[47] N. B. Delone, and V. P. Krainov, J. Opt. Soc. Am. B **8**, 1207 (1991).
[48] J. S. Cohen, Phys. Rev. A **26**, 3008 (1982).
[49] C. R. Feeler and R. E. Olson, J. Phys. B **33**, 1997 (2000).
[50] A. P. R. Ran, Phys. Rep. **110**, 369 (1984).
[51] M. Weckenbrock *et al.*, J. Phys. B **34**, L449 (2001).

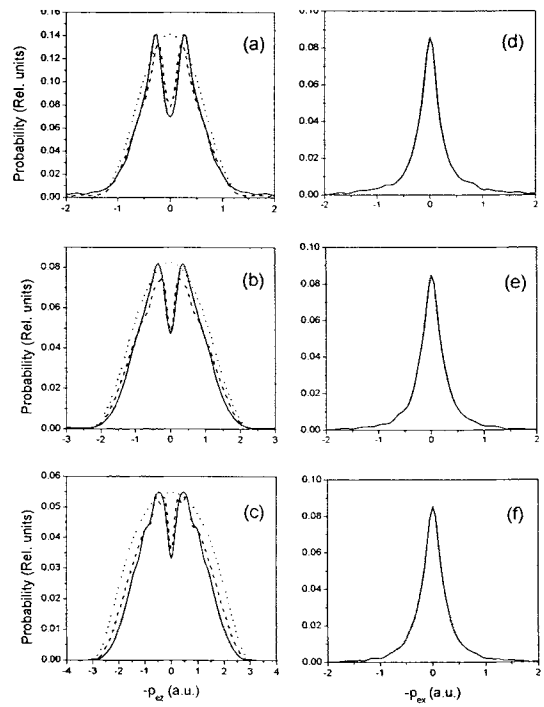

Fig. 1. From top to bottom, momentum distribution of He^+ ions in the parallel direction ((a),(c),(e)) and perpendicular direction ((b),(d),(f)) to the laser polarization. (a), (b): I=2.9 x 10^{14}W/cm^2; (c),(d): 6.6 x 10^{14}W/cm^2 and (e),(f): 1.0 x 10^{15}W/cm^2. Solid line: considering rescattering; dotted line: without rescattering; dashed line: calculation with Coulomb approximation instead of the bound electron (see text).

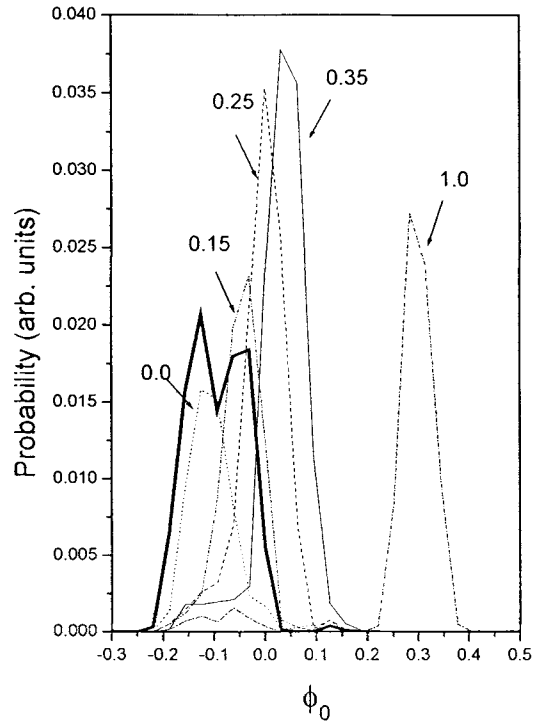

Fig. 2. Distribution of phase Φ_0 corresponding to different momenta except the thick solid line which is for the recombination (see text). The numbers shown represent the electron momentum (in atomic units).

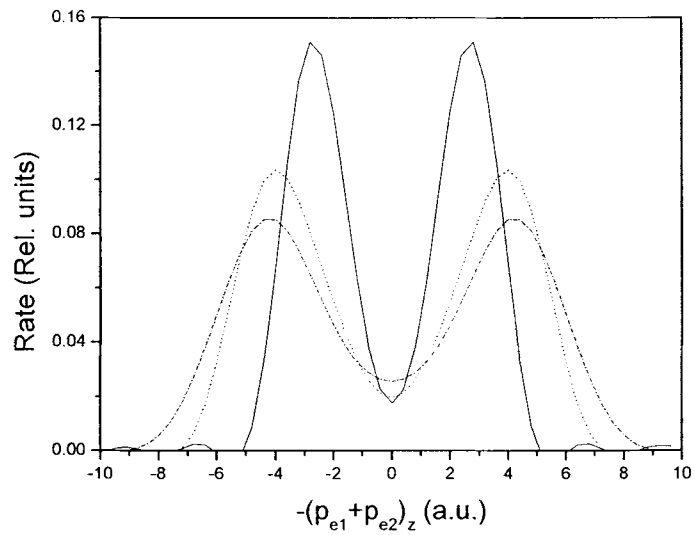

Fig. 3. He^{2+} recoil-ion momentum distributions. Solid line: $2.9 \times 10^{14} W/cm^2$, dotted line: $6.6 \times 10^{14} W/cm^2$ and dash-dotted line: $1.0 \times 10^{15} W/cm^2$.

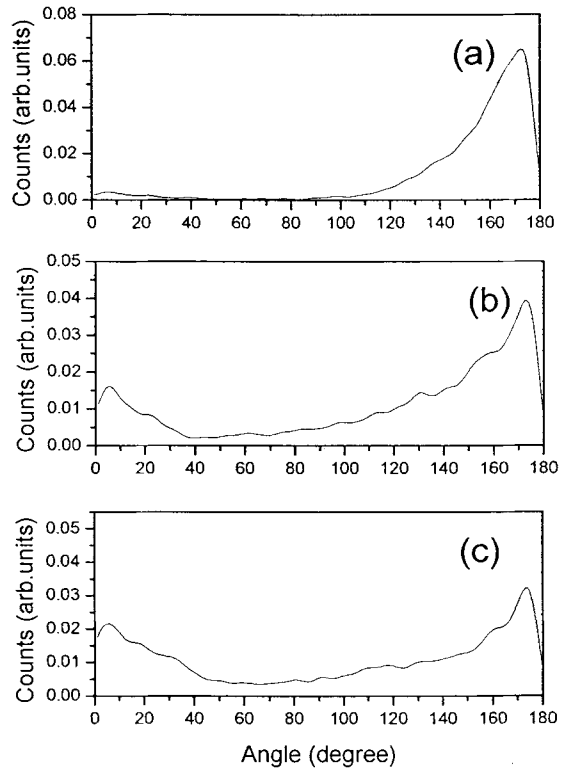

Fig. 4. The angular distributions of two emitted photoelectrons in double ionization at laser intensities (a) 2.9×10^{14}W/cm^2, (b) 6.6×10^{14}W/cm^2 and (c) 1.0×10^{15}W/cm^2.

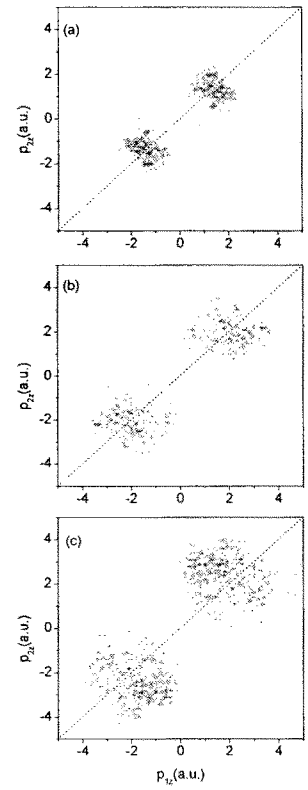

Fig. 5. Density plot of the distribution of the momentum components of electron one and two parallel to the laser polarization direction.

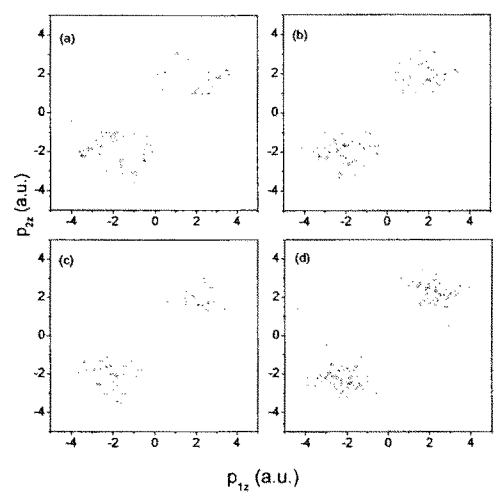

Fig. 6. Momentum correlation between the emitted electrons with different relative transverse momentum δp. (a) $\delta p < 0.5$ a.u.; (b) $0.5 < \delta p < 1.0$ a.u.; (c) $1.0 < \delta p < 1.5$ a.u.; (d) $\delta p > 1.5$ a.u..

A. 2. 3. Frequency dependence of non-sequential double ionization

Frequency dependence of non-sequential double ionization (NSDI) of Ne is studied using a semiclassical rescattering model. It is found that the ratio (Ne^{2+}/Ne^{+}), calculated for the laser intensity of $I=1.0 \times 10^{15} W/cm^2$, increases while the wavelength decreases down to about 250nm, the limit of the applied model. Careful investigation of the trajectories show that there are two categories of double ionization: "instant ionization" and "delayed ionization."By limiting the time interval between the re-collision time and ionization time, the " delayed ionization" is identified to give rise to the high probability of NSDI in the short wavelength region.

In recent years, the study on double (or multiple) ionization of atoms and molecules has attracted considerable attention. After the first observation of unexpected high ion yields in double and multiple ionization in intense, linearly polarized laser pulses [1], which is called non-sequential double (or multiple) ionization (NSDI), several mechanisms have been proposed to explain the observed experimental results. Among them, three are commonly considered. One of them is that the second electron could be shaken-off by a nonadiabatic change of the potential caused by the emission of the first electron, suggested by Fittinghoff *et al.* [2]. Another is the rescattering model proposed by Corkum [3,4], in which the second electron is ionized by a collision with the first tunneled electron when it returns to the parent ion after freely propagating for about half an optical cycle in the external laser field. The third is a "correlated energy sharing" model based on a so-called intense-field many-body S-matrix theory derived by a rearrangement of the usual S-matrix series proposed by Becker and Faisal [5-7]. Since the measurements of the distributions of the recoil momentum of doubly charged He [8] Ne [9] and Ar [10,11] and charge-state resolved above-threshold ionization (ATI) spectra [12,13] in the non-sequential region, intensive theoretical and experimental investigations have been devoted to this interesting topic [14-28]. Now it is commonly accepted that the "shaken-off" model can be ruled out from being a dominant contribution to NSDI since it gives an ion momentum distribution along the field direction peaking at zero, which conflicts with the observation exhibiting distinctive maximums at nonzero momenta [8,9]. The "correlated energy sharing" model and "rescattering" model can both give results consistent with the experiments [9,14,16,18]. The rescattering model and its recent development is more applausive because it gives a

clearer picture of the process: after being ionized by the laser field, the first electron moves in the external field and may return back to the core and collides with the core. Thus the bound electron may be ionized directly by the collision or be driven to excited states and then ionizes via a tunneling process [3,4,19,21,22].

In this paper, we studied the frequency dependence of non-sequential double ionization of Ne using a semiclassical rescattering model developed recently [19]. This model has been applied to quantitatively reproduce the excessive double ionization of He observed in experiments and succeeds in the explanation of the momentum distribution of recoiled ions [18,19,29]. This model has also been used to examine the photoelectron spectra, angular distribution and correlated electron emission observed in more recent NSDI [27,28].

Firstly, we briefly represent the semiclassical rescattering model adopted in our calculations [18,19]. Since we only consider the double ionization problem, a Ne atom is approximated as a two-electron atom. The ionization of the first electron from the bound state to the continuous state is treated by the tunneling ionization theory. The subsequent evolution of the ionized electron and the bound electron in the combined Coulomb potential and laser field is described by classical Newtonian equations. To emulate the evolution of the electron wave packet, a set of trajectories is launched with initial conditions taken from the wave function of the tunneled electron.

Evolution of the two-electron system after the tunnel ionization of the first electron is determined by the classical equations of motion (in atomic units)

$$\frac{d^2\mathbf{r}}{dt^2} = \mathbf{E}(t) - \nabla(V_{ne} + V_{ee}) \quad (1)$$

Here $\mathbf{E}(t)=(0,0,F(t))$ is the electric field and $F(t)=F\cos(\omega t)$. The indices i=1 and 2 refer to the tunnel ionized and the bound electron with ionization potentials I_{p1} and I_{p2}, respectively. The potentials are $V_{ne}=-q_e/|\mathbf{r}_i|$ and $V_{ee}=1/|\mathbf{r}_1-\mathbf{r}_2|$, with q_e being the effective charge of the Ne^+ ion. The initial condition of the first electron is determined by an equation including an effective potential [18,19]. The initial velocities are set to be $v_z=0, v_x=v_{per}\cos(\Theta)$ and $v_y=v_{per}\sin(\Theta)$. The weight of each trajectory is proportional to $w(t_0,v_{per})=w(0)\hat{w}(1)$ [30]. Here $w(0)$ is the tunneling rate in the quasistatic approximation and $\hat{w}(1)=(2|I_{p1}|)^{1/2}/(\varepsilon\pi)\exp(-v_{per}^2(2|I_{p1}|)^{1/2}/\varepsilon)$ is the quantum-mechanical transverse velocity distribution. The initial condition of the second, i.e. the

bound electron is determined by assuming that the electron is in the ground state of Ne^+ under Coulomb approximation and its initial distribution is given by a microcanonical distribution [19,31].

In our computation, 10^5- 3×10^5 points are randomly distributed in the parameter volume $-\pi/2<\phi_0<\pi/2$, $v_{per}>0$ and $0<\Theta<2\pi$, where $\phi_0=\omega t_0$. The trajectories are traced until at least one electron has moved to such a position that $r_i > R$, with R in the range between 200 and 800 a.u.. The number of points and r_i varies with the frequency to ensure the convergence. The intensity of the laser field is chosen as $I=1.0 \times 10^{15}$ W/cm^2. About 1000- 1300 double ionization cases for each frequency are found in our calculation. Then these cases are traced until $t_f=13T$ (T is the period of the laser field) to ensure they are really the double ionization cases (some of them are not double ionization since the electrons may come back to recombine with the core). In this calculation, the amplitude of the field is kept as a constant during $t_0<t<10T$ and drops to zero in a cosine-squared shape during the last three cycles.

The frequency dependence of the ratio of Ne^{2+}/Ne^+ is illustrated in Fig. 1. The ratio increases as the wavelength decreases, i. e. the frequency increases. The maximum is at about 250 nm. When the wavelength decreases further, the ratio drops sharply. This result is not consistent with the prediction of theoretical [7,32] and experimental results [32-34]. In reference [32], the so-called "antena" theory, proposed by Kuchiev [35], was applied to calculate the wavelength dependence of Ar^{2+}/Ar^+. The peak of the ratio appears at about 600 nm. In view of the rescattering model, there are two effects that determine the frequency dependence of NSDI [32]. One is that the pondermotive energy decreases with decreasing wavelength. This will limit the possibilities of NSDI for short wavelength. Another is the diffusion of the electron wavepacket. Under a longer wavelength laser field the width of the wavepacket of the first ionized electron at the rescattering moment spreads wider since the electron will experience longer time before re-collision. Even though the electrons are treated classically in this semiclassical model the assembly of the first electron can be considered as to emulate the electron wavepacket. The longer is the wavelength, the lower is the probability of collision between the first electron and the core with the same initial condition. This explains the reason why the ratio decreases as wavelength increases. However, the increase of the ratio as wavelength decreases until 250 nm is not consistent with the above arguments, though different atoms are used in Ref [32] and this paper. The maximum kinetic energy that the first electron can gain in the field when it comes back to the core is

$E_k=3.17U_p$, where U_p is the pondermotive energy. Under the condition of $I=1.0 \times 10^{15}W/cm^2$ and $E_k=I_{p2}$, we get $\omega=0.126$ a.u., i.e. $\lambda=357$ nm. This means that when the wavelength is shorter than 357 nm, the maximal kinetic energy of the first electron, when it re-collides with the core, is smaller than the ionization potential of the second electron. This indicates that the ratio of the NSDI should reach its maximum at, if not much, longer wavelength than 357 nm for the impact-ionization cross-section of $e\text{-}Ne^+$ decreases very fast above the threshold energy. Moreover, there is another parameter that limits the application of the model. In the semiclassical model, the ionization of the first electron is treated as a tunneling process. Thus the Keldysh parameter ($\gamma=(I_{p1}/U_p)^{1/2}$) should be less than 1. This limit gives that $\omega<0.138$ a. u., or equivalently $\lambda>327$ nm.

The question remaining to be answered is why the probability of NSDI is so high even when the kinetic energy of the returned electron is already too low to ionize the bound electron in the high frequency region. Careful inspection on the trajectories gives some hints on this problem. We find two typical double ionization processes. Figure 2 shows the energy evolution of electrons in these two categories of NSDI cases. In the first category, as shown in Fig. 2a, after collision with the tunneled electron, the energy of the bound electron instantly rises above zero. It can be called as "instant ionization". In the second one, as shown in Fig.2b, the bound electron is at first excited to some energy level lower than zero by the returned electron and then is ionized by the field after a rather long time. It can be called as "delayed ionization". Further investigation shows that the portion of the second category decreases with increasing wavelength.

To quantitatively categorize the trajectories, we define a parameter Δt called an ionization time, which is equal to the interval between the collision time of two electrons and the moment when both of them are ionized, i. e. their energies are above zero. Here the collision time is chosen as the time when the distance between two electrons is the smallest. The curves with differentΔt are plotted in Fig. 3. The frequency dependence with Δt is obtained by counting the double ionization cases after excluding the cases with ionization time longer than Δt. It is obvious that the ratio increases with Δt. Starting from $\Delta t=1.0$ T, the ratio drops fast at higher frequency. When Δt decreases to 0.1T, the shape of the curve becomes stable with a peak at about 600 nm. This curve is quite consistent with that of Ar predicted by the antena model [32]. However, this consistency is not compelling because the atomic species are different.

From the above analysis, it can be concluded that the probability of double ionization in high frequency region is overestimated in the semiclassical model. The cause of this overestimated probability, or in other words, the appearance of large amount of "delayed ionization" cases, is believed to be due to the classical aspect of the model. In the semiclassical model, the evolution of the electrons after the tunneling of the first electron is treated classically. It is well known that the energy of the bound electron is continuous in classical picture. The bound electron can be excited to any higher energy level (but still below zero) via the collision with the tunneled electron and, if the energy is high enough, may be ionized by the external field. Thus the bound electron can still be ionized in this classical way in spite of the insufficient kinetic energy of the returned first electron at short wavelength. This is also believed to be one of the reasons why NSDI ratio is overestimated by the Corkum's theory [4]. Usually the ionization of the excited bound electron by the laser field in the classical way does not occur instantly, contrary to the ionization occurring only by the scattering of the first electron. This characteristic makes it possible to distinguish these two categories of double ionization using the method stated above. Furthermore, the reason why the portion of " delayed ionization" increases with frequency can be understood as follows: as the wavelength decreases, the time that the tunneled electron experiences before rescattering decreases and then the tunneled electron has higher probability to collide with and excite the bound electron. On the other hand, the ionization rate of the bound electron induced by the external field (single ionization rate) also increases with decreasing wavelength [36]. Thus as the wavelength decreases, the bound electron has higher probability to be ionized, which is allowed only classically.

In conclusion, the frequency dependence of non-sequential double ionization of Ne is investigated using a semiclassical rescattering model. The NSDI ratio increases as the wavelength decreases and reaches its maximum at about 250 nm, the limit of the applied semiclassical model ($I=1.0 \times 10^{15} W/cm^2$). Careful investigation of the trajectories shows that there are two categories of double ionization: "instant ionization" that is caused by the collision between the bound and tunneled electrons and "delayed ionization" that occurs through the excitation of the bound electron by the collision with the returned electron and subsequent ionization by the field. Based on the different time intervals for these two processes, a technique is developed to identify the double ionization cases by limiting the time interval between the re-collision time and ionization time. It is found that "delayed ionization" gives rise to the large probability of

NSDI in the high frequency region, which is due to the classical aspect of the semiclassical model. However, so far the comparison between theories and experiments is still poor. Further examination of our calculations will be made in comparison with future experiments and quantum-mechanical calculations.

References

[1] A. L'Huiller *et al.*, Phys. Rev. A **27**, 2503 (1983).

[2] D. N. Fittinghoff *et al.*, Phys. Rev. Lett. **69**, 2642 (1992).

[3] P. B. Corkum, Phys. Rev. Lett. **71**, 1994 (1993).

[4] T. Brabec, M. Y. Ivanov and P. B. Corkum, Phys. Rev. A **54**, R2551 (1996).

[5] A. Becker and F. H. M. Faisal, J. Phys. B **29**, L197 (1996).

[6] A. Becker and F. H. M. Faisal, J. Phys. B **32**, L335 (1996).

[7] A. Becker and F. H. M. Faisal, Phys. Rev. A **59**, R1742 (1999).

[8] Th. Weber *et al.*, Phys. Rev. Lett. **84**, 443 (2000).

[9] R. Moshammer *et al.*, Phys. Rev. Lett. **84**, 447 (2000).

[10] Th. Weber *et al.*, J. Phys. B **33**, L127 (2000).

[11] Th. Weber *et al.*, Nature (London) **405**, 658 (2000).

[12] B. Witzel, N. A. Papadogiannis and D. Charalambidis, Phys. Rev. Lett. **85**, 2268 (2000).

[13] R. Lafon *et al.*, Phys. Rev. Lett. **86**, 2762(2001).

[14] A. Becker and F. H. M. Faisal, Phys. Rev. Lett. **84**, 3546 (2000).

[15] U. Eichmann *et al.*, Phys. Rev. Lett. **84**, 3550 (2000).

[16] M. Lein *et al.*, Phys. Rev. Lett. **85**, 4707 (2000).

[17] H. W. van der Hart and K. Burnett, Phys. Rev. A **62**, 013407 (2000).

[18] J. Chen *et al.*, Phys. Rev. A **63**, 011404(R) (2001).

[19] L. B. Fu *et al.*, Phys. Rev. A **63**, 043416 (2001).

[20] V. R. Bhardwaj *et al.*, Phys. Rev. Lett. **86**, 3522(2001).

[21] G. L. Yudin and M. Yu. Ivanov, Phys. Rev. A **63**, 033404 (2001).

[22] B. Feuerstein *et al.*, Phys. Rev. Lett. **87**, 043003 (2001).

[23] K. Sacha and B. Eckhardt, Phys. Rev. A **64**, 053401 (2001).

[24] S. P. Goreslavskii *et al.*, Phys. Rev. A **64**, 053402 (2001).

[25] E. R. Peterson and P. H. Bucksbaum, Phys. Rev. A **64**, 053405 (2001).

[26] M. Dammasch *et al.*, Phys. Rev. A **64**, 061402(R) (2001).

[27] J. Chen *et al.*, Phys. Rev. A **66**, 043410 (2002).

[28] L. B. Fu *et al.*, Phys. Rev. A **65**, 021406(R) (2002).

[29] J. Chen and C. H. Nam, Phys. Rev. A **66**, 053415 (2002).

[30] N. B. Delone, and V. P. Krainov, J. Opt. Soc. Am. B **8**, 1207 (1991).

[31] J. S. Cohen, Phys. Rev. A **26**, 3008 (1982).

[32] S. Larochelle *et al.*, J. Phys. B **31**, 1201(1998).

[33] K. Kondo *et al.*, Phys. Rev. A **48**, R2531(1993).

[34] D. Charalambidis *et al.*, Phys. Rev. A **50**, R2822 (1994).

[35] M. Y. Kuchiev, Sov. Phys.-JETP **20**, 404 (1987); J. Phys. B **28**, 5093 (1995); Phys Lett. A **212**, 77 (1996).

[36] A. Becker *et al.*, Phys. Rev. A **64**, 023408 (2001).

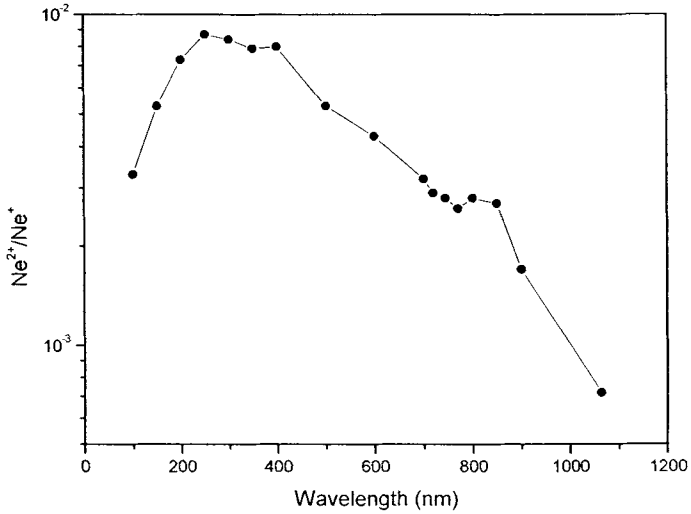

Fig.1. Wavelength dependence of ratio Ne^{2+}/Ne^{+}. I=1.0 x 10^{15}W/cm^2.

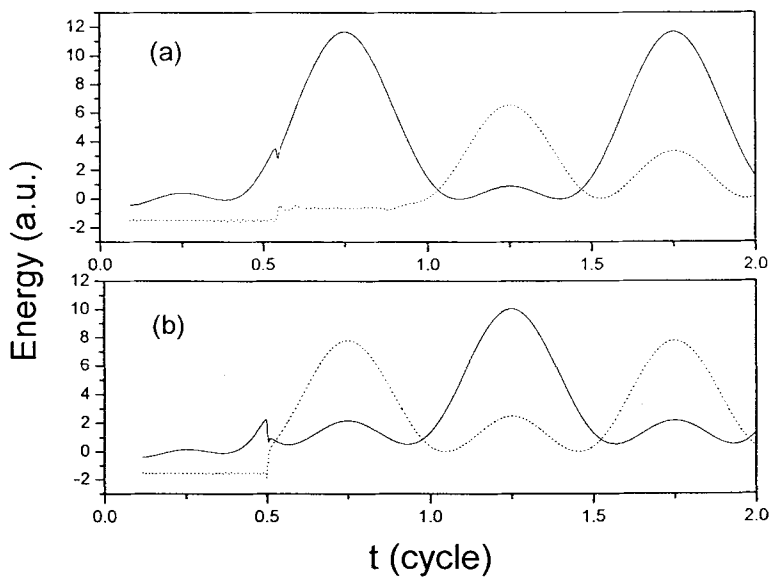

Fig.2. Energy evolution of electrons in double ionization. I=1.0 x 10^{15}W/cm^2, λ=800 nm. Solid line: tunneled electron; dotted line: bound electron. (a) "instant ionization" and (b) "delayed ionization" (see text).

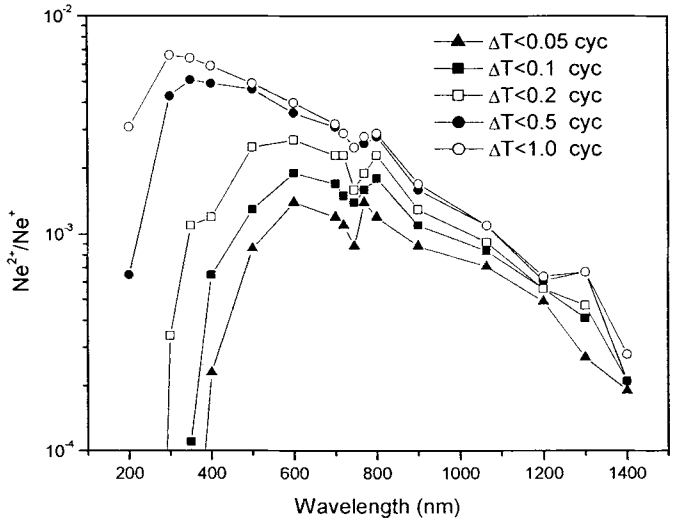

Fig.3. Wavelength dependence of double ionization with different ionization time Δt $I=1.0 \times 10^{15} W/cm^2$.

3 Development of high power femtosecond laser technology

A. 3. 1. Performance improvement of a 1 kHz femtosecond high-power laser

I. Installation of an acousto-optic pulse shaper in a CPA laser

Chirped pulse amplification (CPA) Ti:sapphire lasers have become a standard laser configuration for the generation of high-power femtosecond laser pulses. In the CPA amplifier, output pulses lengthen compared to input pulses because of uncompensated phase error and gain narrowing. Therefore, maintaining the short pulse duration after amplification needs a programmable device that is capable of compensating for large amounts of dispersion over large spectral bandwidths and shaping the spectral amplitude. Several devices have been demonstrated, such as liquid-crystal modulators, deformable mirrors and acousto-optic deflectors. All these devices require high-quality optical elements and the precise alignment because of the use of Fourier plane of a zero-dispersion line. Moreover, they induce the spatio-temporal distortion in the pulse, which is proportion to the magnitude of the shaping. But, the acoustic-optic programmable dispersive filter (AOPDF) proposed in 1997 can shape the spectral phase and amplitude of the pulse without the zero-dispersion line and spatio-temporal distortion.[1,2] As shown in Fig. 1, the AOPDF works through a collinear acousto-optic interaction. The group delay of the diffracted optical pulse is controlled by the acoustic frequency, which is a function of time. Simultaneously, the spectral amplitude of the diffracted optical pulse is controlled by the acoustic signal's power.

The front-end oscillator of the CPA laser system is a long-cavity femtosecond Ti:sapphire laser with an energy of 13 nJ per pulse and a repetition rate of 27 MHz.[3] Laser pulses from the oscillator are stretched to about 220 ps by an all reflective Offner-triplet type stretcher. The pulses are injected into a multi-pass amplifier that consists of a flat gold mirror and two concave dielectric mirrors. The amplifier is pumped by 1-kHz 11-mJ green pulses from a frequency-doubled Q-switched Nd:YLF laser. After the first five passes, the preamplified pulse train is extracted from the amplifier, and pulses are selected using a Pockels cell with 1-kHz repetition rate. The selected pulses are reinjected into the amplifier and their energy is boosted up to 1.5 mJ in the four passes. In this configuration, the Pockels cell not only acts as pulse selector but also suppresses amplified spontaneous emission (ASE). The laser pulses compressed by a grating compressor have a duration (FWHM) of 30 fs and a spectral width of 40 nm. In our CPA laser system, the AOPDF is positioned between the stretcher and the amplifier because of its low damage threshold. When the AOPDF was installed, the gain narrowing and phase errors were compensated for through spectral amplitude and phase shaping before amplification. To obtain the wider spectral width of the pulse by compensating for the gain narrowing, the spectral amplitude was controlled with a minimum transmission at 800 nm. The output pulses were characterized by the frequency-resolved optical gating (FROG) method. To correct the residual phase error, a fourth-order polynomial was fitted to the spectral phase retrieved through the FROG. It was used to calculate the new transfer function for the AOPDF. As the result, the spectral width was 65 nm and the pulse duration was 19.5 fs close to Fourier transform-limited pulse duration as shown in Fig. 2.

II. Generation of 1-kHz high-power sub-10-fs pulses

Laser pulses with a duration as short as 20 fs and the peak power of terawatt level are now available from CPA lasers. High-power sub-10-fs optical pulses, however, cannot be generated directly from CPA lasers because of serious gain narrowing due to a large gain required. The generation of intense few-cycle length pulses requires an extra technique after amplification. One of typical techniques for pulse shortening is to use a single-mode optical fiber for the spectral broadening of laser pulses by self-phase-modulation (SPM), but the use of single-mode fibers limits the pulse energy to a few nanojoules because of material damage and high-order nonlinearities. As a technique for spectral broadening of the high-energy femtosecond pulses, bulk materials have been used.[1] However, unguided propagation in the bulk material leads to nonuniform transverse SPM due to the nonuniform beam transverse intensity profile. In order to overcome these problems, a powerful pulse-shortening technique that combines the benefits of single-mode fiber and bulk material has been demonstrated.[5-9] This technique is based on the spectral broadening in a hollow fiber filled with noble gases and dispersion compensation by chirped mirrors to compress high-energy pulses.

The use of the hollow fiber filled with noble gases has several advantages such as a high threshold for multiphoton ionization and a high critical power for self-focusing due to the single mode guiding with a large mode size. Since wave propagation along a hollow fiber is accompanied with a multiple reflection at the dielectric inner surface of the fiber higher-order transverse modes are suppressed by propagation loss and only fundamental mode (EH_{11} hybrid mode) can propagate in a sufficiently long fiber. By a proper matching between the input beam size and the fundamental EH_{11} mode size the

coupling efficiency for the EH_{11} mode can be larger than 90%.[7] Because the hollow fiber acts as a distributed spatial filter, the output beam is expected to be diffraction limited. The hollow fiber also preserves the polarization of the input beam. Several facts have to be considered when the laser pulses with a peak power of terawatt level are used in the hollow-fiber compressor. Firstly, the type of noble gas and its pressure have to be selected so that the critical power for self-focusing should be larger than the laser peak power. Secondly, the hollow-fiber diameter has to be chosen so that the laser peak intensity should be smaller than the multiphoton ionization threshold of the selected gas.[5,7] With a proper consideration of these facts, the hollow-fiber technique has become applicable to the pulses with the energy as large as a few millijoules.

A schematic of the hollow-fiber compressor is shown in Fig. 3. The laser pulses generated in the CPA system are launched to a hollow fiber with an inner diameter of 320 μm and a length 60 cm. The fiber is kept straight in a V groove made on an aluminum bar placed in a high-pressure chamber with 0.7-mm-thick fused-silica windows with broadband antireflection coating. The chamber is filled with neon gases at the pressure of 2.6 bars, and the laser spectrum is broadened due to the SPM imposed by the optical Kerr effect of the gas. As shown in Fig. 4, the spectrum presents the amplitude modulation due to SPM. The 65-nm-wide (FWHM) input spectrum broadens to more than 200 nm, accompanied by a blueshift. The origin of the blueshift is self-steepening of the laser pulse. The output pulse energy is around 300 μJ, corresponding to 30% coupling efficiency. This low efficiency is partly contributed from the poor spatial profile of the input beam originating from the thermal lensing effect in the multi-pass amplifier. The output beam is recollimated by a f = 1 m gold mirror and reflected

three times off a pair of chirped mirrors for pulse compression. The mirrors have constant negative group-delay dispersion of – 60 fs^2 over the spectral range extending between 650 and 950 nm. For the precise compensation of chirp, the prism – chirped-mirror composite compressor can be used, but the use of the prisms limits the pulse energy to a few microjoules because of the onset of nonlinearities in the prisms at higher pulse energies. Therefore, only chirped mirrors are used for the pulse compression at the millijoule level.

The pulse duration was measured by FROG method based on second-harmonic generation. Figure 5 shows the pulse shape with the duration of 8.3 fs (FWHM) retrieved from FROG measurement. The post-pulses in the temporal intensity profile originate from uncompensated cubic phase.

III. Conclusions

The performance improvement of a 1-kHz CPA laser was carried out in two ways. First, we installed an AOPDF to the 1-kHz CPA laser to obtain broad laser spectrum and compensate for the high-order phase distortion. As a result, we obtained sub-20-fs high-power laser pulses at 1 kHz. Second, we generated 8-fs optical pulses with the energy of 250 μJ at 1 kHz using a pulse compression technique based on the spectral broadening in a hollow fiber filled with neon gas. We investigated the optimal conditions for the good spatial and temporal beam quality. The high-peak-power sub-20-fs/sub-10-fs optical pulses generated in this work are well suited for the high-order harmonic soft-x-ray generation at 1-kHz repetition rate.

References

[1] P. Tournois, Opt. Commun. **140**, 245 (1997)

[2] F. Verluise, V. Laude, Z. Cheng, Ch. Spielmann and P. Tournois, Opt. Lett. **25**, 575(2000)

[3] J. H. Sung, K. H. Hong, Y. H. Cha and C. H. Nam, Jpn. J. Appl. Phys. **41**, 931 (2002)

[4] C. Rolland and P. B. Corkum, J. Opt. Soc. Am. B, **5**. 641 (1988).

[5] M. Nisoli, S. De Silvestri, and O. Svelto, Appl. Phys. Lett. **68**, 2793 (1996)

[6] S. Sartania, Z. Cheng, M. Lenzner, G. Tempea, Ch. Spielmann, and F. Krausz, Opt. Lett. **22**, 1562 (1997).

[7] M. Nisoli, S. De Silvestri, O. Svelto, R. Szipocs, K. Ferencz, Ch. Spielmann, S. Sartania, and F. Krausz, Opt. Lett. **22**, 522 (1997).

[8] M. Nisoli, S. Stagira, S. De Silvestri, O. Svelto, S. Sartania, Z. Cheng, Gabriel Tempea, Christian Spielmann, and Ferenc Krausz, Member, IEEE J. Quantum Electron., **4**, 414 (1998).

[9] G. Cerullo, S. De Silvestri, M. Nisoli, s. Sartania, S. Stagira, and O. Svelto, Fellow, IEEE, IEEE J. Quantum Electron. **6**, 948 (2000).

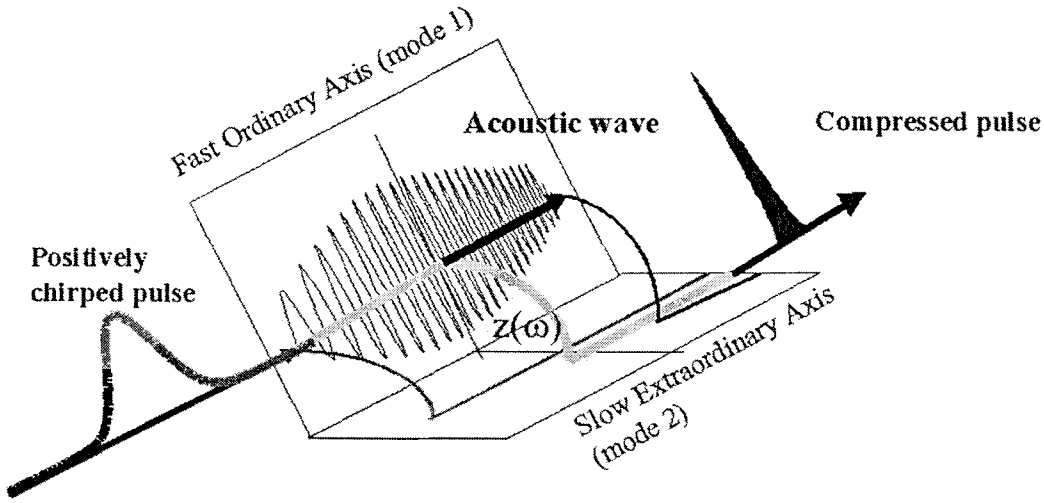

Fig. 1. Schematic of the AOPDF

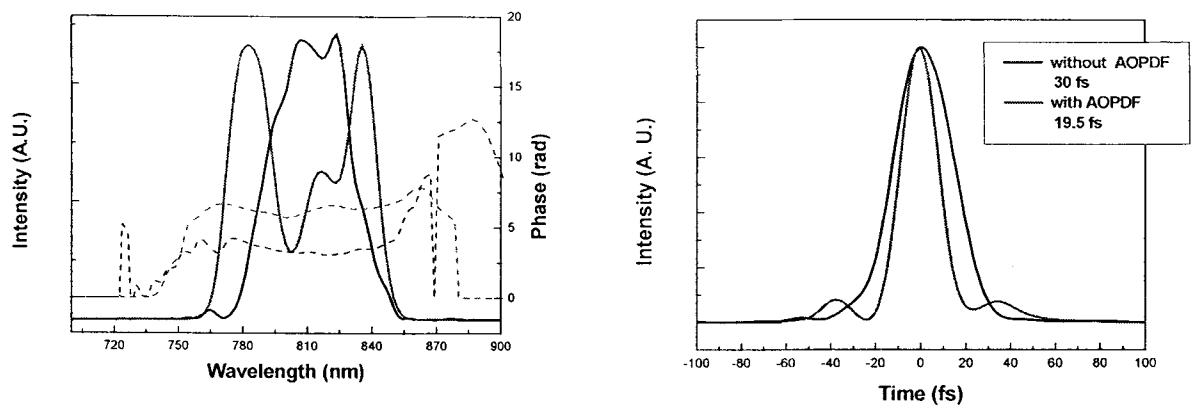

Fig. 2. (a) The spectral intensity and phase (b) Temporal intensity profile

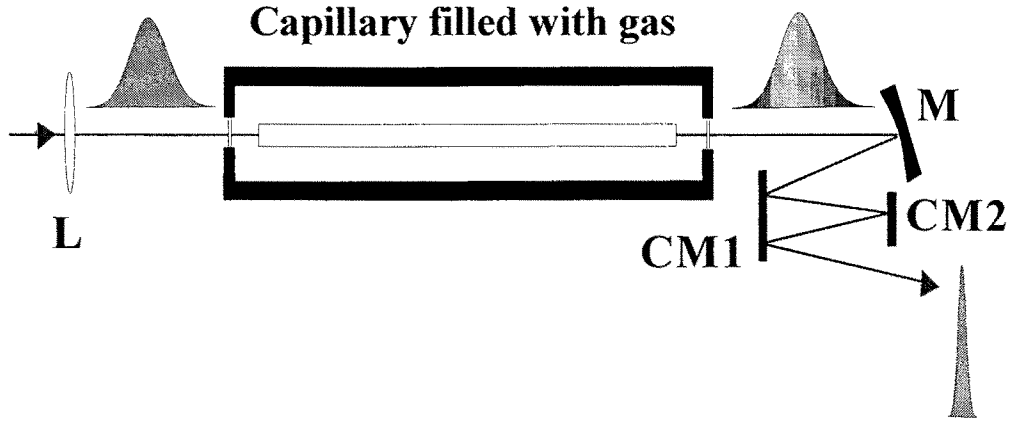

Fig. 3. Schematic of the hollow-fiber compressor. L, AR-coated lens with a focal length of 1 m; M, gold-coated mirror with 2 m radius of curvature; CM1,2, chirped mirrors.

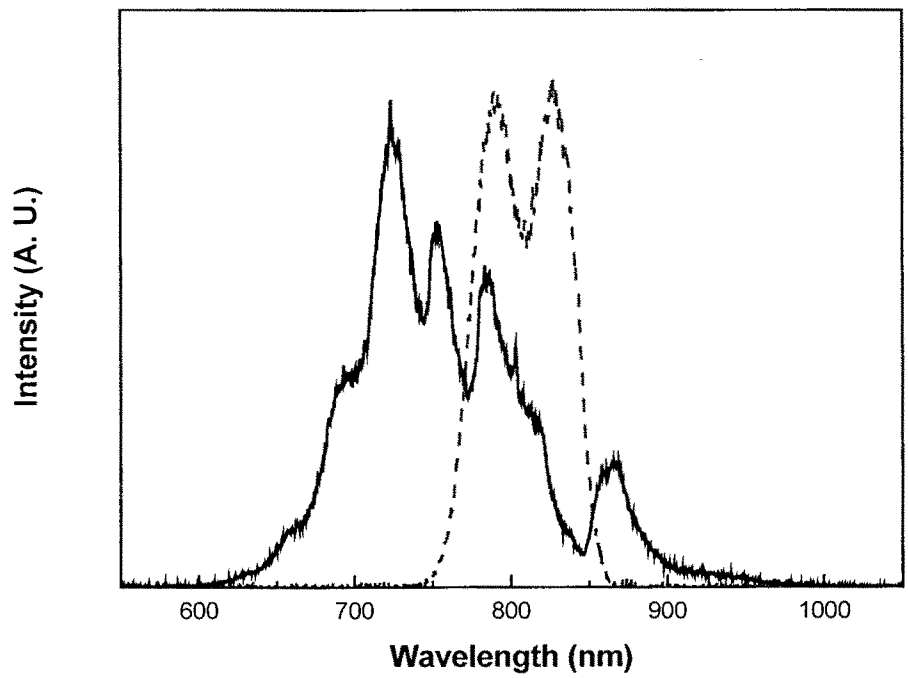

Fig. 4. Spectra for pulses before (dashed curve) and after (solid curve) passing through the neon-filled hollow-core fiber.

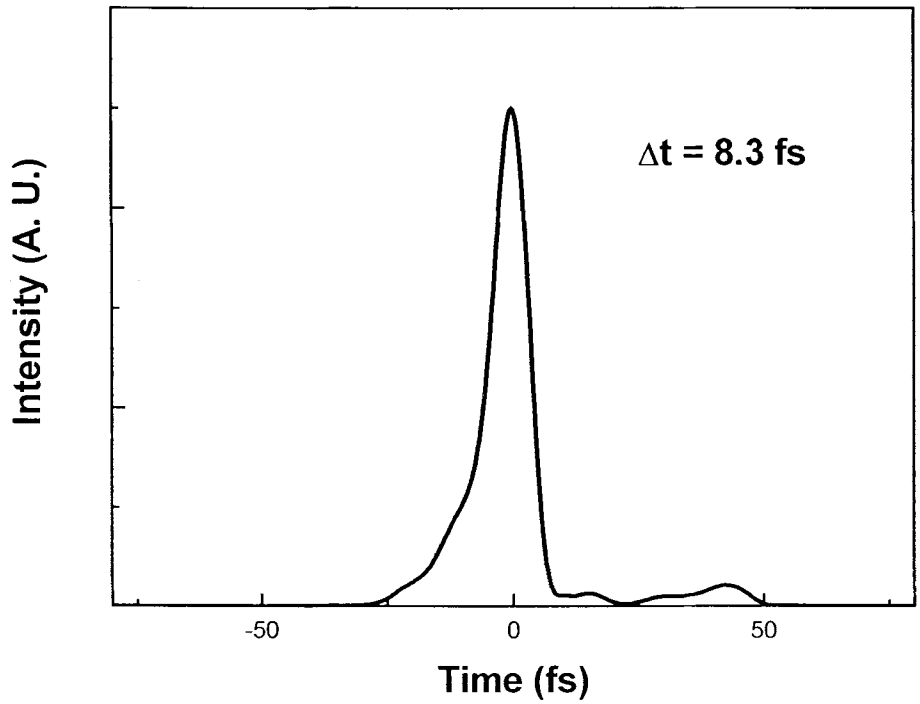

Fig. 5. Temporal intensity profile retrieved from the SHG-FROG trace.

A. 3. 2. Electric-field recovery of sub-10-fs laser pulses from interferometric autocorrelation using an evolutionary strategy

I. Introduction

Recent progress in femtosecond laser technology has made it feasible to routinely generate sub-10-fs optical pulses with energies ranging from a few nJ to 1 mJ [1,2]. Shorter pulse duration, greater is the need for accurate temporal characterization of the femtosecond optical pulses increases. Frequency-resolved optical gating (FROG) and spectral-phase interferometry for direct electric-field reconstruction (SPIDER) have been employed very successfully for the intensity and phase measurement of femtosecond optical pulses, including those of sub-10-fs pulses[3,4]. The (second-harmonic generation; SHG) interferometric autocorrelation (IAC) method, which has been widely used for weak pulses at high repetition rate, is still a valuable tool, and it has also been utilized for the characterization of sub-10-fs pulses[1,5] and for the confirmation of FROG and SPIDER measurements[3,4]. IAC has several experimental advantages to its credit such as easy implementation, self-calibration from interferometric fringes, and alignment confirmation through symmetry and contrast ratio and requires the laser pulses of much lower intensities than FROG or SPIDER, because it does not resolve second-harmonic or sum-frequency-generated spectrum of the laser pulse. It can also be used as a real-time diagnostic because it directly reveals the number of optical cycles and its fringe structure is very sensitive to the intensity and phase of the pulse. IAC would become a even more powerful technique for the temporal characterization of ultrashort pulses if one could recover the intensity and phase from a measured IAC trace.

The intensity and phase recovery from an IAC trace has been investigated using several methods. Diel *et al.*[6] used an iterative fit technique for the characterization of ~100-fs pulses. Their fitting method, however, is inapplicable to optical pulses of arbitrary shape whose spectra are not described in an analytic form. Moreover, the uniqueness of electric field retrieved using this method has not been proved. A drawback of this method is that the pulse duration of sub-10-fs pulses is usually underestimated [4]. Naganuma *et al.*[7] showed that the pulse intensity and chirp can be uniquely retrieved from the autocorrelation measurement using an iterative Fourier-transform algorithm. Their technique, however, is quite complicated because it is based on the analysis of three spectra, i.e., fundamental laser spectrum, SHG spectrum, and power spectrum of the laser intensity. More recently, similar iterative Fourier-transform algorithms, for the temporal decorrelation from an intensity autocorrelation measurement, were demonstrated by Peatross *et al.*[8]. Since the intensity autocorrelation trace is not sensitive to the intensity and phase variation of a laser pulse, the retrieved electric field profile is very sensitive to minute experimental errors. Hence, this method is not of much practical use. In this Letter, we demonstrate a phase retrieval process based on an evolutionary strategy (ES) [9] from an IAC trace, focusing mainly on the reconstruction of sub-10-fs pulses. We shall call this method as the 'Evolutionary Phase Retrieval from Interferometric Auto-Correlation' (EPRIAC) algorithm. The EPRIAC is first tested with numerically generated femtosecond pulses having sufficiently broad spectrum to support sub-10-fs pulse and then applied to experimental measurements. A negatively chirped pulse and a sub-10-fs pulse with high-order phase distortion are retrieved from experimentally measured IAC traces.

Naganuma *et al.*[7] showed that the measurement of both the first-order and SHG IACs allows a unique recovery of the intensity and phase of a laser pulse. Instead of the first-order IAC, we choose to use the fundamental laser spectrum that is equivalent to the first-order IAC and can be easily measured. To uniquely retrieve the spectral phase, the only unknown parameter of the electric field, from an IAC trace, we adopt an ES instead of iterative Fourier transform algorithms. In our algorithm, we explicitly utilize the fringe structure of IAC which is very sensitive to changes in the intensity and phase of the laser pulse, whereas the iterative Fourier-transform algorithm uses the power spectrum of IAC which is not so sensitive to the variation of the intensity and phase of the laser pulse. The general advantages of ESs and other genetic algorithms (GAs) in the search of an optimal solution is that the algorithms can avoid getting trapped in calculating local extrema through random search. Further, a detailed knowledge about the system is also not necessary. Consequently, such algorithms are simple and easy to implement. For these reasons, the GAs have been applied extensively to ultrashort laser technologies such as FROG algorithms [10], an adaptive pulse compression [11], and the control of chemical reactions [12].

II. Procedure of EPRIAC

We demonstrate the EPRIAC using a laser spectrum corresponding to few-cycle pulses. The spectrum, generated in a mirror-dispersion-controlled (MDC) Ti:sapphire laser, covers 650-950 nm with two peaks around 760 nm and 870 nm, as shown in Fig. 1, and supports 7.6-fs pulses in the Fourier-transform limit. The procedure of the EPRIAC algorithm that evaluates full information of the laser pulse is shown in Fig. 2. The first

step of the algorithm is to generate N random 'individuals' representing the spectral phase information of N optical pulses. The phase is calculated using a fourth-order polynomial, obtained from the Taylor expansion of the spectral phase $\tilde{\phi}(\omega)$ about the carrier frequency ω_0, and is expressed:

$$\tilde{\phi}(\omega) = \phi_0 + \frac{d}{d\omega}\phi(\omega_0)(\omega-\omega_0) + \frac{1}{2!}\frac{d^2}{d\omega^2}\phi(\omega_0)(\omega-\omega_0)^2 + \frac{1}{3!}\frac{d^3}{d\omega^3}\phi(\omega_0)(\omega-\omega_0)^3 + \frac{1}{4!}\frac{d^4}{d\omega^4}\phi(\omega_0)(\omega-\omega_0)^4. \quad (1)$$

The Taylor expansion up to the fourth order is appropriate because the third- and fourth-order dispersion (TOD and FOD) terms are dominant dispersion parameters in the formation of sub-10-fs pulses when the laser is operated in the regime of zero second-order or group-delay dispersion (GDD). The first two terms in Eq. (1), representing the absolute phase and the group delay, respectively, can be neglected since they have no effect on the pulse shape and its measurement. Consequently, we should carry out a three-dimensional search to find out the optimal combination of GDD, TOD, and FOD that yields the best fit between the IAC of trial pulse and that of target pulse. These three dispersion terms are set in the range of [0, 200 fs^2], [-5000, 5000 fs^3], and [-50000, 50000 fs^4], respectively, where GDD is taken to be positive because its sign cannot be determined in the IAC measurement. The time direction of the laser pulse and corresponding sign of the spectral phase may be determined separately by an intentional introduction of a certain amount of GDD to the laser pulse.

After randomly generating the dispersion terms, we obtain the temporal amplitude and phase by Fourier transforming the spectral amplitude and phase of each individual. We then calculate the IAC trace using the electric field of each individual. The next step is

the selection process: among the randomly generated N individuals, N_s individuals that yield the best fit to the target or experimentally measured IAC trace are selected for the next 'generation'. The survival parameter of the *i*th individual is define as:

$$S_i = \frac{\int_{-T}^{0} \left| IAC_i(\tau) - IAC_{target}(\tau) \right| d\tau}{\int_{-T}^{0} IAC_{target}(\tau) d\tau}, \qquad (2)$$

where $IAC_i(\tau)$ and $IAC_{target}(\tau)$ are the IAC traces of the *i*th individual and the target pulse, respectively, and $-T$ is the lower limit of the integration below which the IAC signal is close to the background. Upper limit of the integration is set to zero in view of the symmetry of the IAC traces. The oscillatory structure of an IAC trace, corresponding to the carrier frequency, is reflected in the survival parameter because the algorithm is focused on sub-10-fs pulses that do not have many cycles in the pulse envelope. In the case of long pulses with many carrier oscillations, this survival parameter should be properly modified to reduce the calculation load; in this case, the upper and lower envelope functions of the IAC trace will be more suitable than IAC itself. In any case, smaller S_i implies better fit between two IAC traces in the delay range from $-T$ to 0, and thus, the first N_s individuals that yield the smallest value of S_i are selected as the 'parents' of the next generation. The population of the next generation consists of N_s parents and (N-N_s) offspring generated by the crossover and mutation from randomly selected parents, wherein we keep the number of individuals (or the population size) the same (N) throughout all the generations. The ratio between crossover and mutation is chosen to be about 1:4 after some trial and error. The evolution process continues until the enhancement of the fitness (i. e. the decrease of S_i) is negligible.

III. Performance of EPRIAC

To test the performance of EPRIAC, we generate two target IAC traces. The first dispersion parameters of the test pulse chosen arbitrarily were GDD of 40 fs^2, TOD of 1000 fs^3, and FOD of -5000 fs^4. The temporal intensity and phase of the target pulse is represented by circles in Fig. 3(a), and the corresponding IAC trace is shown by circles in Fig. 3(b). If the three-dimensional space generated by the three parameters, GDD, TOD, and FOD, is randomly tested, the algorithm may get trapped in some local minima calculation because reaching the entire three-dimensional search space is very time consuming. We tackle this problem by adjusting the range of each parameter depending on the evolution stage. Since the contribution of GDD is usually much larger than those of TOD and FOD, the GDD value can be approximately determined first and then TOD and FOD values can be sequentially searched. For the realization of this scheme, two-dimensional search in the GDD and TOD space is done for the first 4 generations (the first stage), wherein TOD is kept small and FOD is taken to be zero. After this, the number of search dimension is extended to three for the next 4 generations (the second stage), but the GDD space is restricted around the value obtained in the first stage and FOD is kept nearly zero. For the remaining generations, GDD and TOD spaces are restricted to be close to the values obtained in the second stage and the FOD search is done in the full FOD space. The final result retrieved from the first test pulse is shown as solid lines in Fig. 3(a) and (b). The parameters were chosen as follows: N=50, N_s=10, and T=50 fs. The total number of generations required for convergence was between 11 and 15, which normally requires 2-3 minutes of computation time on a Pentium III computer. The best survival parameter of the first test pulse S_{best}=0.027 and the retrieved values of GDD, TOD, and FOD were 47 fs^2, 900

fs^2, and –4214 fs^4, respectively. Even though the these values were not exactly the same as the target values, 40 fs^2, 1000 fs^2, and –5000 fs^4, the temporal intensity and phase of the retrieved pulse was in good agreement with those of the target pulse.

The second test pulse had a small GDD of 5 fs^2 and was dominated by the higher-order terms, TOD of -500 fs^3 and FOD of 2000 fs^4. This kind of situation is easily observed in an imperfectly compressed pulse. We used the same parameters for the phase retrieval as for the case of the first test pulse. The required number of generations for the convergence was again found to be between 11 and 15. Figures 3(c) and (d) show that the retrieved IAC and electric field, represented by solid lines, have a good fit with the target IAC and electric field, represented by circles, wherein S_{best}=0.035, GDD=22 fs^2, TOD=-400 fs^3, and FOD=65 fs^4. The dispersion terms were, again, not exactly the same as those of the target pulse, but the agreement between the retrieved pulse and the target was still very good.

For demonstrating the applications of EPRIAC to experimental IAC traces, we obtained the IAC traces of optical pulses, generated in the MDC Ti:sapphire laser, using an autocorrelator consisting of a Michelson-type interferometric arm, a 10-μm-thick type I β–BaB_2O_4 crystal and a photo-multiplier tube (PMT). The laser pulse that passed through an output coupler was compressed by the use of a pair of chirped mirrors having a negative dispersion of –60 fs^2 for each bounce. The measured IAC trace of the laser pulse, bounced 4 times off the chirped mirrors, is represented by circles in Fig. 4(a) while the retrieved IAC using EPRIAC is represented by solid line. The corresponding intensity and phase profiles are shown in Fig. 4(b). The GDD of this

pulse was found to be –63 fs^2, and the higher-order terms were negligible (TOD of –40 fs^3 and FOD of 9 fs^4), resulting in a pulse duration of 29 fs; here the sign of GDD was determined from the prior knowledge that this pulse was negatively chirped. This overcompensated laser pulse showed that the optimal number of bounces off the chirped mirrors for the best pulse compression was 3. Figure 4(c) shows the measured IAC trace (represented as circles) and the retrieved IAC trace (represented by solid line) with 3 bounces off the chirped mirrors. The retrieved intensity and phase profile in Fig. 4(d) reveals that the compressed pulse duration is 8.7 fs, which is 1.1 fs larger than that of the transform-limited pulse whose IAC trace and intensity profile are shown as dotted lines in Figs. (c) and (d), respectively. Since the residual GDD is nearly zero (-3 fs^2) whereas the high-order terms are relatively large (TOD of 200 fs^3 and FOD of 460 fs^4), the pulse broadening is mainly due to the residual higher-order dispersion, as is the case with the second test pulse. The survival parameter S_{best} is 0.10 in both the experimental cases. Even though this value is larger than those of the calculated cases due to the experimentally imperfect conditions such as the electrical noise of the PMT and the dispersion of the IAC setup, the retrieved IAC traces mimic every oscillatory structure of the measured IAC very well in the delay region of –40 fs to 0 fs and, hence, the retrieved intensity and phase profiles are also reliable.

V. Conclusion

We have described an evolutionary technique, called EPRIAC, specially suited for the reconstruction of sub-10-fs pulses from their IAC traces. The pulses retrieved by means of EPRIAC showed good agreement with the numerically generated target pulses, indicating that this method could be utilized for analyzing experimentally produced

laser pulses. Application of EPRIAC to the experimental IAC traces of a negatively chirped pulse and a sub-10-fs pulse produced in a MDC Ti:sapphire laser resulted in successful retrieval of their intensity and phase profiles. EPRIAC extends the usage of the IAC down to sub-10-fs regime and offers a reliable, sensitive and convenient method of the complete characterization of femtosecond laser pulses.

References

[1] U. Morgner, F. X. Kartner, S. H. Cho, Y. Chen, H. A. Haus, J. G. Fujimoto, and E. P. Ippen, Opt. Lett. **24**, 411 (1999).

[2] M. Nisoli, S. De Silvestri, O. Svelto, R. Szipocs, K. Ferencz, Ch. Spielmann, S. Sartania, and F. Krausz, Opt. Lett. **22**, 522 (1997).

[3] R. Trebino and D. J. Kane, J. Opt. Soc. Am A **10**, 1101 (1993); Z. Cheng, A. Furbach S. Sartania, M. Lenzner, Ch. Spielmann, and F. Krausz, Opt. Lett. **24**, 247 (1999).

[4] C. Iaconis and I. Walmsley, Opt. Lett. **23**, 792 (1998); L. Gallmann, D. H. Shutter, N Matuschek, G. Steinmeyer, U. Keller, C. Iaconis, and I. A. Walmsley, Opt. Lett **24**, 1314 (1999).

[5] M. R. Armstrong, P. Plachta, E. A. Ponomarev, and R. J. D. Miller, Opt. Lett. **26**, 1152 (2001).

[6] J. C. Diels, J. J. Fontaine, I. C. McMichael, and F. Simoni, Appl. Opt. **24**, 1270-1282 (1985).

[7] K. Naganuma, K. Mogi, and H. Yamada, IEEE J. Quan. Elec. **QE-25**, 1225-1233 (1989).

[8] J. Peatross and A. Rundquist, J. Opt. Soc. Am. B **15**, 216 (1998).

[9] Z. Michalewicz, Genetic Algorithms + Data Structures = Evolution Programs (Springer, Berlin Heidelberg, 1999) Ch.8.

[10] J. W. Nicholson, F. G. Omenetto, D. J. Funk, and A. J. Taylor, Opt. Lett. **24**, 490 (1999).

[11] E. Zeek, K. Maginnis, S. Backus, U. Russek, M. Murnane, G. R. Mourou, H. Kapteyn, and G. Vdovin, Opt. Lett. **24**, 493 (1999).

[12] S. H. Lee, K.-H. Jung , J. H. Sung, K.-H. Hong, and C. H. Nam, J. Chem. Phys.

117, 9858 (2002).

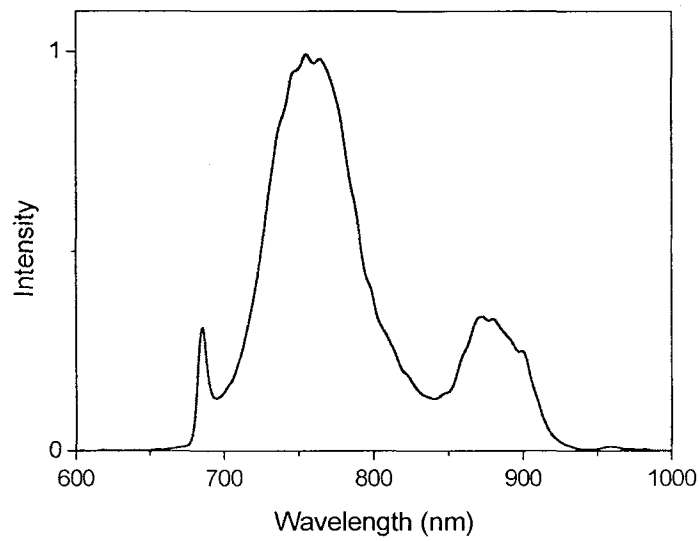

Figure 1. Measured spectrum of a mirror-dispersion-controlled Ti:sapphire laser supporting 7.6-fs pulses.

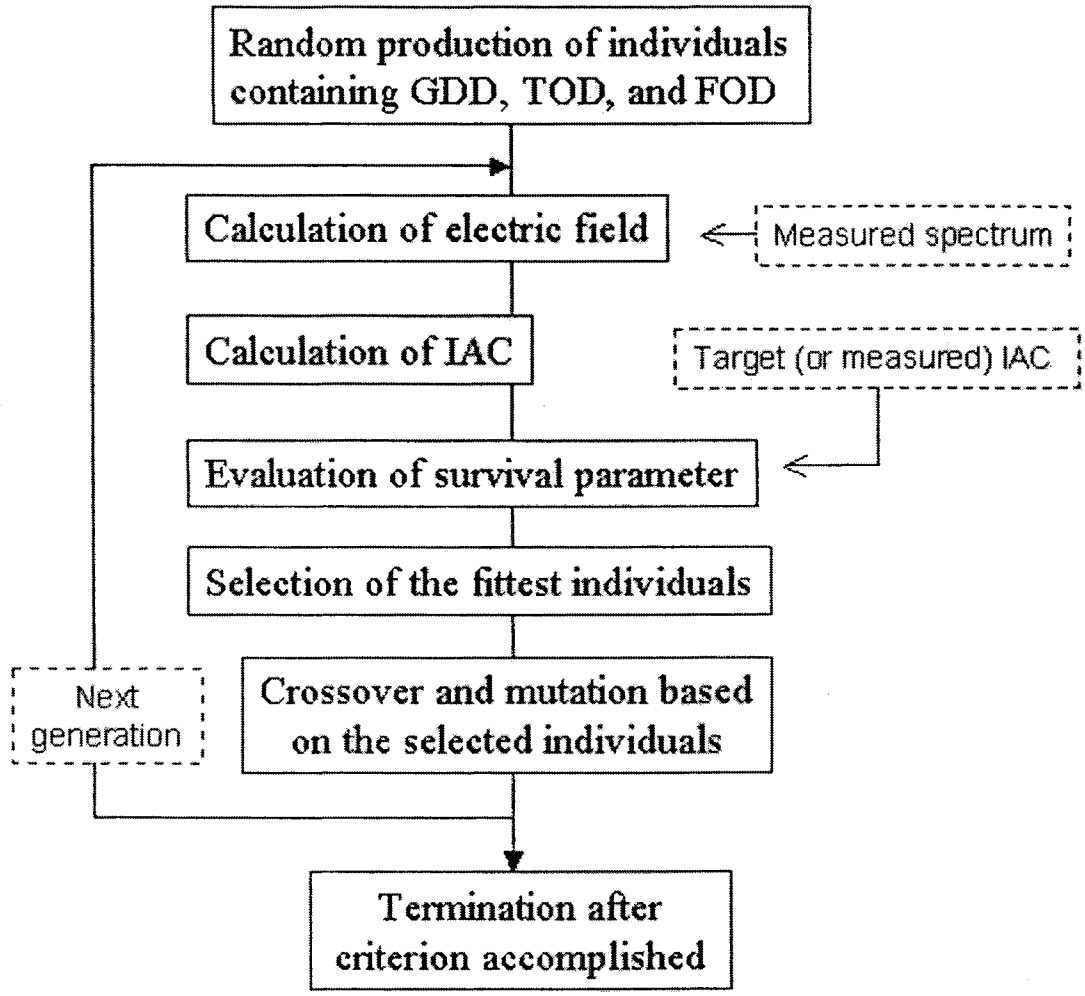

Figure 2. Procedure of the 'evolutionary phase retrieval from interferometric autocorrelation (EPRIAC)' algorithm.

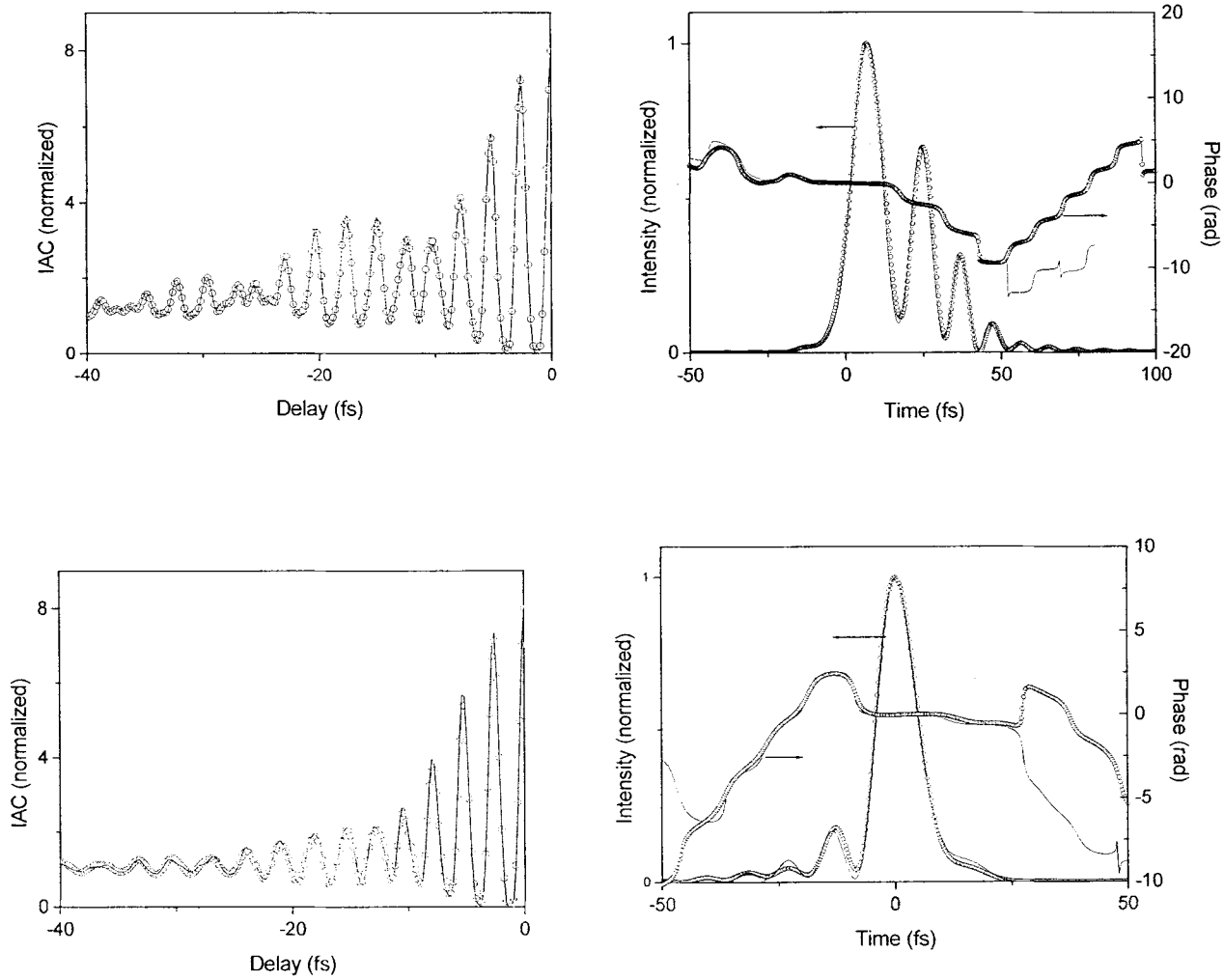

Figure 3. Intensity and phase reconstruction of numerically generated femtosecond pulses using EPRIAC. The target IAC (circles) and retrieved IAC (solid line) of the first test pulse (GDD of 40 fs^2, TOD of 1000 fs^3 and FOD of –5000 fs^4) are shown in (a), and the target electric field (circles) and the retrieved field (solid lines) are shown in (b). The IAC trace and electric field of the second target pulse (GDD of 5 fs^2, TOD of -500 fs^3, and FOD of 2000 fs^4) are shown in (c) and (d), respectively.

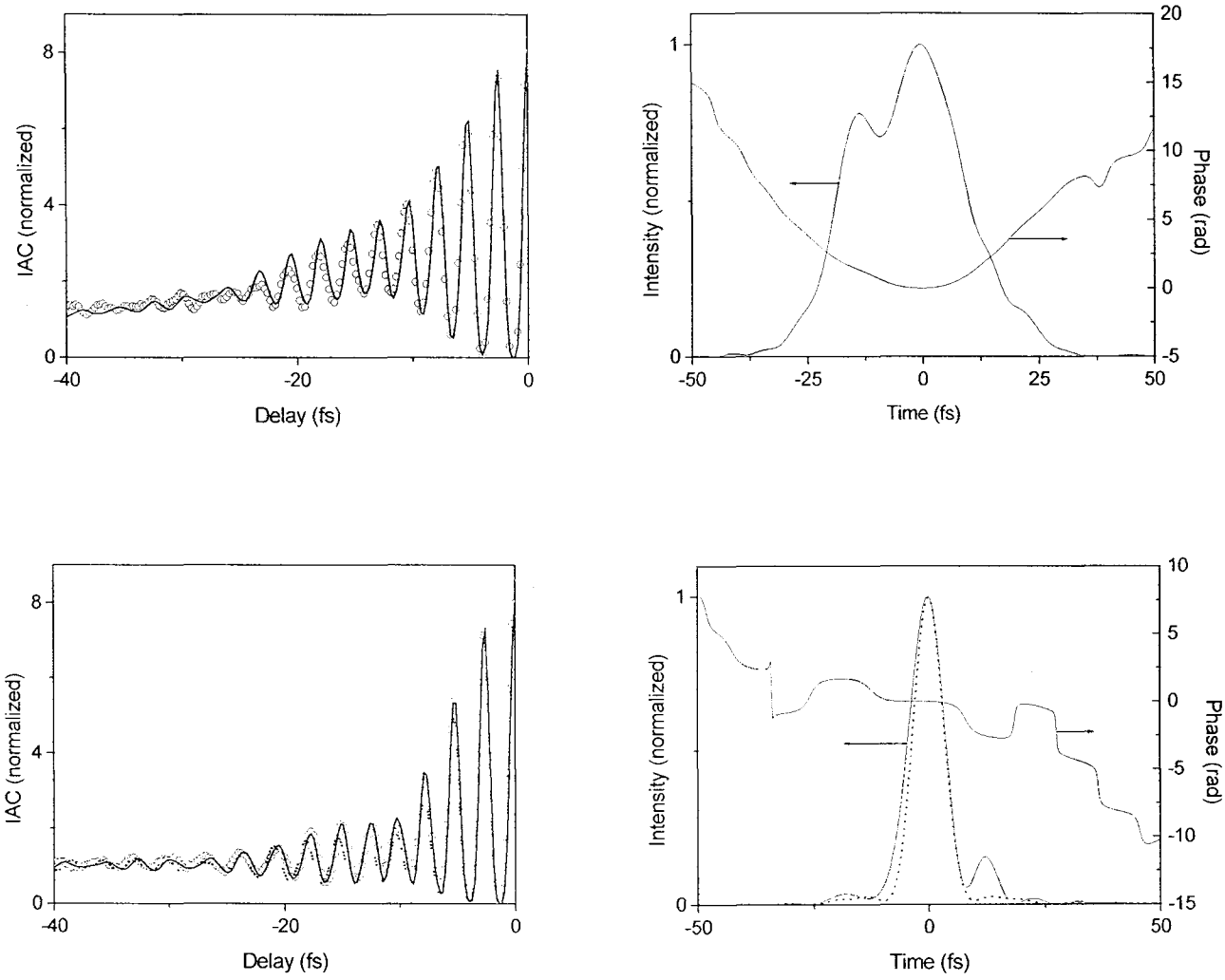

Figure 4. Intensity and phase reconstruction of femtosecond pulses from a MDC Ti:sapphire laser. The measured IAC (circles) and retrieved IAC (solid line) of the negatively chirped pulse (GDD of -63 fs^2, TOD of -40 fs^3, and FOD of 9 fs^4) are shown in (a), and the retrieved electric field in (b). The IAC trace and electric field of the compressed pulse (GDD of -3 fs^2, TOD of 200 fs^3, and FOD of 460 fs^4) are shown in (c) and (d), respectively. The IAC trace and intensity profile of the transform-limited pulse are represented as dotted lines.

A.3.3 Measurement of shot-to-shot carrier-envelope phase slip of femtosecond laser pulses

1. Introduction

With the advancement of sub-10-fs pulse generation technique [1], the description of an optical pulse based on slowly-varying envelope approximation comes to face a new aspect. Unlike many-cycle pulses, the few-cycle pulses are significantly modified in their shape by the phase offset between optical carrier peak and envelope peak, called absolute phase or carrier-envelope phase (CEP). These results show that the light-matter interactions become sensitive to the CEP of the pulse as the laser pulse duration gets shorter than few optical cycles. It has been theoretically known that the spectrum of a femtosecond pulse propagating in a nonlinear medium is dependent on the CEP of the laser pulse[2] and the conversion efficiency of high-order harmonic x-ray generation, which is an extreme nonlinear process, using sub-10-fs pulses is also greatly affected by the CEP[3]. Paulus *et al.* [4] has experimentally observed that photo-ionization process driven by 2-cycle optical pulses depends upon the CEP of the pulses.

For the coherent control of nonlinear optical process and light-matter interaction driven by few-cycle pulses, the random fluctuation of CEP between successive pulses should be suppressed through the stabilization of CEP. Even though an active control of the CEP value of laser pulses has not been realized until now, the measurement and stabilization of shot-to-shot CEP change of mode-locked laser pulses has been intensively investigated using nonlinear interferometry schemes [3,5-7]. Spectral

interferometry method was also proposed as a tool for single-shot CEP measurement [8] and utilized for the measurement of shot-to-shot CEP change [9,10]. Especially, Baltuska *et al.* [10] demonstrated that an optical parametric amplifier seeded by white-light continuum can be a self-stabilized source of few-cycle pulses, wherein the same CEP is reproduced in each laser shot, even though the active control is not still achieved. As in the time-domain applications such as nonlinear optics and light-matter interactions, the CEP of few-cycle laser pulses plays very important role in frequency-domain applications. The stabilization technique of the shot-to-shot CEP slip of a mode-locked laser made a great impact on optical frequency metrology, because it offers a stabilized optical frequency comb in hundreds of THz region, which functions as a simple but highly precise frequency standard [6]. The frequency-domain application is now extended to ultrahigh-resolution spectroscopy [11,12] and optical comb synchronization of two independent lasers [13].

In this Report, we demonstrate the measurement and control of shot-to-shot CEP slip of femtosecond optical pulses generated in a mode-locked Ti:sapphire laser using nonlinear interferometry. The concept of CEP and the measurement principle of shot-to-shot CEP slip using a $2f$-to-f interferometer [3,6] are described in Sec. 2. The experimental setup of the $2f$-to-f interferometer and the measured beat signals depending on laser parameters such as intracavity prism insertion and pumping power are shown in Sec. 3. Section 4 contains conclusions.

2. CEP and shot-to-shot CEP slip of mode-locked laser pulses

An electric field at time t of an optical pulse without frequency chirp can be described as

$$\tilde{E}(t) = E(t)\cos(\omega t + \phi_0), \quad (1)$$

where $E(t)$ is the pulse envelop function, ω is the carrier frequency, and ϕ_0 is the absolute phase or CEP. The pulse shape of a few-cycle pulse depending on the CEP is shown in Fig. 1, where the pulse duration is 6 fs with the center wavelength of 800 nm. We can see that the pulse shape difference with regard to the CEP value is not negligible in spite of the same envelope function. The CEP of a mode-locked laser pulse changes by shot to shot because the velocity of the pulse envelope, i.e., group velocity, is different from the velocity of optical carrier, i.e., phase velocity, and the CEP slip acquired in one cavity roundtrip is not necessarily equal to 2π times an integer. Thus, to obtain the reproducible few-cycle optical pulses with the same CEP value with the ambiguity of 2π times an integer, the shot-to-shot CEP slip should be measured and then stabilized.

Fourier analysis of a mode-locked laser pulse train gives the possibility of measuring the shot-to-shot CEP slip in frequency domain. The optical comb of laser spectrum has a certain amount of offset, δ, as shown in Fig. 2, due to the shot-to-shot CEP slip, $\Delta\phi$. Two quantities have a simple relation given by Fourier transform as follows:

$$\Delta\phi = 2\pi\delta / f_{rep}, \quad (2)$$

where f_{rep} is the repetition rate of the laser. We can thus measure the time-domain quantity $\Delta\phi$ by probing the frequency-domain quantity δ. The measurement of δ can be easily realized if we have a one-octave spectrum that covers from a frequency f to its doubled frequency $2f$. The frequency of the nth optical comb is expressed, in terms of the repetition rate and the frequency offset, as

$$f_n = nf_{rep} + \delta \,. \qquad (3)$$

The second-harmonic frequency of the nth optical comb is given by $f_{SHG} = 2f_n = 2(nf_{rep} + \delta)$, whereas the $2n$th optical comb has the frequency $f_{2n} = 2nf_{rep} + \delta$. Two frequencies, f_{SHG} and f_{2n}, cannot be discriminated in the spectrum, but by interfering f_{SHG} with f_{2n}, we can get the beat frequency of $f_{SHG} - f_{2n} = \delta$, the offset of the frequency comb.

The proper control of δ allows the generation of CEP-controlled optical pulses as long as the change in the repetition rate is negligible. When δ is stabilized to be constant, the frequency of each optical comb is exactly defined, and the CEP difference between successive two pulses is the same as that of the previous two. Especially, in the case of zero δ, all the pulses have the same CEP, and the absolute phase is fixed to an unknown value ϕ_0. The ϕ_0 value can be found out with other method such as high-order harmonic generation or photo-ionization. The physical factors that affect δ in a Kerr-lens mode-locked laser oscillator are intracavity dispersion and Kerr-nonlinearity. Difference between group velocity and phase velocity of a laser pulse is dependent on the path length of intracavity dispersive materials and can be controlled, practically, by adjusting the insertion depth of a prism installed for the intracavity dispersion compensation. The Kerr-nonlinearity that induces an intensity-dependent change of the group velocity can be also controlled by adjusting the intracavity pulse energy through pumping power control.

3. Measurement and control of shot-to-shot CEP slip

The setup of $2f$-to-f self-referencing interferometer consists of a white-light continuum generator and a nonlinear interferometer as illustrated in Fig. 3. A conventional spectrum of a prism-dispersion-controlled Ti:sapphire laser [14] covers the region from 700 nm to 900 nm (or 750 nm to 950 nm), and a mirror-dispersion-controlled (MDC) laser [15], from 650 nm to 1000 nm, which is still not sufficiently broad to cover one octave. The most common technique to obtain an ultrabroadband spectrum is the continuum generation by means of the self-phase modulation (SPM) effect of a high-intensity laser pulse in a solid or an optical fiber. Recently, Ell *et al.* [16] succeeded in generating one-octave spectrum directly from a Ti:sapphire laser by installing an additional SPM arm in the cavity, but they employed specially designed double-chirped mirrors, for the intracavity dispersion compensation, commercially not available. So far, the continuum generation outside the laser cavity is common because it does not require such a special coating and careful intracavity dispersion control. In this work, we use an air-silica microstructure fiber [17] to generate a super-continuum with one-octave spectrum. This fiber significantly reduces the laser intensity required for the wide spectral broadening by SPM. It prevents the laser pulse from being temporally broadened during the SPM process and enhances the spectral broadening during the propagation, because the dispersion at the center wavelength of Ti:sapphire lasers, 800 nm, is negative. The additional nonlinear processes such as four-wave mixing and Raman scattering are also excited in a long fiber, and, as a result, a flattened super-continuum spectrum is obtained. The offset of the optical combs does not change during those nonlinear processes. We focus 30-fs, 3-nJ laser pulses generated from a mode-lcoked Ti:sapphire laser into a 12-cm-long air-silica microstructure fiber using a 40X objective lens and recollimate the generated super-continuum using an another objective

lens. The laser oscillator is capable of delivering three-cycle (7.8-fs) optical pulses, as shown in the inset of Fig. 3, by means of external compression, but the uncompressed (negatively chirped) 30-fs pulses are enough for the nonlinear effect in the air-silica microstructure fiber even with the consideration of additional pulse broadening in the objective lens. The coupling efficiency of two objective lenses and the fiber is 30 %. Figure 4 shows the input laser spectrum in logarithmic scale (a) and generated super-continuum spectra in logarithmic and linear scales (b and c, respectively). The generated super-continuum covers the spectrum from 450 nm to 1150 nm, which is sufficiently broad to cover one-octave. We choose 1064 nm as frequency f_n and 532 nm as f_{2n} or $2f_n$ because Nd:YAG laser optics are conventionally available.

The super-continuum is divided into the infrared (IR) and green parts using a dichroic beamsplitter as in Fig. 3. The IR part containing f_n, 1064 nm, is focused into a 1-mm-thick KTP crystal by use of 10X objective lens to generate its second harmonic frequency, $2f_n$ at 532 nm, and interfered with the green part containing f_{2n}, 532 nm. The delay arm in Fig. 3 ensures the temporal overlap of the two $2f$ ($2f_n$ and f_{2n})- pulses. Since both beams have broad spectra around 532 nm, they are filtered out by two color filters centered at 532 nm with a bandwidth of 1 nm. The second-harmonic ($2f_n$) beam has s-polarization (vertical to optical table), whereas the laser pulse and the generated continuum including f_n and f_{2n} have p-polarization. The $2f_n$ and f_{2n} beams are combined in a polarizing beamsplitter to be spatially overlapped. Since the polarization of one beam is orthogonal to the other, the interference should be occurred at the plane moderately rotated between the vertical and horizontal axes, which can be realized by inserting a linear polarizer. The angle of the polarizer should be properly selected to

enhance the beat signal by equalizing the signal levels of two 532-nm beams because the intensity of f_{2n} beam is usually much stronger than that of $2f_n$ beam. Finally, the beat signal is detected using an avalanche photo-diode (APD) and displayed either on an oscilloscope or on an rf spectrum analyzer.

A typical interference profile obtained at the oscilloscope is shown as Fig. 5(a), where we can observe 116-MHz pulse train with the amplitude modulation representing the beat between the $2f_n$ and f_{2n} beams. The measured rf spectrum is in Fig. 5(b), where we can observe three peaks at the frequencies of f_{rep} and $f_{rep} \pm \delta$. The beat frequency δ manifests itself at the two side-peaks. The observed jitter in δ is ± 50 kHz, indicating an inherent phase error in the CEP slip measurement of ± 2.7 mrad. This jitter comes from the random noise of the unstabilized laser and the nonlinear phase noise in the air-silica microstructure fiber due to the fluctuation of coupling energy [18]. Mechanical vibration of the optical table is the most serious factors that magnify both noises. The thermal noise of Ti:sapphire crystal and the flow of air were found to be negligible in the short-term stability.

After attaining the measurement tool, we controlled δ by changing the insertion depth of an intracavity prism and pumping power. Figure 6(a) shows the prism-insertion dependence of δ. The CEP slip occurring when a medium length is extended from l_0 to l is given by $\Delta\varphi = 2\pi\left(\frac{dn}{d\lambda}\right)(l - l_0)$, where n is the refractive index. The intracavity prisms are made of fused silica whose $dn/d\lambda$ value at 800 nm is -0.0173 μm^{-1}. The fitting curve calculated from the $dn/d\lambda$ value and the prism insertion depth has a slope

of –0.307 rad/μm and shows good agreement with the experimental measurement. The intracavity power dependence of δ at a fixed prism insertion is shown in Fig. 6(b). The linear regression shows that the slope of the line is –0.316 rad/nJ. By finely tuning two parameters, we could slow down δ to nearly zero, in which case the beat frequency was changing at around the jitter level. Figure 6(c) depicts a 280-kHz pure beat signal in time domain. We obtained it by removing the 116-MHz pulse trains from the original interference profile using two additional APDs, represented by ADP2 and APD3 in Fig. 3, and a subtraction circuit. This low-frequency beat signal endures without dephase for several milliseconds and then fluctuates, implying that the pulses with the same CEP can be generated every 3.6 μs for several milliseconds in the unstabilized laser used here. When the beat frequency is further reduced below ~280 kHz, the sinusoidal beat signal was not regularly observed due to the jitter. Perfect isolation of the optical table and experimental setup from the environment will significantly improve the CEP stability and allow the further reduction of the phase jitter. To obtain a jitter-free δ and, ultimately, zero δ for relatively long time (a few seconds), a laser stabilization process is absolutely required through the feedback control of the prism insertion depth or pumping power. The quantitative characterization of shot-to-shot CEP slip of the laser pulses demonstrated in this work is a basic process for the fabrication of a required feedback loop and the laser stabilization process.

4. Conclusions

We measured the shot-to-shot CEP slip of a mode-locked Ti:sapphire laser using a $2f$-to-f self-referencing interferometer. A 20-cm air-silica microstructure fiber was used for the generation of one-octave spectrum, and a nonlinear interferometer was employed for

the observation of beat signal between $2f_n$ and f_{2n} components. The measured beat frequency (δ) has a jitter of 120 kHz, which corresponds to the phase error of 6.5 mrad in the shot-to-shot CEP slip measurement. We also controlled δ by changing the insertion depth of an intracavity prism and the laser pumping power and, by finely adjusting two parameters, slowed down δ to nearly zero close to the jitter level. The perfect isolation of the optical table and experimental setup from environment is required to significantly reduce the jitter, and an active stabilization of the laser is necessary for the jitter-free operation. The measurement of the parameter dependence of δ done in this work will allow the suitable design of a feedback control loop to stabilize δ to a certain frequency and fix it to be zero for the generation of CEP-locked sub-10-fs laser pulses.

References

[1] U. Morgner, F. X. Kartner, S. H. Cho, Y. Chen, H. A. Haus, J. G. Fujimoto, and E. P. Ippen, Opt. Lett. **24**, 411 (1999); M. Nisoli, S. De Silvestri, O. Svelto, R. Szipocs, K. Ferencz, Ch. Spielmann, S. Sartania, and F. Krausz, Opt. Lett. **22**, 522 (1997); K.-H. Hong, Y. S. Lee, and C. H. Nam, Opt. Lett. (submitted).

[2] D. K. Skripov and V. A. Trofimov, Tech. Phys. Lett. **27**, 575 (2001).

[3] A. Apolonski, A. Popper, G. Tempea, C. Spielmann, T. Udem, R. Holzwarth, T. W. Hansch, and F. Krausz, Phys. Rev. Lett **85**, 740 (2000).

[4] G. G. Paulus, F. Frasbon, H. Walther, P. Villoresi, M. Nisoli, S. Stagira, E. Priori, and S. De Silvestri, Nature **414**, 182 (2001).

[5] H. R. Telle, G. Steinmeyer, A. E. Dunlop, J. Stenger, D. H. Shutter, and U. Keller, Appl. Phys. B **69**, 327 (1999).

[6] D. J. Jones, S. A. Diddams, J. K. Ranka, A. Stentz, R. S. Windeler, J. L. Hall, and S. T. Cundiff, Science **288**, 635 (2000).

[7] U. Morgner, R. Ell, G. Metzler, T. R. Schibli, F. X. Kartner, J. G. Fujimoto, H. A. Haus, and E. P. Ippen, Phys. Rev. Lett. **24**, 5462 (2001).

[8] M. Mehendale, S. A, Mitchell, J.-P. Likforman, D. M. Villeneuve, and P. B. Corkum, Opt. Lett. **25**, 1672 (2000).

[9] M. Kakehata, H. Takada, Y. Kobayashi, K. Torizuka, Y. Fujihira, T. Homma, and H. Takahashi, Ultrafast Optics 2001, Mon01 (2001).

[10] A. Baltuska, T. Fuji, and T. Kobayahsi, Phys. Rev. Lett. **88**, 133901 (2002).

[11] R. Holzwarth, Th. Udem, T. W. Hansch, J. C. Knight, W. J. Wadsworth, and P. St. J. Russell, Phys. Rev. Lett. **85**, 2264 (2000).

[12] T. H. Yoon, A. Marian, J. L. Hall, and J. Ye, Phys. Rev. A **63**, 011402(R) (2001).

[13] J. Ye, S. T. Cundiff, S. Foreman, T. M. Fortier, J. L. Hall, K. W. Holman, D. J. Jones, J. D. Jost, H. C. Kapteyn, K. A. H. V. Leeuwen, L. S. Ma, M. M. Murnane, J. L. Peng, and R. K. Shelton, Appl. Phys. B **74**, S27 (2002).

[14] Y. H. Cha, K. T. Lee, H. M. Park, J. M. Han, and Y. J. Rhee, J. Korean Phys. Soc. **40**, 250 (2002); J. H. Sung, K.-H. Hong, Y. H. Cha, and C. H. Nam, Jp. J. Appl. Phys. **41** L931 (2002).

[15] Y.-S. Lim, H.-S Jeon, Y.-C. Noh, K.-J. Ye, D. S. Kim, J.-H. Lee, J.-S. Chang, and J.-D. Park, J. Korean Phys. Soc. **40**, 837 (2002).

[16] R. Ell, U. Morgner, F. X. Kartner, J. G. Fujimoto, E. P. Ippen, V. Scheuer, G. Angelow, T. Tschudi, M. J. Lederer, A. Boiko, and B. Luther-Davies, Opt. Lett. **26**, 373 (2001).

[17] J. K. Ranka, R. S. Windeler, and A. J. Stentz, Opt. Lett. **25**, 796 (2000).

[18] T. M. Fortier, J. Ye, S. T. Cundiff, and R. S. Windeler, Opt. Lett. **27**, 445 (2002).

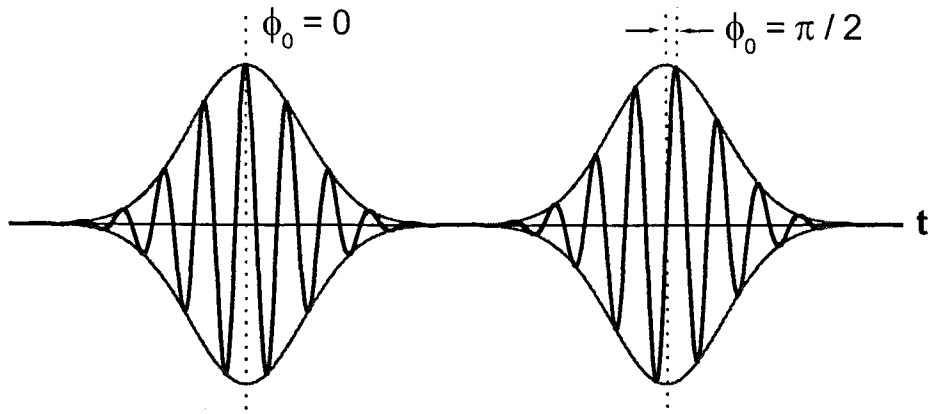

Fig. 1 CEP and pulse shape of two-cycle laser pulses.

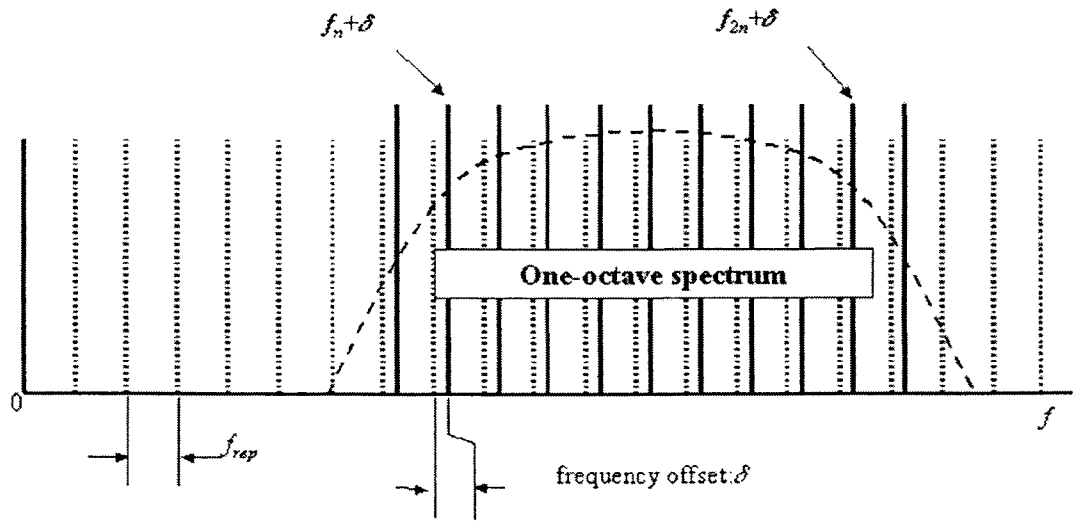

Fig. 2 Optical comb structure of one-octave spectrum.

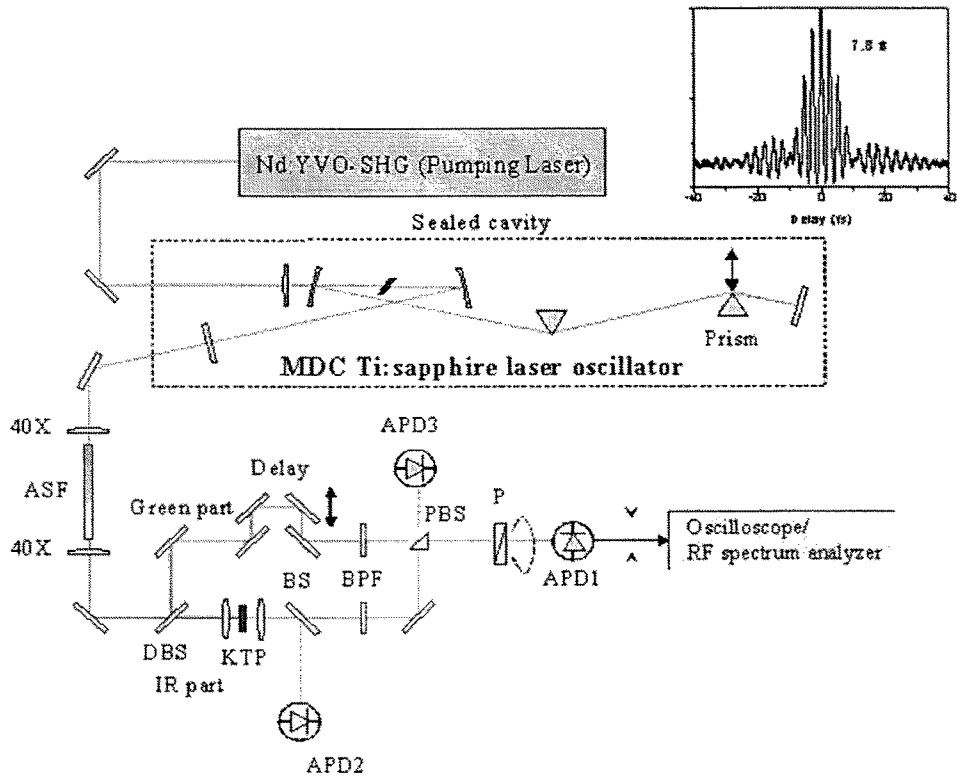

Fig. 3 Experimental setup for the measurement of shot-to-shot CEP slip. The laser source is an MDC mode-locked Ti:sapphire laser capable of delivering 3-cycle (sub-8-fs) optical pulses. ASF: air-silica microstructure fiber, DBS: dichroic beamsplitter, KTP: KTP crystal, 40X: 40X objective lens, BS: beamsplitter, BPF: band-pass filter at 532 nm PBS: polarizing beamsplitter, P: linear polarizer, APD: avalanche photo-diode.

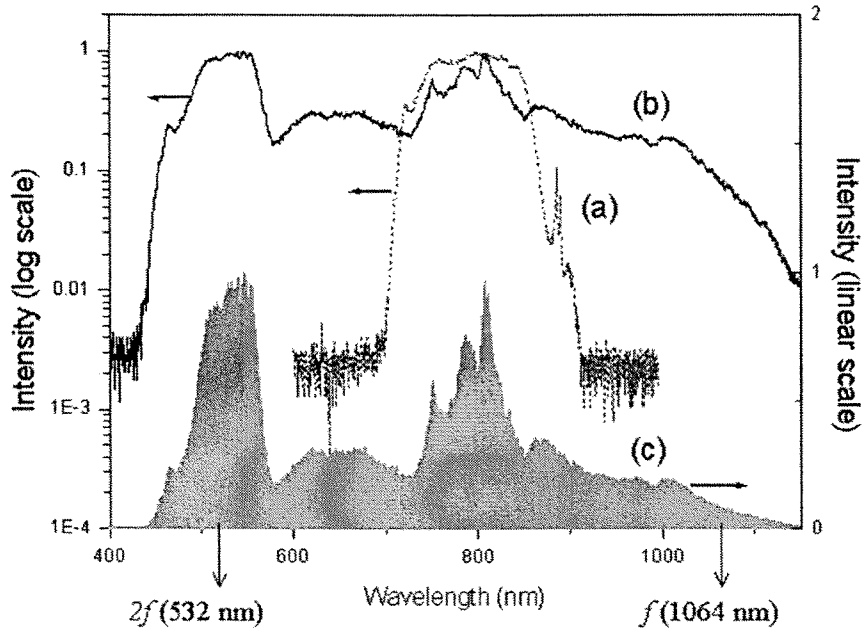

Fig. 4 One-octave spectrum generated in a 12-cm-long air-silica microstructure fiber. Input laser spectrum is shown as (a) in log-scale, while the one-octave spectra as (b) and (c) in log- and linear-scales, respectively.

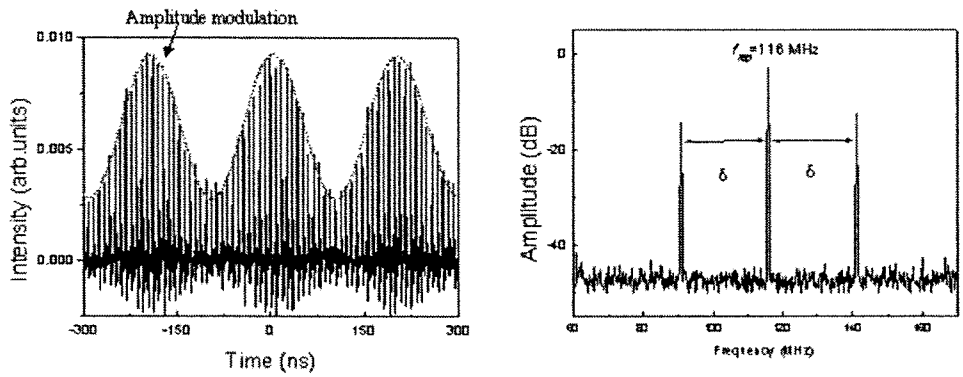

(a) (b)

Fig. 5 Measured beat signals in time (a) and frequency (b) domains. Amplitude modulation frequency in (a) corresponds to the offset frequency, δ, in (b).

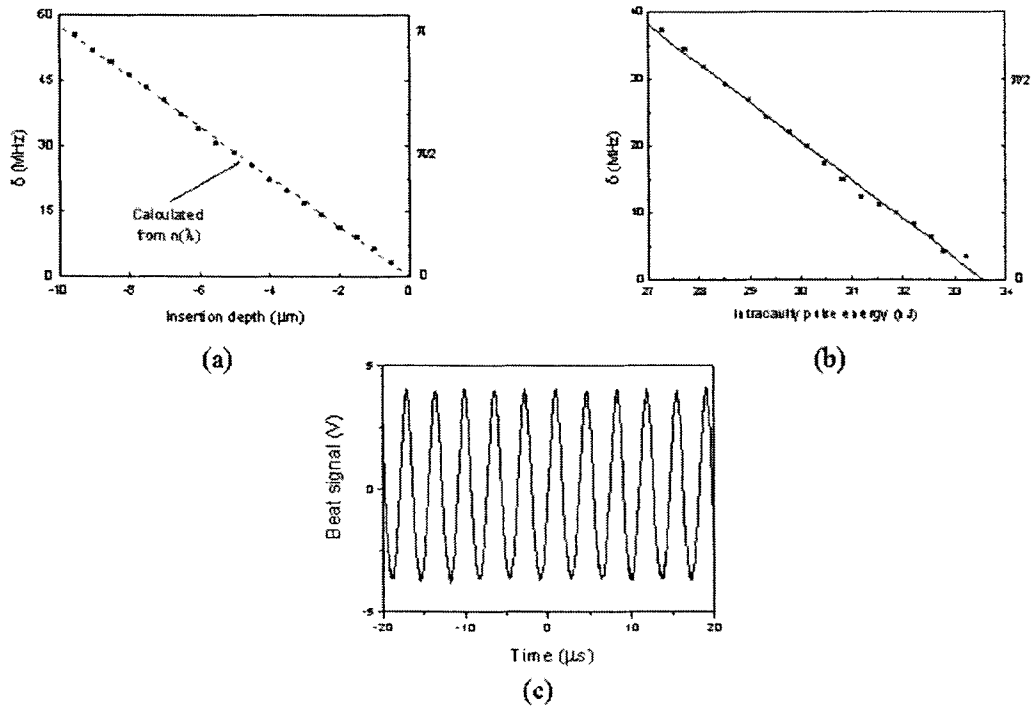

Fig. 6 Parameter dependence of δ and slowing down CEP slip. The δ values versus prism insertion depth and intracavity pulse energy are shown in (a) and (b), respectively. Right axes are corresponding CEP slip. A low-frequency (280-kHz) pure beat signal obtained by a fine adjustment of the two parameters is shown in (c).

특정연구개발사업 연구결과 활용계획서

사업명	창의적 연구진흥 사업		
	-		
과제명	초강력 펨토초 레이저마당 내의 원자조작을 통한 결맞는 X-선 광원개발		
연구기관	한국과학기술원	연구책임자	남창희
총연구기간	1999년 10월 16일 ~ 2002년 9월 30일 (36 개월)		
총 연구비 (단위 : 천원)	정부출연금	민간부담금	합계
	1,530,000,000		1,530,000,000
기술분야	미래원천기술		
참여기업	없음		
공동연구기관	〃		
위탁연구기관	〃		

연구결과활용 (해당항목에(∨) 표시)	1. 기업화 ( )	2. 기술이전( )	3. 후속연구추진( )	4.타사업에 활용( )
	5. 선행 및 기초연구(O)	6. 기타목적활용 (교육,연구)( )	7. 활용중단(미활용)( )	8. 기타( )

특정연구개발사업 처리규정 제 31조(연구개발결과의 보고) 제 2항에 의거 연구결과 활용계획서를 제출합니다.

첨부 : 1. 연구결과 활용계획서 1부.
2. 기술요약서 1부

2002 년 11 월 30 일

연구책임자 : 남 창 희
연구기관장 : 홍 창 선 (직인)

과학기술부장관 귀하

[첨부1]

연구결과 활용계획서

1. 연구목표 및 내용

1) 고출력 펨토초 레이저 기술 개발
- 강력한 레이저와 원자와의 상호작용을 연구하기 위해 1kHz의 반복율을 갖는 10펨토초 0.1테라와트의 고출력 고반복 펨토초 티타늄 사파이어 레이저를 개발. 그리고 개발된 고출력 펨토초 레이저의 시공간적 특성을 측정.

2) 원자와 초강력 레이저장과의 상호작용을 규명
- 강력한 레이저장과 원자와의 상호작용에 의한 고차조화파 발생의 실험적 측정 및 분석과 전산시늉을 포함한 이론적 분석을 통하여 그 발생 메카니즘을 구체적으로 규명.

3) 파장가변 결맞는 엑스선 광원 개발
- 고차조화파의 결맞는 조절을 통하여 조화파의 선폭과 세기에 대한 최적화를 수행하고, 조화파의 청색변이를 이용하여 연속적으로 파장가변이 가능한 펨토초 고차조화파 엑스선 광원 (소형화된 싱크로트론)을 개발.

2. 연구수행결과 현황(연구종료시점까지)

가. 특허(실용신안) 등 자료목록
해당사항 없음

나. 프로그램 등록목록
해당사항 없음

다. 노하우 내역

1) 1 kHz의 고반복율을 갖는 고출력 펨토초 레이저 개발기술 보유
2) 10 펨토초 이하의 고출력 극초단 펄스 발생 기술 보유
3) 펨토초 테라와트 사파이어 레이저의 최적상태 운전기술 보유
4) 고출력 펨토초 레이저의 시공간적인 특성을 측정하는 기술보유
5) 파장가변 결맞는 엑스선 발생 기술 보유

라. 발생품 및 시작품 내역
해당사항 없음.
마. 논문게재 및 발표 실적

○논문게재 실적(필요시 별지사용)

학술지 명칭	제목	게재연월일	호	발 행 기 관	국명	SCI 게재 여부
Phys. Rev. A	Enhanced spectral resolution of high-order harmonics by the coherent sum of dipole spectrum	2000	62	APS	미국	O
Opt. Commun.	Incorporation of a cavity-dumped oscillator in a long-wavelength injected femtosecond terawatt Ti:sapphire laser	2000	185	Elsevier	네덜란드	O
Appl. Phys. Lett.	Enhancement of soft X-ray emission from a cryogenically cooled Ar gas jet irradiated by 25 fs laser pulse	2000	76	AIP	미국	O
J. Korean Phys. Soc.	Investigation of an optical-field-ionized oxygen plasma for a table-top soft X-ray laser	2000	36	KPS	한국	O
Phys. Rev. E	Soft X-ray emission from small-sized Ne clusters heated by intense, femtosecond laser pulse	2000	62	AIP	미국	O
Elec. Lett.	Generation of Passively Q-switched and Mode-locked pulse from Nd:YVO4 Laser with Cr4+:YAG Saturable Absorb	2000	36	IEEE	미국	O
Opt. Appl.	Femtosecond-pulse-driven soft X-ray laser studies using a gas puff target irradiated with a Ti:Sapphire laser	2000	30		폴란드	O
Phys. Rev. A	Selection of high-order harmonics from a single quantum path for the generation of an attosecond pulse train	2001	63	APS	미국	O
Phys. Rev. A	Nonspreading wave packets of diatomic molecules: Generation and control	2001	63	APS	미국	O
Phys. Rev. A	Nonadiabatic blueshift of high harmonic from Ar and Ne atoms in an intense femtosecond laser field	2001	63	APS	미국	O
Phys. Rev. A	Wigner Time-Frequency Distribution of High-Order Harmonics	2001	63	ASP	미국	O
J. Korean Phys. Soc.	High Harmonic Spectra from Neon Atoms in an Intense Femtosecond Laser Field	2001	39	KPS	한국	O

학술지 명칭	제목	게재연월일	호	발 행 기 관	국명	SCI 게재 여부
J. de Phys. IV	Tunable coherent femtosecond x-ray source driven by an intense femtosecond laser	2001	11	EDP science	프랑스	O
J. de Phys. IV	Interaction of intense, femtosecond laser pulse with small-sized Ne cluster	2001	11	EDP science	프랑스	O
J. de Phys. IV	Investigations on femtosecond-pulse-driven softx-ray lasers using a gas puff target irradiated with a Ti:Sapphire laser	2001	11	EDP science	프랑스	O
J. de Phys. IV	Coherent Control of High-Order Harmonics with Chirped Femtosecond Laser Pulser	2001	11	EDP science	프랑스	O
J. Korean Phys. Soc.	High Harmonic Spectra from Neon Atoms in an Intense Femtosecond Laser Field	2001	39	KPS	한국	O
Phys. Rev. A	Plasma-induced frequency chirp of intense femtosecond lasers and its role in shaping high-order harmonic spectral lines	2002	65	APS	미국	O
Laser Part.Beam	Investigation of soft x-ray emission from Ar clusters heated by ultrashort laser pulses	2002	20		미국	O
Phys. Rev. E	Emission of a hot electron jet from intense femtosecond laser-cluster interactions	2002	66	APS	미국	O
Phys. Plasma	Measurement of energetic electrons from atomic clusters irradiated by intense femtosecond laser pulses	2002	9	AIP	미국	O
Japan. J. Appl. Phys.	13-fs, 1-MW Ti:sapphire laser oscillator in a long-cavity configuration	2002	41	일본응용물리학회	일본	O
Appl. Phys. B	Time-frequency analysis of chirped femtosecond pulses using Wigner distribution function	2002	74	Springer	독일	O
Japan. J. Appl. Phys.	Regenerative third-harmonic FM mode-locking in a bulk Nd:YLF laser	2002	41	IPAP	일본	O
Appl. Phys. Lett.	Generation of bright low-divergence high-order harmonics in a long gas jet	2002	81	AIP	미국	O
J. Chem. Phys.	Adaptive quantum control of DCM fluorescence in the liquid phase	2002	117	AIP	미국	O

학술지 명칭	제목	게재연월일	호	발 행 기 관	국명	SCI 게재 여부
Opt. Commun.	Temporal characterization of chirped femtosecond laser pulses	2002	213	Elsevier	네덜란드	O
Phys. Rev. A	Momentum distribution of single and double ionization	2002	66	APS	미국	O
계: 28 건						

ㅇ학술회의 발표 실적(필요시 별지사용)

학술회의 명칭	제목	게재연월일	호	발 행 기 관	국명
7th Int. Conf. on X-ray Lasers	Tunable coherent femtosecond X-ray source drinven by an intense femtosecond laser	2000			프랑스
Atoms, Molecules and Quantum Dots in Laser Fields	Tunable high harmonic generation from atoms driven by intense femtosecond laser	2000			이태리
Asia Pacific Laser Symposium	Femtosecond terawatt Ti:sppphire laser at KAIST	2000			중국
OECD Global Science Forum on Compact High-Intensity Short Pulse Lasers	VUV coherent source with high-order harmonics	2001			일본
SPIE's 46th Annual Meeting	Efficient high-order harmonic generation using a long gas jet	2001			미국
IFSA 2001	Measurement of energetic hot electrons from atomic Xe and Ar clusters irradiated by intense femtosecond laser pulses	2001			일본
14th Annual Meeting of the IEEE Laser & Electro-Optics Society	Coherent Femtosecond X-Ray Source Based on High-Order Harmonics	2001			캐나다
8th Int. X-ray Laser Conference	High-order harmonics as a continuously tunable coherent femtosecond x-ray sourc	2002			미국
3rd Asia Pacific Laser Symposium	Generation of high harmonics with low beam divergence and good wavelength tenability	2002			일본

학술회의 명칭	제목	게재연월일	호	발 행 기 관	국 명
CLEO/QELS 2000	Generation of high-order harmonics originated from a single quantum path	2000			미국
CLEO/QELS 2000	Soft X-ray emission from small-sized Ar clusters heated by intense, femtosecond laser pulse	2000			미국
Atoms, molecules and quantum dots in Laser fields	Control of the high-harmonic spectral structure for attosecond pulse generation	2000			이태리
Atoms, molecules and quantum dots in Laser fields	Enhanced spectral resolution of high-order harmonics by the coherent sum of dipole spectra	2000			이태리
XXVI European Conference on Laser Interaction with Matter	Soft X-ray emission from Ar clusters heated by ultrashort laser pulses	2000			체코
7th Int. Conf. on X-ray Laser	Interaction of intense, femtosecond laser pulse with small-sized Ne cluster	2000			프랑스
7th Int. Conf. on X-ray Laser	Investigations on femtosecond-pulse-driven soft X-ray laser	2000			프랑스
Asia Pacific Laser Symposium	Spectroscopic study of Ne clusters irradiated by an intense, femtosecond laser	2000			중국
CLEO/Pacific Rim 2001	Temporal characterization of compressor-controlled chirped pulses from a CPA Ti:sapphire laser	2001			일본
CLEO/Pacific Rim 2001	Time-Frequency Characterization of High-Harmonics Generation by Intense Femtosecond Laser Pulses	2001			일본
Ultrafast Optics 2001	Time-Frequency Analysis of Chirped Femtosecond Pulses Using the Wigner Distribution Function	2001			캐나다

학술회의 명칭	제목	게재연월일	호	발 행 기 관	국 명
Ultrafast Optics 2001	Plasma-Induced Frequency Modulation of High-Order Harmonics	2001			캐니다
Applications of High Field and Short Wavelength Sources IX	Generation of low beam divergence harmonics using a long gas jet	2001			미국
Applications of High Field and Short Wavelength Sources IX	Chirp analysis of high-order harmonics from atoms driven by intense femtosecond laser pulses	2001			미국
3rd Asia Pacific Laser Symposium	Highly Efficient High-order Harmonic Generation at 13 nm with a Long Gas Jet	2002			일본
3rd Asia Pacific Laser Symposium	Generation of high-power sub-10 fs optical pulses at 1 kHz repetition rate	2002			일본
계: 25 건					

3. 연구 성과

(1) 파장가변 결맞는 엑스선을 발생에 대한 물리적 메카니즘 분석
(2) 아토초 펄스를 발생을 구현할 수 있는 기본적인 실험결과를 획득
(3) 파장가변 펨토초 결맞는 X-선 광원개발
(4) 펨토초 테라와트 레이저 개발과 극자외선 분광기술개발
(5) 고출력 펨토초 레이저와 계측 기술의 국산화

4. 기술이전 및 연구결과 활용계획

가. 당해연도 활용계획

창의적 연구과제인 초강력 펨토초레이저 마당내의 원자조작을 통한 결맞는 X-선 광원개발을 통하여 1단계의 소기의 목적을 달성하였다. 2002 년 10월부터 시작되는 2단계 연구에서는 결맞는 엑스선 연구단에서 개발된 결맞는 엑스선 광원을 이용하여 엑스선 간섭계실험, 엑스선 홀로그라피, 엑스선 리소그라피 광학계 계측과 초고속 분광학 등의 폭넓은 응용분야의 실험을 수행할 것이다.

나. 활용방법

고출력 펨토초 레이저 개발 기술과 안정된 운전 능력 확보를 통하여 우수한 특성의 결맞는 엑스선을 안정적으로 생성하게 될 것이다. 초강력 펨토초 레이저 마당내의 원자조작을 통해서 생성된 결맞는 엑스선 광원은 엑스선 광학계를 통하여 여러 응용실험 장치들로 공급됨으로써 적은 유지보수비와 소규묘 시스템으로도 방사선 가속기를 이용하는 여러 연구들이 갖는 한계성을 극복하여 펨토초나 아토초의 극초단 X-선 분광학 분야나 우수한 공간 결맞음성을 갖는 X-선 간섭계에 활용될 것이다.

다. 차년도이후 활용계획

펨토초 레이저 개발기술과 이를 이용한 결맞는 엑스선 발생기술은 결맞는 엑스선 연구단에서 2단계 창의적 연구과제인 "초강력 펨토초 레이저마당 내의 원자조작을 통한 결맞는 X-선 광원개발"에 활용되어서 X-선 간섭 광학과 초고속 X-선 분광학 분야 등의 응용분야의 실험을 수행할 것이다.

5. 기대효과

펨토초 테라와트 레이저 개발과 극자외선 분광기술개발은 펨토초 레이저와 고출력 펨토초 레이저 기술의 국내 보급과 극자외선 분광기 기술의 국내 정착을 가져온다. 펨토초 레이저는 화학·물리 등의 기초과학 연구에서 그 활용도가 급격히 늘고 있으며, 초미세 가공이나 새로운 LASIK용 레이저로서 펨토초 레이저가 이용되기 시작하여 산업적·의료적 응용이 증대되고 있다. 이와 같은 고가의 고급레이저 기술인 펨토초 레이저 기술의 국산화는 국내 레이저 산업의 경쟁력 확보측면에서도 크게 이바지할 것으로 기대된다. 따라서, 이러한 고출력 펨토초 레이저 기술은 물리·화학·생물분야등 기초과학분야 뿐만 아니라 공학·의료·군사 분야에서도 매우 필요한 기술로서 앞으로 활용도가 크게 증가될 것이다.

6. 문제점 및 건의사항(연구성과의 제고를 위한 제도·규정 및 연구관리 등의 개선점을 기재)

해당사항 없음.

[첨부2]

기술 요약서

■ 기술의 명칭

펨토초 테라와트 레이저와 결맞는 X-선 광원개발 기술

■ 기술을 도출한 과제현황

과제관리번호				
과제명	초강력 펨토초 레이저 마당내의 원자조작을 통한 결맞는 X-선 광원개발			
사업명	창의적 연구진흥 사업			
연구기관	한국과학기술원		기관유형	대학
참여기관(기업)	없음			
총연구기간	1999년. 10월. 16일. ~ 2002년. 9월. 30일.			
총연구비	정부(1,530,000,000)천원 민간( )천원 합계(1,530,000,000)천원			
연구책임자	성명	남 창 희	주민번호	
	근무기관 부서	한국과학기술원 물리학과	E-mail	chnam@mail.kaist.ac.kr
	직위/직급	교수	전화번호	(042)868-2574
실무연락책임자	성명	이 동 근	소속/부서	한국과학기술원/물리학과
	직위/직급	연수 연구원	E-mail	donggun@mail.kaist.ac.kr
	전화번호	(042) 869-8422	FAX	(042) 869-2510
	주소	(305 - 701) 대전광역시 유성구 구성동 373-1		

■ 기술의 주요내용

[기술의 개요]

(1) 펨토초 테라와트 레이저 기술
(2) 극자외선 분광기술
(3) 파장가변 펨토초 결맞는 X-선 광원기술

<기술적 특징>

(1) 펨토초의 짧은 펄스폭과 우수한 결맞음성을 가진 X-선 광원
(2) 고가의 고급레이저 기술인 고출력 펨토초 레이저 기술의 국산화
(3) 극자외선 분광기 기술의 국내 정착

[용도 · 이용분야]

(1) 결맞는 엑스선광원은 초고속 X-선 분광학, 비선형 X-선 광학등에 활용
(2) 펨토초 레이저는 화학 · 물리 등의 기초과학 연구에 이용
(3) 초미세 가공이나 새로운 LASIK용 레이저로서 펨토초 레이저의 활용

■ 기술의 분류

[기술코드] 8 2 9 (3 Digit) (KISTEP 홈페이지 기술요약서용 기술분류표 참조)

[기술분야] (1개만 선택(∨로 표시)하여 주십시오)

□ 정보산업	□ 기계설비	□ 소재	□ 정밀화학 · 공정	□ 생명과학
□ 원자력	□ 자원	□ 에너지	□ 항공 · 우주	□ 해양
□ 교통	□ 보건 · 의료	□ 환경	∨ 기초 · 원천	□ 기타

[기술의 활용유형] (1개만 선택(∨로 표시)하여 주십시오)

∨ 신제품개발 □ 신공정개발 □ 기존제품개선 □ 기존공정개선
□ 기 타 ( )

[기술의 용도] (복수 선택(∨로 표시)가능합니다)

□ 기계설비	∨ 부품소자	□ 원료재료	□ 소프트웨어
□ 가공처리기술	□ 자동화기술	□ 불량률 감소 등 현장애로기술	

□ 제품설계기술 □ 공정설계기술 □ 기 타 ( )

■ 산업재산권 보유현황(기술과 관련한)

권리유형	명 칭	국가명	출원단계	일자	등록번호
특허	토로이드거울이 부착된 평면결상형 극자외선 분광기의 정렬장치	한국	특허 등록됨	1999. 3. 25	0204113

* '권리유형'란에는 특허, 실용신안, 의장, 컴퓨터프로그램, 노하우 등을 선택하여 기재
* '출원단계'란에는 출원, 공개, 등록 등을 선택하여 기재

■ 기술이전 조건

해당사항 없음.

■ 기술의 개발단계 및 수준

[기술의 완성도] (1개만 선택(∨로 표시)하여 주십시오)

∨	① **기초, 탐색연구단계** : 특정용도를 위해 필요한 신 지식을 얻거나 기술적 가능성을 탐색하는 단계
	② **응용연구단계** : 기술적 가능성의 실증, 잠재적 실용화 가능성의 입증 등 실험실적 확인 단계
	③ **개발연구단계** : Prototype의 제작, Pilot Plant Test 등을 행하는 단계
	④ **기업화 준비단계** : 기업화에 필요한 양산화 기술 및 주변 기술까지도 확보하는 단계
	⑤ **상품화 완료단계**

[기술의 수명주기] (1개만 선택(∨로 표시)하여 주십시오)

	① **기술개념 정립기** : 기술의 잠재적 가능성만 있는 단계
∨	② **기술실험기** : 기술개발에 성공했으나 아직 실용성, 경제성 등이 확실치 않은 단계
	③ **기술적용 시작기**: 최초의 기술개발국에서만 활용되고 있는 단계
	④ **기술적용 성장기**: 기술개발국 및 일부 선진국에서 활용되고 있는단계
	⑤ **기술적용 성숙기**: 선진국사이에서 활발한 기술이전이 일어나며, 기술의 표준화가 되어가는 단계
	⑥ **기술적용 쇠퇴기**: 선진국에서 개도국으로 기술이전이 활발하게 일어나고, 선진국에서는 기술의 가치가 저하되나, 개도국에서는 아직 시장의 가치가 높은 기술

[기술발전 과정상의 기술수준] (1개만 선택(∨로 표시)하여 주십시오)

	① **외국기술의 모방단계** : 이미 외국에서 개발된 기술의 복제, reverse Eng.
	② **외국기술의 소화·흡수단계** : 국내시장구조나 특성에 적합하게 적응시킴
	③ **외국기술의 개선·개량단계** : 성능이나 기능을 개선시킴
∨	④ **신기술의 혁신·발명단계** : 국내 최초로 개발

■ 본 기술과 관련하여 추가로 확보되었거나 개발중인 기술

[기술개요]

기술명	
개발단계	□ **연구개발 계획** □ **연구개발 중** □ **연구개발 완료**
기술개요	

[기술을 도출한 과제현황]

과제관리번호				
과제명	초강력 펨토초 레이저마당 내의 원자조작을 통한 결맞는 X-선 광원 개발			
사업명	창의적 연구 진흥사업			
연구기관	한국과학기술원		기관유형	학술연구
참여기관(기업)	없음			
총연구기간	1999.10.16 ~ 2002.9.30			
총연구비	합계 : (1,530)백만원 - 정부 : (1,530)백만원 민간 : ( )백만원			
연구책임자	소속	한국과학기술원 물리학과	성명	남 창 희
	전화번호	(042)869-8423	E-mail	chnam@mail.kaist.ac.kr

연구개발 주요내용

1) 고출력 펨토초 레이저 기술 개발
- 강력한 레이저와 원자와의 상호작용을 연구하기 위해 1kHz의 반복율을 갖는 20펨토초 0.1테라와트의 고출력 고반복 펨토초 티타늄 사파이어 레이저를 개발함. 그리고 개발된 고출력 펨토초 레이저의 시공간적 특성을 조사함.

2) 원자와 초강력 레이저장과의 상호작용을 규명
- 강력한 레이저장과 원자와의 상호작용에 의한 고차조화파 발생의 실험적 측정 및 분석과 전산시늉을 포함한 이론적 분석을 통하여 그 발생 메카니즘을 구체적으로 규명함.

3) 파장가변 결맞는 엑스선 광원 개발
- 고차조화파의 결맞는 조절을 통하여 조화파의 선폭과 세기에 대한 최적화를 수행함. 조화파의 청색변이를 이용하여 연속적으로 파장가변이 가능한 펨토초 고차조화파 엑스선 발생 (소형화된 싱크로트론)을 입증함.